

ECIO 2014

European Conference on Integrated Optics

Nice, France

Collected Manuscripts

(c) Copyright 2014 The ECIO Board. All rights reserved.

Contents

ID	Author	Title
Tu1abPL1	G. Roelkens	Photonic integration: beyond telecom and datacom
Tu2aI1	J. Čtyroký	Computational Analysis of Subwavelength Grating
Tu2aR1	Emil Kleijn, Meint K. Smit and X	Amplitude and phase error correction in 3×3 MMIs
Tu2bI1	Meint K. Smit	Foundry based approach for InP based PIC development
Tu2bR1	R. Guzman, A. Jimenez, G. Carpin	Dual-Wavelength AWG based Lasers for Narrow Linewidth Heterodyne Beat-Note Generation
Tu2bR2	D. D'Agostino, R. Broeke, M. Boe	AWG based wavelength-meter with pm resolution
Tu3aI1	Shinji Matsuo	Photonic crystal lasers for computercom networks
Tu3aR1	Koop van Dalfsen, Shanmugam Arav	1.6-W, Highly Efficient Laser at 2 μm in a Potassium Double Tungstate Channel Waveguide
Tu3aR2	Sergio A. Vázquez-Córdova, Edwar	High-gain spiral amplifiers in a-Al2O3:Er3+ on a silicon chip
Tu3aR3	D. D'Agostino, D. Lenstra, H.P.M	A Coupled Cavity Laser based on a Multimode Interference Reflector
Tu3aR4	A. Aghajani , G.S. Murugan, N.P.	Ytterbium-Doped Tantalum Pentoxide Waveguide Lasers
Tu3aR5	A. Choudhary, S. Dhingra, B. D'U	PLD-grown Yb:Y2O3 waveguide laser Q-switched by a graphene saturable absorber
Tu3aR6	A. Corradi, G. Carpintero, E. Sm	Characterization of an AWG-based dual-wavelength ring laser
Tu3bI1	T. Suhara, M. Uemukai	Grating Coupler Integrated Semiconductor Laser Diodes
Tu3bI2	T. Watanabe and Y. Kokubun	Fan-in/Fan-out Three-dimensional Polymer Waveguide for Uncoupled Multi-core Fibers
Tu3bR1	Y. Kobayashi, K. Warabi, R. Kou,	Selectively formed spot-size converters for efficient coupling in graphene-integrated silicon photonics
Tu3bR2	D. Melati, F. Morichetti, G. G.	Scattering-related crosstalk in photonic waveguides
Tu3bR3	B. Gargallo and P. Muñoz	Interleave-chirp arrayed waveguide grating on InP generic technology
We2abPL2	Kenichi Iga	VCSEL -Its History and Prospects for Green Microoptics
We2aTU1	A. Ortega-Moñux, D. Pérez-Galach	Design of integrated photonic devices for high-speed high coherent receivers
We2bTU2	Hirochika Nakajima	40 years anniversary of Ti:LiNbO3 and beyond
We3aI2	T. Tanemura, M. Zaitsu, and Y. N	Self-aligned InP polarization converters for monolithic polarization-multiplexed PICs
We3aI3	K.A. Williams and R. Stabile	Integrated Optical Switch Matrices
We3aR3	E. Bitincka, R. G. Broeke and M.	Electrical Method for On-Wafer Modal Gain Characterization of Semiconductor Optical Amplifiers
We3aR4	C. D. Gordon, R. Guzman, A. Jime	Colliding Pulse Mode-Locked Laser Diode using Multimode Interference Reflectors
We3bI1	S. Höfling , J. Beetz, M. Lermer	Integrated Single Photon Circuits
We3bI2	Raffaele Santagati, Joshua W. Si	A silicon quantum photonics chip for generation and analysis of entanglement
We3bR1	T. Meany, L. A. Ngah, M. J. Coll	Hybrid Integration for Single Photon Generation
We3bR2	L.A. Ngah, V. D'Auria, L. Labont	Ultra-fast Photon Pair Sources for Quantum Networking
We4aI1	N. Courjal, M.P. Bernal, C. Guyo	Low-loss LiNbO3 integrated photonic crystals
We4aR1	Javier Martínez, Airán Ródenas,	3D Direct-Laser-Written Mid-Infrared Waveguide Circuits in Fused Silica and Crystalline Quartz
We4aR2	Chun-Hao. Yang, Kai.-Hsun. Chang	Mobility-controlled Method to Construct QPM Devices

We4aR3	Heinrich Sieber, Uwe Hollenbach,	Optical Waveguides Processed by Internal Diffusion in Photosensitive Doped Host/Guest Polymer
We4aR4	J. Martínez de Mendíbil, G. Lifa	Ridge waveguide structures in KYW crystals produced by beam-multiplexed fs-laser writing
We4aR5	V. Prajzler, P. Nekvindová, M. V	Nanocrystalline Diamond Optical Planar Waveguides
We4aR6	S.M. Kostritskii, Yu.N. Korkishk	Subsurface Disorder and Electro-Optical Properties of Proton-Exchanged LiNbO3 Waveguides Produced by Different Techniques
We4bI1	N. Hanzawa, K. Saitoh, T. Sakamo	PLC-based three-mode multi/demultiplexer for mode division multiplexing transmission
We4bR1	A. Creux, A. Warzecha, A. Morand	A fully static OCT sensor using glass integrated optics system based on the LLIFTS technology
We4bR2	Markus Pollnau, Manfred Hammer,	Sub-base-pair Resolution During DNA Separation in an Optofluidic Chip
We4bR3	David J. Rowe, Nicholas D. Evans	Ta2O5 Waveguides for Mid-infrared Evanescent Sensing of Stem Cell Differentiation
We4bR4	Edward H. Bernhardi, Kees O. van	Intra-laser-cavity Sensing with a Dual-wavelength Distributed-feedback Laser
We4bR5	M. Bunsen, T. Hisaoka, T. Sato,	Demodulation of Holographically Reconstructed 2-D Signals with Spatial Quadrature Amplitude Modulation
We4bR6	Dzmitry Pustakhod, Emil Kleijn,	AWG-based integrated fiber-Bragg-grating interrogator with improved sensitivity
Th1PL4	L. Vivien, D. Marris-Morini, L.	High speed germanium and silicon optoelectronic devices
Th2aI1	F. Laurell, S. Müller, T. Calman	A fs-laser written waveguide in periodically poled Rb:KTiOPO4 for efficient second harmonic generation
Th2aI2	C. Ozanam, L. Lanco, X. Lafosse,	Guided-wave AlGaAs optical parametric oscillator
Th2aR1	O. Stepanenko1, I. Krasnokutska1	Highly confining nonlinear proton exchanged embedded waveguides on z-cut lithium niobate.
Th2aR2	I. Krasnokutska, O. Stepanenko,	Second-Order Nonlinear Characterizations of NonHomogeneous Quasi-Phase-Matched Waveguides
Th2bI1	Stefania Malaguti, Gaetano Bella	Ultracompact photonic crystal integrated circuits: connecting tiny devices to achieve high-performances
Th2bI2	Rajeev J. Ram	CMOS Photonic Integrated Circuits and Systems
Th2bR1	K. Thyagarajan, Surajit Paul	An enhanced wavelength tolerant design for the Generation of N-partite single photon W-states
Th2bR2	R. Baños, A.L. Giesecke, J. Bolt	Reflective Arrayed Waveguide Grating with Sagnac Loop Reflectors in Silicon-on-Insulator with Gaussian Pass-band
Th4aI2	I. Favero, C. Baker, D. Parrain,	On chip gallium arsenide optomechanical systems
Th4aR07	Mohammad N. Uddin, H. Bingzhou,	First Observation of Photon-Photon Resonance in Active Multimode Interferometer Laser Diode
Th4aR08	Asako Kikuchi, Tomoyuki Miyamoto	Study on Optical Confinement of Small Size VCSEL Using Index Change of QWI
Th4aR10	M. Marconi, J. Javaloyes, S. Bal	Passive Mode-Locking and Tilted Waves in Broad-Area Vertical Cavity Surface-Emitting Lasers
Th4aR11	S. Takeuchi, K. Kato, S. Hisatak	Sub-THz Carrier Frequency Generation Stabilized by Mach-Zehnder Interferometric Phase Detection Scheme
Th4aR12	L. Shen, S.P. Bhat, Y. Jiao, J.J	Towards a high bandwidth waveguide photodetector in an InP membrane on Silicon

Th4bI1	Kiichi Hamamoto	Optical Mode Switch for Future Optical Router
Th4bR1	T. Inoue, T. Suhara	High Performance Electro-Optic Polarization Conversion Type Modulator for Short-Wavelength Light Using Periodically Poled MgO:LiNbO3
Th4bR2	Q. Cheng, A. Wonfor, J. L. Wei,	Dilated 2×2 Hybrid MZI-SOA Switch Circuit Routing 100Gb/s DWDM Data
Th4bR3	S. Inoue1, F. Koyama1	High-Contrast Grating Spatial Mode Filter for Widely Tunable Vertical Surface Emitting Laser
Fr2aI4	Fabio Sciarrino	Quantum simulation with integrated photonics
Fr2aR3	P. L. Mennea, J. B. Spring, J. C	Engineering waveguide arrays for high-purity matched four-wave mixing photon sources
Fr3aI3	Keijiro Suzuki, Ken Tanizawa, Ta	Si-Wire based 8 × 8 strictly-Non-Blocking PILOSS Switch
Fr3aI4	R. Kou, S. Tanabe, T. Tsuchizawa	Graphene Integrated Silicon Photonics
Fr3aR3	S. Grillanda, F. Morichetti, M.	Transparent Monitoring of Light in Integrated Optics
P001	Christoph Vannahme, Cameron L. C	Optimized Distributed Feedback Dye Laser Sensor for Real-Time Monitoring of Small Molecule Diffusion
P002	L. Bastard, H. Ouslimani, G. Gro	Stabilization of Q-switched operation in glass waveguide lasers
P003	S.-C. Huang, Y.-Y. Lai, T.-L. Ho	Study on Confinement Scheme of GaN-based VerticalCavity Surface-Emitting Lasers
P004	R. Baños, P. Muñoz, J.D. Doménec	Opto-electronic wavelength tracker in Silicon-on-Insulator
P005	Jen-Fa Huang, Hsu-Chih Cheng, Ch	Optical samples measurement based on orthogonally polarized light over phase-shifting FD-OCT
P006	A. Crespo-Poveda, K. Biermann, A	Integrated Photonic Devices Driven by Surface Acoustic Waves
P007	E. Delcourt, L. Bodiou, J. Charr	Integrated polymer waveguides incorporating nonlinear chromophores for all-optical signal processing
P008	M.A. Butt, R. Solé, M.C. Pujol,	Fabrication of Y-Splitters and Mach-Zehnder interferometers on (Yb, Nb):RbTiOPO4/ RbTiOPO4 epitaxial layers by Reactive Ion Etching and on RbTiOPO4 by Cs+ diffusion
P009	L.Bodiou, J. Charrier, J. Lemait	Carbon nanotubes incorporated-hybrid waveguides for photonics applications
P010	Fabrice Thomas, Mikhael de Mengi	Near and Mid Infrared Lithium Niobate based Integrated Optics Interferometer based on SWIFTS-Lippmann
P011	G. Lafleur, A. Larrue, G. Almune	Vertically-coupled AlGaAs microdisks using selective lateral oxidation
P012	J. Martínez de Mendíbil, A. Bena	Step-index Nd:YAG ceramic buried channel waveguides fabricated by direct laser writing
P013	R. Braive, V. Tsvirkun, A. Chowd	Optomechanics with 2D photonic crystals membrane
P014	T. Hansson, S. Wabnitz	Dual Pump Microresonator Frequency Comb Generation and Optical Buffer Memories
P015	A.J. Millán-Mejía , J.J.G.M. van	Design of a phase shifter in InP Membranes On Silicon based on a slot-waveguide with liquid-crystal
P016	V. Doya, F. Gustave, C. Michel,	Phase-space control of unconventional modes for SDM
P017	W. Yao, G. Gilardi, M. K. Smit,	Electrical Crosstalk Simulation of InP-based PhaseShifters from a Generic Photonic Integration Platform
P018	Girish Semwal and Vipul Rastogi	Design of Long Period Waveguide Gratings for Broad Band Polarization Filters
P019	A. Tsarev, E. Kolosovsky	Optimization of silicon wire waveguide crossing by means of vertical coupling with a polymer waveguide
P020	A. Tsarev, A. Shklyaev,	Radiation of photonic crystals with multiple cavities

P021	M. Jubera, A. García-Cabañes, J.	Particle Patterning on Lithium Niobate waveguides via photovoltaic tweezers
P022	Y. Shoji, T. Nemoto, T. Mizumoto	Analysis of Temperature Dependence of Ce:YIG for Athermal Waveguide Optical Isolator
P023	J.P. Garayt, E. Jordan, F. Parsy	Study of the magneto-optical interaction in a hybrid nonreciprocal mode converter
P024	Chyong-Hua Chen	Cross-Connected Notch Filter with a Flat Stopband and Double Free-Spectral-Range
P025	H. Asakura1 and H. Tsuda1	Loss Uniformity Improvement of Arrayed-waveguide Grating Router using Interleaved Chirped Array
P026	Hideki Yokoi, Daisuke Tamura, Yu	TE-TM Mode Conversion Optical Isolator Employing Halfwave Plate Integrated with Spot-Size Converters
P027	Jian Chen, Nikos Bamiedakis, Ric	Bandwidth and Offset Launch Investigations on a 1.4 m Multimode Polymer Spiral Waveguide
P028	Aiko Takahashi, Kensuke Inoshita	Bit-Error-Rate Performance in Optical 16QAM Recognition with Integrated-Optic Circuit
P029	P. Aschieri, V. Doya D. Makarov	Two beam multiplexing in a multimode periodic segmented waveguide
P030	Y. Jiao, D. Heiss, L. Shen, S.P.	Design and Fabrication Technology for a Twin-Guide SOA Concept on InP membranes
P031	S. Stopinski, M. Malinowski, R.	Photonic integrated transceivers for data read-out systems
P032	X.Pommarede, A.Talneau, A.Lupu a	Wavelength-Selective Nanopatterned III-V on Si Hybrid Photonic Waveguide
P033	H. Rabbani Haghighi, P.J. van Ve	Generic InP-based Photonic Integration Technology Platform for Long Wavelength Applications
P034	A. Motogaito, Y. Morishita, H. M	Polarization Property of a Double-layer Wire Grid Polarizer and the Mechanism of Transmission
P035	A. Motogaito, S. Nakamura, J. Mi	Excitation of Surface Plasmon Polariton at the GaP–Au Interface in a High-Refractive-Index Medium
P036	I. Suárez, E. P. Fitrakis, R. Ab	QD-PMMA nanocomposite plasmonic waveguides
P037	Yuhsin Chang, Chyong-Hua Chen	1×3 plasmonic power splitter for various splitting ratio
P038	B. Gargallo, P. Muñoz, J.D. Domé	Arbitrary coupling ratio multimode interference couplers in Silicon-on-Insulator
P039	A. Tsarev	The fundamentals of multi-splitting filtering technology
P040	K. Thyagarajan, Ruchi Gupta	Coherent Tunnelling Adiabatic Passage in Fiber Geometry

Photonic integration: beyond telecom and datacom

G. Roelkens[1,2]

[1] *Photonics Research Group, Ghent University/imec, Belgium*
gunther.roelkens@intec.ugent.be
[2] *Center for Nano- and Biophotonics (NB-Photonics),Ghent, Belgium*

Abstract: In this paper we elaborate on the use of silicon photonic integrated circuits for sensing applications. We will discuss disposable bio-sensing chips, chips for biomedical applications such as optical coherence tomography and laser doppler vibrometry as well as integrated spectroscopic sensors based on Raman spectroscopy and vibrational spectroscopy.

Silicon photonics has emerged as a prominent platform for the realization of high data-rate transceivers for use in optical interconnect and telecommunication applications. Silicon photonics leverages the existing technologies in advanced CMOS fabs, which has resulted in a very fast progress in this field as well as the development of an industrial supply chain. The available high refractive index contrast also allows for unprecedented miniaturization. The market potential for silicon photonics is however much broader than datacom and telecom, and there are especially opportunities in the area of lab-on-a-chip. In this paper we will elaborate on the development of a disposable biosensor platform for the detection of biomolecules, a technology that starts to become commercially available. Current research efforts focus on the realization of spectroscopic sensor systems, both in the near-infrared (Raman spectroscopy using SiN waveguide technology) and the mid-infrared (vibrational spectroscopy using Si/Ge technology), in order to enhance the selectivity of currently available sensors. Also in the biomedical field silicon photonic integrated circuits for e.g. optical coherence tomography and laser doppler vibrometry are of interest.

Computational Analysis of Subwavelength Grating Waveguide Structures

J. Čtyroký

Institute of Photonics and Electronics,
Academy of Sciences of the Czech Republic, Prague, Czech Republic
ctyroky@ufe.cz

Abstract: After brief introduction into the theory of electromagnetic Bloch modes in 1-D periodic structures, specific features of our in-house 3-D Fourier Modal Method used for numerical modelling of waveguide structures will be briefly presented. Then, dispersion properties of longitudinally uniform subwavelength grating waveguides (SWG) will be discussed. Finally, results of modelling of more complex SWG waveguide structures, especially tapers and mode transformers, will be shown. Influence of random positional errors of SWG elements on the spectral characteristics of these devices will be mentioned, too.

Introduction Very high-contrast waveguide components, especially those based on silicon-on insulator (SOI) platform, are very perspective due to their small dimensions and strongly reduced bending loss, which allows for larger scale photonic integration. However, for some applications, the refractive contrast of SOI devices is too high. A very elegant way to overcome this problem consists in segmenting the silicon waveguide into sections of a subwavelength size that are embedded into a low-index environment such as SiO_2[1,2]. In accordance with the effective medium theory, by changing the "Si filling fraction" of such a subwavelength grating (SWG) waveguide, its "average refractive index" can be tuned essentially to any value between that of SiO_2 and Si. However, for technological reasons, the size of the smallest features should not decrease below about 50–100 nm, being thus only about an order of magnitude smaller than the operation wavelength. The assumptions of the effective medium theory are thus violated. As a result, rigorous bi-directional 3-D full-vector electromagnetic modelling is required for proper analysis and design of SWG waveguide structures.

Modelling method Full-vector bidirectional methods are required for rigorous modelling of SWG waveguides. One of them, the in-house 3-D full-vector Fourier modal method (FMM) BEX3 has been recently developed in our laboratory[3]. It is based on 2-D sine and cosine Fourier series expansions within the computational window bordered with perfectly conducting electric or magnetic walls. Perfectly matched layers are implemented in the form of the complex coordinate transformation[4]. Electromagnetic eigenvalue problem is formulated in terms of transversal magnetic field components that are continuous in the (nonmagnetic) waveguide structure. For wave propagation along the structure, numerically stable scattering matrix formalism is used. Since most of the computational tasks consist of problems of linear algebra, Matlab programming environment is used to advantage.

Bloch modes The subwavelength grating waveguide (Fig. 1) is longitudinally periodic, its eigenmodes are thus *Bloch modes*. The corresponding eigenvalue problem can be formulated with the help of the scattering matrix of a single period **S** as

$$\begin{pmatrix} \mathbf{0} & \mathbf{S}_{12} \\ \mathbf{I} & -\mathbf{S}_{22} \end{pmatrix} \cdot \mathbf{B} = \begin{pmatrix} -\mathbf{S}_{11} & \mathbf{I}+\mathbf{S}_{12} \\ \mathbf{I}+\mathbf{S}_{21} & -\mathbf{S}_{22} \end{pmatrix} \cdot \mathbf{B} \cdot (\mathbf{I}+\boldsymbol{\Gamma})^{-1},$$

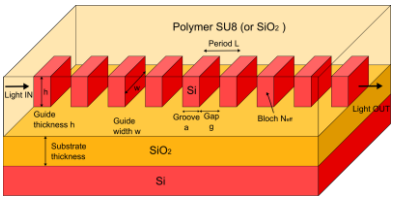
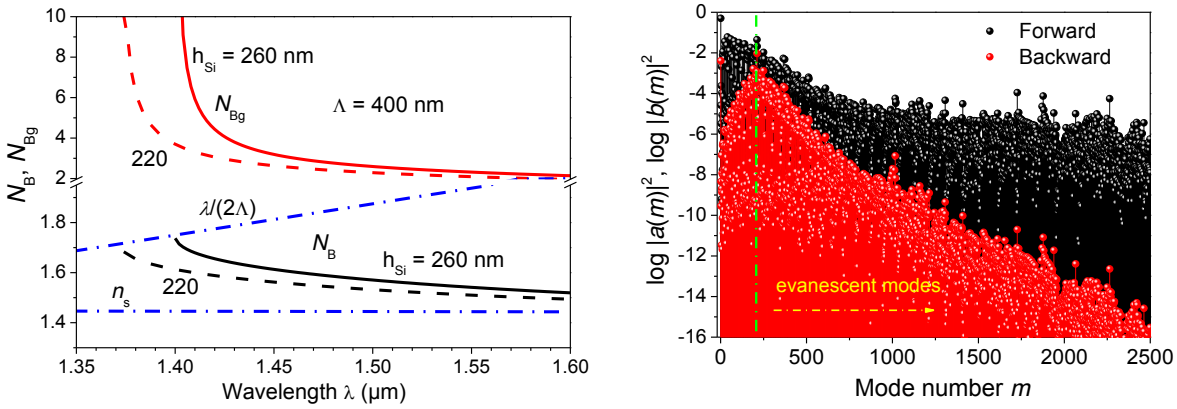


Fig. 1. SWG waveguide

where $\mathbf{S}_{11}$, $\mathbf{S}_{12}$, $\mathbf{S}_{21}$, $\mathbf{S}_{22}$ are submatrices of the scattering matrix **S,** $\boldsymbol{\Gamma}$ is a diagonal matrix with elements $\Gamma_{mn} = \delta_{mn} \exp(i\beta_{B,m}\Lambda)$, Λ is the period length, $\beta_{B,m}$ is the propagation constant of the *m*-th Bloch mode, and **B** is the transformation matrix from the linear space of complex amplitudes of *local normal modes* at the particular waveguide cross-section into the space of Bloch modes. For lossless propagation, the effective refractive index of the Bloch mode must lie above that of the substrate but below the Brillouin zone edge, $n_s < N_B < \lambda/(2\Lambda)$. For N_B approaching the Brillouin zone edge $\lambda/(2\Lambda)$, the group velocity of the mode decreases and enters the *slow-light regime*.



a) *b)*

Fig. 2. a) Dispersion characteristics of Bloch modes of SWG waveguides, b) An example of the content of complex amplitudes of local modes within the Bloch mode of a SWG waveguide.

Phase and group effective refractive indices N_m and $N_{B,g}$ of the Bloch mode of the SOI SWG waveguide 350 nm wide with the Si thickness of 220 and 260 nm are shown in Fig. 2a). In Fig. 2b), the content of forward and backward propagating local modes within the Bloch mode .is depicted.

Photonic wire to SWG waveguide coupler An efficient coupler from a normal mode of a photonic wire into the Bloch mode of a SWG waveguide has been recently described in[1]. The length of the device is about 50 μm long, it consists of more than 300 longitudinally uniform segments, from which over 200 are of different dimensions, and its reliable full-vector modelling is thus rather challenging. However, just this kind of structures can be numerically analyzed using FMM without excessive hardware requirements thanks to the fact that the eigenmode problems in individual longitudinally uniform segments are mutually independent.

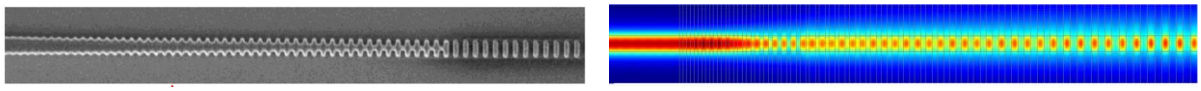


Fig. 3. a) Microphotograph of a part of the photonic wire to SWG waveguide coupler[1]. b) Calculated optical field distribution in the part of the coupler.

The microphotograph of a part of the coupler[1] is shown in Fig. 3a), the calculated optical field distribution is presented in Fig. 3b). The graph of the modal spectral transmittance of the coupler in Fig. 4 documents very high coupling efficiency within the bandwidth of more than 100 nm. Its abrupt decrease for short wavelengths is due to close proximity of the Brillouin zone edge.

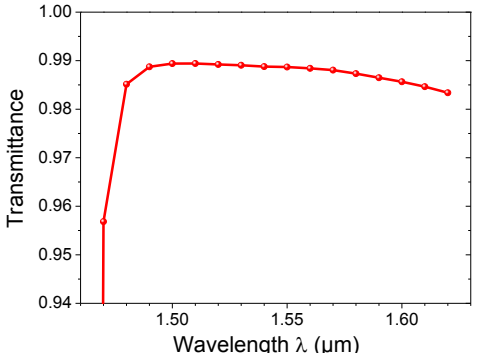


Fig. 4. Spectral dependence of the coupling efficiency of the SWGW coupler

Conclusions It has been demonstrated that SWG waveguide structures can be efficiently numerically analyzed using the Fourier modal method.

References

1. P. J. Bock, P. Cheben, J. H. Schmid, J. Lapointe, A. Delage, S. Janz, G. C. Aers, D. X. Xu, A. Densmore, and T. J. Hall, *Optics Express* **18**, 20251-20262 (2010).
2. P. J. Bock, P. Cheben, J. H. Schmid, J. Lapointe, A. Delage, D. X. Xu, S. Janz, A. Densmore, and T. J. Hall, *Optics Express* **18**, 16146-16155 (2010).
3. J. Čtyroký, *J. Lightwave Technol.* **30**, 3699-3708 (2012).
4. J. P. Hugonin, and P. Lalanne, *J. Opt. Soc. Am. A* **22**, 1844-1849 (2005).

Amplitude and phase error correction in 3×3 MMIs

Emil Kleijn, Meint K. Smit and Xaveer J. M. Leijtens
COBRA Research Institute, Eindhoven University of Technology, 5600 MB Eindhoven, The Netherlands. e.kleijn@tue.nl

Abstract: We present a correction algorithm that is able to reduce the influence of amplitude and phase errors in a 3×3 MMI. When used in a phase estimator, our method reduces the maximum estimation error from 8° to 0.3°.

1 Introduction

A wavelength meter can be used for various applications ranging from monitoring laser diodes to Fiber Bragg Grating read-out systems [1]. On-chip wavelength estimation can be realized by using an imbalanced Mach-Zehnder Interferometer combined with an optical hybrid [2]. In such a system, the MZI is used to map a shift in wavelength to a phase difference between the arms. The phase difference between arms is then estimated by the optical hybrid. A 3×3 Multimode Interference coupler (MMI) can be used as a 120° optical hybrid [3]. By using the outer two inputs of the MMI, a high level of symmetry is obtained, resulting in optimum balance. Figure 1 shows a schematic of the readout system. Ideally, the outputs of the MMI are perfectly balanced and spaced by 120 degrees in the phase domain. In practice, there will be imbalances of a few tenths of a dB and a phase error of a few degrees. This results in a wrong estimation of the phase difference between the MZI arms. To improve the accuracy of the phase estimation, a correction algorithm can be applied. Reyes et al. proposed a linear correction scheme [4], but the system is also subject to non-linear distortion. In this paper we describe a calibration method that also corrects for non-linear distortion, thereby reducing the estimation error caused by imperfections in the MMI.

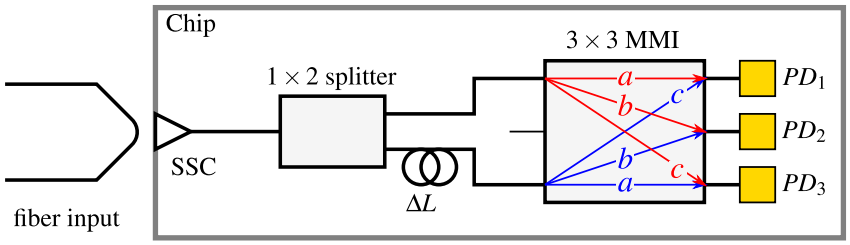


Fig. 1: Schematic of a wavelength meter system. SSC: spot size converter, PD: photo-diode.

2 System

In the system shown in figure 1, there are three photo-diodes connected to each of the MMI outputs. The purpose of this system is to determine the phase difference $\Delta\phi$ between the two MZI arms from the measured photo-currents. The current I_i that can be measured at detector PD_i is described by the following set of equations.

$$\begin{aligned} I_1 &= 0.5 \cdot R\eta P_{\text{in}} \left(|a|^2 + |\alpha c|^2 + 2|ac\alpha| \cos(\Delta\phi - \phi_{\text{MMI}}) \right) \\ I_2 &= 0.5 \cdot R\eta P_{\text{in}} \left(|b|^2 + |\alpha b|^2 + 2|bb\alpha| \cos(\Delta\phi) \right) \\ I_3 &= 0.5 \cdot R\eta P_{\text{in}} \left(|c|^2 + |\alpha a|^2 + 2|ca\alpha| \cos(\Delta\phi + \phi_{\text{MMI}}) \right) \end{aligned} \tag{1}$$

with $\Delta\phi = 2\pi N_{\text{eff}}(\lambda)\Delta L\lambda^{-1}$, $\phi_{\text{MMI}} = \arg\{c\} - \arg\{a\} = 120^\circ + \varepsilon_\phi$, and with R the detector responsitivity, η the input coupling efficiency comprised of SSC loss and 1×2 splitter loss, P_{in} the applied input power, α the MZI balance, ε_ϕ the phase deviation from 120°.

3 Calibration method

Our calibration method consists out of three steps. First, the device has to be characterized by performing a wavelength sweep over a single free spectral range of the MZI, while recording the photo-currents of the detectors. These measurements are subject to noise, among which the dark-current. In the absence of any input light, the mean of the dark-current of every detector can be measured, and then subtracted from the photo-current before further calculations. The second step is to fit the measured results to the equations of (1). Using a non-linear least squares fit method, the coefficients a, b, c, α, ϕ_{MMI} and of the combined term $0.5 \cdot R\eta P_{\text{in}}$ can be estimated. Additionally, the phase difference $\Delta\phi$ needs to be expressed in terms of λ. This results in three more fitting parameters: C_1, C_2, C_3.

$$\Delta\phi = 2\pi\lambda^{-1}C_1 + (\lambda - \lambda_0)C_2 + (\lambda - \lambda_0)^2 C_3 \tag{2}$$

Finally, the third step is using the obtained parameters to correct for a non-ideal MMI response. In order for the correction scheme to work, the applied input power needs to be known. An estimate of this value can be obtained by summing the three photo-currents.

$$I_1 + I_2 + I_3 = 0.5 \cdot R\eta P_{\text{in}} \left[(1 + |\alpha|^2)(|a|^2 + |b|^2 + |c|^2) + 2|\alpha|(2|ac| \cos(\phi_{\text{MMI}}) + |b|^2) \cos(\Delta\phi) \right] \tag{3}$$

Using $\cos(\phi_{\mathrm{MMI}}) = \cos(120^\circ + \varepsilon_\phi) \approx -\frac{1}{2} - \frac{\sqrt{3}}{2}\varepsilon_\phi$, results in

$$I_1 + I_2 + I_3 \approx 0.5 \cdot R\eta P_{\mathrm{in}} \left[(1+|\alpha|^2)(|a|^2+|b|^2+|c|^2) + 2|\alpha|(|b|^2 - |ac| - \sqrt{3}|ac|\varepsilon_\phi)\cos(\Delta\phi) \right]$$

When phase and amplitude errors are small, the term $(|b|^2 - |ac| - \sqrt{3}|ac|\varepsilon_\phi)$ can be neglected.

$$I_1 + I_2 + I_3 \approx 0.5 \cdot R\eta P_{\mathrm{in}} (1+|\alpha|^2)(|a|^2+|b|^2+|c|^2) \tag{4}$$

This means all measurements can be normalized by dividing the photo-currents by the sum of the photo-currents and then multiplying by $(1+|\alpha|^2)(|a|^2+|b|^2+|c|^2)$. It can now be shown that the following relations hold:

$$\cos(\Delta\phi) \approx \frac{X(1+|\alpha|^2)(|a|^2+|b|^2+|c|^2) + (1+|\alpha|^2)(|a|^2-2|b|^2+|c|^2)}{4|\alpha||b|^2 - 4|\alpha ac|\cos(\phi_{\mathrm{MMI}})} \tag{5}$$

$$\sin(\Delta\phi) \approx \frac{Y(1+|\alpha|^2)(|a|^2+|b|^2+|c|^2) - \sqrt{3}(|\alpha|^2-1)^2(|c|^2-|a|^2)}{4\sqrt{3}|\alpha ac|\sin(\phi_{\mathrm{MMI}})} \tag{6}$$

$$X = (2I_2 - I_1 - I_3)(I_1 + I_2 + I_3)^{-1}$$

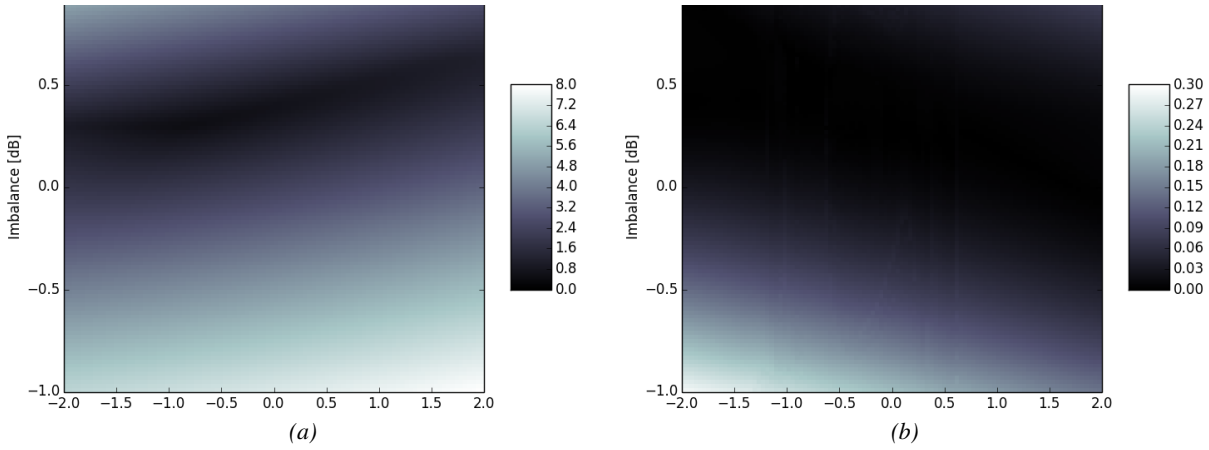
$$Y = \sqrt{3}(I_1 - I_3)(I_1 + I_2 + I_3)^{-1}$$

The phase difference $\Delta\phi$ can now be easily obtained by calculating the arctangent of the sine and cosine terms in (5) and (6).

$$\Delta\phi = \arctan\left(\frac{\sin(\Delta\phi)}{\cos(\Delta\phi)}\right) \tag{7}$$

4 Performance and conclusion

To test the performance of the proposed calibration method, we simulated the estimation error as a function of the MMI phase error and the imbalance. The value for α was kept constant at 0.8, while the values for a and b were kept constant at $\sqrt{0.3}$ and $\sqrt{0.314}$ respectively. The value of c changed with the imbalance of the MMI. The resulting estimation errors without correction and with correction are shown below. Due to the fixed imbalance between a and b, the minimum estimation error does not occur at $(0,0)$. The simulation range corresponds to a typical width error of ± 200 nm in a 12 µm wide indium phosphide based MMI. Our method is able to reduce the estimation error from 8° to less than 0.3° for a wide range of MMI errors. This allows for a more accurate measurement of the wavelength of incoming light.



(a) *(b)*

Fig. 2: Estimation error without (a) and with (b) correction algorithm. Please note the difference in scale.

Acknowledgements

The research leading to these results has received funding from the European Community's Seventh Framework Programme FP7/2007-2013 under grant agreement ICT 257210 PARADIGM.

References

[1] Kersey, A., Berkoff, T., and Morey, W. Jan 1992 *Electronics Letters* **28(3)**, 236–238.

[2] Todd, M., Johnson, G., and Chang, C. Oct 1999 *Electronics Letters* **35(22)**, 1970–1971.

[3] Bachmann, M., Besse, P., and Melchior, H. Jun 1994 *Applied Optics* **33(18)**, 3905–3911.

[4] Reyes-Iglesias, P. J., Molina-Fernández, I., Moscoso-Mártir, A., and Ortega-Moñux, A. Feb 2012 *Opt. Express* **20(5)**, 5725–5741.

Foundry based approach for InP based PIC development

Meint K. Smit

COBRA Research Institute, Eindhoven University of Technology, Eindhoven, the Netherlands
m.k.smit@tue.nl

Abstract: The generic foundry model will reduce the R&D and prototyping costs and the throughput time of Photonic ICs by more than an order of magnitude. The concept of generic photonic integration is discussed and the current status and prospects of generic InP-based integration technology are reviewed.

In photonic integration most integration technologies are developed and optimized for a specific application. As a result we have almost as many technologies as applications, most of them very similar, but sufficiently different to prevent easy transfer of a design from one fab to another. Owing to this huge fragmentation, the market for many of these application-specific technologies is too small to justify their further development into a low-cost industrial volume manufacturing process. And as a result the chip costs remain too high to find wide application.

This is quite different from microelectronics where a huge market is served by a small set of integration processes (most of them CMOS processes). In these processes a broad range of functionalities can be realised from a small set of basic building blocks, like transistors, resistors, capacitors and interconnection tracks. By connecting these building blocks in different numbers and topologies we can realize a huge variety of circuits and systems, with complexities ranging from a few hundred up to over a billion transistors. We call such a process, in which a broad range of functionalities can be synthesized from a small set of basic building blocks, a ***generic integration process***.

In photonics we can do the same. An integration process with building blocks for controlling the basic properties of light: the amplitude, the phase and the polarisation, can support a broad range of functionalities. And by integrating these building blocks with a good waveguide structure we can make interconnections, but also passive components like couplers, filters and demultiplexers. With optical amplifiers (SOA: Semiconductor Optical Amplifier), phase modulators and polarisation converters, for manipulating the amplitude, the phase and the polarisation of the light, the technology can support a broad range of functionalities.

An advantage of generic integration technologies is that because they serve many different applications, they justify the investments in developing the technology for a very high performance and reliability at the level of the building blocks. This will make circuits realised in such a technology highly competitive. A single generic process will not be suited to all applications, of course. Just like in microelectronics we will need a few different generic technologies, optimized for different kinds of applications. But the number of generic technologies can be small, much smaller than the variety in today's technologies.

Such generic integration processes have been developed in the European projects EuroPIC and PARADIGM, and (Dutch) national projects like MEMPHIS, IOP Photonic Devices and STW Generic Technologies for Integrated Photonics. On these experimental platforms more than a hundred different Photonic ICs have been fabricated for applications in telecom, datacom, medical diagnostic, metrology, sensing and security.

Another advantage of a standardized technology is that we can develop design libraries and a related software infrastructure for components or subcircuits that are used by many designers. This leads to a significant reduction of the design time and an increase in the design accuracy, so that fewer design cycles will be necessary to arrive at a required performance.

An important advantage of generic integration technology is that a number of different designs can be combined on the same wafer, because they all use the same fabrication process. Such a wafer is called

a Multi-Project Wafer (MPW). And the Photonic ICs fabricated in such an MPW run are called ASPICs: Application Specific Photonic ICs, the photonic equivalent of an ASIC. *ASPICs are application-specific PICs, realised in a standardized generic process*. This approach leads to a large reduction of the research and development costs. In the development stage often a few design and fabrication cycles are necessary to arrive at the required performance. Usually a few chips out of the wafer are sufficient for testing the design in this stage. By combining a number of designs on a single wafer every designer gets a few chips and the costs of the run can be shared by all participants in the MPW-run. This will lead to a more-than-ten-fold reduction of the costs of a design run.

If the owner of a generic integration process does not provide access to external users the number of companies that can take advantage of this approach remains restricted to a few companies that develop sufficient different products to make a generic approach profitable for themsleves. The corner stone of the generic foundry model is the generic foundry: a chip manufacturer that provides open access to its generic integration process(es). In silicon microelectronics a number of chip manufacturers are providing such foundry access. In Photonics a few companies and institutes have started providing semi-commercial access to generic foundry platforms.

The anticipated large reduction of R&D time and chip manufacturing costs will lead to a large growth of the share of PICs in the photonic components market. So far the commercial deployment of PICs has been mainly restricted to specific areas in telecom core-network applications, where their functionality cannot be matched by competing technologies. Telecom is a relatively niche area for the exploitation of photonic technologies, accounting for about 5% of the global photonics market. Nonetheless the stringent requirements of telecoms are driving PIC research. Thus the opportunities to leverage PIC technology in other established photonic markets such as fibre sensor readout units, medical diagnostic, metrology and many applications where today's photonics does not provide a competitive price level, are immense.

Another important advantage of the generic foundry approach is the short time-to-market. Because the ASPICs are developed in a qualified foundry process upscaling to larger production volumes is straight forward: once the ASPIC design meets the user requirements, the user can order a number of wafers in the same process in which he developed his ASPIC, which he can now fill completely with his design.

All this brings a fundamental change in the business model of photonics and allows commercial and academic groups to co-operate and move forward rather than forever reinventing the wheel.

In the presentation the present status of the InP-based generic foundry approach will be reviewed, and future developments in platform technology development, process design kits and component libraries, generic packaging and testing will be discussed.

References

M. Smit et al, "An introduction to InP-based generic integration technology", accepted for publication in *J. of Semicon. Science and Technology, 2014.*

Dual-Wavelength AWG based Lasers for Narrow Linewidth Heterodyne Beat-Note Generation

R. Guzman[1], A. Jimenez[1], G. Carpintero[1], X.J.M Leijtens[2], K. Ławniczuk[2,3]

[1] Universidad Carlos III de Madrid, Leganes, Madrid, Spain,
rcguzman@ing.uc3m.es, ajgalind@pa.uc3m.es, guiller@ing.uc3m.es
[2] Technical University of Eindhoven, P.O. Box 513, 5600 MB Eindhoven, The Netherlands.
[3] Warsaw University of Technology, Institute of Microelectronics and Optoelectronics, Koszykowa 75, 00-662 Warsaw, Poland

Abstract: Multi-wavelength laser sources based on Arrayed waveguide grating have been shown in order to provide simultaneously multiples wavelengths with a narrow optical linewidth. Two different laser structures have been developed for the millimeter wave signal generation, monolithically integrated using photonic integrated circuits. In this work we report the characteristics of the heterodyne signal in the millimeter wave range. The optical linewidth measured from the modes generated by different channels on each structure can become less than 150 KHz.

Introduction: Millimeter-wave (MMW) frequencies (30 GHz - 300 GHz) have attracted a great interest from industries involved in the development of broadband wireless communication systems because they can provide short range communications with data rates above 1 Gbp/s[1, 2]. Dual wavelength laser sources are useful devices for the generation of high frequency electrical signals over a very wide-range from MHz up to terahertz using heterodyne mixing on a photodiode or another type of opto-electronic transducer. As the beat-note is insensitive to dispersion in optical fiber, it is possible to carry this signal over a long single mode fiber length with very low signal power degradation[3]. The devices presented in this paper were developed within the European Union FP7 iPHOS project to implement an optical technique to generate millimeter waves. The idea is to create 100 GHz and 120 GHz carrier waves with a narrow optical linewidth from each structure. The work described in this paper analyzes to AWG sources, from the point of view of the linewidth of the optical modes, which at the end, determine the electrical beat-note linewidth.

Dual wavelength AWG based lasers (AWGLs): The first device that we studies is an extended cavity laser, based on an array of semiconductor optical amplifiers (SOA) and an AWG. As shown in Fig. 1 (on the right side), the device tested consists of sixteen separated SOAs, one per channel, labeled Channel N (with N = 1 to 16). An additional SOA is located at AWG's common output waveguide arm, to boost the output optical power of the outgoing light. All the SOAs used for the channel waveguide selection are 600 μm long. The length of the Boost SOA is 750 μm. The AWG acts as an intra-cavity filter, to establish the lasing wavelengths by filtering the modes in the laser cavity formed between the cleaved facets of the chip. The AWG central wavelength is λ = 1550 nm, the channel spacing Δλ = 100 GHz (0.8 nm) and the free spectral range (FSR) is 900 GHz (7.2 nm).

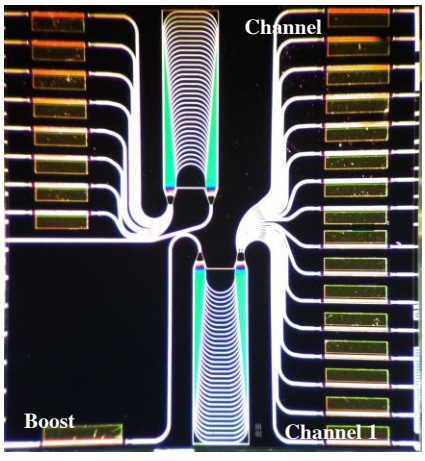


Fig. 1: Monolithically integrated AWG multi-wavelength laser

The second device is the same type of structure, based on an AWG, with 4 input channels and one common output (CO). The main difference is that MMI reflectors are used instead of the chip facets to define the mirrors of the AWG laser, thus producing a fully monolithic device. The dual wavelength output from the CO can now be modulated or processed within the chip, as shown in Fig. 2. In our chip, we placed a Boost SOA to increase the dual mode optical power. Also, the MMI reflectors allow us to reduce the FP cavity length of the laser, increasing the longitudinal mode spacing among the FP cavity modes. An anti-reflective (AR) coating was placed at the cleaved facets to improve the performance of the chip. The AWG designed has a

channel spacing (Δλ) and free spectral range are 0.961 nm (120 GHz) and 5.61 nm (700 GHz), respectively. All the SOAs used both for the channel selection and the common output are 400 μm long. The lengths of the EOPMs are 1000 μm.

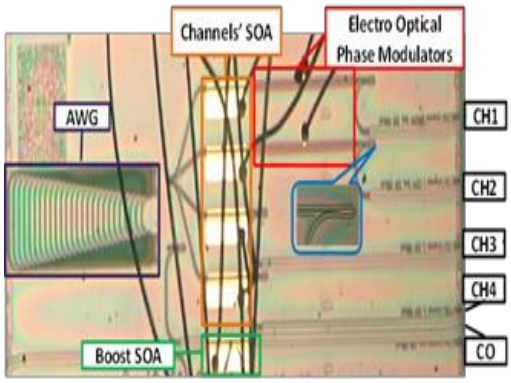


Fig. 2: AWG based laser source using MMI reflectors mirrors.

Linewidth measurements: In order to obtain a single channel emission for both AWG based lasers, the current injected on each separated SOA channel was chosen to achieve single mode operation on the central FSR order, while setting a constant current on the Boost SOA. We obtained the single mode operation for each channel with a side-mode suppression ratio better than 30 dB. We have measured the optical linewidth of the AWG based lasers emission using a self-heterodyne measurement setup, with an optical isolator (OI), an 11 GHz fibered electro-optical phase modulator (EOPM) and a length of 6.8 km of single mode optical fiber between the two arms of the interferometer, as shown in Fig. 3. A polarizer (PC) is included in order to obtain matching of the polarization of light coming from the two arms of the interferometer maximizing the signal at the photo-detector. The beat-note at 11 GHz is sent to an electrical spectrum analyzer (ESA). The -3 dB linewidth of each of the two channels of the AWGLs are evaluated by measuring the beat note spectrum centered at 11 GHz. The red traces in Fig. 4 show the experimental results both for the AWGL1 (Channel 8 and Boost SOA are biased at 38 mA and 50 mA, respectively), and the AWGL2 (Channel 2 and Boost SOA are biased at 60 mA and 30 mA, respectively). The linewidth are extracted assuming a Lorentzian shape, shown as the blue traces in Fig. 4, and the optical -3 dB linewidth is then assumed to be half the -3 dB linewidth of the electrical signal. The optical linewidth measured on both channels give as result 109 KHz and 64 KHz both AWGL1 and AWGL2, respectively. The optical linewidth is below the best figures reported for a dual wavelength source based on two 2,500 μm long DFB lasers and a combiner[3].

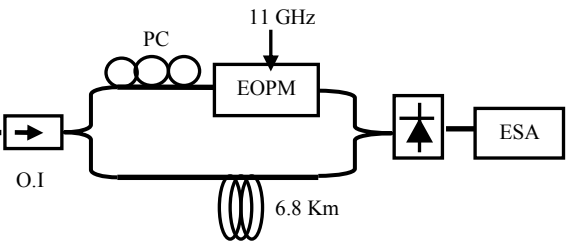


Fig. 3: Optical self-heterodyne linewidth measurement system.

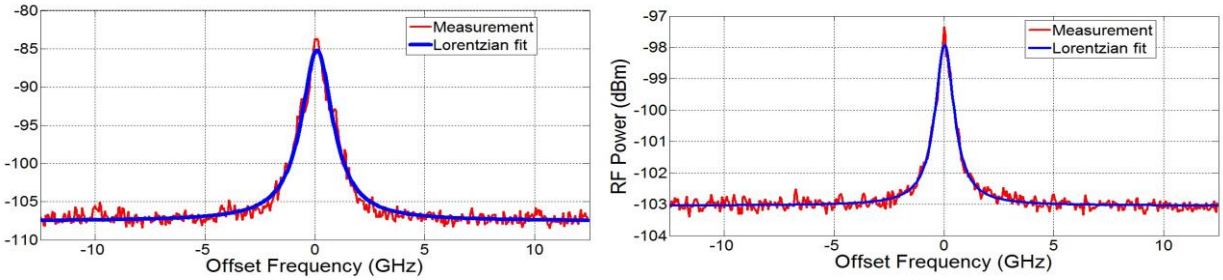


Fig. 4: Optical self-heterodyne linewidth measurement setup both for AWGL1(at the left side, Channel 8 and Boost SOA are biased at 38 mA and 50 mA, respectively (red) and Lorentzian fit (blue)) and AWGL2 (at the right side, Channel 2 and Boost SOA are biased at 60 mA and 30 mA, respectively (red) and Lorentzian fit (blue)).

References

1. G. Fettweis, "WIGWAM: System concept for 1Gbit/s and beyond", in IEEE 802 plenary meeting, November (2005).
2. C.C. Chong et al., "Millimeter-wave wireless communication systems: theory and applications", in EURASIP Journal on Wireless Communications and Networking, (2007).
3.F. Van Dijk, A. Accard, A. Enard, O. Drisse, D. Make and, F. Lelarge "Monolithic dual wavelength DFB for narrow linewidth heterodyne beat-note generation" in Proc. IEEE Int. Top. Meeting on MicrowavePhotonics (MWP), pp. 73-76, 2011, (2001).

AWG based wavelength-meter with pm resolution

D. D'Agostino[1], R. Broeke[2], M. Boerkamp[3], J. Mink[3], H.P.M.M. Ambrosius[1] and M.K. Smit[1]

[1]COBRA Research Institute, Eindhoven University of Technology, 5600 MB Eindhoven, The Netherlands
d.dagostino@tue.nl, hambrosius@tue.nl, m.smit@tue.nl
[2]Bright Photonics BV, 3604 CE Maarssen, The Netherlands.
ronald.broeke@BrightPhotonics.eu
[3]VTEC Lasers & Sensors, 5617 BC Eindhoven, The Netherlands.
martijn.boerkamp@vtec-ls.nl , jan@vtec-ls.nl,

Abstract: This work reports an integrated circuit for the measurement of the wavelength of a coherent light source. The circuit is based on a 1x8 AWG with a 50 nm Free Spectral Range, connected to an array of photo detectors. A change in wavelength can be monitored by evaluation of the photocurrent variation in detectors connected to two adjacent AWG channels. We demonstrate first characterization results obtained from a demonstrator circuit fabricated in a generic foundry process.

1. Introduction

Accurate wavelength measurement is crucial for a high number of applications related to optical sensing. Prominent examples are gas detection and strain sensing based on Fiber-Bragg-Gratings[1,2]. Recently, fiber based monitoring solutions showed great advances with relatively simple fabrication methods[3,4]. However, the high polarization sensitivity of fibers and the necessity of additional equipment is a limiting factor. In this paper we propose a cost efficient Arrayed Waveguide Grating (AWG) approach for accurate and high-speed wavelength measurements. By designing the AWG such that two adjacent channels overlap, a change in wavelength can be monitored by evaluating the photo current of the corresponding photo detectors (PDs). First measurement results of a circuit based on a 1x8 AWG with a 50 nm FSR are presented.

2. Circuit Layout

The circuit is schematically depicted in Fig. 1(a). For simple packaging a straight input is connected to a 1x2 MMI splitter, with one output connected to a reference diode and the other to the AWG. At each of the eight outputs of the AWG, a photo detector is placed. The AWG design employs widened pass bands to increase the crosstalk level between adjacent channels. The wavelength meter is operated around the intersection of adjacent pass bands using balanced detection for increased output power. In Fig. 1(b) we display a photograph of the chip fabricated in the COBRA generic process. The chip contains different AWGs, varying the number of channels employed (three AWGs with eight and one with 16 channels). The metal contacts are conveniently routed to the edge of the chip.

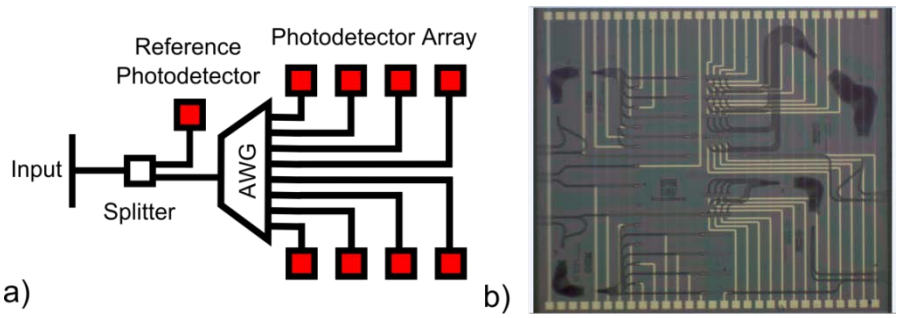


Fig. 1: Schematic of photonic circuit containing integrated detectors, (a) Photo of PIC, containing four AWG based wavelength-meter with up to 16-Channels (b)

3. Measurements

The device has been characterized using the setup depicted in the schematic of Fig. 2 (a). A tunable laser (Agilent 81600B) is coupled via a collimating lense to free space. After passing through the polarizer, the collimated beam is coupled to the device via a microscope objective. A fiberized polarization controler is used to maximize the transmission throught the polarizer set to TE. The device is mounted on a copper element, which is cooled down to 293 K by a water cooler. Small

temperature fluctuations are compensated with a Peltier element which is connected to a temperature controler.

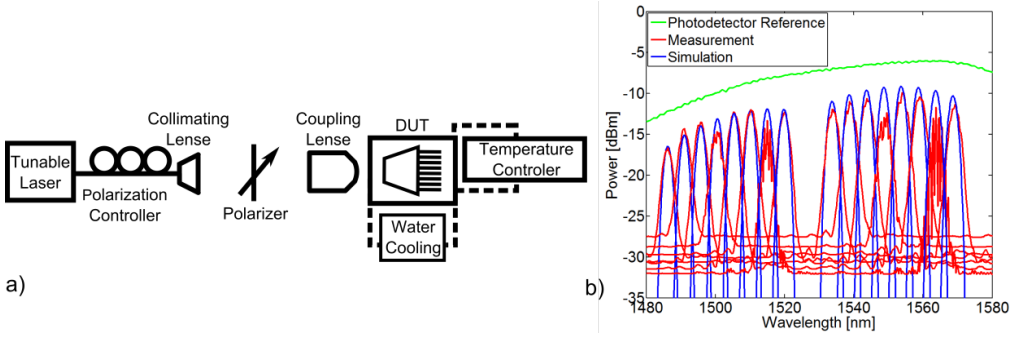


Fig. 2: Schematic of experimental setup, containing water cooling and electrical temperature control via a Peltier element (a). Integrated measurement of 8-channel AWG via detector array (b)

Based on the integrated photo detector array, we measured two FSRs of the AWG, displayed in Fig. 2(b). The response of the photo detectors is sufficient to resolve the pass bands of the AWG over 100 nm. The simulated transmission is calibrated using the detector response and matched to the measurement. The noise floor in the figure is caused by the noise level of the photo detectors and their readout.The sensitivity of the system is tested by using two inverted slopes of adjacent AWG channels, as indicated in Fig. 3 (a). The laser wavelength is set to match the pass band intersection for a time period of 5 s, after which the wavelength is tuned discretely by 5, 10 or 20 pm. The detectors are analysed in steps of 0.1s without averaging. Typical results are displayed in Fig. 3(b). Wavelength steps of a few pm can be clearly distinguished. The resolution limit is given by the standard deviation of the measured signal over time. We measure a typical standard deviation of 0.8 pm over a 10 s period.

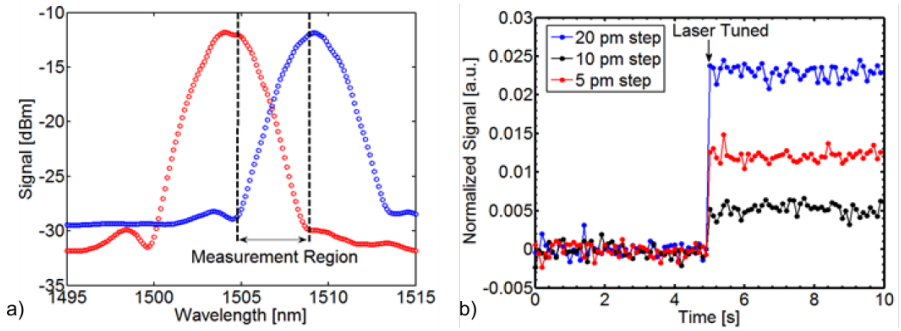


Fig. 3: Integrated measurement of two adjacent AWG pass bands, with indicated wavelength measurement region (a), 5, 10 and 20 pm wavelength steps measured at the crossing point of the AWG channels (b)

5. Conclusion

We fabricated a wavelength interrogator circuit based on a 1x8 AWG connected to an array of photo detectors. By evaluating the photocurrent variation in detectors connected to two adjacent AWG channels, we were able to clearly measure 5 pm changes in the wavelength of a tuneable laser. The standard deviation over a measurement period of 10 s is 0.8 pm. Considering the spectral periodicity of the AWG, the same circuit can be potentially applied over an operating range of above 100 nm.

6. Acknowledgements

The work presented is part of the TULGAS project supported by IOP Photonic Devices and IPC HTSM Fotonica supported by RVO. The authors thank SMART Photonics for the rapid fabrication of the device.

References

1.Hodgkinson J., Tatam R.,*Meas. Sci. Technol.*,**24**, 012004 (2004)
2.Zhang A.P. et al.,*Photonic Sensors*,**2**, pp.1-13 (2012)
3.Wang P. et al.,*Journal of Lightwave Technology*,**30**,pp.1143-1149 (2012)
4.Hatta A.M.,Semenova Y., Farrel G., *Microwave and Optical Technology Letters*,**55**,pp.1645-1649 (2013)
5.Smit M. et al.,*Optoelectronics IET*,**5**,pp.187-194 (2011)

Photonic crystal lasers for computercom networks

Shinji Matsuo[1,2]

[1] *NTT Photonics Laboratories,* [2] *Nanophotonics Center,*
3-1, Morinosato Wakamiya, Atsugi-shi, Kanagawa, Japan
matsuo.shinji@lab.ntt.co.jp

Abstract: Directly modulated lasers with ultralow power consumption are essential for realizing computercom networks, such as chip-to-chip and on-chip optical interconnections. To reduce the operating energy, it is important to reduce the laser active volume. For this purpose, we use a photonic crystal (PhC) cavity with an ultracompact buried heterostructure, which provides good confinement of both carriers and photons. To fabricate current driven PhC lasers with a thin two-dimensional PhC slab (~250 nm), we use a lateral current injection structure with Zn thermal diffusion and Si ion implantation. A fabricated device exhibits ultralow operating energy of less than 10 fJ/bit when it is modulated with 10-Gbit/s NRZ signal.

Introduction: Introducing optical technologies into computercom networks, such as chip-to-chip and on-chip interconnects, is desired because internet traffic is still increasing and optical interconnects provide a potential solution for constructing high-speed networks with low power consumption. However, for optical links in such very-short-reach applications, the operating energy per single bit, defined as the energy cost, has to be less than ~40 and ~10 fJ/bit for chip-to-chip and on-chip interconnects, respectively.[1] To achieve these small energy costs, directly modulated lasers with ultra-small active volume are essential. Therefore, it is important to maintain the cavity Q factor (or photon lifetime) when the cavity size decreases to ~μm^2. In this context, a two-dimensional photonic crystal (PhC) has attracted much attention because it provides a high Q factor (>10^6) with a wavelength-scale cavity.[2] However, high-speed direct modulation and electrical pumping have been difficult to achieve because of both the poor thermal conductivity and lack of a carrier confinement structure.

To overcome these problems, we introduce a buried heterostructure and lateral current injection structure.[3-6] Figure 1(a) shows a schematic diagram of the two-dimensional PhC cavity. The multi-quantum-well (MQW) active region is embedded in an InP-based PhC line-defect waveguide, which is what we call a λ-scale embedded active region PhC or LEAP laser. The optical mode profile calculated using the FDTD method is also shown in Fig. 1(a), and it clearly indicates that the optical mode field is well confined within the active region. Figure 1(b) shows a cross-sectional view of the lateral current injection LEAP laser. The active region is covered with the InP layer to prevent it from being etched during the wet chemical etching of the InAlAs sacrificial layer. Si-ion implantation and Zn thermal diffusion are used for n-type and p-type doping of the undoped InP layer, respectively.

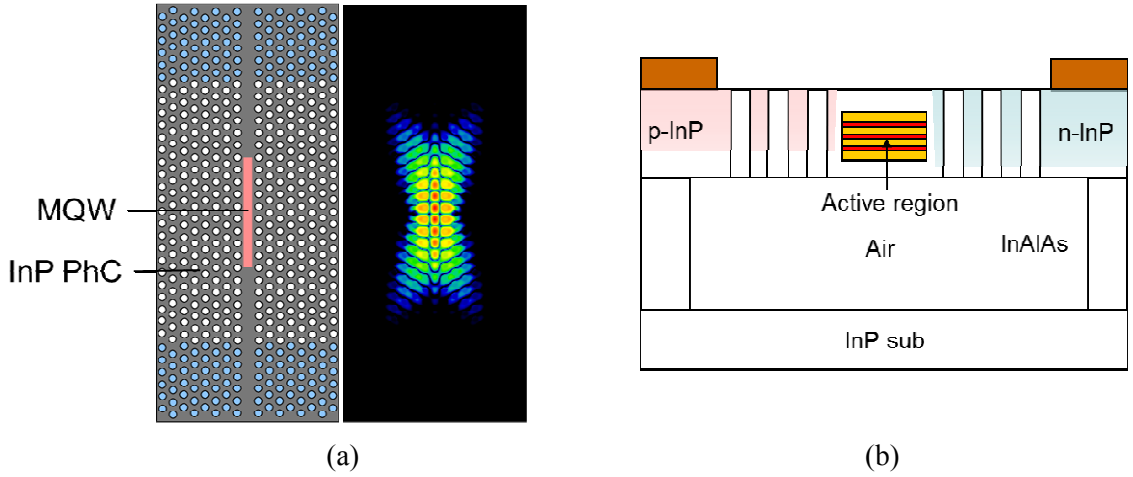
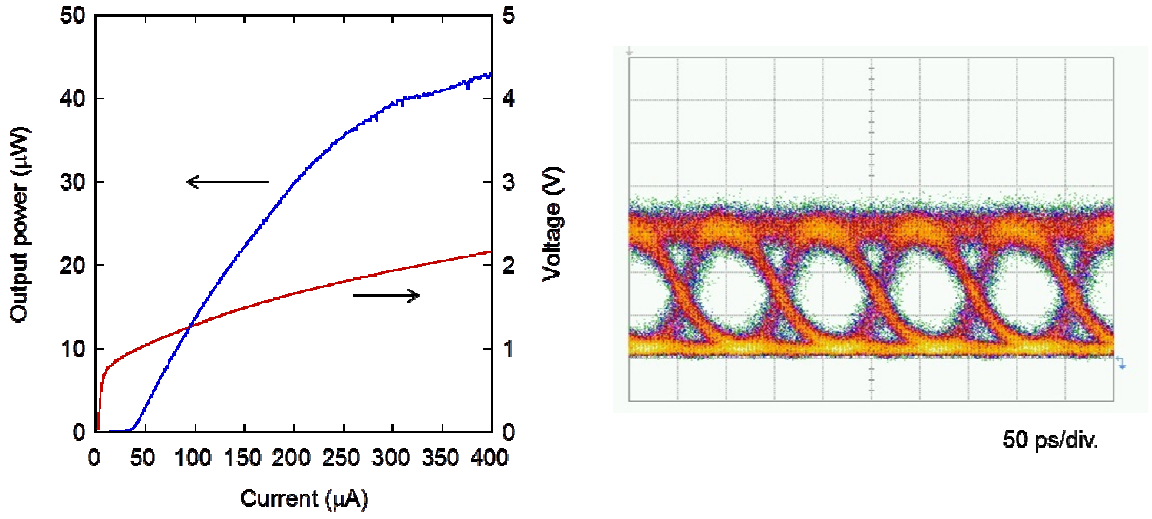


Fig. 1: (a) Schematic diagram and calculated optical mode field of two-dimensional PhC cavity using buried heterostructure. (b) Cross-sectional view of lateral current injection LEAP laser.

Device characteristics: We fabricated a device using InGaAlAs-based six-QW active region. The active region is 2.5 × 0.3 × 0.15 μm^3 (0.12 μm^3). Figure 2(a) shows the injection current dependence of output power and voltage in room-temperature continuous-wave operation. The threshold current was 32 μA and the maximum output power was 43 μW. Differential resistance at threshold was about 6 kΩ. Figure 2(b) shows the eye diagram when the device was operated with 9.953-Gbit/s NRZ signal with PRBS of 2^{31}-1. An air coplanar probe was used to drive the laser without 50-Ω termination. The bias current and voltage were 80 μA and 1.23 V, respectively, resulting in a 9.9-fJ/bit energy cost. As shown in this figure, we obtained clear eye opening with a 10-dB extinction ratio.



(a) (b)

Fig. 2: (a) Injection current dependence of output power and voltage in room-temperature continuous-wave operation. (b) Eye diagram for bias current of 80 μA. 9.953-Gbit/s NRZ signal was used.

Summary: We have developed and electrically driven LEAP laser for use in chip-to-chip and on-chip interconnects. Thanks to the use of an ultracompact buried heterostructure, the device exhibits the maximum output power of 43 μW and clear eye opening when modulated with 10-Gbit/s NRZ signal. These results indicate that the LEAP laser opens the new applications for semiconductor lasers.

Acknowledgements: Part of this work was supported by the New Energy and Industrial Technology Development Organization (NEDO).

References

1. D. A. B. Miller, "Device Requirements for Optical Interconnects to Silicon Chips," *Proc. IEEE* **97**, pp. 1166-1185 (2009).
2. T. Tanabe *et al.*, Trapping and delaying photons for one nanosecond in an ultrasmall high-Q photonic-crystal nanocavity," *Nature Photon.* **1**, pp. 49-52 (2007).
3. S. Matsuo *et al.*, "High-speed ultracompact buried heterostructure photonic-crystal laser with 13 fJ of energy consumed per bit transmitted," *Nature Photon.* **4**, pp. 648-654 (2010).
4. S. Matsuo *et al.*, "Room-temperature continuous-wave operation of lateral current injection wavelength-scale embedded active region photonic-crystal laser,"*Opt. Express* **20**, pp. 3773-3780 (2012).
5. K. Takeda *et al.*, "Few-fJ/bit data transmissions using directly modulated lambda-scale embedded active region photonic-crystal lasers," *Nature Photon.* **7**, pp. 569-575 (2013).
6. S. Matsuo *et al.* "Photonic crystal lasers using wavelength-scale embedded active region," *J. of Phys. D* **47**, 023001 (2014).

1.6-W, Highly Efficient Laser at 2 μm in a Potassium Double Tungstate Channel Waveguide

Koop van Dalfsen[1], Shanmugam Aravazhi[1], Christos Grivas[2], Sonia M. García-Blanco[1], Markus Pollnau[1]

[1] *Integrated Optical Microsystems Group, MESA+ Institute for Nanotechnology, University of Twente, P.O. Box 217, 7500 AE Enschede, The Netherlands*
m.pollnau@utwente.nl
[2] *School of Physics and Astronomy, University of Southampton, Southampton SO17 1BJ, UK*
chr.grivas@gmail.com

Abstract: Buried ridge waveguides are microstructured into a monoclinic potassium double tungstate layer with a composition of $KY_{0.40}Gd_{0.29}Lu_{0.23}Tm_{0.08}(WO_4)_2$ grown onto a $KY(WO_4)_2$ substrate by liquid-phase epitaxy. When pumping with a Ti:Sapphire laser at 794 nm, the fundamental-mode channel waveguide produces laser emission with a slope efficiency of ~80% and an output power of 1.6 W at 1.84 µm in a resonator with 89% output coupling.

Introduction: Dielectric channel waveguide lasers are of great interest because of their low pump thresholds and, even more so, high slope efficiencies resulting from the small transverse channel cross-sections which reduce the volume of active medium that needs to be pumped and the excellent overlap between pump and laser modes. In Tm-doped waveguide lasers operating near 2 µm wavelength, highest reported slope efficiencies are 76% in a $LiYF_4:Tm^{3+}$ planar waveguide with an output power of 560 mW,[1] as well as 70% in Tm^{3+}-doped potassium double tungstate channel waveguides with output powers of 300 mW.[2]

Waveguide fabrication: A co-doped layer of $KY_{0.40}Gd_{0.29}Lu_{0.23}Tm_{0.08}(WO_4)_2$ with a thickness of several tens of micrometers was grown onto a pure $KY(WO_4)_2$ (= KYW) substrate by liquid-phase epitaxy at 920-923 °C.[3-5] The layer was lapped and polished to a thickness of 14.3 µm, covered with a photoresist mask, and patterned 1.9-µm-deep by Ar^+-beam milling.[6] Ridge-type channel waveguides with a maximum loss of 0.11 dB/cm at ~2 µm were produced in this way and overgrown with a pure KYW layer as a cladding to further reduce scattering loss.[7] The channels, having a width of 10−25 µm, which support only the fundamental modes for both the pump and laser wavelengths, were diced to a length of 4.2 mm and end-face polished to an optical finish.

Laser experiments: The Tm^{3+}-doped channel waveguides were pumped at a wavelength of 794 nm with a transverse-magnetic (TM, E||N_p) polarization. As the pump source, a Ti:Sapphire continuous-wave laser was used. In-coupling of pump light into the channel waveguides was optimized using cylindrical lenses of 40 mm and 10 mm in the horizontal and vertical directions, respectively. A dielectric mirror with a reflectivity of 99.9% (HR) at 1900–2100 nm and high transmissions at 790–810 nm (due to an anti-reflection coating at this wavelength) was butt-coupled to the pump in-coupling end-facet of the channel waveguides using index-matching oil (Fluorinert). At the other waveguide end-facet, no dielectric mirror was placed such that feedback was only provided by the Fresnel reflection at the KYW-air interface amounting to ~11% reflection. The laser output power was out-coupled from the channel

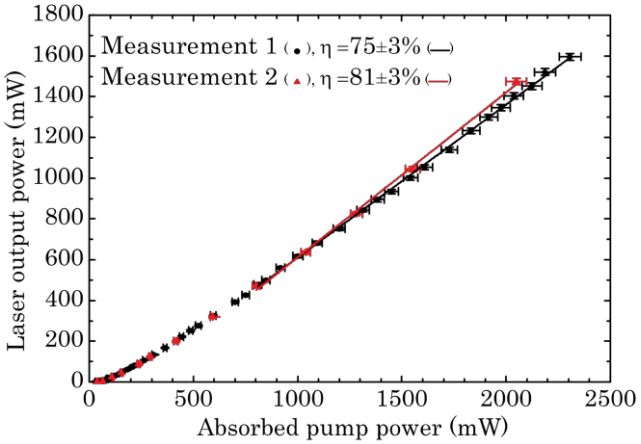


Fig. 1: Laser output power at 1840 nm versus absorbed pumped power at 794 nm in TM-polarization. Shown are two independent measurements (red and black dots), and the linear fits of the laser slope efficiency at higher powers (red and black lines).

waveguides via a 0.25 NA microscope objective and any residual pump power was blocked by a RG1000 filter. The measured laser output power from two independent experiments when pumping at λ_P = 794 nm in TM-polarization is shown in Fig. 1. The highest output power measured is 1594 mW at an absorbed pump power of 2181 mW and the slope efficiency amounts to ~80%. The laser operates at an output wavelength of λ_L = 1840 nm.

Slope efficiency: If ground-state bleaching is absent, from spectroscopic lifetime data[8,9] we derive that the "2 for 1" cross-relaxation process[10] in Tm^{3+} provides a quantum efficiency of η_q = 1.94 for the relevant Tm^{3+} concentration of 5.07×10^{20} cm^{-3}. Furthermore, this laser has a mode overlap of η_{mode} = 1, because the laser-beam size is larger than the pump-beam size, and a Stokes efficiency of $\eta_{St} = \lambda_P / \lambda_L$ = 794 nm / 1840 nm = 0.432. With an out-coupling efficiency equaling the ratio of useful resonator losses, given by the outcoupling transmission of T_{out} = 89%, to total resonator losses, in which also the intrinsic round-trip losses L = 0.015, equaling $\eta_{out} = \ln[1-T_{out}]/\ln[(1-T_{out})(1-L)]$ = 0.993, the theoretical limit of the slope efficiency is

$$\eta_{slope} = \frac{dP_{out}}{dP_{abs}} = \eta_{mode}\eta_{St}\eta_q\eta_{out} = 83.2\% . \quad (1)$$

Thanks to the channel waveguide geometry and the resulting strong confinement of pump and laser modes, the laser overcomes the reabsorption losses from the ground state and is indeed able to operate close to the theoretical slope efficiency, see Fig. 1.

Conclusions: We have demonstrated a 2-μm channel waveguide laser with a slope efficiency exceeding 80% and an output power of 1.6 Watt. At this performance level it may be applied as a compact and inexpensive laser source for real-time monitoring of gases for environmental, industrial, and medical purposes.

References

1. W. Bolaños, F. Starecki, A. Benayad, G. Brasse, V. Ménard, J.-L. Doualan, A. Braud, R. Moncorgé, P. Camy, *Opt. Lett.* **37**, pp. 4032−4034 (2012).
2. K. van Dalfsen, S. Aravazhi, C. Grivas, S. M. García-Blanco, M. Pollnau, *Opt. Lett.* **37**, pp. 887−889 (2012).
3. Y. E. Romanyuk, C. N. Borca, M. Pollnau, S. Rivier, V. Petrov, U. Griebner, *Opt. Lett.* **31**, pp. 53−55 (2006).
4. F. Gardillou, Y. E. Romanyuk, C. N. Borca, R. P. Salathé, M. Pollnau, *Opt. Lett.* **32**, pp. 488−490 (2007).
5. S. Aravazhi, D. Geskus, K. van Dalfsen, S. A. Vázquez-Córdova, C. Grivas, U. Griebner, S. M. García-Blanco, M. Pollnau, *Appl. Phys. B* **111**, pp. 433−446 (2013).
6. D. Geskus, S. Aravazhi, C. Grivas, K. Wörhoff, M. Pollnau, *Opt. Express* **18**, pp. 8853−8858 (2010).
7. K. van Dalfsen, S. Aravazhi, D. Geskus, K. Wörhoff, M. Pollnau, *Opt. Express* **19**, pp. 5277−5282 (2011).
8. F. Güell, Jna. Gavaldà, R. Solé, M. Aguiló, F. Díaz, M. Galan, J. Massons, *J. Appl. Phys.* **95**, pp. 919−923 (2004).
9. O. Silvestre, M. C. Pujol, M. Rico, F. Güell, M. Aguiló, F. Díaz, *Appl. Phys. B* **87**, pp. 707−716 (2007).
10. E. W. Duczynski, G. Huber, V. G. Ostroumov, I. A. Shcherbakov, *Appl. Phys. Lett.* **48**, pp. 1562−1563 (1986).

High-gain spiral amplifiers in a-Al_2O_3:Er^{3+} on a silicon chip

Sergio A. Vázquez-Córdova, **Edward H. Bernhardi, Kerstin Wörhoff, Sonia M. García-Blanco, Markus Pollnau**

Integrated Optical Microsystems Group, MESA+ Institute for Nanotechnology, University of Twente, P.O. Box 217, 7500 AE Enschede, The Netherlands
s.a.vazquezcordova-1@utwente.nl

Abstract: We designed and fabricated integrated optical amplifiers with 20 dB of gain at λ = 1532 nm. Aluminum-oxide films with erbium concentrations of $0.45-3.1\times10^{20}$ cm^{-3} were deposited onto thermally oxidized silicon wafers and microstructured. For a 24.5-cm-long spiral-shaped amplifier with an erbium concentration of 0.95×10^{20} cm^{-3}, a maximum internal net gain of ~20 dB was measured.

Introduction

Rare-earth-doped devices are of great interest for optical amplification due to their weak refractive-index change[1] compared to that typically induced in semiconductor optical amplifiers by electron-hole pairs, their long excited-state lifetimes, their large amplification bandwidth,[2] and the possibility for high-speed amplification.[3] In addition to these properties, giant optical gain of ~1000 dB/cm was measured in a ytterbium-doped crystalline waveguide.[4] Nevertheless, inferior gain performance is commonly observed in amorphous materials due to lower transition cross-sections caused by inhomogeneous broadening, hence only moderate values of gain per unit length have been reported.[5] In this work, we present the design, fabrication, and characterization of erbium-doped amorphous aluminum oxide waveguide amplifiers that exhibit ~20 dB of total internal net gain.

Design and fabrication

The model by Agazzi *et al.*[5] enables a comprehensive study of the spectroscopic characteristics of Al_2O_3:Er^{3+} and, thus, was employed for the design of our waveguide amplifiers. Preliminary simulations employing the model indicated that the doping concentration has to remain below $\sim4\times10^{20}$ cm^{-3} to avoid ETU and fast quenching processes, which were accentuated with the erbium concentration. To ensure that most of the available pump power was absorbed, the amplifier length had to be on the order of tens of centimeters. A spiral-shaped channel waveguide was designed to minimize the footprint of the waveguide. By use of software (*Phoenix B.V.*),[6] mode-field simulations were performed for different ridge channel waveguide cross-sections, and the optimal dimensions were 1 µm height by 1.5 µm width, with a ridge height of 0.35 µm. These waveguide dimensions allowed for good confinement (>80%) of the mode field for both, pump and signal. The targeted maximum bending loss of $\sim10^{-6}$ dB/cm was satisfied in our design for a minimum bending radius of 2 mm.

A ~1-µm-thick layer of Al_2O_3:Er^{+3} was deposited onto a thermally oxidized silicon wafer by RF reactive co-sputtering.[7] The spiral-shaped waveguides were patterned into the Al_2O_3:Er^{3+} film employing common lithographic techniques and reactive ion etching.[8] A protective SiO_2 cladding layer was deposited on top by plasma-enhanced chemical vapor deposition.

Amplifier characterization

Background propagation losses were measured in the spirals using the imaging method.[9] This method consists in analyzing a digital image that records the light scattered from randomly distributed defects within the channel. The light from a fiber-coupled infrared laser (λ = 1320 nm) was butt-coupled to the spiral-shaped waveguide, and the scattered light was captured from the top face of the spiral using an InGaAs camera. Accurate calibration of the images was performed before analysis of the intensity distribution along the channel length in the spiral waveguide. An exponential decay curve as a function of propagation length was fitted to each intensity profile, and background propagation losses were found to be in average (0.2±0.1) dB/cm.

The spiral gain was characterized by employing the pump-probe technique. Pump light from a $\lambda = 976$ nm pig-tailed diode laser was combined with signal light from a tunable laser (λ = 1460−1640 nm) using a fiber-based WDM that was butt-coupled to the input of the spiral-shaped waveguides. At the output end of the waveguide, a second WDM was employed to separate the signal from the residual pump. By lock-in amplification the amplified signal was discriminated from the residual pump and the amplified spontaneous emission coupled to the waveguide. Figure 1 shows an image of a pumped $Al_2O_3:Er^{+3}$ spiral-shaped amplifier. The internal total gain measured in spirals of different length for a doping concentration of 0.95×10^{20} cm^{-3} is shown in Fig. 2. A maximum total gain of ~20 dB is achieved for a 24.5-cm-long spiral. Lower performance in longer waveguides is attributed to insufficient pump power at the end of the spiral, causing lower population inversion and, thus, signal re-absorption at the furthermost part of the spiral.

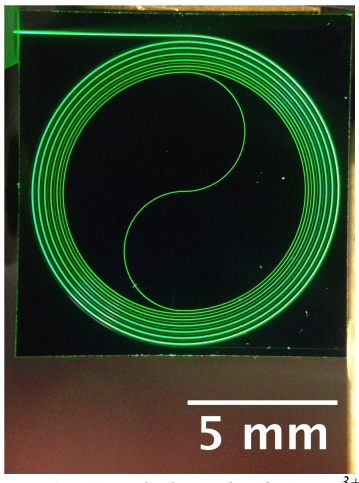


Fig. 1: Spiral-shaped $Al_2O_3:Er^{3+}$ amplifier pumped with a 976 nm pig-tailed diode laser.

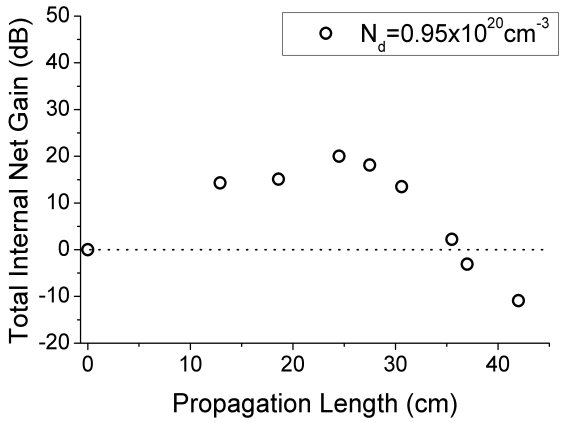


Fig. 2: Maximum total internal gain for different $Al_2O_3:Er^{3+}$ waveguide amplifiers with a doping concentration of 0.95×10^{20} cm^{-3}.

Conclusions

By carefully adjusting the ridge waveguide cross-section, erbium concentration, and waveguide length, we demonstrated 20 dB of internal gain in spiral-shaped $Al_2O_3:Er^{3+}$ waveguide amplifiers on a silicon chip. Further improvement can be expected if the fast quenching process that limits the useful erbium concentration can be diminished.

Acknowledgements

This work was supported by the Dutch Technology Foundation (STW) within the framework of project No. 11689. Sergio A. Vázquez-Córdova gratefully acknowledges CONACyT for its partial scholarship support on his postgraduate studies.

References

1. R. Soulard, A. Zinoviev, J. L. Doualan, E. Ivakin, O. Antipov, R. Moncorgé, *Opt. Express*, **18**, pp. 1553–1568 (2010).
2. J. D. B. Bradley, L. Agazzi, D. Geskus, F. Ay, K. Wörhoff, M. Pollnau, *J. Opt. Soc. Am. B*, **27**, pp. 187–196 (2010).
3. J. D. B. Bradley, M. Costa e Silva, M. Gay, L. Bramerie, A. Driessen, K. Wörhoff, J.-C. Simon, M. Pollnau, *Opt. Express*, **17**, pp. 22201–22208 (2009).
4. D. Geskus, S. Aravazhi, S. M. García-Blanco, M. Pollnau, *Adv. Mater.*, **24**, pp. OP19–OP22 (2012).
5. L. Agazzi, K. Wörhoff, M. Pollnau, *J. Phys. Chem. C*, **117**, pp. 6759–6776 (2013).
6. Phoenix B.V., www.phoenixbv.nl.
7. K. Wörhoff, J. D. B. Bradley, F. Ay, D. Geskus, T. P. Blauwendraat, M. Pollnau, *IEEE J. Quantum Electron.,* **45**, pp. 454–461 (2009).
8. J. D. B. Bradley, F. Ay, K. Wörhoff, M. Pollnau, *Appl. Phys. B*, **89**, pp. 311–318 (2007).
9. Y. Okamura, S. Yoshinaka, S. Yamamoto, *Appl. Opt.*, **22**, pp. 3892–3894 (1983).

A Coupled Cavity Laser based on a Multimode Interference Reflector

D. D'Agostino, D. Lenstra, H.P.M.M. Ambrosius and M.K. Smit

COBRA Research Institute, Eindhoven University of Technology, 5600 MB Eindhoven, The Netherlands.
d.dagostino@tue.nl, d.lenstra@tue.nl, hambrosius@tue.nl, m.smit@tue.nl

Abstract: We demonstrate the first tunable Coupled Cavity Laser fabricated in an InP based generic foundry process. This is achieved by coupling two Fabry-Perot laser cavities with different length via a 2-Port Multimode Interference Reflector. The coupling coefficients of the reflector are designed to enhance the Side Mode Suppression Ratio. The reflector is realized in a deep-etched waveguide process with vertical sidewalls. We measured Side Mode Suppression Ratio close to 40 dB and tuning range of 4.7 nm for 1.2 mm long cavities with a length difference of five percent.

1. Introduction

Coupled Cavity Lasers (CCLs) have been of interest since the beginning of laser integration and are extensively described in literature. A simple and conventional method to create a CCL is by introducing an air gap[1] into a Semiconductor Optical Amplifier (SOA). The yield of this laser is strongly dependent on accurate control of the gap dimension, which ultimately limits the application of CCLs. Recently, new attempts were made to create CCLs using Multimode Interference Devices (MMIs) without imaging properties[2,3]. Although enabling high Side Mode Suppression Ratio (SMSR), these devices suffer from significant loss. In this work we present a novel Multimode Interference Reflector (MIR) with optimal coupling characteristics for CCLs derived from a 3x3 general interference MMI. Combined with existing MIRs[4], the laser can be fully integrated in generic processes[5] that support vertically etched sidewalls. We fabricated a CCL with cavities of approximately 1.2 mm in length, and a difference of five percent. Our first laser shows a SMSR close to 40 dB at 2 mW output power and 4.7 nm tuning range via the integrated phase sections.

2. Laser Design

A schematic of the CCL is given in Fig. 1(a) below. Two cavities, each containing a SOA and a phase control section, are coupled together via a 2-Port MIR with reflectivity R_2 and symmetric amplitude coupling coefficients C_x and C_{bar}. The opposite output mirrors are formed by cleaved facets with reflectivity R_1. The lengths of the cavities are chosen to differ by 5%. The laser is fabricated in the COBRA generic process[5]. As indicated in Fig. 1(b), the mode selection is based on the Vernier-Effect established between the two cavities of different length. Consequently, the laser can be discretely tuned over the combined Free Spectral Range (FSR) by variation of one of the optical cavity lengths. This can be accomplished by biasing one phase control section. Continuous tuning can be achieved by biasing both phase sections with a similar current. Analogous to previously reported CCLs, it is of momentous importance that the phase difference between C_x and C_{bar} is fixed to multiples of 180° [1-3,6]. Light that is cross coupled, amplified and partially added to the originating cavity can thus interfere constructively with the directly reflected components C_{bar}. This can be obtained using directional couplers with three waveguides[7], which adds the condition $|C_x| + |C_{bar}| = 1$ to our coupling element R_2. It was previously theoretically[2] and experimentally[3] demonstrated that SMSR in the 40 dB range can be expected for the case of $C_{bar} \approx 0.85$ and $C_x \approx 0.15e^{j\pi}$.

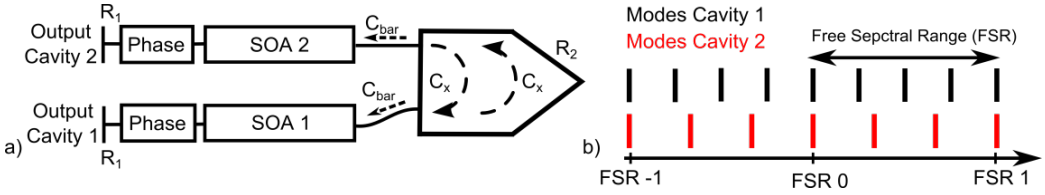


Fig. 1: Schematic of the Coupled Cavity Laser (CCL) (a) with indication of the tuning mechanism (b)

3. MIR Design

The coupling coefficients of a three waveguide coupler are strongly dependent on the accurate control of the gap distances. Previous lasers based on the proposed approach, approximated the right coupling

coefficients with a MMI, at the expense of non-ideal imaging properties[2,3,7]. Here we employ a design which shows both ideal imaging and coupling behaviour. We start from a 3x3 general interference MMI in transmission as depicted in Fig. 2(a) and will derive a related reflector at the end of this section. The 3x3 geometry produces images of equal intensity at the beat length L_π. In Fig. 2(b), we show a numerical example of the propagation inside the multimode section where L_π is indicated. Here it is seen that at $L_\pi/2$ three images are present with unequal intensities such that $C_{bar} \approx 0.21$, $C_{cen} \approx 0.57e^{j\pi/3}$ and $C_x \approx 0.78e^{j\pi}$. By realizing that the condition $|C_x| + |C_{bar}| \approx 1$ is fulfilled, we recognize a potential 2x2 coupler for the laser in Fig. 1(a), if the central waveguide is excluded. Although this implies a significant imaging loss in general, the loss of light is minimized if the two outer inputs are simultaneously excited with almost equal intensities and a phase difference of 180°. In that case, destructive interference occurs in the central output at multiples of $L_\pi/2$, as can bee seen in Fig. 2(c). So far the MMI in transmission. A fully reflective device is obtained by placing a corner mirror at $L_\pi/4$, as indicated in Fig. 2(d). Due to the corner reflection, the coupling coefficients are interchanged. Consequently, the reflector coefficients now read $C_{bar} \approx 0.79$, $C_x \approx 0.21e^{j\pi}$ and $C_{cen} = 0$, which is close to ideal for our laser geometry. Note that these ideal values only occur when the two input intensities are equal and their phase difference is 180°. This property will automatically lead to optimization of the laser operation.

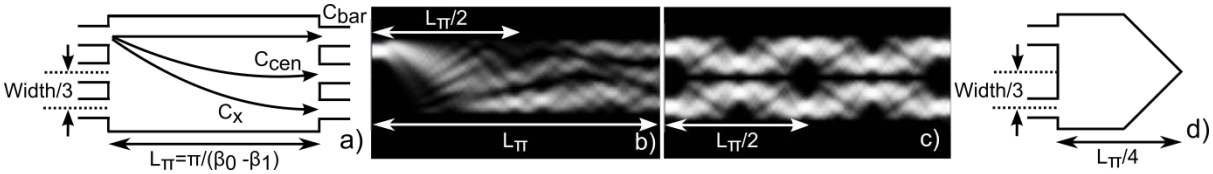


Fig. 2: (a) 2x2 MMI geometry. BPM simulation of (b) Single input excitation of MMI,(c) Anti-resonant excitation of MMI. (d) Related MIR geometry.

4. Measurements

We have fabricated the laser in Fig. 1 (a) with cavities of 1.2 mm length and a length difference of five percent. The MIR is designed 6 µm wide and 25 µm long. The device reaches threshold when 18 mA are injected into SOAs of 500 µm length. Typical spectra of the laser are displayed in Fig. 3, with SMSR close to 40 dB. When a current is injected into the phase control sections, the laser is tuned by 4.7 nm in discrete steps. The inset in Fig. 3 shows a typical L-I curve. The light was collected by a lensed fibre, while injecting current into both SOAs.

5. Conclusion

We have fabricated a Coupled Cavity Laser based on a 2-port Multimode Interference Reflector with optimized coupling characteristics. The laser demonstrates a SMSR close to 40 dB and can deliver several mW output power, when coupled to a lensed fibre. The tuning range of a first, design was 4.7 nm. The fabrication of the device is fully compatible with high-yield waveguide lithography and thus promising for large-scale photonic integrated circuits.

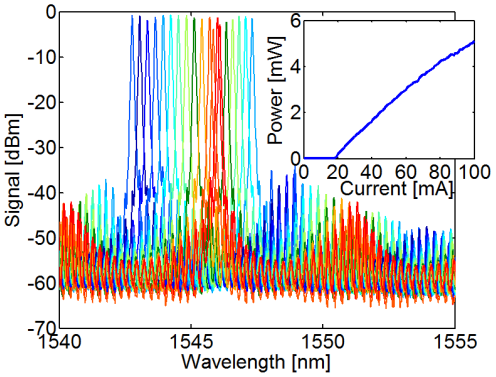


Fig.3: Typical spectrum when 40 mA are injected in both cavities. The phase sections are tuned by current injection. Inset shows a L-I curve obtained with a lensed fiber

6. Acknowledgements

This work is part of the TULGAS project supported by IOP Photonic Devices. The authors thank SMART Photonics for the rapid fabrication of the device.

7. References

1. Coldren L. et al., *Electronics Letters*,**20**,pp.350-356,(1984)
2. Jialiang J. et al.,*Optics Letters* ,**36**,pp.4230-4232 (2011)
3. He J., D. Liu,*Optics Express*, **16**,pp.3896-3911 (2008)
4. Zhao. J. et al.,*23rd International Conference on Indium Phosphide and Related Materials*,pp.1-4,(2011)
5. Smit M. et al.,Optoelectronics, *IET*,**5**,pp.187-194, (2011)
6. Koch T.L., Coldren L.A., *Journal of Applied Physics*,**57**, pp.740-754 (1985)
7. Lin X., Liu D., He J., *Applied Optics*,**48**, F18 (2009)
8. Soldano, L., Pennings, E. , *Journal of Lightwave Technology* ,**13**, pp.615-627, (1995)

Ytterbium-Doped Tantalum Pentoxide Waveguide Lasers

A. Aghajani [1], G.S. Murugan[1], N.P. Sessions[1], V. Apostolopoulos[2], J. S. Wilkinson[1]

[1] Optoelectronics Research Centre, University of Southampton, Southampton, England
aa15v07@soton.ac.uk, smg@orc.soton.ac.uk, nps@orc.soton.ac.uk, jsw@orc.soton.ac.uk
[2] School of Physics and Astronomy, University of Southampton, Southampton, England
v.apostolopoulos@soton.ac.uk

Abstract: We have demonstrated a Yb:Ta_2O_5 waveguide laser fabricated by RF magnetron sputtering on oxidised silicon. The waveguide laser was end-pumped with a laser diode at 977 nm and lasing was observed between 1015 and 1020 nm. The launched pump power threshold and slope efficiency were measured to be ~25 mW and 1.78 %, respectively.

Introduction

Integrated channel waveguide solid-state lasers are key components in the quest for fully integrated optical circuits with advanced functionality such as tunability and pulsed operation. Ta_2O_5 has been selected as the host material for the realization of a compact, integrated ytterbium doped waveguide laser as it offers many important attributes such as good ability to host rare-earth ions, as demonstrated with erbium[1] and neodymium[2], a large third nonlinearity[3] and a high refractive index ($n \approx 2.124$ at $\lambda \approx 980$ nm)[4], and is suitable for mode-locking. High index contrast between the waveguide core and cladding provides for low-loss tight bend radii enabling the development of compact and ultra-small photonic circuits due to the strong confinement of the optical modes.

In this work, we present for the first time lasing behaviour for Yb:Ta_2O_5 rib waveguides and quantify the absorption and emission cross-sections of the material and the threshold, slope efficiency and emission spectrum of waveguide laser.

Device design and fabrication

Rib waveguides in Ta_2O_5 were designed for single mode (SM) operation between 970 nm and 1100 nm, covering the signal and pump wavelengths of Yb-doped materials. Rib waveguide dimensions of 1 μm rib height and 150 nm etch depth were selected using Soref et al.[5] method.

A Yb:Ta_2O_5 film of 1 μm was deposited by RF magnetron sputtering from a power-pressed tantalum pentoxide target, doped with 2.5 wt% of ytterbium oxide (~6.2×10^{20} atoms/cm^3) onto a silicon substrate coated with a 2.5 μm thermally-grown silica layer. The conditions used for the deposition process were 20 and 5 sccm of argon and oxygen gas flow, a substrate temperature of 200°C and magnetron power of 300 W. These conditions were previously optimized for Er:Ta_2O_5 to provide the lowest optical loss with an acceptable deposition rate[6].

The rib waveguides were structured by conventional photolithography and argon ion beam milling (IBM). Channel waveguides were fabricated with an etch depth of 150 nm and with widths ranging from 1 to 10 μm. Once the structuring process was complete, a 1.6 μm thick silica overcladding was deposited on top of the waveguide core, producing a protection layer and a symmetrical waveguide. For preparation for optical measurements the wafer was cut into smaller samples and end facets were polished to optical quality.

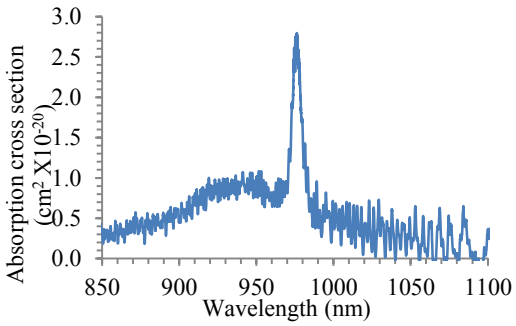


Fig 1: Absorption cross-section

Waveguide and lasing characteristics

The spectral characteristics of Yb:Ta_2O_5 were unknown so an absorption spectrum was obtained to determine the ytterbium cross section at the pump (977 nm) wavelength. Broadband (700 – 1700nm) light from a tungsten halogen lamp was coupled into a 3 mm long waveguide using a monomode fibre and collected at the output using a multimode fiber. The collected light was fed into an optical spectrum analyzer (OSA). Fig 1 shows the absorption cross section of Yb:Ta_2O_5, using the estimated

concentration of ytterbium ions in Ta_2O_5 ($6.2x10^{20}$ atoms/cm^3). The absorption bands of ytterbium at 935 nm and 975 nm are clearly visible with a peak absorption cross section (σ_{abs}) of 2.75 ± 0.17 $x10^{-20}$ cm^2 evident in the pump band at 975 nm. The peak emission cross section (σ_{em}) was also estimated using the reciprocity method from the absorption cross section, giving a peak emission cross section of $2.9 \pm 0.7x10^{-20}$ cm^2 at 975 nm.

A 10.8 mm long laser cavity was formed using the reflections from the parallel optically polished end facets alone, which were estimated to have a Fresnel reflectivity of 12 % at the waveguide-air interface. To demonstrate lasing, the pump was butt-coupled into the end facet of a 3 μm wide waveguide using a monomode fibre, exciting the fundamental mode. Light emerging from the output was collected using a ×40 objective lens and passed through a set of long pass filters with a cut-off wavelength of 1 μm to remove the residual pump radiation. The wavelengths at which lasing occurred ranged from 1015 nm to 1020 nm as shown in Fig. 2b. The lasing output power is plotted against the launched pump power, Fig. 2a, and the laser threshold and single-ended slope efficiency were determined to be ~25 mW and 1.78 %, respectively.

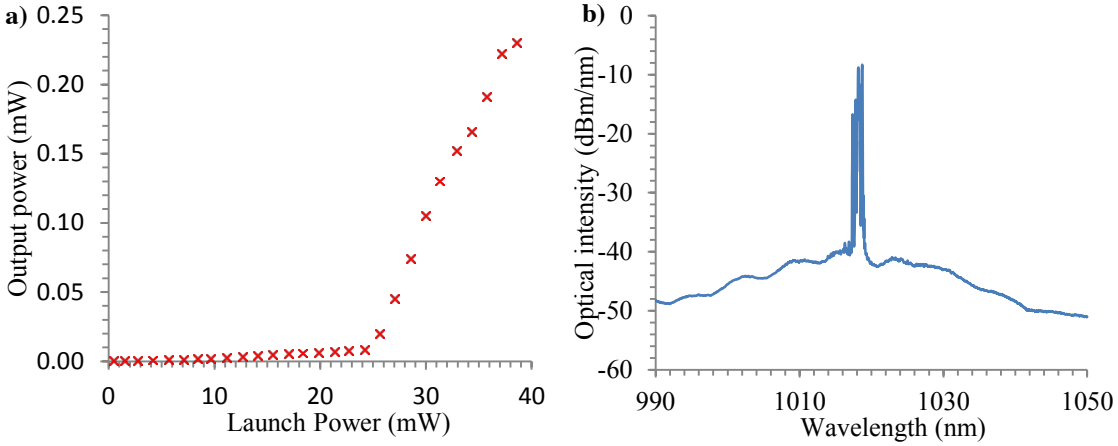


Fig 2: a) Laser output power versus launched pump power b) Lasing spectrum of Yb:Ta_2O_5

Conclusion

In conclusion, we have demonstrated a Yb:Ta_2O_5 waveguide laser fabricated by RF magnetron sputtering on a silicon wafer, and determined spectroscopic parameters and lasing characteristics. The waveguide laser was end pumped with a laser diode at 977 nm and lasing was observed between 1015 and 1020 nm using only the polished facets as mirrors. The launched pump power threshold and slope efficiency were measured to be ~25 mW and 1.78 %, respectively. This material system has demonstrated that compact continuous wave lasing is achievable, providing a platform to develop monolithically integrated components and devices. Improvements in lasing characteristic can be realised through optimisation of cavity mirrors, or with ring resonators exploiting the high index contrast. The gain properties and nonlinearity of the material, and their fabrication with CMOS-compatible processes, offers a potential route to low-cost mass production of highly functional integrated mode-locked and tunable lasers.

Symbols	Definition	Values
N_o	Yb dopant concentration	$6.2x10^{20}$ cm^{-3}
σ_{abs}	Peak absorption cross section	$2.75x10^{-20}$ cm^2
σ_{em}	Peak emission cross section	$2.9x10^{-20}$ cm^2
λ_p	Pump wavelength	977 nm
λ_s	Signal wavelength	1015-1020 nm

Table 1: Spectroscopic parameters for Yb:Ta_2O_5

References

1. A. Z. Subramanian, C. J. Oton, D. P. Shepherd J. S. Wilkinson, *Photon. Technol. Lett,*. **22**, pp. 1571-1573, (2010).
2. B. Unal et al., *J. Quantum Electron*., **41**, pp. 1565-1573, (2005)
3. C. Y. Tai et al., *Optics Express*, **21**, pp 5110 - 5116 (2004)
4. A. Z. Subramanian, *Tantalum Pentoxide Waveguide Amplifier and Laser for Planar Lightwave Circuits*, University of Southampton thesis (2011)
5. R. Soref, J. Schmidtchen, K. Petermann, *J. Quantum Electron*., **27**, pp. 1971-1974, (1991)
6. A.Z. Subramanian, G.S. Murugan, M.N. Zervas, J.S. Wilkinson, *J. Lightwave Technol*., **30**, pp. 1455-1462 (2012).

PLD-grown Yb:Y_2O_3 waveguide laser Q-switched by a graphene saturable absorber

A. Choudhary[1], S. Dhingra[2], B. D'Urso[2], T. L. Parsonage[1], K. A. Sloyan[1], R. W. Eason[1] and D. P. Shepherd[1]

[1] Optoelectronics Research Centre, University of Southampton, Southampton, Hampshire, UK
a.choudhary@soton.ac.uk, tlp1g08@orc.soton.ac.uk, kas@orc.soton.ac.uk, rwe@orc.soton.ac.uk, dps@orc.soton.ac.uk
[2] Department of Physics and Astronomy. University of Pittsburgh, Pennsylvania, USA
shd28@pitt.edu, dursobr@pitt.edu

Abstract: In this paper, we present an Yb^{3+}-doped Y_2O_3 waveguide laser fabricated by pulsed laser deposition (PLD) that is Q-switched using a mono-layer graphene saturable absorber. 140 ns pulses at a repetition rate of 1.21 MHz and pulse energy of 14 nJ are achieved at an absorbed pump power of 528 mW.

Introduction: Pulsed lasers have a range of applications in areas such as medicine, material processing, telecommunications and defence. Waveguide-based pulsed laser systems have the additional potential to be integrated, compact, mass-producible and efficient, making them exciting prospects for future industrial applications. We have recently demonstrated mode-locked femtosecond waveguide lasers at multi-GHz repetition rates[1-3] using semiconductor saturable absorber mirrors (SESAMs). However, SESAMs are expensive, complicated to fabricate and have a narrow operating wavelength range. In the last decade, graphene saturable absorbers[4] have become very popular because of the ease of fabrication and their broadband operation, with Q-switched waveguide lasers[5] and Q-switched mode-locked waveguide lasers[6] being demonstrated. Yttria (Y_2O_3) is a promising laser host due to good thermal properties, ease of rare-earth doping and waveguide fabrication by pulsed laser deposition (PLD)[7]. In this paper, we demonstrate a PLD-grown Yb:Y_2O_3 waveguide laser that has been Q-switched using a mono-layer graphene saturable absorber.

Experimental details and results: A multi-layer clad waveguide structure, consisting of 3-μm-thick Y_2O_3 lower and upper cladding layers and a 6-μm-thick Yb:Y_2O_3 core layer, was grown on a YAG substrate by PLD and end-polished to a final device length of 8 mm. A fibre-coupled laser diode operating at 975 nm was used as the pump source for the initial continuous wave (CW) characterisation of the Yb:Y_2O_3 waveguide laser. The pump output was collimated by an aspheric f = 8 mm lens and launched into the waveguide using a further aspheric lens with f = 8 mm, making a spot size of w_o ~3.3 μm at the input facet. A half-wave plate and a Faraday isolator were installed in the beam path to block any back reflections from the waveguide and to protect the laser diode. The laser cavity was formed by end-butting a 200-μm-thick high reflectivity (HR) mirror at the input-facet, and 200-μm-thick output coupling (OC) mirrors with transmission (@1030 nm) of 0.8%, 2%, 5%, 14% and 19.6%, respectively at the output facet. CW laser action was observed at 1030 nm at a threshold power of 123 mW for the 0.8% OC and a slope efficiency as high as 25% was observed for the 19.6% OC. The laser mode radius was measured to be 3.2 μm in the guided plane and 170 μm in the un-guided plane. The losses were estimated to be 1.6 dB/cm, based on the measured slope efficiency for each output coupler and using Caird analysis[8].

In order to obtain pulsed operation, single-layer graphene was used as a saturable absorber. It was grown on large-domain ultra-flat copper using atmospheric-pressure chemical vapour deposition (APCVD)[9], and was then transferred onto a fused silica substrate using PMMA. The single-layer was subsequently transferred to the waveguide when the substrate was pressed against the output end-facet of the waveguide.

A counter-propagating laser cavity was formed by putting the HR mirror on the output facet of the waveguide and aligning a mirror (2% transmission at 1030 nm, 99.9% transmission at 975 nm) on the input facet. A dichroic mirror (T=99% @ 975 nm, R=97% @1030 nm) was installed before the

launch objective to separate the pump and laser beams. The laser output was reflected by the dichroic mirror and was characterized using a photodiode, a power meter and an optical spectrum analyser.

The output from the waveguide laser was focused on a silicon photodiode (1 ns rise time), which was connected to an oscilloscope (1 GHz bandwidth). On increasing the pump power, CW operation was observed at an absorbed power of 138 mW. At an absorbed power of 292 mW, Q-switched pulses were generated at an average output power of 6 mW. The pulse duration and repetition rate at the threshold for Q-switching were measured to be 310 ns and 830 kHz respectively, and the pulse energy was calculated to be 7 nJ. On increasing the pump power, the pulse duration was found to decrease from 310 ns (at 292 mW) to 140 ns (at 528 mW) and the pulse energy increased from 7 nJ to 14 nJ as seen from Fig.1.a. A maximum output power of 16 mW and a maximum repetition rate of 1.21 MHz were measured at an absorbed power of 528 mW as seen from Fig.1.b. The slope efficiency under Q-switched operation was measured to be 4.4%. In comparison, during CW characterisation (without graphene), the slope efficiency was measured to be 4.9% and a maximum output power of 20 mW was obtained for an HR/2% OC cavity. The output pulse with a full width at half maximum (FWHM) of 140 ns and the pulse train with a repetition rate of 1.21 MHz, measured at maximum pump power are shown in Fig.1.c and Fig.1.d, respectively.

Conclusions: We have demonstrated the first, to the best of our knowledge, Q-switched operation of a PLD-grown waveguide laser. Passive Q-switching was achieved by using CVD-grown graphene as a saturable absorber. A repetition rate as high as 1.21 MHz was obtained with a pulse energy of 14 nJ. Future work would include fabrication of channels to reduce the laser threshold followed by mode-locking experiments.

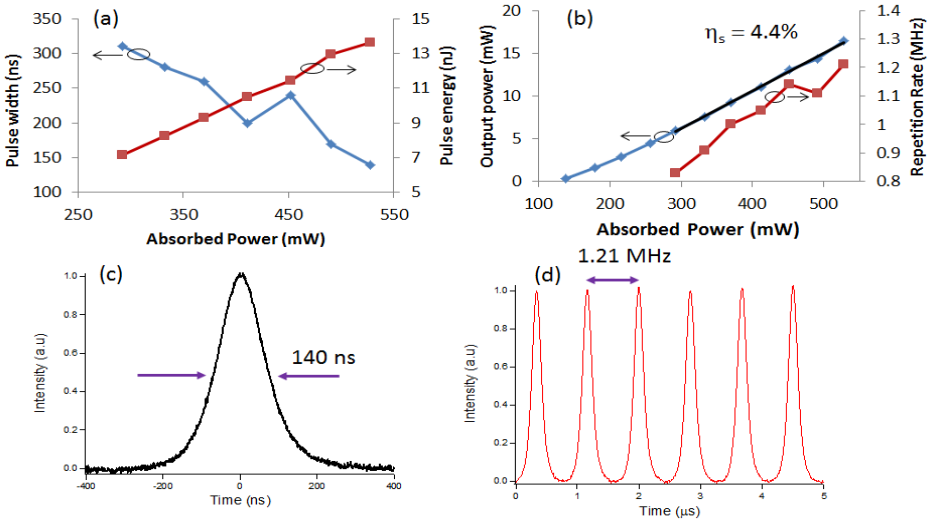


Fig.1. (a) Pulse width and pulse energy vs. absorbed power, (b) Output power and repetition rate vs. absorbed power, (c) 140 ns pulse measured at an absorbed power of 528 mW, and (d) pulse train measured at an absorbed power of 528 mW.

Acknowledgements: This project is funded by the UK Engineering and Physical Sciences (EPSRC) under the projects EP/J008052/1 and EP/L021390. A. Choudhary acknowledges an EPSRC Doctoral Prize.

References

1. A. Choudhary *et al., Optics Letters* **37**, pp. 4416-4418 (2012).
2. A. A. Lagatsky *et al., Optics Express* **21**, pp. 19608–19614 (2013).
3. A. Choudhary *et al*., *Laser Physics Letters* **10**, pp. 105803 (2013).
4. Z. Sun et al., *ACS Nano* **4**, pp. 803-810 (2010).
5. Y. Tan *et al., Optics Express* **22**, pp. 3572-3577 (2014).
6. R. Mary *et al.*, *Optics Express* **21**, pp.7943-7950 (2013).
7. J. W. Szela *et al*., *Optics Express* **21**, pp. 12460-12468 (2013).
8. J. A. Caird *et al*., *IEEE Journal of Quantum Electronics* **24**, pp. 1077-1099 (1988).
9. S. Dhingra *et al.*, *Carbon* **69**, pp.188-193 (2014).

Characterization of an AWG-based dual-wavelength ring laser

A. Corradi[1], G. Carpintero[2], E. Smalbrugge[1], M.K. Smit[1] and E.A.J.M. Bente[1]

[1] *COBRA Research Institute, Eindhoven University of Technology, PhI Group, Eindhoven, The Netherlands, a.corradi@tue.nl, e.smalbrugge@tue.nl, m.k.smit@tue.nl, e.a.j.m.bente@tue.nl*

[2] *UC3M, Universidad Carlos III de Madrid, Madrid, Spain guiller@ing.uc3m.es*

Abstract: In this paper we present characterization results of a monolithically integrated InP-based dual-wavelength laser. The device has been fabricated using active/passive integration technology on a standardized photonic integration platform. In this laser an Array Waveguide Grating (AWG) is used as intra-cavity filter to obtain lasing on two wavelengths using a common optical amplifier in the cavity. A Mach-Zehnder construction allows for controlling the power balance between the two wavelengths. The impact of the crosstalk between AWG channels on the control of the device and the characterization method used to calibrate the Mach-Zender interferometers inside the laser cavity are reported.

Two wavelengths, one common SOA

In this paper we present results on the control and characterization of a photonic integrated dual-wavelength laser for optical-mixed based sub-Terahertz wave generation [1, 2]. Both wavelengths are generated and amplified by one common semiconductor optical amplifier (SOA). As a consequence, λ_1 and λ_2 share the same variations caused by changes in refractive index due to changes in temperature and variations in carrier concentration. This should help in reducing noise in the frequency difference between the two modes.

Design of ring dual-wavelength laser

The schematic representation of the ring dual-wavelength laser is depicted in Fig. 1. An AWG is used as intra-cavity filter to combine the two channels and consequently λ_1 and λ_2. The advantages of using an AWG for this purpose and more details about the design parameters are presented in [3]. In order to achieve lasing action simultaneously on two different wavelengths supported by a single SOA, accurate control of the roundtrip loss in the cavity is required to balance the power of λ_1 and λ_2. This can be obtained through balanced Mach-Zehnder interferometers (MZIs) with voltage controlled electro-optic phase modulators (PHMs) placed in each individual channel. As a drawback, the circuit becomes more complex and the control more difficult compared to two separate lasers.

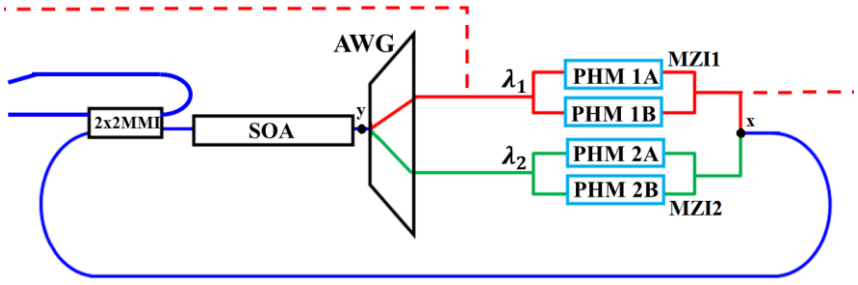


Fig. 1: Schematic of the ring dual-wavelength laser. An SOA provides gain for both wavelengths. An AWG is used as intra-cavity filter to combine λ_1 and λ_2. MZIs are used to compensate losses in the individual channels. A 2x2 multimode interferometer (MMI) couples the light out of the ring cavity.

Preliminary results

All the results reported in this section have been obtained at a temperature of 12°C of the actively cooled aluminum chuck on which the chip is mounted. The SOA and the PHMs on the chip are wire bonded to a simple circuit board from which connections to the current and voltage suppliers are

made. As expected, while biasing the common SOA without balancing the losses in the different channels using the MZIs, the device lases in a single mode; the modes in the other channel are suppressed. The frequency spacing to the side modes matches the expected value of 5.5 GHz related to the cavity length of 15 mm.

Fig. 2 shows that by adjusting the voltage values applied to the PHMs, the losses in the two channels can be balanced and dual-mode operation can be achieved. The SMSR is higher than 25 dB. However, a power difference of 4 dB is still present between λ_1 and λ_2 meaning that the settings are not optimized. The requirement on the power ratio between the two wavelengths is not particularly strict though. A power ratio of 2 for $P\lambda_1$ / $P\lambda_2$ leads to a reduction in difference frequency modulation depth to 0.94 compared the ideal power ratio of 1.

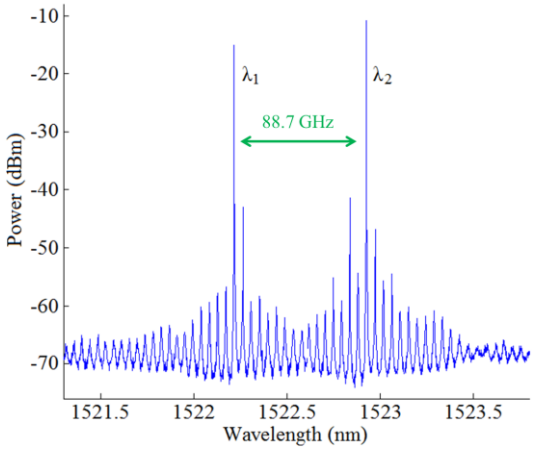


Fig. 2: Output spectra of the ring laser while operating in dual-mode.

The operating point of Fig. 2 has been identified adjusting the settings manually, whereas a more systematic method is desired. Furthermore, the frequency difference between the two lasing wavelengths is 88.7 GHz, considerably smaller than the measured channel spacing of the AWG (120 GHz). This is shown to be due to crosstalk between the two channels in the AWG.

Crosstalk effect and indirect calibration method for PHMs in the MZIs

The crosstalk also complicates the control of the laser because the two channels are not independent from each other. As a consequence, while adjusting losses and tuning of Channel 1, not only λ_1, but also λ_2 is affected. Simulations of the transmission of the filter composed of the AWG and the MZI construction (from point *x* to point *y* in counterclockwise direction in Fig. 1) show that, due to the crosstalk, the settings applied to the PHMs affect in particular the difference in frequency between the maxima of the two channels. As a result, to obtain the desired frequency difference between λ_1 and λ_2 is difficult.

In order to be able to control the device, a precise characterization of the MZIs is needed. Compared to previous devices [4], two additional input/output waveguides (dash lines in Fig. 1) have been placed in the design in order to characterize separately MZI1 using an external laser source (V_π= 6 V, extinction ratio = 15 dB). However, MZI2 must be characterized indirectly since it is placed in the inner part of the ring. The method consists on setting MZ1 to destructive interference configuration forcing the device to lase through Channel 2. Scanning the voltage applied to the PHMs of Channel 2, the threshold current (I_{th}) of the laser changes due to the change of the losses in the cavity. As a result, the transmission function of MZI2 can be extracted. Fig. 3 shows the value of I_{th} while scanning the voltage of PHM2A. When both channels are set to maximum extinction, lasing action takes place through Channel 2: this suggests that the extinction ration is lower in MZI2 than in MZI1. The graph in Fig. 3 shows a value of V_π equal to 6.4 V, consistent with the one measured directly on MZI1, validating the method.

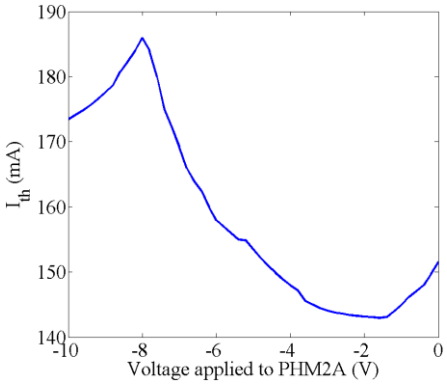


Fig. 3: Values of threshold current as a function of the voltage applied to PHM2A while Channel 1 is set to maximum extinction and PHM2B is grounded. The transmission function of MZI2 can be extracted.

References

1. T. Nagatsuma *et al*., Laser & Photonics Reviews,. **3**, No. 1-2, pp.123-137, (2009).
2. European Union FP7 iPHOS project website www.iphos-project.eu.
3. A. Corradi *et al*., Proceedings of the 16th European Conference on Integrated Optics (ECIO), (2012).
4. A. Corradi *et al*., Proceedings of the 23rd International Semiconductor Laser Conference (ISLC), MB8 (2012).

Grating Coupler Integrated Semiconductor Laser Diodes

T. Suhara, M. Uemukai

Osaka University, Yamada-Oka 2-1, Suita, Osaka, 565-0871 Japan
suhara@eei.eng.osaka-u.ac.jp

Abstract: The work of the author's group will be reviewed on implementation of various integrated photonic devices by monolithic integration of quantum-well DFB/DBR lasers and grating couplers for optical wavefront conversion within the waveguide and/or at the waveguide-free space interface. The devices include integrated photonic sensors, master-oscillator power-amplifier and broad-area lasers with outcouplers, and lasers with couplers for beam shaping.

Introduction: Grating components in an optical waveguide offer various passive functions based upon phase matching and the principle of holography.[1] Variety of integrated photonic devices can be implemented by monolithic integration of quantum-well (QW) DFB/DBR lasers and grating components for optical wavefront conversion within the waveguide and/or at the waveguide-free space interface. The grating components are designed by specifying the patterns required for coupling / wavefront conversion functions, and optimizing the cross-sectional structure parameters to maximize the coupling efficiency, reduce the radiation losses and simplify the fabrication process. In this presentation, the work of the author's group will be reviewed.

Monolithic Integrated Photonic Sensor Devices: Figure 1 shows an integrated photonic interferometer displacement/ position sensor,[2] constructed with a GaAs/AlGaAs SQW DFB laser, photodiodes and grating components in a passive waveguide where the QW is disordered to reduce the propagation loss. The guided wave is outcoupled by a collimator (curved-line) grating coupler to form a sensing beam, and the beam reflected by a moving mirror is back coupled and focused into the PDs by a grating beam splitter. The forward wave is partly reflected and focused by a DBR into the PDs to give reference waves which interfere with the signal wave. The mirror displacement can be measured by monitoring the periodic photocurrent variation. The device was fabricated by MOVPE growth, selective QW disordering, and grating fabrication by EB writing and RIE. The sensor operation of 0.43μm interference period was demonstrated. An integrated photonic disk pickup head with the similar device configuration was also studied.[3]

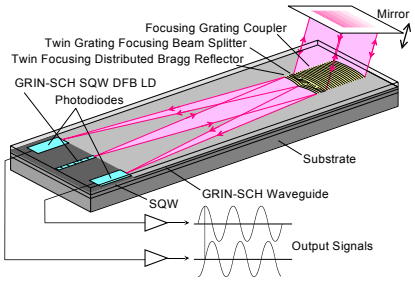


Fig.1: IP displacement sensor.

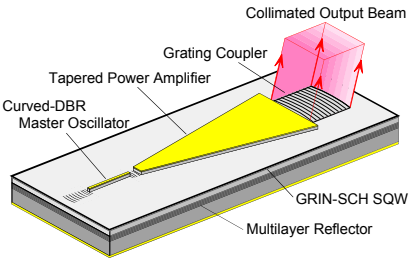


Fig.2: MOPA with grating coupler.

MOPA and Broad-Area Lasers: High-power laser diodes of narrow spectral width integrated with a coupler for output beam collimation or focusing can find many applications as a pump source for nonlinear-optic devices and fiber amplifiers. Figure 2 shows an integrated master oscillator power amplifier (MOPA) with grating outcoupler.[4] The device consists of a DBR oscillator and tapered power amplifier using an InGaAs/AlGaAs QW, and a collimator grating coupler, which eliminates the need of external lens. A curved DBR and a grating coupler of surface groove type are adopted, so that the device can be fabricated without regrowth. The wavefront distortion caused in the amplifier can be compensated for by the appropriate coupler design. Stable single-mode output of power up to CW 183mW (390mW PA output) at 985nm was obtained under 3.0A PA injection. Figure 3 shows a lensless tunable extended-cavity laser using integrated tapered amplifier / grating coupler.[4] Related work includes

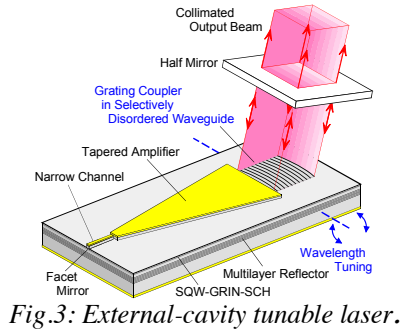


Fig.3: External-cavity tunable laser.

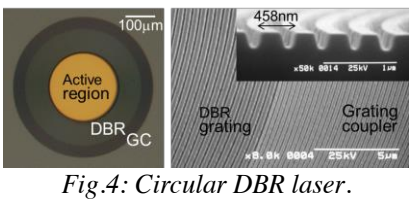


Fig.4: Circular DBR laser.

angled-grating broad-area DBR lasers with grating collimator outcoupler.[5] An unique laser is circular-grating-coupled surface-emitting circular-DBR lasers with focusing function as shown in Fig.4.[6]

Lasers Integrated with Grating Coupler for Beam Shaping: Laser diodes emitting beams focusing into two-dimensional multiple spots are potentially attractive for many applications, such as laser displays, printers, sensing,[7,8] and pumping of multicore fiber amplifiers. By appropriate modification of the focusing grating coupler (FGC) pattern, various beam-shaping functions can be incorporated. Multispot focusing by computer-generated waveguide hologram couplers[9] and integration in semiconductor lasers[10] were reported. A GaInP QW DBR laser with a periodic binary phase-shifted multispot focusing grating coupler was developed as a pump source for bio-fluorescence sensing using a micro fluidic circuit and micro-beads specimen array, and 3×3 square multispot formation of 400μm separation and 0.3mW power at 80mA injection was demonstrated as shown in Fig.5.[11] An integrated laser for producing 6×6 multispot output consisting of four sets of the DBR laser / coupler was demonstrated as shown in Fig.6. A method of designing $n \times n$ spot array output couplers by iterative optimization of a continuous phase shift modulating the FGC pattern was developed, and an integrated laser consisting of a GaInP QW DBR laser oscillator, a power amplifier and a coupler for 7×7 spot array designed by the iterative method as shown in Fig.7 was fabricated. Rotation-symmetric multispot focusing with equal spot intensities by grating couplers with periodic binary phase modulation was also demonstrated as shown in Fig.8.[12] By mixing two laser beams with slightly different wavelengths in a GaAs photoconductive photomixer, coherent THz waves at the beat frequency can be generated.[13] Another application of the phase-shifted FGC under study is integration with two DBR lasers for outcoupling and wavefront superposition toward implementation of a compact THz wave generation system.

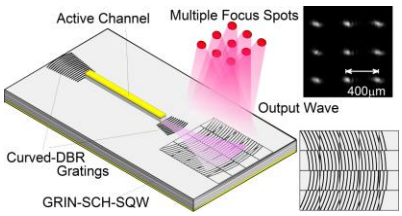


Fig. 5: DBR laser integrated with multispot focusing grating coupler.

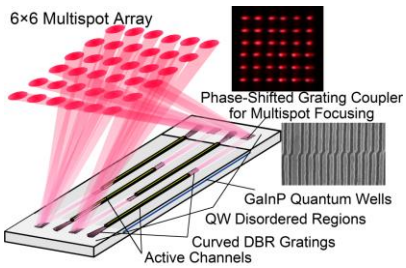


Fig. 6: Integrated multispot lasers.

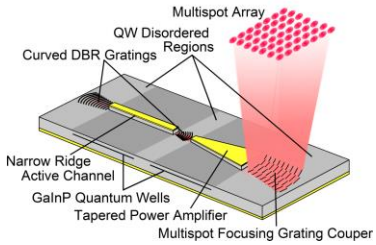


Fig. 7: Multispot MOPA laser.

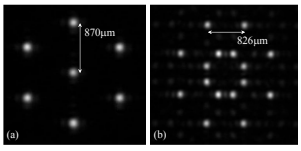


Fig. 8: Rotation-symmetric multi-spot focusing.

Area-Selective QW Disordering: A crucial requirement for the monolithic integration is reduction of passive waveguide losses. An attractive method is area-selective QW disordering. In the previous work, QW disordering by Si ion implantation and impurity-free vacancy diffusion using silica cap layer were employed. Recently, encouraging result has been obtained in disordering by F ion implantation in GaAsP QW.

Nanoimprinting Fabrication of Grating: Although the EB direct writing technique is a versatile and flexible method for accurate fabrication of gratings, the productivity is rather low. Our recent work includes cost-effective grating fabrication by room-temperature nanoimprinting technique using silica master molds fabricated by EB writing, organic Si polymer imprinting layer and RIE.

References

1. T.Suhara and H.Nishihara, *IEEE J. Quantum Electron.*, **QE-22**, pp.845-867 (1986).
2. T.Suhara, T.Taniguchi, M.Uemukai *et al.*, *IEEE Photon. Tech. Lett.*, **7**, pp.1195-1197 (1995).
3. T.Suhara, T.Taniguchi, M.Uemukai *et al.*, *Jpn. J. Appl. Phys.*, **35**, 1B, pp.369-371 (1996).
4. T.Suhara, M.Uemukai, N.Shimada and A.Larsson, *Proc. SPIE*, **4995**, pp.10-21 (2003).
5. M.Uemukai, Y.Kunoh, N.Shimada and T.Suhara, *IEEE J. Sel. Top. Quantum Electron.*, **9**, pp.1191-1195 (2003).
6. A.Saha, M.Uemukai and T.Suhara, *Opt. Rev.*, **21,** no.3 (2014).
7. M.Uemukai, H.Miyamoto, Y. Yamada, Y.Sharma, and T. Suhara, *Jpn. J. Appl. Phys.*, **45**, pp.6738-6741 (2006).
8. M.Uemukai, Y.Yamada and T.Suhara, *Microoptic Conference*, J5, pp.316-317 (2007).
9. M. Li, J.Bengtsson, M.Hagberg, A.Larsson and T.Suhara, *IEEE J. Sel. Top. Quantum Electron.*, **2**, pp.226-235 (1996).
10. P.Modh, J.Backlund, J.Bengtsson, A.Larsson, N.Shimada and T.Suhara, *Appl. Opt.*, **42**, pp.4847-4853 (2003).
11. S.Takushima, M.Uemukai and T.Suhara, *Jpn. J. Appl. Phys.*, **48**, 030206 (2009).
12. K.Uenishi, M.Uemukai and T.Suhara, *Jpn. J. Appl. Phys.*, **51**, 058001 (2012).
13. M.Uemukai, H.Ishida, A.Ito, T.Suhara, H.Kitajima, A.Watanabe and H.Kan, *Jpn. J. Appl. Phys.*, **51**, 020205 (2012).

Fan-in/Fan-out Three-dimensional Polymer Waveguide for Uncoupled Multi-core Fibers

T. Watanabe* **and Y. Kokubun****

Yokohama National University, Graduate School of Eng., 79-5 Tokiwadai, Hodogaya-ku, Yokohama, Japan.
**watanabe-tatsuhiko-hz@ynu.jp, **ykokubun@ynu.ac.jp*

Abstract: Fabrication technologies and device performance of waveguide type fan-in/fan-out device for uncoupled multi-core fiber using Laminated Polymer Waveguide (LPW) are reviewed. The typical coupling loss from a 19-core fiber to nineteen single-core fibers was less than 2.0 dB and the sum of crosstalk from all neighboring cores was lower than -40 dB.

Introduction

Space division multiplexing (SDM)[1] using multi-core fibers (MCFs)[2] is the promising candidate for drastically increasing the transmission capacity. To realize an ultra-high capacity transmission system using the multi-core fiber, a compact integrated fan-in/fan-out device is required for the massive connection. Thus far, several fan-in/fan-out devices such as 3-d waveguide fabricated by ultra-short-pulse laser inscription,[3] tapered MCF connector,[4] thin-fiber bundle type fan-out,[5] grating coupler on Si waveguide[6] and lens coupling apparatus[7] have been reported. However, waveguide-type fan-out devices with mass-productivity, scalability for dense MCFs and the possibility of integration with other waveguide devices have not been reported.

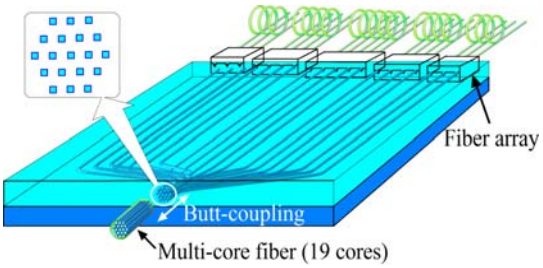


Fig. 1: Schematic view of LPW fan-out device.

In this review, fabrication technologies and device performance of 3-dimentional waveguide fan-in/fan-out device are introduced.

Fabrication

Figure 2 illustrates the fabrication process of the Laminated Polymer Waveguide (LPW). First, the bottom cladding layer is fabricated by the spin-coating and UV-curing of epoxy resin. The epoxy resin is a solvent-free oligomer supplied by NTT-AT. Since the oligomer does not shrink after UV curing, the top surface of the cladding layer can be flattened even if the bottom surface involves the core ridge as shown Fig. 2(c). Then, the core layer is fabricated by the spin-coating of PMMA solution. Here, a polyvinyl alcohol (PVA) layer and another resin layer are formed for the lift-off process. Next, the waveguide pattern is formed by photolithography using a silicone-based photo-resist (FH-SP3CL by Fujifilm) and RIE using O_2 gas. Finally, the mask layer is removed by the lift-off process using water. Then, these steps were repeated to form a multilayer waveguide.

Experimental results

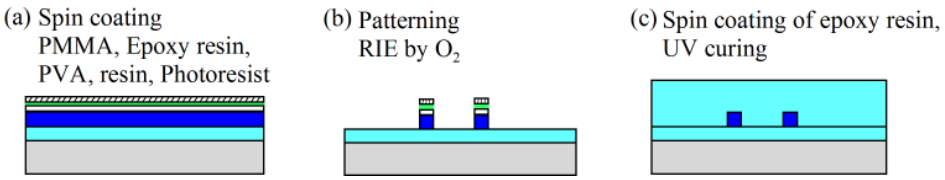
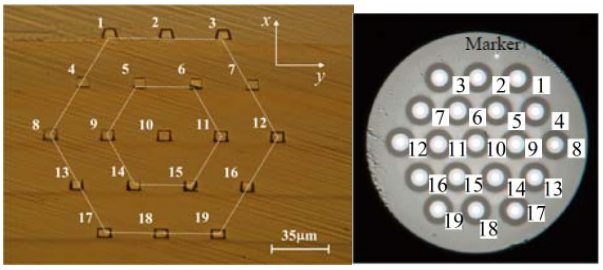


Fig. 2: Fabrication process of laminated polymer waveguide (LPW).

Figure 3(a) and (b) show the cross sectional microscopic images of the fabricated 19-core LPW fan-in/fan-out device and 19-core fiber[8] (supplied by Furukawa Electric Co., Ltd). The cores with the same number were butt-coupled. The core spacing of the multi-core fiber is 35.0 μm and the mode field diameter ranges from 9.56 to 9.85 μm.

First, to asses the coupling loss caused by the offset of core axis and spot sizes (half of MFD) mismatch, the offset loss characteristics were measured. Next, the spot sizes of respective cores of the LPW were evaluated from the measured offset loss characteristics[9]. Then, the spot size mismatch loss and the offset loss were calculated separately from the evaluated spot sizes. In addition, the index contrast Δ of the cores were evaluated by the spot sizes in *x* and *y* directions. The calculated results of the spot size mismatch loss, the offset loss and index contrast of 19 cores are summarized in Fig. 4. The coupling loss was as low as 0.2 - 1.8 dB from the fan-in device to 19-core MCF. The evaluated index contrasts were much smaller than designed value of 0.4%.



(a) LPW fan-in device (b) Multi-core fiber[8]

Fig. 3: Cross-sectional microscopic images

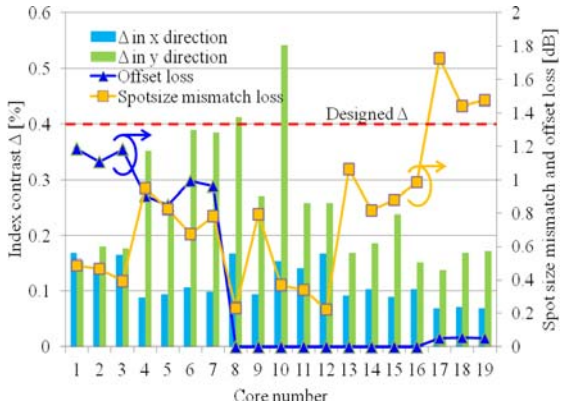


Fig. 4: Evaluated coupling losses and index contrast

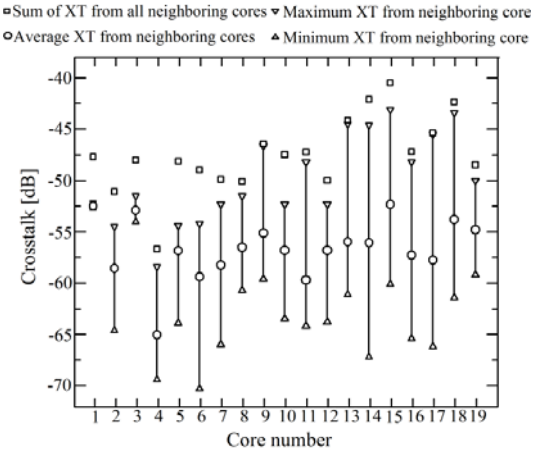


Fig. 5: Measured crosstalk of nineteen cores

Figure 5 shows the measured crosstalks of nineteen cores of fabricated LPW fan-in/fan-out device. In the worst case, the total crosstalk from 6 neighboring cores was less than -40 dB.

Conclusion

The fabrication technique of 3-dimensional multilayer waveguide is promising to not only the fan-in/fan-out devices but also mode multi/demultiplexers for mode division multiplexing. The fabrication error of index contrast will be improved by a careful investigation of UV curing condition and the synthesis process of oligomer material.

Acknowledgement

The authors would like to express their sincere thanks to Dr. M. Hikita of NTT Advanced Technologies Corp. for fruitful discussion. This work was supported by the National Institute of Information and Communication Technology (NICT), Japan.

References

1. T. Morioka, *OECC2009,* FT4 (2009).
2. M. Koshiba, K. Saitoh, Y. Kokubun *ELEX* **6**(2), pp. 98–103 (2009).
3. R. R. Thompson *et al*., *Opt. Express* **15**(18), pp. 11691-11697 (2007)
4. B. Zhu, *et al, Opt. Express* **18**(11), pp.11117-11122, (2010).
5. K. Watanabe, T. Saitoh, K. Imamura and M. Shiino, *OECC2012,* pp475-476 (2012)
6. C. R. Doerr *et al., Photon. Technol. Lett.* **29**(9), pp 597-599 (2011).
7. Y. Tottori *et al., Photon. Technol. Lett.* **24**(21), pp 1926-1928 (2012).
8. K. Imamura, *et al., IEEE Summer Top. Meet. Ser.*, pp 208-209 (2012).
9. T. Watanabe, M. Hikita and Y. Kokubun, *Opt. Express* **20**(24), pp 26317-26325 (2012).

Selectively formed spot-size converters for efficient coupling in graphene-integrated silicon photonics

Y. Kobayashi [1], K. Warabi [1], R. Kou [1,2,3], H. Nishi [2,3], T. Tsuchizawa [2,3], T. Yamamoto [3], K. Yamada [2,3] and H. Nakajima [1]

[1]Gradutate School of Advanced Science and Engineering, Waseda University. 3-4-1, Okubo, Shinjuku-ku, Tokyo 169-8555, Japan
[2]NTT Nanophotonics Center, 3-1, Morinosato Wakamiya, Atsugi, Kanagawa 243-0198, Japan
[3]NTT Microsystem Integration Laboratories, 3-1, Morinosato Wakamiya, Atsugi, Kanagawa 243-0198, Japan
uwr45@ruri.waseda.jp

Abstract: We demonstrate an improvement of coupling efficiency between an optical fiber and graphene-integrated silicon photonics circuit. Selectively formed spot-size converters (SSCs) enable low coupling losses of 1.4 and 2.4 dB/facet for TE and TM modes at 1550 nm without damaging for the single-layer graphene. We achieved broadband coupling from 1300 to 1650 nm. The result maximizes the potential of graphene such as its perfect wavelength independence. Finally, we demonstrate the reductions of coupling loss and ripples by integrating the SSCs on a graphene integrated silicon-ring resonator.

1.! Introduction

Silicon- and graphene-integrated optical devices have recently attracted much attention because graphene has extremely high optical absorption, wavelength independence and high optical nonlinearity [1]. The most well-known silicon- and graphene-integrated optical devices are modulators [2], and photodetectors. However, graphene devices have seriously low coupling efficiency due to the difficulty of depositing SiO_2 on graphene, which is easily affected by oxygen plasma and mechanical stress. Air-cladding two-dimensional grating couplers have been applied to avoid these problems, but high coupling loss (about 3-4 dB/facet for TE and TM modes) and strong wavelength dependence (about 60 and 40 nm in TE and TM modes for 3-dB roll off) are still concerns [2,3]. Therefore, the distinctive feature of wavelength independence in graphene is totally counteracted. On the other hand, we have developed an air-cladding edge coupler to obtain a broadband coupling, but the losses were very high (7.5 and 15.5 dB/facet for TE and TM modes) [4], which caused ripples between input and output surfaces. Thus, we need to enhance the coupling efficiency and broaden the 3-dB spectral bandwidth. In this paper, we propose spot-size converters (SSCs) with selectively formed SiO_2 film for graphene-integrated optical-electrical circuits and bio-chemical sensors.

2.! Design and fabrication

Fig. 1 shows a schematic view of an SSC. We selected three tip widths of 150, 200 and 250 nm to investigate the coupling loss with device fabrication. We estimated the coupling loss to be around 1.5-3 dB/facet by simulation. In the fabrication, we formed a silicon waveguide and inversed-taper waveguide with 400 and 150-250 × 200 nm cores by electron-beam lithography and reactive ion etching on a 4-inch silicon-on-insulator (SOI) wafer. Next, we spin-coated PMMA on single-layer graphene, which had been grown on Cu substrate, and then, after Cu etching, fabricated the graphene pattern on a silicon waveguide. The detailed graphene fabrication process is described in our previous report [4]. Finally, we formed a high-aspect-ratio negative resist on the wafer to avert causing damage to the graphene, and SiO_2 was deposited by electron-cyclotron-resonance chemical-vapor-deposition (ECR-CVD). As a result, a selective overcladding is fabricated on the coupling part after the lift-off process. Fig. 2 shows a schematic view of the device we fabricated and scanning electron microscope (SEM) image. Almost perfect separation can be seen as a boundary between the SSC and graphene integration part.

3.! Devices characteristics

First, we confirmed that our fabrication process didn't cause any remarkable damage to the transferred graphene by μ-Raman spectroscopy. Next, we performed optical spectral measurement in

the SSCs. Fig. 3 shows the spectra for tip widths of 150, 200 and 250 nm in (a) TE and (b) TM modes, acquired by using super luminescent diodes (SLDs). We obtained almost flat coupling properties for each tip width. At tip width of 200 nm, we observed broadband coupling of about 350 and 300 nm in TE and TM modes for 3-dB roll-off and the minimum coupling losses are 1.4 and 2.4 dB/facet at 1550 nm. These coupling losses are approximately 20% for TE and 14% for TM modes, as compared with our previous devices. Toward upcoming applications of graphene-integrated optical-electrical circuits and bio-chemical sensors, we integrated the SSCs onto a graphene integrated silicon-ring resonator which was measured without selective formed SSCs [5]. In this paper, we formed the SSCs in the device to confirm the coupling efficiency improvement. The silicon-ring resonator has a radius of 10μm and a 250-nm gap at the in and out directional couplers, and the graphene integrated on the left side of the ring is 5-μm long and 3-μm wide. A narrow bandwidth tunable laser diode and storage photodetector with a resolution of 1 pm was adopted to clarify the detailed spectral response in the TE mode. Fig. 4 compares spectral transmittance with and without SSCs of graphene-integrated silicon-ring resonators, and inset shows the device schematic. The peak transmittance improved about 10 dB, and resonance ripples are clearly suppressed by integrating SSCs.

4.! Conclusion

With a selective overcladding and inverse-taper waveguide formed on a graphene-integrated Si photonics platform, we demonstrated low coupling losses (1.4 and 2.4 dB/facet for TE and TM modes) and broadband coupling (over 350 and 300 nm in TE and TM modes) without causing damage to the single-layer graphene. We believe that our approach can contribute to future applications of graphene-integrated Si photonics.

References

1.!F. Bonaccorso *et al*., "*Graphene photonics and optelectronics," Nat. Photon*. **4**, pp. 611-622 (2010)
2.!M. Liu *et al*., " *A graphene-based broadbanf optical modulator," Nat. Photon.* **474**, pp. 64-67 (2011)
3.!Z. Cheng *et al*., "*Spectral hole burning in silicon waveguides with a graphene layer on top," Opt. Lett.* **38**, pp. 1930-1932 (2013)
4.!R. Kou *et al*., "*Characterization of optical absorption and polarization dependence of single-layer graphene integrated on a silicon wire waveguide," Jpn. J. Appl. Phys.* **52**, pp. 06203 (2013)
5.!R, Kou *et al*., *"Influence of graphene on quality factor variation in a silicon ring resonator," Appl. Phys. Lett.* **104**, pp. 091122 (2014)

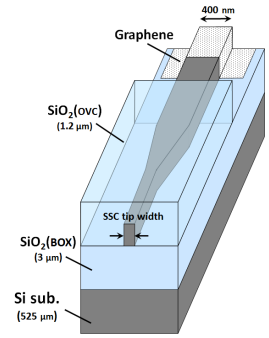


Fig. 1: Schematic view of selective SSC.

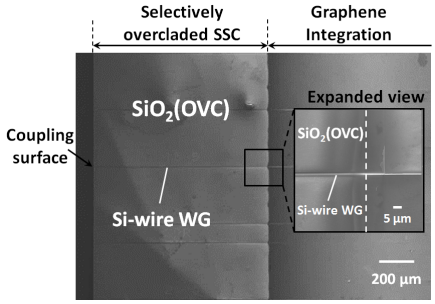


Fig. 2: Scanning electron microscope image of selective integrated part.

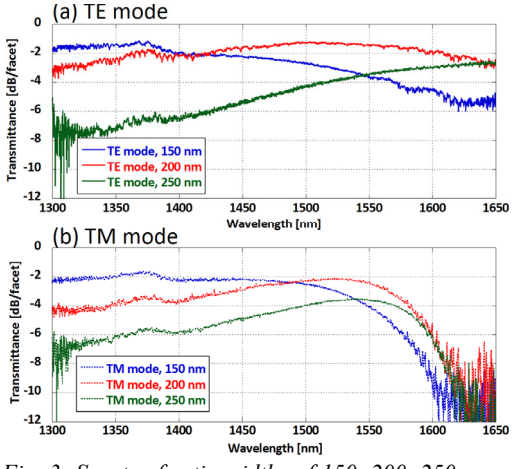


Fig. 3: Spectra for tip widths of 150, 200, 250 nm in (a) TE and (b) TM modes.

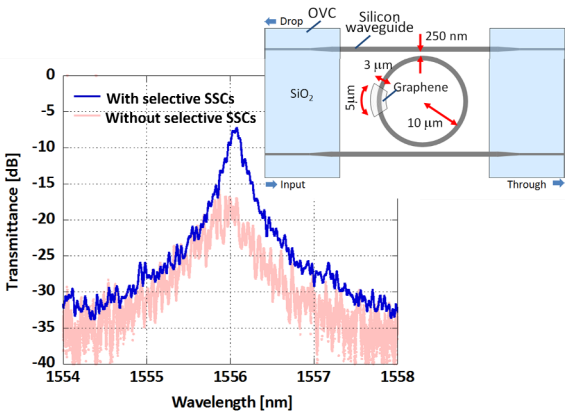


Fig. 4: Comparison of graphene integrated silicon-ring resonators for supression of ripples, and inset is the schematic.

Scattering-related crosstalk in photonic waveguides

D. Melati[1], F. Morichetti[1], G. G. Gentili[1], M. Baier[2], F. M. Soares[2], A. Melloni[1]

[1] *Dipartimento di Elettronica, Informazione e Bioingegneria, Politecnico di Milano, via Ponzio 34/5, Milano*
[2] *Fraunhofer Heinrich Hertz Institute, Berlin, Germany*
daniele.melati@polimi.it

Abstract: A comprehensive analysis of the crosstalk between integrated photonic waveguides generated by roughness-related scattering is presented. A power-law dependence on the waveguide distance is demonstrated, confirmed also by simulations performed with a specifically developed model based on the volume current method.

In the near feature, integrated optics will face a challenging request for larger scale of integration, with the necessity to increase the number of components per unit area of the chips. Crosstalk phenomena will hence become a real limiting factor, eventually compromising the functionality of densely integrated circuits[1]. In particular for high-index-contrast technologies, a source of crosstalk can be represented by the power leakage generated by sidewall roughness[2]. Part of the scattered light can reach a nearby waveguide, causing an unwanted optical power exchange between ideally uncoupled waveguides[3]. In this work we present an experimental characterization of the properties of roughness-induced optical crosstalk in photonic waveguides, demonstrating the emergence of a radiative regime able to support a coupling also beyond the effects of evanescent coupling. The exploited test structure is represented in Fig. 1(a). The device is formed by a S-shaped waveguide comprised between ports A and B (direct waveguide) with a second 3-mm-long straight waveguide (adjacent waveguide) running parallel at a gap distance g and defining the coupling section. Gaps between 2 µm and 30 µm have been considered. The aspect ratio between input port A and output port B is 6 mm × 100 µm and the shape of the device was designed in order to reduce the impact of stray-light generated by the input fibre (port A) on the measured power at ports B and C. Two different waveguides has been considered for the fabrication of the device. The first one, represented in Fig. 1(b), is a shallow etched InP-based rib waveguide with a 1-µm-thick InGaAsP core and an etch depth of 600 nm. The second waveguide is a deeply-etched version of the same cross-section (Fig. 1(c)), with an etch depth of 1.7 µm. In both cases the waveguides are 2 µm wide.

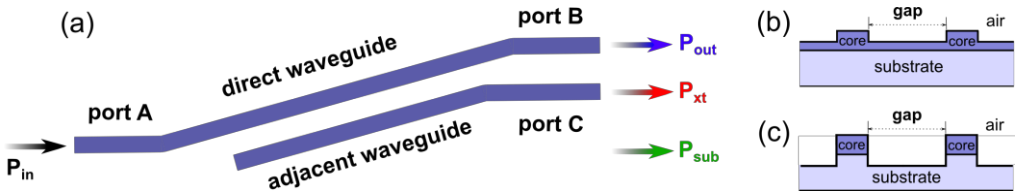


Fig. 1: (a) Design of the test structure exploited for the experimental characterization of the radiative optical crosstalk. Two different cross-sections have been used for the devices: (b) shallow and (c) deeply etched InP-based waveguides.

For all the fabricated structures, the crosstalk was measured coupling light at port A (P_{in}) and measuring the average power at port B (P_{out}) and C (P_{xt}) as function of the gap g. The normalized power $P_{xt}/(P_{xt}+P_{out})$ represents the crosstalk from the direct to the adjacent waveguide. Results for TE polarized light are reported in Fig. 2(a) and 2(b) for the shallow and deeply etched waveguide cross-sections, respectively. In both cases the dynamic range of the measurement is limited by the presence of substrate modes excited by the input fibre and propagating throughout the chip. The power P_{sub} (green squares) carried by these modes was measured laterally shifting the output fibre 50 µm far from port C. For the shallow etched waveguide, the crosstalk is as high as -3dB at g = 2 µm and drops to less than -40 dB at g = 30µm. In order to evaluate the contribution of the pure evanescent coupling to the power transfer between the waveguides, the test structure was simulated with a commercial electromagnetic simulator based on the Film Mode Matching (FMM) method[4] for perfectly smooth sidewalls. Simulation results are shown in Fig. 2(a) with blue and black lines for ports B and C, respectively, and allow to identify different coupling regimes. Evanescent coupling well explains the

-3 dB crosstalk measured at g = 2 μm while, for larger gaps, the measured power coupling largely exceeds the results of the simulations, suggesting the presence of a contribution arising from the roughness-related scattering. For g = 3 μm the device works in an intermediate regime, where the measurements show a power coupling 5 dB higher than the simulated evanescent coupling. For $g \geq$ 5μm only radiative coupling mechanism occurs. Radiative coupling decreases versus distance g with a much slower scaling law than the exponentially decaying evanescent coupling, exhibiting a power-law dependence g^{-x} on the gap distance, with x ≈ 2.8 for the structure under consideration. To support this result, we developed a model to evaluate the expected radiative crosstalk between two parallel waveguides. The model is based on volume current method[5], where roughness on both waveguides is modeled as an array of dipoles. In the direct waveguide the array is excited by the propagating guided mode, generating a radiation field that is collected by the dipoles of the adjacent waveguide. This second dipole array produces itself a scattered field exciting a guided mode in the adjacent waveguide. The results obtained through this model (red dashed line in Fig. 2(a)) well match experimental data, thus confirming the g^{-x} scaling law of the radiative crosstalk versus gap distance (with x ≈ 2.8). For the deeply-etched waveguides of Fig. 2(b), optical crosstalk effects are reduced of more than 15 dB compared to shallow etched waveguides. P_{xt} is as low as -25 dB at g = 2 μm and it drops below the substrate power level (about -35 dB) for a gap distance g > 2 μm. Interestingly, the substrate power level is the same in both cases. Because of the tight confinement of the optical mode in the waveguide, the contribution due to pure evanescent coupling (black line) can be neglected in all the measured structures, so that the weak power transfer between the two waveguides is entirely related to radiation effects. Also in this case the g^{-x} scaling law (x ≈ 2.8) holds well, at least for g ≤ 3 μm. Beyond this limit, substrate modes become predominant, with a contribution P_{sub} independent on the gap distance.

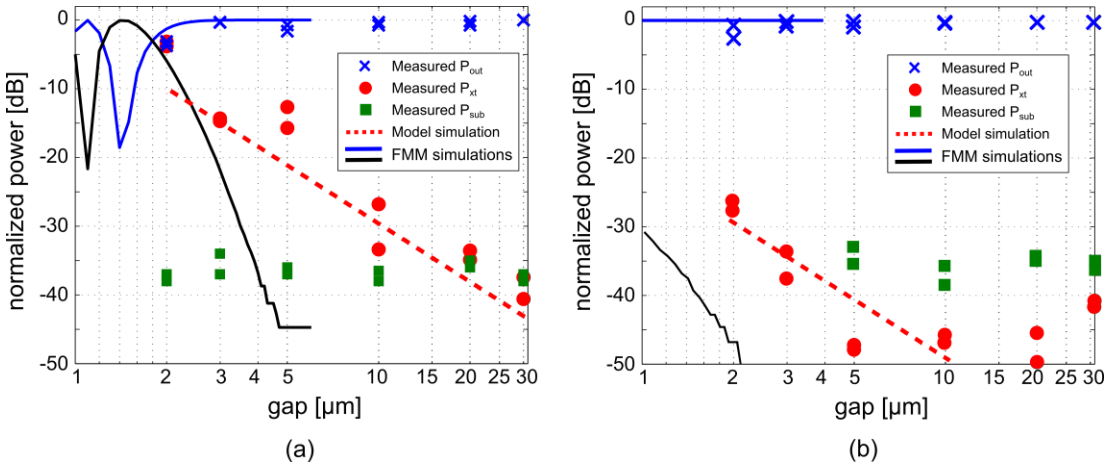


Fig. 2: Power crosstalk as function of the gap between parallel waveguides for (a)shallow and (b) deeply etched waveguides. Both P_{out} (blue crosses) and P_{xt} (red dots) have been measured and compared with FMM simulations of the evanescent power coupling (blue and black solid lines). In both cases, the presence of substrate modes (green squares) limits the dynamic range of the measurement. For shallow etched waveguides, radiative crosstalk shows a power-law dependence on the waveguide distance, confirmed also by the simulations performed with the developed model (red dashed line).

This work was partially supported by the European Community's Seventh Framework Programme FP7/2007-2013 under Grant ICT 257210 (PARADIGM).

References

1. J. Powelson, W. Feng, S. Lin, R. J. Feuerstein, D. Tomic, *Journal of Lightwave Technology* **16** (1998)
2. F. Morichetti, A. Canciamilla, C. Ferrari, M. Torregiani, A. Melloni, and M. Martinelli, *Phys. Rev. Lett.*, **104** (2010)
3. D. Marcuse, *Bell System Technical Journal*, **50** (1971)
4. FIMMWAVE by Photon Design, http://www.photond.com
5. T. Barwicz, H. Haus, *Journal of Lightwave Technology*, **23**, (2005)

Interleave-chirp arrayed waveguide grating on InP generic technology

B. Gargallo[1] **and P. Muñoz**[1,2]
[1]Universitat Politècnica de València & [2]VLC Photonics S.L.
c/ Camino de Vera sn, 46022 Valencia, Spain
pmunoz@iteam.upv.es

Abstract

In this paper the design, fabrication and characterization of an Interleave-chirp Arrayed Waveguide Grating on generic InP technology is reported. The device operates for two wavelength channels spaced 0.8 nm, with a chirp pattern of P=4, unfolding the operation in each wavelength channel to 4 different phases and 2 polarizations, and a free spectral range of 3.2 nm. Polarization splitting is attained through birefringent waveguide cross-sections in the IC-AWG arms. The results show excellent match on the channel spacing, free spectral range, and close to designed targets on the birefringence.

I. Introduction

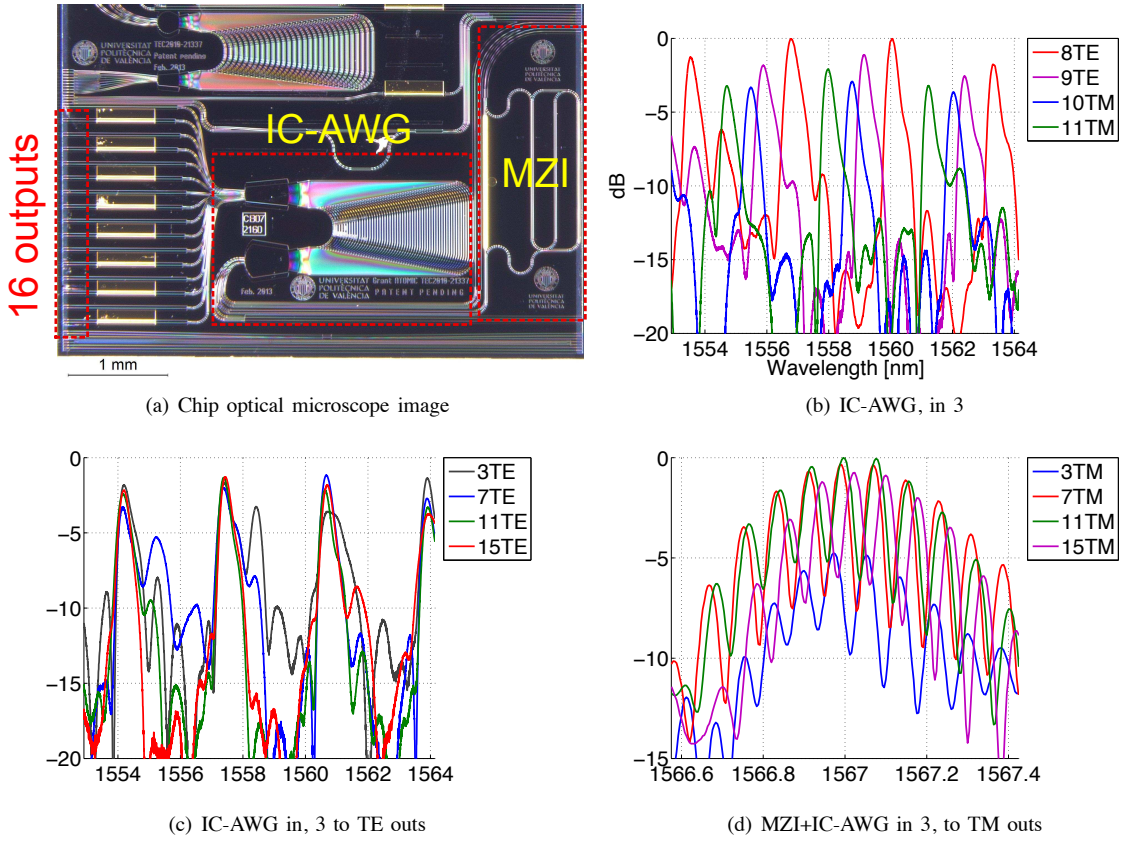
Coherent optical communications have revived in the recent years [1] and high performance photonic integrated circuits (PICs) with real-time operation at aggregate speeds of up to 500 Gb/s have been demonstrated [2]. Currently, the core of integrated optics based coherent receivers are Multi-Mode Interference (MMI) couplers, designed to operate as 90° hybrids. Similar to conventional Intensity Modulated Direct Detection (IM-DD) systems, Wavelength Division Multiplexing (WDM) has been recently brought into PICs for coherent optical communications. The natural combination of on chip demultiplexers, as the Arrayed Waveguide Grating, and optical MMI 90° hybrids have been demonstrated in [2], whereas off-chip optical polarization splitters are used to feed the PIC. Nonetheless, the solution demonstrated by Doerr e.a. [3], in a custom Indium Phosphide (InP) technology platform, in which the AWG arms are modified to enable three fold operation (demultiplexer, polarization splitter, 90° hybrid), is envisaged as the most compact solution for these future on-chip architectures. This device is named Interleaved-Chirp AWG (IC-AWG). In this paper we report on the fabrication of a IC-AWG coherent receiver on generic InP technology.

II. Design, fabrication and characterization

The IC-AWG was designed for the InP technology of JePPIX at the COBRA fab [4]. The technology enables the integration of passive waveguides and active areas, for amplifiers and photo-detectors, on the same chip using a butt-joint regrowth integration scheme. For the design, we followed our methodology described in [5]. Design parameters for the IC-AWG are chirp parameter P=4, channel spacing 0.8 nm, 16 outputs -i.e. 2 wavelength operating channels, P=4 phase relations, and 2 polarizations, TE and TM-, and FSR of 3.2 nm. This resulted in a slab coupler focal length of 384.6 μm, arm length increment of 51 μm, grating order m=107. The waveguides in the array to slab interface were spaced by 2.75 μm, and the curvature radius was 162 μm. The arm waveguide width to attain a birefringence of 1.6 nm, was 2.1 μm on a deeply etched cross section [4]. The chirp pattern was $\{0, 3\pi/4, 0, -\pi/4\}$. The center wavelength was set to 1550 nm. Therefore, each sub-array had a small base incremental length according to this wavelength and the chirp pattern [5]. No optimizations for the i/o waveguides regarding aberrations were done. An auxiliary 2x2 Mach-Zehnder interferometer (MZI) was connected to the input of the IC-AWG, in order to asses on the phase relations of the sub-arrays, similar to [6] for MMI-based 90° hybrids. The MZI has a length increment between arms of 8.124 mm, corresponding to a FSR of 80 pm. The two outputs of the MZI were connected to input positions of the IC-AWG separated corresponding to a spectral separation of the FSR. A microscope picture of the fabricated device is shown in Fig. 1-(a).

The chip was soldered to a submount, that was placed on top of a holder. A temperature controller (TEC) was used to keep the sample at 25° C during the experiments. Light was coupled in/out the chip using edge coupling with lensed fibers. An optical broadband source was used as input, and output traces were recorded with an Optical Spectrum Analyzer (OSA) with 10 pm resolution. All the spectral traces shown are normalized to the maximum value of all traces in the same graph.

Firstly, in order to asses on the birefringence of the IC-AWG arm waveguides, the spectra of 4 consecutive outputs, 8, 9 for TE and 10, 11 for TM, was recorded. The result is shown in Fig. 1-(b). The results show the channels for the same polarization are correctly spaced 0.8 nm as per design. Starting at channel 8TE and looking to shorter wavelengths, channel 10TM should be placed by design at 1.6 nm away, however it appeared at 1.2 nm, confirming the birefringence designed does not match the obtained after fabrication. The obtained FSR is 3.2 nm.



(a) Chip optical microscope image

(b) IC-AWG, in 3

(c) IC-AWG in, 3 to TE outs

(d) MZI+IC-AWG in 3, to TM outs

Fig. 1. Optical microscope image of the fabricated device (a) spectra of 4 consecutive channels to illustrate the birefringence (b), IC-AWG TE outputs (c) and MZI+IC-AWG TM outputs (d).

Secondly, in order to check the interleave-chirp operation, the spectra of 4 outputs spaced the chirp interval P=4 was recorded, i.e. 3, 7, 11 and 15, for TE polarization. The result is shown in Fig. 1-(c). As per design, the same wavelength range is collected at all the outputs. Nonetheless, severe pass-band degradation is observed for channels 3, 7. We attribute this to a very aggressive design, i.e. very narrow channel spacing (0.8 nm) and to the fact no i/o position corrections were done to account for optical aberrations [7] for the present large slab coupler aperture obtained layout. Analog results are obtained for TM, as shown in (d).

Finally, to asses on the phase relations of the IC-AWG, the spectra for a group of 4 outputs spaced the chirp interval P=4 was recorded, but using as input to the IC-AWG the MZI, instead of a directly connected waveguide from the chip facet. The results are shown in Fig. 1-(d). Phase relations are not the designed ones (90,0,180,270). We attribute this either to phase errors in the sub-arrays, or to imprecision's during measurements due to the fact the small FSR MZI (80 pm) might drift between the time required to reposition the output lensed fiber, albeit we are using a TEC.

III. Conclusion

In conclusion we report on the experimental demonstration of an Interleave-Chirp Arrayed Waveguide Grating on generic InP integration technology. The device feature a chirp pattern P=4, 16 channels, with 0.8 nm channel spacing, and had a targeted birefringence of 1.6 nm, therefore allowing to process simultaneously 2 optical channels, with 4 phase relations and 2 polarizations each. The birefringence obtained after fabrication was 1.2 nm. Some channels exhibit considerable pass degradation, that may be corrected using less aggressive layouts and i/o waveguide position corrections to minimize optical aberrations. The transfer function of the joint MZI+IC-AWG allowed to check the different phases provided by each sub-array in the IC-AWG. Finally, we acknowledge funding from the MINECO TEC2010-21337 & TEC2013-42332-P, FEDER UPV 10-3E-492 & 08-3E-008 and FPI BES-2011-046100.

References

[1] K. Kikuchi, in High Spectral Density Optical Communication Technology, Chap. 2, Springer (2010).
[2] R. Nagarajan e.a., Semiconduct. Science and Tech. **27,** 094003 (2012).
[3] C. R. Doerr, L. Zhang and P. J. Winzer, J. Ligthwave Technol. **29,** pp. 536–541 (2011).
[4] E. Bente and M.K. Smit, in Integrated Optoelectronic Devices, pp. 612419-612419 (2006).
[5] B. Gargallo and P. Muñoz, Optics express, **21**(6), pp. 6928–6942 (2013).
[6] L. Zimmermann e.a., IEEE Photon. Technol. Lett, **21**(3), pp. 143–145 (2009).
[7] G. Beelen and H.F. Bulthuis, Gemfire Corporation, US Patent 7,492,991, (2007).

VCSEL -Its History and Prospects for Green Microoptics-

Kenichi Iga
Tokyo Institute of Technology, Emeritus Professor
kiga@vcsel.org

Abstract - *In this talk, we will revie wthe history and the progress of VCSEL technology covering the spectral band from infrared to ultraviolet by featuring materials and fabrication technology. Performances such as threshold, output power, polarization, modulation and reliability are introduced. Lastly, we will touch on its future prospects fro green microoptics for ICT.* **Keywords:** VCSEL, microoptics, green ICT, array, computer mouse, laser printer

I. INTRODUCTION

The vertical cavity surface emitting laser (VCSEL) as shown in Fig. 1 is a popularly known semiconductor laser that can be monolithically fabricated. The present author suggested the device of VCSEL in 1977 [1]. The first device came out in 1979 [2], where we used a 1300nm wavelength GaInAsP/InP material for active region [3]-[5]. VCSELs based on GaAs have been extensively studied[3]-[5]. The first room temperature continuous wave (CW) device using GaAs material was demonstrated in 1988 .

II. DEVICE PHYSICS AND SCALING LAW

The structure common to most of VCSELs consists of two parallel reflectors which sandwich a thin active layer. The reflectivity necessary to reach the lasing threshold should normally be higher than 99.9 %. Together with the optical cavity formation, the scheme for injecting electrons and holes effectively into small volume of active region is necessary for current injection device. The VCSEL structure may provide a number of advantages explained laser [3][4].

A. Threshold Current

The threshold current I_{th} of surface emitting lasers and common to semiconductor lasers, in general, can be expressed by the expression [3];

$$I_{th} \propto V_a \qquad (1)$$

where V_a is the volume of active region.

As seen from this expression, we recognize that it is essential to reduce the volume of active region in order to decrease the threshold current. Assume that the threshold carrier density does not change so much if we reduce the active volume, we can reduce the threshold until we meet an increase of diffraction loss and diffusion of carriers. When we compare the dimensions of surface emitting lasers and conventional stripe geometry lasers, it is noticeable that the volume of VCSEL's could be V=0.06 μm^3, whereas that for stripe lasers remains V=60 μm^3. This directly reflects the threshold currents that the typical threshold of stripe lasers is ranging tens of mA or higher, but that for VCSEL's is able to be less than sub-mA by a simple carrier confinement scheme such as AlAs oxidation. It could be even as low as several ten micro-Amperes by implementing sophisticated carrier and optical confinement structures.

B. Modulation Bandwidth

The 3dB modulation bandwidth is given by [3];

$$f_{3dB} \propto \sqrt{1/V_a}$$

The modulation frequency is inversely proportional to the square root of active volume and it can be larger, if we can reduce the volume as small as possible. Dynamic single mode operation is maintained due to the large mode separation coming from short cavity length of VCSEL's. Wide frequency tuning range is based on the same reason. Due to these physics the VCSEL may provide a number of **advantages** shown below [3];



Fig. 1 A sketch of vertical cavity surface emitting laser (VCSEL) [1].

a) Ultra-low threshold operation is expected from its small cavity volume.
b) Dynamic single mode operation.
c) Wide and continuous wavelength tuning.
d) Large relaxation frequency even at small driving current.
e) Easy coupling to optical fibers.
f) Monolithic fabrication and easy device separation without perfect cleaving requirement.
g) Vertical stack integration by MEMS technology.
h) 2D arrayed configuration.

III. TECHNICAL PROGRESS

Possible choices and technology of semiconductors have been extensively studied for quantum wells and mirror formation, and current confinement scheme. An AlAs oxidation is considered to be the most effective process to perform it.

VCSELs based on GaAs have been extensively studied [1]-[4]. The first room temperature continuous wave (CW) device using GaAs material was demonstrated in 1988. Since 1992, some of 980, 850 and 780nm devices were commercialized into lightwave systems [5],[6].

In the author's group, some key concepts have been proposed; Quantum-well VCSEL, MQB (Multi-Quantum Barrier), 1,200nm GaInAs/GaAs VCSEL, modulation

schemes, phased array VCSEL, Talbot cavity VCSEL, tunneling injection, tandem VCSEL, and so on [5],[6].

Some value-added technologies have been considered such as; continuous tuning, temperature insensitive wavelength (zero temperature coefficient), coherent array (Talbot cavity), MEMS integration, phased array, beam steering, high frequency modulation (>40GHz), hollow-waveguide integration (modulator/slow-light), and nearly unity spontaneous emission factor.

IV. PROSPECT

In Table I, we show possible application areas of VCSELs . The VCSEL itself is basically an exploratory device and generated Gigabit Ethernet and fiber channel applications[5]. It is emerging into higher class of data communication system such as 10 Gigabit Ethernet, high speed LAN's, optical interconnects, optical links, and so on. Moreover, long wavelength VCSELs have been developed toward long distance metropolitan area networks (MAN's). It is noted that continuous and wide range wavelength tunability is a viable solution among many other candidates for this purpose. The VCSEL has been contributing to '**Green ICE**' technology in various aspects by featuring low power and high speed performances. Optical interconnect of LSI chips and circuit boards and multiple fiber systems like in super-computers and PC's is the most interesting field related to VCSELs. Also, VCSEL-based photonics opened up various fields such as laser printers, computer mice, optical sensors, and so on. The arrayed microoptics technology [5] will be very useful for advanced systems.

The concept of VCSEL has been expanded into nano-photonics and photonic crystal field. The ultra-parallel and ultra-high speed photonics based upon sophisticated VCSELs including MEMS and integrated optics will open up a new era in this century.

Several extended applications have been considered; high power lasers, engine ignition, micro-power lasers, 3-color lasers, organic VCSEL (injection scheme and reflector), blue-green VCSEL, single photon VCSELs, and so on.

The author thanks to Prof. F. Koyama and Lab members for collaborations.

References

[1] K. Iga, Laboratory Notebook, March 22, 1977.

[2] H. Soda, K. Iga, C. Kitahara and Y. Suematsu, "GaInAsP/InP surface emitting injection lasers", Jpn. J. Appl. Phys., vol. **18**, no. 12, pp.2329-2330, December 1979.

[3] K. Iga, F. Koyama and S. Kinoshita, "Surface emitting semiconductor lasers", IEEE J. Quantum Electron., vol. **QE24**, no. 9, pp.1845-1855, September 1988.

[4] K. Iga, "Surface emitting laser-its birth and generation of new optoelectronics field," IEEE J. Select. Top. Quantum Electron., invited paper, vol. **6**, no. 6, pp. 1201-1215, Nov. 2000.

[5] K. Iga, "Vertical cavity surface emitting laser: Its Conception and Evolution", Jpn. J. Appl. Phys., Invited Review, vol.**47**, No. 1, pp.1-10, Jan. 2008.

[6] K. Iga, "Vertical Cavity Surface Emitting Laser (VCSEL)", Proc. IEEE, invited paper, vol. **11**, no. 10, pp. 2229-2232, Oct. 2013.

Table I VCSEL Applications and Systems

Technical Fields	Applications and Systems
1. Optical Communications	LANs, Optical links, Mobile links
2. Computer Optics	Computer link, Optical interconnects, High speed/Parallel data transfer
3. Optical Memory	CD, DVD, Near field, Multi-beam
4. Optoelectronic Equipment	Printer, Laser pointer, Mobile tools, Home appliances
5. Information Processing	Optical Parallel processors processing
6. Optical Sensing	Computer mouse, Fiber sensing, Bar code readers, Encoders
7. Displays	Array and surface light sources, High efficiency light-sources
8. Illuminations	Search-lights, Micro illuminators, Car's head lights
9. Laser Machining	Engine ignition, Manufacturing



Kenichi Iga received the B.E., M.E., and Dr. Eng. degrees from the Tokyo Institute of Technology, in 1963, 1965 and 1968, respectively. From 1968, he joined the P&I Lab., Tokyo Institute of Technology, became Associate Professor in 1974 and Professor in 1984. He retired Tokyo Institute of Technology in March 2001 and was awarded by Professor Emeritus. Dr. Iga joined Japan Society for the Promotion of Science (JSPS) as Executive Director from April 2001 to September 2007. He has been serving as the President of Tokyo Institute of Technology from October 2007 till September 2012. From 1979 to 1980, he stayed at Bell Laboratories as Visiting Technical Staff Member.

Dr. Iga first proposed and pioneered the research of surface emitting lasers and microoptics. He is one of the founders of Microoptics Conference.

Prof. Iga received 1992 IEEE/LEOS William Streifer Award, 2003 IEEE Daniel E. Noble Award, 2002 Rank Prize, 2001 Purple Ribbon Prize from the Emperor of Japan, 2003 Fujiwara Award, 2007 C&C Prize, and 2009 NHK Broadcast Cultural Award. In 2013, he was awarded by **Franklin Medal** with the Bower Award and Prize in Science.

Design of integrated photonic devices for high-speed coherent receivers

A. Ortega-Moñux[1], D. Pérez-Galacho[1], C. Alonso-Ramos[1], P. J. Reyes-Iglesias[1], R. Halir[1], R. Godoy-Rubio[1], J. G. Wangüemert-Pérez[1], Í. Molina-Fernández[1], R. Zhang[2], P. Runge[2]

[1] Dpto. Ingeniería de Comunicaciones, ETSI Telecomunicación, Universidad de Málaga, Spain, aom@ic.uma.es

[2] Fraunhofer Inst. for Telecommun., Heinrich-Hertz-Inst., Berlin, Germany

Abstract: In this tutorial we will discuss the most relevant aspects of the design of high performance Photonic Integrated Circuits for Dual Polarization Coherent Receivers suitable for 100GbE applications. Specifically, we will focus our attention on two hot topics: polarization diversity management and colorless operation. Practical issues such as technological constraints and tolerance to fabrication errors will also be covered.

As it is well known, the success of new services such as high definition video streaming or cloud computing and storage require an exponentially increase of available bandwidth. At the same time, these services are affected by severe cost constraints (end-user prices must be kept low), so the existing data communication infrastructure must be maintained with minimum changes.

In order to simultaneously satisfy these two requirements (high bandwidth and low cost), a significant increase of the spectral efficiency of existing long-haul fiber optic communication networks is required, since conventional schemes based on OOK intensity modulation with direct detection are limited to 10-40Gbps per optical carrier and the installation of new fiber links is not an option for economic reasons. The widespread solution to improve the spectral efficiency combines the use of coherent multilevel modulations (e.g. QPSK or 16-QAM) with polarization multiplexing to achieve 100Gbps (or even 400Gbps) per optical carrier in 50GHz grid DWDM systems. Fig. 1.a) schematizes the generation of a Dual Polarization QPSK 100Gbps data stream from four 25Gbps data channels.

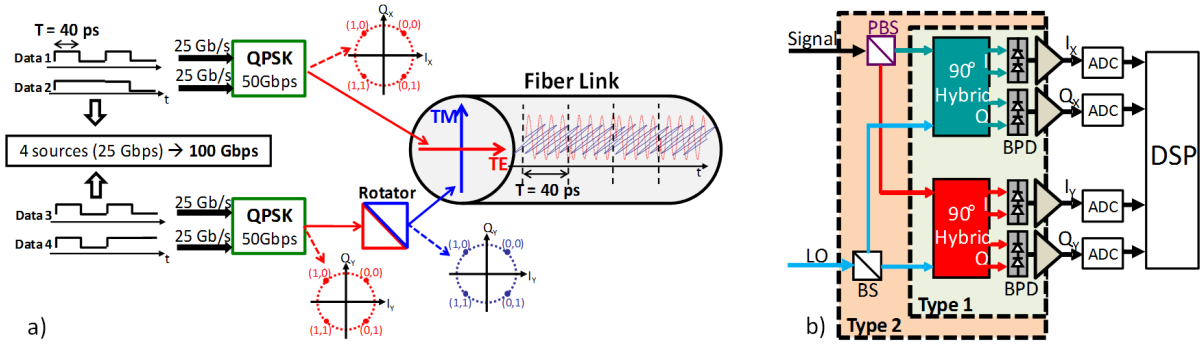


Fig. 1: a) Generation of a DP-QPSK 100Gbps data stream. b) Schematic of an integrated DP coherent receiver.

The first commercially available optical coherent receivers were based on bulk solutions, since the technology of photonic integrated circuits (PIC) was not mature enough. Nevertheless, during the last years a considerable effort has been dedicated to improve integrated solutions and nowadays, commercial products that integrate in a single PIC many of the components of a coherent receiver (e.g. 90º hybrids, Polarization Beam Splitters (PBS), photodetectors, etc.) can be found. Fig. 1.b) shows the functional diagram of an integrated Dual Polarization Coherent Receiver, where two integration levels (Type 1 and Type 2 respectively) have been considered[1]. The most usual approach in commercial products is Type 1, where all the components except the polarization management circuitry are integrated in a single PIC. The PBS is included in the package, but it is implemented in bulk technology and micro-assembled to the chip. On the contrary, receivers of Type 2 are fully integrated solutions where the polarization management circuitry is included, together with the other receiver components, in a single photonic circuit. The fully integrated solution is obviously preferred but it is not widely used in commercial products, since the reduced tolerance to fabrication errors of integrated polarization management devices may decrease the fabrication yield.

In this tutorial we will discuss the most relevant aspects of the design of high performance Photonic Integrated Circuits for Dual Polarization Coherent Receivers suitable for 100GbE applications. Specifically, we will focus our attention on two hot topics: polarization diversity management and colorless operation. Practical issues such as technological constraints and tolerance to fabrication errors will also be covered. For the sake of brevity, we will mainly show results of devices fabricated in InP technology, although the most relevant conclusions of this work can be also applied to other platforms.

Fig. 2.a) shows the widespread implementation of a 90º hybrid in integrated technology. It is composed of a 4x4 multimode interference coupler (MMI 4x4), an optimized output section (four monomode waveguides & two low loss crossings), and two pairs of high speed balanced photodiodes[2]. It must be noticed that the behavior of the 90º hybrid in terms of amplitude and phase imbalance over the complete operation band directly determine the colorless operation of the receiver, so it is worth to spent some time improving the MMI performance.

The design of robust (i.e. highly tolerant to fabrication errors) integrated PBS is a problem that has not yet been fully solved. Fig. 2.b) shows a Mach-Zehnder Interferometer (MZI) PBS fabricated in InP technology[3]. This device is composed of two polarization-independent MMIs and two waveguides with different widths (MZI arms) which exhibit highly dissimilar birefringent behaviors. In this device, active thermal tuning is necessary to compensate the effects of waveguide width fabrication errors. To overcome the drawback of active tuning, a fully passive and highly robust PBS has been recently proposed[4]. In this device, one of the MZI arms is substituted by the waveguide with engineered birefringence drawn in Fig. 2.c). The Si-SiO_2 multilayer structure placed around the core acts as an artificial birefringent material, so the field distributions of TE and TM guided modes (and therefore their propagation constants) are pretty different.

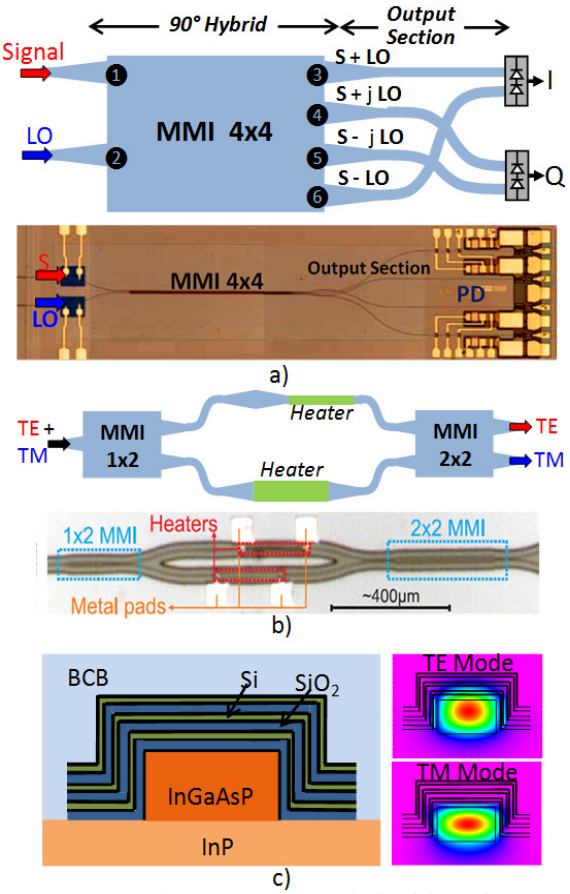


Fig. 2: a) Schematic of a 90º hybrid based on a MMI 4x4 and photograph of a fully integrated coherent receiver fabricated in InP technology[2]. b) Block diagram of a MZI -PBS with thermal tuning and photograph of a fabricated device[3]. c) Geometry of a waveguide with engineered birefringence and mode field profiles[4].

The aforementioned 90º hybrid and the thermally tuned MZI-PBS are the basic components of a fully integrated DP-coherent receiver that fulfill OIF requirements over the complete C-band and allows for reception of data streams up to 224Gbps, which is the highest reported bandwidth for a monolithic coherent receiver[5].

We will finish this tutorial presenting two innovative ideas: a highly tolerant fully passive PBS-less DP-coherent receiver[6] and a broadband colorless receiver based on an integrated 120º hybrid[7].

A significant part of the work that will be shown in this tutorial was developed in the frame of the EU 7th Framework Programme project MIRTHE ICT-2009-5 nº 257980, http://www.ist-mirthe.eu/.

D. Pérez-Galacho is currently at Université Paris-Sud.

References

1. OIF-DPC-RX-01.2 *http://www.oiforum.com/public/documents/OIF_DPC_RX-01.2.pdf*, (2013)
2. R.Kunkel *et al., Indium Phosphide & Related Materials (IPRM), pp. 1-4,* (2010).
3. D. Pérez-Galacho *et al., Journal of Lightwave Technology* **32**, pp. 361-368, (2013)
4. D. Pérez-Galacho *et al., Opt. Express* **21**, pp. 14146-14151, (2013)
5. H. Mardoyan *et al., Optical Fiber Conference Postdeadline Session III (Th5C)*, (2014).
6. C. Alonso-Ramos *et al., Opt. Letters* accepted for publication (2014).
7. P.J. Reyes-Iglesias *et al., Opt. Express* **21**, pp. 23048-23057 (2013).

40 years anniversary of Ti:$LiNbO_3$ and beyond

Hirochika Nakajima

Waseda University, Tokyo, 169-8555 Japan,
chika@waseda.jp

Abstract: This tutorial lecture covers a historical and evolutional developments of Ti:$LiNbO_3$ integrated optics with current status and related future prospects.

Introduction: Ti in-diffused waveguide on $LiNbO_3$ waveguide is one of the most historical player in integrated optics as limited high speed electro-optic device suits to single mode fibers. Ti:$LiNbO_3$ waveguide was first reported in 1974 by I. P. Kaminow et al with Bell Labs.[1] Unfortunately he was lost the last year, however, the devices and basic technologies still survive with several advantages.[2]

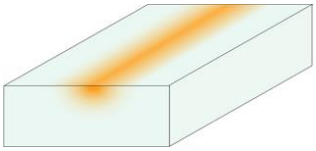


Fig.1 Schimatics of Ti:$LiNbO_3$

History of $LiNbO_3$: Ferroelectric lithium niobate has a pseudo illuminate structure with a trigonal crystal system. 20 years after of its first report in 1928 as a new material, it was successfully grown as a single crystal by flux method in 1949.[3] Then, $LiNbO_3$ and $LiTaO_3$ single crystal of so-called congruent composition without Li/Nb stoichiometric ratio small bowls were first grown by Cz-method in 1965.[4] Both single crystals have been supplied to surface devices mainly for consumer electronics such as oscillators, surface acoustic filters (SAW) and pyro-electric elements until even now evolutionary up to 6" diameter size. On the other hand, at first, their large Pockels coefficients ($r_{33} \cong$ 30 pm/V) and nonlinear optic coefficients were interested for optoelectronic applications with high quality bulk single crystal. However, optical damage and drift problems with high half-wave voltage $V\pi$ up to KV prevented their applications in the real optical fields.

Ti:$LiNbO_3$ as an early integrated optics [5-14]: Since 1974, when we got easy fabrication method to make low-loss single mode waveguides by in-diffusion of Ti on $LiNbO_3$ (not on $LiTaO_3$ with low Tc) wafer around 1000 °C under Curie temperature of Tc ≅ 1130 °C, many reports had done for realization of "integrated optics" not only passive but also functional such as high-speed switch, phase/intensity modulator, TE/TM mode splitter and so on. In the early stage of research period, many types of waveguide structures were introduced; straight line (with curvature), directional coupler (D.C. with perfect coupling length, 3 dB coupling and others), Y-branch, Mach-Zehnder interferometer (MZI) with two Y-branches and arms, balanced bride (B.B.), X or asymmetric-X intersecting. They have relatively large curve radius because of small index change $+\Delta n$ of low Ti-concentration. But, mode size of Ti:$LiNbO_3$ is very close to and single-mode fiber (including polarization maintaining fiber) and they easily couples each other with low loss. And $V\pi$ was dramatically reduced to several volts with appropriate interaction length of electrode and waveguide.

In 1980s, longer wavelength light sources were developed fitting to fiber low-loss wavelength region of (1.3 -) 1.55 μm. This wavelength region is comfortable for Ti:$LiNbO_3$ with high threshold of optical damage, and wider broadband SW/modulators were developed. However, drift problem remained and moreover, pyro-electric induced thermal drift was enlarged on thick dielectric buffer layer putted to compensate lightwave and microwave mismatch with different index caused by large dielectric constant of $LiNbO_3$. Fujitsu group including the author had solved successfuly this thermal drift problem introducing Si coated semi-conducting SiO_2 buffer layer on Z-cut Ti:$LiNbO_3$ in mid 1980s and established first commercially available 10Gbps MZI intensity modulators with automatic bias control for DC drift in 1990. They demonstrated stable operation of fabricated fiber pigtailed package of MZI with hard heat shock test during InterOpto exhibition in Makuhari, Japan for several days in July of the same year. NTT first installed 10 Gbps terrestrial fiber transmission line in early 1990s using this device. TPC-5 undersea cable network also using Ti:$LiNbO_3$ MZI and EDFAs with 5 Gbps was installed in 1996. After then, dense wavelength division multiplexing (DWDM) with AWG (Arrayed Waveguide Grating) and MZI modulators, were rapidly introduced in real fields toward Photonic IT bubble in 2000-2002 as two big players of integrated optics besides of DFB-LDs.

Recent progress of Ti:LibO_3 MZI modulator and applications [15-21] : In mid-2000s after the photonic gracious, digital coherent technologies opened with digital signal processor (DSP). Ti:LiNbO_3 MZI IQ modulators still have important role in them. So-called nested or dual parallel MZI makes not only intensity but also phase of lightwave modulation simultaneously up to multi-QAM. MZI modulators with polarization division multiplexing 100Gbps per λ has been installed in 2012. Compared with other materials of MZI or other principle modulators such as electro absorption (EA), low or less chirp Ti:LiNbO_3 modulators have advantages in long distance transmission. In the other applications out of digital coherent or conventional digital fiber communications, more extinction ratio of MZI is required. Radio over fiber (ROF) is one of the most typical examples. A nested MZI essentially has a potential to get two-tone frequencies with high extinction ratio and effective to even scientific application. However, it has a difficulty of each three MZs individual DC bias control. We recently developed reduced DC bias control at Y-branch of single MZ named active Y-branch to achieve equivalent high extinction ratio. Figure 2 shows a schematic evolution diagram of Ti:LiNbO_3 MZIs starting from a phase modulation by straight line waveguide (1).

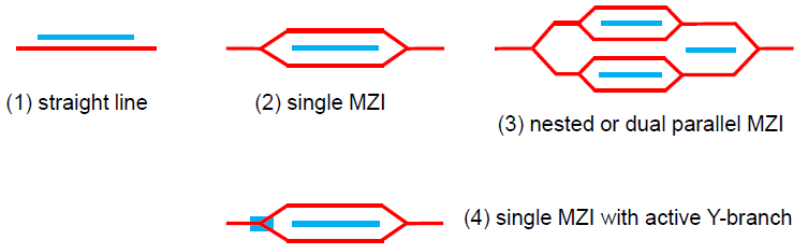


Fig.2 Evolution of Ti:LiNbO_3 MZI modulators

Other LiNbO_3 integrated optics for future possible applications [22-24] : Ti in-diffused waveguide, however, has many disadvantages such as small Δn or weak confinement of guided-wave field. Strong interaction and damage free characteristics are required for non-linear applications. Therefore other structures have been studied except Ti-diffused wavegude. MgO-doping in LiNbO_3 is very effective to reduce optical damage phenomena even in visible wavelength region and various waveguide fabrication technologies have been reported with dry etched rib structure on MgO:LiNbO_3.

Acknowledgements: The author wish to thank his colleagues in Fujitsu and Waseda University. He also thanks to Prof. T. Suhara and member of Microoptics Group in Japan for their encouragements. Present works on active Y-branch studies are partially supported by the National Institute of Information and Communications Technology (NICT) entitled "Agile Deployment Capability of Highly Resilient Optical and Radio Seamless Communication Systems."

References

1. R. V. Schmidt and I. P. Kaminow, *Applied Physics Lett*. 25, pp. 498 (1974).
2. A. Chen and E. J. murphy *edited, "Broadband Optical Modulators", CRC Press* (2012).
3. B. T. Mathias and J. P. Remeika, *Phys. Rev*. **76**, pp. 112 (1949).
4. A. A. Ballman, *J. A. Ceramic Soc*. **48**, pp. 112 (1965).
5. S. E. Miller, *Bell Syst. Tech. J*. **48**, pp. 2059 (1969).
6. H. Kogelnik *et al* , *IEEE J. Quantum Electron*.**12**, pp. 396 (1976).
7. M. Izutsu *et al, IEEE J. Quantum Electron*.**13**, pp. 287 (1977).
8. R. C. Alferness, *IEEE J. Quantum Electron*.**17**, pp. 946 (1981).
9. H. Nakajima *et al, IEEE J. Quantum Electron*.**18**, pp.771 (1982).
10. I. Sawaki *et al, CLEO86, paper MF-2* (1986).
11. M. Seino *et al, ECOC87* **1**, pp. 113 (1987).
12. F. Koyama and K. Iga, *J. Lightwave Tech*. **6**, pp. 87 (1988).
13. H. Nakajima, *IOOC'89* (invited paper) 19D3-3, pp.164 (1989).
14. N. Mekada *et al, Appl. Opt*. **29**, pp. 5096 (1990) .
15. M. Izutsu *et al, IEEE J. Quantum Electron*. **17**, pp. 2225 (1981).
16. R. A. Griffin and A. C. Carter, *Proc. OFC, WX6*, Anaheim, USA (2002).
17. A. H. Gnauck and P. J. Winzer, *J. of Lightwave Tech*. **23**, pp.115 (2005)
18. T. Kawanishi *et al, IEEE J. Sel. Top. Quantum Electron*.**13**, pp. 79 (2007).
19. H. Kiuchi , *et al, IEEE Trans. Microwave Theory Tech*. **55**, pp. 1964 (2007).
20. Y. Ogiso *et al, IEEE Photon. Technol. Lett*., **22**, pp. 941 (2010).
21. Y. Yamaguchi *et al, Proc. ECOC2013, London, UK*, P.2.15 (2013).
22. T. Suhara and M. Fujimura, *"Waveguide Nonlinear-Optic Devices", Springer* (2003).
23. S. Kurimura *et al, Appl. Phys. Lett*. **89**, 191123 (2006)
24. M. Asobe *et al, Opt. Express* **20**, 13164 (2012)

Self-aligned InP polarization converters for monolithic polarization-multiplexed PICs

T. Tanemura, M. Zaitsu, and Y. Nakano

Department of Electrical Engineering and Information Systems, School of Engineering, The University of Tokyo, Tokyo 113-8656, Japan
tanemura@ee.t.u-tokyo.ac.jp

Abstract: We review our recent progress in the development of the half-ridge InP/InGaAsP polarization converters, which can be fabricated by a simple self-aligned high-yield process and monolithically integrated with other active InP components. High polarization conversion efficiency over 96%, low insertion loss below 1 dB, wavelength insensitivity, and monolithic integration with semiconductor optical amplifiers are demonstrated experimentally.

1. Introduction

With the increasing demand for data capacity in the optical networks, use of polarization multiplexing in conjunction with digital coherent technology has become the standard choice for the spectrally efficient long-haul and metro transmission. As 100G dual-polarization quadrature phase shift keying (DP-QPSK) and 16 quadrature amplitude modulation (DP-16QAM) technologies have been developed extensively, there is a growing interest to realize more compact and lower-cost InP-based photonic integrated circuits (PICs) that support polarization-multiplexed signal formats without using bulky optics [1,2]. To this end, simple scheme of manipulating the polarization state inside InP-based PICs is essential.

While various types of InP PC based on asymmetric waveguide structure have been proposed and demonstrated to date [3-6], monolithic integration of PCs with active photonic components, such as laser diodes (LDs) and semiconductor optical amplifiers (SOAs), has been a challenging issue. This is mainly because most of these PCs exhibit relatively large structural mismatch with standard ridge waveguides, which generally leads to large coupling losses. In addition, these schemes often require non-standard fabrication processes, such as slanted dry etching, and/or strict lithographic alignment, which may not be compatible with general LD fabrication procedures.

We have recently proposed and experimentally demonstrated a half-ridge InP/InGaAsP PC, which particularly suits the integration with LDs and other active components owing to its ridge-like structure and simple self-aligned fabrication process [7,8]. In this talk, we review our recent progress in the development of the monolithic InP PCs for polarization-multiplexed PIC applications. In particular, we present our first demonstration of half-ridge InP PCs monolithically integrated with a multiple-quantum-well (MQW) SOA.

2. Half-ridge InP polarization converter

Figure 1 shows the schematic of the proposed half-ridge InP/InGaAsP PC. It exhibits an asymmetric structure, having a shallowly etched ridge profile on one side and a deeply etched high-mesa profile on the other side [7]. Due to the asymmetric cross section, electric and magnetic fields of the two

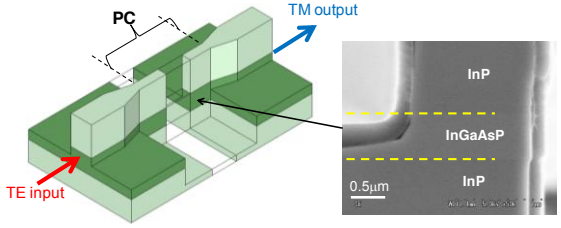


Fig. 1: Schematic of half-ridge InP/InGaAsP PC and SEM image of the fabricated device [8].

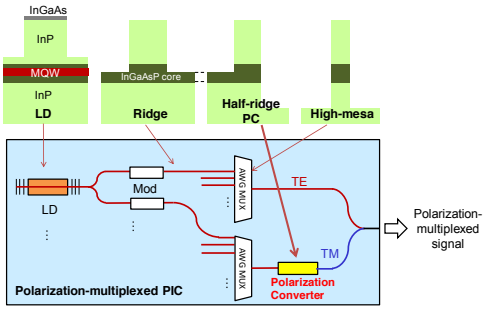


Fig. 2: Schematic of polarization-multiplexed PIC.

lowest-order eigenmodes are tilted from the vertical axis. With a proper choice of the waveguide width and etching depth, these two eigenmodes can be adjusted to have the electric/magnetic field tilted approximately by ±45° [7]. In such a case, incident light with TE (or TM) polarization state excites the two eigenmodes with an equal magnitude. After propagating half a beat length, these eigenmodes recombine into the orthogonal, i.e. TM (TE) polarization state. Owing to the thick InP upper cladding and the half-ridge structure, these modes have large overlap with the TE and TM modes in a symmetric ridge waveguide, which allows low-loss integration with standard ridge LDs and SOAs as shown in Fig. 2.

We have successfully fabricated the half-ridge PCs integrated with symmetric ridge waveguides by using a simple self-aligned high-yield process without the need for any critical lithographic alignment [8]. With a 150-μm-long PC, we have demonstrated TE-to-TM conversion efficiency higher than 96% and insertion loss of less than 1 dB over a broad wavelength range covering from 1510 to 1575 nm. We have also numerically studied the fabrication tolerance of this PC, and demonstrated that it could be extended further by an optimal design [9].

3. Monolithic integration of half-ridge InP polarization converter with SOA

To demonstrate feasibility of monolithic integration with active components, we have fabricated a PIC shown in Fig. 3, where an MQW SOA is monolithically integrated with half-ridge PCs of different lengths (L_{PC}). Fig. 4 shows the measured optical power of the TE and TM components of the output light from two different ports with and without PC. We see that the TE-mode light amplified by the MQW-SOA is effectively converted to TM mode by the PC section. We have thus demonstrated simultaneous emission of both the TE- and TM-mode light from a single InP PIC.

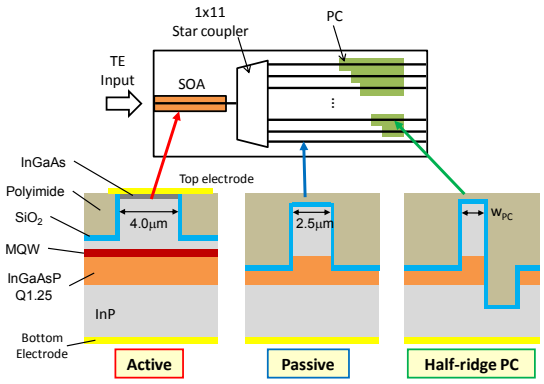


Fig. 3: Schematic of the fabricated PIC with half-ridge PCs and MQW SOA integrated on a single chip.

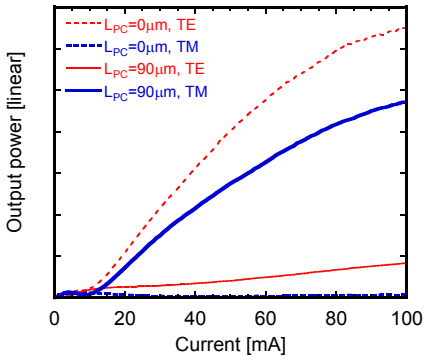


Fig. 4: Measured output power of the TE (red) and TM (blue) components of the light from the ports with PC (solid lines) and without PC (broken lines).

Acknowledgements

This work was supported by the Strategic Information and Communications R&D Promotion Programme (SCOPE), the Ministry of Internal Affairs and Communications of Japan.

References

1. F. A. Kish, *et al*., *J*. *Sel*. *Top*. *Quantum Electron*., **17,** no. 6, pp. 1470-1489 (2011).
2. T. Tatsumi, *et al*., *Proc*. *OFC'14*, paper Tu3H.5, San Francisco, USA (2014).
3. H. El-Refaei, *et al*., *J*. *Lightwave Technol*., **22,** pp.1352–1357 (2004).
4. M.V. Kotlyar, *et al*., *Opt*. *Express*, **13,** pp.5040–5045 (2005).
5. L.M. Augustin, *et al*., *IEEE Photon*. *Technol*. *Lett*., **19,** pp.1673–1675 (2007).
6. C. Alonso-Ramos, *et al*., *Opt*. *Lett*., 37, 335-337 (2012).
7. T. Tanemura, *et al*., *Proc*. *LEOS'09*, paper WF4, Belek-Antalya, Turkey (2009).
8. M. Zaitsu, *et al*., *Optics Express*, **21,** 6, pp. 6910-6918 (2013).
9. M. Zaitsu, T. Tanemura, and Y. Nakano, "Numerical study on fabrication tolerance of half-ridge InP polarization converters," *IEICE Trans*. *Electron*., to be published.

Integrated Optical Switch Matrices

K.A. Williams and R. Stabile

COBRA research institute, Eindhoven University of Technology
k.a.williams@tue.nl, r.stabile@tue.nl

Abstract: High connectivity integrated optical multi-stage switch matrices with up to sixteen input ports and sixteen output ports are demonstrated using active-passive integrated circuits. 192 switching active elements and hundreds of passive components are integrated within the same monolithic chip for establishing optical data connections at the packet time-scale. We trace circuit level performance through to component level design for even higher levels of connectivity.

Optical switching technology has been proposed to enable Terabit class data routing[1]. Integrated optoelectronics can however offer a radical reduction in physical size and avoids the considerable complexity at the circuit assembly stage. Further scaling requires sophisticated multi-stage networks.
Semiconductor optical amplifier (SOA)-based circuits offer the prospect of large-scale integration, broadcast, higher radix switch elements and the possibility to use multiple stages of loss-compensating switch elements. Bandwidths of up to 160 Gb/s have already been demonstrated through a multi-stage 4×4 optical switch[2]. Recently, feasibility studies and experimental work have shown that lossless 16×16 port count can be achieved using cascades of 4×4 devices in an all-active InP/InGaAsP wafer epitaxy[3,4], but the long all-active paths degrade the optical signal-to-noise ratio and requires high operating current.
In this work, we present and analyse active-passive optoelectronic 16×16 switch by monolithically integrating multi-stages of active SOA gate arrays with passive shuffle networks. This allows for loss compensation, lower power consumption, with reduced signal impairment.

16×16 optical switch matrix. A rearrangeably non-blocking switch is designed implementing a hybrid-Benes architecture[5]. The central five stages are collapsed to one stage by using a 4×4 broadcast and select switch architecture and the input and output switching stages are implemented with 2×2 broadcast and select switching elements. Fig. 1 shows a photograph of the switch circuit. Optical fiber connections are made via the facets at the top and bottom of the image. Electrical connections are made from the left and right sides. Bond wires are provided for the input and output switch elements, and also for one of the two planes of switch elements in the center stage.

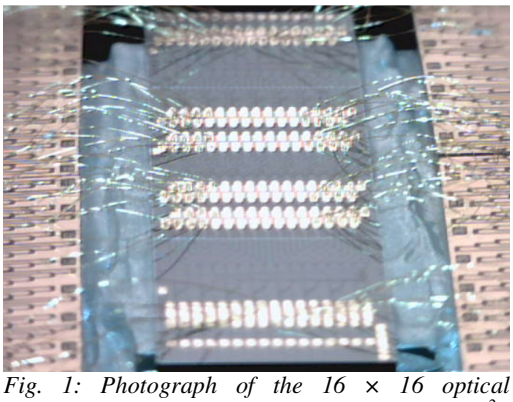


Fig. 1: Photograph of the 16 × 16 optical switching matrix. Chip dimensions are 4 × 14mm^2.

The three cascaded SOA gate stages are implemented across six columns of 30 μm wide and 500 μm long quantum well active islands on a selective area epitaxial regrown InP/InGaAsP wafer. The circuit is fabricated with an eight-mask process. The first waveguide mask defines the waveguide paths: the shortest path is 14 mm and the longest path is 19 mm. The shallow, deep, ultra-deep and electronically isolated waveguides are defined using four photolithographic masks. Inductively coupled plasma etch processing ensures a high side wall verticality to minimize polarization rotation[6]. Waveguide bends with radii as low as 20 μm are implemented in the first mask layer to ensure a compact circuit footprint. The second and third mask patterns define 1.7 μm wide deep-etched 100 μm waveguide bends and 2.2 μm wide shallow-etched straight-waveguides, respectively. The fourth pattern removes p-doped contact layers above the passive waveguides. Mode-matching from deep to shallow waveguides is performed using tapered waveguides. The circuit is planarized before metal evaporation and a lift-off process finally defines the separately addressed p-electrodes. Measurements are performed at 15°C on a temperature stabilized, water-cooled copper mount.

Performance. The switch matrix performance is characterized in terms of gain, loss and noise for paths from the extreme input ports 1 and 16 towards all 16 output ports. Gain and optical signal to noise ratio (OSNR) are initially measured for the enabled path input 1 to output 1 with varied SOA operating condition in Fig 2*a* and *b*.

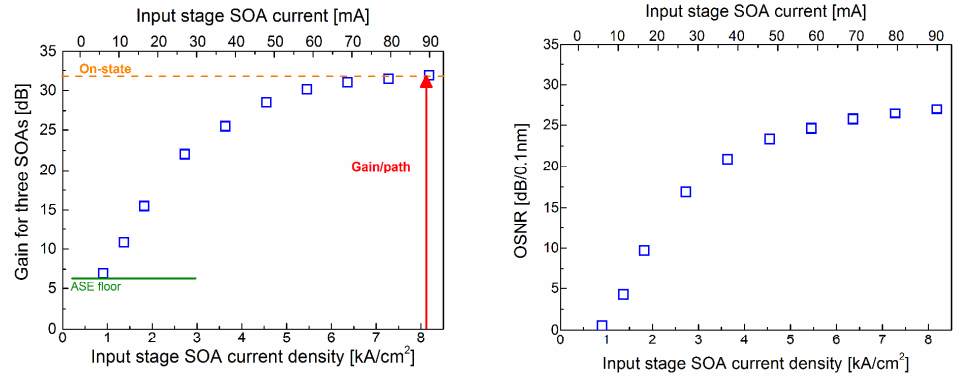


Fig. 2: Gain for three SOAs (a) and optical signal to noise ratio (b) for path 1 to 1 as a function of injected current at the input SOA. The central and output SOA currents are set at 90 mA and 160 mA, respectively.

The net chip gain for path input 1 to output 1 is obtained by normalising the fiber-to-fiber signal losses to the total passive losses of 60.1 dB. A total net gain of up to 10.6 dB per SOA is estimated from the combination of current dependent gain and the anticipated path losses[5]. This shortest path contains up to thirty-eight passive components, as well three active elements, for a net on-chip loss of -17.2 dB. This SOA gain is enough to compensate the inherent splitter losses of 30 dB. The longest paths contribute an additional 8.2dB excess loss due to additional twenty-four components and 5mm waveguide length. Optical signal-to-noise ratio is found to be as high as 28.3dB/0.1nm for the same SOA operating conditions.

To gain insight into circuit level performance, the optical signal to noise ratio is measured for the broad range of paths (Fig. 3). The loss variation per path also leads to a path dependent OSNR in the range from 13.7 up to 28.3 dB. The optical signal to noise ratio is predicted using the anticipated excess losses for the passive components[5], and the observed level of gain and ASE power spectral density from the on-state SOA gates. Excellent agreement is observed, except for the case of the paths from input 16 to output 9-12, due to two imperfectly resolved waveguides. The OSNR approaching 28.3dB/0.1nm already allow for 10Gb/s data routing[5]. The noise figure per stage are estimated to be 14.3, 9.2 and 10.6 dB for the input, central and output SOA, respectively, for a total circuit noise figure of 14.5 dB. These values are due to the low average input powers of -11.9, -21.1 and -36.1 dBm respectively at the first, second and third SOA stage. A considerable enhancement may be anticipated with lower excess losses for the passive components, bringing the circuit level noise figure down to 7.8 dB. This opens a route to further scalability.

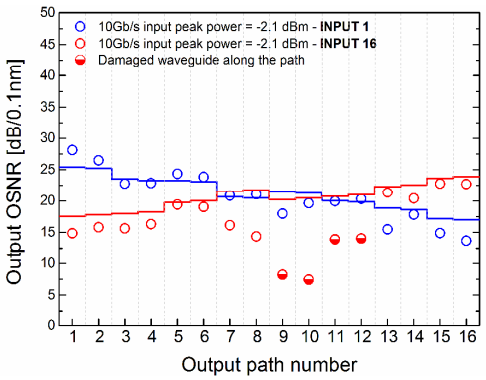


Fig. 3: Path dependent noise performance. Experiment (symbols) and prediction (solid lines).

References

1. N. Sahri *et al.*, Proc. OFC, **4**, pp.PD32-1-PD32-3 (2001).
2. A. Albores-Mejia *et al., Journal of Lightwave Technology*, **28**, pp. 2984–2992 (2010).
3. K.A. Williams *et al., Journal of Optical Networking*, **6**, 189-199 (2007).
4. H. Wang *et al.*, ECOC'10, PD (2010).
5. R. Stabile *et al., Optical Letters*, **37**, pp. 4666–4668 (2012).
6. R. Stabile *et al., Journal of Lightwave Technology*, **29**, pp. 1892-1898 (2011).

Electrical Method for On-Wafer Modal Gain Characterization of Semiconductor Optical Amplifiers

E. Bitincka[1], R. G. Broeke[2] and M. K. Smit[1]

[1] *COBRA Research Institute, Technical University of Eindhoven, 5600 MB Eindhoven, The Netherlands, e.bitincka@tue.nl, m.k.smit@tue.nl*

[2] *Bright Photonics BV, The Netherlands, ronald.broeke@brightphotonics.eu*

Abstract: We present a fast and innovative on-wafer measurement method for modal gain characterization of semiconductor optical amplifiers. It uses a compact integrated spectrometer with electrical control signals only, avoiding, thus the critical and time-consuming optical alignment.

1.Introduction

The generic foundry model[1] reduces the prototyping costs of Photonic Integrated Circuits (PIC) dramatically. One of the main Building Blocks (BB) within the generic foundry approach is the Semiconductor Optical Amplifier (SOA). It is the core element in every integrated laser source. Therefore, its accurate characterization in terms of modal gain is fundamental to the overall performance of the PIC. The main methods proposed for measuring modal gain are the Hakki-Paoli[2], the Thomson[3], and the fitting algorithm method[4]. The draw-back of the Hakki-Paoli method is the need to resolve with very high spectral resolution the longitudinal modes of a laser cavity which includes an SOA and the cleaved facets. For typical chip lengths of several mm this method is not practical since a high resolution spectrometer is needed. The fitting algorithm method[4] makes use of a non linear least square fitting algorithm over the Amplified Spontaneous Emission (ASE) of many SOAs and calculates the modal gain. The draw-back of this method lays in the large number of SOAs needed. The Thomson method in turn needs only two SOAs with length L and $2L$ to determine the modal gain.

Our approach is based on the Thomson method. Its novelty lies in the integration of the SOAs with an optical filter and an array of integrated detectors. The integration of the SOAs with the optical filter and a detector array allows for electrical on-wafer characterization without the need to couple optical signals out of the chip.

2. On-wafer characterization concept

To use the Thomson method a multi-section SOA, a large Free Spectral Range (FSR) Arrayed Waveguide Grating (AWG) and an array of photo detectors (PD) are integrated, see Fig. 1.

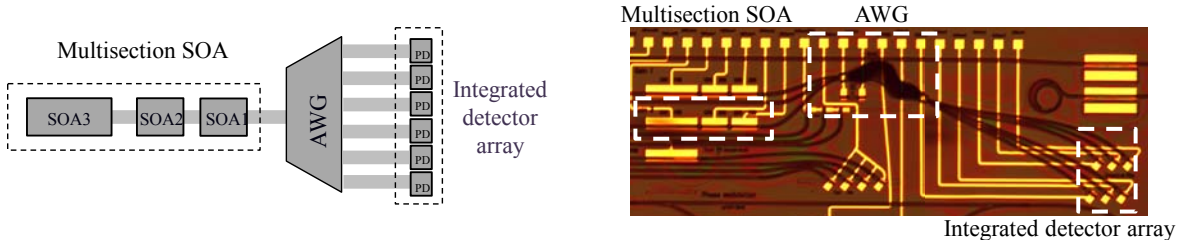


Fig. 1 Schematic of the integrated modal gain measurement (left) and a microscope photograph of the realized circuit (right).

The multi-section SOA consists of SOAs of different length (200-200-400µm). The large FSR AWG (120nm) spectrally resolves the ASE of the SOAs into the PD array. At each of the PDs connected to one of the outputs of the AWG we measure the spectral gain for the corresponding wavelength. The large FSR covers the most important part of the ASE spectra. By pumping different combinations of the three SOAs the following overall SOA length can be obtained: 200-400-800µm. The un-pumped SOAs are always reversely biased (-2V) to absorb incoming light and prevent unwanted feedback. When the feedback is absent the modal gain G and the ASE power are related by[3]:

$$P = \frac{P_{ASE}}{G}\left(e^{GL} - 1\right) \quad (1)$$

With P_{ASE} ASE power and L the SOA length. When comparing two SOAs with length L and $2L$ the analytical solution of (1) gives the net modal gain.

$$G = \frac{1}{L}\left[\ln\left(\frac{P_{ASE_{2L}}}{P_{ASE_L}} - 1\right)\right] \quad (2)$$

3. Experiments

The gain of the 400-800µm long SOA was measured by injecting the same current density (range 1-8kA/cm^2) in each of the two SOA configurations. In Fig. 2 (left) the measured AWG transmission (using an external optical input of the AWG and the detector array) and the simulated one are shown. The SOA ASE power for the 400-800µm long configuration was measured at the PD array, and in Fig. 2 (right) the corresponding gain curves, calculated with (2), are shown.

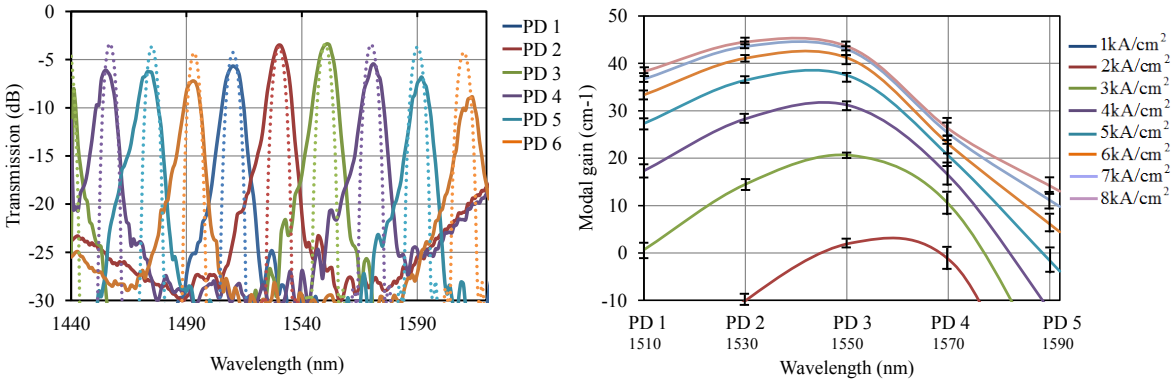


Figure 2 Measurement (cont.) vs. simulation (dashed) AWG transmission (left), and modal gain with error bars (right).

The 20nm measured AWG channel spacing matches very well the simulated one, whereas the measured channel bandwidth was larger than simulated most probably due to phase errors (confirmed by simulations). In Fig. 2 (right) the horizontal axes shows the designed wavelength of the corresponding AWG channel. The typical fabrication tolerance of the central AWG channel is a few nm which translates in a small error in gain estimation shown with the error bars in Fig. 2 (right). These error bars are highest in the outer channels and smaller at the highest gain region (flat gain curve at highest gain point). The typical blue shift of the modal gain at increased pumping current together with a modal gain peak of 45cm^{-1} is clearly observed. Gain saturation appears at ~7 kA/cm^2.

4. Conclusions

We presented for the first time an on-wafer gain measurement test structure using electrical signals only. Avoiding the optical output signals speeds-up the procedure. ASE power is measured in just a few points which is sufficient to calculate the modal gain curves. Characterized amplifiers show a typical modal gain of 45cm^{-1} which agrees well with values measured with other methods

Acknowledgement

The research leading to these results has received funding from the European Community's Seventh Framework Program FP7/2007-2013 under grant agreement ICT 257210 PARADIGM. The authors wish to thank SMART Photonics for the fabrication of the device.

References

1. M. K. Smit *et al., IET Optoelectronics* **5**, pp. 187–194 (2011).
2. B. W. Hakki *et al., Journal of Applied Physics* **46**, pp. 1299–1306, (1975).
3. J. D. Thomson *et al., Applied Physics Letters* **75**, pp. 2527-2529, (1999).
4. B. W. Tilma *et al.*, *Optical and Quantum Electronics* **41**, pp. 735-749 (2009).

Colliding Pulse Mode-Locked Laser Diode using Multimode Interference Reflectors

C. D. Gordon[1], R. Guzman[1], A. Jimenez[1], X. Leijtens[2], G. Carpitero[1]

[1] *Universidad Carlos III de Madrid, Leganes, Madrid, Spain*
ingcarlosgordon@gmail.com, guiller@ing.uc3m.es
[2] *COBRA Research Institute, Eindhoven University of Technology, Eindhoven, Netherlands*
X.J.M.Leijtens@tue.nl

Abstract: We present a novel fully monolithic Colliding Pulse Mode-Locked Laser Diode (CPML) using Multimode Interference Reflectors (MMIRs) to create the laser resonator. We demonstrate experimentally for the first time to our knowledge the Colliding Pulse mode-locking of a laser using MMIRs by observation of the Optical Spectrum and by measuring the frequency spacing between the modes. This component is a promising candidate for Stable Millimeter-Wave Generation in ultra-wideband wireless communication links. Multimode Interference Reflectors are very versatile components that allow avoiding the required cleaved facets to operate.

Introduction: A cost effective technique to increase the data rate of wireless communication systems into multi-gigabit per second is to increase the carrier wave frequency into the millimeter wave region, from the E-band (60 to 90 GHz) to beyond[1]. The challenge to generate signals at this frequency range can be overcome using Microwave Photonic techniques which combine the best of the electronic with the best of photonic techniques[2]. Several reported wireless communication links operating above 100GHz use photonic generation of the carrier frequency. Mode-locked laser diodes (MLLD) are have been successfully used in wireless link demonstration operating at 60GHz[1] and 120GHz[3]. In the latter, the frequency of the pulse train was doubled by an optical clock multiplier (OCM). In the OCM, the pulse train was divided into the two separate legs of a Mach–Zehnder interferometer, and one leg provided a pulse delay.

An alternative approach to increase the repetition rate of a MLLD is by applying Colliding Pulse Mode-locked (CPML) which allows generating higher order harmonics of the cavity round trip frequency, depending on the relative position of the saturable absorber with respect to the mirrors and the length of the resonator[4]. In one hand, if the Saturable Absorber (SA) is located at the middle of the cavity Length (L/2) the CPML is classified as Symmetric Colliding Pulse Mode Locking (S-CPML) which produces optical pulses at twice the cavity round trip frequency. On the other hand, if the Saturable Absorber is shifted from the midpoint toward one facet at an integer fractional position of the cavity length (L/n), it is called Asymmetric Colliding Pulse Mode Locking (A-CPML) which generates the optical pulses at a frequency that is n times the repetition rate defined by the length of the resonator. Besides, the essential components to form the cavity of the resonator are the Multimode Interference Reflectors (MMIRs) which are novel on-chip mirror structures.[5] These are 2-port 50%/50% equal ratio reflection/transmission MMIR.

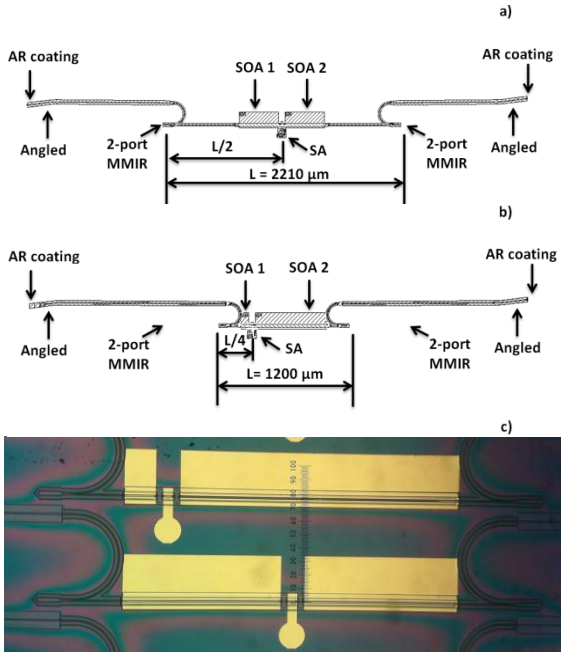


Fig. 1. (a) Symmetric mCPMLLD. (b) Asymmetric mCPMLLD. (c) Microscope Photograph of the Photonic Integrated Circuit.

Device Description: The layout of the S-mCPML where the Saturable Absorber (SA) is located at the middle of the cavity Length (L/2) is depicted in Fig. 1(a). In the A-CPML the Saturable Absorber is located in a position (L/4) toward one faced because we want to generate a harmonic at four times the

repetition rate. Fig. 1(b) shows the layout of the A-CPML.

The device was fabricated in a Multi-Project Wafer (MPW) run for InP-based Photonic Integrated Circuits (PICs), carried out in the clean room at the COBRA Research Institute of the Eindhoven University of Technology (NL). The total length of the cavity in the S-CPML is 2210 µm which allows getting a frequency spacing of 18.67 GHz and the harmonic of 37.34 GHz established by the colliding pulse at midpoint (L/2) of the cavity. The A-CPML with a length of 1200 µm allows obtaining a mode spacing of 34.58 GHz and the harmonic of 138.32 GHz defined by the colliding pulse at one quarter (1/4) point of the cavity. A microscope photograph of the device is shown in Fig. 1(c).

Characterization: The evolution of the optical spectrum of the S-CPML while the current is increased and saturable absorber reverse voltage is fixed at V_{SA} = -3 V is depicted in Fig. 2(a). The light output versus current curve of the S-CPML is shown in Fig. 2(b), where a threshold current of 36 mA is observed. From the comparison between the L-I curve and the optical spectra map we identify different regions of operation of the device. At threshold, the device turns-on as a Fabry-Perot laser, exhibiting lasing on few modes. At 60 mA, the device enters into a colliding pulse mode locked state, up to 100 mA. To confirm the CPML state, the optical pulses were measured on an APE Pulse-Check background-free auto-correlator.

The optical spectrum of the S-CPML in the Colliding Pulse mode-locked state recorded at $I_{SOA\ T}$ = 60 mA (I_{SOA1} = I_{SOA2} = 30 mA), V_{SA} = -3 V, Central wavelength 1560nm and span 40nm in a Yokogawa AQ6370B optical spectrum analyzer is shown in Fig. 3. Inset it shows the mode spacing of 18.67 GHz and the harmonic of 37.34 GHz. We get wide bandwidth which value is BW = 935.53 GHz (7.49 nm) measured at -3 dB. Besides, the A-CPML continues in further studies in order to demonstrate the colliding pulse operation.

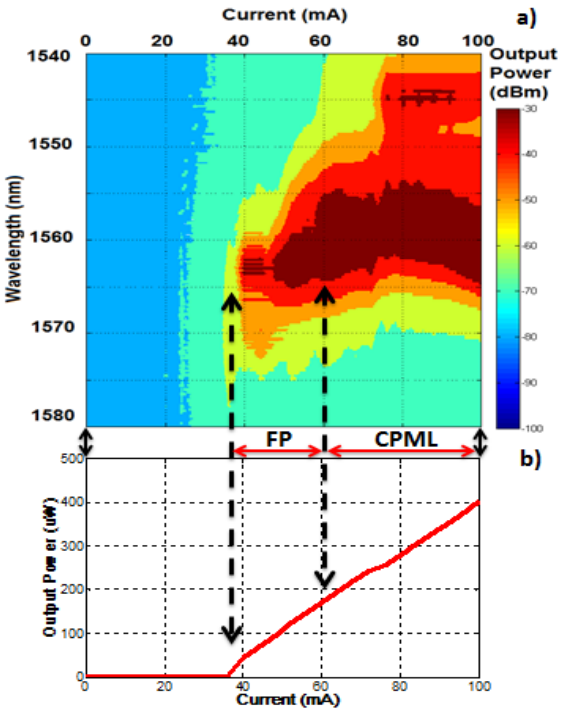


Fig. 2. (a) Evolution of the Optical Spectrum. (b) The Light output versus Current (L-I) curve

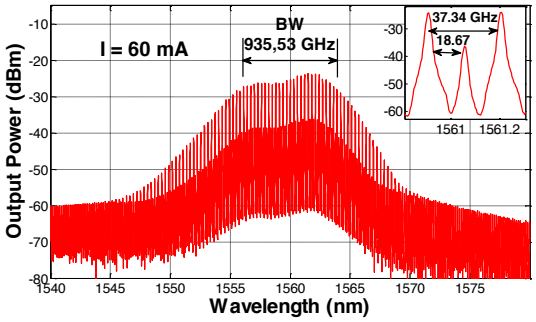


Fig. 3. Optical spectrum of the Symmetric mCPMLLD. Central wavelength 1560nm, span 40nm. Inset it shows the frequency mode spacing.

Conclusion: In summary, the present work is the first demonstration of the fully monolithic Colliding Pulse Mode-Locked Laser Diode reporting experimental data of mode spacing of 18.67 GHz and the harmonic of 37.34 GHz for the Symmetric Colliding Pulse Mode Locking Laser. The device is a novel design that integrates multimode interference reflectors so it does not require cleaved facets, and can be freely located on a Photonic Integrated Circuit (PIC).

References

1. A. Stöhr, A. Akrout, R. Buß, B. Charbonnier, F. van Dijk, A. Enard, S. Fedderwitz, D. Jäger, M. Huchard, F. Lecoche, J. Marti, R. Sambaraju, A. Steffan, A. Umbach, and M. Weiß *et al*., *Journal of Optical Networking* **8**, pp. 471–487 (2009).
2. A. Stohr *et al*., *Topical Meeting on Microwave Photonics (MWP)*, pp. 7–10 (2010).
3. A. Hirata, M. Harada, and T. Nagatsuma *et al*., *Lightwave Technology* **21**, pp. 2145–2153 (2003).
4. T. Shimizu, I. Ogura, and H. Yokoyama *et al*., *Electronics Letters* **33**, pp. 1868–1869 (1997).
5. E. Kleijn, M.K. Smit, X.J.M. Leijtens *et al*., *Lightwave Technology* **31**, pp. 3055–3063 (2013).

Integrated Single Photon Circuits

S. Höfling[1], J. Beetz[1], M. Lermer[1], T. Hoang[2], S. Fattah poor[2], L. Midolo[2], D. Sahin[2], A. Gaggero[3], R. Leoni[3], A. Fiore[2], M. Kamp[1]

[1]Technische Physik, Universität Würzburg, Würzburg, GERMANY
[2]COBRA Research Institute, Eindhoven University of Technology, Eindhoven, THE NETHERLANDS
[3]Istituto di Fotonica e Nanotecnologie (IFN), CNR, Rome, ITALY
sh222@st-andrews.ac.uk

Abstract: Quantum technologies can be utilized for secure communication or computational speed-ups. Waveguide integrated quantum photonic circuits are promising for large scale integration of photonic quantum bit functionalities on a single-chip and we report the development of such a platform on GaAs. This includes waveguide single photon sources based on InGaAs quantum dots, superconducting single photon detectors, electro-optic tuners, directional couplers and splitters. Single-photon sources coupled to waveguides are realized with quantum dots in photonic crystal cavities [1]. Waveguide single-photon detectors are demonstrated by patterning superconducting NbN nanowires on top of ridge waveguides [2], which they can be utilized for on-chip photon auto-correlation measurements [3] and photon number resolved detection [4].

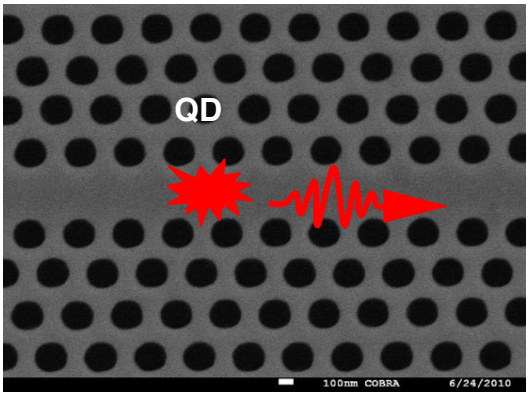


Fig. 1. Photonic crystal waveguide structure with integrated quantum dots for on-chip single photon generation.

References

1. A. Politi *et al*., *Science* ***325***, *pp*. *1221 (2009)*..
2. T. B. Hoang *et al*., *Appl*. *Phys*. *Lett*. ***100***, *061122 (2012)*.
3. J. P. Sprengers *et al*., *Appl*. *Phys*. *Lett*. ***99***, *181110 (2011)*.
4. D. Sahin *et al*., *Opt*. *Express* ***21***, *pp*. *11162 (2013)*.
5. D. Sahin *et al*., *Appl*. *Phys*. *Lett*. ***103***, *111116 (2013)*.

A silicon quantum photonics chip for generation and analysis of entanglement

Raffaele Santagati[1], Joshua W. Silverstone[1], Damien Bonneau[1], Michael J. Strain[2], Marc Sorel[2], Jeremy L. O'Brien[1], and Mark G. Thompson[1]

[1] *Centre for Quantum Photonics, H. H. Wills Physics Laboratory & Department of Electrical and Electronic Engineering, University of Bristol, Merchant Venturers Building, Woodland Road, Bristol BS8 1UB, United Kingdom*

[2] *School of Engineering, James Watt South Building, University of Glasgow, Glasgow G12 8QQ, United Kingdom*

mark.thompson@bristol.ac.uk

Abstract: We present a silicon-on-insulator quantum photonic device able to generate and analyze two maximally entangled qubits. Quantum interference between resonant four-wave mixing sources, phase-stable frequency-selection, and quantum state tomography are shown.

1. Introduction

Silicon quantum photonics promises to take quantum optics to the large scale, where single photons carry the quantum information which can accelerate difficult computational problems, provide perfectly secure communication, or allow high-accuracy measurements. The silicon photonics platform offers miniature, high-yield, and high-performance photonic systems which can be integrated with CMOS electronics and telecommunications-band (1550-nm) optics. However, before large-scale quantum optics can be realized in silicon, several technological hurdles must be overcome.

To date, only non-scalable photon-pair sources, based on spontaneous four-wave mixing [1] (SFWM) in straight silicon waveguides have been shown to interfere [2]. These sources are unsuitable for scaling up, due to limitations

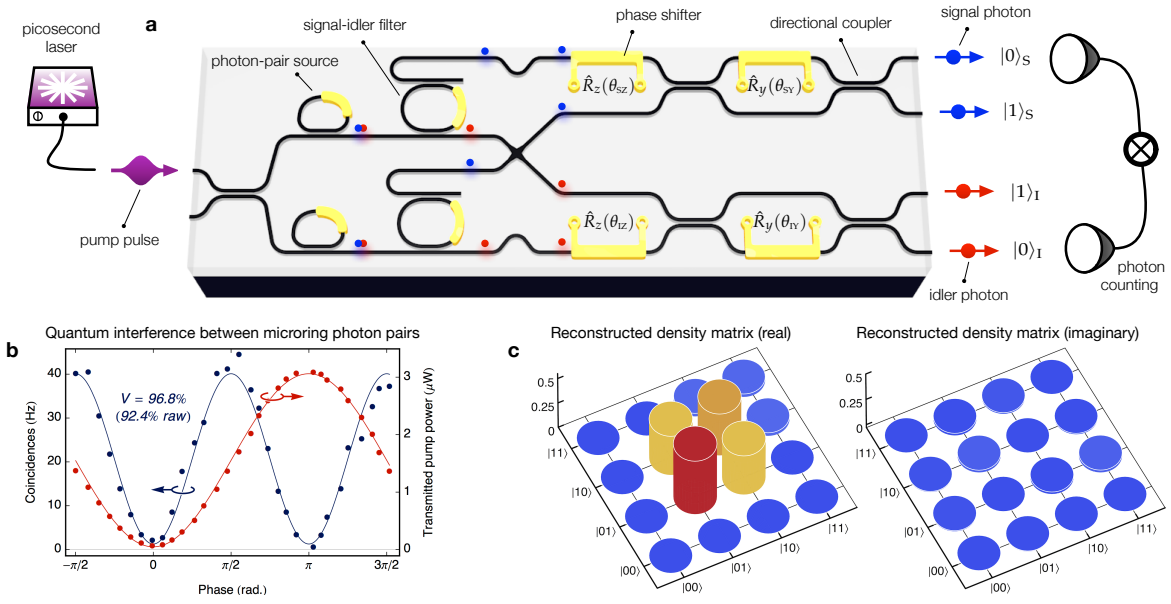


Fig. 1. a) Schematic and operation of the device. b) Quantum and classical interference fringes (on θ_{IZ}) between photon-pair sources. c) Reconstructed density matrix real and imaginary parts.

in brightness and spectral correlation. In this work, we use bright and potentially spectrally uncorrelated [6] silicon microring resonator sources of SFWM photon-pairs, pumped by a picosecond pulsed laser.

Until now, single-photon experiments in silicon [3] have exclusively used an off-chip apparatus, such as a silica arrayed waveguide grating, to control and manipulate photon frequency. Here, we show the first use of phase-stable on-chip wavelength-division multiplexing (WDM) elements. As pictured in Fig. 1a, we use two four-port racetrack resonators to separate the signal photon from each co-propagating pair. The phase-stability of this arrangement is important for the final step of our quantum circuit: two-photon quantum state tomography [4].

By creating a photon pair in a superposition between the two sources, then separating the signal photon from each part of that superposition and relabeling the four waveguides, we generate a maximally entangled state of two path-encoded qubits—a Bell state. The final interferometers of our circuit execute $\hat{R}_Y$ and $\hat{R}_Z$ rotations on those qubits, such that we can infer what the on-chip state is, via quantum state tomography. This is the first time an entangled state of photonic qubits has been both generated and analyzed on-chip.

2. Results

2.1. *Source interference*

Using this device, we demonstrate high-visibility interference between two microring sources, analogous to our demonstration with straight-waveguide sources in [2]. After detuning the WDM resonators, and configuring $\theta_{\mathrm{IY}} = \pi/2$ (such that the interferometer surrounding the sources is closed), we varied the phase θ_{IZ} to obtain the fringe shown in Fig. 1b, with an accidental-subtracted visibility of 96.8%. This high-visibility indicates that the two microring sources are spectrally well overlapped, and that any other effects due to the resonant sources also introduce negligible additional distinguishability.

2.2. *Quantum state tomography*

With good source interference established, we setup the Bell state via the 17-dB extinction WDM resonators, and used maximum likelihood quantum state tomography to reconstruct the state, using the phases θ_{SZ}, θ_{SY}, θ_{IZ}, and θ_{IY} (see Fig. 1a). We collected an over-complete set of 36 measurements which included the complete POVM sets [4] by building projectors from the single-qubit states $|0\rangle$, $|1\rangle$, $|+\rangle$, $|-\rangle$, $|+i\rangle$, and $|-i\rangle$. The reconstructed density matrix is plotted in Fig. 1c. We compared the reconstructed state to the target Bell state $|\Psi^+\rangle$ by computing the fidelity as $F = \langle\Psi^+|\rho|\Psi^+\rangle = 0.88$.

3. Conclusion

We observe high-visibility interference between pairs from different microring sources, pumped by a picosecond pulsed laser. These sources, pumped in this way, could produce spectrally disentangled photon pairs [6], which could be used in integrated multiphoton systems. Our reconstructed Bell state has a total system fidelity ($F = 0.88$) approaching that of the previous post-selected state-of-the-art [5] of $F \in [0.885, 0.947]$ for the four Bell states. This fidelity could be improved (ex. with improved tomography calibration, or with a tuned first coupler), but is nonetheless quite high.

These results represent a new state-of-the-art in functionally integrated quantum photonics. We have presented an integrated photonic device able to generate photon pairs, perform phase-stable frequency selection, and analyze the state of two qubits, via on-chip quantum state tomography. We showed that two scalable SFWM sources generate highly indistinguishable photons with high contrast interference. The designed frequency selection elements showed high extinction, and we were able to successfully reconstruct the on-chip state using the built-in tomography components.

References

1. J. E. Sharping *et al.*, Opt. Express **14**, pp. 12388–12393 (2006).
2. J. W. Silverstone *et al.*, Nature Photon. **8**, pp. 104-108 (2014)
3. D. Bonneau *et al.*, New J. Phys. **14**, pp. 045003 (2012)
4. D. F. V. James *et al.*, Phys. Rev. A **64**, pp. 052312 (2001).
5. P. Shadbolt *et al.*, Nature Photon. **6**, pp. 1749–4885 (2012)
6. L. G. Helt *et al.*, Opt. Lett. **35**, pp. 30063008 (2010).

Hybrid Integration for Single Photon Generation

T. Meany[1], L. A. Ngah[2], M. J. Collins[3], A. S. Clark[3], R. J. Williams[1], B. J. Eggleton[3], M. J. Steel[1], M. J. Withford[1], O. Alibart[2], and S. Tanzilli[2]

[1]Centre for Ultrahigh bandwidth Devices for Optical Systems (CUDOS), MQ Photonics Research Centre, Department of Physics and Astronomy, Macquarie University, North Ryde, 2109 NSW, Australia
[2]Université de Nice-Sophia Antipolis, Laboratoire de Physique de la Matiére Condensée, CNRS UMR 7336, Parc Valrose, 06108 Nice Cedex 2, France.
[3]CUDOS, Institute of Photonics and Optical Science (IPOS), School of Physics, University of Sydney, New South Wales 2006, Australia.

Abstract: A key resource for quantum optics experiments and applications are on-demand sources of single and multiple photon states at telecommunication wavelengths. We report a hybrid integrated source of heralded photons combining periodically poled lithium niobate waveguides, laser inscribed circuits and fibre Bragg gratings to demonstrate the spatial multiplexing of four identical photon pair sources. The achieved results reveal the large potential of such an approach for designing tools for advanced quantum applications.

Introduction

For over thirty years the role of single photons has evolved from a merely fundamental concept to a resource for quantum information science (QIS). Despite advances in genuine single photon sources [1], spontaneous parametric downconversion (SPDC) is the most common method for generating single and paired photons thanks to unrivalled simplicity and versatility. However, SPDC sources have a non-negligible probability to produce multiple pairs preventing an increase to the emission rate at will. Although some schemes exploit this feature [2], in most QIS experiments this multi-photon contribution results in reduced quantum state fidelities [3]. Temporal multiplexing schemes have been used to increase photon production rates by increasing the pump repetition rate [4]. A spatial multiplexing scheme can also be used to increase source brightness, while maintaining a fixed noise contribution [5]. This method uses multiple heralded single photons actively routed to a single output [6,7]. Integrated optics stands as an enabling technology for QIS experiments [8], where integrated waveguides in periodically poled lithium niobate (PPLN) [9] have proven to be a flexible platform for on-chip experiments [10,11]. However, PPLN is less suited to the implementation of complex linear components. The femtosecond laser direct-write (FLDW) technique permits the rapid prototyping of 3D waveguide circuits [12] in glass substrates including fibre Bragg gratings (FBG) and waveguide circuits [13]. Here, we combine the potential of linear FLDW laser written circuits and PPLN waveguides to collect and filter four heralded, spatially separated photons from a PPLN chip. Such a hybrid approach provides scalability and can immediately leverage any improvements in transmission, detection and photon production efficiencies.

Experiment

The experiment interfaces laser written waveguides, directly written in glass substrates with PPLN waveguide SPDC sources (See Fig. 1). The PPLN waveguides act as heralded single photon sources. In this process one photon of a downconverted pair heralds the existence of its complementary photon. The pump laser emits picosecond pulses at 710 nm. This laser is coupled into an optical fibre pigtailed to a FLDW 4-port beamsplitter in order to pump four identical PPLN waveguides. The nonlinear interaction produces 1310 nm (idler) and 1550 nm (signal) paired photons. Those pairs are then split deterministically using laser written wavelength demultiplexers (WDM) and subsequently coupled into single mode fiber in a V-groove array. Upon the detection of one out of four 1310 nm photons, the complementary 1550 nm photon is heralded and routed to a single output thanks to fast optical switches. The heralded single photon rate is recorded and the signal to noise is characterized by measuring the coincidence-to-accidental ratio (CAR), calculated by taking the ratio of coincident arrivals of signal and idler photons from the same pulse with those from subsequent pulses.

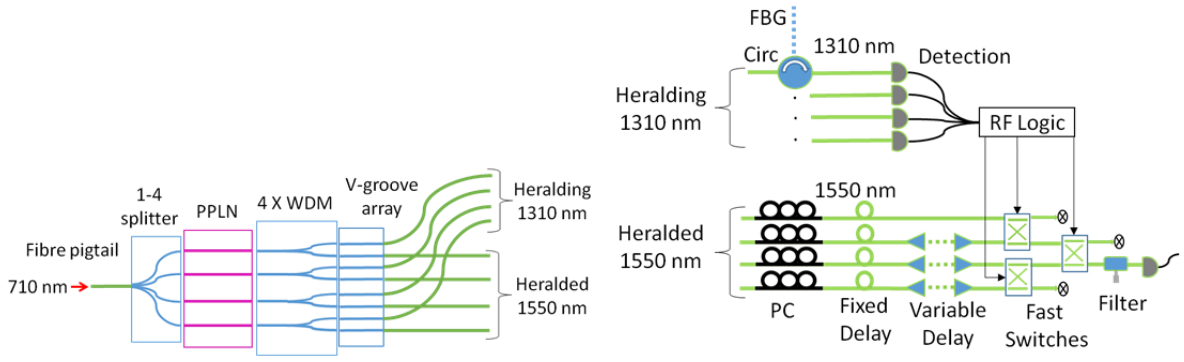


Fig.1: (left) A picosecond laser pumped array of 4 identical PPLN waveguides, where a pair of FLDW chips couple light in and out of the device. (right) The output of the WDMs is sent to a multiplexing setup. Four single photon channels at 1310 nm, which are filtered by FBG and circulators (Circ), herald the arrival of 1550 nm photons. Radio frequency (RF) electronics control the switches for routing the 1550 nm photons.

Results

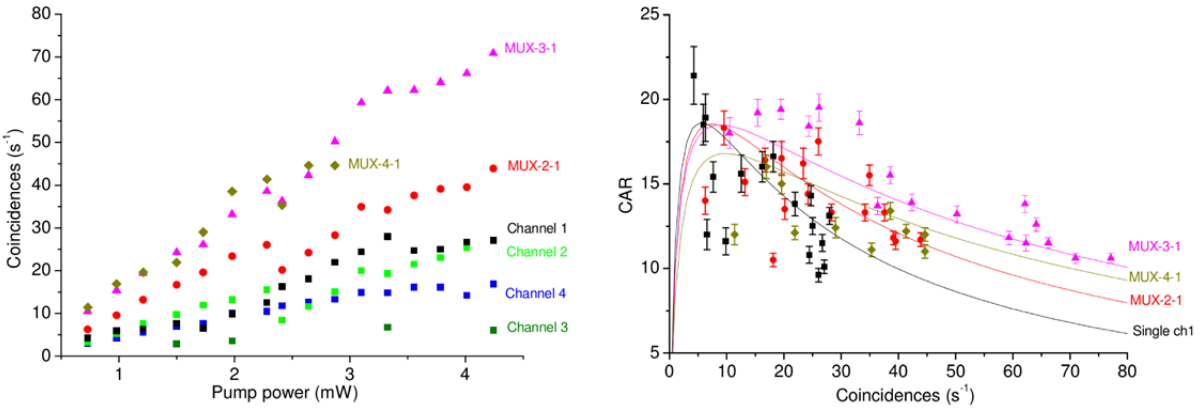


Fig.2: (left) Heralded photon rate vs. pump power for single channels and a 4-1 multiplexing scheme. (right) CAR vs. coincidences for multiplexing 2, 3 and 4 channels. Single channel 1 is shown for comparison.

Fig.2 clearly shows an increased photon rate, while maintaining a fixed signal-to-noise ratio through multiplexing. The overall results is in practice comparable to existing waveguide based photon sources due to high overall losses in the setup and one failing source (channel 3).

Conclusion

We have interfaced the largest number of SPDC sources on a single chip which is comparable to bulk optic demonstrations. This shows the practicality of hybrid integration for the preparation of single and multiple photon states. By increasing photon rates, while maintaining a fixed signal-to-noise ratio through multiplexing, we have demonstrated the scalability of our technique.

References

[1] O. Gazzano *et al., Phys. Rev. Lett.* **110**(25), 250501 (2013).
[2] J. C. F. Matthews *et al., arXiv*:1307.4673v2 (2013).
[3] J. L. Smirr *et al., J. Opt. Soc. Am. B* **28**(4), 832–841 (2011).
[4] T. Inagaki *et al., Opt. Express* **21**(20), 23241–23249 (2013).
[5] A. Migdall *et al., Phys. Rev. A* **66**(5), 053805 (2002).
[6] X. s. Ma *et al., Phys. Rev. A* **83**(4), 043814 (2011).
[7] M. J. Collins *et al., Nat. Commun.* **4**, 2582 (2013).
[8] S. Tanzilli, *et al., Laser & Phot. Rev.* **6**, 115-143(2012).
[9] F. Kaiser, *et al., Las. Phys. Lett.* **10**, 045202 (2013).
[10] S. Krapick *et al., New J. of Phys.* **15**(3), 033010 (2013).
[11] A. Martin *et al., New J. of Phys* **14**, 2 025002 (2012).
[12] T. Meany *et al., Appl. Phys. A* **114**, 113–118 (2013).
[13] T. Meany *et al., Opt. Express* **20**(24), 26895–26905 (2012).

Ultra-fast Photon Pair Sources for Quantum Networking

L.A. Ngah, V. D'Auria, L. Labonté, O. Alibart, S. Tanzilli

Laboratoire de Physique de la Matière Condensée (LPMC), Université Nice Sophia Antipolis, CNRS UMR 7336, Parc Valrose, 06108 Nice, France,
lutfi-arif.bin-ngah@unice.fr, dauria@unice.fr, laurent.labonte@unice.fr, olivier.alibart@unice.fr, sebastien.tanzilli@unice.fr

Abstract: We report on the realization of ultra-fast photon pair source, capable of delivering high-quality single photon pairs, guaranteeing efficient operational condition for advanced quantum networking by taking advantage of high-performance telecom components and integrated optics.

The role of entanglement, which was initially categorized as a theoretical ground in quantum physics, is now considered as a resource for enabling various implementations of complex quantum information science (QIS) protocols. Taking advantage of strong correlations between entangled photons allows QIS protocols to reach their fullest potential in term of long operational distances. One of the most investigated protocols for quantum networking, involving entanglement as a genuine resource, is the quantum relay configuration.[1, 2] With that being said, the success rates of complex protocols such as QR, are highly affected by the non-deterministic nature of spontaneous parametric down conversion (SPDC), usually exploited for photon pairs generation. In favor of achieving higher success rates, we exploit here high-speed performance offered by state-of-the-art telecom laser technology and guided-wave optics.

Generating photon pairs at telecom wavelength by SPDC requires pumping any suitable non-linear crystals at visible wavelength. To achieve this, most of the demonstrated QIS protocols adopt solid-state, mode-locked lasers producing optical pulses around 780 nm as the pump beam whose repetition rate is inherently limited to a few hundreds of MHz. In contrast, state-of-the-art, ultra-fast fiber laser is readily available in the 1550 nm telecom band exhibiting picoseconds pulses whose repetition rate is adjustable up to 10 GHz. On the other hand, the very high efficiency of periodically poled lithium niobate (PPLN) waveguides has led to the investigation of sequential non-linear processes *i.e*. two PPLN waveguides are arranged in a cascade manner for which each particular waveguide plays a specific designated role. In such configuration, the non-linear interaction of second harmonic generation (SHG) up-converts the incident lights from 1560 nm to 780 nm, then through SPDC in the second PPLN waveguide, photon pairs back in the 1560 nm band are created.[3] What we propose here is to use such fast laser pulses at 10 GHz rate, feeding the cascaded PPLN waveguides to generate photon pairs at telecom wavelength at ultra-high repetition rate.

In this paper, we demonstrate the realization of ultra-fast photon pair sources and their characterization in terms of coincidence-to-accidental ratio, as well as the spectral "purity" which are essential for efficient quantum networking.[4] For that purpose, a standard arrangement of Hanbury Brown and Twiss (HBT) experiment is implemented and this conveniently gives access to *P1,* the probability of registering a "heralded" photon given the other counterpart "heralding" photon is detected, and to $g^{(2)}(0)$, the second order auto-correlation function which quantifies the "singleness" of the emitted photon pairs. On the other hand, the picosecond laser regime has been identified to be optimal for generating "pure" photon states in the spectral domain, *i.e.* Fourier-transform limited within the duration of the pump pulses, since suitable spectral filtering in standard telecom channels can be achieved using competitive off-the-shelves, high-performance, low-loss and relatively inexpensive fiber components.[5] We have further tested the indistinguishability of the produced photons using a Hong-Ou-Mandel (HOM) type setup.[6]

As illustrated in Fig.1, using ultra-fast, 10 GHz picosecond pulses, the figures of merit *P1* and $g^{(2)}(0)$ are measured. Pairs of photons are generated in a PPLN waveguide, using frequency-doubled 10 GHz laser (1540 nm → 770 nm). The slightly non-degenerate, energy-matched photon pairs are deterministically separated thanks to a combination of a wavelength division multiplexor (DWDM) and a fiber Bragg grating (FBG) filter, in predefined ITU 42 and ITU 50 telecom channels, respectively. Through the employed HBT setup, the correlation in terms of coincidences between the

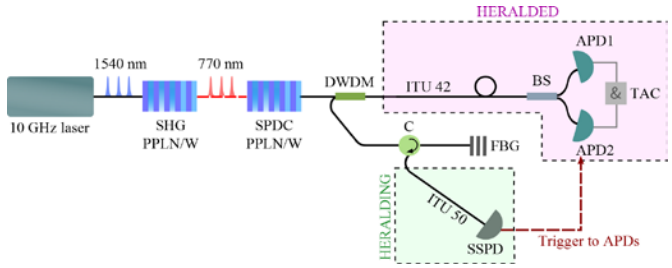


Fig. 1: The multi-pair contributions is characterized using a HBT

two heralded avalanche photodiode (APD) detectors is registered. For the moment, our source exhibits a *P1* of 0.385 and a $g^{(2)}(0)$ of 0.09 at a heralding rate about 2.3 MHz. Moreover, high purity of the photons has been demonstrated with the arrangements shown in Fig. 2. At this stage, we simply used a much slower, solid-state, Coherent MIRA 900 laser (770 nm, 76 MHz, 1 ps temporal duration pulses). By adjusting the temporal overlap of interfering photons at the beam splitter (BS), we reveal a raw dipping signature during the acquisition of four-fold coincidences of 98.6% visibility. This indicates the high degree of indistinguishability of our single photon preparation stage, making it suitable for quantum networking. In addition, the measured false four-fold coincidence rates are closed to the estimated, pure APD dark counts contribution which suggests negligible presence of photonic noise in the setup. This is achieved by implementing better filtering scheme with optimum rejection and also by employing high-performance telecom fiber components.

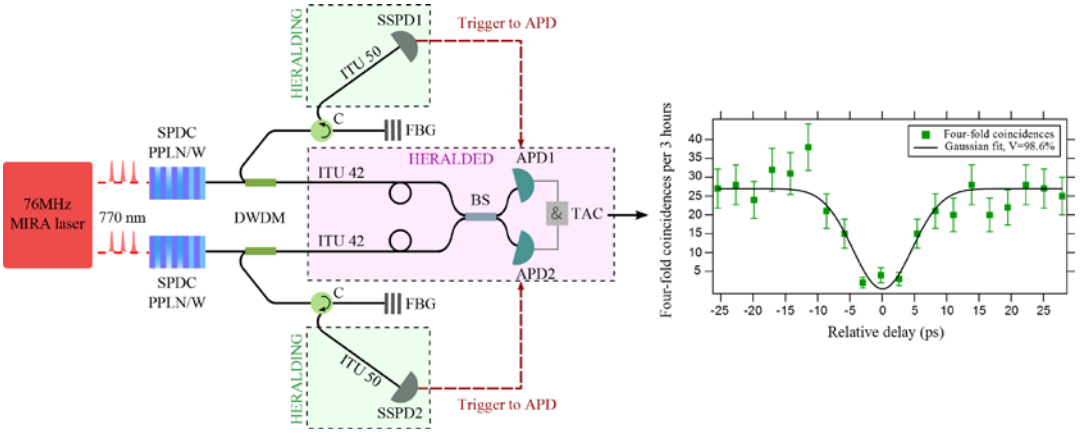


Fig. 2: The accumulated four-fold coincidences are registered for single photon indistinguishability measurement using a much slower MIRA laser.

So far, promising results have been obtained, gauging the quality of our experimental approaches. The next step is to perform a two-photon interference experiment at 10GHz repetition rate. We therefore expect achieving better results, namely, high four-fold coincidence rates, up to 1000 coincidences per an hour of measurement, while keeping an excellent visibility for the HOM dip. This should demonstrate the effectiveness of our high-speed photon pair sources for quantum networking.

References

1. R. Kaltenbaek *et al., Physical Review A* **79**, pp. 040302, (2009).
2. M. Halder *et al., Nature Physics* **3**, pp. 692–695, (2007).
3. Q. Zhang, *et al., Optics Express* **15**, pp. 10288–10293, (2007).
4. J. B. Spring, *et al., Optics Express* 2**1**, pp. 13522–13532, (2013).
5. P. Aboussouan *et al., Physical Review A* **81**, pp. 021801, (2010).
6. C. K. Hong *et al., Physical Review Letters* **59**, pp. 2044–2046, (1987).

Low-loss $LiNbO_3$ integrated photonic crystals

N. Courjal[1], M.P. Bernal[1], C. Guyot, F. Henrot, G. Ulliac, W. Qiu, F. Baida

[1] *FEMTO-ST Institute, Besançon, France,*
Nadege.courjal@femto-st.fr

Abstract: We report $LiNbO_3$-based photonic components consisting of low-loss ridge waveguides and high aspect ratio photonic crystals. The components include spot-size converters to efficiently couple light from a SMF28 fiber into the ridge waveguide. The coupling losses and propagation losses are measured to be as low as 0.8 dB per facet and 0.2 dB/cm respectively, for both TE and TM polarizations. High aspect ratio photonic crystals are inscribed in the confined ridge waveguides by focused ion beam (FIB) milling. These developments open the way to compact low-power photonic circuits. For the sake of example, we present ultra-sensitive temperature sensors with an active length of only 30 µm and new photonic structures.

Tunable photonic crystals (PhCs) represent a stimulating challenge for advanced functionalities in compact optical devices. Lithium niobate ($LiNbO_3$) substrates appear as excellent candidates for such realizations, due to their well-known nonlinear, piezoelectric and electro-optic properties. However, the integration of $LiNbO_3$ PhCs in photonic circuits faces two major issues. The first one is related to the weak confinement of light in $LiNbO_3$ waveguides: the maximum index change produced by standard techniques is quite small ($\Delta n<0.01$), and the resulting mode is broadly distributed. Thin films of $LiNbO_3$ providing strong light confinement are now available [1], but the confinement is achieved at the expense of the insertion losses. Secondly, the production of high aspect ratio PhCs is severely hindered by the matter redeposition occurring during the dry etching processes.
Here we show an alternative approach that relies on high aspect ratio ridge waveguides [2,3] with low insertion losses. The guided light is submitted to a large lateral index contrast resulting in a strong lateral confinement of light. An innovative vertical transition enables low coupling losses between the SMF28 fiber and the ridge. These ridges can lead to temperature sensors with unexpectedly high temperature sensitivity (8 nm/°C), and to high aspect ratio photonic crystals with insertion losses lower than 5 dB.

Firstly a planar waveguide is produced either by Ti-indiffusion, Annealed Proton Exchange (APE) or by a combination of both techniques. The ridge structure is made in a second step by "optical grade dicing" with a circular precision saw (DISCO DAD 321) [1]. Hence, ridges with aspect ratios (width:depth) larger than 500 can be achieved. The optimal propagation losses are as low as 0.2dB/cm for both TE and TM polarizations, and the related confinement is twice stronger than the one of standard waveguides. Stronger confinements can be achieved by combining Ti-indiffusion and APE techniques.

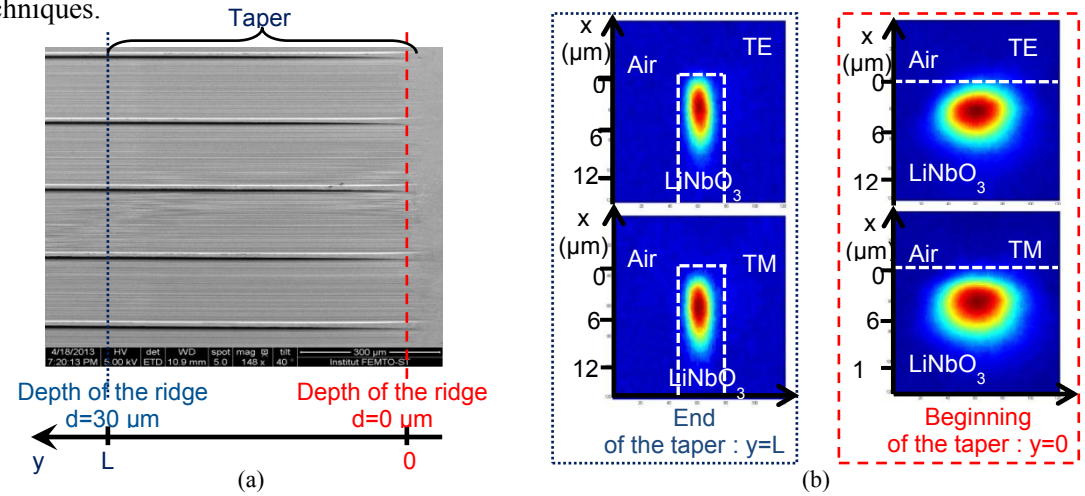
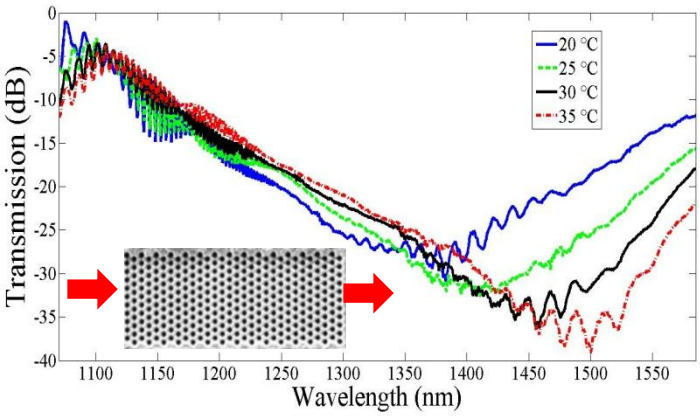


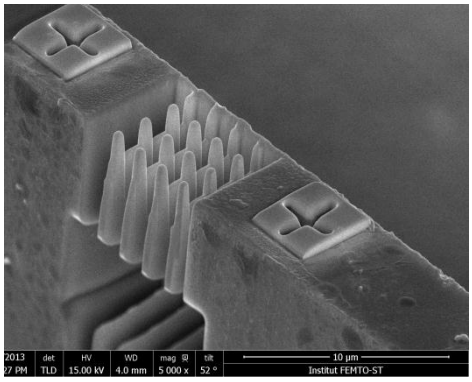
Figure 1. Vertical tapers made with a circular precision saw. (a) SEM view of five tapered ridges: the depth of the ridge is progressively increased. (b) Optical modes visualized with an infrared vidicon camera and a X20 microscope objective. Lefts: Mode at the end of the taper. Rights: the mode at the input of the taper. Width of the Ti-indiffused ridge: 6µm.

New challenges arise with the achievement of confined waveguides. Indeed, standard SMF28 fibers exhibit a broadly distributed mode that weakly overlaps with confined modes. This issue is addressed with a vertical taper between the ridge and the fiber in order to ensure a spot size conversion of the guided mode. The taper is made simply by lifting the blade before the end of the ridge waveguide (see Figure 1(a)). As a result, the section of the waveguide in contact with the fiber is weakly confined and strongly overlaps with the fiber's mode, while the end of the taper in contact with the ridge is strongly confined for both TE and TM polarizations (see Figure 1(b)). The taper contributes to reduce the coupling losses from 2.8 dB (ridge in direct contact with fiber) to 0.8 dB (taper in contact with fiber) per facet: this achievement is of great relevance for the production of compact low-power PhCs-based components.

Photonic structures are made in a second time by focused ion beam (FIB) milling. These developments have been successfully exploited for the experimental demonstration of low-power-consuming tunable PhCs. For the sake of example, a single triangular PhC inscribed in a Ti-indiffused APE ridge waveguide has shown an enhanced temperature sensitivity of 8 nm/°C (Figure 2(a)), which can be regarded as a record in comparison with other all-dielectric temperature sensors. The device could be advantageously exploited as temperature or electric field sensors.



(a)



(b)

Figure 2. (a) Measured optical transmission through a triangular lattice of holes in a (Ti-APE) $LiNbO_3$ ridge waveguide, as a function of temperature. The results have been obtained by normalizing the optical intensity light transmitted through the nanostructured waveguide with the intensity through a single ridge waveguide made in the same conditions without any PhC. The guided light is TE-polarized. Insert: top view of the PhC (b) SEM views of a free standing 3D $LiNbO_3$ photonic crystal

Recently we have also demonstrated photonic crystals with extremely high aspect ratios by inscribing the photonic patterns through the side of the ridges [3]. An illustration is given in Figure 2(b), where a SEM picture shows a free standing three dimensional $LiNbO_3$ photonic crystal. Optical characterizations have been performed on various high aspect ratio $LiNbO_3$ PhCs: the reflectivity is now measured to be higher than 80% in the photonic bandgap for both TE and TM polarizations, and the insertion losses are lower than 5 dB. Such PhCs with high reflectivity can advantageously be implemented into photonic resonators. It is worth noting that the characterization method relies on an optical coherence tomography (OCT) based system that works in reflection as well as in transmission. This approach enables the assessment of reflectivity, transmission and losses, which is of great relevance for the optimization of various photonic structures.
These results open the way toward low consumption compact electro-optic components.

This work was supported by the ANR Matériaux et Procédés pour les Produits Innovants 2012 under project CHARADES, by the SNIFER DGA RAPID project contract number 112906210, by the Labex ACTION program (contract ANR-11-LABX-01-01) and by the Conseil Régional de Franche-Comté, France. The work was partly supported by the French RENATECH network and its FEMTO-ST technological facility.

References

1. A. Guarino, et al., Nature Photonics, **1**, pp. 407 - 410 (2007)
2. N. Courjal, et al., J. Phys. D: Appl. Phys, **44**, pp. 305101, (2011)
3. C. Guyot, et al., Optics Letters, **39** (2), pp. 371-374 (2014)

3D Direct-Laser-Written Mid-Infrared Waveguide Circuits in Fused Silica and Crystalline Quartz

Javier Martínez[1], Airán Ródenas[1], Toney Fernandez[3], M. Aguiló[1], Javier Rodríguez Vázquez de Aldana[2], Javier Solis[3] and Francesc Díaz[1]

[1] Física i Cristal•lografia de Materials (FiCMA), Universitat Rovira i Virgili (URV), 43007, Tarragona, Spain, javier.martinez@urv.cat, airan.rodenas@urv.cat, magdalena.aguilo@urv.cat, f.diaz@urv.cat
[2] Grupo de Óptica, Facultad de Ciencias, Universidad de Salamanca, 37008 Salamanca, Spain, jrval@usal.es
[3] Laser Processing Group, Instituto de Óptica-CSIC, Madrid 28006 Spain, toney.teddyfernandez@gmail.com, j.solis@io.cfmac.csic.es

Abstract: We report on the fabrication, for the first time to our knowledge, of mid-infrared step-index waveguides in fused silica substrates and mid-infrared cladding waveguides in crystalline quartz. Both types of waveguides can be designed to be multimode or single mode for wavelengths up to the transparency limits of the materials, around 4 μm wavelengths. For the case of step-index core waveguides in fused silica we demonstrate core to cladding index steps in the 0.01 range with core sizes around 10 μm x10 μm, this enabling for low coupling losses to optical fibers. We also demonstrate the capability of writing waveguide circuits deeply embedded inside silica substrates down to the mm scale, this enabling the design and 1-step fast fabrication of advanced 3D mid-IR waveguide circuits for future light processing chips for chemical sensing, astrophotonics, or any other mid-IR related application.

Introduction: In recent years there is an increasing interest in exploiting the range of longer wavelengths called the mid-infrared (MIR) range which spans from 2.5 to 20 μm [1]. Femtosecond (fs) pulse direct laser writing (DLW) is a novel technique which has been demonstrated to be capable of producing three-dimensional (3D) waveguide designs and configurations which are required for efficient and low-loss interconnection between different components, such as optical fibers and waveguide chips [2]. In this work we explore the possibility of fabricating, with this technique, MIR waveguides in fused silica and crystalline quartz, which are transparent from the ultraviolet to up to the MIR at around 4 μm.

Femtosecond pulse laser 3D fabrication: Low OH-concentration fused silica glass and standard α-quartz c-cut crystal, are employed as substrate materials for the waveguides. Fig. 1 shows examples of fabricated waveguides in crystalline quartz and fused silica. Our presentation will show how we can create lowered refractive index structures in crystalline quartz, and increased refractive index structures in fused silica glass. In the case of the crystal, we have designed and fabricated cylindrical cladding structures which can sustain light propagation in the whole transparency range of the crystal. On the other hand, in fused silica the ultrashort pulses can induce a local increase of the index, from which we benefit to design step-index core waveguides which can guide light through bends and also feature low loss butt-coupling to commercial fibers.

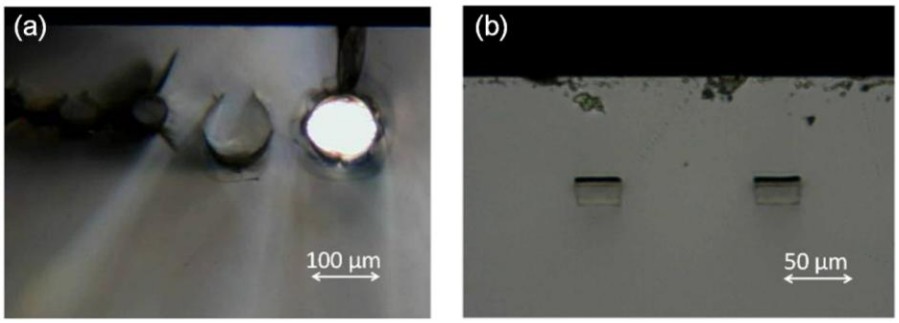


Fig. 1. Microscope images of fabricated waveguides in (a) α-quartz crystal and (b) fused silica glass.

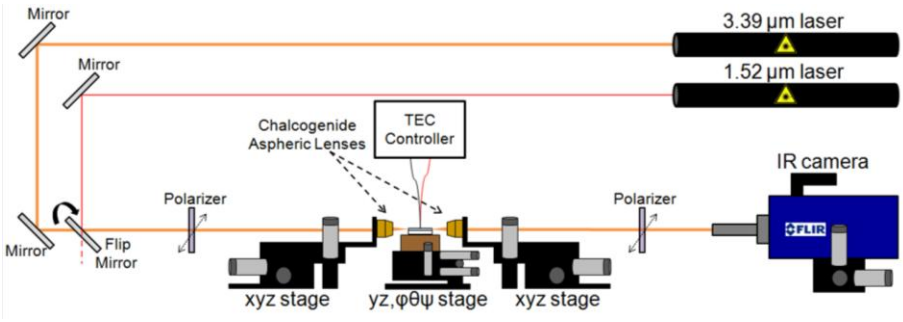


Fig. 2. Scheme of the optical setup used for modal characterization of NIR and MIR waveguides

Optical mid-infrared waveguide characterization: We have built a complete setup for NIR and MIR optical characterization of waveguides (see Fig. 2). Modal and propagation loss measurements of the waveguides are possible up to 5 µm, and spectroscopic characterization of waveguides transmission up to 12 µm with a fiber coupled FTIR spectrometer are also being performed. Some examples of modes measured at 3.39 µm wavelength in the MIR range are shown in Fig. 3. For α-quartz, two different types of cladding waveguides are shown: the first one is monomode (Fig. 3(a)) whereas the second one is much larger in size and supports a great number of modes (Fig. 3(b)). In the case of step index waveguides made in fused silica glass, we show here the observable modes for the waveguides shown in Fig.1b. Three different modes can be excited almost independently.

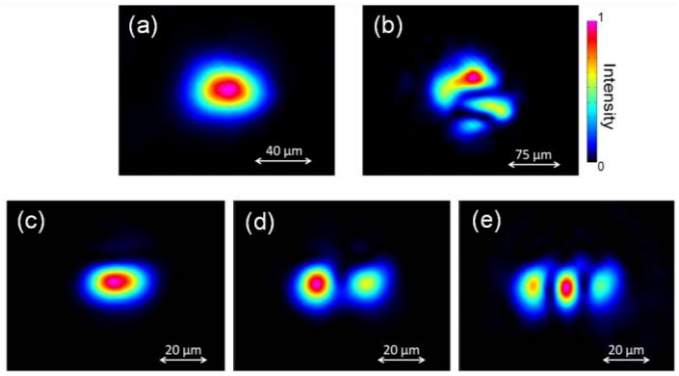


Fig. 3. Measured near-field intensity mode profiles for selected waveguides at 3.39 µm. (a) Monomode and (b) multimode waveguides made in α-quartz. (c), (d), (e) First three modes supported by a step-index waveguide made in fused silica.

Conclusions: MIR waveguides embedded in glass and crystal are being developed by the femtosecond laser writing technique. Properties such as size, light confinement, modal behavior or 3D propagation path can be easily controlled. An optical setup allows modal characterization of fabricated waveguides and testing of the performance providing feedback for fabrication optimization. The obtained waveguides will serve as MIR sensors and first results will be shown.

Acknowledgments: This work has been partially supported by the Spanish Government under projects MAT2011-29255-C02-O2, MINECO TEC2011-22422, by the Catalan Government under Project 2009SGR235 and 2014FI_B 00274 and by the European Commission under ACP2-GA-2013-314335- JEDI ACE.

References

[1] Airán Ródenas, Guillermo Martin, Brahim Arezki, Nickolas Psaila, Gin Jose, Animesh Jha, Lucas Labadie, Pierre Kern, Ajoy Kar, and Robert Thomson, "Three-dimensional mid-infrared photonic circuits in chalcogenide glass," Opt. Lett. 37, 392-394 (2012)

[2] K. M. Davis, K. Miura, N. Sugimoto, and K. Hirao, "Writing waveguides in glass with a femtosecond laser," Opt. Lett. 21, 1729-1731 (1996)

Mobility-controlled Method to Construct QPM Devices

Chun-Hao. Yang[1], Kai.-Hsun. Chang[1], Lung-Han. Peng[1], A-H. Kung[2], and A. Boudrioua[3]

[1] National Taiwan University, Taipei, Taiwan, R.O.C.,
peng1@ntu.edu.tw
[2] National Tsing-Hua University, Hsinchu, Taiwan, R.O.C. and Academia Sinica, Taipei, Taiwan, R.O.C.
[3] Institut Galile'e, UMR 7538 – CNRS, Universite' Paris 13, Villetaneuse, France.

Abstract: Periodically poled quasi-phase-matching (QPM) devices were studied by means of mobility-controlled method to realize the ferroelectric domains at desirable quasi-phase-matching periodicity and duty cycle. Fidelity of domain shape and duty cycle were ascribed to the extremely low value of lateral domain mobility of ~0.01 mm^2/kV-sec found on the –Z face of PPLT and ascribed to the +Z face anchoring effect from the charged barriers formed by the diffusion process. Examples were illustrated on 20mm-long PPLT optical parametric oscillator with low threshold of 30 MW/cm^2 and slope efficiency of 45% for broad 1060nm-band generation.

Introduction: The quasi-phase-matching (QPM) materials represent an important selection as laser light sources for scientific investigation and industrial application. Entangled photon pair-generation for quantum information process, multi-harmonics generation for optical pulse synthesis, parametric generation of mid-infrared (IR) sources for spectroscopy and bio-imaging are the representative applications benefited from the QPM devices[1]. For the QPM materials made on the ferroelectric nonlinear crystals such as lithium niobate ($LiNbO_3$) or lithium tantalite ($LiTaO_3$), the limiting factors constraining the photon conversion efficiency are due to the inverted domain periodicity and duty cycle. For the conventional wisdom where the inverted domains were formed by the pulse electric poling method, the fringing field effect plays an essential role in affecting the domain fidelity. The fringing field, however, was known to arise from the dielectric discontinuity across the corrugated interfaces between the poling electrodes and the ferroelectric crystals, and was an inherent issue in dealing with the periodically poled devices.

In this work, we reported the use of a two-step of diffusion-poling scheme to control the lateral motion of inverted domains in PPLN/LT. Our model led to a high-field mobility of ~0.01 mm^2/KV-s in constraining the lateral motion of inverted domains in LT. This number is two-order of magnitude lower than that (~1.6 mm^2/KV-s) previously observed in poling of LN[2]. It therefore allows us to realize 20mm-long PPLT with good control of domain fidelity and reach slope efficiency of 45% when degenerately-pumped by 532nm Q-switched laser to render broad-spectral generation of 1060nm-band infrared sources.

Experiments and Results: Our device fabrication procedures first began with deposition of a thin layer of stripe pattern of Ni/Zn on the +Z face of the $LiTaO_3$ or $LiNbO_3$ substrate. The coated substrates were then subject to a thermal diffusion process at temperature slightly lower than the material's Curie temperature. The purpose of this treatment is to introduce periodically inverted surface domains which can serve as distributed charged barriers against the merging with the nearby electrically poled domains. The latter phenomenon can be seen from Fig.1 where an external voltage of 16KV was applied across a 0.5mm-thick Z-cut LN substrate. We notice that the inverted vertical domains (dark regions in Fig.1) can be well confined between the hemispheric-shape of inverted domains. The latter reflects regions where the process of Li out-diffusion can cause thin surface inverted domains (dark regions), thereby forming charged barriers due to the divergence effect of the polarization (P_s) against the virgin crystal.

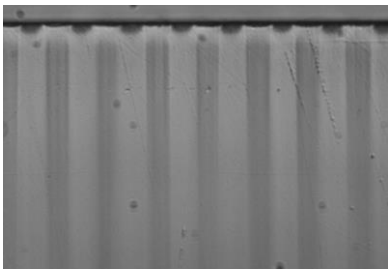


Fig. 1: PPLN sample made by the proposed two-step poling process.

In order to quantity the parameters responsible for the lateral expansion of the inverted domains, we analysed the digital images taken from the optically polished y-faces of PPLN or PPLT. Sketched in Fig. 2 are (a) our suggestive trapezoidal domain shape analysis for (b) inverted domain at the –Z face of our study. By examining the sidewall expansion distance as a function of the polarization

switching field and the switching time, we observed in Fig.2(c) an extremely low value of domain mobility 0.01 mm^2/kV-sec on the –Z face of PPLT. We note this value is two-order of magnitude lower than that of free expansion value in the –Z face of inverted LN domains. The latter can be ascribed to the surface constraint exerted by the charged barriers underneath the +Z face of this study.

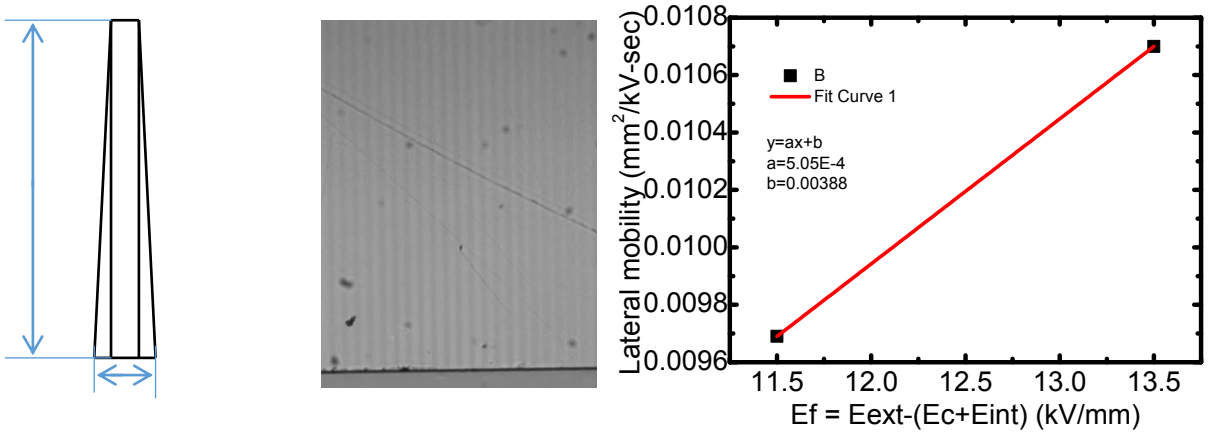


Fig. 2 (a): Trapezoid domain shape analysis, (b) inverted domain, (c) field-dependent mobility for Z-cut PPLT.

We further applied this proposed method to realize a 20mm-long PPLT crystal and built up a spectrally-tuned infrared OPO. The latter was degenerate-pumped by a Q-switch 532nm SHG green laser of 5ns width and 500Hz repetition rate. The corresponding (a) temperature-dependent IR OPO output spectra and (b) conversion efficiency, were displayed in Fig.3, respectively. Here we denote a continuously shift of the 1060nm-band lasers to 1060± 50nm with ± 5°C temperature tuning. The splitting of signal/idler spectra can be analysed to have a Lorentzian gain profile of 20nm (~140cm^{-1}) width and dispersed with ~14cm^{-1} mode spacing. The latter is ascribed to a thin (~250μm) OPO output mirror which also plays a role of intra-cavity etalon. The OPO characteristics data in Fig. 3(b) reveals a threshold of 85mW and slope efficiency more than 45%.

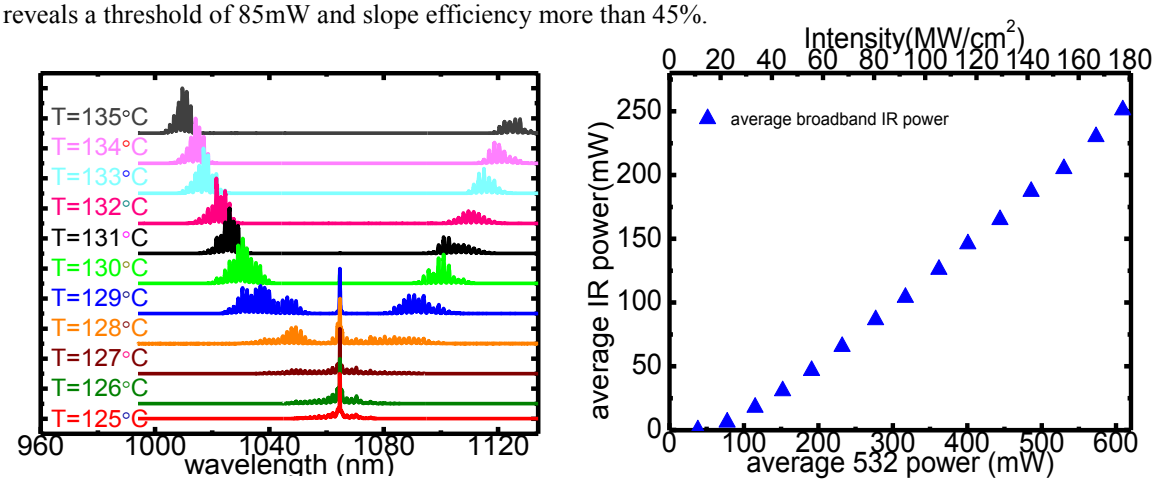


Fig. 3 (a)Temperature-tuning, and (b) slope efficiency of a 20mm-long PPLT-OPO build-up by this proposed method.

Conclusions: We demonstrated the use of two-step, i.e., diffusion followed by pulse field poling procedure to realize QPM devices on PPLN and PPLT. An extremely low value of lateral domain mobility of ~0.01 mm^2/kV-sec can be found on the –Z face of PPLT and was ascribed to the +Z face anchoring effect due to the charged barriers formed by the diffusion process.

References

1. P. Ferraro, S. Grilli, P. De Natale, "*Ferroelectric Crystals for Photonic Applications*,"(2nd Ed, Springer,2014).
2. L. -H. Peng, Y. -C. Fang, and Y. -C. Lin, "Polarization switching of lithium niobates with giant internal field," Appl. Phys. Lett. **74**, 2070 (1999).

Optical Waveguides Processed by Internal Diffusion in Photosensitive Doped Host/Guest Polymer

Heinrich Sieber[1], Uwe Hollenbach[1], Jürgen Mohr[1], Karl Pfeiffer[2], Ute Ostrzinski[2], Gabi Grützner[2]

[1] *Institute of Microstructure Technology (IMT), Karlsruhe Institute of Technology (KIT), Karlsruhe, Germany, heinrich.sieber@kit.edu, uwe.hollenbach@kit.edu, juergen.mohr@kit.edu*

[2] *micro resist technology GmbH (MRT), Berlin, Germany, k.pfeiffer@microresist.de, u.ostrzinski@microresist.de, g.gruetzner@microresist.de*

Abstract: We report on manufacturing and characterization of planar optical single mode waveguide structures in a photosensitive negative tone resist. The resist is based on a two component host/guest-polymer. Diglycidester-oligomer as host polymer is doped with a special glycidyl-monomer. The refractive index of the mixture is adjustable by an internal diffusion processes during the pre- and post- exposure bake. This allows a "one-material" processing which avoids chemical wet etching after exposure. The refractive index distribution shows nearly step index profiles. The near field intensity distributions present perfect Gaussian modes. Prototype CWDM waveguide structures have been fabricated.

Introduction: Today optical fibers are used as point to point interconnects between separated electrical boards for data transfer between electrical processors. In view of higher data rates optical parallel processing on optical printed circuit boards (OPCB's) is under development. It needs a higher integration of optical network routing using hybrid integrated optical circuits. Polymeric multimode (MM) waveguide structures for applications in OPCB's are described in [1]. We are focusing on the development of an easy handling process which is suitable for single mode (SM) waveguide fabrication using UV- lithography or direct laser writing at 365nm.

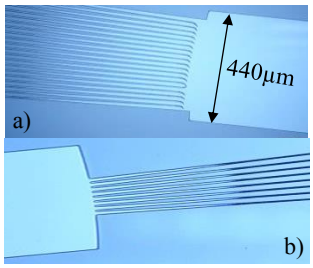


Fig. 1. Pictures of CWDM parts; a) AWG out at star coupler, b) 8x WG output

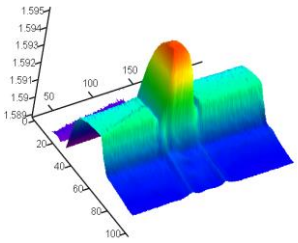


Fig. 2. RI- profile across WG core, w=h=6µm, Δn~0.0050, @ 678nm

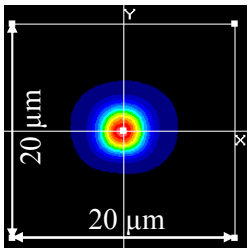


Fig. 3. NFP of a SM-WG, $\omega_{x,y}$=5.9µm ($1/e^2$), @ 808nm

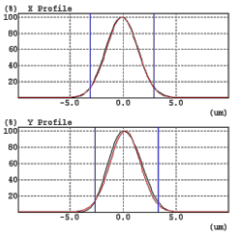


Fig. 4. x-y-intensity profiles of NFP, and Gauss fits @ 808nm

Polymer Synthesis: We developed a novel mixed polymer to improve the condition for an internal diffusion which allows refractive index (RI) adjustment between cladding and core. This resist was developed and tested in a 3-years project named POLINA [2]. A diffusible additive glycidyl-monomer is used as low RI solvent of 15-30w% in 80-65w% of oligomer (pre linked units of bisphenol-A-diglycidether) which is the curable high RI part of the mixed polymer approach. The catalytic accelerator in the photosensitive polymer is a 5w% standard photo acid generator (PAG, bis/thio- triarylsulfonium hexafluoroantimonate).

Polymer Processing: The basic process steps to fabricate waveguide cores in polymers are well known [3] and encompass a) spin coating, b) pre bake (PB), c) UV- exposure, d) post exposure bake (PEB) and hard bake (HB). Basic carrier is a 4-inch diameter Si-substrate. At first we prepare an app. 20µm thick under-cladding followed by the manufacturing of the waveguide (WG) core layer in a thickness of app. 5-6µm and 8-9µm for different operation wavelengths of 780-980nm and 1260-1600 nm respectively. Finally we cover the WG core layer by an over-cladding of app. 20µm to protect the WG cores. The structuring of the core layer is done using standard i-line lithography at 365nm and a light field COG-mask. The UV-light activates the PAG and during the PEB at temperatures up to 95°C the polymerization is only possible outside of the core structures. The crosslinking runs a) inter- and b) intra-molecular between the oligomers and c) between the oligomers and the dopant

monomers. Therefor the concentration of free monomers decreases quickly and the dopant monomer diffusion starts in plane from the core area into the cladding area. Additionally in both areas an out-of-plane diffusion of free dopant monomers runs which, due to the polymerization, is much stronger in the core area than in the cladding area. This leads to the required RI difference between the waveguide core and cladding. Instead of UV- lithography we also demonstrate direct laser writing at 365nm for waveguide patterning. After PEB and crosslinking of the cladding the whole layer is flood exposed and in a second PEB also the core structures are cured. At last a hard bake up to 180°C is done to shift the glass temperature up to app. 160°C.

Results: After the WG structure processing (see Fig. 1) we analyze the RI using a scanning RNF-method at 678nm (Fig. 2). The RI profile gradients show nearly step index distribution and the RI contrast Δn is about 0.005 (0.006) for a core size of 6µm x 6µm (8µm x 8µm). The near field intensity pattern (NFP) is given in Fig. 3. The fundamental modes have perfect Gaussian shapes and the x-y mode field intensity diameters are 5.9µm (8.0µm) at the $1/e^2$ intensity levels at 808nm (1310nm). The far field intensity patterns (FFP) have divergence angles of app. 15° at the 1% intensity levels at 808nm which is consistent to an aperture value of NA=0.13. The typical (best) insertion loss values are 0.25dB/cm (0.14dB/cm) at 808nm and 0.42dB/cm (0.33dB/cm) at 1310nm. Polarization analysis shows PDL values of <0.3dB which is the limit of our Jones-matrix method accuracy.

Based on the encouraging results with different test structures (straight WG with different mask widths, curved WG with diff. radius and arc-lengths) we produce functional structures like splitters, symmetrical and asymmetrical interferometers, couplers for 780/905nm, 850/960nm and 1310/1550nm and CWDM wavelength filters for 1300nm. Exemplarily the characterization of a 1x8 channel CWDM structure is shown in Fig. 5. The design for a first prototype has a structure size of L x W=36mm x 3mm (Fig. 5a). The arrayed WG (AWG) contains only N=20 WG to minimize the chip size.

The intensity distribution in the front and middle of the AWG is shown in Fig. 5b-c. The output spectral transmission has a smallest insertion loss (IL) of 5dB at 1285nm using a Super-Continuum-Laser (Fig. 5d) and 4 dB at 1305nm using a tunable laser source. The cross talk depression is >20dB at channel center and >10dB in spans of ±6.5nm side wall distance around 1305nm. The aimed channel space of 20nm is realized to 19.6nm with ±0.9nm standard deviation. The thermal sensitivity of the CWDM chip was tested between RT and 70°C and the drift coefficient is about -0.11nm/K.

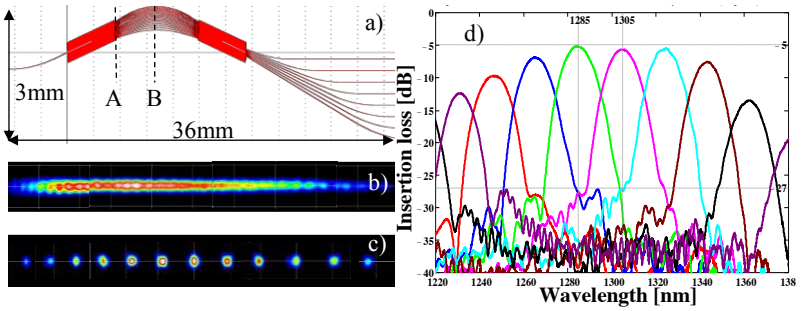


Fig. 5. a) 1x8 CWDM design; b-c) Int. distribution in front (cut A in 5.a) and middle (cut B in 5.a) of the AWG; d) Spectral transmission at the output ports 1-8 using Super-Continuum-Laser @ 1200 – 1400 nm

Resume: Our newly developed and applied mixed polymer was demonstrated in a "one-material"-technique of WG core formation based on internal diffusion of dopant monomers. It simplifies the manufacturing and avoids wet etching steps. Rapid prototyping and cost efficient manufacturing for examples guides to complex functional structures such as splitters, interferometers for app. 780-980 nm and couplers for 1310/1550nm wavelength range. Furthermore we realized CWDM's for 1250-1350nm wavelength ranges where SM and high degree MM structures are operated in combination.

Acknowledgement: The POLINA- project "Polymere Lichtwellenleiter für die Nanophotonik" was sponsored by the German Federal Ministry of Economics and Technology under grant BMWi-AIF (ZIM) KF 2308201MF9.

1. Fuad E. Doany, et al, *IEEE Transactions on Advanced Packaging*, **Vol. 32**, No. 2, May 2009, P. 345 – 359
2. Heinrich Sieber, et al, *Proc. of Photonics Europe, Bruxelles*, 2012, **Series 8431**
3. A. del Campo, et al, *J. Micromech. Microeng.*, **17** (2007), R81-R95

Ridge waveguide structures in KYW crystals produced by beam-multiplexed fs-laser writing

J. Martínez de Mendíbil[1], G. Lifante[1], J. del Hoyo[2], J. Solís[2], M. C. Pujol[3], M. Aguiló[3] and F. Díaz[3]

[1] Dept. de Física de Materiales, C-04, Universidad Autónoma de Madrid, 28049-Madrid, Spain
jon.martinez@uam.es, gines.lifante@uam.es
[2] Laser Processing Group, Instituto de Optica, CSIC, Serrano 121, 28006-Madrid, Spain
j.hoyos@io.cfmac.csic.es, j.solis@io.cfmac.csic.es
[3]Física i Cristal·lografia de Materials i Nanomaterials (FiCMA-FiCNA), Universitat Rovira i Virgili (URV), Campus Sescelades, c/ Marcel.lí Domingo, s/n, E-43007, Tarragona, Spain
mariacinta.pujol@urv.cat, magdalena.aguilo@urv.cat, f.diaz@urv.cat

Abstract: Femtosecond laser structuring using a multiplexed beam has been used to produce ridge waveguides in KYW crystals. The initial structure consists on a planar waveguide where a cladding is added by LPE technology. Then, the cladding is structured by fs-laser processing is such a way that lateral confinement of the light is achieved by a local increase of the effective refractive index of the planar waveguide. The proposed waveguide geometry allows the propagating mode to be confined in a region far from the lateral walls of the ridge, thus avoiding losses that could arise from the roughness of the walls at the high-index material/air interfaces.

Introduction. Double tungstates, such as $KY(WO_4)_2$, have been widely studied for photonic applications[1,2]. In particular, their optical transparency, high refractive indices, and the high absorption and emission cross sections when doped with rare earths, make them good candidates for developing integrated optical devices. Combining Liquid Phase Epitaxial (LPE) with Reactive Ion Etching (RIE) o Ar milling techniques for the surface micro-structuring, low losses (< 0.25 dB/cm) waveguides have been reported, and efficient waveguide lasers have been demonstrated[3]. Alternatively, channel waveguides can be structured by fs-laser writing[4], although wall roughness can induce undesired propagation losses. Here we propose and study numerically a ridge waveguide structure which avoids losses from the roughness at the high-index material/air interface. These structures have been fabricated in KYW crystals by LPE followed by fs-laser processing structuring. Experimental results have been then compared with predictions based on numerical modelling.

Ridge structure. Figure 1 shows the cross-section of the proposed ridge structure with the relevant size parameters. It consists of a film of refractive index n_{core} and thickness h_1, which acts as the waveguide core, sandwiched by a uniform substrate (n_{subs}) and a structured cladding made with of the same material ($n_{clad} = n_{subs}$). In the figure h_2 represents the residual cladding thickness.

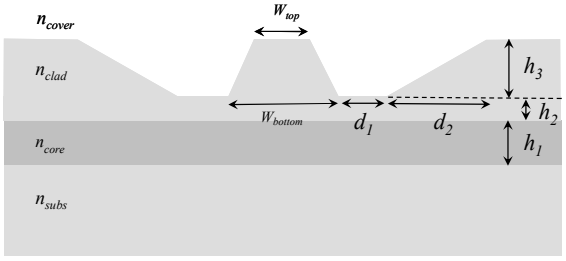


Fig. 1: Transversal section of the ridge structure.

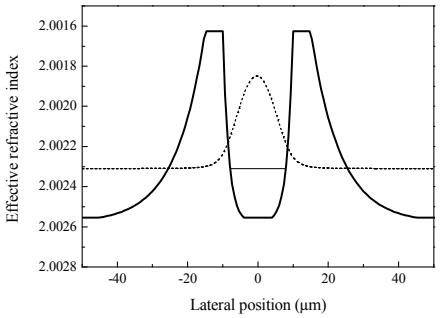


Fig. 2: Effective index and mode profiles using EIM.

The transversal structure has been analyzed by means of the effective index method[5] (EIM). For such a purpose, the effective index corresponding to the fundamental mode of the asymmetric planar waveguide obtained by vertical cuts from the original structure is obtained as function of the total cladding thickness (h_2+h_3 in figure 1), and then it is parameterized to an exponential function. In the model, $n_{clad} = n_{subs} = 2.000$ (KYW crystal), and $n_{core} = 2.005$, that is, a 5×10^{-3} index increase respect to

the substrate index, which is a typical value obtained in LPE epitaxial layers. The core thickness is h_1 = 4 μm, and the working wavelength is λ = 1.55 μm. Figure 2 plots the effective index profile (thick line) along the horizontal direction obtained by the EIM. That index profile was obtained with: h_2 = 0.5 μm, h_3 = 8 μm, W_{bottom} = 20 μm, W_{top} = 10 μm, d_1 = 5 μm and d_2 = 30 μm. The modal intensity profile of the fundamental mode (dashed line) and its effective index (horizontal line) are also plotted in figure 2. As the resulting 2D-waveguide consists on light confinement between two low-index optical barriers, some losses are expected coming from tunneling through the low-index barriers, similar to those found in ion implanted waveguides. In this case, the calculated propagation loss of the mode at 1.55 μm is 0.25 dB/cm. The losses can be reduced either by increasing the residual cladding (h_2) or by increasing the lateral distance d_1 (or even d_2).

Following this concept, a ridge waveguide has been fabricated on an oriented KYW substrate grown by the TSSG method[1]. A layer of 0.5% Er^{3+}-0.5% Yb^{3+} KYW was deposited by LPE[6], with a final thickness of 4 μm. After that, a 8 μm cladding of pure KYW was additionally grown. The three-layer sandwich was then processed with a multiplexed fs-laser beam, using a spatial light modulator, as described in Ref.4, in order to produce ridge structures similar to those shown in figure 3 (left, center). After end-face polishing, the mode profile of the waveguides at 1640 nm was measured (figure 3, top-right) showing a good mode confinement of the ridge structure and negligible propagation losses. In the same figure (bottom-right) the mode intensity profile obtained by imaginary-distance 3D-BPM has been included, using the parameters derived from the experimental profile dimensions and the refractive indices of the substrate and core layers. Also, the measured losses at this wavelength are lower than 0.5 dB/cm.

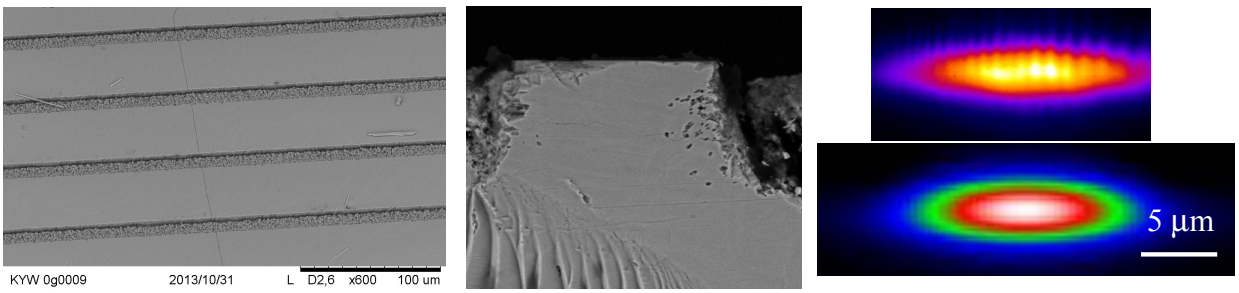


Fig. 3: Left and center: Typical SEM images appearance of the ridge structures produced before end facets polishing. Right: measured (top) and simulated (bottom) waveguide mode at 1640 nm.

Conclusions. A waveguide ridge structure has been proposed to generate lateral confinement on planar structures grown by KYW crystals fabricated by the LPE. This structure has been fabricated by fs-laser processing, and the results of light propagation have been compared with numerical simulations. The good accordance between experiments and simulations indicate that this a promising route for fabricating channel waveguides in KYW crystals and its isostructural family.

Acknowledgements. This work has been supported by the Spanish Government under projects MAT2011-29255-C02-01/02, and by the Generalitat de Catalunya under project 2009SGR235.

References

1. X. Mateos et al., *Opt. Mat.* **28**, pp. 423-431 (2006).
2. S. Bjurshagen et al., *Appl. Opt.* **45**, pp. 4715-4725 (2006).
3. W. Bolaños et al., *Opt. Express* **18**, pp. 26937-26945 (2010).
4. J. Cugat et al., *J. Light. Technol.* **31**, pp. 385–390 (2013).
5. G. Lifante, *Integrated Photonics: Fundamentals. John Wiley & Sons, 2003.*
6. W. Bolaños et al., *Cryst. Growth Des.* **9**, 3525-3531 (2009).

Authors are asked to submit an acrobat reader (pdf) version electronically on the conference's website http://www.atout-org.com/eciomoc2014).

Nanocrystalline Diamond Optical Planar Waveguides

V. Prajzler[1], P. Nekvindová[2], M. Varga[3], Z. Remes[3], A. Kromka[3]

[1] Czech Technical University, Prague, Czech Republic,
xprajzlv@feld.cvut.cz
[2] Institute of Chemical Technology, Prague, Czech Republic,
pavla.nekvindova@vscht.cz
[3] Institute of Physics, Academy of Sciences of the Czech Republic, Prague, Czech Republic,
varga@fzu.cz, remes@fzu.cz, kromka@fzu.cz

Abstract: We report about properties of nanocrystalline diamond planar waveguides. Design of the presented planar waveguides was done on the bases of modified dispersion equation and experimental samples were fabricated by microwave plasma enhanced chemical vapor deposition on silica-on-silicon substrates. Waveguiding properties of our samples were examined by prism coupling technique at 473 nm, 632.8 nm, 964 nm, 1310 nm and 1550 nm wavelengths. It was found that the diamond thin films guided one fundamental mode for all measured wavelengths.

Introduction

Nanocrystalline diamond (NCD) thin films have been of special interest for photonics application in the past few years because they exhibit beneficial chemical and physical properties. NCD thin films have high thermal conductivity, high density, large Young's modulus and high stability under extreme operating conditions [1-3]. Natural diamonds have also high refractive index. Though refractive index of synthetically prepared NCD film is usually lower than that of natural one, NCD deposited on silica-on-silicon substrate still has enough high refractive index contrast. The waveguides created this way are known as high index contrast (HIC) waveguides. Useful HIC waveguides can be used for small bending radius structures or compact and ultra dense photonics integrated circuits. One of the most important NCD thin films properties is its ability to act as a single photon source by incorporating N-V centres in diamond matrix. This opens a possibility of using NCD for quantum key distribution. Therefore development of waveguide in NCD films is an important first step towards a monolithic platform and all-diamond devices [4].

Design and fabrication of the NCD waveguides

In this paper we are going to describe design and fabrication of NCD planar waveguides deposited on silica-on-silicon substrate. The dimensions of the NCD planar waveguides were calculated by using modification dispersion equation. From the calculations it follows, e.g., that if we want the deposited film to guide one single mode, the thickness of the diamond film (h_{NCD}) should not exceed 200 nm at 632.8 nm, and for the 1550 nm the diamond film (h_{NCD}) should not be thicker than approx. 450 nm [5]. The thickness of the buffer SiO_2 film (h_{SiO2}) was set according to the calculated one, which ensures that the out-coupled energy of the evanescent wave would be less than 1 %. Calculations made clear that to ensure the above-mentioned conditions the thickness of the silica film should not be smaller than 900 nm for all considered wavelengths. Therefore we used silica-on-silicon substrate with thickness of the silica film to be around 1420 nm, which is fully sufficient.

After designing of the NCD planar waveguides we fabricated NCD waveguides by using microwave plasma enhanced chemical vapor deposition (MW PECVD) on silicon substrate bearing 1420 nm thick silica film. The NCD deposition was done from a gas mixture of methane and hydrogen (for NCD1 sample the hydrogen gas flow was 400 sccm and methane gas flow was 2 sccm while for the NCD2 sample the hydrogen gas flow was 500 sccm and methane gas flow was 1.5 sccm, resp.) in a MW PECVD reactor using an ellipsoidal cavity resonator [5, 6].

Results

Morphology of the NCD layers was investigated by Raman spectrometer (Renishaw InVia Reflex) with the excitation wavelength of 325 nm and the obtained data are shown in Fig. 1. Raman spectrum exhibits two sharp peaks, first one is centered at 521 cm^{-1} and it is assigned to the silicon substrate; the second one centered at 1332 cm^{-1} is well known as the so called diamond peak and it is related to sp^3

bonds. The wide band located at 1580 cm^{-1} is assigned to the G-band ("graphite-band") and is related to the sp^2 phases (i.e. amorphous phases) preferentially localized at grain boundaries [6]. The NCD2 sample was done at lower concentration of methane in the reaction mixture and it revealed lower rate of sp^2 ordering than NCD1.

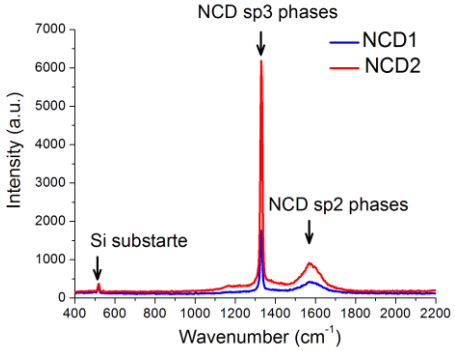


Fig. 1: Raman spectrum of the deposited NCD.

Waveguiding properties of the NCD films were measured by prism-coupling system using Metricon 2010 prism-coupler at five wavelengths: 473 nm, 632.8 nm, 964 nm, 1311 nm and 1552 nm. Measurements of the mode spectra for both polarizations (TE and TM) proved that the values of the refractive indices for TE and TM modes are almost identical. Based on this observation, we will in the following text for simplicity show only the TE modes. Refractive indices of the deposited films were calculated using the angles given for sample NCD1 in Fig. 2a, the wavelengths of the measurement and, if needed, the thickness of the NCD waveguiding films (380 nm). NCD2 sample that had lower rate of sp^2 we did not succeeded to get the refractive index value for 473 nm. Fig. 2b plots refractive indices of our NCD films against the values of natural diamond [8]. According to the calculations mentioned above it was expected that the deposited NCD film having a thickness of 380 nm will support 2 TE modes at the wavelengths of 964 nm and shorter. At the longer wavelengths there would be noticeable one TE mode only. However, the measurement showed that the deposited films actually supported always just one mode at all applied wavelengths. The value of the refractive indices of our NCD film much more resemble refractive indices of natural diamond than the films reported in [7], what make us to believe in high optical quality of our products.

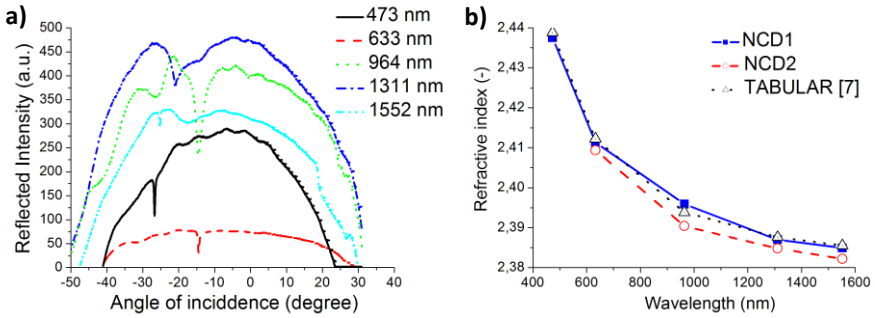


Fig. 2: a) TE guided mode spectrum for the NCD1 sample, b) Comparison of refractive indices of our NCD waveguides and natural diamond.

Conclusion

In this paper we presented a modified approach to deposit diamond thin layers. Waveguiding structure of our deposited layers was calculated for various operating wavelengths using modified dispersion equation. The NCD waveguides were fabricated by MW PECVD on silica on silicon substrate. The comparison with cited references [7] shows the merit of our work, as refractive index of our diamond is very close to natural diamond.

References

1. P. Achatz, et al., *Applied Physics Letters* **88**, 101908 (2006).
2. D.M. Gruen, *Annual Review of Materials Science* **29**, pp. 211–259 (1999).
3. O.A. Williams, et al., *Chemical Physics Letters* **495**, pp. 84–89 (2010).
4. M.P. Hiscocks, et al., *Conference on Photonics: Design, Technology, and Packaging III*, SPIE **6801**, (2008).
5. V. Prajzler, et al., *Optics Express* **21**, pp. 8417-8425 (2013).
6. A. Kromka, et al., *Vacuum* **86**, pp. 776–779 (2012).
7. E. D. Palik, *Handbook of Optical Constants of Solids* (Academic Press, 1985).

Acknowledgments

Our research is supported by the Grant Agency of the Czech Republic under grant number GA14-05053S.

Subsurface Disorder and Electro-Optical Properties of Proton-Exchanged $LiNbO_3$ Waveguides Produced by Different Techniques

S.M. Kostritskii[1], Yu.N. Korkishko[1], V.A. Fedorov[1], V.P. Mitrokhin[1], O.G. Sevostyanov[2], I.M. Chirkova[2], M. De Micheli[3], O. Stepanenko[3]

[1]RPC Optolink Ltd, 124489, Zelenograd, Russia,
skostritskii@optolink.ru, korkishko@optolink.ru, fedorov@optolink.ru, mitrokhin@optolink.ru,
[2]Phys. Dept., Kemerovo State University, 650043, Kemerovo, Russia,
olsevos@yahoo.com, irina1989_2@mail.ru
[3]LPMC, Université de Nice Sophia-Antipolis, 06108 Nice Cedex 2, France,
marc.de-micheli@unice.fr,

Abstract: It has been established, that subsurface disorder in soft proton-exchanged (SPE) waveguides is much smaller than in annealed proton-exchanged (APE) ones. The experimental samples of phase modulators fabricated by SPE technique exhibit the improved electro-optical efficiency and superior propagation losses compared to the $LiNbO_3$ modulators produced by the standard and improved APE techniques. According to our data, low DC bias drift behavior of such SPE modulators is expected.

Introduction: Proton exchange is now an established technique for fabricating integrated optical devices in $LiNbO_3$, as it offers potential possibility of obtaining low-loss waveguides with a good electro-optical (EO) performance[1]. Note that a significant degradation (more than one order of magnitude) of the EO coefficients occurs immediately after the proton exchange process[1,2]. However, after appropriate annealing the EO coefficients are almost re-established and reach maximum values in the so-called α-phase annealed proton-exchanged $LiNbO_3$ waveguides[2]. By the way, EO coefficients cannot be restored completely even after a long annealing at the standard fabrication conditions that is in common use today[1-3]. It was shown[4] that the extended annealing in dry air at $T \geq 320\ ^oC$ leads to the precipitation of disordered phases in a subsurface layer (depth $\leq 0.5\ \mu m$), causing undesirable degradation of the EO properties of the waveguide. Such degradation could be interpreted as the field-screening effect in the highly structurally disordered parts of the proton exchanged regions below the surface. Besides, these structural defects are observed to increase the conductivity, believed to be a key reason for a DC-voltage bias drift of the EO modulators[4]. Besides, it was recently reported[3] that this subsurface disorder provides some marked level of propagation loss related mainly to guided mode scattering within inhomogeneous near-surface part of waveguide. It has been established[4] that the loss of water during annealing is a major contributor to the formation of crystalline disorder and, hence, annealing under a high pressure of water vapor is shown to decrease such a disorder. However, this method allows only for partial suppression of the both subsurface disorder and related degradation of waveguide properties. To avoid these undesirable effects completely, the method of the soft proton exchange (SPE) has been proposed to use in this work, as there is no any water losses when the α-phase waveguides are fabricated by SPE[5].

Samples Fabrication and Characterization Techniques: APE waveguides were fabricated with standard technique[2] (APE1 sample was annealed in dry air at 360 °C) and improved APE technique[4] (APE2 sample was annealed for appropriate time[2] in wet air at 360 °C). SPE waveguides were fabricated by special method[5] with benzoic acid melts containing the various concentration of lithium benzoate (LB): for SPE1 and SPE2 samples [LB] was 2.4 and 1.5 mol%, respectively.

Subsurface disorder was studied by depth profiling with micro-Raman spectrometer and oblique IR-reflection with spectrophotometer. Electro-optic coefficient r_{33} values were estimated from data[2] on band gap and disorder factor F values in different waveguides. Finally, the fiber-pigtailed phase modulators were formed on basis of these waveguides and effective values of r_{33} were measured with the aid of a fiber-optical Sagnac interferometer.[2]

Experimental Results: Broadening of Raman phonon bands is well-established clear indication[2,6] of a marked structural disorder in $LiNbO_3$. According to the significant difference in FHWM (Fig.1 and Table 1) between waveguides studied, it's evident that subsurface disorder in SPE waveguides fabricated at optimal [LB] values is much smaller than in any APE samples.

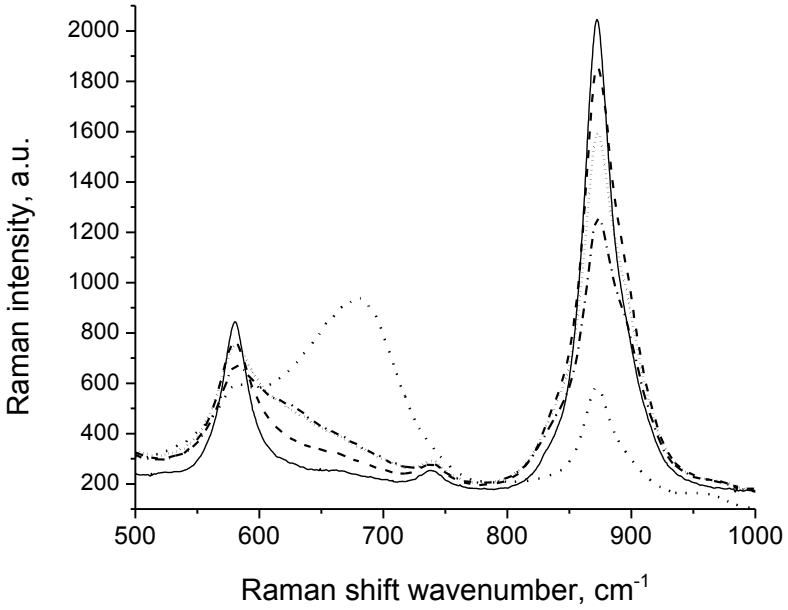


Fig. 1. Raman spectra of a subsurface part of the different samples: PE, APE1, APE2, SPE1 and z0 (notation meaning is given in text). This samples order corresponds to spectra sequence from bottom to top at 871 cm^{-1}.

Attenuation of Raman intensity (I_{LO}) of the LO-phonon band at 871 cm^{-1} and intensity (I_{extra}) increase of specific extra band at 656-690 cm^{-1} are related to decrease of local electro-optic response[2,6]. Indeed, a local value of electro-optic coefficient r_{33} may be rather smaller than its effective value because of the field-screening effect in a disordered subsurface part of waveguide[2].

Table 1. Sample notation, FWHM of Raman band at 871 cm^{-1}, disorder factor F, Raman intensities (I_{LO} and I_{extra}) of LO-phonon and extra Raman bands, and the effective values of electro-optic coefficient r_{33}.

sample	*FWHM, cm^{-1}*	*F*	*I_{LO}, a.u.*	*I_{extra}, a.u.*	*r_{33}*
z0, (pure LN)	29.7	0	3.5	0	1
SPE1	35.3	0.05	3.2	0.14	0.90
SPE2	38.7	0.074	2.7	0.3	0.82
APE2	40.5	0.082	3.1	0.18	0.85
APE1	44.1	0.095	3.0	0.24	0.80

The experimental samples of phase modulators fabricated by SPE technique exhibit the improved electro-optical efficiency (Table 1) and superior propagation losses compared to the $LiNbO_3$ modulators produced by the standard and improved APE techniques. Low DC bias drift is expected in SPE modulators, as subsurface disorder is shown[4] to be a key reason of such a drift.

References

1.M. Rottschalk *et al*, *Opt. Commun.* **9**, pp. 19-23, (1988).
2. S.M. Kostritskii *et al*, *Ferroelectrics* **440**, pp. 47-56, (2012).
3. T.T. Lay *et al*, *IEICE Transactions* **E74**, pp. 3870-3872, (1991).
4. H.G. Muller *et al*, *J. Appl. Phys.* **110**, 033539, (2011).
5. M. De Micheli *et al*, *J. Lightwave Techn.* **4**, pp. 743-745, (1986).
6. Yu.N. Korkishko *et al*., *J. Appl. Phys.* **84**, pp. 2411-2419, (1998).

PLC-based three-mode multi/demultiplexer for mode division multiplexing transmission

N. Hanzawa[1], K. Saitoh[2], T. Sakamoto[1], T. Matsui[1], K. Tsujikawa[1], T. Uematsu[2], M. Koshiba[2], and F. Yamamoto[1]

[1] NTT Access Network Service Systems Laboratories, Tsukuba, Ibaraki, Japan,
hanzawa.nobutomo@lab.ntt.co.jp
[2] Hokkaido University, Sapporo, Hokkaido, Japan,

Abstract: We realized a three-mode multi/demultiplexer (MUX/DEMUX) using parallel waveguides with a uniform height for mode division multiplexing transmission. We achieved the mode coupling of the LP_{01} mode to the LP_{21} mode by using the LP_{11}b mode, which we generated by rotating the waveguide 90 degrees with the mode coupling of the LP_{01} mode to the LP_{11}a mode. The mode conversion of the LP_{01} mode to the LP_{11} and LP_{21} modes in the C-band was achieved using our fabricated MUX/DEMUX.

Introduction: The transmission capacity in single-mode fiber (SMF) achieved by employing wavelength division multiplexing (WDM) and a multi-level modulation format is limited to around 100 Tbps owing to the input power and bandwidth limitations of an optical amplifier as shown in Fig. 1.[1] Recently, space division multiplexing (SDM) transmission with multi-core fiber and mode division multiplexing (MDM) transmission using few-mode fibers have been intensively studied and are attracting a lot of interest because of their potential for improving transmission capacity.[2-4] An optical fiber and a mode multi/demultiplexer (MUX/DEMUX) are the key components for realizing an MDM transmission. A mode MUX/DEMUX compatible with the LP_{21} mode has been realized using free space optics.[5]

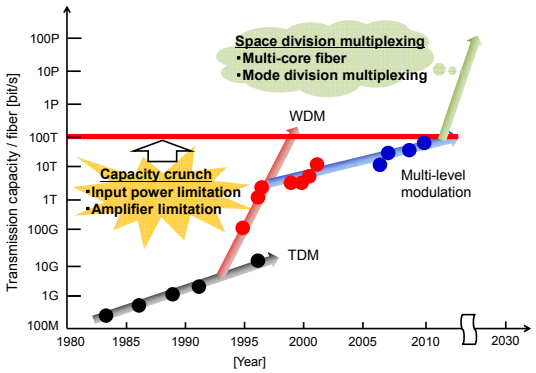


Fig. 1: Increase in single-mode fiber capacity.

We have already proposed a silica-based PLC-type two-mode MUX/DEMUX with a low insertion loss and a wide wavelength range.[6,7] The PLC-type device has distinctive advantages such as a small size, a high yield rate, and a low cost. Therefore, in terms of mass production, the use of a PLC with a uniform height as a mode MUX/DEMUX is a very promising approach, especially as the number of modes increases. In this paper, we report on a three-mode MUX/DEMUX for LP_{21} mode conversion. It was designed and fabricated using parallel waveguides with a uniform height.

Design of mode MUX/DEMUX for LP_{21} mode: Figure 2 shows the structure of our proposed three-mode MUX/DEMUX. The basic concept is the same as for LP_{21} mode coupling. Since the LP_{01} mode cannot be directly coupled to the LP_{21}a mode by matching the effective index, it was realized by using the LP_{11}b mode. The LP_{11}b mode is generated by rotating the LP_{11}a mode 90 degrees since it is also impossible to couple the LP_{01} mode to the LP_{11}b mode. The LP_{01} mode from port 1 is converted to the LP_{11}a mode, and the LP_{01} mode from port 2 is directly output at the output port. The LP_{01} mode from port 3 is converted to the LP_{11}a mode, and the LP_{11}b mode is generated from this LP_{11}a mode by rotating the waveguide 90 degrees,

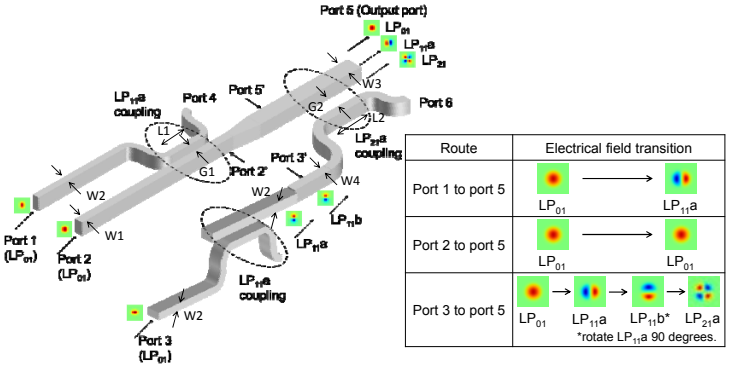
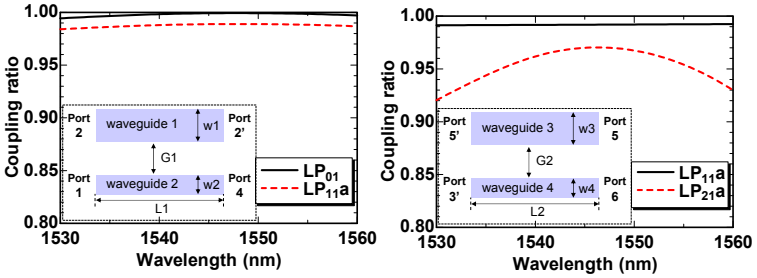


Fig. 2: Diagram of fabricated three-mode MUX/DEMUX.

which is converted to the $LP_{21}a$ mode. Here, we assumed the relative index difference and the waveguide height to be 0.45% and 9.0 μm, respectively. We then calculated the mode coupling ratios of the LP_{01} mode to the $LP_{11}a$ mode and the $LP_{11}b$ mode to the $LP_{21}a$ mode with three-mode multiplexing when we adopted w1, w2, w3, w4, G1, G2, L1, and L2 values of 12.9 μm, 4.5 μm, 19.1 μm, 7.0 μm, 4.0 μm, 9.0 μm, 0.65 mm, and 8.9 mm, respectively. Figure 3(a) and (b) show the wavelength dependence of the coupling ratios from port 1 or 2 to port 2' and from port 3' or 5' to port 5. The solid and dashed lines, respectively, show the coupling ratios of the LP_{01} and $LP_{11}a$ modes in Fig. 3(a) and those of the $LP_{11}a$ and $LP_{21}a$ modes in Fig. 3(b). The coupling ratios of the $LP_{11}a$ and $LP_{21}a$ modes exceeded 98% and 92%, respectively, between 1530 and 1560 nm. We consider the mode crosstalk to be relatively small since the coupling ratios of the LP_{01} and $LP_{11}a$ modes in a straight port exceeded 99%.



(a) (b)

Fig. 3: (a) $LP_{11}a$ mode coupling ratio dependence on wavelength. (b) $LP_{21}a$ mode coupling ratio dependence on wavelength.

Experimental results: We fabricated three-mode MUX/DEMUXs using the above parameters. In the experiment, a four-mode fiber supporting the LP_{01}, LP_{11}, LP_{21}, and LP_{02} modes in the C-band was connected to the output port of the PLC, and a conventional SMF was connected to ports 1, 2, and 3. Figure 4 shows near field patterns (NFPs) measured at the output port when a CW light with a wavelength between 1530 and 1565 nm was input into ports 1, 2, and 3. The LP_{11} and LP_{21} mode patterns were clearly observed by converting the LP_{01} mode from ports 1 and 3 to the LP_{11} and LP_{21} modes in the waveguide. As a result, we confirmed that the three modes were multiplexed by the fabricated MUX/DEMUX in the C-band.

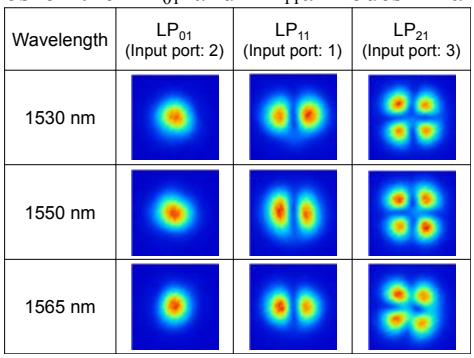


Fig. 4: NFP of output port from each input port.

We then observed the three-mode multi/demultiplexing. Figure 5 shows the eye patterns when the signals of an individual mode and three multiplexed modes were input into the three-mode DEMUX. Here, we used a 10 Gbps NRZ signal with a $2^{31}-1$ PRBS. The first, second, and third rows in Fig. 5 are the eye patterns of the LP_{01}, LP_{11}, and LP_{21} modes, respectively. Although the eye patterns of the third column were slightly degraded compared with those when the individual modes were input into the mode DEMUX, we confirmed that we could obtain relatively clear eye patterns with our fabricated three-mode DEMUX.

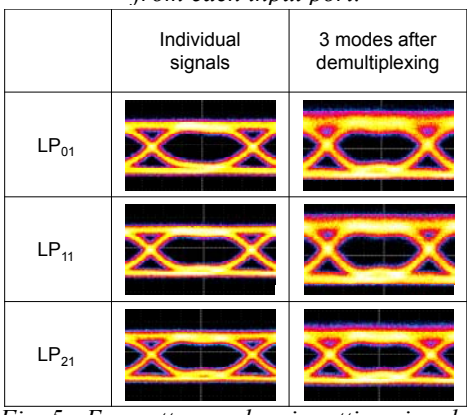


Fig. 5: Eye patterns when inputting signals of individual modes and three multiplexed modes.

Conclusions: We designed and fabricated a multi/demultiplexer for LP_{01}, LP_{11}, and LP_{21} mode conversion operating in the C-band using a silica-based PLC with a uniform height.

References

1. T. Morioka et al., IEEE Comm. Mag. **50**, p.s31-s42, (2012).
2. T. Mizuno et al., Proc. OFC2014, Th5B.2, (2014).
3. V.A.J.M. Sleiffer et al., Opt. Express, **20**, pp. B428-B438, (2012).
4. R. Ryf et al., Proc. OFC2013, PDP5A.1, (2013).
5. G. L. Cocq et al., Opt. Express **20**, pp. 27051-27061, (2012).
6. N. Hanzawa et al., Opt. Express **21**, pp. 25752-25760, (2013).
7. T. Uematsu et al., Proc. OFC2013, OTh1B.5, (2013).

A fully static OCT sensor using glass integrated optics system based on the LLIFTS technology

A. Creux[1], A. Warzecha[1], A. Morand[1], P. Benech[1], F. Thomas[2], E. Lecoarer[2], R. Puget[3], C. Bonneville[3], B. Martin[3], C. Cassagnettes[4] and D. Barbier[4].

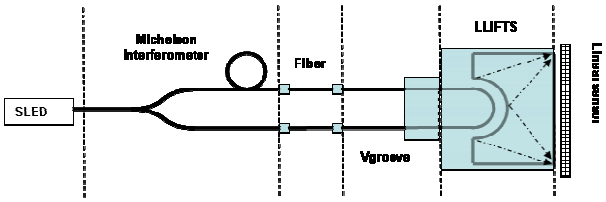
[1] IMEP-LAHC, Minatec, 3 Parvis Louis Néel, CS 50257, 38016 Grenoble, France
warzecha@minatec.inpg.fr, morand@minatec.inpg.fr, pierre.benech@phelma.grenoble-inp.fr
[2] UJF-Grenoble 1/CNRS-INSU, IPAG UMR 5274, Grenoble, F-38041, France
Etienne.Le-Coarer@obs.ujf-grenoble.fr, fabrice.thomas2@obs.ujf-grenoble.fr,
[3] Resolution Spectra System 13 chemin du vieux chêne, F-38240 Meylan, France
christophe.bonneville@resolutionspectra.com, renaud.puget@resolutionspectra.com, bruno.martin@resolutionspectra.com
[4] TeemPhotonics 61 chemin du vieux chêne, F-38240 Meylan, France
c.cassagnettes@teemphotonics.com, d.barbier@teemphotonics.com

Abstract: Optical Coherence Tomography (OCT) sensors traditionally use optical delay line with moving parts. In other way, OCT systems with linear detector array are more simples and do not need moving elements. They can be based on the measurement of a Fourier interferogram made along the linear pixel array. Nevertheless, optical bulk parts are often used. In this paper, an entire integrated system is proposed from the two input signals to compare (reference and probe) to the linear optical detector. Leaky Loop Integrated Fourier Transform (LLIFTS) technology is used to have a fourier interferogram along an edge of the glass chip which is glued on a CCD linear detector array without protective glass window. After describing the system principles, first measurements are presented.

Introduction: Nowadays a lot of kind of OCT sensors using different technologies as optical delay line (displacement of a reference mirror), optical grating or tunable source (SWEPT)[1] are available. The integration of theses systems can be complex to realize and not enough robust for easy use. The solution proposed in this paper is to use a linear optical coherence technology[2] for making a Fourier interferogram on a linear photodetector array. For example, this solution has been used with the analysis of the Young interference pattern issued from the superposition of two diffraction beams coming from two fibers, reference and probe signals. Using initially a SLED source, a fringe packet is observed. Its maximum position gives the optical phase difference between the two signals and the packet amplitude can give the amplitude probe signal. The FWHM of the SLED is directly related to the phase shift resolution and the size of the interferogram gives the accessible phase range or the imaging depth of a real sample to analyze. Due to the numerical aperture of single mode fiber, the size of the interferogram is limited in this configuration. In this paper, we propose to use glass integrated optic function to obtain the Fourier interferogram on the edge of the glass chip. For this purpose, a LLIFTS function is used[3]. In order to have a compact system, the CCD linear photodetector array is glued on this edge without optical lenses in order to have a stable module with an unique calibration table. The LLIFTS permits to increase the interferogram size and ideally the interferogram size would be limited only by the length of the linear sensor. In this paper, a 4096 pixels linear photodetector array is used with a square pixel pitch of $10\text{x}10\mu\text{m}^2$.

Description and realization of the system: The integrated optics glass chip is composed of two input single mode waveguides working in the wavelength range of 700-1000nm made by ion exchanged technology (Ag^+/Na^+). Each input waveguide is followed by a bend waveguide forming a loop. A planar waveguide is realized near the loop waveguide characterized by a gap between the two structures. Following the gap, a part of the light leaks in the planar waveguide tangentially of the bend waveguide. The planar waveguide allows this light part to reach the edge of the glass chip thanks to the vertical confinement. The modulation of the gap controls the amplitude and the size of the optical beam at the end of the component. The superposition of the two beams coming from the loop gives access to the fourier interferogram. The spatial fringes period at the end of the waveguide is enlarged due to the symmetry of the device. It must also be sampled by a linear detector array. This period is $\Lambda = (\lambda L)/(2nR)$ with L the length of the plane waveguide, R the radius of the loop and n the

refraction index of the glass. Three to four pixels are used to obtain a correct sampled interferogram. Using this method, a spectrometer has been already proposed with a spectral resolution close to 4nm at λ=850nm[4]. The linear detector array without the protective glass window has been approached mechanically to have a distance close to 60µm in order to reduce the diffracted effect at the output of the glass chip. For this purpose, the device is initially set on a large support which is then glued on the optoelectronic module as shown in Fig. 1.



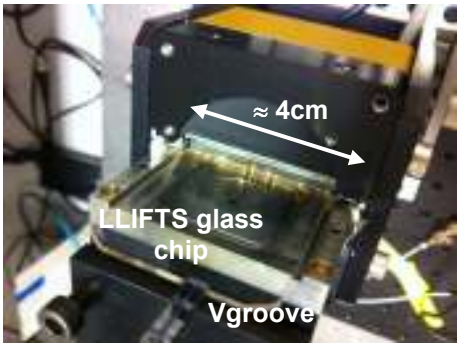
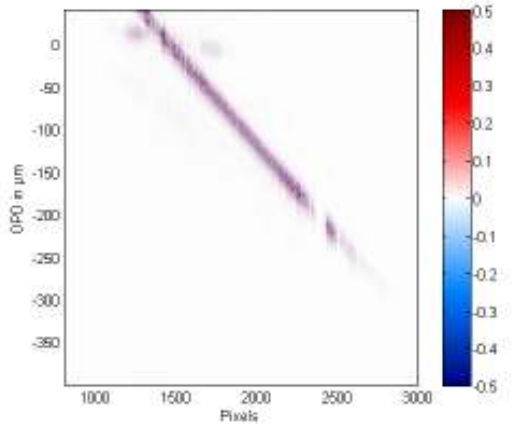


Fig. 1: Left: optical set up used to analyse the displacement of the fringe packet along the linear sensor. Right: picture of the sensor composed of two input fibers, the glass chip and the linear photodetector array.

First measurements: To analyze this system, an optical set-up is used to have two optical signals coming from a single SLED. For that, we use a Michelson interferometer permitting to have two different signals injected in two respective fibers. A displacement of one of the two mirrors allows the control of the Optical Phase Difference (OPD) between the two input signals. On Fig. 2, the position of the fringe packet can be observed following the OPD. A linear evolution of the maximum is observed over the mirror distance of around 300µm which is related to a pixel range of 1200 of the linear camera. With this linear detector array and a larger interferogram, OPD close to 1mm can be expected using this kind of static device. OCT analysis over a depth of this distance can be then investigated.



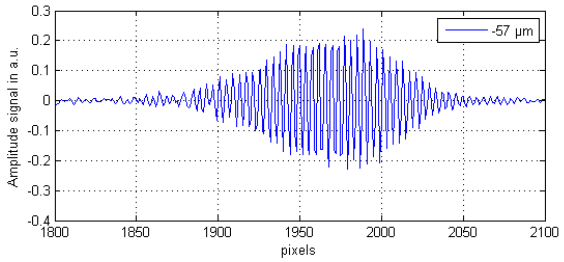


Fig. 2: Left: Evolution of the Fourier interferogram versus the OPD. Only the envelope has been eliminated to observe the useful interferogram. Right: zoom on the fringe packet at the OPD=-57µm of the SLED characterized by a wavelength center 870nm and a FWHM of 100 pixels (around 25 optical fringes).

It will be show that after a calibration step or basic signal treatment, the results can be improved. The perspective is to increase the integration, adding the y-junction after the SLED. Only two fibers will be used to reach a reference mirror and the sample under test.

Acknowledgement: The authors are thankful to the help of French ministry through an ANR Emergence project OCT-LLIFTS.

References

1. A. F. Fercher e*t al., Rep. Prog. Phys* **66**, pp. 239–303 (2003).
2. C. Hauger *et al., Appl. Opt.*. **42**, pp. 3896–3902, (2003).
3. B. Martin *et al*, *Opt. Lett.* **34**, pp. 2291-2293 (2009).
4. A. Creux *et al*, *Proc. of SPIE.* **8267** (2013).

Sub-base-pair Resolution During DNA Separation in an Optofluidic Chip

Markus Pollnau, Manfred Hammer, Chaitanya Dongre, Hugo J. W. M. Hoekstra

Integrated Optical Microsystems Group, MESA+ Institute for Nanotechnology, University of Twente, P.O. Box 217, 7500 AE Enschede, The Netherlands
m.pollnau@utwente.nl

Abstract: Applying capillary electrophoresis, we separate and detect two sets of fluorescent-labeled DNA molecules in the 150–1000 base-pair range and achieve a sizing accuracy of 4×10^{-4}, thereby enabling micro-chip analysis of genetic illnesses with single-base-pair deletion/insertion.

Introduction: DNA sequencing in a lab-on-a-chip aims at providing cheap, high-speed analysis of low reagent volumes to, e.g., identify genomic deletions or insertions associated with genetic illnesses. Detecting single base-pair insertions or deletions from DNA fragments in the diagnostically relevant range of 150–1000 base-pairs requires a sizing accuracy of $S < 10^{-3}$, while only $S < 10^{-2}$ were reported.[1] Here we demonstrate a sizing accuracy of 4×10^{-4}, thereby paving the way for the envisaged applications.

Experimental: A commercial microfluidic chip (LioniX BV), as displayed in Fig. 1, was post-processed by femtosecond-laser writing of an optical waveguide.[2] Two sets of DNA molecules were permanently end-labeled with different dyes to identify their origin.[3] The 12 blue-labeled (Alexa fluor 488) and 23 red-labeled (Alexa fluor 647) DNA fragments were separated in size by capillary electrophoresis,[1,3] each set excited exclusively by either of two lasers power-modulated at different frequencies of 17 Hz and 31 Hz and launched through the optical waveguide, their fluorescence detected by a sensitive photomultiplier, and blue and red signals distinguished by Fourier analysis.[3] The results are displayed in Fig. 2.

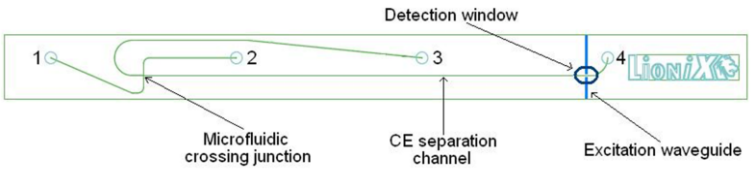


Fig. 1: Schematic of optofluidic chip.

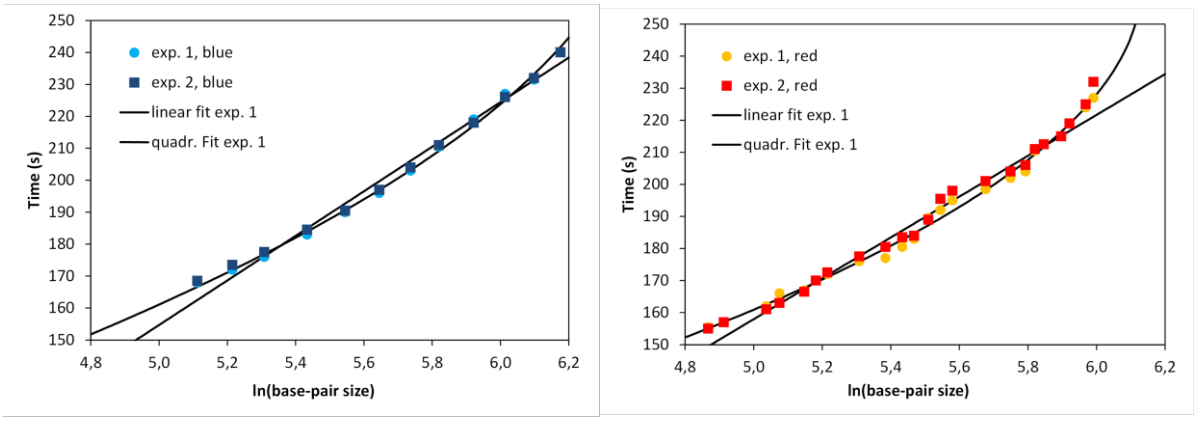


Fig. 2: Migration time (linear scale) vs. DNA base-pair size (logarithmic scale) of (a) 12 blue-labeled and (b) 23 red-labeled DNA molecules simultaneously migrated and separated in experiment 1 (circles) and experiment 2 (squares).

Data analysis: Different calibration strategies for the dependence of migration time on base-pair size in a given experimental situation were tested: a) use either set of DNA molecules as reference to calibrate the set-up and identify the base-pair sizes of the other set in the same flow experiment,

thereby eliminating variations in temperature, wall-coating and sieving-gel conditions, and actuation voltages; b) use the same molecular set as reference and sample (in a real-life experiment the reference set would be the healthy counter-part of an unknown, potentially malign sample set) with the same fluorescence label, flown in consecutive experiments; c) perform cross-experiments based on different molecular sets with different labels, flown in consecutive experiments; also d) self-calibration in the same experiment was analyzed. Results of the analysis are displayed in Fig. 3.

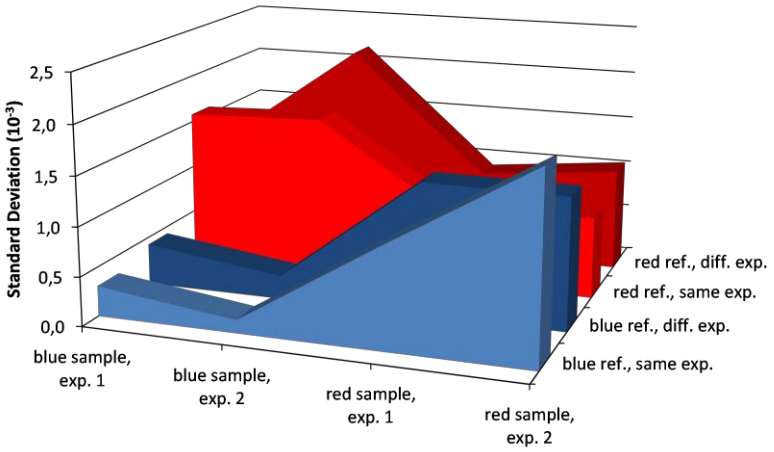


Fig. 3: Standard deviation of measured data from quadratic fit function.

Discussion: From the experimental results displayed in Fig. 2 and their analysis shown in Fig. 3 we conclude the following:

1) Applying quadratic instead of the usual linear fit functions improves the accuracy of calibration.

2) Blue-labeled molecules, see Fig. 2(a), are separated with higher accuracy than red-labeled molecules, see Fig. 2(b), hence different dye labels influence the DNA flow differently.

3) Different dye labels affect the formation and microfluidic flow of individual DNA plugs more severely than variations in temperature, wall-coating and sieving-gel conditions, and actuation voltages between consecutive experiments.

4) Choosing a single, suitable dye label, combined with reference calibration and sample investigation in consecutive experiments, see the left-hand side of the dark-blue curve in Fig. 3, results in a sizing accuracy of $S = 4 \times 10^{-4}$, enabling detection of single base-pair insertion/deletion in a lab-on-a-chip.

Conclusions: Choice of a suitable dye label, combined with reference calibration and sample investigation in consecutive experiments, results in capillary electrophoretic separation of fluorescent-labeled DNA molecules in the 150–1000 base-pair range with sub-base-pair resolution, thereby enabling detection of single base-pair insertion/deletion in a lab-on-a-chip with low reagent volumes in a few-minute experiment.

References

1. C. Dongre, J. van Weerd, G. A. J. Besselink, R. van Weeghel, R. Martínez Vázquez, R. Osellame, G. Cerullo, M. Cretich, M. Chiari, H. J. W. M. Hoekstra, M. Pollnau, *Electrophoresis* **31**, pp. 2584–2588 (2010).
2. R. Martínez Vázquez, R. Osellame, D. Nolli, C. Dongre, H. H. van den Vlekkert, R. Ramponi, M. Pollnau, G. Cerullo, Lab Chip **9**, pp. 91–96 (2009).
3. C. Dongre, J. van Weerd, G. A. J. Besselink, R. Martínez Vázquez, R. Osellame, G. Cerullo, R. van Weeghel, H. H. van den Vlekkert, H. J. W. M. Hoekstra, M. Pollnau, Lab Chip **11**, 679–683 (2011).

Ta_2O_5 Waveguides for Mid-infrared Evanescent Sensing of Stem Cell Differentiation

David J. Rowe[1], Nicholas D. Evans[2], Stuart J. Pearce[3], Ganapathy Senthil Murugan[1], James S. Wilkinson[1]

[1] Optoelectronics Research Centre, University of Southampton, Highfield, Southampton SO17 1BJ, UK, d.rowe@soton.ac.uk, jsw@ecs.soton.ac.uk, smg@orc.soton.ac.uk

[2] Institute for Developmental Sciences, School of Medicine, University of Southampton, Tremona Rd, Southampton SO16 6YD, UK, n.d.evans@soton.ac.uk

[3] Nano Research Group, School of Electronics and Computer Science, University of Southampton, Highfield, Southampton SO17 1BJ, UK, sp3@ecs.soton.ac.uk

Abstract: Stem cell differentiation is a fundamental biological process of particular interest for regenerative medicine. Differentiated cells have been characterised using mid-infrared FTIR microscopy but the use of spatially unresolved spectroscopy remains unexplored. Evanescent waveguide sensing may allow non-contact, label-free and real-time monitoring of differentiation. We report preliminary FTIR-ATR measurements which successfully distinguish between lysates of cells grown under different conditions and initial results on the fabrication of mid-infrared Ta_2O_5 waveguides. We also identify potential routes to a wholly self-contained analytical device.

Introduction: The vibrations of molecular bonds give characteristic absorptions in the mid-infrared (MIR) range of the electromagnetic spectrum (wavelengths of 2 to 20 μm), where the absorption frequencies correspond to vibrational resonant frequencies. MIR spectroscopy can therefore be used to identify the composition of a sample or changes thereof.

Evanescent field perturbation of an unclad optical waveguide is a stable and controllable method of performing spectral absorbance measurements. Geometric variation of the waveguide cross-section allows optimisation of field perturbation for maximal sensitivity. Ideally the waveguide should guide a single mode over the range of wavelengths of interest for unambiguous interpretation.

Silicon photonics has been able to take advantage of a wealth of fabrication techniques developed by the microelectronics industry. However, the low transmission of silicon outside the 3 - 5 μm[1] wavelength range severely restricts its use for biomedical sensing in the MIR. The dominant absorptions within this range are those of water and hydrocarbon bonds, which are ubiquitous in organic media and therefore offer limited specificity. In this work we demonstrate tantalum pentoxide to be a viable alternative.

Mid-infrared Ta_2O_5 waveguides: Ta_2O_5 films have previously been demonstrated to offer high refractive index and low loss in the MIR region.[2] Ta_2O_5 offers better biocompatibility, lower chemical reactivity and higher mechanical durability in comparison with alternative materials including Bi_2O_3, HfO_2 and the chalcogenide glasses.

The use of Ta_2O_5 to guide light restricts the choice of substrate material to the halides for suitably high transmission and low index to achieve a strong index contrast over the whole MIR region. Of the most commonly available halides (CaF_2, BaF_2, KBr, NaCl, NaF), CaF_2 was chosen for having the best mechanical rigidity and lowest reactivity, hygroscopicity and cost. Soref's expression[3] was used to choose the design of a single-mode rib waveguide of unclad Ta_2O_5 on CaF_2, resulting in rib height = 4 μm, rib width = 4 μm and slab height = 3 μm.

50 × 50 × 2 mm CaF_2 substrates were obtained from Crystran (Poole, UK) and cleaned for 15 minutes in each of acetone, IPA and DI water with an ultrasonic bath, and then cleaned for 30 minutes in a microwave-frequency oxygen plasma with a plasma asher. Ta_2O_5 thin films were then deposited on the substrates using both a Leybold Optics Helios sputtering tool for reactive sputtering and an OIPT tool for direct sputtering, using tantalum and tantalum oxide targets respectively. The chief advantage of the reactive sputtering process is in using an oxygen sensor to control the oxygen content of the plasma, which ensures the film is not depleted of oxygen and therefore does not need to be deposited

at elevated temperature or annealed. This is particularly important due to the large difference in the thermal expansion coefficients of Ta_2O_5 and CaF_2; direct sputtering cannot be used to deposit adequately oxygen-rich tantala without destroying the film integrity. The slab waveguide loss was measured as 0.88 dB/cm at $\lambda = 1550$ nm using prism coupling (Metricon). Waveguides of 1 to 10 µm width and 100 µm pitch were defined in S1813 photoresist using photolithography and etched to a depth of 1 µm using ion beam milling. The end facets were polished to achieve an optical quality surface finish. Exemplar waveguides are shown in Fig. 1.

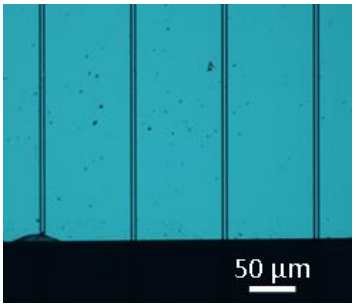


Fig. 1: Polished Ta_2O_5 waveguides on CaF_2.

The waveguides were subsequently aligned with an infrared camera using a HeNe laser and butt coupled to a tunable QCL source. However, optimisation of the polishing procedure included repeatedly mounting and demounting the waveguides on a jig with wax. This gradually introduced irremovable surface defects into the Ta_2O_5 film, which formed scattering centres and prevented waveguiding. MIR characterisation of higher quality Ta_2O_5 waveguides is in progress.

Stem cell differentiation: Cells were used from M57 and M67 human osteosarcoma lines. Two populations were grown from each line for three weeks: M67 cells were grown in basal and osteogenic media (TLBM and OGM) and M57 cells were grown in basal and adiopogenic media (BM and AM). M67 TLBM and M57 BM remained undifferentiated. M67 OGM differentiated to mineral rich bone-type cells and M57 AM differentiated to fatty cells as expected. Each culture was visually verified with a microscope. The cells were then removed from their respective growth media and resuspended in lysis buffer.

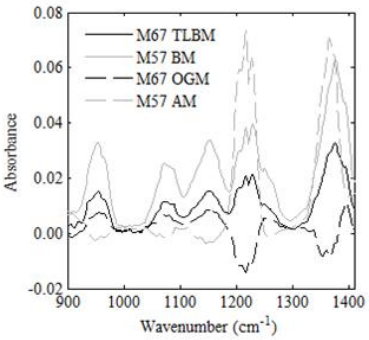


Fig.2: 900–1400 cm^{-1} region of lysate absorbance spectra.

An Agilent FTIR spectrometer was used in conjunction with a ZnSe ATR trough plate for evanescent spectral absorbance measurements. Each cell lysate-lysis buffer mixture was pipetted onto the ATR plate and absorbance spectra recorded in the frequency range 600 – 6000 cm^{-1}. Each measurement was taken relative to pure lysis buffer so the result is effectively that of the lysed cells only. The changes between M67 OGM and M67 TLBM are markedly different from the changes between M57 AM and M57 BM at many points throughout the spectrum. As an example, one region of interest is the peak at 1220 cm^{-1} ($\lambda = 8.2$ µm) shown in Fig. 2. Such differences are probably due to differences in the extracellular matrices from the different growth conditions.

Conclusions: MIR Ta_2O_5 waveguides can be directly integrated with a polymer microfluidic interface, based on previous work[4] and shown in Fig. 3, for continuous flow characterisation. Additional microfluidic functionality for cell growth and lysis[5] should be integrated to allow on-chip stem cell manipulation. The preliminary data on evanescent spectroscopy of stem cell lysates show that the morphology of cells and extracellular matrices does not necessarily need to be known for continuous, non-contact, label-free and real-time monitoring of differentiation. These data also show promise for Ta_2O_5-based integrated MIR optics as a generic biosensing platform and specifically for characterising stem cell differentiation.

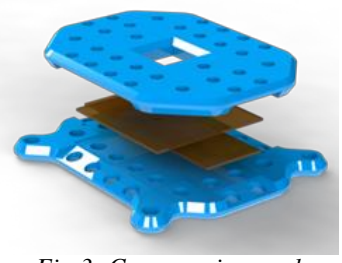


Fig.3: Compression-seal microfluidic manifold.

References

1. Si data sheet, Crystran, www.crystran.co.uk/optical-materials/silicon-si [accessed 24 March 2014].
2. J.D. Traylor Kruschwitz and W.T. Pawlewicz, *Applied Optics* **36**, pp. 2157-2159 (1997).
3. R.A. Soref *et al*., *IEEE Journal of Quantum Electronics* **27**, pp. 1971-1974 (1991).
4. D.J. Rowe *et al*., *Sensors and Actuators B: Chemical* **169**, pp. 213-221 (2012).
5. S.-H. Park *et al*., *PLOS ONE* **7**, e46689 (2012).

Intra-laser-cavity Sensing with a Dual-wavelength Distributed-feedback Laser

Edward H. Bernhardi[1], Kees O. van der Werf[2], Anton J. F. Hollink[1], Kerstin Wörhoff[1], Vinod Subramaniam[2], Markus Pollnau[1]

[1] Integrated Optical Microsystems Group, MESA+ Institute for Nanotechnology, University of Twente, P.O. Box 217, 7500 AE Enschede, The Netherlands
m.pollnau@utwente.nl
[2] NanoBioPhysics Group, MIRA Institute for Biomedical Technology and Technical Medicine & MESA+ Institute for Nanotechnology, University of Twente, P.O. Box 217, 7500 AE Enschede, The Netherlands
v.subramaniam@utwente.nl

Abstract: An integrated intra-laser-cavity microparticle sensor based on a dual-wavelength distributed-feedback channel waveguide laser in $Al_2O_3:Yb^{3+}$ on silicon is demonstrated. Real-time detection and accurate size measurement of single micro-particles with diameters of 1–20 μm are achieved. A limit of detection of ~500 nm is deduced. The sensing principle relies on measuring changes in the frequency difference between the two longitudinal laser modes as the evanescent field of the dual-wavelength laser interacts with micro-sized particles on the waveguide surface.

Introduction: Lasers find numerous applications in spectroscopy, optical communications, and optical sensing. These applications place stringent requirements with respect to efficiency, output power, spectral characteristics, compactness, robustness, and thermal stability on the laser. Waveguide lasers allow one to realize compact, rigid, and robust optical devices, since the entire laser cavity can be fabricated on the same substrate. In this work, surface-corrugated Bragg gratings are integrated with $Al_2O_3:Yb^{3+}$ channel waveguides to realize a monolithic distributed-feedback (DFB), dual-wavelength laser and demonstrate intra-laser-cavity micro-particle sensing.

Sample fabrication: 1-μm-thick $Al_2O_3:Yb^{3+}$ layers with a doping concentration of 5.8×10^{20} cm^{-3} were deposited onto standard thermally oxidized silicon wafers.[1] 10-mm-long, 2.5-3.0-μm-wide ridge channel waveguides supporting single-transverse-mode operation at the pump and laser wavelengths were etched to a depth of ~0.1 μm via a chlorine reactive ion etching process.[2] A SiO_2 cladding layer was deposited on top of the ridge waveguides by plasma enhanced chemical vapor deposition. Surface-relief Bragg gratings were fabricated on the top surface of the SiO_2 cladding by means of laser interference lithography. A grating pattern was defined in a 120-nm-thick negative resist layer on top and etched into the SiO_2 cladding using a $CHF_3:O_2$ reactive ion plasma.[3] The grating period is 316 nm, resulting in a Bragg wavelength of ~1020 nm. The waveguide propagation losses, including grating-induced scattering losses, are as low as 0.14 dB/cm. With a grating coupling coefficient of κ = 6.5 cm^{-1}, the 1-cm-long Bragg gratings possess reflectivities higher than 99% for TE polarization.[4] A quarter-wavelength phase shift was induced by adiabatic widening of the waveguide, resulting in a resonance with a passive Q-factor up to 1.35×10^6.

Distributed-feedback lasers: The single-longitudinal-mode $Al_2O_3:Yb^{3+}$ DFB laser,[5] which is diode-pumped at 976 nm, has a threshold of 5 mW. The laser operates at a wavelength of 1022.2 nm, where the maximum measured laser output power exceeds 55 mW at a launched pump power of 91.5 mW, resulting in a slope efficiency of 67%. Based on two 2-mm-long quarter-wavelength phase shifts centered at 3.5 mm and 5.5 mm (as measured from the end-facet from where the light is launched) in a DFB cavity, a dual-wavelength $Al_2O_3:Yb^{3+}$ DFB laser is demonstrated. A stable electrical beat signal is created at the output of a photodetector, with the frequency of the beat signal corresponding to the wavelength spacing of the two optical waves.[6] The two resonances share a common cavity which consists of both phase-shift regions, and the wavelength spacing between these resonances depends on the spatial separation and values of the respective phase shifts. The laser output was measured with a photodetector and an electrical spectrum analyzer, which confirmed a microwave beat signal at 15.0426 GHz. The long-term frequency stability of the microwave beat signal was measured over a period of 45 min. with a 100 ms interval. The standard deviation of the microwave frequency during this period was found to be ±2.5 MHz.

Intra-laser-cavity sensing: An integrated intra-laser-cavity microparticle sensor based on this dual-wavelength DFB channel waveguide laser in Al_2O_3:Yb^{3+} is demonstrated.[7] Real-time detection and accurate size measurement of single micro-particles with diameters ranging between 1 µm and 20 µm are achieved, which represent the typical sizes of many fungal and bacterial pathogens as well as a large variety of human cells. The sensing principle relies on measuring changes in the frequency difference between the two longitudinal laser modes as the evanescent field of the dual-wavelength laser interacts with micro-sized particles on the surface of the waveguide.

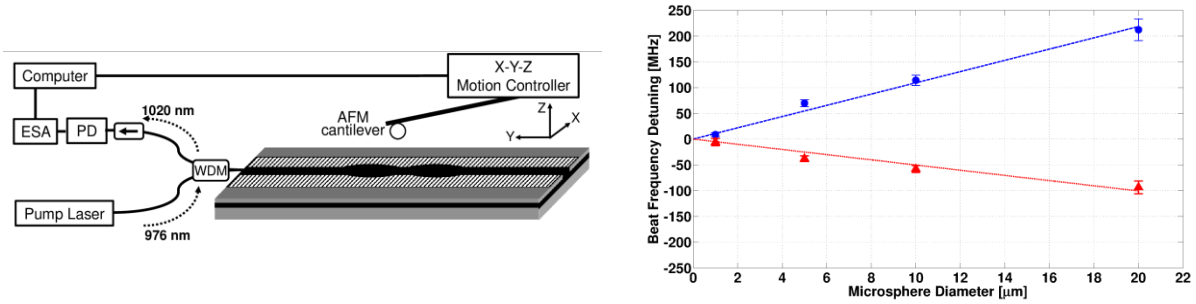


Fig. 1: (left) Experimental setup used to characterize the intra-laser-cavity micro-particle dual-wavelength laser sensor. ESA: Electronic spectrum analyzer;PD: Photodetector; WDM: Wavelength division multiplexing fiber; AFM: Atomic force microscope. (right) Laser microwave beat frequency detuning as a function of microsphere diameter. The red triangles were measured in the center of the phase shift on the pumped side, while the blue circles were measured in the center of the phase shift on the unpumped side of the laser cavity.

We demonstrate optical sensing by systematically probing the intra-cavity evanescent laser fields with various borosilicate glass microspheres of diameters ranging between 1 µm and 20 µm, attached to an atomic-force-microscope cantilever mounted on a 3-dimensional computer-controlled translation stage as shown in Fig. 1 (left). Each microsphere was scanned across the waveguide laser in the center region of each of the two phase shifts with a lateral resolution of 25 nm, while the frequency detuning of the microwave beat signal was observed, see Fig. 1 (right). Inside the first phase-shift region, the largest investigated microsphere with a diameter of 20 µm induced a 94 MHz decrease in the microwave beat signal, while the smallest microsphere, with a diameter of 1 µm, induced a frequency decrease of 6 MHz. In the second phase-shift region, the largest and smallest microspheres induced an increase in the microwave beat signal of 212 MHz and 9 MHz, respectively. Assuming that the frequency detuning of the laser-generated beat signal has a linear dependence on microsphere size, the resolution of the sensor is currently limited to particles of ~500 nm diameter. This size limitation is due to the free-running frequency stability of the laser of ~5 MHz, which is most likely due to fluctuations in the pump power as well as some optical back-reflections into the laser cavity.[6]

Conclusions: We have demonstrated DFB channel waveguide lasers in Al_2O_3:Yb^{3+} on silicon substrates with an output power of 55 mW and a slope efficiency of 67%. A dual-phase-shift DFB laser with dual-wavelength emission was operated and a stable microwave beat signal at ~15 GHz was created via heterodyne photo-detection. By measuring changes in the microwave signal, we could detect single micro-particles with diameters between 1 µm and 20 µm on the waveguide surface.

References

1. K. Wörhoff, J. D. B. Bradley, F. Ay, D. Geskus, T. P. Blauwendraat, M. Pollnau, *IEEE J. Quantum Electron.* **45**, pp. 454–461 (2009).
2. J. D. B. Bradley, F. Ay, K. Wörhoff, M. Pollnau, *Appl. Phys. B* **89**, pp. 311–318 (2007).
3. E. H. Bernhardi, H. A. G. M. van Wolferen, L. Agazzi, M. R. H. Khan, C. G. H. Roeloffzen, K. Wörhoff, M. Pollnau, R. M. de Ridder, *Opt. Lett.* **35**, pp. 2394–2396 (2010).
4. E. H. Bernhardi, Q. Lu, H. A. G. M. van Wolferen, K. Wörhoff, R. M. de Ridder, M. Pollnau, *Photon. Nanostruct.* **9**, pp. 225–234 (2011).
5. E. H. Bernhardi, H. A. G. M. van Wolferen, K. Wörhoff, R. M. de Ridder, M. Pollnau, *Opt. Lett.* **36**, pp. 603–605 (2011).
6. E.H. Bernhardi, M.R.H. Khan, C.G.H. Roeloffzen, H.A.G.M. van Wolferen, K. Wörhoff, R.M. de Ridder, and M. Pollnau, *Opt. Lett.* **37**, pp. 181–183 (2012).
7. E. H. Bernhardi, K. O. van der Werf, A. J. F. Hollink, K. Wörhoff, R. M. de Ridder, V. Subramaniam, M. Pollnau, *Laser Photonics Rev.* **7**, pp. 589–595 (2013).

Demodulation of Holographically Reconstructed 2-D Signals with Spatial Quadrature Amplitude Modulation

M. Bunsen[1], T. Hisaoka[1], T. Sato[1], M. Takabayashi[2], A. Okamoto[3]

[1] Fukuoka University, Fukuoka, Japan,
bunsen@fukuoka-u.ac.jp
[2] Graduate School of Computer Science and Systems Engineering, Kyushu Institute of Technology, Iizuka, Fukuoka, Japan,
takabayashi@ces.kyutech.ac.jp
[3] Graduate School of Information Science and Technology, Hokkaido University, Sapporo, Japan,
ao@optnet.ist.hokudai.ac.jp

Abstract: Demodulation of holographically recorded and retrieved signal beams, whose intensities and phases are spatially modulated with multiple values, is experimentally demonstrated to increase the storage capacity of holographic data storage. The intensity and phase modulated signal beams are generated by serially arranged two liquid crystal spatial light modulators and recorded in the holographic material. The intensity and the phase of the reconstructed signal are demodulated by the phase-shifting interferometry. Feasibility and potential of this kind of modulation are discussed with the constellation plots of the demodulated signals.

1. Introduction

Recent years, spatial quadrature amplitude modulation (SQAM) has been expected as one of the signal modulation methods to increase the capacity of holographic data storage (HDS).[1] Although two-dimensional intensity distribution of the signal beam is modulated merely in two brightness levels in the conventional modulation method, both the intensity and the phase of the signal beam are spatially modulated with multiple values in SQAM. To detect the SQAM signals, phase-shifting interferometry (PSI) which requires plural interferograms having the different spatial phase from each other is generally employed.[2] However, this technique decreases the data transfer rate of HDS because multiple interferograms should be captured per a datapage. To improve the data transfer rate, we have proposed the novel detection technique for SQAM-based holographic data storage system referred to as phase-shift embedding method.[3] In ref.3, only the spatial phase of the signal beam was modulated in order to simply confirm the basic operation principle of our proposing method.

In this paper, we experimentally demonstrate the demodulation of holographically recorded and retrieved SQAM signals in which both the intensity and the phase are fully modulated with multiple values. The SQAM signal beams are generated by serially arranged two liquid crystal spatial light modulators and recorded in the holographic material. The intensity and the phase of the reconstructed signal are demodulated by the PSI. Note that the demodulation is implemented by conventional four-step PSI in this paper because the main purpose of the experiment is experimental realization of modulation and demodulation of fully intensity- and phase-modulated SQAM signal. Feasibility and potential of this kind of modulation are discussed with the constellation plots of the demodulated signals.

2. Spatial Quadrature Amplitude Modulation and Phase-shifting Interferometry

Figure 1 shows the conceptual diagram of the holographic data storage system with SQAM. Both the intensity and the phase of the signal beam are modulated with multiple values. At the moment, the combination of the intensity-type and the phase-type spatial light modulators (SLMs) is used to generate the SQAM signal. In this paper, we adopt conventional four-step phase-sifting interferometry to demodulate the SQAM signal where the intensity and the phase of the signal beam is calculated by the following well-known equations.[2]

$$I(x,y) \propto \left\{I_4(x,y) - I_2(x,y)\right\}^2 + \left\{I_1(x,y) - I_3(x,y)\right\}^2 \tag{1}$$

$$\phi(x,y) = \tan^{-1}\left[\left\{I_4(x,y) - I_2(x,y)\right\} / \left\{I_1(x,y) - I_3(x,y)\right\}\right] \tag{2}$$

$I_j(x,y)$ denotes the intensity distribution of the interferogram of the signal beam recalled from the hologram and the reference beam with the phase retardations of 0 (j=1), π/2 (j=2), π (j=3) and 3π/2 (j=4).

3. Experiment

We experimentally demonstrate holographic recording, retrieving, and demodulation of the SQAM signal with PSI. Figure 2 shows the experimental setup. The diode-pumped solid state laser of the wavelength of 532nm is used as the light source. The SAQM signal beams are generated by serially arranged two liquid crystal spatial light modulators. Here LC-2002 (Holoeye) and LCOS-SLM x10468 (Hamamatsu Photonics) are used as the intensity and the phase spatial modulators, respectively. The spatial distributions of the intensity and the phase of the signal beam are two-dimensionally modulated according to the patterns with 8×8 pixels as shown in Fig.3. In Fig.3 (b), the gray-level indicates the depth of the phase modulation, and the black (0) and the white (255) correspond to 0 deg. and 360 deg., respectively. The SQAM signal is demodulated by the four-step PSI in which the phase retardation of the reference beam 2 in Fig.2 is sequentially changed by the piezo-driven mirror, and the four interferograms with the phase-shifts of 0, π/2, π and 3π/2 are captured. In the following, we denote the number of the intensity modulation level N_I and that of the phase modulation level N_P as (N_I, N_P). The demodulated symbols of the SQAM signals are plotted in the constellation diagrams in Fig.4. It is shown that the constellation points of (2, 4), (2, 8) and (3, 4) can be separably recognized, although discrimination of the symbols of (2, 16), (3, 8) and (3, 16) are relatively difficult. Increase of the dispersion in the constellation plots is considered to be caused by the error in the shift amount of the piezo-driven mirror, aberration of the lenses and so on.

4. Conclusions

Holographically recorded and retrieved signal beams, whose intensities and the phases are spatially modulated with multiple values, have been successfully demodulated by the phase-shifting interferometry. Increasing the number of pixels and intensity/phase levels are future subjects as well as the quantitative evaluation of the demodulated signals.

References

1. A. Okamoto *et al., Opt. Express.* **19**, pp. 13436-13444 (2011).
2. D. Malacara: Optical Shop Testing (Wiley, New York, 2007) 3rd ed.
3. M. Bunsen *et al.*, *Jpn. J. Appl. Phys* **52**, pp. 09LD04-09LD09 (2013).

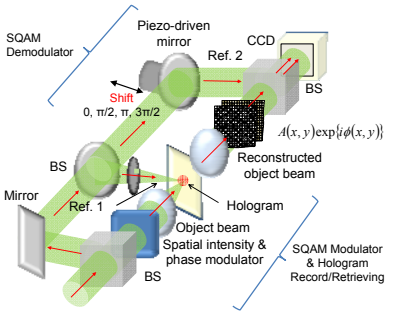


Fig. 1: Conceptual diagram of holographic data storage system with SQAM signal.

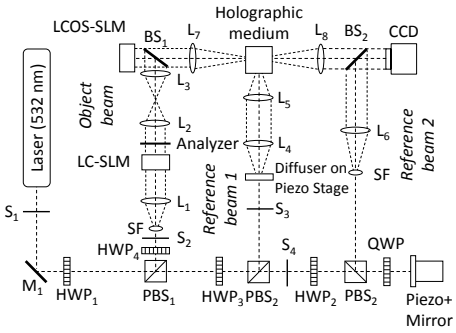
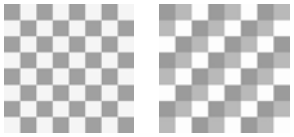
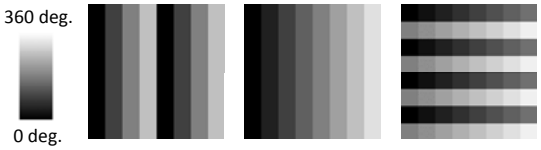


Fig. 2: Experimental Setup.

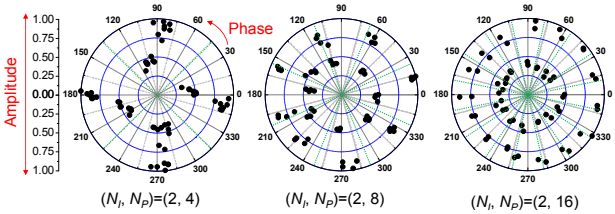


(a) 2- and 3-valued intensity modulation patterns

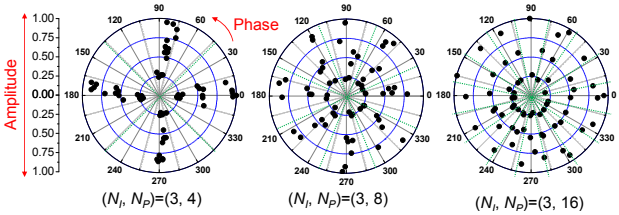


(b) 4-, 8- and 16-valued phase modulation patterns

Fig. 3: Intensity and phase modulation patterns.



(a) 2-valued intensity modulation with 4-, 8- and 16-valued phase modulations from left to right



(b) 3-valued intensity modulation with 4-, 8- and 16-valued phase modulations from left to right

Fig. 4: Constellation plots of demodulated SQAM signals.

AWG-based integrated fiber-Bragg-grating interrogator with improved sensitivity

Dzmitry Pustakhod, Emil Kleijn, Meint K. Smit, and Xaveer J. M. Leijtens
COBRA Research Institute, Eindhoven University of Technology, 5600 MB Eindhoven, The Netherlands
d.pustakhod@tue.nl

Abstract: A Fiber Bragg Grating interrogator based on an AWG with custom design of the inputs is described. The proposed modifications ensure a non-zero readout signal on at least two detectors for any wavelength. It is shown that the combined readout allows to track wavelength changes with a resolution better than 5 pm.

1 Introduction

Fiber Bragg Grating (FBG) sensors are used in many applications[1]. In such sensors, the FBG plays the role of a wavelength-specific reflector. Any change of the measured physical parameter, e.g. temperature or strain, leads to a change of the wavelength of the reflected signal. To track this change of wavelength, FBG interrogators are used. Integrated photonic technologies make it possible to use a miniaturized photonic circuit as such an interrogator. In this paper we present the design and measured performance parameters of a manufactured integrated FBG interrogator device.

2 Fiber Bragg Grating Interrogator Design

The design is based on an arrayed waveguide grating (AWG)[2]: light is coupled into the input of the AWG and is collected at the outputs of the AWG by an array of integrated PIN detectors. Depending on the incoming wavelength, the optical signal is directed to different outputs. In a standard AWG the passbands from a single input to the output channels are spaced by the channel spacing Δf_{ch}. Since there is only a small overlap between two adjacent channels, the signal is mainly present at a single output for a particular wavelength. For a wavelength close to the edge of a passband only a small signal is transferred to at most two outputs.

In order to ensure a readout on at least two detectors, we modify the input waveguide by inserting a 1×2 MMI (see figure 1, a) and connecting both outputs (α and β in figure 1) to the Free Propagation Region (FPR) of the AWG with a distance between them corresponding to $2.5 \times \Delta f_{\mathrm{ch}}$. Another way to guarantee readout on two detectors is to place the MMI directly at the FPR (figure 1, b).

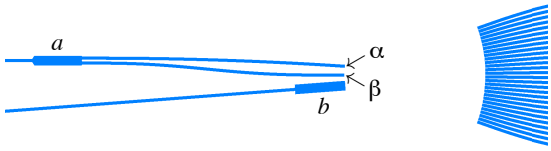


Fig. 1: Design of AWG input waveguides. a—1×2 MMI in the middle, α, β—outputs of the MMI. b—MMI at the end of input.

In this paper we study only the design shown in figure 1, a. Another modification of the AWG design was to reduce the spacing between the output waveguides from the normal value of 1 μm to 0.4 μm, thereby increasing the crosstalk between the channels, which is good for this application.

The manufacturing of the device was carried out as a part of Multi-Project Wafer (MPW) run, following a generic integration methodology, using standard building blocks such as waveguides, AWGs, and detectors. No detailed knowledge on the manufacturing process is required by the designer. Moreover, the costs of prototyping are shared among all the users participating in the MPW run.

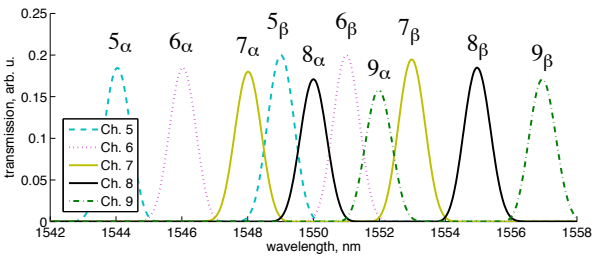


Fig. 2: Simulation of the AWG passbands. Only channels 5–9 are shown.

3 Simulations

The response of the AWG was simulated using an analytical model[3]. The results are shown in figure 2. Each output has two peaks in the passband (α and

β), the separation between them $\Delta\lambda_{\alpha,\beta} = 2.5\Delta\lambda_{ch}$ is determined by the distance between inputs α and β in figure 1. Channel spacing is $\Delta\lambda_{ch} = 2\,\text{nm}$.

4 Measurements

The device was fabricated in an InP active-passive MPW carried out at Oclaro Technology Ltd. within the Memphis project. In order to characterize the transmission properties of the device, we couple light from a laser into the chip with a lensed fiber tip and record the photocurrent from reversely biased detectors. The photocurrent for three channels is shown in figure 3. The channel spacing of the fabricated device $\Delta\lambda_{ch} = 2.0 \pm 0.1\,\text{nm}$ and the distance between the peaks $\Delta\lambda_{\alpha,\beta} = 5\,\text{nm}$ correspond to the design values. The passbands are wider than simulated, due to a reduced etch depth in between the closely spaced output waveguides.

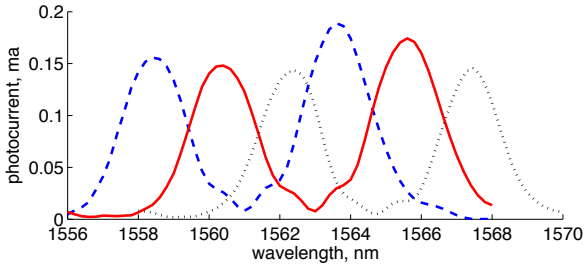


Fig. 3: Measured wavelength response of the AWG outputs.

5 Performance analysis

We calibrate the interrogator before the measurements. First, we record the readouts of each detector $I_i(\lambda)$ using a reference laser signal with a known wavelength. Based on this data we divide the AWG free spectral range (FSR) into wavelength regions and map each of them to a pair of detectors, which have a non-zero readout in this region. The readout signals from the corresponding detectors, I_a and I_b, are combined into $I(\lambda) = (I_a - I_b)/(I_a + I_b)$. To reconstruct the wavelength during measurements we use the readout from the two detectors with the maximum photocurrent, labelled a and b, and their combined response $I(\lambda)$.

The error in the wavelength value can be expressed as $\Delta\lambda = |\mathrm{d}\lambda/\mathrm{d}I|\,\Delta I = |\mathrm{d}I/\mathrm{d}\lambda|^{-1}\,\Delta I$. Based on the known detector responses $I_i(\lambda)$ the intensity noise ΔI can be translated into wavelength noise $\Delta\lambda$. In figure 4 the readout $I(\lambda)$ over time is shown for two wavelengths, λ and $\lambda + 5\,\text{pm}$. The change of the readout value due to wavelength change of 5 pm is clearly seen and the standard deviation of the readout corresponds to 0.8 pm.

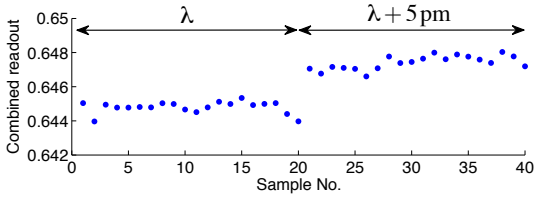


Fig. 4: Measured readout $I(\lambda)$ from a pair of detectors. A step change is due to wavelength change of 5 pm.

The current accuracy limitation is from a slow drift of the readout signal in our measurements due to the fiber-to-chip coupling which causes first order mode excitation. This effect can be reduced by improving the stability, e.g. by packaging the device.

6 Conclusions

We fabricated and characterised an integrated Fiber Bragg Grating interrogator with an FSR of 20 nm, 10 output channels, and a footprint around 1 mm^2, which can be used to track wavelength shifts with a resolution better than 5 pm, which corresponds to 0.025 % of the FSR.

Acknowledgements

This research is carried out in the ProCon Project 11369, supported by the Dutch Technology Foundation STW, which is part of the Netherlands Organization for Scientific Research (NWO), and which is partly funded by the Dutch Ministry of Economic Affairs.

References

[1] Hill, K. O. and Meltz, G. Aug 1997 *Journal of Lightwave Technology* **15(8)**, 1263–1276.

[2] Smit, M. K. and Van Dam, C. Jun 1996 *IEEE Journal of Sel. Topics in Quantum Electronics* **2(2)**, 236–250.

[3] Kleijn, E., Smit, M. K., and Leijtens, X. J. M. Oct 2013 *Journal of Lightwave Technology* **31(20)**, 3309–3314.

High speed germanium and silicon optoelectronic devices

L. Vivien[1*], D. Marris-Morini[1], L. Virot[1,2,3], D. Perez-Galacho[1], P. Damas[1], G. Rasigade[1], J-M. Hartmann[2], E. Cassan[1], P. Crozat[1], S. Olivier[2], C. Baudot[3], F. Boeuf[3], J-M. Fédéli[2]

[1]Institut d'Electronique Fondamentale, Univ. Paris-Sud, CNRS UMR 8622, Bât. 220,91405 Orsay, France;
[2]ST Microelectronics, 850 rue Jean Monnet 38920 Crolles, France
[3]CEA, LETI, Minatec Campus 17 rue des Martyrs, 38054 Grenoble cedex 9 France
[4] Alcatel-Lucent Bell Lab France, Nozay, France
[*]laurent.vivien@u-psud.fr

Abstract: Silicon photonics has generated a strong interest for the development of high-speed optical transceivers The co-integration of photonics and electronics in the same circuit will allow a strong reduction of photonic system costs and the increase of the number of functionalities on the same integrated chip. In this paper, we will present recent results on 40Gbit/s optical modulators based on carrier depletion effect and germanium photodetectors integrated in silicon on insulator (SOI) waveguides.

Short-link optical communications including communications in datacentre and in integrated circuits are considered as the main application for silicon photonics [1]. For this purpose, numerous studies on the development of optoelectronic devices have been performed including III-V on silicon laser [2], germanium laser [3], electro-refraction modulators based on the carrier depletion [4-7], electro-absorption modulators based on Franz Keldysh effect [8] and quantum confined stark effect [9,10] and germanium photo-detectors [11-13].

In this paper, we present a 40Gbit/s silicon modulator based on carrier depletion in lateral pn junction and a 40Gbit/s lateral pin germanium photodetector integrated in a Silicon-On-Insulator (SOI) waveguide. Both optoelectronic devices have been separately fabricated in a 300-mm Complementary Metal Oxide Semiconductor (CMOS) pilot line. The use of such a technological platform opens the route towards high volume production for optical interconnects applications. Furthermore, the use of a 300 mm CMOS platform enables the access of state of the art technological including immersion deep-UV lithography, leading to sub-50-nm resolution.

Silicon modulators: Carrier depletion effect in lateral pn diode was used to induce phase variation in silicon waveguide. Intensity variation was obtained by inserting this diode in both arms of a 950µm long Mach-Zehnder interferometer. A schematic view of the phase shifter cross-sections is shown in Fig1a. The waveguide geometry was: 400 nm wide and 220 nm thick silicon rib waveguides. The etching depth was 120 nm. The characterization were performed for TE polarization in the 1.55µm telecom wavelength range. A modulation efficiency $V_\pi L_\pi$ of 2.2 V.cm was achieved and a -3 dB cut-off frequency as high as 26 GHz was demonstrated. Finally, a 40 Gbit/s eye diagram of MZ modulator is reported in Fig 1b. Extinction ratio of 7.8 dB was obtained for insertion loss as low as 4 dB.

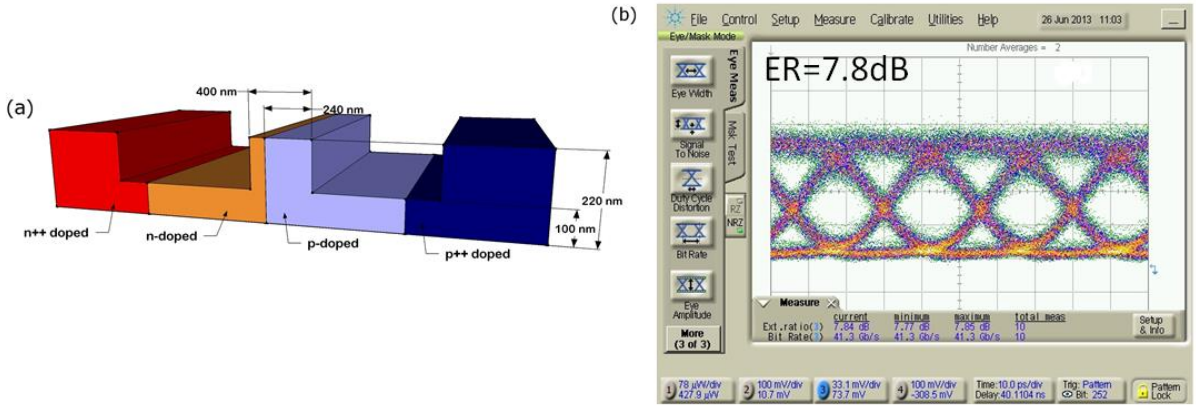


Fig. 1: (a) Schematic view of lateral pn diode; (b) 40Gbit/s eye diagram at a wavelength of 1.55µm

Germanium photodetectors: A lateral pin Ge photodiodes integrated in silicon waveguide was used for high-speed detection (fig.2) [13]. The doping levels of both p and n doped regions were 1.10^{19} cm^{-3} to ensure good contact resistances. The intrinsic region width of the pin diode was 700 nm, enabling high speed operation as well as high responsivity. Under a reverse bias of 1V, dark current was as low as 6nA. Under illumination, photo-generated current were collected with a responsivity higher than 0.5 A/W. -3 dB cut-off frequency higher than 50GHz under zero bias was achieved as well as a 40Gbit/s data transmission.

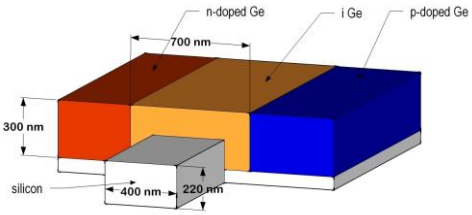


Fig. 2. Schematic view of the lateral pin Ge photo-detector integrated in a Si waveguide.

In conclusion, both Si modulator and Ge photodetector exhibited 40Gbit/s operation with competitive characteristics. A point to point 40Gbit/s optical link including one modulator chip and one photodetector chip, both connected with an optical fibre has been demonstrated [14]. The obtained overall optical loss was lower than 18dB including 4 dB losses per coupler (i.e. 12 dB for light coupling), waveguide propagation (<1dB) and 5dB insertion loss from the optical modulator.

References

1. International Technology Roadmap for Semiconductors, http://www.itrs.net/
2. Liepvre, A.L.; Accard, A.; Poingt, F.; Jany, C.; Lamponi, M.; Make, D.; Lelarge, F.; Fedeli, J.-M.; Messaoudene, S.; Bordel, D.; Duan, G.-H., Wavelength Selectable Hybrid III–V/Si Laser Fabricated by Wafer Bonding, IEEE Photonics Technology Letters 25 (16), 1582,1585 (2013)
3. Rodolfo E. Camacho-Aguilera, Yan Cai, Neil Patel, Jonathan T. Bessette, Marco Romagnoli, Lionel C. Kimerling, and Jurgen Michel, "An electrically pumped germanium laser," Opt. Express 20, 11316-11320 (2012)
4. D. J. Thomson, F. Y. Gardes, Y. Hu, G. Mashanovich, M. Fournier, P. Grosse, J-M. Fedeli, and G. T. Reed, "High contrast 40Gbit/s optical modulation in silicon," Opt. Express 19, 11507-11516 (2011)
5. D. Marris-Morini, C. Baudot, J-M. Fédéli, G. Rasigade, N. Vulliet, A. Souhaité, M. Ziebell, P. Rivallin, S. Olivier, P. Crozat, X. Le Roux, D. Bouville, S. Menezo, F. Bœuf, and L. Vivien, "Low loss 40 Gbit/s silicon modulator based on interleaved junctions and fabricated on 300 mm SOI wafers," Opt. Express 21, 22471-22475 (2013)
6. P. Dong, L. Chen, Y-K Chen "High-speed low-voltage single-drive push-pull silicon Mach-Zehnder modulators" Optics Express, 20 (6), 6163-6169 (2012).
7. Melissa Ziebell, Delphine Marris-Morini, Gilles Rasigade, Jean-Marc Fédéli, Paul Crozat, Eric Cassan, David Bouville, and Laurent Vivien, "40 Gbit/s low-loss silicon optical modulator based on a pipin diode," Opt. Express 20, 10591-10596 (2012)
8. Ning-Ning Feng, Shirong Liao, Dazeng Feng, Xin Wang, Po Dong, Hong Liang, Cheng-Chih Kung, Wei Qian, Yong Liu, Joan Fong, Roshanak Shafiiha, Ying Luo, Jack Cunningham, Ashok V. Krishnamoorthy, and Mehdi Asghari, "Design and fabrication of 3μm silicon-on-insulator waveguide integrated Ge electro-absorption modulator," Opt. Express 19, 8715-8720 (2011)
9. P. Chaisakul, D. Marris-Morini, M-S Rouifed, G. Isella, D. Chrastina, J. Frigerio, X. Le Roux, S. Edmond, J-R. Coudevylle, and L. Vivien, "23 GHz Ge/SiGe multiple quantum well electroabsorption modulator", Optics Express, 20 (3) (2012)
10. P Chaisakul, D Marris-Morini, J Frigerio, D Chrastina, M-S Rouifed, S Cecchi, P Crozat, G Isella, L Vivien, Integrated germanium optical interconnects on silicon substrates, Nature Photonics 8, 482–488 (2014)
11. L. Vivien, J. Osmond, J-M. Fédéli, D. Marris-Morini, P. Crozat, J-F. Damlencourt, E. Cassan, Y. Lecunff, S. Laval, "42 GHz p.i.n Germanium photodetector integrated in a silicon-on-insulator waveguide," Opt. Express 17, 6252-6257 (2009)
12. T. Tsuchizawa, K. Yamada, T. Watanabe, S. Park; H. Nishi, K. Rai, H. Shinojima, S-I. Itabashi, "Monolithic Integration of Silicon-, Germanium-, and Silica-Based Optical Devices for Telecommunications Applications," IEEE J. Select. Top.Quant. Elec., 17, 516-525 (2011)
13. L. Vivien, A Polzer, D Marris-Morini, J Osmond, J-M Hartmann, P Crozat, E Cassan, C Kopp, H Zimmermann, J-M Fédéli, "Zero-bias 40Gbit/s germanium waveguide photodetector on silicon," Opt. Express 20, 1096-1101 (2012)
14. D. Marris-Morini, L. Virot, C. Baudot, J.-M. Fédéli, G. Rasigade, D. Perez-Galacho, J.-M. Hartmann, S. Olivier, P. Brindel, P. Crozat, F. Bœuf, and L. Vivien, "A 40 Gbit/s optical link on a 300-mm silicon platform," Opt. Express 22, 6674-6679 (2014)

A fs-laser written waveguide in periodically poled Rb:$KTiOPO_4$ for efficient second harmonic generation

F. Laurell[1], **S. Müller**[2], **T. Calmano**[2], **P. Metz**[2], **C. Kränkel**[2], **C. Canalias**[1], **C. Liljestrand**[1], **and G. Huber**[2]

[1] *Department of Applied Physics, Roslagstullsbacken 21, 106 91 Stockholm, Sweden KTH, Stockholm, Sweden,*
[2] *Universität Hamburg, Institut für Laser-Physik, Luruper Chaussee 149, 22761 Hamburg, Germany*
fl@laserphysics.kth.se

Abstract: A femtosecond Ti:sapphire laser was used to inscribe low loss waveguides with the double-track method in a 9.5 mm long periodically poled Rb:$KTiOPO_4$ sample. 76mW of stable blue light was obtained in a second harmonic generation experiment using a fundamental power of 1.6W from a continuous wave Ti:Sapphire laser at a wavelength of 943.18 nm resulting in a normalized conversion efficiency of 4.6%$W^{-1}cm^{-2}$.

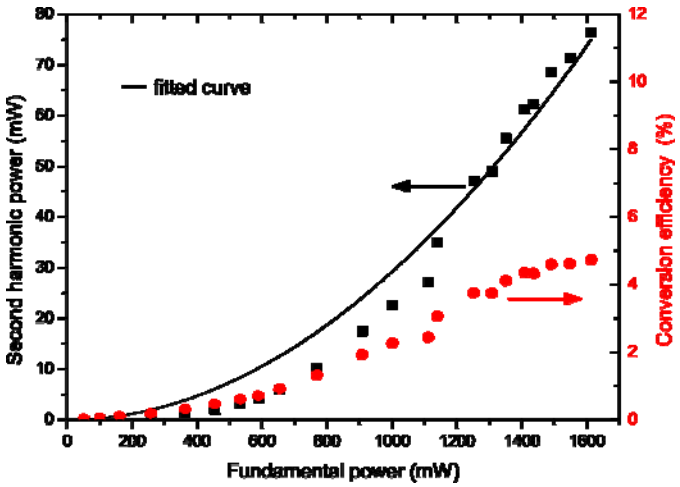
Introduction: Three dimensional microstructures can be formed in transparent dielectrics by intense laser radiation. Fs-laser radiation focused underneath the material surface creates a refractive index modification or micro destruction[1]. By proper choice of the fabrication parameters and the arrangement of the modifications, waveguiding structures in passive and active glasses as well as in crystals have been realized[2]. The so called "double-track method" in which waveguiding is appearing between the tracks has in most cases given waveguides with the lowest loss in crystalline materials[3].
With the advent of periodic poling (PP) efficient quasi-phasematching (QPM) has become a versatile technique in nonlinear optics. PP-crystals from the $KTiOPO_4$ (KTP) family are preferred for the generation of visible light thanks to their strong resistance to optical damage and the possibility to pole dense gratings of high quality. Rb doped KTP (RKTP) is the latest introduced material in this class where the slight Rb-doping facilitates the periodic poling, and reduces the linear absorption[4]. Ion-exchanged waveguides in $KTiOPO_4$ (KTP) have been extensively used in nonlinear applications[5]. However, at high power operation the electric field drives the diffused ions deeper into the substrate and the effective mode indices changes, which also shifts the phase matching condition. This is detrimental in most cases[6].
Laser writing is a potentially interesting, novel, alternative to ion-exchanged, ion-implanted and diffused waveguides for nonlinear optical applications. Fs-laser inscribed waveguides in PPKTP were first demonstrated by Campbell *et al.*[7]. They achieved 0.22%W^{-1} normalized conversion efficiency in first order QPM second harmonic generation (SHG) of 980 nm and 0.02%W^{-1} third order QPM of 800 nm radiation. In our recent work we introduced the double-track writing method and obtained low loss waveguides in KTP and used those for broad bandwidth type II SHG generating 1.3 mW of green light[7]. In this work we applied the writing method to PPRKTP and demonstrate efficient blue light quasi-phasematched SHG without any long term drift as previously observed with ion-exchanged KTP waveguides[6].

Experiment: A 1 mm thick RKTP crystal was periodically poled with a 6.03 μm period and a grating length of 8 mm. Prior to waveguide writing the bulk PPRKTP sample was characterized for SHG with a Ti:sapphire-laser. A maximum power of 0.45 mW at 180 mW launched IR radiation at 943.40 nm was measured after the sample, corresponding to a normalized conversion efficiency of 1.74%$W^{-1}cm^{-1}$ and an effective nonlinear coefficient, d_{eff} = 11pm/V.
For waveguide fabrication a chirped pulse femtosecond Ti:sapphire amplifier was employed. The radiation was focused 250 μm underneath the polished surface of an 11 mm long, 1 mm thick *z*-cut PPRKTP crystal. During the writing process, the crystal was translated along the *x*-axis with a velocity of 25 μm/s, using a motorized translation stage. Several waveguides were written with different track distances and pulse energies and finally the end faces were polished giving a device length of 9.5 mm. The waveguide, which later gave the highest SHG and conversion efficiency was written with a pulse energy of 3.2 μJ and a track distance of 18 μm. The losses were measured with a HeNe-laser at

632.8nm and a cw Ti:sapphire-laser at 940 nm. The lasers were vertically polarized to excite the TM modes. The combined incoupling and propagation losses for the above mentioned waveguide were 2.2 dB in the IR and 1.6 dB in the visible, respectively.

The Ti:sapphire laser was then used as the fundamental source for the SHG measurements. The sample was temperature controlled at room temperature. 76 mW of stable blue light were obtained for an incident fundamental power of 1610 mW at 943.18 nm (see Fig. 1). This corresponds to a conversion efficiency of η = 4.7% and a normalized conversion of η_{norm} = 4.6%$W^{-1}cm^{-2}$. The phase-matching bandwidth, 3.3 °C, was the same as for the bulk measurement indicating a homogeneous waveguide.

In the figure a square-fit of the SH power vs. incident fundamental is depicted. One can see a slight deviation from a smooth fit at around 1.1 W of input power caused by thermally induced dephasing. To compensate for it a minor wavelength adjustment was done. The dephasing comes from the non-negligible absorption in the visible for RKTP[8], which leads to heating of the waveguide at high power and a small shift of the phase-matching wavelength. The phase-matching wavelength could be temperature tuned from 942.36 nm at 8.5°C to 945.35 nm at 65°C, i.e. by 0.053 nm/°C. The mode sizes of the fundamental and second harmonic were both elliptically shaped with dimensions of 12.8 µm × 22.3 µm (IR) and 9.4 µm × 11.8 µm (blue), but with their center of gravity at almost the same spatial position, which is important for getting a good mode overlap and high conversion efficiency. The latter is in contrast with the case of SHG in annealed proton-exchanged waveguides in $LiNbO_3$, where the visible mode is strongly bound close to the surface, while the fundamental mode penetrates much deeper into the substrate, which reduces the overlap and hence ultimately limits the conversion efficiency.



Conclusions: Efficient and stable second harmonic generation into the blue spectral region has been demonstrated using a femtosecond-laser written waveguide in PPRKTP. The waveguide losses were estimated to be < 2.2 dB at 940nm and a maximum output power of 76 mW was obtained at 471.6 nm with an incident fundamental power of 1610 mW. The normalized conversion efficiency was η_{norm} = 4.6%$W^{-1}cm^{-2}$. Absorption of second harmonic led to heating of the waveguide and a weakly distorted phase-matching curve at maximum power. To a large extent this can be compensated for by slight cooling of the sample and it represents only a small reduction of the efficiency. If a waveguide with higher confinement could be fabricated and/or higher fundamental power used the SH power could hence be increased much further.

We believe that the waveguide fabrication process can be improved by optimizing the fs-laser writing parameters. A higher confinement, reduced waveguide loss and even better overlap between the fundamental and SHG modes are the primary properties to address. This new type of nonlinear waveguide device could have interesting applications, for example in biotechnology or quantum optics, if combined with a wavelength stabilized diode or fiber laser.

The authors are very grateful for the financial support by the graduate school 1355 "Physics with new advanced coherent light sources", the Linnaeus Center ADOPT, and the Swedish Research Council.

References

1. B. C. Stuart, *et al., Phys. Rev. B* **53,** pp. 1749– 1761 (1996).
2. R. Osellame, *et al., J.Opt. Soc. Am. B* **20,** pp. 1559–1567 (2003).
3. T. Calmano, *et al., Appl. Phys. B* **100,** pp. 131–135, (2010).
4. A. Zukauskas, *et al., Opt. Mater. Express* **1,** pp. 201–206 (2011).
5. C. J. van der Poel, *et al., Appl. Phys. Lett.* **57,** pp. 2074–2076 (1990).
6. F. Laurell, *Optical Materials,* **11,** pp. 235–244 (1999).
7. S. Campbell, *et al. Opt. Express* **15**, pp. 17146–17150 (2007).
8. G. Hansson, *et al., Appl. Opt.* **39,** pp. 5058–5069 (2000).

Guided-wave AlGaAs optical parametric oscillator

C. Ozanam[1], L. Lanco[2], X. Lafosse[2], A. Andronico[1], I. Favero[1], S. Ducci[1], G. Leo[1]

[1]Université Paris Diderot, Sorbonne Paris Cité, Laboratoire MPQ, Paris, France,
giuseppe.leo@univ-paris-diderot.fr
[2]Laboratoire de Photonique et Nanostructures, CNRS, Marcoussis, France

Abstract: We demonstrate the first near-infrared integrated optical parametric oscillator in a direct gap semiconductor. This nonlinear device is based on a selectively oxidized GaAs/AlAs heterostructure, the same "AlOx" technology at the heart of VCSEL fabrication. We observe a threshold of 210 mW at degeneracy around 2 µm in the CW regime, with a single-pass-pump doubly resonant scheme. This result marks a milestone for integrated nonlinear photonics and represents a significant step toward the goal of a broadly tunable coherent light source on chip.

The optical parametric oscillator (OPO), one of today's most known optical devices, can be functionally defined as a widely tunable coherent source [1]. With the aim of demonstrating its on-chip electrically pumped version, AlGaAs waveguides raise a big interest because of the direct-gap of this III-V semiconductor, its high $\chi^{(2)}$ susceptibility, wide transparency window, good thermal conductivity and mature technology.

Here we report on the demonstration of a near-IR continuous-wave (CW) OPO in a form-birefringent partially oxidized GaAs/AlGaAs waveguide [2], with a low pump threshold P_{th} = 210 mW. The development of such a source might radically transform a number of applications in near and mid IR up to 3 µm. The structure that we consider here has been designed to operate as an OPO in the near IR, with degeneracy at 1.064 µm. It relies on guided-wave type-I phase matching between a TM_{00} pump mode at wavelength λ_P and two TE_{00} signal/idler modes at wavelengths λ_S and λ_I, respectively. The corresponding vertical layout consists of GaAs (substrate) / 1 µm $Al_{0.92}Ga_{0.08}As$ / 1 µm $Al_{0.7}Ga_{0.3}As$ / 4 × [37.5 nm $Al_{0.98}Ga_{0.02}As$ / 273 nm GaAs] / 37.5 nm $Al_{0.98}Ga_{0.02}As$ / 1 µm $Al_{0.7}Ga_{0.3}As$ / 30 nm GaAs. This heterostructure has been grown by molecular beam epitaxy on a semi-insulating (001) GaAs substrate. Chemically etched guiding ridges (3-4 µm wide, ~ 3 µm deep and 2 mm long) have been defined along the crystalline axis by means of UV photolithography. Then $Al_{0.98}Ga_{0.02}As$ has been selectively transformed into AlOx by thermal wet oxidation [3]. Propagation optical losses mainly stem from the oxidation process. As shown in Fig. 1a, they exhibit two different regimes: 1) Above λ~1.1 µm, they decay as an inverse power law of the wavelength, a fingerprint of scattering due to the AlOx layers rough interfaces; 2) below λ~1.1 µm, losses are much higher (up to 3 cm^{-1}), diverge when λ decreases, and can be reasonably ascribed to Urbach's tail associated to gap levels created during the oxidation process in the GaAs layers adjacent to AlOx [4,5].

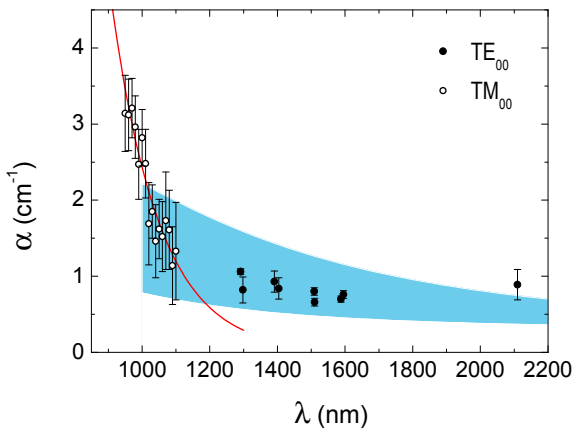


Figure 1. Propagation losses of the fundamental TM and TE modes vs. λ. Below λ~1.1 µm, data are fitted by a decaying exponential (red line). Above λ~1.1 µm, they are compared to a scattering model (blue stripe).

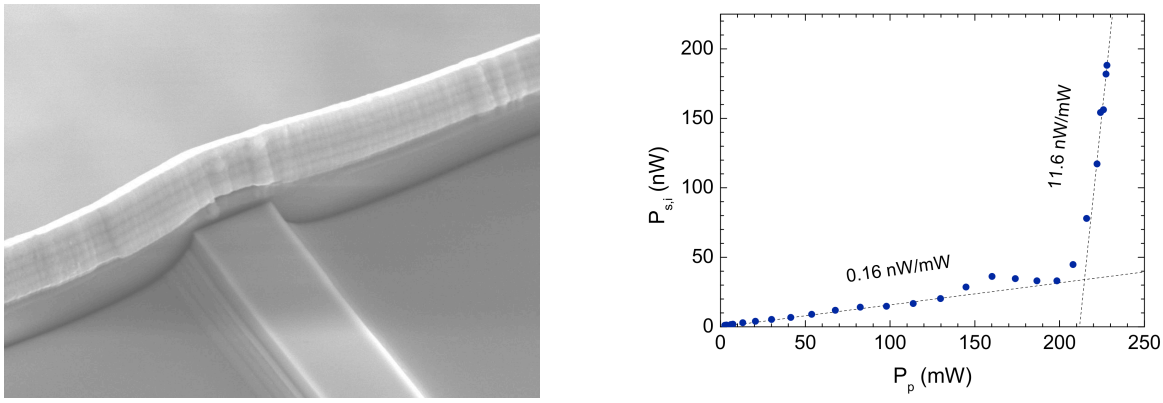


Figure 2. Left: Electron microscope view of a waveguide facet after mirror deposition. Right: OPO power vs. pump power at degeneracy ($\lambda_p \approx 1068.5$ nm, $\lambda_{s,i} \approx 2137$ nm), showing a clear threshold at P_p=210 mW.

We fabricated a doubly resonant OPO (DROPO), by depositing a SiO_2/TiO_2 Bragg dichroic mirrors ($R_{s,i}$ = 90%) on waveguide facets (see Fig. 3 Left). In agreement with our calculations, below threshold we measured a parametric gain coefficient of 4.1 $W^{-1/2}$ cm^{-1} at degeneracy (corresponding to η_{norm} = 1500% $W^{-1}cm^{-2}$) [6]. Although reaching the OPO threshold has been a challenging task due to hardly reproducible losses and mirrors performances, some of our waveguide cavities have allowed us to observe it at P_{th} = 210 mW, as shown in Fig. 2 (Right). With such value of P_{th}, which corresponds to a mode intensity of 0.8×10^7W/cm^2, we can estimate two-photon absorption losses, obtaining $\alpha_{TPA} \approx$ 0.19 cm^{-1}, thus negligible with respect to the linear absorption at pump wavelength. The maximum pump power $P_p \approx$ 230 mW is presently limited by an irreversible thermal damage of the mirrors that occurs after about thirty minutes of CW operation.

Our present efforts are being devoted to increase P_p /P_{th}. To this end, a double-pass-pump scheme can be implemented, leading to a reduction of P_{th} by a factor between 2 and 4, depending on the relative dephasing of pump, signal, and idler modes at the back mirror of our DROPO [38]. Such scheme could also be adopted for a singly resonant OPO for which, despite a higher impact of TPA, we estimate a threshold $P_{th} \approx$ 0.8 W: a reasonable price for its better stability and tunability performance [7]. A further optimization of our AlGaAs/AlOx OPO demands reducing its near-IR linear propagation losses induced by the oxidation process. To this end, we think that the insertion of thin lattice-matched $Ga_{0.5}In_{0.5}P$ barriers between the AlOx and GaAs layers should effectively hamper the diffusion of As-rich oxidation reaction products into the latter, thus preventing the formation of point defects [8]. Finally, for future power scaling, we will explore the option of encapsulating the guiding ridge in e.g. benzocyclobutene (BCB), so that the mirrors can be deposited on wider facet areas, with an advantage in terms of uniformity and heat sink.

Besides improving the optically pumped OPO reported here, we also envisage to fabricate its electrically injected counterpart. We estimate that such VCSEL-like engineering of current and light confinement will lead the way to an electrically pumped OPO.

References

1. M. Ebrahim-Zadeh et al., Handbook of Optics, Optical Society of America, 2nd Ed., Vol. IV (McGraw Hill, 2001).
2. A. Fiore et al., *Nature* **391**, 463 (1998).
3. K. Choquette et al., *IEEE J. Sel. Top. Quant. Electron.* **3**, 916–926 (1997).
4. J. A. Kash et al,. *Appl. Phys. Lett.* **67**, 2022–2024 (1995).
5. J. F. Chen et al., *J. Appl. Phys.* **99**, 023711 (2006).
6. E. Guillotel et al., *Appl. Phys. Lett.* **94**, 171110 (2009).
7. J. E. Bjorkholm et al., *IEEE J. Quantum Electron.* **QE-6**, 797-799 (1970).
8. S.-C. Lee et al., *Jpn. J. Appl. Phys.* **39**, 2583-2584 (2000).

Highly confining nonlinear proton exchanged embedded waveguides on z-cut lithium niobate.

O. Stepanenko[1], I. Krasnokutska[1], E. Quillier[1], P. Baldi[1], M. De Micheli[1]

[1] *University Nice Sophia Antipolis, LPMC UMR 7336, France,*
marc.de-micheli@unice.fr

Abstract: In this work, to fabricate highly confining embedded waveguides on LN without degradation of the nonlinear coefficient, we combined a modified direct exchange we call High Index Soft Proton Exchange (HISoPE) and a reverse proton exchange (RPE) processes. The kinetics of the RPE process is discussed, as well as its influence on the index profile. Linear and nonlinear characterizations are performed on a first realization, that illustrates the complexity of the obtained index profile.

Introduction. Fabrication of highly confining nonlinear waveguides on lithium niobate (LN) has always been a challenge. The proton exchange (PE) technique proposed in the 1980's is able to achieve a high value of $\delta n_e = 0.1$, however such waveguides no longer benefit from the intrinsic nonlinear properties of the substrate.[1] Since then, many modifications of the PE process have been tested in order to find a compromise between the confinement and the nonlinearities. Techniques such as Annealed Proton Exchange (APE) and Soft Proton Exchange (SPE) do realize waveguides with preserved nonlinear coefficients but with a rather weak confinement, the value of the index change, being in any cases lower than 0.03 at $\lambda = 1.55$ µm.[2-5] We have developed a new Proton Exchange process, which allows realizing waveguides on LN with a δn_e of 0.1 and without degradation of the nonlinear coefficient. However, to avoid strains and stresses due to an important lattice parameters mismatch, which is typical for H:LN structures with high concentration of protons, we reconstructed the LN substrate near the surface using the Reverse Proton Exchange (RPE) process.[6] Embedding a waveguide in such a way, allows "erasing" the surface layer presenting the higher mismatch and preserving the deeper part of waveguide whose index increase is at least equivalent to SPE waveguides. However, this approach is difficult to control, as the kinetics of RPE depends on the crystalline phase of the initial proton exchanged LN.[7] In the present work, we discuss the main problems that one can meet during the fabrication of nonlinear waveguides using a combination of PE and RPE processes.

Planar waveguide fabrication and characterizations. 3" Z-cut wafers were used for the waveguides fabrication. The PE consists in immersing the crystal in a bath of benzoic acid (BA) containing a certain percentage of lithium benzoate (LB), which is chosen low to obtain waveguides with high index change (Fig. 1). But on the other hand this concentration is chosen as high as possible to avoid the degradation of the nonlinearities. Waveguides are fabricated in a hermetically closed and

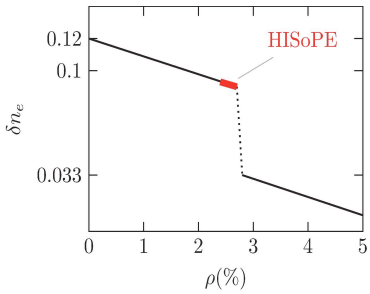


Fig. 1: Concentration of LB used for waveguide fabrication.

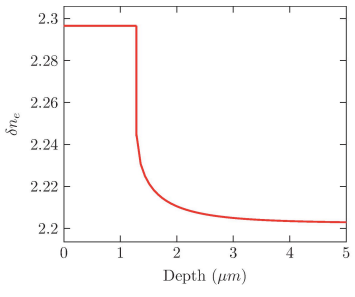


Fig. 2: Typical index profile of HISoPE waveguides.

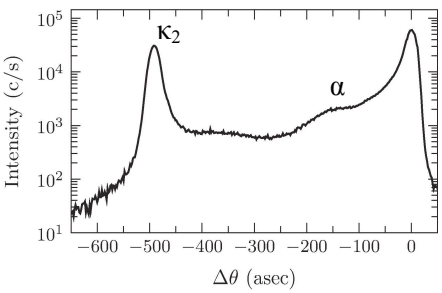


Fig. 3: X-ray rocking curve of (00.12) atomic planes of HISoPE waveguide.

evacuated down to 3 mbar metallic container at a temperature of 300°C. The exchange time can vary from several hours to several days depending on the desired depth of the waveguide. Further characterizations of the waveguides reveals that the index profile is composed of a step section followed by a graded index section (Fig. 2) and that the nonlinear properties are non degraded. We

call them High Index Soft Proton Exchanged waveguides, and X-Ray diffraction characterization indicates that these waveguides are composed of κ_2 phase and α phase (Fig. 3).

For the RPE process, the crystal is immersed into a melt of KNO_3:$NaNO_3$:$LiNO_3$ in the proportions 1:1:0.1 and heated up to 300°C. The study of RPE kinetics indicates that the step portion of the index profile is rather rapidly erased while the RPE seems to be much slower in the graded index part of the waveguide (Fig. 4). This behavior is quite interesting and indicates that the tolerances to produce an embedded graded index waveguide should be quite loose.

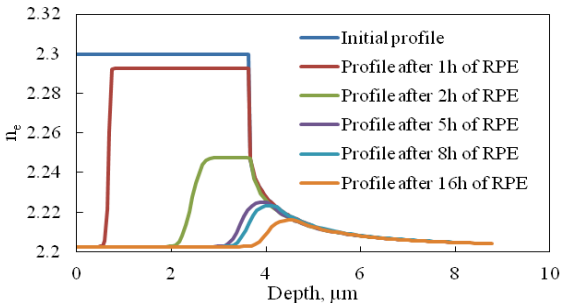


Fig. 4. Index profiles obtained after a direct PE step followed by a RPE process whose duration is varying between 1 and 16 hours.

Channel waveguides fabrication and characterizations. Contrary to what occurs in planar waveguides, the different kinetics of RPE raise a problem for channel waveguides fabrication. Indeed, the κ_2 part of the channel waveguide being erased more rapidly by RPE, the resulting waveguide can be quite complicated (Fig. 5). We will see in the following that a profile corresponding to the one sketched in Fig.5 behave more or less as two highly coupled waveguides.

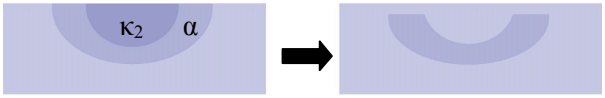


Fig. 5. Channel waveguide before and after RPE.

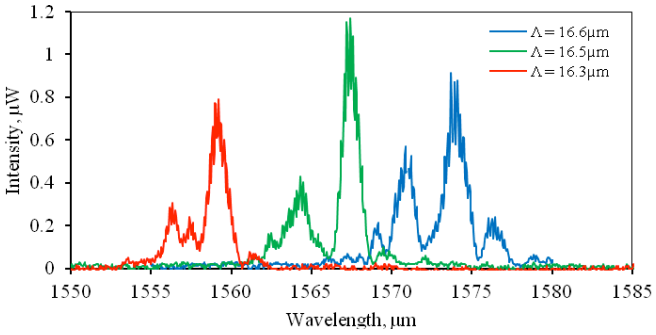


Fig. 7. SHG response in function of the pumping wavelength measured for waveguides with PPLN periods of 16.3, 16.5 and 16.6 µm

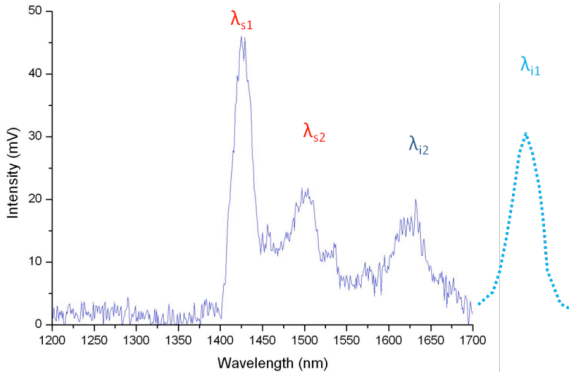


Fig. 6. Observation of the different families of signal and idler frequency in spontaneous parametric down conversion (SPDC) experiment. The idler of the first family is not observable as its wavelength was out of the detector sensibility range.

Indeed, measuring SHG as well as SPDC spectra (Figs. 6-7) of embedded waveguides fabricated in the way described above in PPLN, we could observe multiple peaks of phase matching. The distribution of these peaks cannot be explained by a multimode nature of the waveguide, but fits quite well with the assumption that the embedded waveguide behaves like a directional coupler.

Conclusion. The combination of direct and reverse proton exchange we proposed, allows realizing highly confining (up to δn_e=0.1) embedded waveguides on LN without degradation of the nonlinear coefficient. All the details concerning the first linear and nonlinear channel waveguides characterization will be presented at the conference.

References

1. F. Laurell *et al.*, *Appl. Phys. Lett.*, **60**(3), pp.301-303 (1992).
2. P. Baldi *et al.*, *Opt. Eng.*, **37**(4), pp.1193-1202 (1998).
3. L. Chanvillard *et al.*, *Appl. Phys. Lett.*, **76**, pp.1089-1091 (2000).
4. M. L. Bortz *et al.*, *Opt. Lett.*, **20**(1), pp.49-51 (1995).
5. M. H. Chou *et al.*, *Opt. Lett.*, **24**(16), pp.1157-1159 (1999).
6. J. L. Jackel and J. J. Johnson, *Electron. Lett.*, **27**(15), pp.1360-1361 (1991).
7. Yu. N. Korkishko and V. A. Fedorov., *J. Appl. Phys.*, **82**(3), pp.1010-1017 (1997).

Second-Order Nonlinear Characterizations of Non-Homogeneous Quasi-Phase-Matched Waveguides

I. Krasnokutska, O. Stepanenko, E. Quillier, H. Tronche, P. Aschieri, M. De Micheli, P. Baldi

LPMC, CNRS UMR 7336, University of Nice Sophia Antipolis, Nice, France,
Pascal.Baldi@unice.fr

Abstract: Quasi-Phase-Matched (QPM) waveguides may suffer from the degradation of their optical nonlinear performances like poor efficiency and/or distorted spectra. On a set of non-homogeneous QPM Lithium Niobate waveguides, we used spontaneous parametric down conversion and second harmonic generation as characterization methods. We compared both processes and retrieved back the non-homogeneity along the waveguides.

Introduction: Nonlinear interactions, such as Spontaneous Parametric Down Conversion (SPDC) and Second Harmonic Generation (SHG) in Periodically Poled Lithium Niobate (PPLN) waveguides are nowadays widely employed, for example in quantum telecommunications.[1] However, many teams have reported non standard behavior for the generated power spectrum, with shifted main peak and pronounced side lobes compared to the expected perfect $sinc^2$ form.[2-3] Main reasons of this behavior are inhomogeneity of the waveguide or of the poling. Knowing the origin of these distortions is of great importance as it allows improving the fabrication process and increasing the interaction efficiency. It is thus interesting to have precise nonlinear characterization tools and accurate numerical simulation methods. For our demonstration, we have fabricated a set of on-purpose distorted PPLN waveguides and used SPDC and SHG as characterization methods. We compared both nonlinear processes together and with numerical simulations and concluded that the distortions of spectrum and reduced efficiencies appear from a nonuniform effective index along the waveguides.

Fabrication of the PPLN waveguides: sample fabrication started by poling a 3" wafer using the e-field technique. Periods range from 15.6 to 16.6µm by 0.1µm step. Soft Proton Exchange (SPE) at 300°C for 3 days was then used to fabricate the waveguides.[4] One part of the sample was covered by a standard photolithographic mask with uniform openings of widths ranging from 4 to 8µm by 1µm step, while the other part was covered by a mask with non-uniform widths. The width was linearly increased from w at the input face to w+4 at the middle of the waveguide, and then linearly decreased back to w at the output face (waveguides were thus symmetric). The initial value w was ranging from 4 to 8µm by 1µm step. Sample was then end-faces polished and all waveguides were 4.5cm long.

Nonlinear characterizations of the homogeneous waveguides: the homogeneous waveguides were first characterized using SPDC and SHG. The SPDC experimental set-up is described elsewhere.[5]

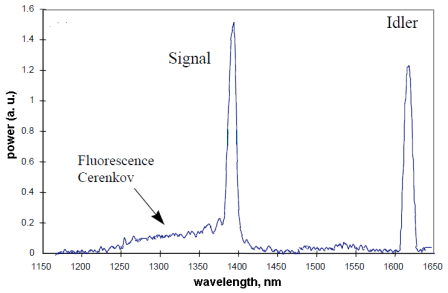


Fig. 1: Expected form of SPDC in an homogeneous waveguide.[9]

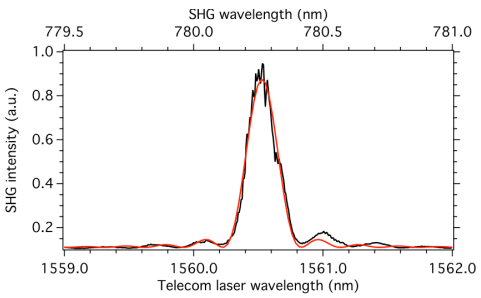


Fig. 2: Expected $sinc^2$ form for the SHG spectrum in an homogeneous waveguide.

The SHG set-up used a Tunics-Plus 10 tunable laser, delivering 5mW from 1500 to 1620nm as the fundamental wavelength. A polarization maintaining fiber allows the light injection into the PPLN waveguide. Light was coupled out from the waveguide using a microscope objective. A system of dichroic mirrors, filters and flip-flap metallic mirrors allowed to measure both fundamental and second-harmonic spectra and to observe on cameras the excited modes. Figs. 1 and 2 show typical spectra with no deviation from the expected forms as it should be in uniform waveguides.

We also performed SPDC in the bulk to check the quality of the poling. Figure 3 shows that we obtained the expected spectrum shape characteristic of non-collinear SPDC. We did not observed any distortions into the sharp break between the signal and idler peaks, confirming that the poling was uniform.

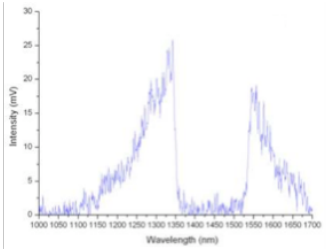


Fig. 3: Non-collinear SPDC in the bulk PPLN for Λ=15.μm And λ_p=712.6nm.

SPDC and SHG in the non-homogenous waveguides: Figures 4 and 5 report SPDC and SHG respectively for three different waveguide widths.

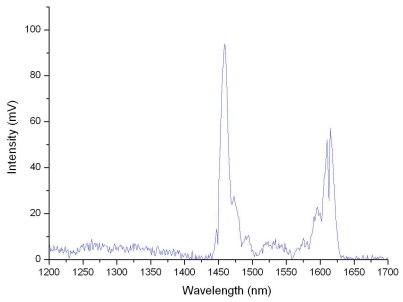


Fig. 4a: spectrum of generated SPDC in a w=4μm width waveguide for Λ=15.6μm and λ_p=763.6nm.

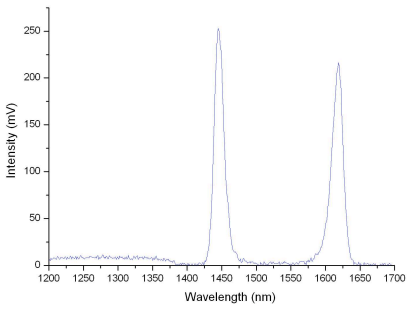


Fig. 4b: spectrum of generated SPDC in a w=6μm width waveguide for Λ=15.6μm and λ_p=764.2nm.

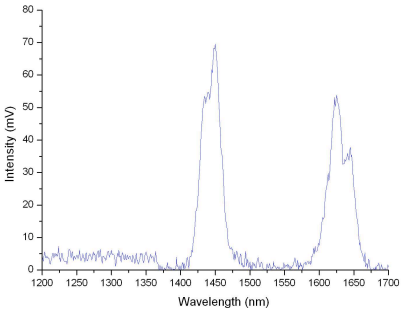


Fig. 4c: spectrum of generated SPDC in a w=8μm width waveguide for Λ=15.6μm and λ_p=766.2nm.

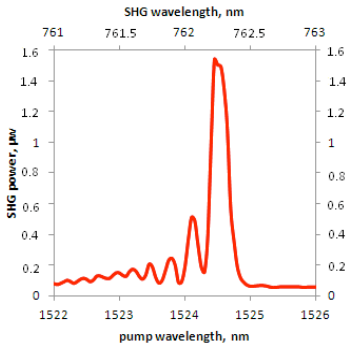


Fig. 5a: SHG in the same than Fig. 5a waveguide.

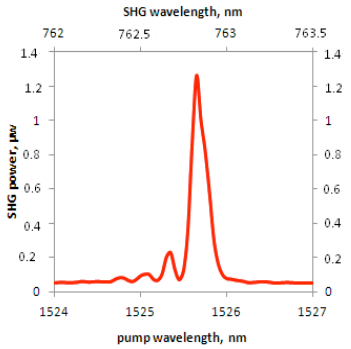


Fig. 5b: SHG in the same than Fig. 5b waveguide.

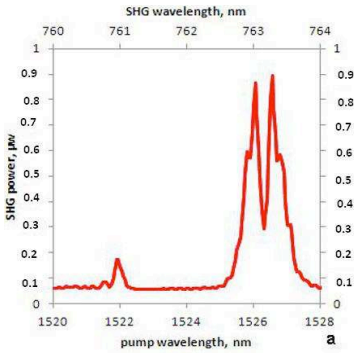


Fig. 5c: SHG in the same than Fig. 5c waveguide.

The distortions in the spectra were in qualitative agreement with the simulated ones. For a given waveguide, the inversion of the side lobes compared to the main peak between SPDC and SHG is due to the phase mismatch term that appears in the governing equations. Because of the waveguide dispersion the side lobes are more pronounced on one side or the other of the main peak depending on w. For w=6µm the nonlinear spectra have almost perfect shape, even if the efficiency η is reduced compared to similar homogeneous waveguide. We obtained comparable values η_{SHG}=(7.9±1.4)%W^{-1}cm^{-2} and η_{SPDC}=(5.9±0.9)%W^{-1}cm^{-2}, indicating that the two nonlinear characterizations are in good agreement. Furthermore the measured bandwidths were also shown to be in good agreement.

Conclusion: we have shown that both SHG and SPDC can be used to characterize the nonlinear optical properties of non-homogenous QPM waveguides. Both characterizations are in good agreement. SHG needs simpler set-up equipments compared to SPDC but requires to know quite accurately the QPM wavelength. SPDC has a much larger acceptance in terms of QPM conditions but requires detecting low (in the pW range) powers.

References

1. S. Tanzilli *et al., Laser Photonics Rev.* **6**, pp. 115–143 (2012).
2. M.M. Fejer *et al., IEEE J. Quantum Electron.* **28**, pp. 2631–2654 (1992).
3. S. Helmfrid *et al., JOSA B* **8**, pp. 797-804 (1991).
4. L. Chanvillard *et al., Appl. Phys. Lett.* **76**, pp. 1089-1090 (2000).
5. P. Baldi *et al., IEEE J. Quantum Electron.* **31**, pp. 997–1008 (1995).

Ultracompact photonic crystal integrated circuits: connecting tiny devices to achieve high-performances

Stefania Malaguti, Gaetano Bellanca and Stefano Trillo

[1] *University of Ferrara, Ferrara, Italy*
gaetano.bellanca@unife.it

Abstract: PhC technology is expected to play an important role in the future of optical telecommunication devices. Results relevant to the design and fabrication of a 4×25 Gbit/s WDM Receiver and of a 100 Gbit/s OTDM Receiver are presented.

Introduction. In the last years, the rapid advances in science and technology, with the disrupting advent of Internet in daily life, have transformed significantly the world of communication and computing. The demands of consumers for higher speeds and greater capacities appear unending. Photonic chips are set to play an important role in the development of future communication and information technologies. Photons (carriers of optical signals) have important fundamental properties that make them superior to electrons (carriers of electrical signals) for representing and transmitting data, as demonstrated by long distance communication networks. However, as the bandwidth increases, the advantages of optics even holds for very short transmission distances, such as between high-speed processors in a computer, and ultimately, across individual computer chips. Although electronics continues to remain unbeaten for performing high-level data processing (such as that performed by modern computers), the growth in performance is today falling short of earlier predictions: electrical interconnects, in fact, are the key factor limiting the speed and the integration level of electronic circuits. Faster switching is possible with current transistor technology, but it takes too much power and generates too much heat to send information across the chip at higher data rates. Photonics has therefore a crucial role to play in global interconnects, but this is a difficult challenge as, to be competitive, the size and power consumption of traditional photonic devices must be reduced by more than two orders of magnitude. Photonic Crystals (PhCs) based technology seems to address these issues and be able to provide devices capable of meeting these challenges. In the framework of the European Project COPERNICUS, researches of different institutions developed the technology needed to provide 100 Gbit/s WDM and OTDM receivers based on PhCs. The main steps needed to get devices that can satisfy these challenging specifications and ensure the required performances, are summarized in the following.

Modeling. Effective designs for complex devices as the ones based on PhCs requires accurate theoretical modeling and simulation tools. To achieve the expected results, a wide range of steady-state and time-domain approaches have been developed. In particular, the Finite Difference in the Time Domain (FDTD) has proven to be accurate for simulating linear responses of the investigated components[1]. However, other approaches were pursued, in particular for nonlinear modeling[2] and coupling with electrical/thermal simulations[3].

Material Engineering. For device fabrication, III-V semiconductor PhC membranes have been used[4,5]. This platform is ideally suited for both wavelength filtering/routing, high-speed/low power optical switching and detection. In particular, GaAs and InP technology were pursued. GaAs has the key advantage of a short carrier lifetime, which is attractive for AOGs, whereas InP is compatible with active telecom devices such as InGaAs photodetectors/laser/amplifiers. For the planar technology, both air-bridged and Benzocyclobutene (BCB)-encapsulated PhC membranes were pursued. The former for AOGs[6], whereas the latter for WDM devices with integrated photodetectors[7].

Device Fabrication and Measurements. Fig. 1 (on the left) shows an example of a 4-channel WDM Receiver. The fabrication of this component required the design of both the key elements (the PhC cavities) and the optical circuitry (waveguides, bends, tapers). Optimizations of each component is fundamental to guarantee a device that satisfies the challenging specifications and ensures the required performances. The same figure reports also (on the right) the eye diagram evaluations at the different ports of the receiver[8].

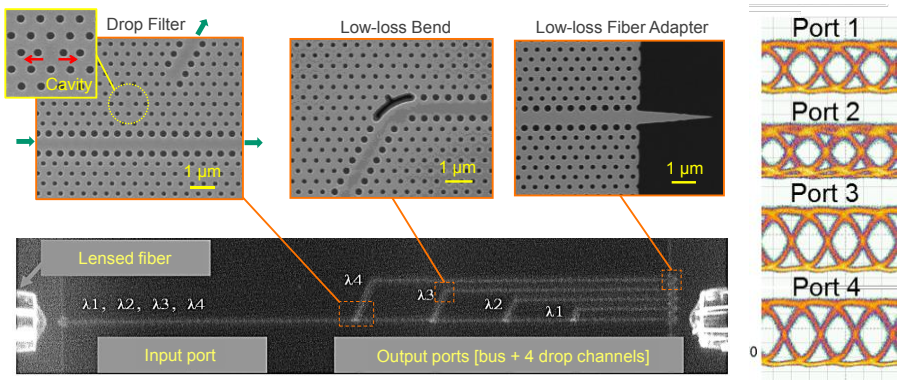


Fig. 1 Image of the 4-channel WDM demultiplexer (left) with magnifications of the resonant cavity, low-loss bend and fiber adapter. Eye diagrams of 100 Gbit/s signal after demultiplexing into 4×25 Gbit/s signals (right).

The All Optical gate (AOG) is the key component of the OTDM Receiver. The basic principle of the AOG is the optically induced spectral shift of a microcavity, which is configured to operate as a band-pass filter. Through this mechanism, the transmission spectrum near the cavity resonance is dynamically controlled. Different configurations for this device have been investigated. The left panel of Fig. 2 shows a layout based on two H0 coupled cavities on a PhC air-suspended InP membrane[6]. Switching obtained on a non-degenerate pump-probe experiment (pump shifted of about 10 nm from the signal) is also illustrated (center-left panel). Measurements showed that this AOG follows a clock of 20 Gbit/s. An alternative configuration based on a hybrid III-V photonic crystal nanobeam cavity on a silicon on insulator (SOI) waveguide[9] is reported in the center-right panel of the same figure. A switching time of 12 ps, with an energy of 40 fJ, has been measured (Fig. 2 on the right).

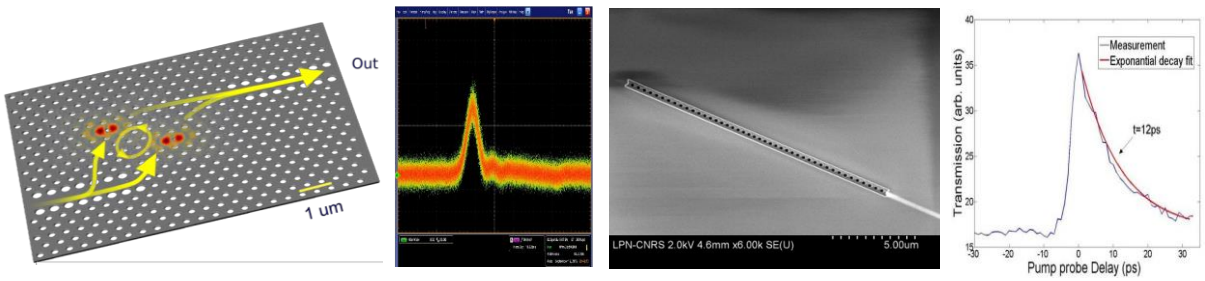


Fig. 2: On the left: layout of the two coupled H0 cavities forming the PhC "molecule" AOG and (center-left) response to a single short pulse in non-degenerate pump-probe measurement of the nonlinear dynamics. Center-right: two-port AOG based on a hybrid III-V PhC nanobeam cavity on a (SOI) waveguide and switch demonstration on a degenerate pump-probe experiment (on the right).

Acknowledgments. The authors acknowledge the contributions of all the partners of the COPERNICUS Project (FP7 ICT 2009.3.8.b 249012): M. Gay, M. Thual and L. Bramerie (CNRS-FOTON, France), A. Bazin, F. Raineri and R. Raj (CNRS-LPN, France), L. Ottaviano and K. Yvind (DTU FOTONIK, Denmark), A. De Rossi and S. Combrié (Thales Research and Technology, France), S. Formont and L. Menager (Thales Systemes Aeroportes, France), S.Kaunga-Nyirenda, H. Dias, S. Bull and E. Larkins (University of Nottingham, UK), M. Serbay (u2t Photonics, Germany).

References

1. S. Malaguti *et al*., *Optical and Quantum Electronics* **45**, pp. 329–342 (2013).
2. P. T. Kristensen *et al*., *Applied Physics Letters* **102**, 041107, (2013).
3. H.K. Dias *et al*., *IET Optoelectronics* **8**, pp. 58–63 (2014).
4. K. Lenglé *et al*., *Optics Express* **20**, 16154, (2012).
5. F. Raineri *et al*., *CLEO 2012, CTu21.5*, (2012).
6. S. Combrié *et al*., *Applied Physics Letters* **103**, 193510 (2013).
7. L. Ottaviano *et al*., *Conference on Lasers and Electrooptics (CLEO 2012)*, CM1A.2 (2012).
8. K. Lenglé *et al*., *IEEE Photonics Technology Letters* **24**, pp. 2109–2111 (2012).
9. F. Raineri *et al*., *International Conference on Transparent Optical Networks (ICTON), Cartagena*, (2013).

CMOS Photonic Integrated Circuits and Systems

Rajeev J. Ram

Massachusetts Institute of Technology, Cambridge MA 02139

rajeev@mit.edu

Abstract: Integrated photonic-electronic components and subsystems are designed and demonstrated for microprocessor-to-memory interconnection. Monolithically integrated receivers and transmitters are demonstrated in both zero-change silicon-on-insulator CMOS as well as custom bulk CMOS processes.

CMOS photonics applications include medium reach links for data center backhaul, short reach links for optical backplanes, optical implementations of peripheral hardware bus (PCI-type), memory-to-core links, and core-to-core links. Here we consider one particular application – memory-to-core links required for the continued scaling of multicore microprocessors.

Here, I review the progress made towards building systems utilizing CMOS electronics and photonics fabricated simultaneously within a state-of-the-art CMOS manufacturing flow. I will focus primarily on the recent results of devices and systems resulting from an on-going collaboration between my group (the Physical Optics and Electronics Gorup) at MIT, Vladimir Stojanovic's Group at UC Berkeley, and Milos Popovic's Group at the University of Colorado at Boulder. Recently, we have successfully demonstrated monolithic integrated electronic-photonic integration of transmitters (modulators and drive electronics) and receivers (photodetectors and circuits) in both foundry silicon-on-insulator processes as well as custom bulk CMOS processes.

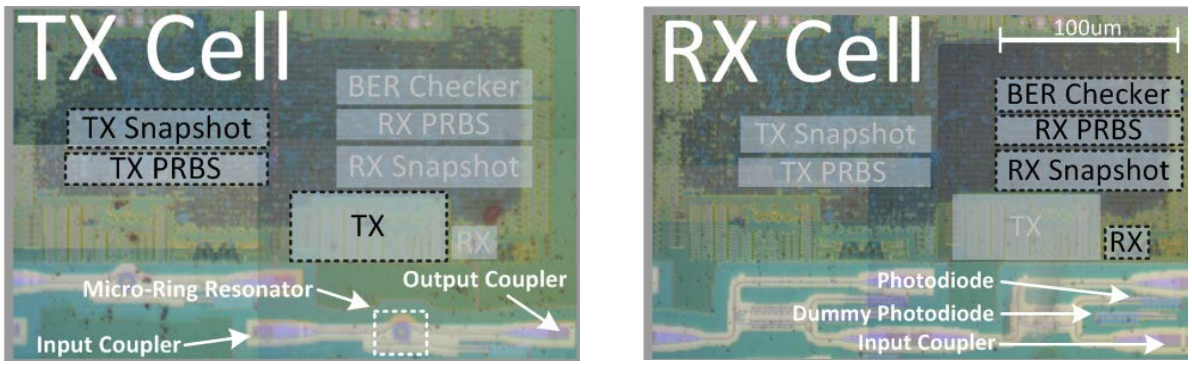


Fig. 1 a) Monolithically integrated transmitter in 45nm SOI with digital back-end. The micro-ring resonator uses interleaved p-n junctions to achieve efficient tuning in depletion mode. B) Monolithically integrated receiver in 45nm SOI utilizing SiGe photodetector.

Zero-change silicon-on-insulator CMOS photonics has been demonstrated using the IBM 45nm SOI platform. This unmodified platform is used for a wide range of products from supercomputers to servers to gaming consoles. Our team has demonstrated high-performance resonant modulators utilizing the crystalline (body) silicon as a waveguide layer. Optimized devices demonstrate 5 Gbps data transmission with an extinction ratio of 8 dB an insertion loss of 1.5 dB [1]. Interleaved p-n junctions are operated in depletion by virtue of electrical contacts distributed within the inner circumference of the ring-resonant modulator. The low capacitance of this structure results in a low-energy per bit of < 5fJ/bit for the intrinsic modualtor. When driven with an CMOS driver, the total energy consumption for the transmitter block is 20 fJ/bit at 2 Gbps [2]. To the best of our knowledge, this is the lowest energy consumption for an integrated transmitter. The receiver in this chip is realized by

exploiting interband absorption in the SiGe p-doped strain layers. These are the first waveguide infrared photodetecotrs implemented in a zero-change CMOS process. The 10% quantum efficiency detectors are coupled to an on-chip transimpedance amplifier and digital sense amplifier. The total power dissipation for the receiver is 220 fJ/bit at 2 Gbps [2].

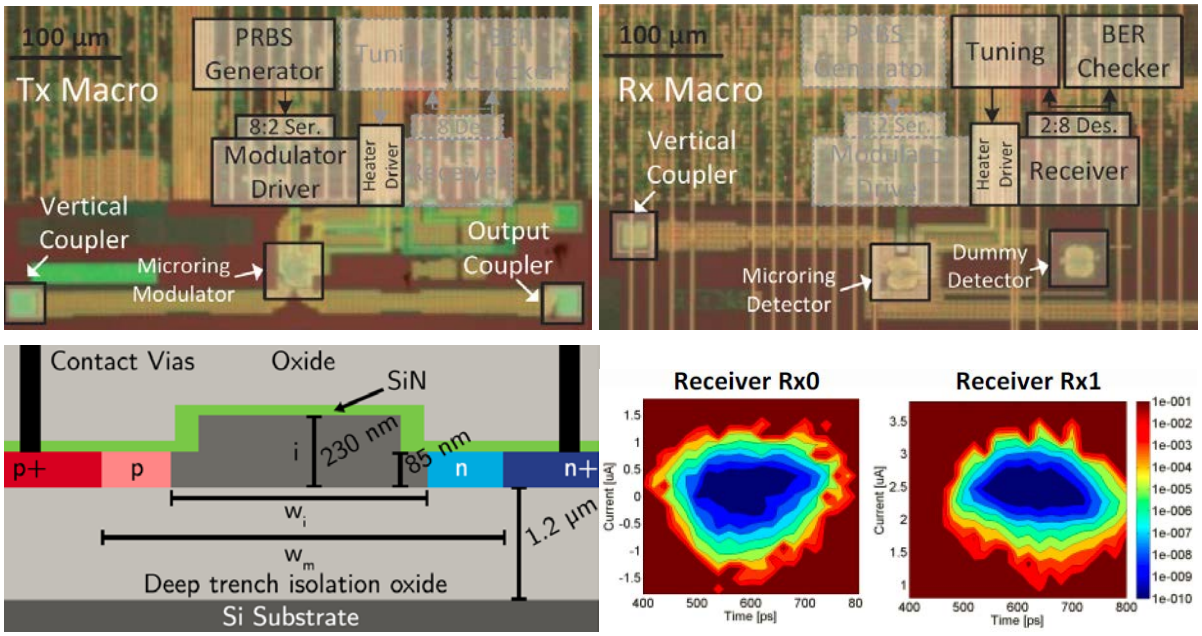


Fig. 2 a) Monolithically integrated transmitter in Bulk CMOS with digital back-end. A simple ridge waveguide microring resonator is used for transmission. b) Monolithically integrated 1280nm receiver in using defect state absorption in polysilicon based microring resonator. c) The cross-section of the polysilicon detector showing the layers for the polysilicon ridge waveguide and deep trench oxide. d) Link data transmission at 5 Gbps with direct fiber connection from chip-to-chip. The BER for the dual-data rate receivers is below 1e-10 for 5 Gbps operation.

Because of pricing sensitivity in a very competitive market, DRAM is fabricated only in bulk CMOS processes. Hence, the transmitter and receiver must be fabricated from a polysilicon layer that is deposited on a deep trench oxide. A complete photonic link has been demonstrated at 5 Gbps that transfers digital information from one Bulk CMOS Photonics chip to another [3]. A single-polysilicon deposition and lithography mask were used to simultaneously define the transistor gate, the low-loss waveguides, the depletion modulators, and the photodetectors [4]. The process was finely tuned to adjust the density of localized electronic states associated with the grain-boundaries in polysilicon. A low-defect state density was utilized for the waveguide and modulator layers. This defect state density could be tuned to be higher for the all-silicon photodetectors. The resulting microring resonant detectors exhibit a 20% quantum efficiency with 9.7 GHz bandwidth over a wide range of wavelengths [5]. For link tests, 1280nm laser was coupled into the transmitter chip, modulated, and then coupled into a receiver chip several meters away.

1. M. Wade, et al. Optical Fiber Conference, 2014.

2. M. Georgas, et al. VLSI Symposium, 2014.

3. C. Sun, et al. VLSI Symposium, 2014

4. R. Meade, et al. VLSI Symposium, 2014

5. K. K., Mehta, et al. Optics Letters, 2014

An enhanced wavelength tolerant design for the Generation of *N*-partite single photon *W*-states

K. Thyagarajan[1], Surajit Paul[2]

Department of Physics, Indian Institute of Technology Delhi, New Delhi – 110016, India
[1]ktrajan@physics.iitd.ac.in
[2]surajitpaul26@gmail.com

Abstract: Recently integrated optic solutions for generation of *N*-partite *W*-state have been proposed using a 1-D array of '*N*' identical single mode optical waveguides. The proposed design exhibits very low tolerance to the input wavelength. Here we propose an alternative design of a waveguide array consisting of (2*N*-1) waveguides to create '*N*' partite *W* state that exhibits much greater tolerance to the input wavelength thus making it easy for experimental realization.

It is well known that entanglement plays a crucial role in various phenomena in the field of quantum computation[1], quantum cryptography[2-3], teleportation[4], quantum key distribution etc. Among various kinds of non-classical entangled states, *W* states are important as their entanglement is less fragile against loss of any qubit whereas the other class of entangled states i.e. GHZ states become fully separable after qubit loss[5]. For the realization of such non-classical *W* states, quantum optics provides an elegant platform[6].

Recently integrated optic solutions for generation of *W*-states have been proposed using a 1-D array of *N* identical single mode optical waveguides, which are coupled via nearest neighbor interaction[7]. The flow of a single photon through such structure is governed by a set of Heisenberg equation of motion:

$$i\frac{d\hat{a}^{\dagger}}{dz} = K\hat{a}^{\dagger} \qquad (1)$$

where $\hat{a}^{\dagger}$ is the creation operator representing the z dependence of the field in each of the waveguides and given by $\hat{a}^{\dagger} = \left[\hat{a}_1^{\dagger}, \hat{a}_2^{\dagger}, ...\hat{a}_N^{\dagger}\right]^T$ and K is the coupling matrix representing the coupling co-efficient between adjacent waveguides. Solution of eqn. (1) gives the evolution of the z-dependence of the field as

$$\hat{a}^{\dagger}(z) = e^{-iKz}\hat{a}^{\dagger}(0) \qquad (2)$$

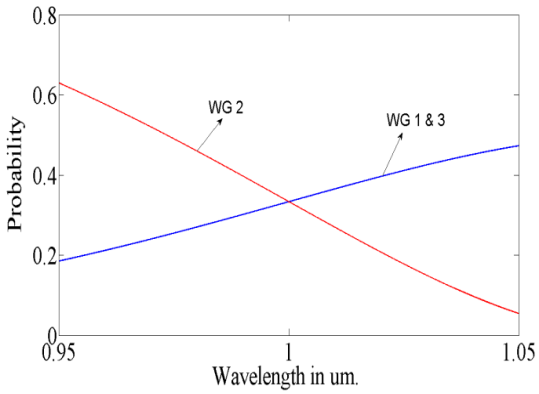


Fig. 1: Wavelength variation of probability of finding a single photon in an array of 3 equally spaced waveguides

Here the term e^{-iKz} acts as the z-evolution operator corresponding to the z-dependence of field in each waveguide. It is well known that for an array consisting of three equally spaced identical waveguides, for a single photon incident in the central waveguide a three partite *W*-state is formed at a propagating distance $z_0 = \left[\tan^{-1}\left(\pm\sqrt{2}\right) + n\pi\right] \Big/ \sqrt{2}\kappa_0$. The major problem with the above mentioned design is that the tolerance to the wavelength of the input single photon for the generation of the *W*-state is very critical. Figure 1 shows the variation of probability of finding the photon in an array of 3 equally spaced ($d = 12\mu m$) identical waveguides as a function of input wavelength, for a device of length $z = 2.48\, cm$ designed to provide a *W*-state at $\lambda_0 = 1\mu m$. Even a change of the input wavelength by ± 0.5 nm. (≈ ±0.05 %) leads to deviation from the *W* state with variation in probabilities of about ± 0.5 %. Such critical tolerance can lead to problems in practical applications of such devices.

To overcome this problem and for a better experimental feasibility of *W* states, we propose an alternative design of a waveguide array consisting of $(2N-1)$ waveguides to create an *N* partite *W* state that exhibits much greater tolerance to the input wavelength.

For example to generate a 3-partite *W*-state, we have considered an array of five waveguides with unequal coupling coefficients given by $\kappa_{2,3}=\kappa_{3,4}=\kappa_0$ and $\kappa_{1,2}=\kappa_{4,5}=\tilde{\kappa}_0$. Now, if a single photon is incident at the central waveguide, then the initial state of the photon at z = 0 i.e. $|\psi_{in}(z=0)\rangle=|00100\rangle=\hat{a}_3^{\dagger}(0)|00000\rangle_{z=0}$ evolves along the propagating distance to a superposition of states

$$|\psi_{out}(z)\rangle=\sum_{p=1}^{5}(T)_{p,3}^{*}\,\hat{a}_p^{\dagger}(z)|00000\rangle_z \qquad (4)$$

where

$$(T)_{1,3}^{*}(z)=(T)_{5,3}^{*}(z)=\frac{\kappa_0\tilde{\kappa}_0}{2\kappa_0^2+\tilde{\kappa}_0^2}\left[-1+\cos\left(\sqrt{2\kappa_0^2+\tilde{\kappa}_0^2}\,z\right)\right] \quad (5)$$

$$(T)_{2,3}^{*}(z)=(T)_{4,3}^{*}(z)=-\frac{i\kappa_0}{\sqrt{2\kappa_0^2+\tilde{\kappa}_0^2}}\left[\sin\left(\sqrt{2\kappa_0^2+\tilde{\kappa}_0^2}\,z\right)\right] \quad (6)$$

$$(T)_{3,3}^{*}(z)=\frac{\tilde{\kappa}_0^2}{2\kappa_0^2+\tilde{\kappa}_0^2}+\frac{2\kappa_0^2}{2\kappa_0^2+\tilde{\kappa}_0^2}\left[\cos\left(\sqrt{2\kappa_0^2+\tilde{\kappa}_0^2}\,z\right)\right] \quad (7)$$

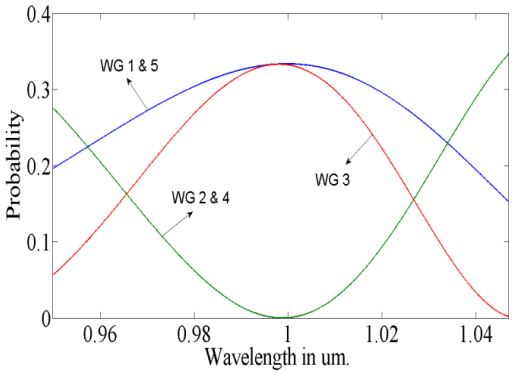


Fig. 2: Wavelength variation of probability of finding a single photon in an array of 5 waveguides (according to our design)

Now, our aim is to generate a 3 partite *W* state in the array of 5 waveguides i.e probability of finding the photon in WG#1, WG#3, WG#5 should be the same (equal to 1/3) and in WG#2, WG#4 it should be zero. This can be achieved by a proper selection of ratio of the propagation distance (z) to the coupling coefficients $(\kappa_0,\tilde{\kappa}_0)$. To demonstrate the idea, simulations have been performed for an array of length $z=7.24\,cm$, consisting of planar waveguides each of width 4 μm. Figure 2 shows the variation of probability of finding the photon in an array of 5 waveguides as a function of input wavelength. The figure clearly demonstrates the much enhanced tolerance of ± 2.5 nm. (≈ 0.25%) to the input wavelength thus clearly showing improved performance of the proposed configuration. Simulations for the generation of 5 partite *W*-states using 9 waveguides show similar enhanced tolerance. The enhanced spectral bandwidth of the proposed device can be used for the generation of *W*-states using pulsed single photon sources with picosecond pulse width.

In conclusion, we have shown that an appropriately designed 1-D array of $(2N-1)$ identical waveguides can lead to *N*-partite *W*-state with much greater tolerance to the input wavelength than the earlier proposed designs.

References

1. M. A. Nilsen and I. L. Chuang, *Quantum Computation and Quantum Information* (Cambridge University Press, Cambridge, UK, 2000).
2. W. Tittel, J. Brendel, H. Zbinden, and N. Gisin, Phys. Rev. Lett. **84**, 4737 (2000).
3. T. Jennewein, C. Simon, G. Weihs, H. Weinfurter, and A. Zeilinger, Phys. Rev. Lett. **84**, 4729 (2000).
4. D. Bouwmeester, J.-W. Pan, K. Mattle, M. Eibl, H. Weinfurter,and A. Zeilinger, Nature (London) **390**, 575(1997).
5. W. Dur, G. Vidal and J. I. Cirac, Phys. Rev. A **62**, 062314 (2000).
6. G. Beneti, G. Casati, and G. Strini, *Principles of Quantum Computation and Information* (World Scientific, Hackensack, NJ, 2004).
7. A. Perez-Leija, J. C. Hernandez-Herrejon, H. Moya- Cessa, A. Szameit and D. N. Christodoulides, Phys. Rev. A. **87,** 013842 (2013).
8. Y. Bromberg, Y. Lahini, R. Morandotti and Y. Silberberg, Phys. Rev. Lett. **102**, 253904 (2009).

Reflective Arrayed Waveguide Grating with Sagnac Loop Reflectors in Silicon-on-Insulator with Gaussian Pass-band

B. Gargallo[1], **P. Muñoz**[1,2], **R. Baños**[1], **A.L. Giesecke**[3], **J. Bolten**[3], **T. Wahlbrink**[3] **and H. Kleinjans**[3]

[1]Universitat Politècnica de València & [2]VLC Photonics S.L.
Camino de Vera sn, 46022 Valencia, Spain - pmunoz@iteam.upv.es
[3]AMO GmbH, Otto-Blumenthal-Straße 25, 52074 Aachen, Germany - kleinjans@amo.de

Abstract

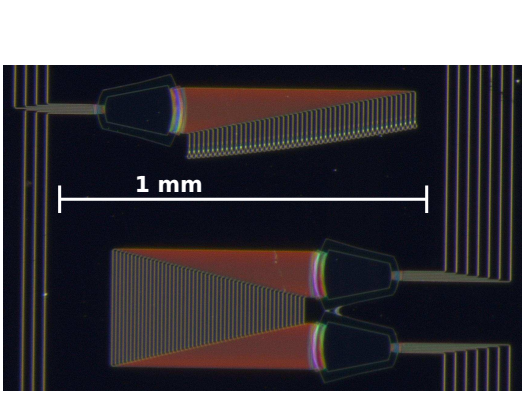
In this paper the experimental demonstration of a Silicon-on-Insulator Reflective Arrayed Waveguide Grating (R-AWG) is reported. The device employs one Sagnac loop mirror per arm in the array, built with a 1x2 input/outputs, 50:50 splitting ratio, Multimode Interference coupler, for total reflection. The spectral responses obtained are compared to those of regular AWGs fabricated in the same die.

Wavelength multi/demultiplexers are central components in optical communications. Their cost when implemented as an integrated circuit is closely related to its footprint [1]. Reflective multiplexers as the Echelle Diffraction Grating (EDG) achieve considerable size reduction [2]. One issue with EDGs is to maximize the reflection on the grating, in order to minimize the overall insertion losses, with the deposition of metal layers at the edge of the grating [3], or the addition of other structures as Bragg reflectors [4]. Metal deposition provides broadband reflectors, but it requires additional fabrication steps. Conversely, Bragg reflectors can be manufactured in the same process, but the reflection bandwidth is inversely proportional to their strength [5]. Reflective Arrayed Waveguide Grating (R-AWG) with reflectors implemented in similar ways exist, with coatings on the facet of the chip [6], [7], photonic crystals [8], external reflectors [9] and Bragg reflectors [10]. A common issue of all the described approaches for the reflector is that broadband full reflectivity requires additional fabrication steps, increasing the cost. In [11] a configuration for a R-AWG, where Sagnac Loop Reflectors (SLRs) are used at the end of the arrayed waveguides, was demonstrated in Silica. These reflectors are broadband, supply total reflection, and can be fabricated in the same lithographic process as the AWG. Moreover, the reflection of a SLR depends on the coupling constant of the coupler. Hence, it can be different for each of the waveguides in the array. In this paper we report on the experimental demonstration of a Silicon-on-Insulator (SOI) R-AWG with Gaussian response, based on SLRs with 50:50 coupling ratio. This opens the door to further research on non Gaussian response R-AWGs, using MMIs with coupling ratios other than 50:50 as we describe in [12].

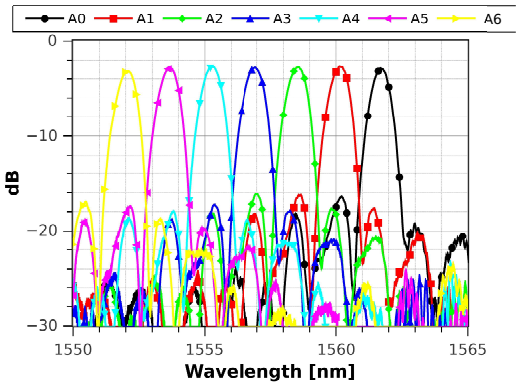
Following the model and methodology from [12], regular and reflective AWGs were designed for target polarization TE on SOI substrates consisting of a 3 μm thick buried oxide layer and a 220 nm thick Si layer, with no cladding. The effective indexes, calculated using a commercial software, are 2.67 in the arrayed waveguides (n_c) -waveguide with 0.8 μm to minimize phase errors [13]- and 2.83 in the slab coupler (n_s). The R-AWG parameters are: center wavelength 1550 nm, 7 channels with spacing 1.6 nm and free spectral range of 22.4 nm, focal length 189.32 μm, length increment 36.03 μm and the number of arms is 49. The R-AWG footprint is 350x950 μm^2 with an orthogonal layout. The fabricated devices are shown in Fig. 1-(a). Each waveguide in the R-AWG array is terminated by a SLR built with a 1x2 Multimode Interference coupler, with 50:50 splitting ratio for ideally full reflectivity. The input/output waveguides are equipped with focusing grating couplers (FGCs).

The waveguides are fabricated by Electron Beam Lithography (EBL) and dry etching in a two-step process. First, using hydrogen silsesquioxane negative tone resist in combination with a high contrast development process [14] all device features are defined and fully etched to the buried oxide using an HBr-based ICP-RIE process [15]. In a second step, a positive tone ZEP resist mask is carefully aligned to those features, exposed and used to define the shallow etched parts of the devices using a C4F8/SF6-based dry etching process. For both process steps a multi pass exposure approach is used to further reduce the sidewall roughness of the photonic device, hence minimizing scattering losses in those devices. Furthermore, special care is taken to guarantee accurate critical dimensions of all parts of the device by applying a very accurate proximity effect correction in combination with a well-balanced exposure dose [16].

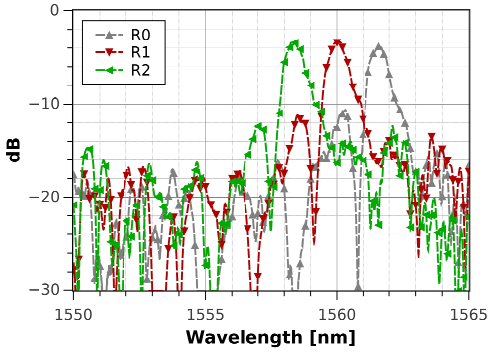
For spectral characterization, a broadband source was employed in the range of 1525-1575 nm, and traces were recorded using a Optical Spectrum Analyzer with 10 pm resolution. All the traces were normalized with respect



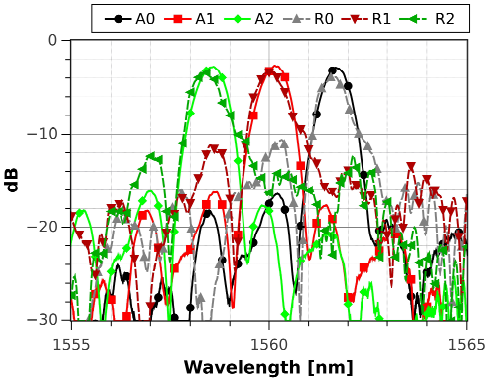
(a) Optical microscope image of the fabricated devices



(b) AWG spectra



(c) R-AWG spectra



(d) Comparison R-AWG vs AWG

Fig. 1. Optical microscope image of the fabricated AWGs (a) and spectral traces, (b) regular AWG, (c) R-AWG and (d) comparison.

to a straight waveguide. The results are shown in Fig. 1. Panel (b) shows the spectra for the seven channels of the AWG, from the central input. Peak insertion loss is approximately 3 dB. Note this value is subject to small variations in the performance of the FGCs (expected ± 0.4 dB). The highest side lobe level is 12 dB below the pass band maximum. Panel (c) shows the spectra for the three inner channels from the central input, for the R-AWG. The other three channels were not designed to be measured, as they end in the same side of the chip. Finally, (d) shows the comparison of both AWG and R-AWG. Two main differences are clearly visible in the figure, between the AWG and the R-AWG. These can be seen in (d) comparing for instance traces A0 and R0. First, the shape of the pass band is slightly degraded towards longer wavelength, for the R-AWG, where broadening happens at 6 dB below maximum. Second, the side lobe level is increased by 4 dB in the R-AWG as compared to the AWG. Being the only difference between both devices the presence of SLRs, these degradations are likely to be due to phase/amplitude imperfections in the reflectors.

In conclusion, we have reported the experimental demonstration of a SOI reflective Arrayed Waveguide Grating, with Sagnac mirrors and Gaussian spectral response. The performance of this first prototype is comparable to that of a regular twin AWG in the same die. Differences, likely due to dissimilarities between reflectors, are subject of current on-going research. Finally, we acknowledge funding from the Spanish MINECO TEC2010-21337 & TEC2013-42332-P, FEDER UPV 10-3E-492 & 08-3E-008, and FPI BES-2011-046100.

References

[1] R. Kirchain and L. Kimerling, Nat. Photon. **1**, 303–305 (2007).
[2] R.J. Lycett, D.F.G. Gallagher, and V.J. Brulis, IEEE Photon. J. **5**(2), (2013).
[3] D. Feng e.a, IEEE Photon. Technol. Lett. **23**(5), 284–286 (2011).
[4] E. Ryckeboer e.a., Opt. Express **21**(5), 6101–6108 (2013).
[5] M.W. Pruessner, T.H. Stievater, and W.S. Rabinovich, Opt. Lett. **32**(5), 533–535 (2007).
[6] Y. Inoue e.a., Electron. Lett. **31**(9), 726–727 (1995).
[7] J.B.D. Soole e.a., Electron. Lett. **32**(19), 1769–1771 (1996).
[8] D. Dai e.a., Opt. Lett. **35**(15), 2594–2596 (2010).
[9] L.G. de Peralta e.a., IEEE Photon. Technol. Lett. **16**(3), 1041–1135 (2004).
[10] K. Okamoto and K. Ishida, Opt. Lett. **38**(18), 3530–3533 (2013).
[11] Y. Ikuma e.a., in Proc. European Conference on Optical Communications (ECOC), (2007).
[12] B. Gargallo and P. Muñoz, arXiv preprint arXiv:1402.4395 (2014).
[13] W. Bogaerts e.a., IEEE J. Sel. Topics Quantum Electron. **12**(6), 1394–1401 (2006).
[14] W. Henschel, Y.M. Georgiev and H. Kurz, J. Vac. Sci. Technol. B 21(5), 2018-2025 (2003)
[15] M.C. Lemme e.a, Microelec. Eng. 73 346-350 (2004)
[16] J. Bolten e.a., Microelec. Eng. 8710411043 (2010)

On chip gallium arsenide optomechanical systems

I. Favero,[1] C. Baker,[1] D. Parrain,[1] W. Hease,[1] D.T.Nguyen,[1] E.Gil Santos,[1] J.Restrepo,[1] C.Ciuti,[1] P. Senellart[2], A.Lemaître[2], S.Ducci,[1] G.Leo[1]

[1] *Laboratoire Matériaux et Phénomènes Quantiques, Université Paris Diderot, CNRS UMR 7162, Sorbonne Paris Cité, 10 rue Alice Domon et Léonie Duquet, 75013 Paris*
[2] *Laboratoire de Photonique et Nanostructures, CNRS, Route de Nozay, 91460 Marcoussis*

I will present our recent research on Gallium Arsenide disk optomechanical resonators confining photons and phonons in a sub-micron interaction volume [1], and reaching an extreme optomechanical coupling of several MHz [2,3]. The understanding of mechanical and optical dissipation in these resonators [4], together with its control to the ultra-low dissipation limit [5], will be exposed. With their strong optomechanical cooperativity, these miniature disks are also compatible with on-chip integration [6] and optoelectronics technologies based on III-V semiconductors. We have taken advantage of these assets to explore the fluidic operation of Gallium Arsenide devices, their close-to-quantum operation, and their interface with Quantum Dots or Quantum Wells for novel polariton-optomechanical scenarios [7].

References

[1] L. Ding et al. Physical Review Letters 105, 263903 (2010).
[2] L. Ding et al. Applied Physics Letters 98, 113108 (2011).
[3] C. Baker et al. arXiv:1403.4269 (2014), to appear in Optics Express.
[4] C. Baker et al. Applied Physics Letters 99, 151117 (2011).
[5] D. Parrain et al. Applied Physics Letters 100, 242105 (2012).
[6] D. T. Nguyen et al. Applied Physics Letters 103, 241112 (2013).
[7] J. Restrepo et al. Physical Review Letters 112, 013601 (2014).

First Observation of Photon-Photon Resonance in Active Multimode Interferometer Laser Diode

Mohammad N. Uddin[1], H. Bingzhou[1], A. Tajima[2], K. Kato[3] and K. Hamamoto[1]

[1] *Interdisciplinary Graduate School of Engineering Sciences, Kyushu University, 6-1, Kasuga-Koen, Kasuga, Fukuoka 816-8580, Japan.*
mohammad.nasir.uddin.656@s.kyushu-u.ac.jp, 5ES13004T@s.kyushu-u.ac.jp, hamamoto@asem.kyushu-u.ac.jp
[2]*Green Platform Research Laboratories, NEC Corporation, kanagawa, Japan.*
a-tajima@bk.jp.nec.com
[3]*Graduate School of Information Science and Electrical Engineering, Kyushu University, Fukuoka, Japan.*
kato@ed.kyushu-u.ac.jp

Abstract: Active multimode interferometer laser diode (MMI-LD) with split pump section have been fabricated to achieve high 3 dB bandwidth. Higher photon density using split pump scheme and high-frequency photon-photon resonance has been exploited to extend the direct modulation bandwidth. The split pump active MMI design allows interaction between the lasing mode and a second mode used as catalyst in the pumping section to achieve PPR peak along with the higher photon density delivered by the MMI pumping section towards the modulation section, which allowed us to reach a more than 15.2 GHz of extended 3 dB bandwidth for the active MMI LD.

Introduction: Due to recent rapid growth of data traffic, direct modulation laser diode has been widely researched especially for short distance application [1]. Some of the promising approaches to enhance the modulation bandwidth are increasing the photon density in the modulation section and exploration of the photon-photon resonance. By utilizing the split pump section in 1.55 μm active multimode interferometer laser diode (active MMI LD), combination of higher photon density and photon-photon resonance (PPR) has been achieved. Significant enhancement of 3 dB bandwidth up to 15.2 GHZ from 2.6 GHz has been confirmed successfully for a directly modulated MMI LD.

Device Concept: Figure 1 shows a schematic view of the actually implemented active multimode interferometer laser diode. Pumping region, separated from modulation region, is consisted of MMI waveguide that enables the emission of larger optical power compared to single stripe waveguide [2]. The MMI, which enables the single-mode optical field at the input to be identically imaged at the MMI output, has a wider area than the single-mode waveguides. The larger active area contributes to the enhancement of the output power. As the existence of multiple mode is necessary condition for the PPR, so the advantage of having multimode section in active MMI LD allows us to design lateral mode locking for exploration of photon-photon resonance (PPR) [3]. The photon density in the modulation region is enhanced significantly from this MMI configuration, which enhances the carrier photon resonance (CPR) [4] peak and eventually helps us to get CPR peak close to the PPR peak to achieve a flat response between them. The designed MMI is connected asymmetrically to single mode high mesa waveguides. For the actually implemented devices, the total length of the cavity was 315 μm. The MMI section width was set to 8 μm. The length of the MMI section was 133 μm and with both edges connected to a 2 μm oppositely off-centered single mode waveguide of 3 μm width. The length of the pumping section was set to be 265 μm and the modulation section was set to be 50 μm. The high mesa asymmetric configuration ensures single wavelength characteristics for the actual implemented device.

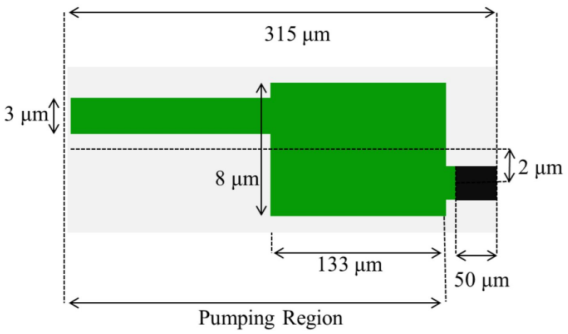


Fig. 1: Schematic view of pumping region split active multimode interferometer laser diode

Results and discussion: Semiconductor lasers carrier photon resonance (CPR) is limited by the relaxation time of the excited electrons. However it is possible to extend the cutoff frequency beyond usual limitations by using a higher order resonance like the PPR, which is related to the roundtrip time of the photons in the laser cavity. A necessary prerequisite for the PPR is the existence of a weak

additional mode used as a catalyst. The second mode has to be placed on the longer wavelength side of the main mode in a distance equal to the desired position of the PPR [5]. To excite a PPR peak at around 11 GHz, the distance of the main mode and the second mode has also to be 11 GHz, corresponding to a wavelength difference of ~ 0.08 nm. The device emits at a wavelength of 1561.95 nm with a side mode suppression ratio (SMSR) of about 35 dB as shown in Fig. 2. Inset picture shows the magnified peak of the emission. Inset picture in Fig. 2 also shows the wavelength difference of the phase locked mode, which is around 0.08 nm. Figure 3 (a) shows the experimental data of small signal response of an asymmetric active MMI LD with photon-photon resonance. A second strong resonance peaks can be seen in the figure, which is due to multiple lateral mode phase locked condition. For having PPR peak the mode locking must be stable over time. So the existence of PPR peak verifies the constant phase difference for long time [6]. Large enhancement in modulation bandwidth of over 15.2 GHz can be experimentally obtained, which corresponds to more than 12.6 GHz improvement compared to 2.6 GHz previously reported for MMI LD [7]. The amplitude of the second resonance can be tuned, depending on the injected pump current, from a relatively strong peak to a relatively flat response (Fig. 3 (a)). With increasing pump current flat response between CPR and PPR can be achieved. This second resonance peak is caused by the interaction of the main mode and a weak additional mode on its long wavelength side. Change of the amplitude of second resonance (PPR) influenced by the pump current is presented in Fig 3 (b). This shows the linear increasing trend of the PPR peak with increasing pump current. This may cause due to the contribution of the increasing coupling of the phase locked weak mode with the increasing pump current. Figure 3 (b) also shows the frequency shift of the PPR peak with increasing pump current. From this figure it is evident that the PPR frequency is not much affected by any variation of pump current. Which is expected for photon-photon resonance peak, if the phase tuning section is not present in laser [8] and experimentally verified.

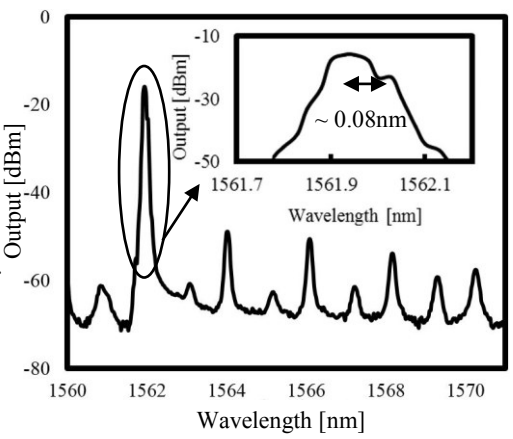


Fig. 2: Optical spectrum

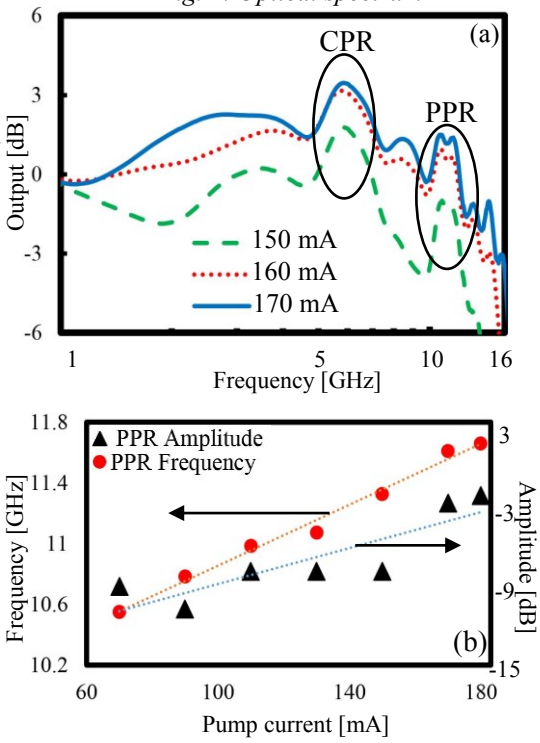


Fig. 3: (a) Small signal frequency response of MMI LD (b) PPR peak amplitude with increasing pumping current and dependency of PPR frequency on pump current

Conclusion: Extended 3dB modulation bandwidth of more than 15.2 GHz has been experimentally verified for the first time in active MMI LD. The Modulation response shows a second resonance peak above the relaxation oscillation frequency with a value that corresponds the lateral mode frequency separation showing an evidence of lateral mode locking.

Acknowledgement: A part of this work was supported by JSPS KAKENHI #C24560047.

References

1. T. Tadokoro, *et al.,OFC/NFOEC*, pp. 1–3 (2011).
2. K. Hamamoto *et al., ECIO'97*, pp. PD 5–1, (1997).
3. A. Laakso, *et al., Opt Quant Electron,* **42**, pp. 785-791, (2011)
4. M. N. Uddin, *et. al., OECC/PS,* paper TuPK-7 (2013).
5. F. Gerschutz *et al., OPTICS EXPRESS*, **16,** pp. 5596-5600, (2008).
6. M. Dumitrescu *et al., OFC/NFOEC,* paper JW2A.33 (2013).
7. K. Hamamoto, *et. al., OFC/NFOEC*, 4, pp. 3 (2005).
8. P. Acedo, *et al., IEEE Photon. Technol. Lett.,* **14**, pp. 1055- 1057, (2002).

Study on Optical Confinement of Small Size VCSEL Using Index Change of QWI

Asako Kikuchi, Tomoyuki Miyamoto

P&I Lab., Tokyo Institute of Technology, Yokohama, Kanagawa, Japan,
asako.kikuchi@ms.pi.titech.ac.jp, tmiyamot@pi.titech.ac.jp

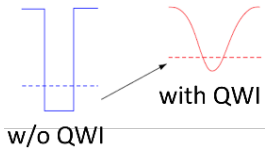
Abstract: We investigated the applicability of quantum well inter-mixing (QWI) for VCSEL to use its low refractive index difference. As the result of numerical simulations, we shows that by combining an oxidation layer and a QWI layer appropriately, an small sized VCSEL is realizable.

1. Introduction Since amount of the information increases with advanced and diversified needs of information, it is necessary to improve the performance of information systems like computers continuously. Metal wirings that transmit the electrical signal have become the bottleneck of the improvement in system performance due to band-limitation, cross-talk, and high power consumption. Therefore, introduction of optical interconnection is required.

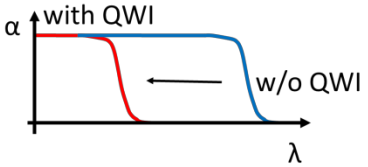
Vertical-cavity surface-emitting laser (VCSEL) which has been used in board-to-board optical-interconnection has advantages of low power consumption and dense array light source. However, it is necessary for VCSEL to become more low power consumption for future applications. To achieve it, 1μm diameter class of active region of VCSEL is needed. VCSEL has used selective oxidation technology for reducing the active region diameter.[1] However the selective oxidation technology has large refractive index difference around the oxidation aperture. It causes the scattering of light and the diffraction, and these influences are increased when the device size is decreased. Therefore, a novel technology which can suppress the light scattering and apply a waveguide effect is necessary for solving the problems.

In this study, we proposed and investigated novel VCSELs that consist of a low refractive index difference structure formed by the quantum well inter-mixing (QWI) technology. We report the numerical analysis results of the improved cavity characteristics of small sized VCSELs.

2. Refractive Index Change by QWI The QWI technology has been used for control the position dependent bandgap energy. The structure is formed by introducing the vacancy or defects around quantum wells and then heating. The interdiffused atoms between well and barrier layer causes change of the bandgap in quantum well.[2] In this study, we use the refractive index change in the QWI which is caused by change of the absorption spectrum shown as Fig. 1. The refractive index change by the QWI has been studied and the change of up to 0.09 was reported.[3, 4] In the following numerical analysis, we assumed that the refractive index change was 0.05.



(a) Bandgap change



(b)Change of absorption spectrum

Fig. 1: Principle of QWI.

3. Numerical Simulation Model of QWI-VCSEL A schematic structure of QWI-VCSEL is shown in Fig. 2. The QWI layers are inserted in the DBR. The QWI is introduced in the outer area of VCSEL mesa and the center area is maintained the original QW. The structure is considered as a waveguide using relatively low index difference. Therefore it can reduce light scattering and light diffraction.

Assumed VCSEL model has the 0.98μm band of GaInAs active layer on the GaAs substrate. Upper and bottom DBRs have 25 and 30 pairs, respectively. As the detail of QWI structure, one pair of three-QW layer which has shorter wavelength than 0.98 μm is inserted near a node of the standing wave in the upper DBR. The total thickness of the one pair of QWI is 35 nm. We inserted one

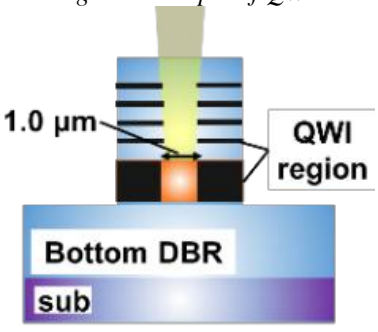


Fig. 2: Analyzed VCSEL model.

selective oxidation layer for the purpose of current confinement. In this study, the target aperture diameter of the QWI and the oxidation area is 1 μm. The cavity loss was analyzed as photon lifetime, from the time decay of the light intensity using the two-dimensional FDTD.

4. Results and Discussions Figure 3 shows the photon lifetime dependence on the number of QWI layer. A oxidation layer is inserted just above the active layer and the QWI layers are inserted above the oxidation layer. The plot on the left y-axis shows a conventional VCSEL structure which has one oxidation layer without QWI layer. In these structures, by decreasing the aperture diameter, photon lifetime decreased due to increase of the scattering and diffraction. In the case of 1 μm aperture, by introducing the QWI layer, photon lifetime was increased to 12.1 ps at 10 QWI layers, that is about three times of the conventional VCSEL. The value is larger than that of the conventional VCSELs with large apertures. It means that low power consumption almost proportional to the aperture size will be expected. On the other hand, it is noted that increased layers of more than 10 caused decrease of the photon lifetime.

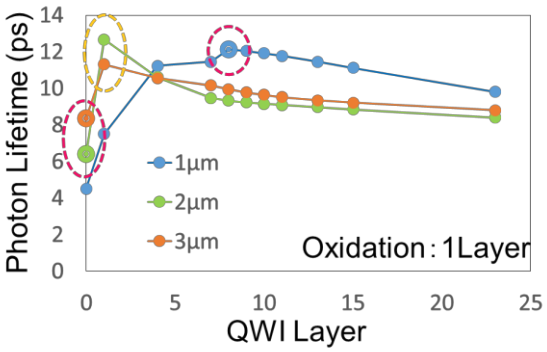


Fig. 3 Photon lifetime dependence on the QWI layer in DBR.

We can consider three effects of the QWI layers. The first one is that the QWI structure suppresses the diffraction loss because it is regarded as a waveguide, and the increase of the number of QWI layers cause increase of the photon lifetime. Secondly, since the QWI layer does not form a completely waveguide, the light is scattered in each layer without QWI. It lead to the reduction of photon lifetime by increasing the number of QWI layers. Thirdly, there is a mode coupling between the oxidation aperture and the QWI aperture. As a result, effect of the first comes out strongly when the number of layers is small, but if the number of layers is large, the effect of secondly comes out strongly. So there are the optimum number of layers. The highest photon lifetime was obtained at a few QWI layer when aperture is 2 and 3 μm. This is because that the beam spot is large and the effect of the light diffraction is small. Therefore scattering effect was increased by increase of the QWI layer.

Figure 4 shows the effect of the coupling loss between the oxidation aperture and the QWI aperture. In this calculation, oxide aperture diameter is fixed at 1 μm. When the QWI aperture is smaller than 1 μm, photon lifetime is reduced. On the other hand, the photon lifetime become highest when the 1.2 μm QWI aperture. It is because that the transverse mode size of the light in the QWI layer has larger spot size due to small index –step in comparison with oxidation layer.

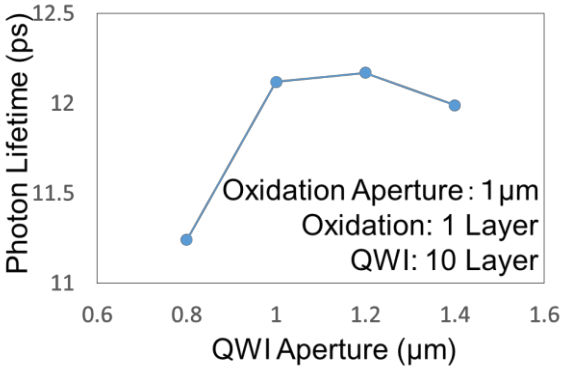


Fig. 4 QWI aperture dependence of photon lifetime.

5. Conclusions We investigated VCSELs which uses the refractive-index change by QWI for optical confinement. By combining an oxidation layer and a QWI layer appropriately, a small size VCSEL with decreased cavity loss is realizable.

References

1. *D. L. Huffaker, D. G. Deppe, K. Kumar, and T. J. Rogers*, *Appl. Phys. Lett.*, **65**, pp. 97-99 (1994).
2. *W. D. Laidig, N. Holonyak, Jr., and M. D. Camras*, *Appl. Phys. Lett.*, **38**, pp. 776-778 (1981).
3. *T. Wolf, C. L. Shieh, R. Englemann, K. Alavi, and J. Mantz*, *Appl. Phys. Lett.*, **55**, pp. 1412-1414 (1989).
4. *T. C. Kleckner, A. S. Helmy, K. Zeaiter, D. C. Hutchings, and J. S. Aitchison*, *IEEE JQE*, **42**, pp. 280-286 (2006).

Passive Mode-Locking and Tilted Waves in Broad-Area Vertical Cavity Surface-Emitting Lasers

M. Marconi[1], J. Javaloyes[2], S. Balle[3], M. Giudici[1]

[1] *Institut Non Linéaire de Nice, Valbonne, France*
[2] *Departament de Fisica, Universitat de les Illes Baleares, E-07122, Palma de Mallorca, Spain.*
[3] *Institut Mediterrani d'Estudis Avançats, E-07190 Esporles, Spain.*

Abstract: We show experimentally that an electrically biased 200 μm multi-transverse mode VCSEL can be passively mode-locked using optical feedback from a distant Resonant Saturable Absorber Mirror. Optical feedback selects a tilted wave propagating along the transverse section of the VCSEL and leading to mode-locking of the external cavity modes. A large portion of the VCSEL transverse section contributes to mode-locked pulse emission with pulses of approximately 1 W peak power and 10 ps width.

Passive Mode-Locking (PML) is arguably one of the most elegant methods to obtain short and intense pulses in the output of a laser. It is achieved by combining two elements, a laser amplifier providing gain, and a saturable absorber (SA) acting as a pulse shortening element. The different dynamical properties of the SA and of the gain can create a window for amplification only around the pulse, thus leading to a pulsed emission [1,2]. While dye and solid-state lasers are generally used to generate the shortest and most intense pulses, semiconductor lasers are interesting for applications because of their compactness, low costs, high repetition rate and high plug-in efficiency. In semiconductor lasers, PML can be achieved by coupling Vertical External Cavity Surface-Emitting Lasers (VECSEL) with a Semiconductor Saturable Absorber Mirror (SESAM) [4]. The external cavity is designed to operate in the fundamental gaussian mode since the presence of higher order transverse modes is usually perceived as detrimental for PML stability. Nevertheless, the possibility of achieving a cooperative effect of transverse modes for which they would contribute to longitudinal mode-locking is very attractive for increasing pulse power.

In this work, we propose a scheme for achieving PML using an electrically biased 200 μm multi-transverse mode VCSEL. This device is mounted in an external cavity configuration closed by a Resonant Saturable Absorber Mirror (RSAM). Instead of using a self-imaging configuration in which the VCSEL transverse profile is mapped onto the RSAM, we form an image of the VCSEL onto the front focal plane of the collimating lens placed before the RSAM (Fig. 1). This has the effect to inject the Fourier Transform (i.e. the far-field) of the VCSEL near-field profile onto the RSAM. In addition the VCSEL profile is (inversely) imaged onto itself after one round-trip. Since VCSEL and RSAM lie on Fourier planes, any plane wave emitted by the VCSEL yields a spot on the RSAM and vice-versa. We therefore induce strong local saturation of the RSAM while gain section experiences low power density, which favors the onset of mode-locked pulses [3].

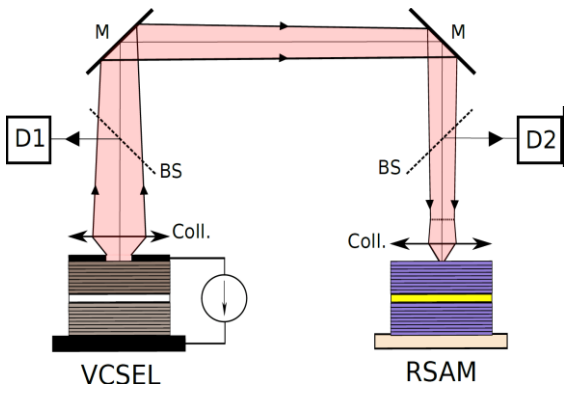


Fig.1: Experimental setup. Temperature stabilized VCSEL and RSAM. Coll : aspheric lens, BS: Beam Splitter, M : Mirror

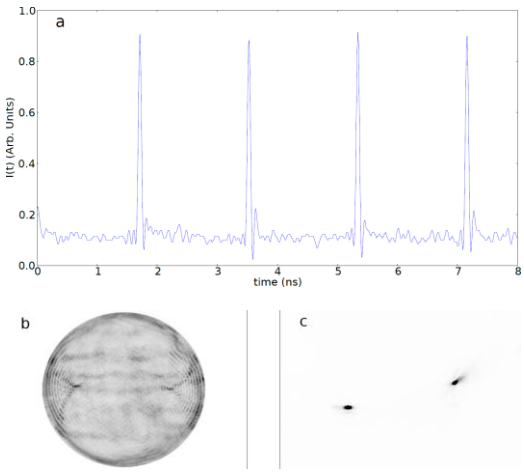


Fig. 2 : a)Total intensity output from the VCSEL in the mode-locking regime, b) near-field profile of the VCSEL, c) far-field profile of the VCSEL

Panel a) in Fig. 2 displays the time trace of the VCSEL in the mode-locking regime which consists of a regular train of pulses with a period equal to the roundtrip time in the external cavity (τ = 1.8 ns) and a pulse width equal to 10 ps FWHM. The time-averaged far-field of the VCSEL exhibits two bright off-axis spots that indicate the presence of two tilted waves travelling in the external cavity. The transverse wave-vector of each of these waves is related in direction and modulus to the position of the spots and their symmetry with respect to the optical axis indicates that the two transverse wave-vectors are one opposite to the other.

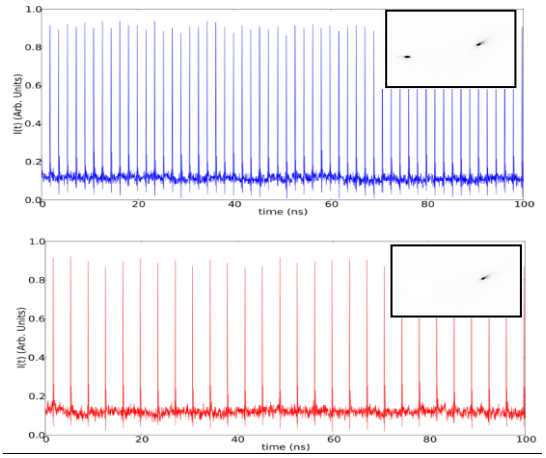


Fig.3 upper panel: Intensity output from the VCSEL obtained when detecting the two spots of the far-field emission (inset) of the VCSEL. Lower panel: Intensity output from the VCSEL obtained when detecting only one spot of the far-field emission (inset) of the VCSEL.

Remarkably, however, no interference pattern is visible in the VCSEL near-field emission. This implies that the transverse waves must not be simultaneously present. This is shown in Fig. 3 where we plot the intensity output from only one of the bright spots in the Far-Field. It consists also of a periodic train of pulses, but the period is now 2τ, thus showing that the two tilted waves are alternating each other after every round-trip.

This mode-locked dynamics doesn't critically depend on the transverse wave-vector selected by the system. Such value can be modified by adjusting the external cavity alignment, namely tilting one of the mirrors M in the setup or slightly displacing the collimator off the axis defined by the center of the VCSEL and the RSAM. On the other hand wave-vector selectivity may also arise from any imperfections on the RSAM/VCSEL mirrors that break the spatial invariance.

References:

- [1] : H. A. Haus**,** Journal of Applied Physics, vol. **46**, pp. 3049–3058, 1975.

- [2] : H. A. Haus, Quantum Electronics, IEEE Journal of, vol. 11, pp. 736–746, 1975.

- [3] : H. A. Haus, IEEE J. Selected Topics Quantum Electron., vol. 6, pp. 1173–1185, 2000.

- [4] : U. Keller and A. Tropper, Physics Reports 429,67-120, 2006

Sub-THz Carrier Frequency Generation Stabilized by Mach-Zehnder Interferometric Phase Detection Scheme

S. Takeuchi[1], **K. Kato**[1], **S. Hisatake**[2], **T. Nagatsuma**[2]

[1] *Kyushu University, Fukuoka, Japan, 2ie13166t@s.kyushu-u.ac.jp*
[2] *Osaka University, Osaka, Japan*

Abstract: We propose a Mach-Zehnder interferometric phase detection for low phase noise sub-terahertz (THz) carrier frequency generation. In this scheme, phase fluctuation between two optical signals can be detected as the interference between their optical sidebands. Experimental result shows that, by controlling the interference to be constant, the phase noise is successfully reduced, which indicates effectiveness of the proposed method.

Introduction: For sub-terahertz (THz) wireless communications, high carrier frequency generation with two different optical frequencies extracted by an arrayed-waveguide grating (AWG) filter from an optical frequency comb (OFC) has attracted a great deal of interest.[1,2] For reducing a phase noise of sub-THz carrier, the difference of optical path lengths between two optical frequencies should be detected and controlled to be constant. One of the approaches for detecting the difference of two optical path lengths is to dither optical path lengths and deduce relative optical phase fluctuations.[1] Recently, we have proposed another approach in which two optical paths configure a Mach-Zehnder interferometer (MZI) and the interference of an additional lightwave is detected as the relative optical phase fluctuation.[3] We demonstrated in this approach that the phase noise could be reduced at a generation of 50 GHz carrier frequency. In this paper, further developing the interferometric phase detection method, we proposed a simple and practical phase detection scheme without any additional lightwave and successfully demonstrated the phase stabilization at the generation of a 300 GHz carrier frequency.

Phase stabilization system: Figure 1 shows the conceptual diagram of the sub-THz wave generation system with our proposed phase detection scheme in which two optical paths are configured as a MZI. The single-mode wave (the optical carrier frequency is f_0) output from a narrow linewidth laser is phase-modulated at the frequency f_{RF} with an electro-optic modulator (EOM1) to generate the OFC. The two optical signals of different frequencies (f_{-n} and f_{+n}) are extracted from the OFC by an AWG filter. Two optical fibers between the AWG filter and the 50:50 optical coupler (OC) are almost equal in their length in order to work as a kind of a MZI. Note that this configuration is not a conventional MZI because optical frequencies going through two optical paths are different and they never interfere with each other by themselves.

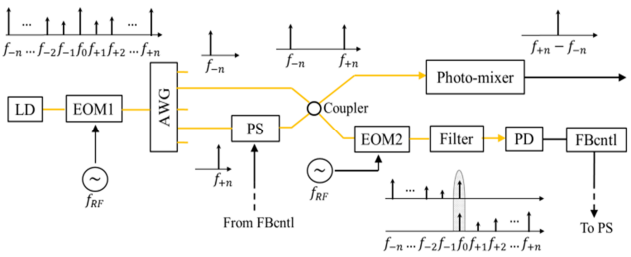


Fig. 1: Mach-Zehnder Interferometric phase stabilization scheme

Assuming f_{-n} is smaller by $n \times f_{RF}$ than f_0 and f_{+n} is larger by $n \times f_{RF}$ than f_0, their waves after the OC (F_{-n} and F_{+n}) could be expressed as follows using the Bessel function J_n:

$$F_{-n}(t) = J_{-n}(m)cos[2\pi f_0 t + (-n)2\pi f_{RF} t] \quad (1)$$

$$F_{+n}(t) = J_{+n}(m)cos[2\pi f_0 t + (+n)2\pi f_{RF} t + \Delta\varphi(t)] \quad (2)$$

where $\Delta\varphi$ is the phase difference between F_{-n} and F_{+n} which originates from the optical path length fluctuations between the AWG filter and the OC, and m is the modulation index which is proportional to the input voltage of EOM1. In our experiment, the voltage was set at such a value that $|J_{-n}|$ and $|J_{+n}|$ get maximum in order to obtain a large signal-to-noise ratio.

One set of optical signals from the optical coupler is input to the photo-mixer which generates the sub-THz beat frequency ($f_{+n} - f_{-n}$). The other set of optical signals is modulated with another

electro-optic modulator (EOM2) at the same voltage and frequency as EOM1. As a result, the two optical signals generate the OFCs with an interval of f_{RF}, in which both the OFCs have the same optical frequencies of f_0. Thus, the optical wave (F_0^*) at the frequency f_0 is expressed as follows by using (1) and (2):

$$F_0^*(t) = J_{+n}(m)J_{-n}(m)\cos 2\pi f_0 t + J_{-n}(m)J_{+n}(m)\cos[2\pi f_0 t + \Delta\varphi(t)]. \quad (3)$$

This equation shows that F_0^* includes the phase fluctuation $\Delta\varphi$ between the two optical paths. Thus, we can detect $\Delta\varphi$ by monitoring the interference of F_0^*. To observe interference of F_0^*, we used an optical band-pass filter with the center frequency of f_0 and a photodiode (PD). As the interference after EOM2, the PD output voltage (V) is expressed as follows:

$$V \propto \sin\Delta\varphi(t). \quad (4)$$

The detected phase fluctuation is fed back to be constant using the phase shifter (PS) through PID controller, so as to stabilize the phase fluctuation of the sub-THz beat frequency.

Results and discussion: The laser output wave of $f_0 = 193.75$ THz was modulated with EOM1 at $f_{RF} = 25$ GHz and the voltage was set at such a value that $|J_{-6}|$ and $|J_{+6}|$ get maximum to generate the OFC. The AWG filter extracted -6th and 6th optical sidebands from the OFC. The photo-mixer generated a 300 GHz beat signal from these optical sidebands. EOM2 modulated the two sidebands at the same frequency as that of EOM1 to generate the optical frequencies of $f_0 = 193.75$ THz. The optical interference at f_0 was extracted by the optical band-pass filter and detected by the PD. The PD output voltage was fed back to the PS which consists of a piezo-electric device, so as to control the voltage to be constant. Figure 2(a) shows the PD output voltage without phase control observed at an oscilloscope. From equation (4), the output voltage fluctuation has a sinusoidal function with the phase fluctuation as a valuable. From this, we estimated that the voltage change of 260 mV corresponds to the phase fluctuation of π. Figure 2(b) shows the PD output voltage with phase control. The output voltage is stabilized so that the fluctuation is within ± 50 mV. This corresponds to phase stabilization with an accuracy of 0.2 π or less. Figure 3 shows the relative phase noise intensity spectra obtained by Fourier transform of the waveforms in Fig. 2(a) and (b). The phase noise in the region below 5 Hz decreases significantly with our phase stabilization system.

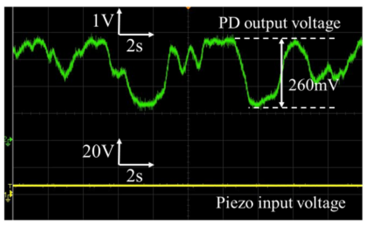


Fig. 2(a): Interfered light power without control

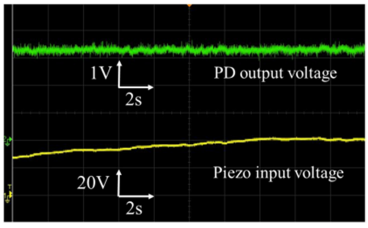


Fig. 2(b): Interfered light power with control

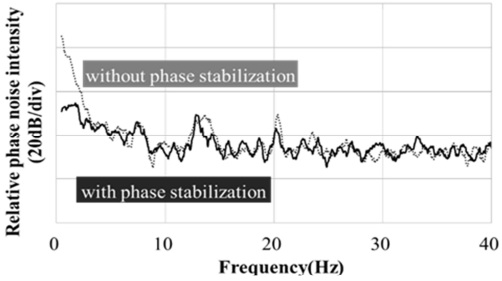


Fig. 3: Relative phase noise intensity spectra

Conclusions: We proposed and demonstrated the MZ interferometric phase detection scheme for low phase noise sub-THz carrier frequency generation. The phase fluctuation between two optical signals can be detected as the interference between their optical sidebands and successfully stabilized by a feedback controller.

Acknowledgement: The authors thank NTT Photonics Laboratories for their experimental support. This work was supported by the Strategic Information and Communications R&D Promotion Programme (SCOPE) 2013, from the Ministry of Internal Affairs and Communications, Japan.

References

1. Y. Yoshimizu *et al, J. Comm. and Networks,* Vol. 15, No. 6, pp. 569-575, (2013).
2. A. Kanno, *et al, Opt. Express,* Vol. 19, No.26, (2011).
3. S.Takeuchi, *et al,* submitted to *IEICE Trans. Electron.*(Japanese Edition).

Towards a high bandwidth waveguide photodetector in an InP membrane on Silicon

L. Shen[1], S.P. Bhat[1], Y. Jiao[1], J.J.G.M. van der Tol[1], G. Roelkens[1,2], M.K. Smit[1]

[1] *Eindhoven University of Technology, Eindhoven, the Netherlands,*
l.shen@tue.nl, s.p.bhat@tue.nl, y.jiao@tue.nl, j.j.g.m.v.d.tol@tue.nl, m.k.smit@tue.nl
[2] *Ghent University - IMEC, Ghent, Belgium,*
gunther.roelkens@intec.UGent.be

Abstract: An InP membrane based waveguide photodetector is designed to reach a 3 dB bandwidth beyond 100 GHz. A uni-traveling-carrier (UTC) configuration is used for minimizing the carrier transit time. A novel double-side process technology is developed to enhance the bandwidth. In addition, a low resistance n-type contact technology is optimized to control the metal spiking into semiconductors.

Introduction and design: InP Membrane on Silicon (IMOS) technology provides a new platform for integration of passive and active photonic devices on top of CMOS chips.[1] These devices are fabricated in an InP-based membrane which is bonded to a silicon wafer by using benzocyclobutene (BCB). Recently, a uni-traveling-carrier photodetector (UTC-PD) in the IMOS platform is being developed for high speed applications. The carrier transport in UTC-PDs is dominated by electrons due to the utilization of a p-type doped absorption layer.[2] The higher velocity of electrons compared to holes results in a higher bandwidth than in conventional PIN-PDs.

The designed structure is shown in Fig. 1. The width of the PD mesa is designed as 3 μm. A 300 nm thick intrinsic InP layer is used both as the passive waveguide and as the electron collector (depleted) in the UTC region. A 150 nm thick p-type doped InGaAs layer is used both as the absorber and the p-contact. This layer is doped with a gradient concentration from 10^{18} cm^{-3} at the collector-absorber interface to 10^{19} cm^{-3} at the contact surface. Optical simulation gives a modal absorption coefficient of 3600 cm^{-1} at 1.55 μm. This high absorption is due to the strong confinement of the optical mode in such a high index contrast membrane. The PD is designed to be 10 μm long, which is sufficient for an absorption efficiency of 97%. The small device area results in a junction capacitance of less than 10 fF.

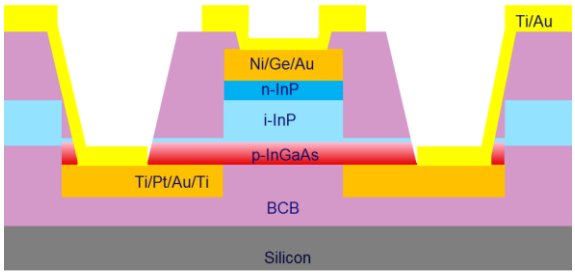


Fig. 1: Cross-section of the UTC-PD.

The carrier transit time of a UTC-PD consists of two components: the electron diffusion time in the p-type InGaAs absorber, and the electron drift time in the depleted InP collector. The first term can be reduced below 1 ps with the doping gradient in the p-type InGaAs layer.[2] In terms of the electron drift time, UTC-PDs can be set with an optimal bias voltage so that electrons travel at the velocity overshoot (above 2×10^{7} cm/s).[2] At this bias, the electron drift time through the 300 nm collector is only 1.5 ps. The bandwidth limited by a total transit time of 2.5 ps is calculated to be 150 GHz.

Double-side process technology: While the transit time and the capacitance are minimized, the high sheet resistance of a thin membrane device remains the major limiting factor for the bandwidth. In order to reduce the series resistance of the p-contact layer, a double-side process scheme (Fig. 2) is used to evaporate the p-metal (Ti/Pt/Au) at the back side of the device before bonding to Si. In this way the spacing between p-metal can be made sufficiently narrow to minimize the series resistance. An optimized spacing of 3 μm (equal to the mesa width) is chosen as a trade-off between the metal loss and the resistance (Fig. 3). At this point, the metal loss (340 cm^{-1}) is very limited compared to the modal absorption (3600 cm^{-1}). The resistance is simulated by considering a conductivity of 9000 S/m and a specific contact resistance of 3×10^{-6} Ω cm^{2} of the InGaAs layer. In case of p-metal on top of the membrane (n-side, same side as the mesa), a practical limit from lithography determines the smallest

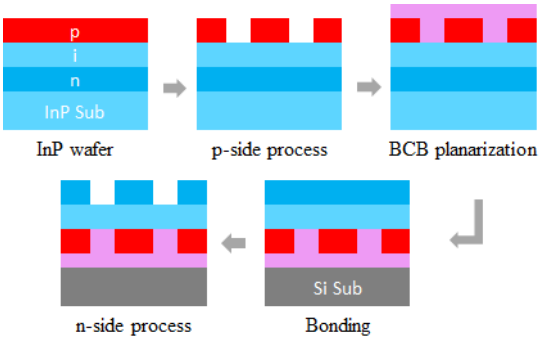


Fig. 2: Overview of double-side process.

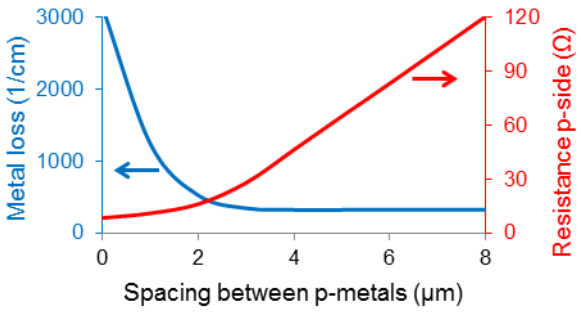


Fig. 3: Trade-off between metal loss and resistance.

spacing to be around 7 μm, which will result in a high resistance of 100 Ω. With a metal spacing of 3 μm which can be made with a p-side process, the resistance can be reduced below 30 Ω.

After processing on the p-side, planarization with BCB is required for the subsequent bonding process. In order to accurately control the BCB thickness and have a good thermal contact, an etch-back is usually performed. However, the etch-back on completely cured (at 280 ºC) BCB creates uniformity issues and affects the bonding. To mitigate this, a new technique involving partial cure at 180 ºC, followed by etch-back and complete cure, is developed. Experiments show good uniformity and reproducibility. The remaining processes are performed from n-side after the bonding.

N-type contact technology: Another contribution to the RC constant limitation comes from the n-type contact on the top of the PD. The specific contact resistance has to be optimized below 1×10^{-6} Ω cm^2 for a total resistance of the PD of less than 50 Ω. In our tests, Ni/Ge/Au based n-type contact shows a low contact resistance of 4×10^{-7} Ω cm^2 after 15 s annealing at 400 ºC. However, Au spiking during high temperature process is a well-known problem of this type of contact. This is critical for thin membrane devices: the Au spiking into the active layers can cause high optical loss and large leakage current. Therefore a new contact technology is developed by controlling the Au addition to the Ni/Ge contact. A circular transfer length method (CTLM) is used to measure the specific contact resistances of samples with different amount of Au participating in the annealing. The samples without Au addition give higher specific contact resistances (above 2×10^{-6} Ω cm^2). This is consistent with previous research showing the contribution of Au to the ohmic behavior.[3] Interestingly, by adding a very small amount of Au (20 nm deposition) the resistance drops to 7×10^{-7} Ω cm^2. As can be seen from Fig. 4a, this limited addition of Au leads to a very sharp and uniform interface between metal and InP. A thickening layer of Ti/Au can be deposited after the annealing without affecting the interface. Compared to the rough interface (over 100 nm Au penetration, Fig. 4b) made by the conventional contact (with 250 nm Au), this new technique provides a way to control the spiking while maintaining a low resistance.

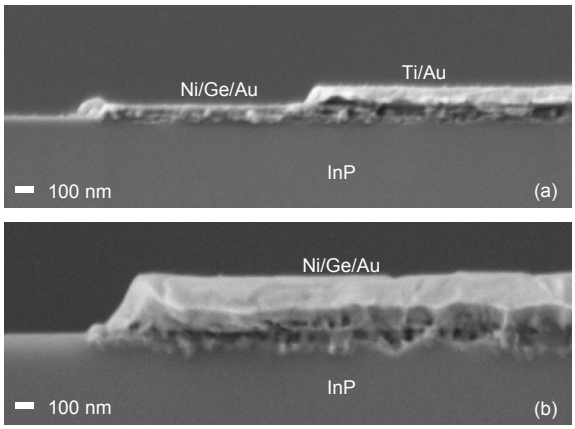


Fig. 4: SEM pictures of cleaved cross-sections.

Conclusion: A high-speed UTC-PD is designed in the IMOS platform. The carrier transit time is minimized below 2.5 ps by using the UTC structure. The strong absorption in the membrane leads to a compact size and a capacitance below 10 fF. A new double-side process technology and an optimized n-type contact scheme are developed to reduce the total resistance below 50 Ω. A 3 dB bandwidth beyond 100 GHz can be reached based on these values. Realization of the device is underway.

References

1. J. van der Tol *et al.*, *IET Optoelectronics* **5**, pp. 218–225, (2011).
2. T. Ishibashi *et al.*, *IEICE Transactions on Electronic* **E83-C**, pp. 938–949, (2000).
3. H. Kawata *et al.*, *Journal of Applied Physics* **75**, pp. 2530–2537, (1994).

(Invited) **Optical Mode Switch for Future Optical Router**

Kiichi Hamamoto

Interdisciplinary Graduate School of Engineering Sciences (I-EggS), Kyushu University
6-1, Kasuga-Koen, Kasuga, Fukuoka 816-8580, Japan
hamamoto@asem.kyushu-u.ac.jp

Abstract: We have proposed novel optical mode switch, which overcomes matrix size limitation issue that has been a general issue for waveguide optical space switch, because of its simple fiber coupling configuration. In addition, it contributes to loss-less mux/demux function like wavelength-multiplexing with power-less mode-conversion unlike wavelength-conversion.

Introduction: Due to the recent data traffic increase with high power consumption, optical router has been researched intensively [1] as it avoids energy-exchanges between optical signal and electric one that is one of the main cause of the high power consumption. Optical switch is one of the key devices to realize such that optical router. Among them, waveguide optical switch is attractive because of the potential of high-speed operation and low power consumption [2-3], however, there has been a limitation in the switch matrix size. One of the reason that limits the matrix size of the optical space switch is that it is required to connect to fiber-array, that arises the necessity of S-bending region integration to open up the input and output ports to a certain (typically 125mm) adjacent spacing of the fiber-array even if the main switch matrix configuration itself can be shrunk by using latest advanced waveguide technologies including Si-photonics and others. To overcome this issue, we have proposed novel optical mode switch [4-5]. It overcomes matrix size limitation issue because it requires only single fiber (in this case, few mode fiber or multi-core fiber) connection at the both input and output port. In addition, it contributes to loss-less mux/demux function like wavelength-multiplexing with power-less mode-conversion unlike wavelength-conversion. In this paper, we explain the concept, the principle, and the scalability will be discussed.

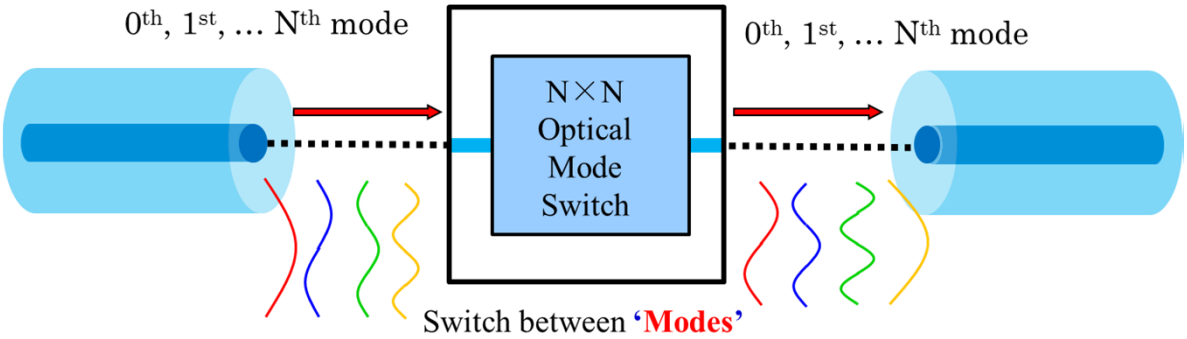


Fig.1: Schematic configuration of optical mode switch module.

Concept: The waveguide-based optical space switch has always a matrix size limitation issue mainly due to S-bend region, needed for fiber array connection, that prevents large scale integration. The optical mode switch solves this issue. Instead of switching port information, it switches "optical mode". As each optical mode is orthogonal in principle, the input and the output ports can be summarized into single space ports, respectively, as is shown in Fig. 1. S-bend region is no more required that results in downsizing or higher integration. Moreover, the optical mode switch also offers a merit of low power consumption. The optical mode exchange itself does not need energy unlike wavelength, while the optical mode also realizes loss-less mux/demux like wavelength. The remaining issue was to prove the principle of the optical mode switch.

Device principle: Typical optical mode switch for two modes has two symmetric Y-junction waveguides as 3dB splitter and coupler. It also has a phase shifter region. At the phase shifter region, the refractive index is variable and can be controlled by injecting current. The width of the input and the output ports are set to be twice compared to branch waveguides. When 0th mode is injected in the input port, it is going to split into two 0th modes with same phase at the 3dB splitter. While when 1st mode is injected, it is split into two 0th modes with phase π difference each other.

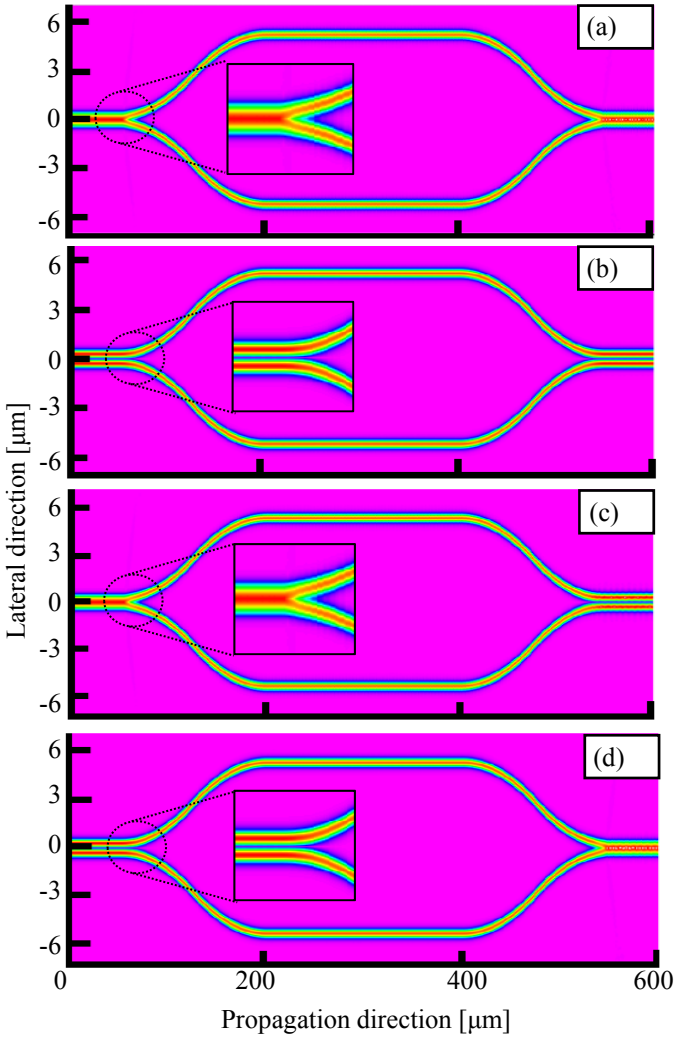


Fig.2: Simulated results of optical mode switch.

To realize such that four modes switching, it is consisted from the following five regions as is shown in Fig. 3; Region 1: 3dB divider up to 3rd order. The divided light propagates as up to 1st order mode in each arm. One arm is consisted of π phase shifter (section A) for 1st mode. Region 2: 3dB divider up to 1st order mode. The divided light propagates as fundamental mode. The center arm is shared with two 3dB couplers. Region 3: π phase shifter (section D, E and F). Region 4: 3dB coupler up to 1st order mode. One arm of one coupler is consisted of π phase shifter (section C) for 1st mode. Region 5: 3dB coupler up to 3rd order. As is shown here, only 6 phase shifters are needed in this configuration.

Figure 2 shows the beam propagation method (BPM) simulation results of the optical mode switch between 0th and 1st modes. When the phase shifter is OFF state (Fig. 2 (a), (b)), the modes propagate and then couple at the mode coupler into the same modes as the injected modes. When a certain current is injected into the phase shift region and the phase shifter is ON state (Fig. 2 (c), (d)), the phase of the one split 0th mode is shifted with π. Thus, these are coupled as 1st mode at the end. While the injected 1st mode is converted into the two 0th modes in the same phase, and then couple as the 0th mode. Thus, this structure realizes the switching between 0th mode and 1st mode.

Scalability: Figure 3 shows a schematic of the optical mode switch for four modes. The device switches one mode to another mode each other like space cross-bar switch among 0th, 1st, 2nd, and 3rd modes. In case "space port information" is replaced to "mode information", this switch configuration corresponds to 4 × 4 matrix space switch. As it requires to be connected with single fiber (few mode fibers or multi-core fibers instead of array fiber) at the input and the output ports, the size of it can be shrunk down within 0.033mm^2 that corresponds to approximately 10 times less than conventional 4 × 4 matrix switch due no need of S-bend fiber connecting region.

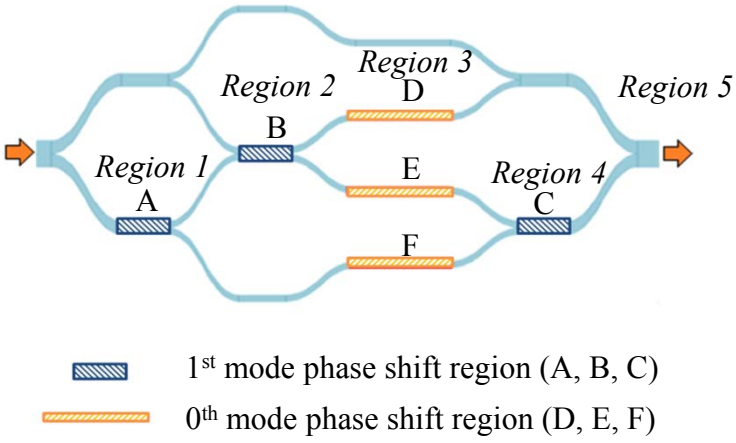


Fig.3: Schematic configuration of four mode optical mode switch.

Summary: We have proposed optical mode switch to overcome matrix size issue in addition to low power consumption. This work has been supported by NICT, Japan.

References

1. R Urata, *et al.*, Proc. ECOC, **6.3.1**, 2009
2. J. V. Campenhout, *et al.*, Opt. Express, **17** (26), pp. 24020–24029, 2007
3. P. Dong, *et al.*, Tech. Dig. OFC., **OWZ4**, 2011
4. M. Jizodo, *et al.*, Tech. Dig. OECC/PS, **TuPT-1**, 2013
5. R. Takakura, *et al.*, Tech. Dig. MOC, **H1**, pp. 56-57, 2013

High Performance Electro-Optic Polarization Conversion Type Modulator for Short-Wavelength Light Using Periodically Poled MgO:$LiNbO_3$

T. Inoue, T. Suhara

Osaka University, Suita, Osaka, Japan,
tinoue@ioe.eei.eng.osaka-u.ac.jp

Abstract: We fabricated an EO polarization conversion type modulator for short-wavelength light using periodically poled MgO:$LiNbO_3$ and evaluated the characteristics by using an external grating complex resonator laser. The maximum conversion efficiency 91% was obtained. The wavelength selectivity of the modulator was in good agreement with the calculated value.

Introduction: Ferroelectric $LiNbO_3$ (LN) crystal has large nonlinear-optic (NLO) and electro-optic (EO) coefficients. Periodically poled LN (PPLN) has been applied to NLO quasi-phase-matched wavelength conversion devices and EO devices.[1–6] One of the EO devices is a polarization conversion type modulator, and the intensity modulation of the near-infrared light has been demonstrated.[3–5] Recently, we reported the polarization conversion type modulator for short-wavelength light using periodically poled MgO:LN (PPMgLN).[6] PPMgLN has not only excellent EO properties but also higher resistance to photorefractive damage than non-doped LN. Therefore it is suitable for the modulation of high power and short-wavelength light. Since this modulator has narrow wavelength-bandwidth, wavelength selective modulation and multi-channel modulation for optical communication and signal processing can be realized by cascading a number of modulators with slightly different grating periods. In this paper, we report fabrication of a compact EO polarization conversion type modulator using PPMgLN and evaluation of the modulation characteristics by using an external grating complex resonator GaN laser.

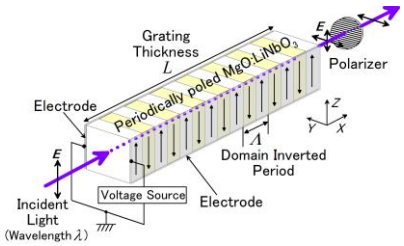


Fig. 1: EO polarization conversion type modulator using PPMgLN.

Operation Principle: A schematic illustration of EO polarization conversion type modulator using PPMgLN is shown in Fig. 1. When an electric field parallel to Y axis is applied to MgO:LN, the optical principal axes of the index ellipsoid rotate and non-diagonal components of the dielectric tensor are generated through the EO effect. When the appropriate field is applied to PPMgLN with the period to satisfy the phase matching condition between the ordinary and extraordinary polarized lights, the polarization conversion takes place. The grating period required to satisfy the phase matching condition is given by $\Lambda = \lambda/(n_o - n_e)$, where λ is the wavelength, n_o and n_e are the ordinary and extraordinary refractive indices. From the coupled-mode equations, the conversion efficiency under the phase matching condition can be written as

$$\eta = \sin^2 [2Lr_{51}(n_e^3 n_o^3)^{1/2} E/\lambda], \quad (1)$$

where L is the grating thickness, r_{51} is the EO coefficient and E is an applied electric field parallel to Y axis. To modulate the violet light with λ = 407 nm (n_e = 2.31, n_o = 2.42),[7] we determined the grating period Λ = 3.6 μm. For the grating thickness L = 1.0 mm and r_{51} = 28 pm/V,[8] the applied field required for η = 100% was estimated as $E_{\eta\max}$ = 0.86 kV/mm.

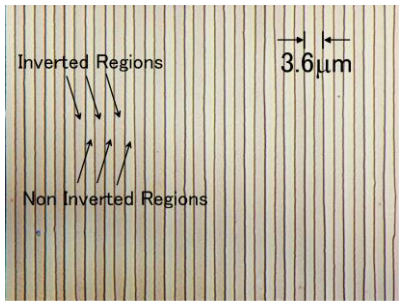


Fig. 2: Fabricated domain-inverted structures after etching.

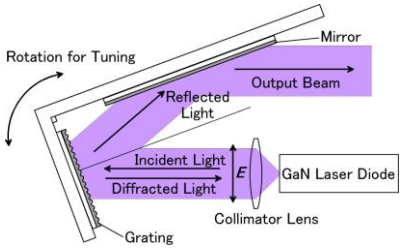


Fig. 3: Complex resonator laser using external grating.

Fabrication: We fabricated domain-inverted structures with 3.6

μm period by applying voltage in 0.2 mm[t] Z-cut MgO (5 mol%) : LN.[6, 9] Figure 2 shows the micro-photograph of the fabricated structures after etching. High-quality domain-inverted gratings were obtained over 1.0 × 1.0 mm^2 area. Fabricated PPMgLN was annealed at 600°C for 15 hours in the O_2 atmosphere to reduce the relaxation phenomena during the modulation.[2] The ±X and ±Y faces were polished, and Al electrodes for the modulation were deposited on the ±Y faces. The size of the crystal was 2.3 mm (Y direction) × 5 mm (X direction). The required applied voltage for $\eta = 100\%$ was estimated as 2.0 kV.

Evaluation of modulation characteristics: The spectrum width of an ordinary Fabry-Perot GaN laser is broad due to multi-mode lasing. Therefore it is difficult to obtain high conversion efficiency in the modulator which has narrow wavelength bandwidth (< 1nm). We constructed a complex resonator laser using an external grating as shown in Fig. 3. The beam from the GaN laser diode was collimated by a lens and incident to the grating of 3600 lines/mm (Littrow mounting configuration). As shown in Fig. 4, the spectrum width (FWHM) of the complex resonator laser was < 0.04 nm, which was much narrower than that of the laser without the grating. Also, the wavelength tuning over a range of ~1.5 nm was obtained by changing the angle of the grating.

We evaluated the characteristics of the fabricated modulator. The beam of the complex resonator laser ($\lambda = 407$ nm) was incident as the ordinary or extraordinary polarized light in PPMgLN. The voltage was applied to the modulator, and the vertical and horizontal polarization components of the output light were measured using a polarizer and a photodiode. The measured dependence of the horizontally and vertically polarized light powers upon the applied voltage is shown in Fig. 5. In Fig. 5(a), the vertically (horizontally) polarized light power was maximum (minimum) at 2.6 kV, and the maximum conversion efficiency 89% (= max converted light power / total light power) was obtained. In Fig. 5(b), the horizontally (vertically) polarized light power was maximum (minimum) at 2.6 kV, and the maximum efficiency 91% was obtained. Next, the wavelength selectivity of the modulator was measured. Figure 6 shows the dependence of the conversion efficiency upon the incident light wavelength. The FWHM of the experimental result was 0.7 nm, which was in good agreement with the calculated value 0.6 nm. This result means that fabricated domain-inverted structures has good uniformity.

Conclusions: We fabricated the EO polarization conversion type modulator using PPMgLN and evaluated the modulation characteristics. The maximum conversion efficiency as high as 91% was obtained. The wavelength selectivity of the modulator was in good agreement with the calculated value.

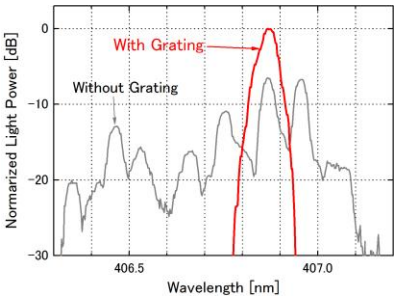
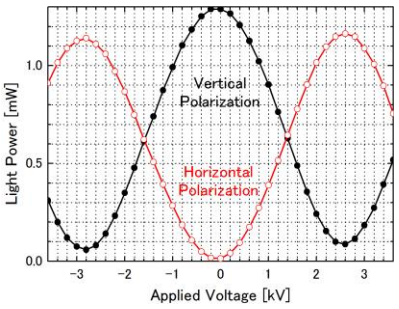
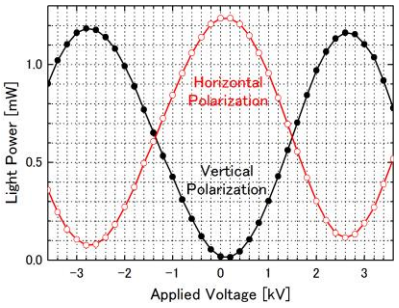


Fig. 4: Comparison of oscillation spectra. (Resolution: 0.04nm)



(a) Input: Vertical polarization



(b) Input: Horizontal polarization

Fig. 5: Dependence of powers of polarization components upon applied voltage.

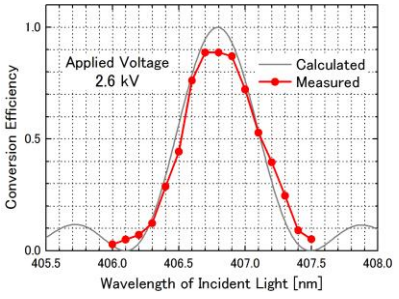


Fig. 6: Dependence of conversion efficiency upon wavelength. (Input: Vertically polarized light)

References

1. T. Suhara and M. Fujimura, *Waveguide Nonlinear-Optic Devices* (Springer-Verlag, Berlin, 2003).
2. T. Inoue and T. Suhara, *IEEE Photon. Technol. Lett.* **23**, pp. 1252–1254 (2011).
3. Y. Lu *et al.*, *Appl. Phys. Lett.* **77**, pp. 3719–3721 (2000).
4. X. Chen *et al.*, *Opt. Lett.* **28**, pp. 2115–2117 (2003).
5. L. Shi *et al.*, *J. Appl. Phys.* **112**, 073103 (2012).
6. T. Inoue and T. Suhara, *The 18th Microoptics Conference*, G–6, Tokyo (2013).
7. D. E. Zelmon *et al.*, *J. Opt. Soc. Am. B* **14**, pp. 3319–3322 (1997).
8. E. H. Turner, *Appl. Phys. Lett.* **8**, pp.303–304 (1966).
9. N. Horikawa *et al.*, *Jpn. J. Appl. Phys.* **46**, pp.5178–5180 (2007).

Dilated 2x2 Hybrid MZI-SOA Switch Circuit Routing 100Gb/s DWDM Data

Q. Cheng, A. Wonfor, J. L. Wei, R. V. Penty, I. H. White

Centre for Photonic Systems, University of Cambridge, Cambridge, CB3 0FA, United Kingdom
qc223@cam.ac.uk

Abstract: This paper presents a dilated 2×2 hybrid MZI-SOA switch circuit routing 10 wavelengths of 10Gb/s/channel DWDM data. MZI switches using a dilated approach provide low loss high speed routing with short SOAs integrated primarily to enhance extinction. Better than -38dB signal to crosstalk ratio has been achieved for each of the ten channels. An input power dynamic range of greater than 10dB is observed for penalties of less than 0.5 dB at the aggregate 100 Gb/s /port data rate.

An optical switch fabric is regarded as a potential key component for future optical interconnects and access networks to meet the substantial and increasing demand for communications bandwidth[1]. Packet switches with nanosecond reconfiguration times are of particular interest and therefore semiconductor optical amplifier (SOA) and Mach-Zehnder interferometer (MZI) based switches have received much attention. However, the ultimate port count of SOA switches is restricted by the accumulation of noise and distortion[2]; while the scalability of MZI switches is limited by the poor crosstalk performance and high insertion loss[3].

We therefore have proposed a novel MZI-SOA hybrid approach, using dilated MZI switches to route signals and using short SOAs in between to enhance extinction and compensate MZI losses with reduced amplified spontaneous emission (ASE) noise[4]. A schematic of the operating principle of the hybrid design is shown in Fig. 1(a). Using this approach, a monolithically integrated 2×2 MZI-SOA hybrid switch module has been fabricated, as shown in Fig. 1(b). The routing performance of a single wavelength has been reported with up to -40dB extinction/crosstalk ratio, 3ns switching times, and almost penalty-free operation[5]. In this paper, we demonstrate the first 10×10Gb/s dense wavelength-division multiplexed (DWDM) routing using the monolithic 2×2 hybrid switch. Crosstalk performance for all the ten channels is assessed and penalties are measured.

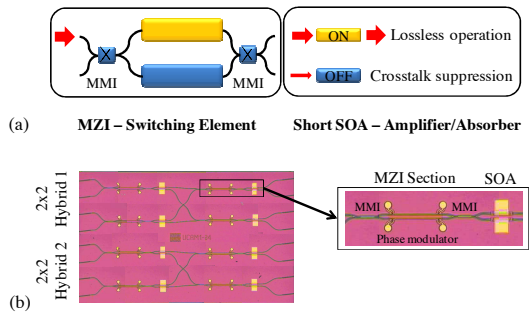


Fig. 1: (a) Schematic of operating principle. (b) Photograph of the fabricated hybrid switch.

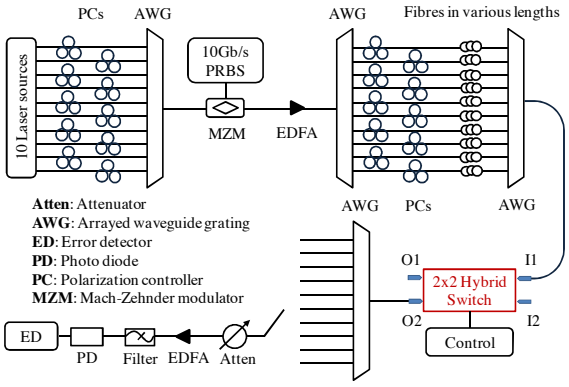


Fig. 2: Schematic of the experimental test-bed.

The switch device was designed and fabricated on a multi-project wafer using a generic foundry process within the EU FP7 PARADIGM project[6]. The chip comprises two dilated 2×2 hybrid switches and each is 2mm × 6mm in size. The 2x2 switch comprises four MZIs each output of which being followed by a 170μm long SOA gate. An MZI structure comprises two MMI couplers, two 800μm long phase modulators and input/output passive waveguides. The SOAs act to provide gain in the ON state but also provide significant crosstalk suppression in the OFF state.

A schematic of the experimental test-bed is shown in Fig. 2, where an array of 10 tunable lasers is operated at wavelengths from 1547.7 nm to 1554.9 nm with 100GHz spacing. The ten channels are combined by an arrayed waveguide grating (AWG) and a 2^{31}-1 pattern length 10Gb/s pseudorandom

bit sequence (PRBS) is imposed by a Mach-Zehnder modulator. The fibers carrying the different wavelengths between the two additional AWGs differ in length so as to decorrelate the channels. This produces 100Gb/s aggregate DWDM data. Lensed fibers are used to couple light in and out of the chip. The switch is mounted on a thermoelectric cooler and operated at 20°C.

The DWDM crosstalk performance is first assessed by comparing the power at both output arms of the switch as a function of wavelength. The device configuration state (bar or cross state) can be switched by tuning the biasing conditions of the SOAs (0mA to 14mA) and phase modulators (-0.5V to -6.5V). It can be seen from Fig. 3 that the crosstalk ratio of the ten wavelengths lies between -38dB to -40dB and up to 42dB signal to noise ratio in a 0.1 nm bandwidth is achieved. The crosstalk of the dilated MZI structure is around 20dB and the short SOAs provide 18dB extinction enhancement. The measurement is performed with an aggregate optical input power of 8dBm (-2dBm per channel on average). Higher input power leads to a reduced crosstalk performance due to SOA power saturation.

By placing an AWG at the switch output, the routing performance of each sub-wavelength can be evaluated separately, by connecting to an optically pre-amplified and filtered receiver and error detector. Fig. 4 shows the switch power penalty at a BER of 10^{-9} as a function of on-chip input power per wavelength for both single and 10 wavelength with the switch operating in the cross state. It can be seen that the single wavelength input power dynamic range (IPDR) exceeds 26dB for a power penalty less than 0.5dB. The multi-wavelength operation however sees a more restricted operating regime owing to the increased aggregate optical power. The IPDR curve of channel 4 (1550.1 nm) shown in Fig. 4, which represents an average performance in the 10 channels, has a dynamic range of more than 10dB. The worst case is channel 8 (1553.3 nm) but still achieves penalties less than 0.3 dB with a dynamic range of 8dB. When routing 100Gb/s DWDM data, the switch device only consumes 0.3pJ/bit energy. The excellent performance and reduced power consumption are attributed to the use of short SOAs.

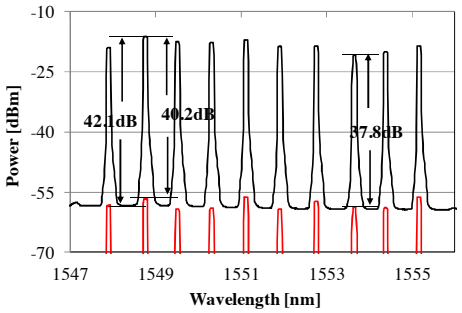


Fig. 3: Crosstalk measurement of 10 channels (the upper black curves represent the routed signal, while the lower red show the crosstalk signal).

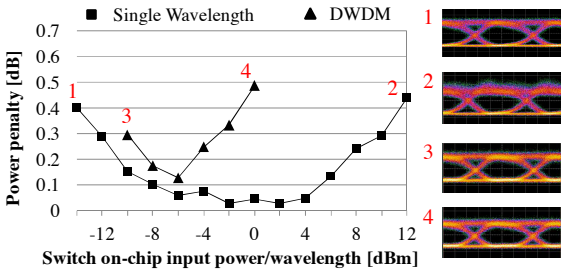


Fig. 4: IPDR curves for both single wavelength and DWDM operation eye diagrams shown for the numbered operating points.

In conclusion, better than -38dB crosstalk ratio and large IPDR (in excess of 10dB for less than 0.5dB penalty) has been reported for a monolithic 2×2 hybrid MZI-SOA switch routing 100Gb/s DWDM data. The excellent performance demonstrates this to be a promising approach for large-scale high-bandwidth monolithic circuit design.

The research leading to these results has received funding from the UK EPSRC through the INTERNET, STAR and COPOS II grants and the European Commission under FP7 grant agreement ICT 257210 PARADIGM. We would also like to acknowledge the Greentouch consortium.

References

1. R. Tucker, *IEEE J. Sel. Topics Quantum Electron.*, **2**, pp. 261- 274, (2011).
2. A. Wonfor, *et.al*, *IEEE J. Opt. Commun. Netw.*, **8**, pp. A32-A39, (2011).
3. D. H. P. Maat, *et.al*, *IEEE Photon. Technol. Lett.*, **3**, pp. 284-286, (2000).
4. Q. Cheng, *et.al*, *J. Lightw. Technol.*, **18**, pp. 3077- 3084, (2013).
5. Q. Cheng, *et.al*, *in Optical Fiber Communication Conference*, paper W4C.6, (2014)
6. M. Smit, *et.al*, *in Optical Fiber Communication Conference*, paper OM3E.3, (2012).

High-Contrast Grating Spatial Mode Filter for Widely Tunable Vertical Surface Emitting Laser

S. Inoue[1], F. Koyama[1]

[1] *Photonics Integration System Research Center, Tokyo Institute of Technology, shunya.inoue@ms.pi.titech.ac.jp*

Abstract: We present the highly angular dependent High-Contrast Grating (HCG) mirror functioning as a spatial mode filter for widely tunable single-mode VCSELs. The incident angular dependence of GaAlAs/air HCG mirror was calculated for TE mode light using Rigorous Coupled-wave Analysis (RCWA). We are able to use the angular dependence of HCG for the transverse-mode control of widely tunable VCSELs by filtering out high-order transverse-modes. The modeling results show HCG offers the spatial mode filtering for a wide wavelength range over 60 nm at 980 nm band. This result may lead to widely tunable single transverse mode VCSELs with high-output power.

Vertical Cavity Surface Emitting Lasers (VCSELs) are key devices for optical communications and optical sensors. They offer low threshold operations and hence low power consumptions with help of their small active region. However their single-mode output power is limited by their large thermal resistance caused by the small cavity volume. Expanding active region enables us to improve manufacturing tolerance and to increase single-mode output power. A key challenge is how to control the transverse mode for single-mode operations. There have been various reports on the transverse-mode control, which include surface relief structures, metal apertures, multi-oxide layers and so on[1-3]. Their basic common idea is to use spatial mode filtering with adding excess losses for high-order modes. We proposed and demonstrated the engineered angular dependence[4] of high contrast grating (HCG)[5, 6] for the transverse-mode control of VCSELs[7, 8]. On the other hand, widely tunable VCSELs are attracting much attention for use in Optical Coherent Tomography (OCT). There is a strong demand to boost the single-mode output power over a few tens mW.

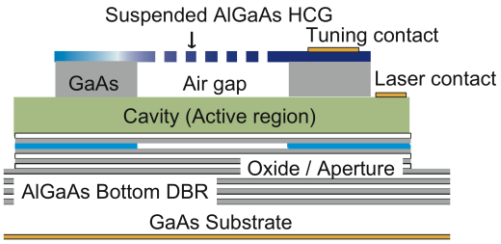


Fig.1 Device structure of the HCG MEMS VCSEL

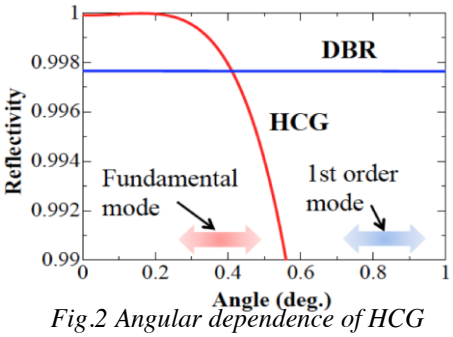


Fig.2 Angular dependence of HCG and DBR mirror

In this paper, we present the modeling of highly angular dependent HCG functioning as a spatial mode filter in broad wavelength range. The result shows a possibility of widely tunable single-mode VCSELs with high output power.

Figure 1 shows the schematic structure of a tunable VCSEL with a membrane HCG mirror. The basic idea for the transverse mode control of HCG VCSELs is illustrated in Fig. 2. The transverse spatial frequency and propagation angle of each transverse mode are different. A fundamental mode has the smallest propagation angle and high-order modes show larger angles. Thus we are able to select only a fundamental mode using the highly angular dependent reflectivity of HCG. This advantage is to avoid all the higher-order modes. This would come from the spatial frequency filtering thanks to the highly angular dependence.

We calculated the reflectivity of HCG using the RCWA method. The high-index material of HCG is $Al_{0.65}Ga_{0.35}As$ and surrounded by air. The grating parameters are grating

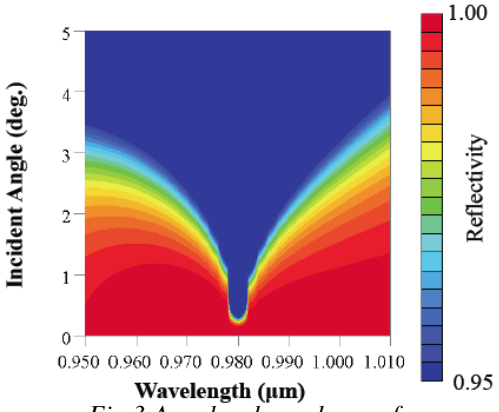


Fig.3 Angular dependence of reflectivity versus wavelength

thickness, period and duty cycle. Figure 3 shows the incident angle dependence of reflectivity versus wavelength. We see the large angular dependence, but it is dependent on the operating wavelength. We carried out the optimization of grating parameters for a wide wavelength range. We define a single-transverse mode condition when the difference in reflectivity between the fundamental transverse mode and the 1st order mode is >0.5%. We found the grating thickness is an important parameter for expanding a wavelength region. By calculating the propagation angle and reflectivity at incident angle, we obtain the maximum active region size for single transverse mode operation as shown in Fig. 4(a). Additionally, a high reflectivity is needed for low threshold operations. Figure 4(b) shows the reflectivity mapping for the normal incidence as function of wavelength. From these results, we show the maximum active region size that meets >99% of reflectivity as shown in Fig. 4(c). The orange and red areas in Fig. 4(c) indicate the capability of single-mode active region size of >20μm. The result indicates a wide wavelength range of over 60nm for single-transverse-mode operations.

In conclusion, we present the engineered angular dependence of HCG for widely tunable single-mode VCSELs. The high angular dependence of HCG enables us to expand an active region of over 20 μm, which is several times larger than that of conventional single-mode VCSELs. We expect a high single-mode output power of a few tens mW and wide wavelength tunability at the same time. This could make great contributions for bio-medical applications of VCSELs such as OCT.

Acknowledgement: This work was supported by Grant-in-Aid for Scientific Research from the Ministry of Education, Science, Sport and Culture.

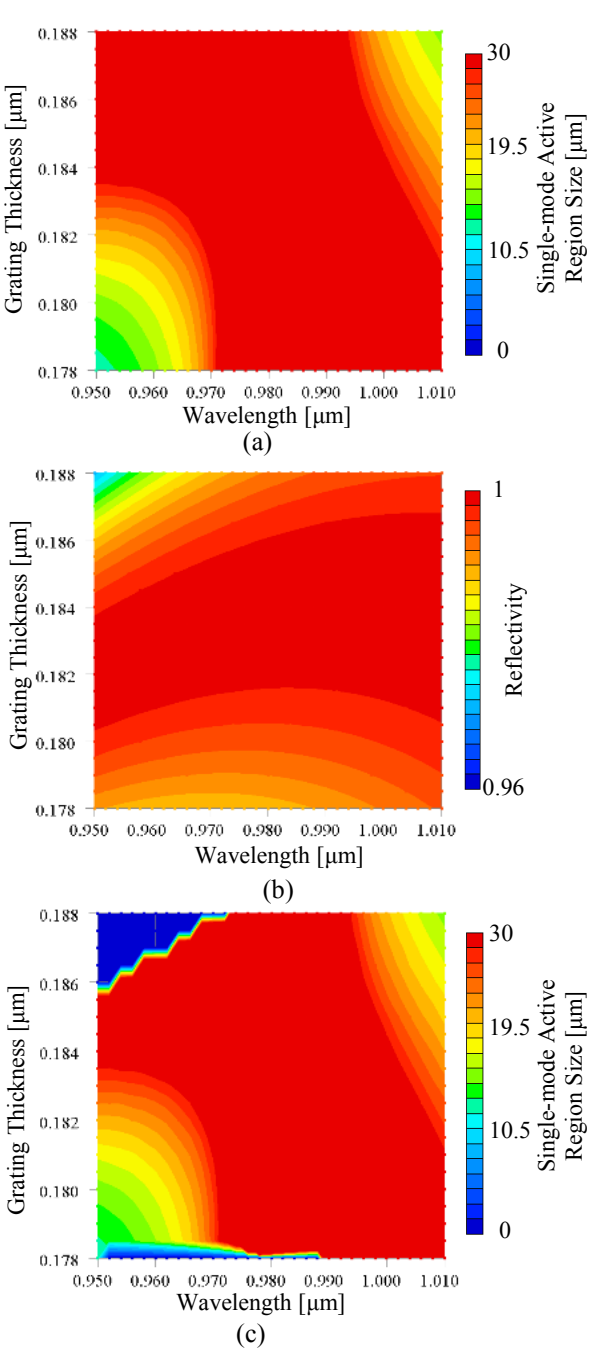


Fig.4: (a)Single-mode active region size (b)Reflectivity to normal incidence (c)Single-mode active region size that meets high reflectivity to normal incidence

References

1. H. J. Unold, M. Grabherr, F. Eberhard, F. Mederer, R. Jäger, M. Riedl and K. J. Ebeling, Electron. Lett., vol. 35, pp. 1340-1341, 1999.
2. R. A. Morgan, G. D. Guth, M. W. Focht, M. T. Asom, K. Kojima, L. E. Rogers and S. E. Cails, IEEE Photon. Technol. Lett., vol. 4, pp. 374-377, 1998.
3. N. Nishiyama, M. Arai, S. Shinada, K. Suzuki, F. Koyama and K. Iga, IEEE Photon. Technol. Lett. Vol.12, No 6 pp.606-608, 2000.
4. A. Imamura, W. Yang, J. Ferrara, Y. Hasidume, X. Gu, F. Koyama and C. J. Chang-Hasnain, 16th OECC, Kaohsiung, 2011.
5. C.F.R Mateus; M.C.Y Hunang; Yunfei Deng; A.R. Neureuther; C.J. Chang-Hansnain; IEEE Photon. Technol. Lett., vol.16, no.2, pp.518-520, 2004.
6. C. Chase, Y. Rao, W. Hofmann, C.J. Chang-Hasnain, Optics Express, vol.18, 15468 2010.
7. J. Kashino, A. Imamura and F. Koyama, 17th Microoptics Conference (MOC'11), H-24, 2011
8. J. Kashino, S. Inoue, A. Matsutani, H. Ohtsuki, T. Miyashita, F. Koyama, IEEE Photonics Conference 2013, TuE2.2, pp. 244-245, 2013.

Quantum simulation with integrated photonics

Fabio Sciarrino

Dipartimento di Fisica, Sapienza Università di Roma,
Piazzale Aldo Moro, 5, I-00185 Roma, Italy
http://quantumoptics.phys.uniroma1.it
www.3dquest.eu

Integrated photonic circuits have a strong potential to perform quantum information processing [1, 2]. Indeed, the ability to manipulate quantums states of light by integrated devices may open new perspectives both for fundamental tests of quantum mechanics and for novel technological applications [3,4]. Within this framework we have developed a directional coupler, fabricated by femtosecond laser waveguide writing, acting as an integrated beam splitter able to support polarization-encoded qubits [5]. As following step we addressed the implementation of quantum walk. This represents one of the most promising resources for the simulation of physical quantum systems, and has also emerged as an alternative to the standard circuit model for quantum computing. Up to now the experimental implementations have been restricted to single particle quantum walk, while very recently the quantum walks of two identical photons have been reported. For the first time, we investigated how the particle statistics, either bosonic or fermionic, influences a two-particle discrete quantum walk [6]. Such experiment has been realized by adopting two-photon entangled states and integrated photonic circuits. As following step we have exploited this technology to simulate the evolution for disordered quantum systems observing how the particle statistics influences Anderson localization. Finally we will discuss the perspectives of optical quantum simulation: the implementation of the boson sampling to demonstrate the computational capability of quantum systems [7] and the development of integrated architecture with three-dimensional geometries [8,9].

References

[1] T. D. Ladd, et al, "Quantum computers", *Nature* **464**, 45–53 (2010).

[2] J. L. O'Brien, A. Furusawa, and J. Vuckovic, "Photonic quantum technologies", *Nature Photonics* **3**, 687 (2009).

[3] P. Kok, et al, "Linear optical quantum computing with photonic qubits", *Rev. Mod. Phys.* **79**, 135 (2007).

[4] A. Politi, J. Matthews, M. Thompson, and J.O'Brien, "Integrated quantum photonics", *Selected Topics in Quantum Electronics, IEEE Journal of QE* **1673**, 15 (2009).

[5] L. Sansoni, F. Sciarrino, G. Vallone, P. Mataloni, A. Crespi, R. Ramponi, R. Osellame, "Polarization entangled state measurement on a chip", *Phys. Rev. Lett.* **105**, 200503 (2010).

[6] L. Sansoni, F. Sciarrino, G. Vallone, P. Mataloni, A. Crespi, R. Ramponi, R. Osellame, "Two-particle bosonic-fermionic quantum walk via 3D integrated photonics", P*hys. Rev. Lett.* **108**, 010502 (2012); A. Crespi, R. Osellame, R. Ramponi, V. Giovannetti, R. Fazio, L. Sansoni, F. De Nicola, F. Sciarrino, and P. Mataloni, Anderson localization of entangled photons in an integrated quantum walk, Nature Photonics 7, 322–328 (2013) doi:10.1038/nphoton.2013.26.

[7] A. Crespi, R. Osellame, R. Ramponi, D. J. Brod, E. F. Galvao, N. Spagnolo, C. Vitelli, E. Maiorino, P. Mataloni, and F. Sciarrino, "Experimental boson sampling in arbitrary integrated photonic circuits", Nature Photonics 7, 545 (2013).

[8] . Spagnolo, C. Vitelli, L. Aparo, P. Mataloni, F. Sciarrino, A. Crespi, R. Ramponi, and R. Osellame, "Three-photon bosonic coalescence in an integrated tritter", Nature Communications 4, 1606 (2013) doi:10.1038/ncomms2616.

[9] N. Spagnolo, L. Aparo, C. Vitelli, A. Crespi, R. Ramponi, R. Osellame, P. Mataloni, and F. Sciarrino, Quantum interferometry with three-dimensional geometry, Sci. Rep. 2, 862 (2012).

Engineering waveguide arrays for high-purity matched four-wave mixing photon sources

P. L. Mennea[1], J. B. Spring[2], J. C. Gates[1], B. J. Metcalf[2], P. C. Humphreys[2], M. Moore[2], M. T. Posner[1], N. K. Langford[2], W. S. Kolthammer[2], I. A. Walmsley[2], P. G. R. Smith[1]

[1] Optoelectronics Research Centre,University of Southampton, Southampton, UK
plm1v07@southampton.ac.uk,
[2] Clarendon Laboratory, University of Oxford, Oxford, UK,
j.spring1@physics.ox.ac.uk

Abstract: We present recent developments in integrated four-wave mixing photon source arrays, produced via direct UV-writing in a silica-on-silicon substrate. These sources are of high purity and are mode-matched to optical fibre. Matching of the source arrays is demonstrated in initial results from quantum interference experiments, and efforts to further integrate these experiments are discussed.

Introduction

Significant advancements have recently been made in on-chip quantum optics experiments, highlighting the importance of integration in scaling to larger systems. Waveguide-integrated photon sources have been demonstrated in a variety of platforms, in the form of both single-photon emitters and photon-pair generation via non-linear processes. A key challenge in this area has been the difficulty of matching multiple sources without drastic reduction in count rates, particularly in an integrated format[1].

In this work we demonstrate that birefringent-matched four-wave-mixing (FWM) sources in UV-written silica-on-silicon waveguides possess sufficient uniformity for high quality quantum interference to be observed between photons emitted by independent guides in an array. This technology has previously been used in a range of two- and three-photon quantum circuits[2].

Fabrication

The UV-writing process utilized here involves a local refractive index increase induced in a photosensitive glass layer through absorption of a focused UV beam, translated across the substrate to inscribe a series of buried channel waveguides[3]. The silica core and cladding layers were fabricated on a thermally oxidised silicon substrate via Flame Hydrolysis Deposition (FHD), the former of these being doped with germanium and boron for photosensitivity and the latter with boron and phosphorus.

The birefringence of the resulting waveguides is dominated by the locked-in stress due to the different consolidation temperatures of these two FHD layers, which may be controlled by adjusting the dopant concentrations. This ability to tune the birefringence of the fabricated waveguides is invaluable since it allows the phase-matching to be tuned to place the signal and idler photons away from the Raman noise peak.

This approach produces waveguides which are highly uniform in both birefringence and effective index over chip scales, and may be fabricated reproducibly.

Characterisation

Characterisation of the source array was conducted by free-space launching into pairs of waveguides, via a free-space optical delay stage for one input, with an 80 MHz Ti-sapphire pump at 760 nm. The signal and idler outputs from each source were then separated and launched into separate fibres after filtering of the pump. The two signal photons were detected by Avalanche Photodetectors (APDs) and used to herald the idler photons, which were interfered at a 50-50 fibre beam splitter before being detected at two further APDs. The peak wavelength of the signal and idler photons, 670 nm and 820 nm respectively, were consistent with a waveguide birefringence of 1.2×10^{-4}.

Fig. 1a displays the coincidence count rates as a function of delay stage position for one pair of sources, both with and without minimal filtering. The Hong-Ou-Mandel (HOM) interference dip visibility is also plotted for four pairs of sources (Fig. 1b); these values demonstrate high quality non-classical interference, close to the calculated theoretical maximum for the system, for all four pairs of waveguides.

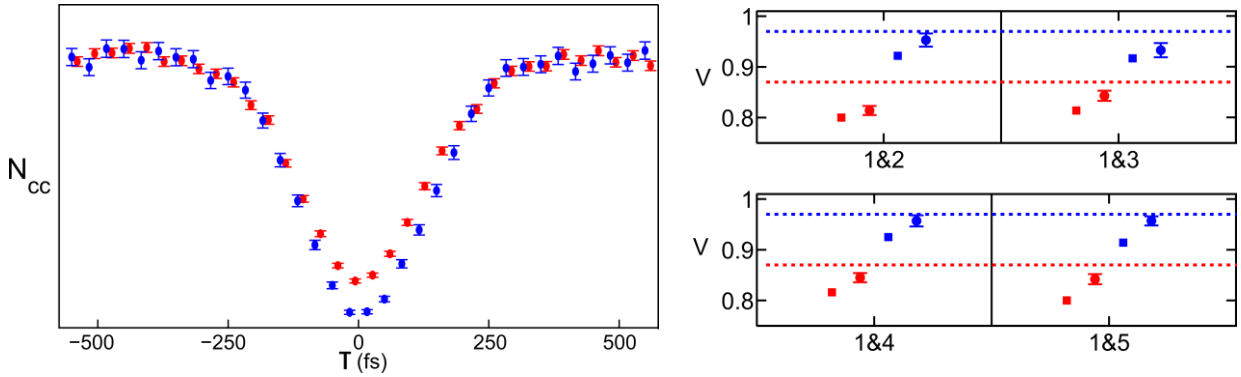


Fig. 1: a) Coincidence count rate as a function of delay for a representative source pair on the fabricated

Conclusion

We report the fabrication of matched UV-written waveguide arrays for FWM photon sources, and present non-classical interference between pairs of sources in a set of four. Results suggest that many on-chip sources of identical photons are possible in this platform with minimal additional development.

Further integration of these sources is also being explored; in particular the UV-written approach permits high-quality Bragg gratings to be incorporated readily, allowing for on-chip pump suppression. Additionally, a 1-N splitter at the input would reduce the number of free space launches, permitting scaling to larger numbers of sources.

References

1. T. Meany, L. A. Ngah, M. J. Collins, A. S. Clark, R. J. Williams, B. J. Eggleton, M. J. Steel, M. J. Withford, and O. Alibart, "Hybrid photonic circuit for multiplexed heralded single photons," *pre-print*, arXiv:1402.7202 [quant-ph], 2014.
2. B. J. Metcalf, N. Thomas-Peter, J. B. Spring, D. Kundys, M. a Broome, P. C. Humphreys, X.-M. Jin, M. Barbieri, W. S. Kolthammer, J. C. Gates, B. J. Smith, N. K. Langford, P. G. R. Smith, and I. a Walmsley, "Multiphoton quantum interference in a multiport integrated photonic device.," *Nature communications* **4**, p. 1356, Jan. 2013.
3. C. Sima, J. C. Gates, H. L. Rogers, P. L. Mennea, C. Holmes, M. N. Zervas, P. G. R. Smith, *Optics Express* **21**, pp. 15747–15754 (2013).

Si-Wire based 8 × 8 strictly-Non-Blocking PILOSS Switch

Keijiro Suzuki, Ken Tanizawa, Takashi Matsukawa, Guangwei Cong, Sang-Hun Kim, Satoshi Suda, Morifumi Ohno, Tadashi Chiba, Hirofumi Tadokoro, Masashi Yanagihara, Yasushi Igarashi, Meishoku Masahara, Shu Namiki, and Hitoshi Kawashima

National Institute of Advanced Industrial Science and Technology, Tsukuba, Ibaraki, Japan
k.suzuki@aist.go.jp, ken.tanizawa@aist.go.jp, t-matsu@aist.go.jp, gw-cong@aist.go.jp, sanghun-kim@aist.go.jp, s-suda@aist.go.jp, morifumi-ohno@aist.go.jp, tadashi-chiba@aist.go.jp, h-tadokoro@aist.go.jp, masashi-yanagihara@aist.go.jp, yasushi-igarashi@aist.go.jp, m.masahara@aist.go.jp, shu.namiki@aist.go.jp, kawashima-h@aist.go.jp

Abstract: We present a Si-wire waveguide based 8×8 path-independent insertion-loss (PILOSS) switch, which has a record-small footprint of 3.5×2.4 mm^2. The PILOSS switch includes 64 thermooptic Mach-Zehnder switches and 49 intersections. These switches and intersections employ directional couplers, which enable to comprise a low loss PILOSS switch. We demonstrate successful switching of digital-coherent 43-Gbps QPSK signal by the PILOSS switch.

1. Introduction

There is a continuing demand for strictly non-blocking high-port-count $N\times N$ optical switches in an integrated form [1, 2]. A standard $N\times N$ switch topology is a path-independent insertion loss (PILOSS) topology [3], in which light passes through N element switches and $N-1$ intersections for all the N^2 ways. The number of ON (the switch with electric power applied is in ON state) elements is N in the PILOSS topology. Another option is a "switch-and-select" topology, in which the switch is composed of $1\times N$ switch units arrays [4-6]. The number of ON switch elements depends on a path setting, and the average number of ON elements is proportional to $(\log_2 N)$ N. Comparing the two topologies, the PILOSS switch is more energy efficient due to less ON switch elements. For this reason, we believe that the PILOSS remains prospective for long-term scalability towards larger N.

In this paper, we report the implementation of an 8×8 PILOSS switch using Si-wire waveguides. The PILOSS switch has record-small footprint of 2.4 × 3.5 mm^2. Crosstalk of the PILOSS switch is as low as −23.1 dB, comparable to the switch based on the thick (~1.5 μm) Si-rib waveguides [7]. For circuit switch applications, 43-Gbps digital-coherent QPSK signals switching is also demonstrated.

2. Results and discussion

The 8 × 8 PILOSS switch chip fabricated by use of *e*-beam lithography and CMOS-compatible process are shown in Fig.1(a). The PILOSS switch includes 64 Mach-Zehnder (MZ) switches and 49 intersections. A Si-wire waveguide dimension is 430 × 220 nm^2, buried by SiO_2 over cladding. The MZ switch is composed of directional couplers and thermooptic phase-shifters with TiN heaters. A footprint of the PILOSS switch is 3.5 × 2.4 mm^2, which is 1/550 as small as that of the silica PLC switch [3], 1/4 as small as that of the thick Si-rib waveguide based switch [7]. The measured insertion losses at a wavelength of 1.55 μm are shown in Fig. 1(b). The average on-chip loss is 6.5 ± 1.0 dB, where the on-chip loss is defined as the loss without the coupling loss. This small loss variation clearly warrants the merit of the PILOSS topology. Figure 1(c) plots the crosstalk for all switch states (8! = 40,320) that was estimated from the results of the loss measurement [8]. The crosstalk is lower than −18.3 dB, and its median is −23.1 dB. The crosstalk is limited by the switch-to-switch variation of the minimum-crosstalk wavelength, which is estimated to be ~5 nm.

We evaluated the switching characteristics of a digital-coherent 43-Gbps QPSK signal between two switch states. Figure 2 shows the measured constellation diagrams of each output port for the state 1 (input-output connections are 1-8, 2-7, 3-6, 4-5, 5-4, 6-3, 7-2, and 8-1) and 2 (1-1, 2-6, 3-4, 5-2, 6-5, 7-3, and 8-8). It is found that there are clearly separated symbols and not any degradation at both switch states compared to the back-to-back result. The measured error vector magnitude is approximately 13.4%, corresponding to a BER of less-than 1×10^{-12}.

These results demonstrate that the Si-wire based PILOSS switch can be a good candidate for the high-port-count strictly-non-blocking $N \times N$ switch in the integrated form. The wavelength and polarization dependence of the PILOSS switch are yet challenges to be solved [9].

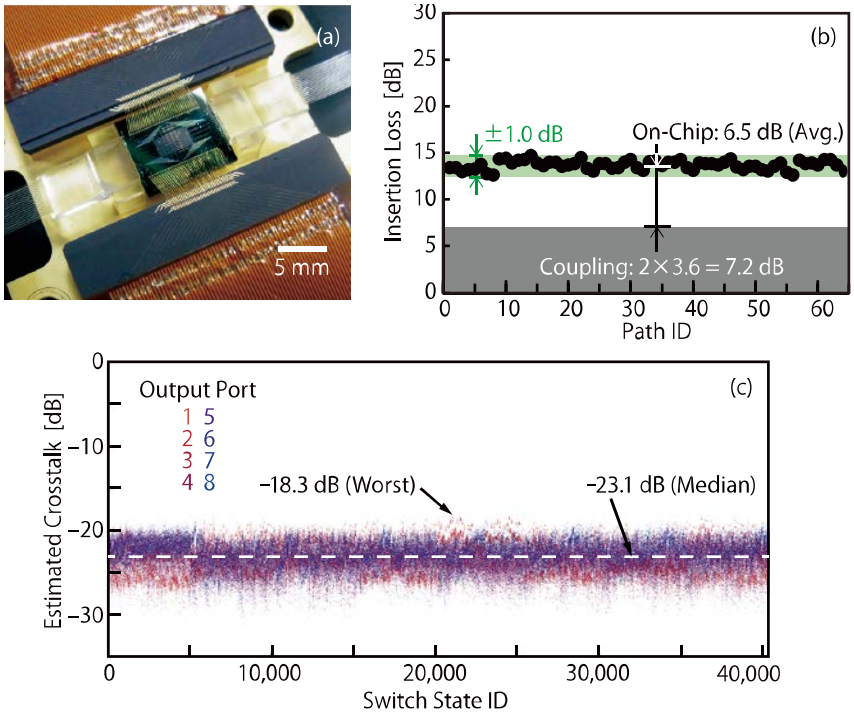


Fig. 1: (a) Fabricated 8×8 PILOSS switch on ceramic mount. (b) Fiber-to-fiber insertion loss of 8^2 =64 paths. (c) Estimated crosstalk at eight output ports for all possible switch state (8! = 40,320).

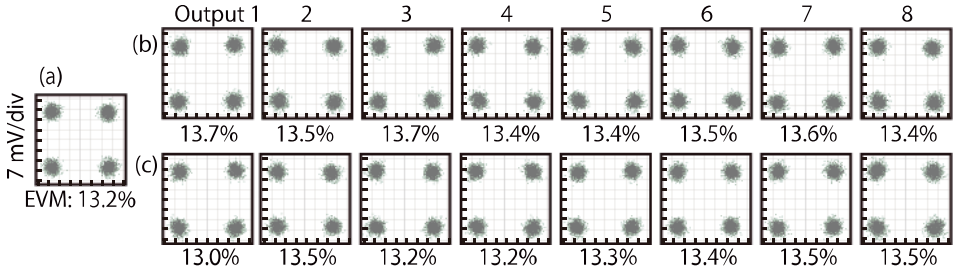


Fig. 2: Measured constellation diagrams. OSNR = 20 dB. (a) Back to back. (b) State A (input-output: 1-8, 2-7, 3-6, 4-5, 5-4, 6-3, 7-2, and 8-1). (c) State B (1-1, 2-6, 3-4, 5-2, 6-5, 7-3, and 8-8). EVM: Error Vector Magnitude.

Acknowledgement

This work was partly supported by Project for Developing Innovation Systems of MEXT, Japan.

References

1. S. Namiki, *et al.*, *IEEE J. Sel. Top. Quantum Electron.* **17**, pp.446-457 (2011).
2. K. Ishii, *et al.*, *Proc. SPIE* **8646**, pp.86460A (2013).
3. T. Goh, *et al.*, *J. Lightwave Technol.* **17**, pp.1192-1199 (1999).
4. L. Chen, *et al.*, *Opt. Express* **20**, pp.18977-18985 (2012).
5. M.-J. Kwack, *et al.*, *Opt. Express* **20**, pp.28734-28741 (2012).
6. S. Nakamura, *et al.*, OFC/NFOEC'12, OTu2I.3 (2012).
7. S. Nakamura, *et al.*, Proc. OFC'11, OTuM2 (2011).
8. K. Suzuki, *et al.*, *Opt. Express* **22**, pp.3887-3894 (2014).
9. S.-H. Kim, *et al.*, ECOC, We.4.B.5 (2013).

Graphene Integrated Silicon Photonics

R. Kou [1,2,3], S. Tanabe [4], T. Tsuchizawa [1,2], K. Warabi [3], Y. Kobayashi [3], S. Suzuki [4],
H. Hibino [4], T. Yamamoto [2], H. Nakajima [3], K. Yamada [1,2]

[1]*NTT Nanophotonics Center, 3-1, Morinosato Wakamiya, Atsugi, Kanagawa 243-0198, Japan*
[2]*NTT Microsystem Integration Laboratories, 3-1, Morinosato Wakamiya, Atsugi, Kanagawa 243-0198, Japan*
[3]*Gradutate School of Advanced Science and Engineering, Waseda University. 3-4-1, Okubo, Shinjuku-ku, Tokyo 169-8555, Japan*
[4]*NTT Basic Research Laboratories, 3-1, Morinosato Wakamiya, Atsugi, Kanagawa 243-0198, Japan*
takahashi.rai@lab.ntt.co.jp

Abstract: We have investigated light-matter interactions in monolayer graphene integration on a silicon-photonic waveguide in telecommunications bands of 1.5 μm. The passive integration scheme and device characteristics are discussed with our recent experimental results and analysis.

1. Introduction

Devices based on silicon photonics technologies provide various advantages in optical communications systems. Except for a monolithic light source, those devices have been comprehensively developed over the last ten years [1]. The next step for enhancing device integration density and operation bandwidth, reducing cost and power consumption requires innovative approaches. Here, we propose the use of graphene, which is composed of carbon-atoms with honeycomb structure. The unique linear energy dispersion in grapheme (Fig. 1) provides remarkable optical features, such as wavelength-independent light absorption (2.3 %/layer), ultrahigh carrier mobility (10^6 cm^2/Vs), a saturable absorption effect, and a tunable Fermi level and band gap (with bilayer graphene). These features would contribute to overcoming the limitations of silicon photonic devices. In this paper, we describe how we apply existing silicon photonics technologies as an integration platform to maximize graphene's potential for achieving future ultrahigh performance opto-electro integrated circuits.

2. Device design and integration process

Fig. 2(a) shows the target structure for monolayer graphene integration on a silicon-photonic waveguide. Thanks for the large evanescent field surrounding the silicon waveguide core, the interaction between light and grapheme is very strong as shown in Fig. 2(b), which corresponds to the propagation mode profile for TE polarization. To realize this basic structure, we developed the integration process briefly summarized in Fig. 3. Large-scale monolayer graphene (50×50 mm^2) grown on copper foil by the CVD method is transferred onto a 4-inch as-etched silicon waveguide SOI wafer. Then, we define graphene patterns using photolithography and O_2 plasma etching. This process enables us to obtain a high-resolution and a flexible shape in graphene.

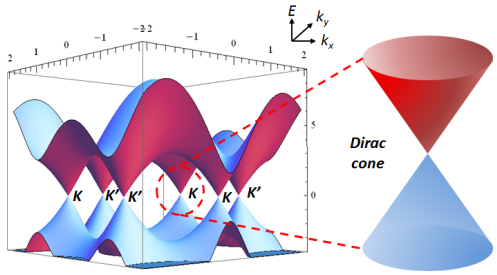


Fig. 1. Energy dispersion in graphene

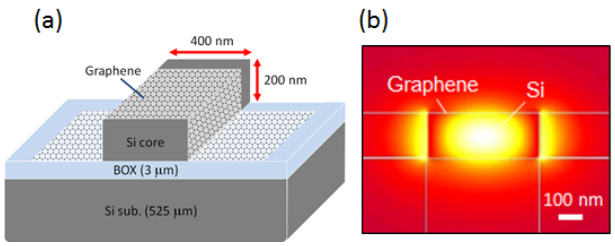


Fig. 2. (a) Schematic of graphene integration on silicon waveguide (b) Calculated mode profile with graphene

3. Device characterization

Fig. 4 shows optical microscope and SEM images of the integration, and micro-Raman spectra from the circled areas in the images. The graphene integrated part (circle 1) has the obvious inherent

response of monolayer graphene. In the optical measurement, we first investigated the light-absorption efficiency of the graphene on a silicon waveguide, and polarization dependence by changing the integrated graphene length from 2.5 to 200 μm. The measured efficiencies were 0.09 dB/μm in the TE mode, and 0.05 dB/μm in the TM mode. From measurement results and numerical analysis, we found that the lower absorption efficiency in the TM mode is due to strong p-doing in the transferred graphene. The p-doping causes surface-plasmon polariton propagation, which results in the low-loss propagation [2]. Next, we investigated the influence of graphene on the resonance Q factor variation by integrating graphene on a silicon-ring resonator. Fig. 5(a) shows a schematic of the sample, where parameter $L_{Gr.}$ corresponds to graphene length from 0 to 20 μm. As shown in Fig. 5(b), the initial Q factor of 7900 drastically decreased to 1200 at $L_{Gr.}$ of 20 μm [3]. We analysed this phenomenon by mode calculation and theoretical approaches and then found that it can be explained by linear graphene absorption on the silicon waveguide. Currently, the only remaining issue for forming passive graphene integrated devices is fiber coupling. Since graphene is a single-atomic-layer material, damage caused by the upper over-cladding layer is very serious. We recently proposed the use of an efficient (1.4 and 2.4 dB/facet in the TE and TM modes) and ultra-broadband (> 300 nm at 3-dB roll off in the both polarizations) selective spot-size converter as a way to solve the problem [4].

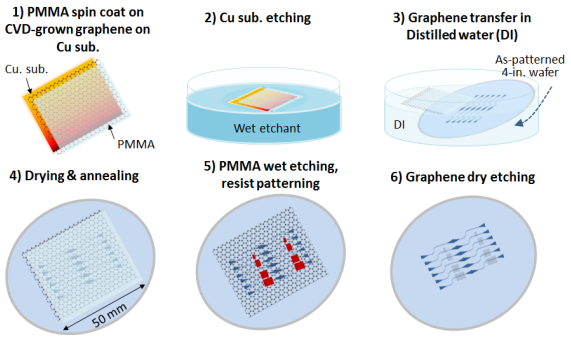


Fig. 3. Fabrication process flow for integration of graphene and silicon photonics

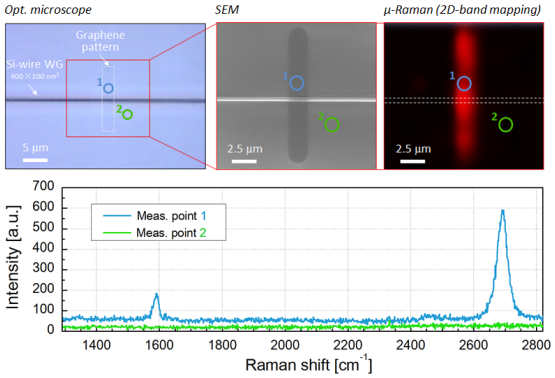


Fig. 4. Optical microscope and SEM images of integration, and micro-Raman spectra. The spectra correspond to each measurement point.

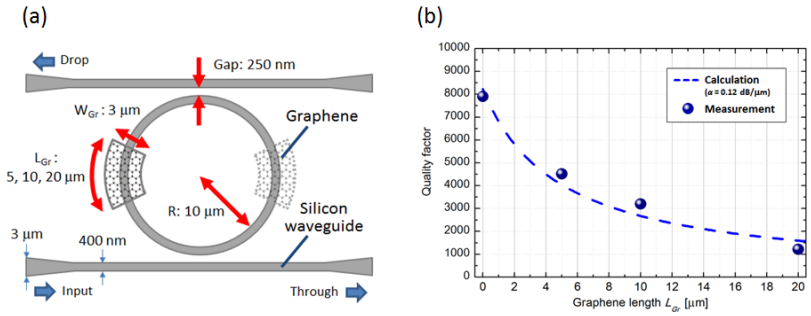


Fig. 5 (a) Partial graphene integration on a silicon ring-resonator. (b) Q factor variation by changing graphene length.

4. Conclusion

We introduced our recent activities on passive graphene integration with silicon-photonic circuits, such as a simple straight waveguide, ring resonator, and selectively spot-size converter. Our results will contribute to the development of large-scale and high-performance circuits using group-IV materials of silicon and graphene in the near future.

References

1. B. Analui, D. Guckenberger, D. Kucharski et al. *IEEE J. Solid-State Circuits* **41**, 12, pp. 2945-2955 (2006).
2. R. Kou, S. Tanabe, T. Tsuchizawa et al. *Jpn. J. Appl. Phys.* **52**, 6, 060203 (2013).
3. R. Kou, S. Tanabe, T. Tsuchizawa et al. *Appl. Phys. Lett.* **104**, 9, 091122 (2014).
4. R. Kou, Y. Kobayashi, K. Warabi et al. *IEEE Photon. J.* **6**, 3, 6600409 (2014).

Transparent Monitoring of Light in Integrated Optics

S. Grillanda, F. Morichetti, M. Carminati, P. Ciccarella, G. Ferrari, M. Sampietro, and A. Melloni

Dipartimento di Elettronica, Informazione e Bioingegneria, Politecnico di Milano, via Ponzio 34/5, 20133 Milano, Italy
andrea.melloni@polimi.it

Abstract: We demonstrate transparent monitoring of light in photonic integrated circuits, based on silicon and indium phosphide platforms, by means of a novel integrated photonic probe. In silicon waveguides our transparent probe enables light observation over 30 dB dynamic range, down to -20 dBm sensitivity, and on a microsecond time scale. Application to the tuning of the resonant wavelength of a silicon microring resonator is shown.

1. Introduction

Photonic integrated circuits are fundamental building blocks enabling high-speed, low power and small footprint wavelength division multiplexing (WDM) optical interconnects. However, because of their strong sensitivity to fabrication tolerances, thermal drifts, laser fluctuations, crosstalk effects etc., their operation needs to be continuously monitored and stabilized. Active tuning techniques for the feedback control of the resonator wavelength have been recently demonstrated [1-2], however they require the use of tap photodetectors to monitor the current status of the circuit, condition that should be avoided for large scale integration circuits, where hundreds of components are integrated on the same chip.

In this contribution we demonstrate a ContactLess Integrated Photonics Probe (CLIPP), that neither taps additional photons from the waveguide nor introduces significant perturbations of the optical field [3]. Our technique, that exploits the measurement of the variation of the waveguide electric conductance associated with intrinsic surface-state absorption (SSA), is inherently CMOS compatible, enables multi-point light monitoring on chip, and proves its utility for the tuning and control of photonic integrated devices.

2. The CLIPP concept

Figure 1(a) shows a schematic view of the CLIPP, that consists simply of two metal electrodes placed on top a photonic waveguide (here demonstrated for Si and InP technologies) covered by an insulating top cladding layer. The inset of Fig. 1(b) reports the case of a Si waveguide where two Au electrodes are deposited on top of a Si core waveguide (w = 480 nm, h = 220 nm) surrounded by SiO_2. The metal pads are placed at 1 µm distance from the Si core to avoid any additional optical loss, and at a mutual distance of 100 µm. Owing to the typical doping of SOI wafers (10^{15} cm^{-3}), in the electrical domain the Si core acts essentially as a resistor of conductance G, whereas the insulating top cladding provides an access capacitance from the metal to the Si core.

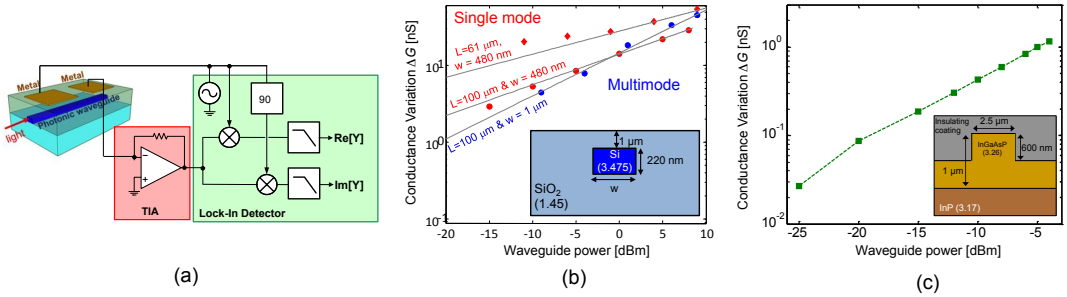


Fig. 1: (a) Schematic view of the CLIPP integrated with a generic photonic waveguide and measurement setup composed of a transimpedance amplifier (TIA) and a lock-in detector. (b) Light induced conductance change measured by the CLIPP in a Si waveguide as a function of the optical power for single and multimode waveguides and different CLIPP configurations and (c) in a InGaAsP/InP waveguide (coated with Si_3N_4).

As the light propagates in the waveguide, carriers are generated at the Si core boundaries by intrinsic surface-state-absorption (SSA) mechanisms, thus modifying the electric conductance G of the waveguide. No specific treatment was performed at the Si/SiO_2 interface. In order to measure the conductance change ΔG induced by optical power P, one of the CLIPP electrodes is excited with an electrical signal (voltage V_e = 1 V, and frequency f_e = 1 MHz), while the electric current at the other

electrode is collected by means of a transimpedance amplifier (TIA) and a lock-in detector, measuring the complex (amplitude and phase) electric admittance Y. The electrical frequency f_e was chosen in order to bypass the access capacitance (~ 5 fF), thus probing directly the conductance of the Si core.

Figure 1(b) shows the measured ΔG as a function of optical power P on TE polarization and at a 1550 nm wavelength, for single (w = 480 nm) and multimode (w = 1 µm) waveguides and different distances L between the CLIPP electrodes. Light monitoring was performed over a dynamic range of 3 orders of magnitude, down to -20 dBm, thanks to a sensitivity in the conductance measurement of better than 1 nS. The non-invasive behavior of the CLIPP was confirmed by the absence of a significant modulation effects in the output optical signal at the electric read-out frequency f_e: in fact, with a driving voltage of 1 V, the CLIPP introduces a phase perturbation as low as 0.4 mrad, corresponding to less than 0.2 ppm change of the waveguide effective index [3]. This negligible perturbation, that is induced by a tiny electro-optic effect, is comparable to that that would be induced by a temperature change smaller than 3 mK, that is far below the thermal stability of conventional thermoelectric coolers.

The CLIPP effectiveness was also demonstrated for InGaAsP/InP waveguides [Fig. 1(c)], here covered with Si_3N_4, where light induced ΔG was measured across 20 dB dynamic range and down to -25 dBm.

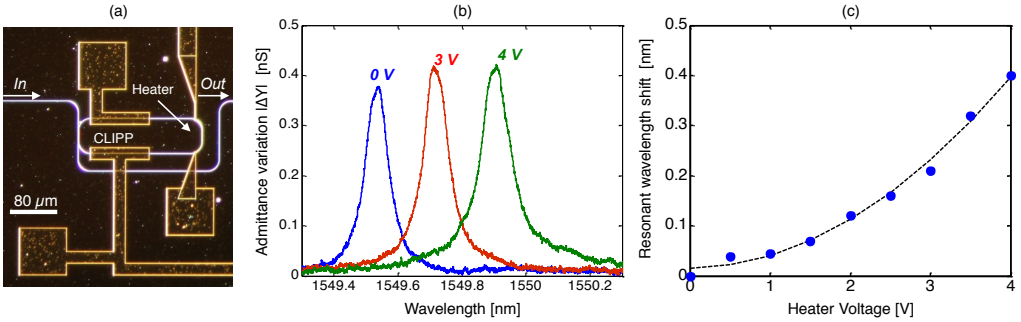


Fig. 2: (a) Top-view photograph of the Si ring resonator, onto which a CLIPP and a thermal actuator are integrated; (b) spectral response of the resonator measured by the CLIPP for different voltage applied to the heater; (c) resonant wavelength shift measured by the CLIPP when the heater is driven from 0 to 4 V.

3. Tuning of a Si resonator wavelength

Transparent monitoring of light can be exploited for the tuning of the spectral response of microring resonators. Figure 2(a) shows a top-view photograph of a Si ring resonator, in an all-pass-filter configuration, onto which a CLIPP and a thermal actuator are integrated. The resonator is 516 µm long (free-spectral-range FSR = 138.6 GHz) and has a linewidth of 87 pm (10.8 GHz). The CLIPP, that is placed inside the resonator, enables to monitor the light stored inside the ring, that is not accessible with an external photodetector or optical-spectrum-analyzers. As the thermal actuator is driven from 0 to 4 V, the ring spectral response, that is measured by the CLIPP, redshifts accordingly [Fig. 2(b), showing the magnitude of the electrical admittance variation $|\Delta Y|$]. Neither a change in the quality factor of the resonator (that is around 18000) is observed when the CLIPP and the heater are switched on, nor a significant crosstalk between the heater and the CLIPP electrical signals. Figure 2(c) reports the resonant wavelength of the filter, measured with the CLIPP, exhibiting a quadratic dependence with the heater voltage, as expected.

4. Conclusion

We demonstrated transparent monitoring of light in Si and InP photonic waveguides by means of a novel non-invasive detector, that neither taps additional photons, nor introduces significant perturbations of the optical field. Furthermore, we show the utility of the CLIPP to assist the tuning of the transfer function of a Si resonator.

This work was supported by the European Project BBOI of the 7th EU Framework Program. The authors are grateful to D. Melati from Politecnico di Milano for support in the measurements, to M. Sorel and M. Strain from Glasgow University for the fabrication of the Si chips, and to F. M. Soares and M. Baier from HHI for the fabrication of the indium phosphide chips.

References

1. K. Padmaraju *et al., J. of Lightwave Technol.* **32**(3), pp. 505-512 (2014).
2. W. A. Zortman *et al.*, *IEEE Micro* **33**(1), pp. 42-52 (2013).
3. F. Morichetti *et al., J. Sel. Top. Quantum Electron.* **20**(4), pp. 1-10 (2014).

Optimized Distributed Feedback Dye Laser Sensor for Real-Time Monitoring of Small Molecule Diffusion

Christoph Vannahme, Cameron L. C. Smith, Martin Dufva, Anders Kristensen

Technical University of Denmark, Department of Micro- and Nanotechnology, DTU Nanotech, Ørsteds Plads, Building 344, DK-2800 Kgs. Lyngby, Denmark
christoph.vannahme@nanotech.dtu.dk, cameron.smith@nanotech.dtu.dk, martin.dufva@nanotech.dtu.dk, anders.kristensen@nanotech.dtu.dk

Abstract: Nanoimprinted distributed feedback dye laser sensors featuring multilayer slab waveguides are presented. A simple yet precise analytical model is used to optimize the lasers in order to give highest sensitivity and it is found that the thickness of a high index TiO_2 top layer is the most important parameter for optimization. Using such laser sensors in an imaging spectroscopy setup, real-time label-free monitoring of sugar molecule diffusion in water is demonstrated. This method could potentially pave the way towards the analysis of small molecule diffusion in various media, e.g. protein signaling processes in tissue.

Organic dye-based distributed feedback (DFB) lasers have gained significant interest as widely tunable laser light sources in the visible wavelength regime. They are inexpensive and feature simple fabrication, low threshold, and single-mode emission.[1] Recently, they have been found to be highly sensitive refractive index and label-free bio-sensors where a change in the cladding refractive index results in a laser wavelength shift which is used as sensor signal.[2,3] Label-free sensing is very promising for the measurement of diffusion properties of small molecules in different media. These properties could not be measured with label-based methods as the labels would affect the diffusion. On a longer term, label-free monitoring of signaling proteins in tissue could be achieved this way leading to deeper understanding of the pathways that exist in tissue.[4]

Figure 1a shows a scheme of a 2nd order DFB dye laser sensor featuring a Pyrromethene 597 doped Ormocomp layer structured by UV nanoimprinting with a grating period of Λ = 384 nm.[5] In addition, the structure exhibits a thin TiO_2 top layer which is deposited by ion beam evaporation and significantly enhances the sensitivity of the sensor. This is proven by simulations with a simple yet precise model for calculating the emission wavelength of multilayer DFB lasers.[6] In contrast to choosing the DFB emission wavelength and solving for the corresponding propagation constant, here the propagation constant, β, is chosen to be $\beta = m\pi/\Lambda$, where m is the Bragg order. Thus, a more straightforward calculation yields the emission wavelength directly and the approach avoids several common approximations.

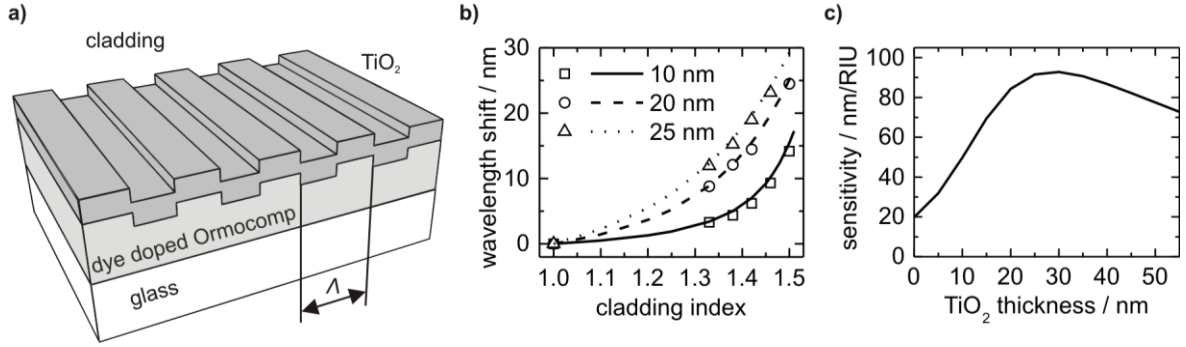


Fig. 1: a) Schematic of DFB dye laser sensor. b) Measured (symbols) and calculated (lines) wavelength shift for varying TiO_2 thickness. Ormocomp thickness is 400 nm. c) Calculated sensitivity as function of TiO_2 thickness.

Figure 1b shows the simulated and measured emission wavelength shift of DFB lasers with TiO_2 thickness of 10 nm, 20 nm, and 25 nm. Very good agreement between experimental data and simulations is evident. Thus, using this model is valid for optimizing the sensitivity of the lasers which is defined as wavelength change per refractive index unit. The plot in Fig. 1c shows the sensitivity as function of the TiO_2 layer thickness. It can be seen that the sensitivity can be improved

by a factor of 5 in comparison to a laser without TiO_2 top layer and that there is an optimal thickness of approx. 30 nm. This way, a detection limit of $8 \cdot 10^{-6}$ RIU is achieved.[5]

With these optimized lasers real-time monitoring in time and one dimension of space of sugar molecules diffusion in water is feasible. In order to achieve this, a microscope setup with an imaging spectrometer[7,8] is used, see Fig. 2a. Here, the green pump laser light (ns pulses at 532 nm) is focused onto the DFB dye laser sensor. The laser emits laser light of longer wavelength. For analysis the pump light is blocked by a dielectric mirror and the DFB laser light is used to project an image of the device surface onto a CCD for position control, Fig. 2b. Via a beamsplitter, the same image of the device surface is projected onto the slit of an imaging spectrometer (Acton SP-2756 imaging spectrograph with PIXIS00B digital CCD camera). The laser is oriented such that the imaged grating lines are parallel to spectrometer slit. Analysis of the spectrometer CCD image gives the emission wavelengths as function of the y-position where the spectrum of each row is analyzed and the emission wavelength is found with a center-of-mass approach.[5] 12 CCD images per second are taken. Each image gives one column with emission wavelengths for 100 y-positions corresponding to 100 rows on the CCD. In order to prove the functionality of the setup, a fluidic well on top of the laser is filled with water and a small piece of sugar is added. Thereupon, the sugar is dissolved in the water and the refractive index of the solution increases. The surface plot in Fig. 2c shows how the wavelength is changing as the sugar concentration is increasing. It is expected that this method can be used to analyze the diffusion of small molecules in various media on the milli- and micrometer scale and in real-time.

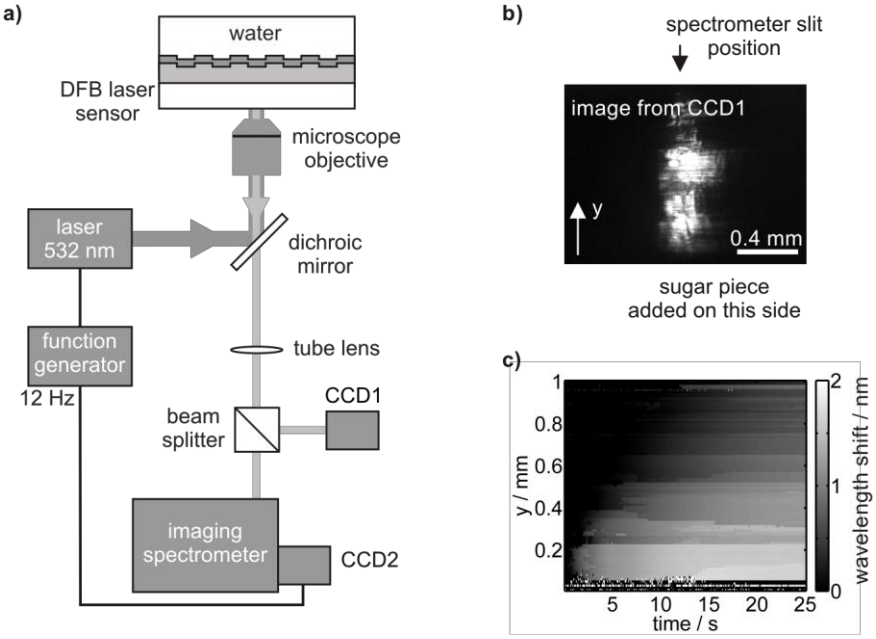


Fig. 2: a) Schematic of setup for real-time monitoring of sugar diffusion in water with DFB laser sensor. b) Image of laser emission on the surface indicating the position of the spectrometer slit. c) Wavelength shift occurring when a piece of sugar is added to water plotted as function of y-position and time as obtained from the imaging spectrometer data.

References

1. C. Grivas and M. Pollnau, *Laser Photonics Rev*. **6**, pp. 419–462, (2012).
2. M. Lu, S.S. Choi, C.J. Wagner, J.G. Eden, B.T. Cunningham, *Appl. Phys. Lett*. **92**, pp. 261502, (2008).
3. Y. Tan, A. Chu, M. Lu, B.T. Cunningham, *IEEE Sens. J*. **13**, pp. 1972–1978, (2013).
4. H. Youk and W. A. Lim, *Science* **343**, pp. 1242782, (2014).
5. C. Vannahme, M.C. Leung, F. Richter, C.L.C. Smith, P.G. Hermannsson, A. Kristensen, *Laser Photonics Rev*. **7**, 1036–1042, (2013).
6. C. Vannahme, C.L.C. Smith, M. B. Christiansen, A. Kristensen, *Appl. Phys. Lett*. **101**, pp. 151123, (2012).
7. J. Fallert, R.J.B. Dietz, J. Sartor, D. Schneider, C. Klingshirn, H. Kalt, *Nat. Photonics* **3**, pp. 279–282, (2009).
8. W. Chen, K.D. Long, M. Lu, V. Chaudhery, H. Yu, J.S. Choi, J. Polans, Y. Zhuo, B.A.C. Harley, B.T. Cunningham, *Analyst* **138**, 5886–5894, (2013).

Stabilization of Q-switched operation in glass waveguide lasers

L. Bastard[1], H. Ouslimani[1], G. Grosa[1], J.E. Broquin[1]

[1] IMEP-LaHC, Grenoble, France,
lionel.bastard@minatec.grenoble-inp.fr, hana.ouslimani@minatec.grenoble-inp.fr,
gregory.grosa@minatec.grenoble-inp.fr, jean-emmanuel.broquin@minatec.grenoble-inp.fr

Abstract: In this paper, we study the stability of integrated pulsed lasers. The devices are realized on rare-earth-doped glasses by the ion-exchange technique. The influence of the cavity design on the pulsation regime (Q-switching, mode-locking or Q-switched mode-locking) is analyzed. We show that unwanted Q-switched mode-locked operation is obtained in Fabry-Perot waveguide lasers. However, when replacing one of the mirrors by a Bragg grating, the mode-locking is suppressed and a stable Q-switch operation can be obtained. The behavior has been observed for Er/Yb co-doped and Yb doped laser.

Introduction: Q-switched lasers are used in many applications, ranging from sensing to micro-machining. In sensor applications such as LIDARS, either time-of flight[1] or Doppler[2] measurements can be used. However, depending on the parameters of the laser cavity, unwanted mode-locking can appear within the Q-switched pulses (referred to as Q-switched mode locking operation), leading to a more complex pulse envelope and a higher optical bandwidth. This mode of operation is detrimental for both types of LIDARs: the leading edge of the pulse is not smooth, decreasing hence the accuracy of time-of flight measurements, while the higher optical bandwidth is detrimental for Doppler measurements. It is thus interesting to realize devices in which the Q-switched mode locking regime cannot be attained.

In the literature, tailoring of the mode of operation of pulsed lasers is generally made through the design of the saturable absorber[3]. In this paper, we show that the mode of operation can be chosen thanks to the cavity design. For this purpose, we present the design, realization and characterization of different Q-Switched lasers with different cavity configurations (Fabry-Perot, distributed Bragg reflectors, distributed feedback). All these lasers are based on ion-exchanged waveguides made in rare-earth-doped phosphate glasses since this versatile technology already allowed the realization of compact and efficient CW and pulsed lasers[4].

Realization: All lasers use a channel waveguide realized by ion exchange in a doped glass as the optical amplifier element. Phosphate glass substrates are provided by Schott™, they are either doped with Ytterbium (4,6 wt%) or co-doped Erbium (2,2wt%) and Ytterbium(3,6 wt%). Diffusion apertures are formed by a standard photolithographic process in a 30 nm Silicon thin film deposited by RF sputtering. This process allows the realization of 4 cm-long straight waveguides with 3µm wide diffusion apertures. The ion exchange was carried-out at 330 °C in a molten salt bath containing 20% of $AgNO_3$ and 80% of $NaNO_3$. The exchange time was set in order to obtain single mode waveguides at the signal wavelength (λ=1534 nm for Erbium/Ytterbium codoped glass and λ=1030 nm for Ytterbium doped glass).

To obtain a passively Q-switched operation, a saturable absorber element has been added to the laser cavity. In the case of Erbium lasers, a commercially available SESAM element was stuck on the output facet of the waveguide. The relaxation time of the SESAM was 10ps and its modulation depth was 50%. For Ytterbium lasers, a dye (BDN) was embedded in a polymer and cast on top of the waveguides. In this case, the saturable absorber interacts with the evanescent tail of the guided mode[5]. The BDN relaxation time is 5ns and its concentration in the polymer was set to $4.2 \times 10^{23} m^{-3}$, which corresponds to an 80% modulation depth. Finally, the laser cavity was closed by a mirror or by a Bragg grating. Four different lasers have thus been realized. They will be referred to with letters A, B, C and D. Device A is a Fabry-Perot Erbium laser using a 4% reflection mirror on one facet and the SESAM on the other. B is a DBR Erbium laser identical to A, but the 4% mirror was replaced by a 1cm long, 10% reflection Bragg Reflector realized on top of the waveguide. C is a Fabry-Perot

Ytterbium laser terminated by 4% and 84% reflection mirrors, the saturable absorber is a BDN-doped polymer deposited on top of the waveguides. Finally, D is identical to C except that the 4% mirror is replaced by a 50% reflection Fiber Bragg Grating (FBG). The reflection of the FBG is centered on λ=1030 nm.

Characterization: Both spectral and temporal characteristics of lasers A, B, C and D have been measured. For spectral measurements, an OSA with a 0.07nm-resolution is used. Temporal measurements are carried-out with a fast photodetector (10 GHz bandwidth for 1.5 µm wavelength lasers and 25 GHz for 1µm lasers). The photodetector is connected to a 6 GHz bandwidth oscilloscope.

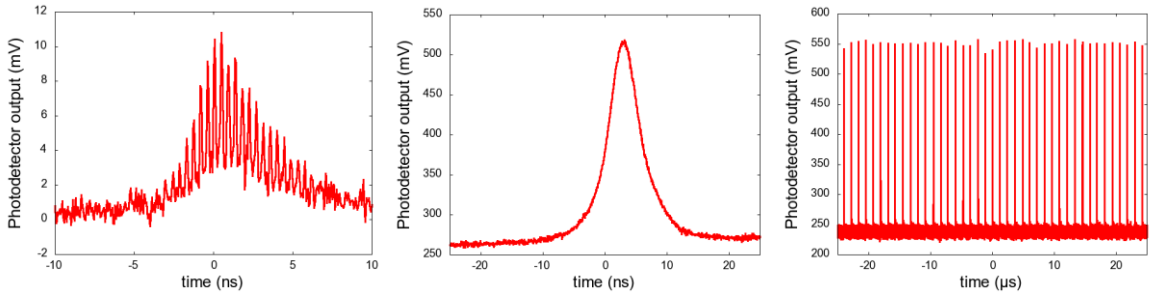


Figure 2: temporal characteristics of lasers. a): device A exhibits a Q-switched mode-locked operation. b) and c): device B is purely Q-switched.

Devices A and B both operate at a 1.53 µm-wavelength and are similar, except that A is a Fabry-Perot and B is a DBR laser. Both devices have an output power of 10 mW for an injected pump power of 300 mW. However, their spectra are different: for A it is 1 nm-wide whereas for B it is limited by the resolution of the OSA (0.07 nm). The results of the temporal measurements are presented on figure 2: a) is the pulse shape obtained with device A, b) is the pulse shape obtained with device B and c) is a pulse train from device B. In both cases, pulse width is about 4 ns and repetition rate varies from a few tens of kHz to 1 MHz depending on the pump power, but it can be clearly seen that device A presents a Q-Switched Mode-locked operation, while a pure Q-switched operation is ensured for laser B thanks to the integrated Bragg reflector.

Devices C and D have been realized in an Ytterbium-doped glass and were characterized with the same setups. The spectrum obtained with device C presents several emission lines between 1000 and 1020 nm, which respective power fluctuates randomly. This behavior is attributed to the very wide inhomogeneous emission linewidth of Ytterbium combined with the low spectral filtering of the Fabry-Perot cavity. On the other hand, the spectrum obtained with device D consists of a unique emission line at 1030 nm (the reflection wavelength of the FBG). The pulse width of both devices is around 9 ns and a repetition rate of 10 kHz can be observed under pumping at 300 mW. As with the Erbium lasers, Q-switched mode-locking is observed for device C whereas device D exhibits a pure Q-switched operation.

Conclusion: In this paper we reported the realization and characterization of Yb-Er and Yb integrated passively Q-Switched lasers for LIDAR application. We showed experimentally that the use of a Bragg Reflector for closing the laser cavity allows obtaining quite high power densities while maintaining a pure and stable Q-switched operation. Current work is focused on the realization of single-frequency passively Q-switched lasers thanks to the implementation of a DFB cavity

References

1. Warburton *et al*., *Optics letters* 32.15, pp. 2266-2268 (2007)
2. S. Kameyama *et al*,. *Applied Optics* 46.11, pp. 1953-1962 (2007)
3. U. Keller *et al*., *IEEE Selected Topics in Quantum Electronics*, pp. 435-453 (1996)
4. J-E. Broquin *et al*, *Symposium on Integrated Optics*, pp. 105-117 (2001)
5. B.Charlet *et al*, *Optics letters* 36.11, pp. 1987-1989 (2011)

Study on Confinement Scheme of GaN-based Vertical-Cavity Surface-Emitting Lasers

S.-C. Huang, Y.-Y. Lai, T.-L. Ho, T.-C. Lu*, and S.-C. Wang

National Chiao Tung University, Hsinchu, Taiwan
**timtclu@mail.nctu.edu.tw*

Abstract: The GaN-based vertical-cavity surface-emitting lasers (VCSELs) with three sorts of current-confined structure are numerically studied. The simulation results illustrate the proposed hybrid VCSEL design, which shows apparently lower threshold current and turn-on voltage, has superior performance due to the uniformly spread of current distribution and increased lateral optical confinement. These beneficial enhancements reflect the lateral multimode lasing behavior is suppressed via the smaller aperture size. As a result, the consideration provides a very promising design for the high-performance of GaN-based device.

Introduction

Development of potential nitride semiconductors and their applications such as light emitting diodes and laser diodes has attracted momentous attention.[1] The continuous wave (CW) current injection of GaN-based VCSELs was illustrated.[2-3] The current-confined aperture becomes electrically non-conducting layer hence the injected current will be confined into the central region of the VCSELs. This technique has been applied to GaN-based VCSELs where fractional oxidation of a high Al-content layer gives an aperture for current and optical confinement in the transverse direction.

Device Structure and Technical Methods

There are three structures demonstrated in this work, noting as original aperture inside the Indium-tin-oxide (ITO) layer (Type Ⅰ), AlN-aperture inside the p-GaN (Type Ⅱ), and the proposed hybrid structure with the ITO current spreading layer and the AlN current aperture (Type Ⅲ). The original structure is based on our previous report[4] of the room-temperature operated GaN-based device with emission wavelength of 410-nm. The proposed structure has a 7λ thick cavity surrounded by a bottom 29-pair AlN/GaN epitaxial distributed Bragg reflector (DBR) and a top 10-pair Ta_2O_5/SiO_2 dielectric DBR. The cavity composes of a n-GaN layer (900 nm), a 5-pair of $In_{0.2}Ga_{0.8}N$ (3 nm)/GaN (8 nm) multiple quantum wells (MQWs), a AlGaN electron blocking layer (20 nm), a AlN-aperture (30 nm) inserted into a p-GaN layer (100 nm), and a ITO current spreading layer (40 nm). The simulation model owing to the cylinder-symmetry structure can be simplified to the two-dimensional (2D) scheme, defined by the vertical (longitudinal) direction Z and the lateral (transverse) direction R.

Simulation Results

The key essential role to affect the laser behavior is that the overlapping percentage, which determined by the distribution of the cavity modes and the optical gain in the active region. The VCSEL with a small aperture can support only the zeroth-order mode, and other multimode will be suppressed. The main cause to influence on the threshold condition among several designs would be the lateral optical confinement. Here the investigation of the buried AlN-aperture case would not be discussed in the following due to the edge accumulated gain distribution and high absorption loss at the central region.

According to the simulation results as shown in Fig. 1(a), the Type Ⅰ device was set at the node position of the optical field to diminish the absorption loss. We further generalized from the Type Ⅰ design: the smaller overlapping percentage brought about a higher threshold current among smaller aperture size. The consequence of gain-optical zeroth-order mode overlapping percentages for 3.5 μm, 4 μm, and 5 μm devices were 65.7%, 79.6%, and 83.6%, respectively. Besides, the Type Ⅲ had better lateral confinement compared to the Type Ⅰ with the same radius by virtue of AlN-aperture. To accomplish single mode operation, the AlN aperture size should be declined to increase the

overlapping between gain region and the zeroth-order mode. Moreover, the device with 4.5 μm aperture size had lowest threshold of zeroth-order mode lasing as a result of much relatively higher gain-optical zeroth-order mode overlapping percentage and relatively smaller gain-optical first-order mode overlapping percentage, as shown in Fig. 1(b).

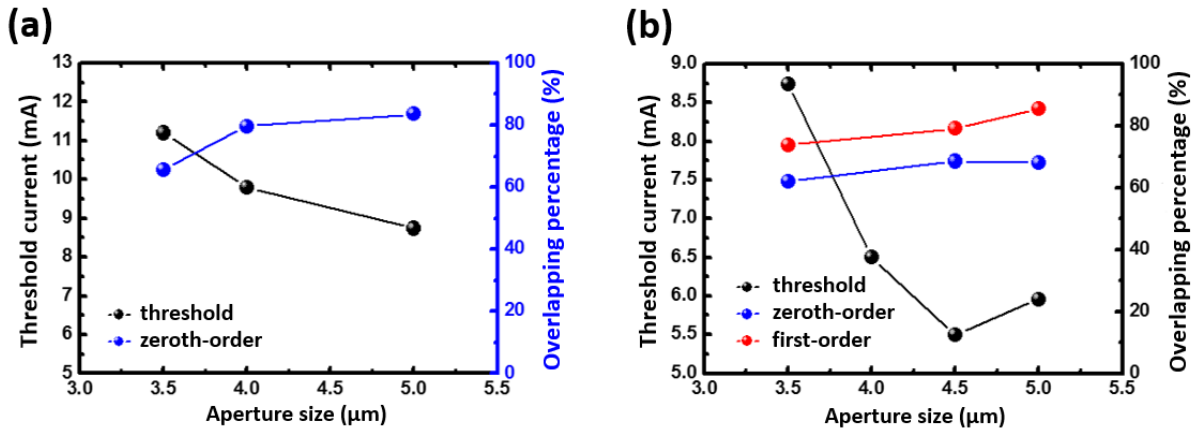


Fig. 1: (a) Threshold and gain-mode overlapping percentage as a function of aperture sizes. (b) Threshold (black dot) and gain-mode overlapping percentage of zeroth-order (blue dot), and first-order (red dot) optical mode as a function of aperture sizes.

Fig. 2 shows the light output power-current-voltage (L-I-V) curves of above mentioned distinct schemes. The Type Ⅲ design had considered the benefits of superior current spreading ability of the ITO layer and optical confinement of the AlN-aperture. The threshold current would be lower even half of the Type Ⅰ. The lager contact area between ITO layer and p-GaN contributed to superior injection ability and current spreading. Such method could provide an omnipotent solution for high performance GaN VCSELs.

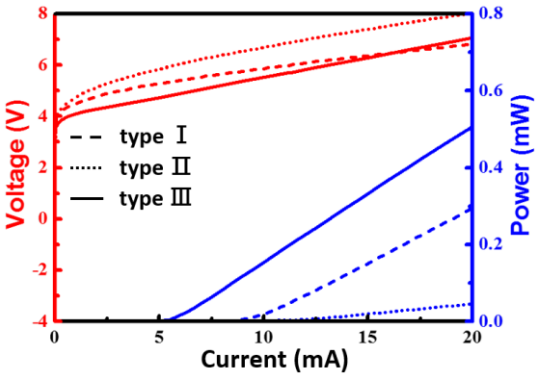


Fig. 2: The calculation of light output power (blue line) and contact voltage (red line) characteristics of Type Ⅰ (dash line), Type Ⅱ (dot line) and Type Ⅲ (solid line) VCSELs with various injected currents.

Conclusions

In conclusion, we have analysed a better design for confinement characteristics of VCSEL structures to identify the proper structure for GaN-based VCSELs. The enhanced confinement leads to lower threshold current and turn-on voltage. Our proposed structure not only improves the current crowding issue but also provides gain enhancement of single-mode operation. Above mentioned propose a better examination than ever before, which can be utilized novel design of GaN-based VCSELs.

References

1. S. Nakamura *et al*., *Appl. Phys. Lett*. **70**, pp. 4056–4058 (1996).
2. T. C. Lu, *et al*., *Appl. Phys. Lett*. **92**, pp. 141102, (2008).
3. T. C. Lu, *et al*., *Appl. Phys. Lett*. **97**, pp. 071114, (2010).

Opto-electronic wavelength tracker in Silicon-on-Insulator

J.D. Doménech[1], **J.S. Fandiño**[2], **R. Baños**[2] **and P. Muñoz**[1,2]
[1]VLC Photonics S.L., c/ Camino de Vera sn, 46022 Valencia, Spain
david.domenech@vlcphotonics.com
[2]Universitat Politècnica de València c/ Camino de Vera sn, 46022 Valencia, Spain
pmunoz@iteam.upv.es

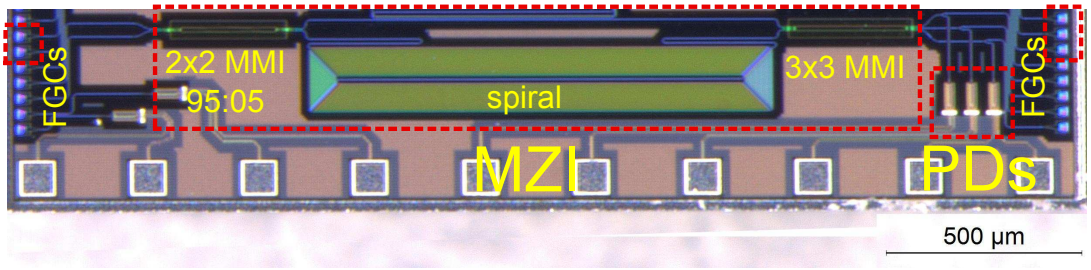
Abstract

In this paper the experimental demonstration of a Silicon-on-Insulator opto-electronic wavelength tracker is reported. The device consist of a 2x3 Mach-Zehnder interferometer with 10 pm resolution and photo-detectors integrated on the same chip. The design provides three complementary, with 120° phase relations, responses. Optical input/output responses exhibit rejection as good as 15 dB, thanks to asymmetric design for the input coupler. Synchronized recorded DC electronic responses for the three photo-detector outputs reproduce the MZI de-phased characteristic, allowing for monitoring wavelength changes with sign.

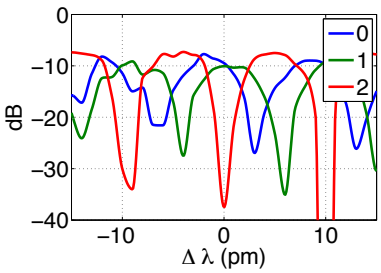
Wavelength tracking (WVLT) devices are of application in the fields of optical communications, instrumentation and sensing. These devices allow for monitoring changes in the wavelength of an optical signal caused by different phenomena, such as strain, temperature and humidity, among other. There have been a significant number of WVLT implementations with discrete components, [1] [2] are good examples, and most of the commercial implementations use such assemblies. A versatile well known layout for a WVLT makes use of an imbalanced Mach-Zehnder interferometer (MZI), where each arm of the interferometer has a different length. The imbalanced MZI has a periodic power spectral response that follows a cosine square expression (see theory in [3]). The spectral period, commonly named free spectral range (FSR) is inversely proportional to the length difference between the two arms of the MZI. To be precise, FSR = $\lambda^2/(n_g \Delta L)$., where λ is the operating wavelength, n_g is the group index for, and ΔL is the length difference between, the arm waveguides. Furthermore the MZI can be integrated on a photonic chip, with photo-detectors. MZI based WVLTs can make use either of 2 or 3 complementary outputs. The former usually provides outputs with a phase relation of 180°, whereas the latter are commonly designed for the optical outputs to have phase relations of $\{-120°, 0°, 120°\}$. While both configuration allow for monitoring the change in wavelength through the relative power change between the output signals, the 3 output port configuration enables to determine the sign of change as well. Integrated WVLT MZIs based on Multimode Interference (MMI) couplers have been reported in different technologies, and a remarkable layout for Silicon-on-Insulator (SOI) technology is proposed in [4], where Harmsma and co-workers made a 2x3 MZI SOI device with 0.55 nm FSR. In this paper we report on the experimental demonstration of a WVLT photonic chip based on a 2x3 MZI with integrated photo-detectors (PDs) in SOI technology. The device has a FSR of 10 pm and a footprint of 2.5x0.5 mm^2.

The devices were designed for, and fabricated in, a multi-project wafer technology by the OpSIS platform at IME Singapore [5]. The process allows for passive and opto-electronic active areas, as p-n junction modulators and photo-detectors. An optical microscope picture of the device is given in Fig. 1-(a). The device is composed of a 2x2 MMI input coupler and a 3x3 MMI output coupler. The couplers are designed in a shallowly etched areas, and designed following the rules in [6]. The output coupler has a 33:33:33 coupling ratio. The inputs/outputs to the couplers are tapered and all the dimensions were numerically optimized using a Beam Propagation Method (BPM) commercial software [7]. The two outputs of the first coupler are connected to the top and bottom inputs of the output coupler with strip waveguides of 450 nm width. One of the connections is a straight waveguide, whereas the other is a spiral waveguide of 56 mm, which for a group index of 4.25 corresponds to a FSR of 10 pm. The input coupler is designed to have a 95:05 coupling ratio, so as to compensate the large loss imbalance between the short and long arm, in order to attain the maximum rejection in the MZI spectral response. The output coupler outputs are connected to Y-branches. One output of each Y-branch is connected to a PD, and the other is used as test optical output. Focusing grating couplers (FGCs) are used as light input/output structures.

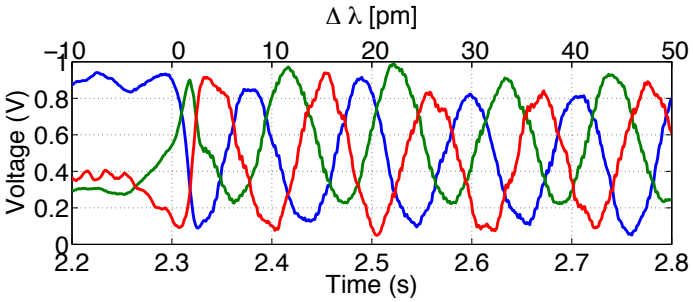
The chip was held in a vacuum chuck, whose temperature was kept to 25° C using a temperature controller (TEC). Fibers, at angle of 74° from the chip normal, were aligned to the input/output FGCs using motorized translation stages. Firstly, the spectral response of the MZI was measured. A tunable laser source synced with an an Optical Spectrum Analyzer (OSA) was used to acquire traces with 1 pm resolution. The traces, normalized with respect of a straight waveguide, are shown in Fig. 1-(b) for a wavelength interval around 1549.83 nm for the three outputs labeled 0, 1 and 2 in the figure. The spectral displacement between the traces correspond



(a) Optical microscope image of the fabricated devices



(b) Optical I/O MZI response



(c) Opto-electronic synchronized response

Fig. 1. Optical microscope image of the fabricated device (a) MZI I/O spectral traces with respect of 1549.83 nm (b) and synchronized electronic traces (c) for the three WVLT channels.

approximately to one third of the FSR, in agreement with the designed phase relations for the output MMI coupler. Despite the chip temperature was controlled, we observed spectral drifts of ± 1 pm in the measurements from a nominal position, in the scale of several tens of seconds, which we attributed to the limited resolution of the TEC. The rejection ratio attained in all the responses , defined as the difference between maximum and minimum value in a period, is at least around of 15 dB, thanks to the asymmetric input MMI coupler.

Secondly, the setup was conditioned to measure the opto-electronic response of the WVLT. Probes were used to contact the PD pads, Fig. 1-(a) lower right corner. Each probe was then loaded with a 10 kΩ resistor, and the PDs were biased at -2V. In absence of optical input we observed a dark current of 2 μA. The three resistors where then probed and connected to three channels of a data acquisition (DAQ) card, which allows for recording simultaneously the voltage corresponding to the current change in the three PDs. A tunable laser (TL) was then used as input, to be swept in steps of 1 pm. Furthermore, LabView^{TM} programs were deployed to control simultaneously the TL sweep and the DAQ recording, in order to obtain synchronized data at all the outputs. The results are shown in Fig. 1-(c). They correspond to smoothed data using a moving average of 10 points. The TL start and end wavelengths were set to 1550 nm and 1550.090 nm respectively, and the sweep was started iteratively. The traces in (c) are shown in a given time where, on the left hand side, the currents acquired have random value, since the TL is returning to the start wavelength. After this period of time (around 2.3 s in the figure) the sweep starts and the voltages recorded reproduce the sinusoidal variation of (b), with a one third period de-phased relation as well. Panel (c) top axis shows the sweep time translated into wavelength change from 1550 nm (negative values are arbitrarily labeled to represent the TL return time).

In conclusion, we have reported the experimental demonstration of a SOI opto-electronic wavelength tracker. The device is based in a 2x3 Mach-Zehnder interferometer, with 10 pm resolution, equipped with photo-detectors. The optical transfer function exhibits the phase relations of one third of the FSR, as expected from the design of the output MMI coupler. The optical rejection attained is at least as good as 15 dB. The opto-electronic transfer functions, recorded synchronously at the photo-detectors, reproduce the targeted tracking responses. Finally, we acknowledge funding from the Spanish CDTI NEOTEC, MINECO TEC2010-21337 & TEC2013-42332-P, FEDER UPV 10-3E-492 & 08-3E-008, FPI BES-2011-046100 and FPU AP2010-1595.

REFERENCES

[1] A.D. Kersey, T. Berkoff, and W.W. Morey, Optics letters, **18**(16), pp.1370–1372 (1993).
[2] M.D. Todd, G.A. Johnson, and B.L. Althouse, Measurement Science and Technology, **12**(7), pp.771–777 (2001).
[3] M.C. Teich and B.E.A Saleh. Fundamentals of photonics, 2nd ed., Wiley Interscience, (2007).
[4] P. Harmsma e.a., in Proc. CLEO/Europe and EQEC 2011 paper CK_P26 (2011).
[5] C. Galland e.a., in Proc. ECOC 2013, paper Mo.3.B.2 (2013).
[6] L.B. Soldano and E.C.M. Pennings, J. Lightwave Technol., **13**(4), pp.615–627 (1995).
[7] FieldDesigner and OptoDesigner software packages, http://www.phoenixbv.com/,

Optical samples measurement based on orthogonally polarized light over phase-shifting FD-OCT

[1]Jen-Fa Huang, [2]Hsu-Chih Cheng, [3]Chia-Tsai Huang

[1,3]Advanced Optoelectronic Technology Center, Institute of Computer&Communications Engineering, Department of Electrical Engineering, National Cheng Kung University, Tainan, Taiwan.
huajf@ee.ncku.edu.tw
[2]Department of Electro-Optical Engineering, National Formosa University, Yunlin, Taiwan.
chenghc@nfu.edu.tw

Abstract: An improved structure of Frequency-Domain Optical Coherence Tomography (FD-OCT) is proposed to simultaneously measure thickness and refractive index of unknown samples. In conventional FD-OCT, the generated mirror signals will cause the measurement range be cut half. The goal of this study is to increase measurement range and to eliminate unnecessary correlation and mirror signals. By phase-shifting algorithms over orthogonally polarized light, eliminating those unnecessary noise terms becomes possible, and the measurement range is doubled. The proposed FD-OCT thus achieve simultaneous measurements of optical samples in a full-range and one-shot scheme.

As shown in Figure 1, the proposed FD-OCT setup consists of a low-coherence light source, two polarizers, two beam splitters, a polarization beam splitter, a quarter-wave plate, three mirrors and a spectrometer. The SLD light source is divided into three optical paths (M1-arm, M2-arm, M3-arm) by beam splitters BS1 and BS2. The path M1-arm is a reference arm used to detect, M2-arm is another reference arm, and M3-arm is a sample arm. $E_o(\omega)$ is the electric field emitted from the SLD light source, passing through the polarizer P1 placing 45° and then through a quarter-wave plate Q placing 0°.[1] The emerged light is a circularly polarized electric field $E_i(\omega)$. The electric field $E_o(\omega)$ and $E_i(\omega)$ can be expressed as follows:

$$E_o(\omega) = a(\omega)exp[-i(\omega t + \kappa z)] \quad (1)$$

$$E_i(\omega) = J_Q(0°)J_P(45°)E_o(\omega) = a(\omega)exp(-i\frac{\pi}{4})\begin{bmatrix} exp[-i(\omega t+\kappa z)] \\ i\ exp[-i(\omega t+\kappa z)] \end{bmatrix}$$

$$= a(\omega)exp(-i\frac{\pi}{4})\begin{bmatrix} exp[-i(\omega t+\kappa z)] \\ exp[-i(\omega t+\kappa z)+\frac{\pi}{2}] \end{bmatrix} \quad (2)$$

where $a(\omega)$ is the electric field amplitude, ω, t, κ, z are frequency, time, wave number and distance, respectively. $J_Q(0°)$ and $J_P(45°)$ are the Jones matrix formalism of quarter-wave and polarizer.

The horizontal and vertical polarized light is received by the OSA. The intensity of polarization light is the dot product of electric fields[2] and can be expressed as:

$$I_i(\omega,\Delta z) = \langle E_i(\omega,\Delta z)\,, E_i{}^*(\omega,\Delta z)\rangle$$
$$= \langle E_{si}(\omega,\Delta z)\,, E_{si}{}^*(\omega,\Delta z)\rangle + \langle E_{ri}(\omega,\Delta z)\,, E_{ri}{}^*(\omega,\Delta z)\rangle$$
$$+2\Re\{\langle E_{si}(\omega,\Delta z)\,, E_{ri}{}^*(\omega,\Delta z)\rangle\} \quad (3)$$

where the index i can be replaced with h or v to denote horizontal and vertical polarization channels. In (3), the first and the second terms are self-coherence interference, and the third term is cross-coherence interference.

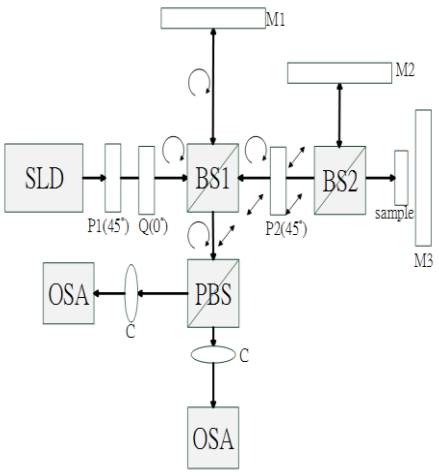


Fig. 1: Schematic illustration of the proposed FD-OCT scheme. (**SLD**: Super-luminescent diode; **P1, P2**: polarizer; **Q**: Quarter wave plate; **BS**: beam splitter; **PBS**: polarization beam splitter; **M1, M2, M3**: mirrors; **C**: collimator; **OSA**: optical spectrum analyzer.)

The complex intensity consists of $I_H(\omega, \Delta z)$ and $I_V(\omega, \Delta z, \phi=\pi/2)$, which can be expressed as[3]

$$I(\omega) = I_H(\omega,\Delta z) + i\,I_V(\omega,\Delta z,\varphi=\pi/2) \quad (4)$$

$$\Delta S(\tau) = \mathcal{F}^{-1}\{I(\omega)\} - \mathcal{F}^{-1}\{I^*(\omega)\} \quad (5)$$

When (4) substituted into (5), the symmetry mirror image and autocorrelation terms are eliminated. It is with such π/2-phase-shifting algorithm we can achieve a double measurement range.

The reason on adding the second reference arm is that the conventional FD-OCT needs two stages of measurements (place sample and remove sample) on the refractive index of the unknown samples. After adding the second reference arm, it needs only one-shot measurement on the thickness and the refractive index of the unknown samples.

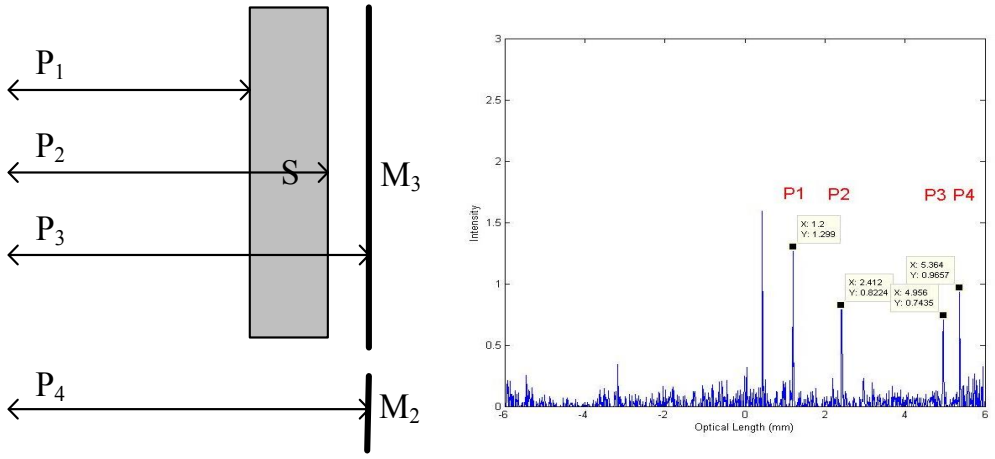


Fig. 2. (a). The optical path length of each surface by the M2 and M3 arm. (P_1~P_4 are optical path length of reflected light from different surface.) (b). The demodulated signal of the interferogram.

The simultaneous measurement method is shown in Figure 2(a). The demodulated signal of the interferogram is as shown in Figure 2(b). The optical path difference (i.e., P_2-P_1 and P_3-P_4) can be obtained by the experiment when substituted into (6) and (7). The thickness L and the refractive index n_s of the unknown sample can therefore be obtained:[4]

$$n_s = n_a \times \frac{P_2 - P_1}{(P_2 - P_1) - (P_3 - P_4)} \quad (6)$$

$$P_2 - P_1 = n_s \times L \quad (7)$$

Where n_s is the refractive index of samples, n_a is the refractive index of air, L is the thickness of the unknown sample. The values of the thickness and refractive index are calculated to be 0.82 mm (the real thickness is 0.8 mm) and 1.4878 (the real refractive index is 1.502), respectively.

References

1. Y. Watanabe, Y. Hayasaka, M. Sato, and N. Tanno, "*Full-field optical coherence tomography by achromatic phase shifting with a rotating polarizer*," *Appl. Opt.* **44**, pp. 1387–1392, (2005).

2. H.C. Cheng, M.S. Shiu, "Experimental demonstration of high-speed full-range Fourier domain optical coherence tomography imaging using orthogonally polarized light and a phase-shifting algorithm," Appl. Opt. 51(36), pp. 8762-8768, (2012).

3. R.A. Leitgeb, C.K. Hitzenberger, A.F. Fercher, and T.Bajraszewski, "*Phase-shifting algorithm to achieve highspeed long-depth-range probing by frequency-domain optical coherence tomography*," *Opt. Lett.* **28**, pp. 2201–2203, (2003).

4. H.C. Cheng and Y.C. Liu, "*Simultaneous measurement of group refractive index and thickness of optical samples using optical coherence tomography*," *Appl. Opt.* **49**, pp. 790-797, (2010).

Integrated Photonic Devices Driven by Surface Acoustic Waves

A. Crespo-Poveda[1], K. Biermann[2], A. Tahraoui[2], P. V. Santos[2], B. Gargallo[3], P. Muñoz[3], A. Cantarero[1], and M. M. de Lima, Jr.[1]

[1]*Universitat de València, Materials Science Institute, PO. Box 22085, ES46071 Valencia, Spain*
Antonio.Crespo-Poveda@uv.es, Mauricio.Morais@uv.es, Andres.Cantarero@uv.es
[2]*Paul Drude Institute for Solid State Electronics, Hausvogteiplatz 5-7, DE10117 Berlin, Germany*
biermann@pdi-berlin.de, tahraoui@pdi-berlin.de, santos@pdi-berlin.de
[3]*iTEAM Research Institute, Universitat Politècnica de València, Camino de Vera s/n, ES46022 Valencia, Spain*
pmunoz@iteam.upv.es, bergarja@iteam.upv.es

Abstract

A compact tunable photonic modulator driven by surface acoustic waves in the GHz frequency range is reported. The device follows a well-known Mach-Zehnder interferometer structure with three output channels, built upon multi-mode interference (MMI) couplers. The light continuously switches paths between the central and the side channels, avoiding losses and granting a 180°-dephasing synchronization between them. The modulator was monolithically fabricated on (Al,Ga)As, and can be used as a building block for more complex photonic functionalities. Light modulated at multiples of the fundamental acoustic frequency can be accomplished by adjusting the applied acoustic power.

A great effort has been made during the past decades to increase the integration level in photonic circuits. Although integration levels of up to a few hundreds of components per chip have been accomplished, photonic integrated circuits are still far from reaching the same development followed by its electronic counterpart. The search for solutions that allow devices that are at the same time fast, compact, inexpensive, and compatible with nowadays integration technology is of paramount importance. The external control of light propagation inside the devices allows for a reduction in the dimensions, favouring the integration and giving rise to novel functionalities. A promising approach consists of using a surface acoustic wave (SAW) to modulate single or multiple ridge or slot waveguides through the acousto-optical effect, with the possibility of adressing several devices with the same SAW beam. This method presents an excellent compromise between speed and size, and can be implemented in almost any material platform such as Silicon, (In,Ga)P or $LiNbO_3$. In this contribution, we will address the design, fabrication, and characterization of a three output photonic modulator driven by surface acoustic waves in the GHz frequency range, in which the light is continuously splitted, with a 180° -dephased synchronization, between the central and side waveguides. This is in contrast with most of the previous works, which explored designs with a single output [1]–[3] or, very recently, two outputs [4].

The device consists of a Mach-Zehnder interferometer (MZI) structure with three output waveguides, built upon multi-mode interference (MMI) couplers with the same coupling length [Fig. 1(a)]. The first coupler is a balanced (50:50) splitting ratio MMI that splits the incoming light into two identical optical beams which are then modulated by a SAW beam propagating perpendicularly to them (MWG_1 and MWG_2). The SAW beam is generated by an interdigital transducer (IDT). A second MMI coupler combines the input light into three output waveguides (OWG_L, OWG_C and OWG_R) with different power distribution depending on the phase and intensity of the light coming from the active region of the device. The spatial separation between the waveguides in the active region must be set to $(2m+1)\lambda_{SAW}/2$, where λ_{SAW} is the surface acoustic wave wavelength, and m is an integer. This ensures that each of the MWGs suffers a change in the effective refractive index of equal magnitude but opposite phase, maximizing therefore the acousto-optical modulation.

The response of the device was simulated using a finite difference beam propagation (BPM) method implemented via the RSoft package. Assuming either the transverse electric (TE) or the transverse magnetic (TM) polarizations at the input waveguide, we tracked the propagation of the optical field throughout the device. The width and length of the MMI couplers in the devices were optimized to operate at 900 nm. The device was fabricated on a sample grown by molecular beam epitaxy on a (001) GaAs wafer. The sample consists of a 300-nm-thick GaAs film forming the guiding layer, deposited on a 1500-nm-thick $Al_{0.2}Ga_{0.8}As$ buffer layer. The modulator was fabricated in two steps using contact optical lithography. First, Ti/Al/Ti IDT in a split finger configuration for efficient SAW generation was fabricated using a lift-off process. The IDT was designed for

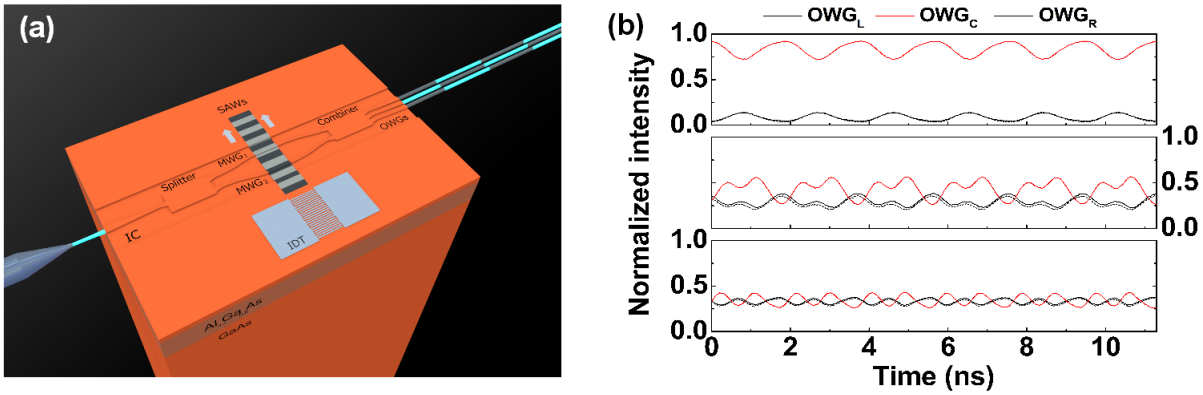


Fig. 1. *(a) Illustration (not to scale) of the SAW-driven Mach-Zehnder interferometer with three output waveguides, fabricated on (Al,Ga)As. (b) Time-resolved traces recorded for the light leaving the* OWG_{L} *(dotted black line),* OWG_{C} *(solid red line) and* OWG_{R} *(solid black line), measured for the TE polarization and RF powers of* $P_{\mathrm{IDT}} = 6.8$ *mW (upper panel),* $P_{\mathrm{IDT}} = 68.3$ *mW (central panel), and* $P_{\mathrm{IDT}} = 108.3$ *mW (bottom panel).*

an operation wavelength of $\lambda_{\mathrm{SAW}} = 5.6$ μm [5] (corresponding to a resonance frequency of approximately 520 MHz), with finger width and spacing of 700 nm. A second step of plasma etching was employed to create the 137-nm-deep grooves delimiting the rib waveguides of the device.

The device was optically characterized by coupling light into the input waveguide using a tapered optical fiber probe with a lensed tip. As light source, we used a superluminescent diode with peak emission centered at the wavelength $\lambda = 920$ nm, with a full width at half maximum of approximately 40 nm. The transmitted light was detected using a Si avalanche photodiode with a time resolution of 500 ps, synchronized with the RF signal driving the IDTs. Time-resolved transmission traces were recorded for different RF powers (P_{IDT}) applied to the IDT, and light with TE polarization (similar behavior was observed for light with TM polarization). The total transmission is normalized to 1. At small P_{IDT} [Fig. 1(b), upper panel], the light is modulated at the SAW fundamental frequency (f_{SAW}), with the central waveguide contributing to nearly 80% of the total transmission. When P_{IDT} increases, the presence of higher harmonics becomes evident. At $P_{\mathrm{IDT}} = 68.3$ mW [Fig. 1(b), central panel], the modulation at the first harmonic is less intense with a simultaneous increase in the modulation at the second harmonic. At $P_{\mathrm{IDT}} = 108.3$ mW [Fig. 1(b), bottom panel], the light modulation is entirely dominated by the second harmonic.

In conclusion, we have developed an acoustically driven photonic modulator based on a Mach-Zehnder interferometer that operates in the GHz range. The lateral channels are 180°-dephased with respect to the central one, whose phase and amplitude response can be changed by varying the applied acoustic power. The device was monolithically fabricated on (Al, Ga)As, although it can be easily implemented in other material platforms (InP, $LiNbO_3$), or even in non-piezoelectric materials, such as Si. In this case, SAWs can be generated by IDTs placed on a piezoelectric overlayer. Modulation at the second harmonic of the SAW driving frequency (1.03 GHz) is accomplished. The large phase coherence of the surface acoustic waves allows for the modulation of several ridge or slot waveguides using the same acoustic beam. The modulator can be used as a building block for more complex photonic functionalities. This research has been supported by the Spanish MINECO Projects TEC2010-21337 and MAT2012-33483. Financial support through FPI grants BES-2010-036846 and BES-2011-046100 is gratefully acknowledged.

REFERENCES

[1] M. M. de Lima Jr., M. Beck, R. Hey, and P. V. Santos, *Appl. Phys. Lett.* **89**, 121104 (2006).
[2] M. Beck, M. M. de Lima, Jr., E. Wiebicke, W. Seidel, R. Hey, and P. V. Santos, *Applied Physics Letters* **91**, 061118 (2007).
[3] M. Beck, M. M. de Lima, Jr., and P. V. Santos, *Journal of Applied Physics*, **103**, 014505 (2008).
[4] A. Crespo-Poveda, R. Hey, K. Biermann, A. Tahraoui, P. V. Santos, B. Gargallo, P. Muñoz, A. Cantarero, and M. M. de Lima, Jr., *Optics Express* **21**, 21669 (2013).
[5] M. M. de Lima, Jr., F. Alsina, W. Seidel, and P. V. Santos, *J. Appl. Phys.* **94**, 7848 (2003).

Integrated polymer waveguides incorporating nonlinear chromophores for all-optical signal processing

E. Delcourt[1], L. Bodiou[1], J. Charrier[1], S. Achelle[2], J. Lemaitre[1], N. Lorrain[1] and D. Bosc[1]

UEB, Université Européenne de Bretagne, Université de Rennes 1, France
[1]CNRS UMR 6082 FOTON, Enssat, 6 rue de Kerampont, BP 80518, 22305 Lannion, France
[2] UMR 6226 Institut des Sciences Chimiques de Rennes, IUT de Lannion, rue Ed.Branly, BP 30219, F22302 Lannion Cedex, France
delcourt@enssat.fr, loic.bodiou@univ-rennes1.fr, joel.charrier@univ-rennes1.fr, lemaitre@enssat.fr, nathalie.lorrain@univ-rennes1.fr, bosc@enssat.fr, sylvain.achelle@univ-rennes1.fr

Abstract: In order to obtain non-linear waveguides for all-optical signal processing, new nonlinear polymer waveguides incorporating chromophores have been designed and processed using standard photolithographic steps. Polymer refractive index changes with chromophore concentration are presented. Waveguides exhibiting single mode propagation and high optical field confinement are demonstrated and optical propagation losses of 4.1 dB/cm at 1550 nm are measured.

Introduction:

Passive and active optical components for applications in optical fiber communications, optical interconnects inside and between CMOS chips, and in biophotonics (integrated sensors, lab-on chips) are readily available due to progresses in silicon photonics technologies. One of the major future challenge still concerns the development of compact optical components operating at low power, to process high-bit rate signals (about 100 Gbit/s and above). Although several high-speed components have been demonstrated using the high third-order nonlinearity of silicon based waveguides[1], these devices suffer from limitations arising from two-photon absorption (TPA) and free-carrier absorption processes in silicon. To overcome these detrimental effects, integrated structures based on higher bandgap materials, such as AlGaAs, GaInP or chalcogenide glasses have emerged[2]. An alternative approach, which we describe in this paper, could take benefit from the potentially larger third-order susceptibility $\chi^{(3)}$ of organic based materials. Indeed, nonlinear refractive index (n_2) values for organic materials like Polydiacetylene para-toluene sulfonate (PDA-PTS) or Poly(p-PhenyleneVinylene) (PPV) can reach 2.10^{-16} $m^2.W^{-1}$ which is one order of magnitude larger than conventional inorganic semiconductors ($Al_{0.2}GaAs$, Si) or chalcogenides (As_2Se_3).

Design and fabrication:

A molecular engineering methodology is now emerging to further improve the nonlinear efficiency of these organic molecules[3]. The current knowledge of the structure-property relationships indicates a certain number of important trends[4] to design efficient third-order NLO materials as increasing the conjugation length for quasi one-dimensional molecules (such as polymethines), enhancing the intramolecular charge transfer by heteroatomic conjugation incorporation or designing quadrupolar (D-π-A-π-D like DDMEBT molecule[5] used by Koos and co-workers to demonstrate all-optical demultiplexing[5]) and octupolar structures. Following these guidelines, quadrupolar molecules based on pyrimidine and triphenylamine units with a D-π-A-π-D structure[6] have been synthesized via short and high-yielding reactions. Polymeric buried waveguides with different core dimensions have been processed using standard i-line photolithography and reactive ion etching process. PMATRIFE (Poly(2,2,2 MethAcrylate of TRIFluoro-Ethyl) was used for both lower and upper claddings (n=1.41 at 1.55 µm). The waveguide core of the structure is made from chromophores (*Fig. 1a*) incorporated (20 % by weight) in PolyMethyl MethacrylImide (PMMI). *Fig. 1b* shows the cross section of one of the processed waveguides. Using the prism coupling technique, the refractive index of this core layer was measured to range from n=1.515 to 1.55 at a wavelength of 1.55 µm depending on the chromophores concentration (see *Fig. 1c*). UV-Visible spectra (not shown) of chromophores dissolved in in CH_2Cl_2 show two absorption bands located at 301 and 427 nm. All polymer layers were deposited by spin-coating. To avoid subsequent dissolution, thin inorganic barriers layers (SiO_2 or SiN_X) were

deposited by PECVD between the different organic layers. The core dimensions were designed using Olympios software to maximize the optical density in the nonlinear region of the waveguide.

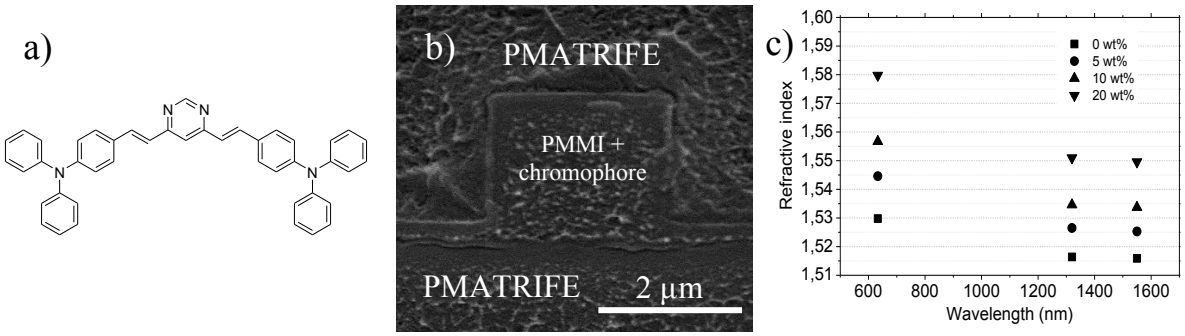


Fig. 1: a) Molecular structure of the chromophores, b) SEM image of the waveguide cross section and c) Wavelength dependence of the core material refractive index for different chromophore concentrations.

Optical characterizations of waveguides:

To minimize coupling losses, microlensed fibers were used to launch a broadband laser source around 1550 nm into the waveguides and to collect outcoming light. Using far field experiments, mode diameter of 2.2 µm were measured at 1550 nm for microlensed fibers. Single mode propagation in the waveguide was confirmed by imaging the output facet of the waveguide on an infrared camera through a high magnification and numerical aperture microscope objective (*Fig. 2a*). A 2.4 µm mode field diameter was measured (at $1/e^2$) by comparing this intensity profile to that of microlensed fibers. Waveguide propagation losses of 4.1±0.3 dB/cm were determined using the cut-back technique (*Fig. 2b*). Several waveguides of the same size (width=1.5 µm, height=2 µm) were characterized for three different sample lengths (0.4, 1.2 and 1.6 cm) without facet polishing after cleaving.

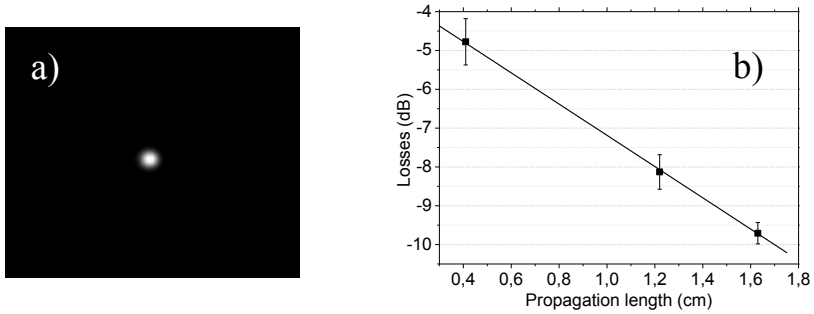


Fig. 2: a) Intensity profile of the waveguide output (w=1.5 µm, h=2 µm) b) Loss measurements of the polymer waveguide (w=1.5 µm, h=2 µm) derived from the by cutback method.

Conclusions:

Nonlinear molecules potentially fulfilling simultaneously the main requirements of all-optical processing applications (large nonlinear refractive index n_2 at 1.55 µm, reduced losses related to TPA around 1.55 µm and ultrafast response (<ps) of the nonlinear refractive index) have been synthesized. The fabrication process of single mode organic-based nonlinear waveguides exhibiting propagation losses of 4.1±0.3 dB/cm has been described. These results show that the incorporation of nonlinear chromophores in standard polymers could be a way to implement waveguides dedicated to efficient all-optical signal processing.

References

[1] E. Dulkeith *et al*., *Optics Express*, **14**, 5524 (2006).
[2] H. Oda *et al*., *Applied Physics Letters*, **90**, 231102 (2007), S. Combrié *et al.*, *Applied Physics Letters*, **95**, 221108 (2009) and K. Suzuki *et al*., *Optics Express*, **17**, 22393 (2009)
[3] J.M. Hales *et al*., *Science*, **327**, 1485 (2010).
[4] R.R. Tykwinski *et al*., *Journal of Physical Chemistry B*, **102**, 4451 (1998).
[5] B. Esembeson *et al*., *Advanced Materials*, **20**, 4584 (2008) and C. Koos *et al*., *Nature Photonics*, **3**, 216 (2009).
[6] S. Achelle *et al*., *Journal of Organic Chemistry*, **74**, 3711 (2009).

Fabrication of Y-Splitters and Mach-Zehnder interferometers on (Yb, Nb):$RbTiOPO_4$/ $RbTiOPO_4$ epitaxial layers by Reactive Ion Etching and on $RbTiOPO_4$ by Cs^+ diffusion

M.A. Butt[1], R. Solé[1], M.C. Pujol[1], A. Ródenas[1], G. Lifante[2], J.S. Wilkinson[3], A. Choudhary[3], G.S. Murugan[3], D.P. Shepherd[3] , M. Aguiló[1] and F. Díaz[1]

1. Física i Cristal·lografia de Materials i Nanomaterials (FiCMA-FiCNA) and EMaS, Universitat Rovira i Virgili (URV), Marcel·lí Domingo s/n, E-43007 Tarragona, Spain,
2. Departamento de Física de Materiales, Universidad Autónoma de Madrid 28049 Madrid, Spain,
3. Optoelectronics Research Centre, University of Southampton, Southampton, SO171BJ, United Kingdom
** mariacinta.pujol@urv.cat, rosam.sole@urv.cat*

Abstract We present the fabrication and characterization of Y-splitters and Mach-Zehnder Interferometers by the two different techniques of reactive ion etching and ion exchange on (Yb,Nb):$RbTiOPO_4$/ $RbTiOPO_4$ and $RbTiOPO_4$, respectively. Liquid phase epitaxy was used to grow planar thin films followed by reactive ion etching for fabrication of structures over it. Cs^+ ions were used for diffusion process because they produce a significant increase in the refractive index and the ionic radius is close to the Rb^+ radius. It has been found that these structures can guide light with TM polarization at 1520 nm.

1. **Introduction:** Rubidium titanyl phosphate $RbTiOPO_4$ (RTP) belongs to a highly diverse and versatile structural family and is of interest because of its large non-linear optical coefficients, wide transparency, high laser damage threshold, high chemical stability and low dielectric constants.[1] RTP has similar non-linear optical coefficients to $KTiO(PO_4)$ (KTP) but, unlike KTP, it can be doped with Yb^{3+} to obtain a high enough concentration to allow efficient laser action.[2] Thus, RTP is a strong candidate as a platform material for integrated photonics. Reactive ion etching (RIE) is a commonly used method in etching of semiconductors, but there is little literature available on the plasma-based etching of RTP. Recently, Cs^+ ion exchange channel waveguides on RTP have been reported.[3] Cs^+ ions were used for diffusion process because they produce a significant increase in the refractive index and the ionic radius is close to that of Rb^+ . The motivation for the current work is to make use of all these excellent properties of RTP (001) to fabricate integrated EO devices such as Mach-Zehnder Interferometers (MZIs) by different techniques like RIE and Cs^+ ion difusion.

2. Experimental details: RTP single crystals were grown by the top-seeded solution growth-slow cooling (TSSG) technique. Thin plates with (001) orientation were obtained to be used as substrates for Liquid Phase Epitaxy (LPE) growth and Cs^+ diffusion. RTP single crystals are orthorhombic biaxial crystals, and the (001) plane contains the optical phase matching direction for doubling light at 1 μm. LPE was used to obtain (Yb,Nb):RTP/RTP(001) in a well-isolated cylindrical vertical furnace with practically zero thermal gradient. The refractive indexes of the epitaxial layer and the substrate have been measured at 1550 nm by the dark mode method.

RIE on (Yb,Nb):$RbTiOPO_4$/$RbTiOPO_4$ epitaxial layers for the fabrication of Y-splitters and MZIs: After obtaining 6-7 μm thickness epitaxial layers, a metal layer was deposited on it which acts as a hard mask during RIE. Channel designs were transferred to the mask by conventional photolithography and the sample was etched with metal etchant to remove the unwanted parts of the metal mask. Finally**,** the samples with hard metal mask were reactive ion etched in a Plasmalab 80Plus (OIPT) to fabricate the structures. The process was carried out at 250 W, with 40 mTorr pressure and a gas combination of Ar (10 sccm) and SF_6 (10 sccm), which was optimized in previous work.[4] Etching times were in the range of 200-600 min. The width and height of the designed patterns were 6-9 μm and 5 μm, respectively, to support a fundamental mode at wavelengths near 1520 nm. A

thin layer of RTP was grown using the LPE technique at the end of the fabrication process to act as cladding for increasing light confinement, and also serves to lower the propagation losses.

Y-splitters and MZIs on $RbTiOPO_4$ by Cs^+ ion Exchange: A Ti layer was deposited on the RTP (001) substrate by sputtering. The designs of Y-splitters and MZIs of 9 mm in length and 6 µm in width along ***b*** direction were transferred onto a photoresist by photolithography. After developing the exposed part, the design was transferred to the Ti mask by etching it with H_2O_2:NH_4OH in 2:1 molar ratio. Cs^+ diffusion was carried out by immersing the sample with the Ti pattern horizontally in a crucible containing 25 g of $CsNO_3$ at 698 K for 2 h, rotating at 40 rpm.

3. Results and discussion: We have obtained very high quality crystals with dimensions close to 17x18x18 mm^3 along the **a**, **b** and **c** directions respectively, without any cracks and inclusions. The same is applicable for epitaxial layers grown by LPE. With RIE, a maximum etch rate of 8.5 nm/min for the epitaxial layer was obtained, and the deepest etch achieved was 2.8 µm. Figure 1a) shows an ESEM image of a part of the MZI design etched on an epitaxial layer. The LPE growth of cladding shows a clear interface of growth, as shown in figure 1b). Optical waveguiding of the fundamental mode at 1520 nm was observed.

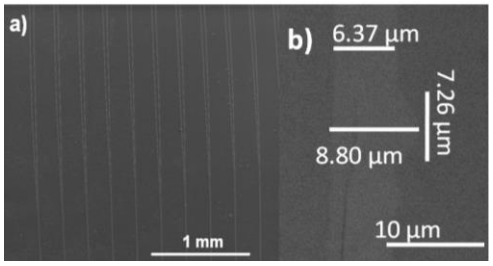


Fig. 1: a) Input section of the MZIs fabricated on (Yb,Nb):RTP/RTP; b) cross sectional view of a MZI .

In case of Cs^+ diffused channels**,** EPMA analysis show traces of Cs^+ along ***c*** direction to a depth of 6 µm. In all the MZIs and Y-splitters, the 1520 nm light was guided only in the TM polarization because of the existing relatively higher n_z refractive index contrast as compared to n_x and n_y . Figure 2 shows the horizontal intensity cross section (a) and the measured near field pattern (b) of the output guided modes in a 9 mm long Y-splitter. A Gaussian profile with dimensions of 15.6 µm x 9.0 µm for the left arm and 13.2 µm x 8.5 µm for the right arm in the ***b*** and ***c*** directions was measured.

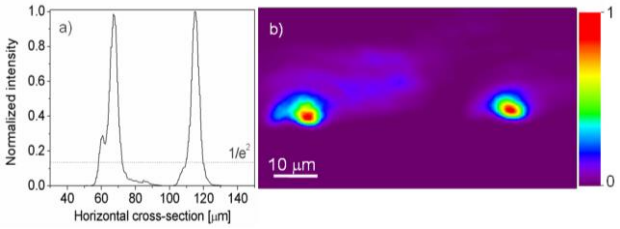


Fig. 2: a) Horizontal intensity cross section of the near field profile and b) measured near-field image, of the fundamental mode at 1520 nm wavelength of a Y-splitter.

4. Conclusion: RIE was used to fabricate Y-splitters and MZIs on (Yb,Nb):RTP/RTP(001) samples. Y-splitters and MZIs in RTP fabricated by Cs^+ ion exchange have been reported for the first time to our knowledge. Optical waveguiding was achieved at a wavelength of 1520 nm using both the RIE and Cs^+ diffusion.

Acknowledgments. This work was supported by the Spanish Government under MAT2011-29255-C02-02, TEC2010-21574-C02-01, TEC2010-21574-C02-02, by the Catalan Authority under 2009SGR235 and by the European Union under Project No. FP7-SPA-2010-263044. M. Ali Butt thanks the Catalan Government for the FI-DGR fellowship 2012FI-B 00192.

References

1. M.N. Satyanarayan, A. Deepthy, and H.L Bhat, *Crit. Rev.Solid State Matter. Sci.*, vol. **24**, no. 2, 103-191(1999).
2. X.Mateos, V.Petrov, A.Peña, J.J.Carvajal, M.Aguiló, F.Díaz, P. Segonds, B. Boulanger, *Opt.Lett.* **32**,1929-1931(2007).
3. J. Cugat, R. Solé, J.J. Carvajal, X. Mateos, J. Massons, G. Lifante, F. Díaz, and M. Aguiló, *Opt. Lett*, **38**,323-325 (2013).
4. A. Choudary, J. Cugat, K. Pradesh, R. Solé, F. Díaz, M. Aguiló, H.M.H. Chong and D.P. Shepherd, *J. Phys. D: Appl. Phys.* **46**,(6pp),145108 (2013).

Carbon nanotubes incorporated-hybrid waveguides for photonics applications

L.Bodiou[1], J. Charrier[1], J. Lemaitre[1], E. Delcourt[1] and D. Bosc[1]

M. Guézo[2], T. Batte[2], Q. Gu[2], J. Le Pouliquen[2], H. Folliot[2]

UEB, Université Européenne de Bretagne, Université de Rennes 1, France
[1]CNRS UMR 6082 FOTON, Enssat, 6 rue de Kerampont, BP 80518, 22305 Lannion, France
[2]CNRS UMR 6082 FOTON, INSA, avenue des buttes de Coësmes, CS 70839, 35708 Rennes Cedex, France
loic.bodiou@univ-rennes1.fr, joel.charrier@univ-rennes1.fr, lemaitre@enssat.fr, delcourt@enssat.fr, bosc@enssat.fr, maud.guezo@insa-rennes.fr, thomas.batte@insa-rennes.fr, qingyuan.gu@insa-rennes.fr, julie.le-pouliquen@insa-rennes.f, herve.folliot@insa-rennes.fr

Abstract: Semiconducting carbon nanotubes (CNT) exhibit large nonlinear- and strong quasi-one dimensional excitonic optical properties. Their integration in integrated waveguides could lead to very efficient light-emitting devices or optical signal processing functions. We described the fabrication and optical characterization of hybrid planar waveguides incorporating CNT. Ways of further enhancing light interaction with the CNT namely ridge waveguides processing and CNT alignment are also presented.

Introduction:

Carbon nanotubes (CNT) and graphene have attracted large research interest due to their unique optical, electrical, chemical and mechanical properties. Semiconducting carbon nanotubes have found photonics applications as nanoscale light emitters and photovoltaic devices[1] or as saturable absorber for passive mode locking of different laser types or optical switching[2]. Indeed, LED operations have been demonstrated using CNT[3] as well as CNT guided luminescence[4] and optical gain[5]. All-optical signal processing functions have also been developed using highly nonlinear waveguides. Wavelength conversion based on four wave mixing has been obtained using CNT deposited on top of tapered fiber[6], D-shaped fiber[7] or integrated waveguide based on Ge doped silica[8]. In these devices, CNT were interacting with the optical beam through evanescent field. To further benefit from the very large nonlinear refractive index of CNT, which surpasses that of silicon by several orders of magnitude, we proposed to use direct interaction between the CNT and the laser beam.

Fabrication:

A hybrid structure composed of a lower polymer cladding made of benzocyclobutene (BCB) and silicon nitride (SiN_x) core incorporating single-walled carbon nanotubes (SWCNT) was designed.

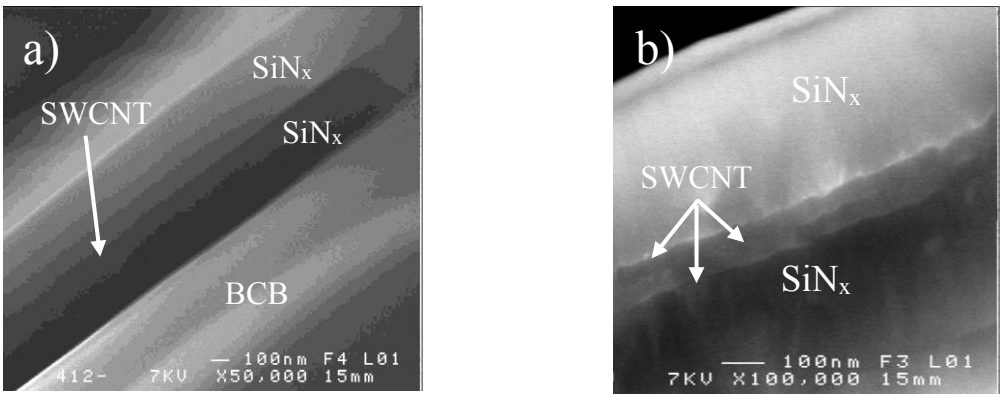


Fig. 1: SEM pictures of planar waveguides incorporating a) one SWCNT layer or b) three SWCNT layers.

BCB (5µm thick) was deposited on Si substrate by spin-coating from solution at a speed of 1500 rpm followed by soft bake at 120°C for 2 minutes and hard bake under nitrogen at 250°C for an hour. The waveguide core is made of two SiN_x layers between which one or three thin SWCNT layers are deposited by spray coating. The SiN_x layers were deposited by sputtering and their total thickness is

640 or 870 nm for one- or three SWCNT layers cavity respectively (*Fig. **1***). For the second sample, a 30 nm-thick spacer was deposited between the three SWCNT layers (*Fig. 1b*). SWCNT surrounded by micelle were obtained by mixing 10 mg of pristine HiPCO single-walled CNT powder to a 20 ml of 2% sodium cholate water solution followed by sonication for 1 hour, ultracentrifugation at 25000×g for 1 hour and filtration of the upper suspension layer. Linear absorption spectra indicate that the SWCNT first excitonic transition energies are suitable for 1550 nm-window photonics applications[2].

Optical characterization and discussion:

Planar waveguides with air as upper cladding were first characterized. To minimize coupling losses, microlensed fibers with optical mode diameter of 2.2 µm were used to launch a broadband laser source around 1550 nm into the waveguides. Optical propagation at 1550nm in 3.5 mm long-waveguides was confirmed by imaging the output facet of the waveguide on an infrared camera through a high magnification and numerical aperture microscope objective (*Fig. 2a*).

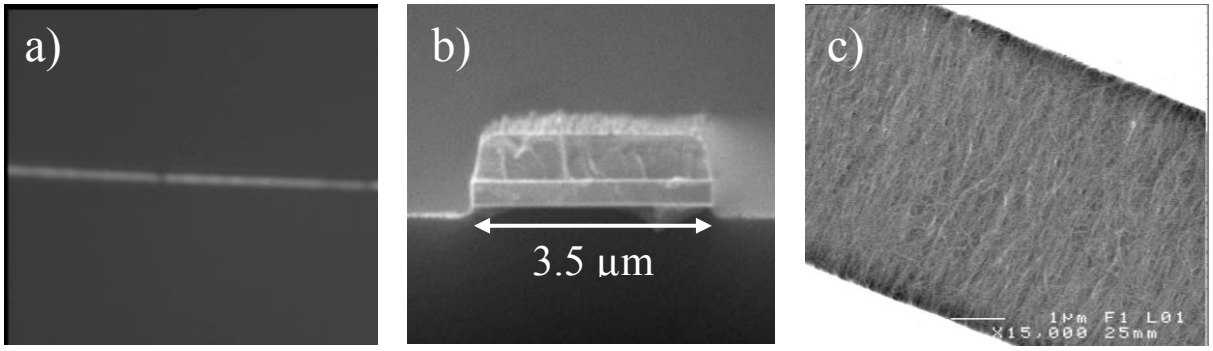


Fig. 2: a) Intensity profile of the planar SWCNT incorporated-waveguide output, b) SEM picture of ridge SiN_x waveguide with BCB lower cladding (resin was not removed) c) SWCNT aligned by dielectrophoresis between gold electrodes.

Ridge waveguides have been processed using standard i-line photolithography and SF6 based reactive ion etching (*Fig. 2b*) process for samples with BCB lower cladding layers and SiN_x core without SWCNT. For samples incorporating SWCNT in the waveguide core, worm-like defects occurs during the post-exposure bake. A modification of the thermal steps of BCB curing and photolithographic process could help overcoming these defects[9]. Interaction of SWCNT with the optical beam could be further improved by aligning SWCNT. To this end, electrophoresis experiments[10] have been performed. *Fig. 2c* shows the preliminary results obtained on the alignment of SWCNT. Transferring this technology to integrated waveguides incorporating CNT should pave the way to the development of efficient devices dedicated to optical signal processing or light emission.

Conclusion:

Waveguides with BCB lower cladding and SWCNT-incorporated SiN_x core have been processed. If problems occurring during photolithographic steps have hindered the optical characterization of ridge waveguides, optical propagation through the planar structure has been observed. These results prove that waveguides with SWCNT incorporated-core could be very promising structures to implement nanoscale light emitters or optical signal processing functions.

References

[1] P. Avouris *et al*., *Nature Photonics*, **2**, 341 (2008)
[2] H. Nong *et al*., *Applied Physics Letters*, **96**, 061109 (2010)
[3] S. Wang *et al*., *Nano Letters*, **11**, 23 (2011) and M. Kinoshita et al., *Optics Express*, **18**, 25738 (2010).
[4] E. Gaufrès *et al*., *ACS Nano*, **6**, 3813 (2012).
[5] E. Gaufrès *et al*., *Applied Physics Letters*, **96**, 231105 (2010).
[6] K.K. Chow *et al*., *Applied Physics Letters*, **96**, 061104 (2010).
[7] K.K. Chow *et al*., *Optics Express*, **17**, 15608 (2009).
[8] K.K. Chow *et al*., *Optics Letters*, **35**, 2070 (2010).
[9] D. Bosc *et al*., *Applied Surface Science*, **253**, 6162 (2007).
[10] S. Shekhar *et al*., *ACS Nano*, **5**, 1739 (2011).

Near and Mid Infrared Lithium Niobate based Integrated Optics Interferometer based on SWIFTS-Lippmann

Fabrice Thomas[1], Mikhael de Mengin[1], , Samuel Heidmann[1], Nadege Courjal[2], Gwenn Ulliac[2], Alain Morand[3], Pierre Benech[3], Etienne Le Coarer[1], and Guillermo Martin[1]

[1]UJF-Grenoble 1/CNRS-INSU, Institut de Planétologie et d'Astrophysique de Grenoble (IPAG) UMR 5274, Grenoble, F-38041, France
fabrice.thomas2@obs.ujf-grenoble.fr, mikhael.demenginpoirier@obs.ujf-grenoble.fr, samuel.heidmann@gmail.com, Etienne.Le-Coarer@obs.ujf-grenoble.fr, guillermo.martin@obs.ujf-grenoble.fr
[2] FEMTO-ST, Université de Franche-Comté, Besançon, 25030, France
gwenn.ulliac@femto-st.fr, nadege.bodin@univ-fcomte.fr
[3]IMEP-LAHC, Minatec, 3 Parvis Louis Néel, CS 50257, 38016 Grenoble, France
morand@minatec.inpg.fr, pierre.benech@phelma.grenoble-inp.fr

Abstract: High resolution spectrometers are nowadays achievable in compact devices using integrated optics. The approach developed here consists in obtaining a static interferogram by means of a Fresnel reflection at the waveguide output (Lippmann interference between forward and backward beams) and then sample the fringes by periodically etching the waveguide with transverse nano-grooves, that will collect a negligible part of the flux. We present the first SWIFTS-Lippmann interferometer in the near and mid-infrared, thanks to high form factor grooves obtained by focused ion beam in lithium niobate, which opens the way to electro-optic modulation of the interferogram and thus, sampling on-chip, without any moving part.

Introduction: High resolution integrated spectrometers are an active field of research, thanks to progress in microtechnologies and materials research, aiming at miniaturization and access to different spectral windows [1, 2, 3, 4, 5, 6]. We present in this work the developments of SWIFTS-Lippmann integrated interferometer based on lithium niobate (LN) waveguides in the near and mid-infrared. SWIFTS is the acronym for Stationary Wave Integrated Fourier Transform-Spectrometer [7], where a high resolution integrated optics spectrometer can be obtained by periodically sampling the stationary wave obtained by superposition of direct and backward guided optic beams, using evanescent out-coupling thanks to nanodots or dielectric discontinuities periodically distributed along the surface of a waveguide [8, 9]. In order to sample the stationary wave, we use Focused Ion Beam technology (FIB) to realize high aspect ratio grooves perpendicular to the waveguide and use the diffused energy to sample the optical field. Here we present the realization of high form factor FIB grooves in a LN channel waveguide, its near- and mid-infrared characterization and the application to measurement of effective refractive index of the waveguide and high resolution spectroscopy. The use of an electro-optical material such as LN opens the way to internally scan the fringes under the grooves in order to improve sampling, or shift the wide-band interferogram towards the desired sampling region (i.e. avoiding bad sampling centers) by using a phase modulation stage prior to the Lippmann interference.

Theoretical Model: In a SWIFTS-Lippmann configuration, the superposition of forward and backward reflected beams in a channel waveguide (X-cut, Y-propagation) is given by:

$$I(\lambda, y, E) = I_0 \, \mathrm{e}^{-\alpha y}\left[1 + R\,\mathrm{e}^{-4\alpha(L-y)} - 2\sqrt{R}\,\mathrm{e}^{-2\alpha(L-y)}\cos\left[\frac{2\pi}{\lambda}n(\lambda, E)2(y-L)\right]\right] \qquad (1)$$

Where n(λ,E) is the effective refractive index of the fundamental mode and R is the Fresnel reflexion intensity coefficient of LN waveguide/air interface. The period of the static interferogram is given by i=λ/2n. At a fixed position y (i.e. at a given diffusion center) the intensity of the radiated signal oscillates with wavelength. The period of this signal is given by, in terms of wavenumber:

$$\Delta\sigma = \Delta\lambda/\lambda^2 = 1/2ny \qquad (2)$$

, where y is the distance to the waveguide facet. By measuring the period of the fringes at different (but very close) wavelengths at a given position y, one can recover the effective refractive index of the waveguide.

Fabrication: We firstly produced the optical waveguides for X-cut $LiNbO_3$ wafers, through diffusion of 180-nm thick 12 µm wide ribs of titanium at 1030°C for 50 hours. Then, we realized the grooves, perpendicular to the waveguide direction, by Focused Ion Beam. The FIB grooves where realized at FEMTO-ST Beam (FIB Dual Beam FEI Helios 600i) in four hours with a probe current of 24 pA, a step size of 12 nm, and a dwell-time of 0.1 ms. We realized 50 grooves, 170nm wide, 633nm deep, with a period of 10 µm, giving a total sampling length of 500 µm (see fig.1).

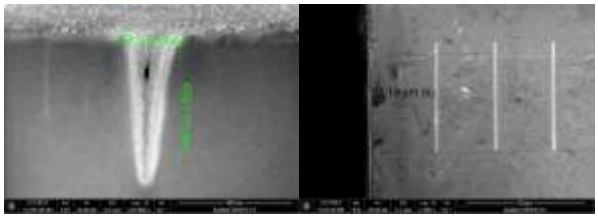


Figure 1: Left: MEB image of groove, showing typical dimensions (170nm long, 633nm depth). Right: Periodicity of the grooves, transverse to the waveguide, and distance from the edge.

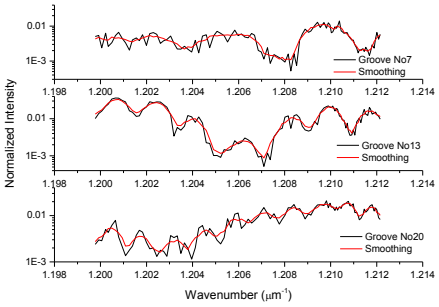


Figure 2: Normalized intensity diffused by different grooves depending on the distance y to the edge (see eq.2). (up): 7,81 µm; (middle): 141µm and (bottom): 211 µm.

We have used a minimum sampling period of 0.1 nm and focused on the first 25 diffusion centers. Theoretical values for spectral resolution, S.R., and spectral window, $\Delta\sigma$, are $S.R.=2nL/\lambda$ and $\Delta\sigma=1/4n\Delta L$ [7]. With L=500 µm (length of the sampling region), n=2.26 the effective refractive index and λ=0.85 µm, we expect S.R.=2350, which is insufficient to resolve the Sacher Laser Diode linewidth (500 kHz), but gives an idea of the spectral resolution we can obtain in this simple device. The spectral window is $\Delta\sigma=0.0125\ \mu m^{-1}$ with ΔL=10 µm the distance between grooves.

Results: Using a Sacher tunable source, we scanned the wavelength from 825 to 833 nm, while observing the signal diffracted by the grooves. As given by eq. 2, at a given position y (i.e. observing the light diffused by a given groove), the intensity oscillation varies more and more rapidly as we move away from the waveguide edge (as y increases). The first images of sampling where obtained by using a Sacher tunable source, that allowed us to scan between 825 - 833 nm with a step of 0.1 nm. The results are shown in figure 2. Studying the first 25 grooves, we obtain the period of the sampled signal for different sampling centers as a function of their distance to the edge and can extract the effective refractive index of the fundamental mode of the waveguide with high accuracy.

Results in mid IR as well as simulations on the radiated field as a function of the grooves form factor will also be presented.

References

1. S. Rommeluere et al. *Proceedings of SPIE*, **5406**, pp. 170-177, (2004).
2. R.F. Wolffenbuttel, *J. Micromech. Microeng.* **15**, Issue7, pp. S145-S152, (2005).
3. J. Bland-Hawthorn, A. Horton, *Proceedings of SPIE*, **6269**, 62690N-1-14, (2006).
4. M. Froggatt and T. Erdogan, *Opt. Lett*, **24**, Issue 14, pp. 942-944, (1999).
5. D. Knipp et al., *IEEE Trans. On Electron Devices* **52** (3), pp. 419-426, 2005.
6. P. Cheben et al., *Opt. Exp.* **15**, pp. 2299-2306, (2007).
7. E. Le Coarer, S. Blaize, P. Benech, I. Stefanon, A. Morand, G. Lérondel, G. Leblond, P. Kern, J.M. Fedeli, P. Royer, *Nature Photonics*, **1** (8), pp.473-478, (2007).
8. C. Bonneville et al, *SPIE MOEMS Photonics West*, (2013).
9. F. Thomas et al, *SPIE OPTO Photonics West*, (2014).

Vertically-coupled AlGaAs microdisks using selective lateral oxidation

G. Lafleur[1,2], A. Larrue[1,2], G. Almuneau[1,2], P.-F. Calmon[1,2], A. Arnoult[1,2], O. Gauthier-Lafaye[1,2], S. Calvez[1,2]

[1] LAAS-CNRS, 7 avenue du Colonel Roche, BP54200, F-31400 Toulouse, France, and
[2] Univ de Toulouse, Université Paul Sabatier, LAAS, F-31400 Toulouse, France
glafleur@laas.fr, almuneau@laas.fr, ogautie@laas.fr, scalvez@laas.fr

Abstract: This paper presents a planarization-free method to realize microdisk resonators that are vertically-coupled to buried access waveguides. The novel 3-dimensional integration scheme exploits selective lateral oxidation of aluminum-rich AlGaAs layers. Microdisk devices resulting from a first fabrication run demonstrate the proof-of-principle of this approach. Their optical characterization is currently being carried out and will be presented at the meeting.

Introduction

Integrated whispering gallery mode (WGM) resonators in the form of micro-ring, micro-disk or micro-racetrack resonators have attracted a lot of attention since they can provide large field enhancement in a compact format and, thereby, enable the fabrication of selective filters, low-threshold emitters, high-speed modulators, sensitive sensors or nonlinear converters [1-3].

In order to couple light in and out of these resonators, most devices use evanescent coupling which can be realized either by lateral integration i.e. by having the access waveguide and the resonator in the same plane or by vertical integration where the waveguide lies (typically) below the resonator. The latter approach is generally preferred as it offers greater fabrication tolerances and enables different materials to be used for the resonator and its access waveguide. The conventional method[4,5] to make such vertically-coupled resonators begins with the definition of the access channel waveguides followed by the deposition of a cladding layer. The surface of this overlayer is corrugated and needs to be planarized to be able to make the desired high-quality factor resonators. Furthermore, the thickness of this cladding layer also needs to be precisely controlled since it adjusts the degree of coupling, making this planarization a critical processing step. Finally, after re-alignment, the definition of the resonator completes the device fabrication sequence.

Here, we report an alternative method to fabricate such vertically-coupled resonators which exploits the lateral oxidation of buried layers and thus does not require any planarization.

Microdisk device design

The device design consists in a buried oxide-confined rib waveguide that is vertically-coupled to a GaAs-based microdisk resonator. The multi-layer stack is based on AlGaAs alloys. The waveguide claddings ($Al_{0.7}Ga_{0.3}As$ and $Al_{0.3}Ga_{0.7}As$) were chosen to be asymmetric such that a greater field penetration occurs towards the resonator. The 716nm-thick resonator/waveguide coupling region includes two 68nm-thick $Al_{0.98}Ga_{0.02}As$ layers to be laterally oxidized, sandwiched between three $Al_{0.3}Ga_{0.7}As$ layers. The partial oxidation of these layers will form oxide apertures and thus induce lateral waveguiding. The upper layer (located at 100-nm beneath the disk core) is also used to increase the vertical confinement in the disk whilst the lower is essentially there to set the lateral confinement of the access waveguide. This layer was positioned relatively far (150-nm-away) from the GaAs-based core of the access waveguide to provide single-mode operation for (weakly-confined ($\Delta n \sim 10^{-2}$)) large-width modes, thereby reducing the dependence on lateral offset of the waveguide/resonator coupling. The (0.68μm) thickness of the GaAs-core resonator was also set to support vertically only the quasi-TE fundamental mode.

Fabrication process

The AlGaAs (vertical) structure was grown on a (100) GaAs substrate by molecular beam epitaxy (Riber 412). The wafer was post-processed using two photolithography steps using direct laser writing

(Heidelberg DWL 200). The two mask levels are respectively used to define the access waveguides and the resonators in SPR700 photoresist with a re-alignment accuracy estimated to be better than 0.25µm. These patterns were transferred in the AlGaAs stack by an ICP-RIE plasma etch using a $Cl_2/N_2/Ar$ gas mixture and the etch depth was monitored by optical reflectometry. Simultaneous wet thermal oxidation of both $Al_{0.98}Ga_{0.02}As$ layers was carried out in a custom furnace with in-situ optical monitoring[6], equipment now commercially available from AET Technologies. During the oxidation, the sample was held at a substrate temperature of 420°C, in a reduced pressure environment (~0.5 atm.), and exposed to a mixed $H_2/N_2/H_2O$ gas steam generated by an evaporator-mixer system at 95°C. The oxidation front progressed linearly at a rate of 0.31µm/min and was stopped when the oxide aperture width reached 4µm. The samples were then polished to a substrate thickness of ~150µm, cleaved and mounted on Si sub-mounts.

Figure 1 shows a top-view optical microscope image of one of the fabricated micro-disks with schematic cross-sections. We note that the oxidation of the two AlGaAs layers is not strictly identical, a phenomenon we believe to be the result of oxide-induced strain distribution in the asymmetric vertical structure. The bottom waveguide aperture width was measured to be ~3.7µm by using a focused ion beam (FIB) and scanning electron microcopy (SEM) characterizations, while the upper confining layer aperture width was observed to be ~1.8µm larger.

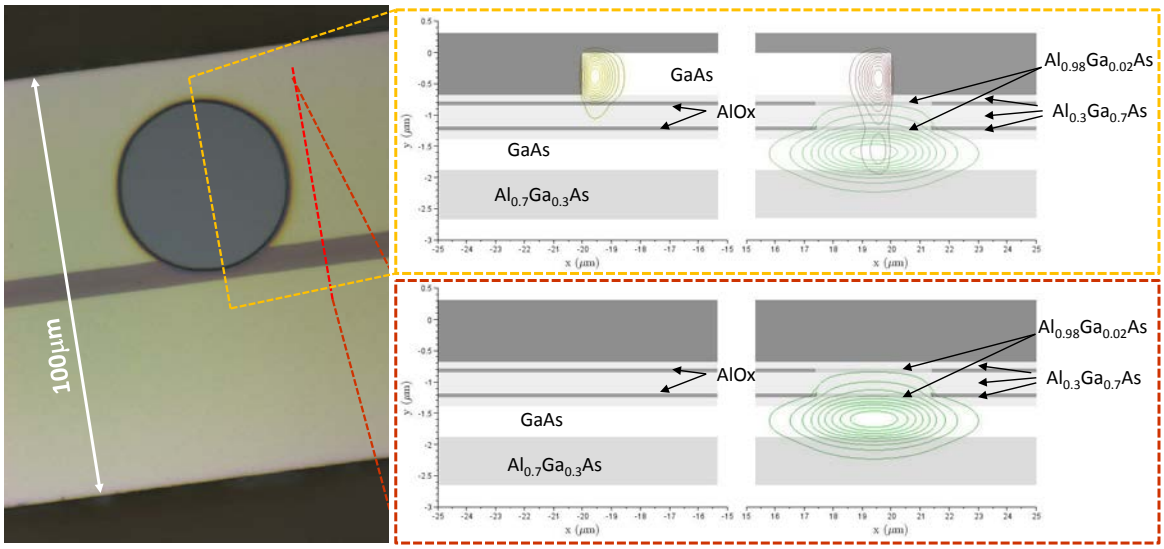


Fig. 1: Top-view optical microscope image of a fabricated AlGaAs/AlOx vertically-coupled microdisk resonator and rib waveguide, and associated schematic cross-sections showing the corresponding vertical structure and calculated normalized E-field profiles[7,8].

Conclusion

We have devised a novel approach to vertically integrate microdisk resonators on top of their access waveguides by exploiting selective lateral oxidation of aluminum-rich layers on a GaAs platform. The optical characteristics of the devices are being assessed and will be reported.

Acknowledgement: This work was partly supported by the French RENATECH network and by the CNES R&T contract R-S13/LN-0001-025.

References

1. K.J. Vahala., *Nature,* **424**, pp. 839–846, (2003).
2. J. Ward *et al., Laser Photonics Review,* **5**, pp. 553–570, (2011).
3. S. Feng *et al., Laser Photonics Review,* **6**, pp. 145–177, (2012).
4. L. Razzari *et al., Nature Photonics,* **4**, pp. 41–45, (2009).
5. M. Ghulinyan *et al., Photonics Technology Letters,* **23**, pp. 1166–1168, (2011).
6. G. Almuneau *et al., Semiconductor Science and Technology,* **23**, pp. 105021, (2008).
7. A.B. Matsko *et al.*, *Journal of Selected Topics in Quantum Electronics,* **12**, pp3-14 (2006)
8. A.B. Fallahkhair *et al.*, *Journal of Lightwave Technology,* **26**, pp1423-1431 (2008)

Step-index Nd:YAG ceramic buried channel waveguides fabricated by direct laser writing

J. Martínez de Mendíbil[1], A. Benayas[1,2], D. Jaque[1], A. K. Kar[3], A. Ródenas[4] and E. Cantelar[1]

[1] Departamento de Física de Materiales, Facultad de Ciencias, Universidad Autónoma de Madrid, Madrid 28049, Spain

[2]Univ Quebec, Inst Natl Rech Sci Energie Mat & Telecommun, Varennes, PQ J3X 1S2, Canada

[3]School of Engineering and Physical Sciences, David Brewster Building, Heriot Watt University, Edinburgh EH14 4AS, UK

[4]Física i Cristal·lografia de Materials i Nanomaterials(FiCMA-FiCNA). Universitat Rovira i Virgili (URV), Campus Sescelades c/ Marcel·lí Domingo, s/n. E-43007 Tarragona, Spain

Abstract: Multi-scan femtosecond laser writing has been used for the fabrication of high contrast buried channel waveguides in Neodymium doped YAG ceramics. The fabricated structures have been demonstrated to be capable of light confinement in the near infrared. Confocal fluorescence microscopy has been used to elucidate the femtosecond assisted modifications induced in the Nd:YAG network. Based on the obtained fluorescence images the mechanisms leading to the refractive index increment at the modified zone have been discussed. The near infrared laser properties of the fabricated structures have been also investigated.

Since the pioneering work of Davis et al.,[1] direct laser writing (DLW) with subpicosecond pulses has become a well-established and versatile technique for the microprocessing of transparent media for integrated optics applications. Because of its inherent advantage for three dimensional (3D) processing inside the bulk of substrates, ultrafast DLW has already been used for the straightforward demonstration of numerous photonic devices such as 3D photonic crystals,[2] photonic lanterns,[3] integrated gratings,[4] and near-field lenses.[5] Ultrafast DLW has also been proved to be an almost universal technique for waveguide (WG) writing in almost any transparent material.[6-8] Within the field of solid state lasers, Neodymium doped ceramic yttrium aluminum garnet (Nd:cYAG) is of special relevance.[8] So far, the DLW process in Nd:YAG has been based on the direct creation of surface or volume damage,[9,10] and on the use of the collateral strained regions as waveguide cores.[6,8] Indeed, the fabricated structures were found to retain the outstanding spectroscopic properties of Neodymium ions in the as-fabricated YAG ceramics. As a matter of fact the fabricated waveguides were found to be highly efficient laser sources.[11] Most of the structures reported up to now were based on the refractive index changes produced by the combination of lattice damage at focus (refractive index decrease) and lattice compression in the surroundings of damage volumes (this yielding to a refractive index increment). This approach, although demonstrated to provide excellent results, has the main drawback that propagating radiation along the waveguides has a non-negligible overlap with damage volumes leading to residual propagation losses. In addition, the stress based waveguides fabricated in Nd:cYAG were not able of optical confinement for wavelengths longer than 1300 nm.

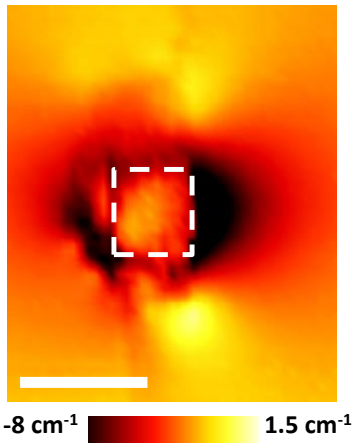


Figure 1.- *Typical fluorescence image (in terms of spectral induced displacements) corresponding to a step-index Nd:YAG ceramic buried channel waveguides fabricated by direct laser writing*. Scale bar is 10 μm.

In this work we have demonstrated the fabrication of buried channel waveguides in Nd:cYAG ceramics by the multiscan direct laser writing method in absence of drastic damage.[12] Waveguiding is provided by the refractive index increment created at focus. The advantage of the waveguides reported here over the typically used Type II stress-induced ones is their capability for light confinement for wavelength longer than 1.3 μm, as well as the ease with which the core parameters, such as size and contrast, can be tailored. Luminescence images of the waveguides have revealed that the writing process causes a complex distortion of the Nd:cYAG network (see **Figure 1**). A great variety of novel and unexpected phenomena have been observed including, as an example, the site-redistribution of Neodymium ions in the YAG network very likely related to the formation of ion pairs during laser writing procedure. The possible physical mechanisms at the origin of the refractive index increment have been discussed and compared to those previously reported for stress based channel waveguides also fabricated in Nd:cYAG waveguides. The potential use of the fabricated structures as integrated laser sources is discussed on the basis of their fluorescence images. We provide on the first, up to the best of our knowledge, laser action demonstration in multi-scan fabricated Nd:cYAG waveguides**.**

REFERENCES

1. 1. K. M. Davis et al. *Opt*. *Lett*. **21**, 1729 (1996).
2. G. Zhou et al., *Opt*. *Lett*. **31**, 2783 (2006).
3. R. R. Thomson, et al. *Opt*. *Express* **19**, 5698 (2011).
4. G. D. Marshall et al., *Opt*. *Lett*. **33**, 956 (2008).
5. J. Barrio et al. *Appl*. *Phys*. *B* **103**, 51 (2011).
6. J. Burghoff et al. *Phys*. *Lett*. **89**, 081108 (2006).
7. V. Apostolopoulos et al. *Appl*. *Phys*. *Lett*. **85**, 1122 (2004).
8. A. Ródenas et al. *Appl*. *Phys*. *B* **95**, 85 (2009).
9. G. A. Torchia et al., *Opt*. *Express* **15**, 13266 (2007).
10. A. Ródenas et al.. *Appl*. *Phys*. *Lett*. **93**, 151104 (2008).
11. G. A. Torchia et al. *Appl*. *Phys*. *Lett*. **92**, 111103 (2008).
12. A. Rodenas, et al. *Opt*. *Lett*. **36**, 3395 (2011).

Optomechanics with 2D photonic crystals membrane

R. Braive[1,2], V. Tsvirkun[2], A. Chowdhury[2], I. Robert-Philip[2], K. Makles[3], P.-F. Cohadon[3], T. Briant[3], S. Deleglise[3], A. Heidmann[3]

[1] *University Paris 7, Paris, France,*
remy.braive@lpn.cnrs.fr
[2] *CNRS – Laboratory for Photonics and Nanostructures (LPN), Marcoussis, France*
[3] *Laboratory Kastler Brossel (LKB), Paris, France*

Abstract: Cavity optomechanics exploits the coupling of mechanical oscillators to the light field via the optical force. In our work, the optomechanical resonator is a suspended 2D photonic crystal structure. We investigate experimentally the mechanical behavior exhibited by a conventional two dimensional photonic crystal acting as a mirror or including a cavity of diffraction-limited size. Due to their geometry and very small scales, the optomechanical mirrors sustain mechanical modes in the MHz frequency range; these modes exhibit a very strong nonlinear behavior. The optomechanical cavities also sustain in the GHz frequency localized mechanical modes, which are confined in the cavity core. In this paper, we will present our work towards fully integrated optomechanical platforms combining the optomechanical resonator and external actuation tools, either by electrostatic actuation via interdigitated electrodes or by optical actuation via an integrated silicon waveguide below the optomechanical resonator.

1- Introduction

Optomechanics utilizes the coupling between light and the geometry of a mechanical oscillator to read or tailor the mechanical motion of the oscillator. Optomechanical coupling can be enhanced by use of an optical cavity. This coupling is also stronger at the nano-scale because of the very small mass of nano-mechanical oscillators. In our work, we investigate the nano-optomechanics of suspended photonic crystal membranes. These structures may combine cavity enhancement and low mass and thus exhibit strong mechanical coupling to light. Optomechanical coupling in 1D photonic crystal cavities has been observed in patterned single and dual nanobeams (zipper cavities). In this work, the mechanical oscillator consists of a suspended nano-scale InP membrane pierced with a regular array of holes constituting a two-dimensional photonic crystal. Depending on the arrangement of holes, it can either act as a deformable end-mirror in a conventional Fabry-Perot cavity or include a cavity of diffraction-limited volume that simultaneously confines both phonons (i.e. mechanical vibrations) and photons.

2- Optomechanical photonic crystal cavities

We first investigated experimentally the mechanical behavior exhibited by a conventional two dimensional photonic crystal including a cavity of diffraction-limited size[1]. This cavity sustains a single optical mode at a telecommunication wavelength with a cold-cavity quality factor of around ten thousand. In our experiment the mechanical modes of the suspended membrane are observed by measuring the frequency noise spectrum obtained by evanescently coupling a laser into the optical cavity and locking it on a side of the resonance. We observe more than 20 mechanical modes in the frequency range between 10 MHz and 1 GHz. These modes can be assigned to two different mode families. Low-frequency modes (below 200 MHz) are flexural modes corresponding to the movement of the whole membrane. The second mode family consists of localized modes corresponding to mechanical displacement of the membrane localized in the cavity core. Due to the strong confinement and colocalization of the optical and mechanical modes within the defect cavity, strong optomechanical coupling is observed for the localized modes.

The observation and actuation of these modes, exploited up to now light coupling to the resonator via a tapered optical fiber placed in the evanescent field of the resonator, restraining the possibility to

combine various optomechanical functionalities on the same chip. An integrated platform has been developed by replacing the usual tapered fiber by a silicon waveguide underneath the suspended photonic crystal membrane (see Figure 1. left). This approach opens the possibility to integrate an extra functionality on the top surface of the planar membrane. The use of this fully-intergrated circuitry on a single planar setting opens the way to their use for RF photonics (microwave oscillators, RF filters...) or chip-scale optomechanical signal processing (wavelength conversion, delay lines...).

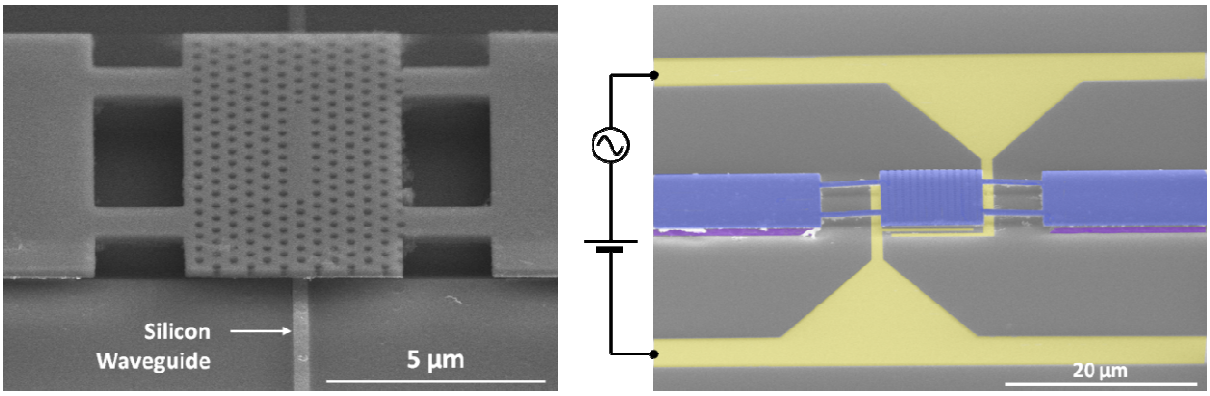


Figure 1: Scanning electron image of (Left) a suspended photonic crystal cavity bonded over an integrated silicon waveguide and (Right) a suspended photonic crystal mirror bonded over interdigitated electrodes.

3- Optomechanical photonic crystal mirrors

Photonic crystal slabs with a square lattice of holes have been used as mirrors operating at normal incidence in active (VCSEL) and passive optical resonators. We extended their use to optomechanics[2], by demonstrating experimentally that such slabs sustain vibrational modes in the MHz range while their reflectivity at normal incidence at 1064 nm is higher than 95 %. These two features, combined with their very low mass, open the way to the use of such periodic structures as deformable end-mirrors in Fabry-Perot cavities for the investigation of cavity optomechanical effects.

Due to their geometry and very small scales, these resonators exhibit a very strong nonlinear behavior, in particular mechanical bistability[3]. This feature turns out to have a dramatic impact on the dynamics of a mechanical mode, as well as an intermodal effect observed on the frequency shift of a second mode when a first mode is actuated in its nonlinear regime. We also observed in particular the emergence of a phase conjugate mechanical response to a weaker probe actuation; the mechanical response exhibits both a resonance at a frequency above the pump frequency and a spontaneously generated mechanical motion at a lower frequency symmetrically located below the pump frequency.

Most of these experiments used an external piezoelectric actuation of the mechanical motion. Such actuation scheme could be strongly enhanced by using integrated electrostatic actuation tools. Such scheme can be achieved by integrating interdigitated electrodes below the membrane (see figure 1 right). Applying an AC voltage (superimposed to a DC voltage) on the electrodes, induces an electrostatic force that is applied on the membrane and thus that actuates mechanical motion. In our preliminary experiments, we observe that the increase of the applied DC voltage (an thus of the force) induces a parabolic shift of the mechanical frequency, as predicted by our numerical simulations.

The authors acknowledge financial support from the French National Research Agency (ANR) through the MINOTORE project and from the European Commission through the CQOM ITN project,

References

1. E. Gavartin *et al., Phys. Rev. Lett.* **106**, 203902 (2011)
2. T. Antoni *et al., Opt. Lett.* **36**, 3434 (2011)
3. T. Antoni *et al., Europhys. Lett.* **100**, 68005 (2012)

Dual Pump Microresonator Frequency Comb Generation and Optical Buffer Memories

T. Hansson, S. Wabnitz

University of Brescia, Brescia, Italy,
tobias.hansson@ing.unibs.it, stefan.wabnitz@unibs.it

Abstract: We analyse the dynamics and stability of Kerr frequency comb and soliton generation in a microresonator pumped by two cw lasers. The beating of the pumps leads to a temporal modulation which permits the stable holding of externally injected pulses into a practical, chip-scale optical data buffer for packed-switching networks based on microring resonators.

Optical microresonators are currently being actively investigated, as they may enable a new class of chip-scale frequency comb sources for spectroscopy and metrology applications[1]. Most research to date has focused on pumping the microresonator with a single cw laser. We analyse here an alternative configuration where the cavity is simultaneously pumped at two different frequencies. Dual pumping can be implemented either using two separate cw laser sources, or by modulating a single cw pump laser in order to simultaneously excite two modes separated by some multiple of the free-spectral-range. Such a configuration allows the generation of frequency combs without a pump intensity threshold in both the normal and the anomalous dispersion regime[2].

Moreover, dual pumped microresonator may also provide the necessary long-term stability of recirculating pulses in optical soliton memories[3]. Indeed, for enabling secure all-optical photonic transparent IP networks, one needs routing devices for the optical packets. However, packet switching based on header information is currently hampered by the lack of practical optical memories for buffering the data while the header bits are processed. Current optical memories are based on active re-circulating loops of silica fiber which are bulky and require optical amplification to compensate for the cavity loss, thus adding noise to the data. Such types of memories are thus power hungry and not cost-effective as they cannot be integrated on the chip of a photonic integrated circuit. A different type of optical memory can be based on a passive ring cavity pumped by a cw holding beam[4]. We show here that a dual pumped microresonator may potentially lead to a stable and fully integrable optical data buffer.

We model a bi-chromatically pumped microresonator by the mean-field approach: for two equal amplitude pumps with a common phase detuning, the intracavity field can be described by the driven and damped nonlinear Schrödinger equation

$$A_\tau + i\beta A_{tt} - i|A|^2 A = -(1+i\delta_0)A + f_0 \cos(\Omega t). \quad (1)$$

Here t is the ordinary (fast) time variable which describes the temporal profile of the field, and τ is the slow time-scale for the evolution of this profile over successive round-trips. The field A is periodic with the cavity round-trip time, i.e., $A(t+2\pi,\tau) = A(t,\tau)$[5]. Moreover, β is the second-order dispersion coefficient, δ_0 is the cavity detuning, f_0 is the external pump field and Ω is the pump modulation frequency.

To gain insight into the comb generation dynamics, we derived a truncated four-wave model involving the two strong pump modes and the dominant sideband pair, which allows us to capture much of the essential dynamics of Eq.(1). This allows us to predict the existence and stability of the stationary comb states of the dual pumped microresonator (see Fig.1, left).

Based on the four-wave model predictions, we numerically analyzed the different mechanisms for comb generation: Fig.1, right, demonstrates stable primary comb generation in the normal dispersion regime, with a comb line spacing given by the pump modulation frequency Ω. Fig.2, left, illustrates an example of secondary, background-free (i.e., with no dc component) comb which is generated in the anomalous dispersion regime and for negative cavity detuning. However, anomalous dispersion combs are generally unstable if they possess a dc component.

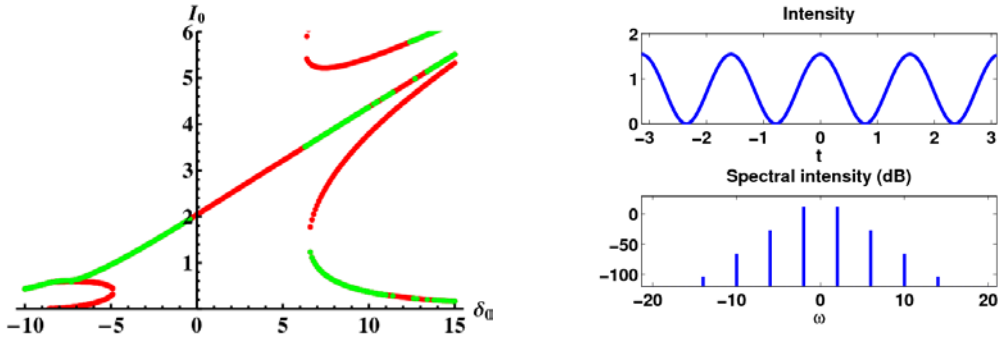


Fig.1: (left): Pump mode intensity I_0 vs. detuning δ_0, for $\kappa = \beta\Omega^2 = -1$ and $|f_0|=9$. Green (red) curves indicate stable (unstable) intensities; (right): normal dispersion, background-free primary frequency comb.

One of the most interesting properties of the dual pumped configuration is that is also capable of supporting cavity solitons, i.e., isolated pulses that exists on a background, and that have smooth spectral profile that involves all cavity modes with the fundamental mode spacing of a single free-spectral-range. Cavity solitons can be created by injecting a similar writing pulse into the cavity, which forms an optical soliton buffer[4]. The advantage of using a dual pump scheme is to suppress interactions between individual solitons[3]. In fact, the pumping of two modes that are separated by multiples of the free-spectral-range introduces a low intensity pattern of non interacting clock pulses whose number can be controlled by the modulation frequency in order to determine the number of bits in the cavity. These clock pulses provide a fixed background onto which the cavity solitons can be written, and the modulation frequency can be selected so that only a single cavity soliton will fit onto each clock pulse. The clock pulses could also be used to provide a re-timing feature in order to synchronize detection. The same pulses that are used to write the cavity solitons can also be used to erase an optical bit for a proper choice of amplitude and width, thus allowing the cavity to function as a logical XOR gate. The entire pattern can moreover by erased by lower the pump amplitude below the threshold for cavity solitons. An example of stable storage of the 16 bit word 0100100001010111 where ones are represented by cavity soliton pulses is shown in Fig.2, right.

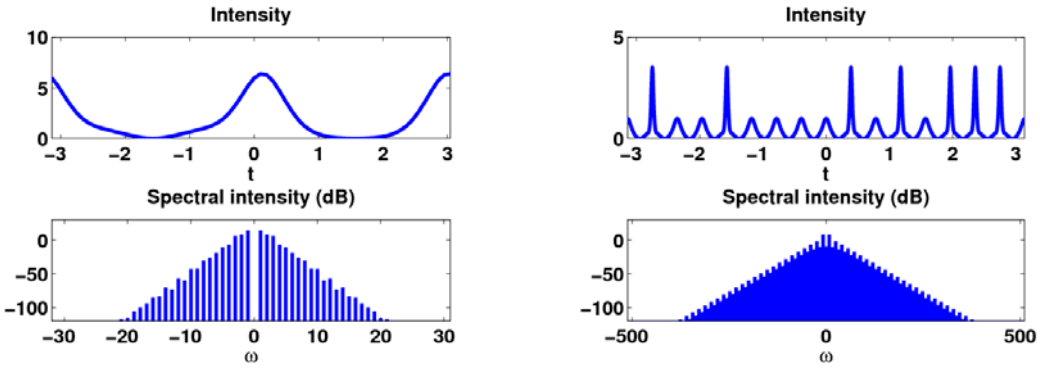


Fig.2: (left): Stable anomalous dispersion frequency comb without a background component but with even modes filled in due to secondary comb generation; (right): Coexistence of multiple injected cavity solitons on top of a stationary 16 bit pattern of low-intensity clock pulses.

In summary, we have shown that a dual pumped microresonator is capable of generating background-free frequency combs both in the anomalous and in the normal dispersion regime. Additionally, we proposed a long term stable optical buffer memory with suppressed pulse interactions. This research was funded by Fondazione Cariplo (grant no. 2011-0395).

References

1. T. J. Kippenberg *et al., Science* **332**, 555-559 (2011).
2. D. Strekalov and N. Yu, *Physical Review A* **79**, 041805(R) (2009).
3. S. Wabnitz, *Optics Letters* **18**, 601-603 (1993).
4. F. Leo *et al., Nature Photonics* **4**, 471-476 (2010).
5. T. Hansson *et al., Phys. Rev. A* **88**, 023819 (2013).

Design of a phase shifter in InP Membranes On Silicon based on a slot-waveguide with liquid-crystal

A.J. Millán-Mejía , J.J.G.M. van der Tol, and M.K. Smit

Photonic Integration Group (PhI), Dept. of Electrical Engineering, Technische Universiteit, Eindhoven, Den Dolech 2, 5612 AZ Eindhoven, The Netherlands
A.Millan.Mejia@tue.nl, J.J.G.M.v.d.Tol@tue.nl, M.K.Smit@tue.nl

Abstract: In the development of the InP Membranes On Silicon (IMOS) platform, phase shifters are essential elements for switches or tunable filters. The simulation of slot-waveguides with an organic liquid crystal (5CB) shows that high performance devices with a theoretical predicted optical voltage-length product of $U_\pi L = 0.0607\, Vmm$ are possible. These devices present sub millisecond response (~300 μs) and low energy consumption (~10 $pJ\ per\ transition$).

Introduction

In the last years, optical interconnects are becoming an essential technology for short distance links. A need for higher speed communication and lower energy consumption devices inside computer chips are the two key factors for this change. The use of a thin optical layer of InP material bonded with BCB on top of silicon wafers is an attractive solution (InP membranes On Silicon (IMOS))[1]. One important element for this platform is a phase shifter. This component allows constructing complex devices such as switches and tunable filters.

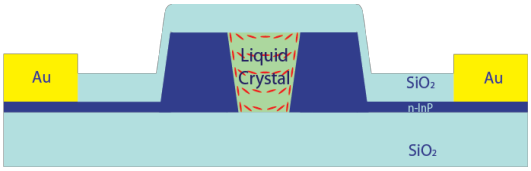


Fig. 1: Schematic of the phase shifter

Important results in modulators using slot waveguides with electro optical polymer have been demonstrated in Silicon On Insulator (SOI) platform. Low voltage devices ($V_\pi = 0.25\ V$)[2] and high speed modulators (40 $Gbit/s$) with only 250 μm length[3] are relevant examples. These results make this structure appealing to be implemented in IMOS platform.

The slot-waveguide is a configuration where the TE optical mode is mostly confined in the low refractive material due to boundary conditions, creating large discontinuities in the electric field at the high index contrast interfaces. Contrary to previous slot waveguide devices, this structure is covered with a SiO_2 layer, and due to the small dimension of the slot; a gap of almost the same dimension of the slot is created. By making openings at the extremes of the slot waveguides and deposit a drop of LC in one side, the capillary forces will fill the created gap with LC. This configuration will provide a protection of the LC, making a most durable device than solutions presented previously in literature[4]. Because a huge part of the optical mode overlaps with the LC, when an electric field is applied, E_0 control the orientation of the LC molecules and a large variation of the refractive index is obtained. Figure 1 show a schematic representation of the slot waveguide phase shifter.

In terms of the electrical part, an n-doped layer of InP next to the slot waveguide will provide the connection with the contacts allowing a high electric field present inside the slot due to the small slot dimension. The integration of the phase shifter with strip waveguides developed in the IMOS platform is obtained by using logarithmic tapered converters[5]. This geometry allows adiabatic transition in a reduced length (~10 µm) and provides electrical isolation, requirements needed for this device.

Geometry optimization

In order to make an optimization of the structure, we assume that the LC molecules inside the slot are aligned parallel to the sidewall of the InP waveguides. In the absence of an electric field ($V = 0$) the electric component of the optical mode is then perpendicular to the LC molecules, obtaining a refractive index inside the slot $n_\perp = 1.51$. When a high voltage is applied, (V>>0) the LC molecules orientate in the direction of the electric field applied, which is parallel to the electric component of the optical mode. In this condition, the refractive index in the slot is $n_\parallel = 1.68$. We define these as the two states of the phase shifter. The phase difference obtained between these two states is related with the effective refractive index difference (Δn_{eff}). We plot this parameter versus the geometry

parameters which are the width of the slot and the sidewall angle. The height of the waveguides was defined to be 300 nm and the connection n-doped InP layer is 50 nm thick. This is compatible with the passive elements already developed for this platform[6]. The width of the strip waveguides was selected to be 240 nm, this was optimized in our previous study of a slot modulator with electro optical polymer[7]. The optimization study was carried out with an eigen mode solver (Lumerical ™ MODE solver).

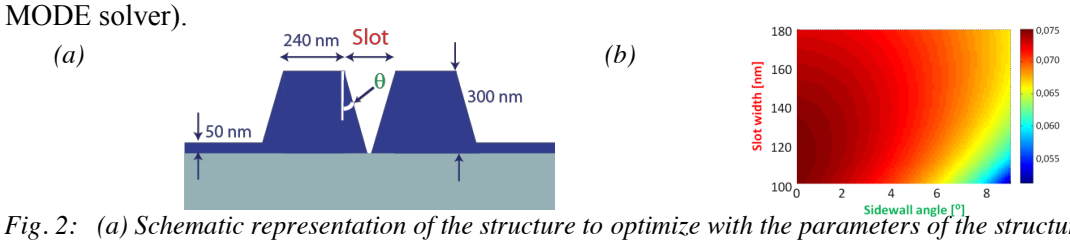


Fig. 2: (a) Schematic representation of the structure to optimize with the parameters of the structure indicated. (b) Effective refractive index difference (Δn_{eff}) between the two liquid crystals states.

In the fabrication of passive elements in IMOS, a sidewall angle between 2° and 5° is obtained depending on the etching process used. As can be seen from figure 2 (b), the maximum of the Δn_{eff} with a sidewall angle of 5° is found with a slot of $140\ nm$ with $\Delta n_{eff} = 0.0715$.

Performance

To analyze the performance of this device, calculation in the phase change versus the length of the device is needed. We consider a complex propagator $\exp(-\beta z)$, the difference in phase is defines as $\Delta\phi/L = \beta(V=0) - \beta(V >> 0) = 2\pi\Delta n_{eff}/\lambda$, if we consider a wavelength of $\lambda = 1.55\ \mu m$, we obtain $\Delta\phi/L = 92\,\pi/mm$. Taking into account the saturation on the orientation of the LC molecules is around $\sim 40V/\mu m$ [5], which correspond to $5.6\,V$ applied between the electrodes, we obtain an voltage-length product of $U_\pi L = 0.0607\ Vmm$. Another important parameter is the time response of the device. It is well known that for planar aligned LC cells the time response is defined by the relaxation time, $\tau_{fall} = \gamma_1 d^2/\pi^2 K_{11}$ [8]. In the case of 5CB LC, and considering a slot of $140\ nm$, $\tau_{fall} = 303.44\ \mu s$. This time can be reduced using different techniques such as bias voltage effect or transient nematic effect. The RC time constant for $1mm$ length device is around $\tau_{RC} = 2\ ps$, leaving room of improvement if different LC with better performance is used. To calculate the energy consumption, we consider the LC works as insulator material without current flowing through this material, so our device works as a capacitor. Miller [9] establishes for devices as the one presented here, the energy consumption is the one needed to charge and discharge the electrodes, which can be calculated as $\Delta E = CV^2$ per cycle. In case we consider a switching of a device of $1\ mm$ length, and the dielectric permittivity $\epsilon_{\|} = 18$, the capacitance of the device is $C = 341.52\ fF$. With an operational voltage V=5.6V, the energy consumption per cycle is $E = 10.71\ pJ$. If we switch at $500\ kHz$, which is close to its speed limit. The power needed will be $17\ \mu W$. This is around 2 orders of magnitude lower than high performance thermo optical devices[10].

Conclusions

The use of a slot waveguide connected with n-doped InP layers to the contacts allows for high overlap of the electrical and optical mode with the liquid crystal. These characteristics allow a low energy consumption ($\sim 17\ \mu W$) and high efficiency phase shifter ($U_\pi L$ = 0.0607 Vmm). The time response is in microsecond ($\sim 300\ \mu s$). We consider this device can provide a high performance phase shifter for the IMOS platform and the protection layer of SiO_2 will make it durable. The fabrication of this device is underway.

References

1. J. van der Tol *et al*., *IET Optoelectronics*, **5**, pp 218-225 (2011)
2. T. Baehr-Jones *et al*. *Applied physics letters*, 92, pp 163303-1- 163303-3 (2008)
3. R. Palmer *et al*., *OFC conference*, (2014)
4. J. Pfeifle *et al*., *Optics express*, **20**, pp. 15359-15376 (2012)
5. R. Palmer *et al*., *IEEE Photonics Journal*, **5**, (2013)
6. J Pello *et al*., *Proceedings Symposium IEEE Photonics Society Benelux*, pp. 213-216 (2011).
7. A.J. Millan Mejia *et al*., *Proceedings Symposium IEEE Photonics Society Benelux*, pp. 195–198 (2013).
8. Yadav *et al*., *Acta physyca polonica A*, **119**, pp. 824-828, (2011)
9. David A.B. Miller, *Optics Express*, **20**, pp. A293-A308, (2012)
10. Lian-Wee Luo *et al*. *Optics Express*, **18**, pp 23079-23087, (2010)

Phase-space control of unconventional modes for SDM

V. Doya*, F. Gustave, C. Michel, P. Aschieri

Laboratoire de Physique de la Matière Condensée,
Université de Nice Sophia Antipolis, CNRS UMR 7336, France,
valerie.doya@unice.fr,claire.michel@unice.fr,pierre.aschieri@unice.fr

Abstract : The modes properties of highly multimode optical fibre are governed by the rays' dynamics in the geometrical limit. Different regimes of dynamics are encountered by modifying the geometry of the transverse cross section of the fibers. We show that the selection of modes in a highly multimode fiber can be simplied thanks to the signature of the rays' dynamics on the waves and exploited for spatial division multiplexing.

Unexploited until now, spatial division multiplexing (SDM) appears as the innovative way to provide the next jump in transmission capacity. A broad variety of technologies are investigated to probe the potential of SDM from multicore fibres, coupled core fibres to multimode fibres[1]. By using multimode fibres, transmission capacity must increase proportionally with the number of modes that act as independent transmission channels. In this active period of prospective investigations on SDM, we propose an original and challenging approach whose interest lies in transferring fundamental concepts of wave propagation in complex media to applied optical telecommunication.
Wave complexity can be induced by the geometry of a medium that governs the rays' dynamics. A silica optical fibre constitutes a natural connection between complexity and applied photonics and telecommunications. Indeed, a multimode optical fibre whom radius R is large compared with the wavelength λ, is a versatile system for investigating different regimes of complex rays' dynamics. Starting from a circular cross section and truncating gradually, different regimes for the dynamics are explored. The dynamics can thus be regular, chaotic or a mixture of chaos and regularity (said mixed), depending on the degree of the truncation (d).

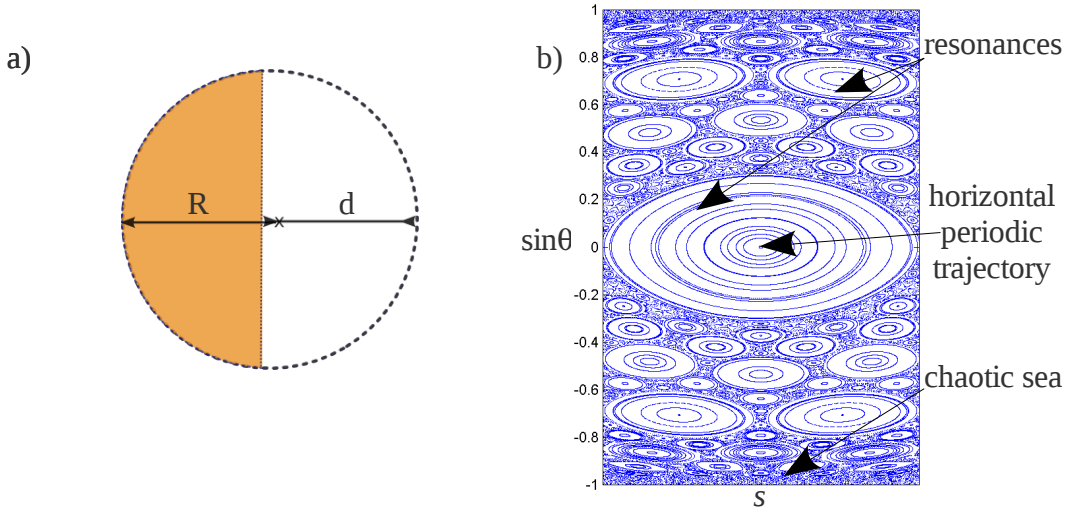


Fig. 1 : Transverse cross section of the guiding part of the multimode fibre (a), R is the radius and d the truncation length (here d=1.05R). Poincaré surface of section associated to a mixed dynamics. s, is the curve abscissa of the ray and θ the angle of the ray at each reflection on the boundary (b).

In the Fig. 1b, the mixed dynamics is caracterised in the Poincaré surface of section (PSS) by the coexistence of regular islands (resonances) and distributed dots (chaotic sea). These regular and chaotic behaviours of the rays' dynamics mark the spatial properties. For instance, the so-called *chaotic* modes exhibit a statistically uniform spatial field distribution whereas the so-

called *regular* modes present enhanced intensity localised on periodic rays' trajectory. The particular regular modes associated to the horizontal trajectory (periodic trajectory that closes itself after two bounces on the boundary of the transverse cross section) are of great interest because they constitute a subset of highly localised and stable modes as they are constructed on the main stable resonance of the PSS (see figure 1b). These properties made these modes more easy to excite that the thousand other modes supported by the fibre. Besides this, these modes can be seen as the longitudinal modes of a stable resonator constituted by a curve and regular reflectors separated from each other by a distance 2R-d. Thus, each mode presents enhanced intensity in the vicinity of the focus point and the value of their associated transverse wave number can easily be deduded from a standard resonance condition along the periodic trajectory :

$$k_{tn}L=2\pi\, n+\Delta\phi+\Delta\varphi_{gouy}, \qquad (1)$$

where L, is the 2 times the width of the resonator, $\Delta\phi$, the phase shift due to the core/cladding interface and $\Delta\varphi_{gouy}$ is the Gouy phase induced by the focus point. A regular mode associated to n=3 is reported in Fig. 2a.

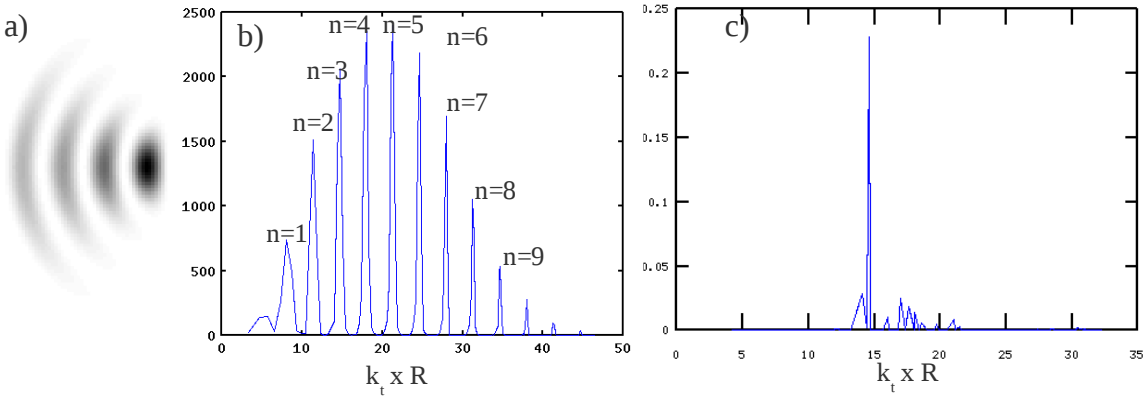


Fig.2 : Intensity of a regular modes associated to n=3 (a). Intensity spectrum resulting from a tilted gaussian beam located on the focus point (b). Intensity spectrum associated to a phase mask illumination with a spatial modulation associated to regular modes of order n=3 (k_t=14.6/R).

Each regular modes are spatially localised, that is, with a reduced spatial overlap with the other modes. Moreover, they have well-separated transverse wavenumbers (see eq. (1)). Consequently these modes should be more robust to crosstalk with other modes that may be induced by stresses on the fibre or curvatures. We claim that they can be good candidates for SDM using individual modes. Fig. 2b also shows that the regular modes can easily be excited and discriminated from the other modes by simply using a focused gaussian beam in the area of maximum of intensity (focus point).
On top of that, we may also be able to perform selective amplification of these modes by introducting a localised gain in the vicinity of the focus point, point of maximum of intensity[2].

References :

1. D. Richardson, J. M. Fini, L. E. Nelson, *Nature Photonics*, 2013.94 (2013).
2. C. Michel, V. Doya, O. Legrand, F. Mortessagne, *Physical Review Letters*, **99**, 224101 (2007).

Electrical Crosstalk Simulation of InP-based Phase-Shifters from a Generic Photonic Integration Platform

W. Yao[1], G. Gilardi[1], M. K. Smit[1], M. J. Wale[1,2]

[1] COBRA Research Institute, Photonic Integration Group, Department of Electrical Engineering, University of Technology Eindhoven, the Netherlands,
w.yao@tue.nl, g.gilardi@tue.nl, m.k.smit@tue.nl
[2] Oclaro Technology Ltd., Caswell, Towcester, Northamptonshire, NN12 8EQ, United Kingdom,
mike.wale@oclaro.com

Abstract: This paper analyzes electrical crosstalk between phase-shifters from a generic photonic integration platform using a full-wave simulation model. The model accurately predicts the microwave performance of a single phase-shifter and is extended to account for two coupled phase-shifters. Electrical crosstalk levels are estimated for varying coupling length and distances and pose a limit to integration density of modulator arrays.

Introduction

With the advent of generic photonic integration platforms low-cost photonic integrated circuits (PICs) can be made available to a broad range of users with a wide application space.[1] One of such applications are low-cost, high-capacity multichannel transmitters for optical transport systems to meet today's huge bandwidth demand. To allow for high-speed operation with a high number of channels, the generic integration platform must offer fast optical modulators and a high integration density. Phase-shifters from the COBRA generic integration process have shown good electrical performance, allowing potentially for 10Gpbs modulation speed when used in a Mach-Zehnder configuration.[2] To reduce chip size, dense packing of modulator arrays is required, which leads to electrical signal crosstalk between channels at high bitrates. Up until now, electrical crosstalk analysis has been limited only to electronic ICs and packages, but to the best knowledge of the authors it has not been properly dealt with on the PIC level. This paper addresses the issue and presents crosstalk simulations on two coupled phase-shifters from the COBRA process.

Simulation Model

To analyze coupling effects between phase-shifters, the commercial 3D field solver CST MWS is used. It has been shown in the literature before, that FDTD- and FEM-based electromagnetic calculations can accurately predict the microwave behavior of optical modulator structures.[3,4] For single phase-shifters fabricated with the COBRA process, this approach already yielded good agreement between simulation and measurement.[2] Here, the same technique is extended to account for two coupled phase-shifters. Each simulation run calculates the electrical scattering parameters of the coupled 4-port structure for a fixed length of 100μm. Transformation from S- to T-matrix and cascade of shorts sections lead to the S-matrix of long coupled phase-shifters.

Results and Discussion

When one of the coupled phase-shifters is driven by a microwave signal, the crosstalk that builds on the second phase-shifter travels to both sides, the near-end (NEXT) and far-end (FEXT) of the electrode. Fig. 1(a) shows both crosstalk contributions of two coupled phase-shifters for three different electrode lengths and an electrode internal distance of 25μm. Both NEXT and FEXT increase with coupling length below 10 GHz. At higher frequencies the periodicity of crosstalk starts to take effect and resembles that of a directional coupler formed by two edge-side coupled microstrips.[5] It can be observed, that FEXT is generally higher than NEXT with peak crosstalk values of -28dB at 13 GHz for L=2000μm. Fig. 1(b) illustrates the electric field distribution when signals from one phase-shifter couples to the other. Major coupling path occurs through air whereas the semiconductor material between the two phase-shifters acts as a shield. The crosstalk field builds up in the guiding layer of the second phase-shifter, which contributes to noise in the optical signal. In the following, the focus lies on FEXT, as it travels alongside the optical signal and is more detrimental to the modulation process.

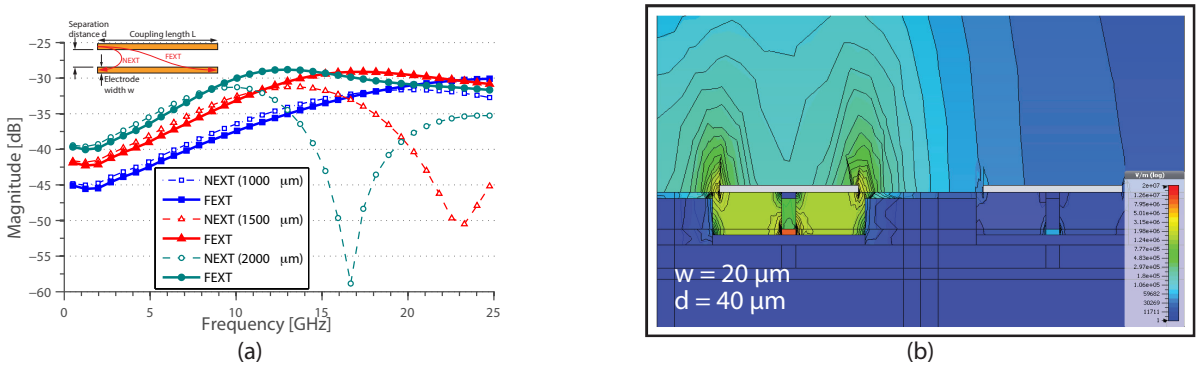


Fig. 1: (a) FEXT and NEXT for d=25µm and (b) electric field distribution of coupled phase-shifters.

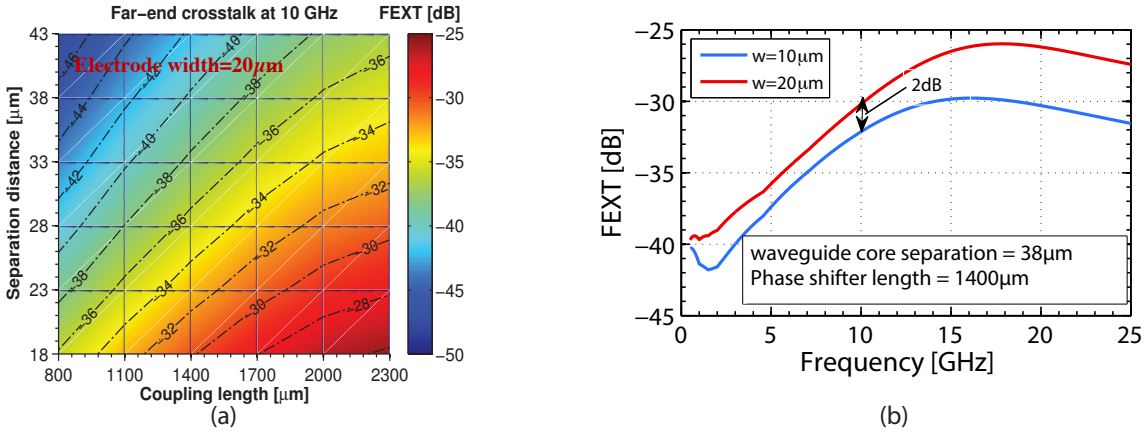


Fig. 2: (a) FEXT for different coupling length and distances. (b) Electrode width influence on crosstalk.

The coupling distance is an important parameter for crosstalk. The closer the coupling distance, the higher is the crosstalk. This is shown in Fig. 2(a) where the amount of FEXT at 10GHz is given for varying coupling length and distances. If -35dB is taken as a tolerable amount of electrical crosstalk, phase-shifters with typical length of 1.5mm should be separated by at least 30μm. Shorter phase-shifters allow for higher integration density, but also lead to an increase in half-wave voltage V_π, posing a trade-off in design. FEXT is also periodic with respect to the coupling length, which can be observed here when L approaches 2300μm. The crosstalk increase approaches a maximum and is expected to decrease again for longer coupling lengths as would be the case for a directional coupler.
Because the electric field coupling occurs through air, the electrode width also influences the crosstalk level. Narrow electrodes have small extension of the field whereas the field of wider electrodes reaches farther. Its effect is shown in Fig. 2(b) where FEXT is plotted for two electrode width values when the coupling length and distance is held constant. Crosstalk reduction of more than 2dB can be expected when the electrode width is reduced from 20μm to 10μm.

Conclusion

Electrical crosstalk effects between phase-shifters from the COBRA generic integration process have been analyzed in this paper. It turns out that the coupling resembles that of an electrical directional coupler, depending on coupling distance, length and electrode width. The given results with respect to geometrical parameters are useful in the design of broadband modulator arrays for transmitter PIC applications. Further experimental work is needed to verify the simulation results and additional analysis of the crosstalk's influence on the optical data signal is essential.

References

1. M. Smit *et al.*, *IET Optoelectronics* **5**, pp. 187-194 (2011).
2. W. Yao *et al.*, *Proceedings of the 18th Annual Symposium of the IEEE Photonics Society Benelux Chapter*, pp. 151-154, (2013).
3. M. Koshiba *et al.*, *IEEE Transactions on Microwave Theory and Techniques* **47**, pp. 1627-1633 (1999)
4. R. Lewen *et al.*, *IEEE Transactions on Microwave Theory and Techniques* **51**, pp. 1117-1128 (2003)
5. F. D. Mbairi *et al.*, *IEEE Transactions on Components and Packaging Technologies* **31**, pp. 601 –610, (2008).

Design of Long Period Waveguide Gratings for Broad Band Polarization Filters

Girish Semwal[1] and Vipul Rastogi[2]
[1]*Instrument Research and Development Establishment, Dehradun,248008, India*
girishsemwal@rediffmail.com
[2]*Department of Physics, Indian Institute of Technology Roorkee, Roorkee, 247667, India*
vipul.rastogi@osamember.org

Abstract: We present long period waveguide grating based broadband polarization filters. Our numerically simulated results show TE-pass and TM-pass filters with polarization extinction ratio in excess of 20 dB over a wavelength band wider than 90 nm.

Introduction

Long-period waveguide gratings (LPWG) have been proposed to overcome the geometry and material limitations of long period fiber grating (LPFG). [1, 2] LPWG devices have become popular for their applications as integrated-optic devices and components for optical telecommunications and sensing technologies. [3, 4] A polarizer is one of the important components in the area of telecommunication and fiber optics gyro to reduce the interference between TE and TM modes. LPWGs presented in Ref. [1] showed the possibility of obtaining very wide rejection band. We utilize this characteristic of LPWG to design broad-band polarization filters. We have optimized waveguide and grating parameters by using the particle swarm optimization (PSO) algorithm to obtain TE-pass and TM-pass polarization filters with polarization extinction ratio (PER) in excess of 20 dB over a wavelength band broader than 80 dB. The design would be useful for applications as integrated optic polarization filters for WDM telecommunication systems.

Numerical Results

A 4-layer planar waveguide structure with finite over cladding proposed in Ref. [1] has been employed to design polarization filters. The waveguide consists of a guiding film deposited on a substrate and a finite over cladding deposited on the guiding film. We have used long period corrugated grating embedded in the guiding film of the waveguide to couple unwanted polarization to one of the cladding modes and to obtain band rejection. We have considered the following values of various waveguide parameters in our calculations:

Substrate index $n_s = 1.5$, guiding film index $n_f = 1.52$, over cladding index $n_{cl} = 1.51$, cover index $n_c = 1$, guiding film thickness $d_f = 2$ μm, and over cladding thickness $d_{cl} = 5.5$ μm.

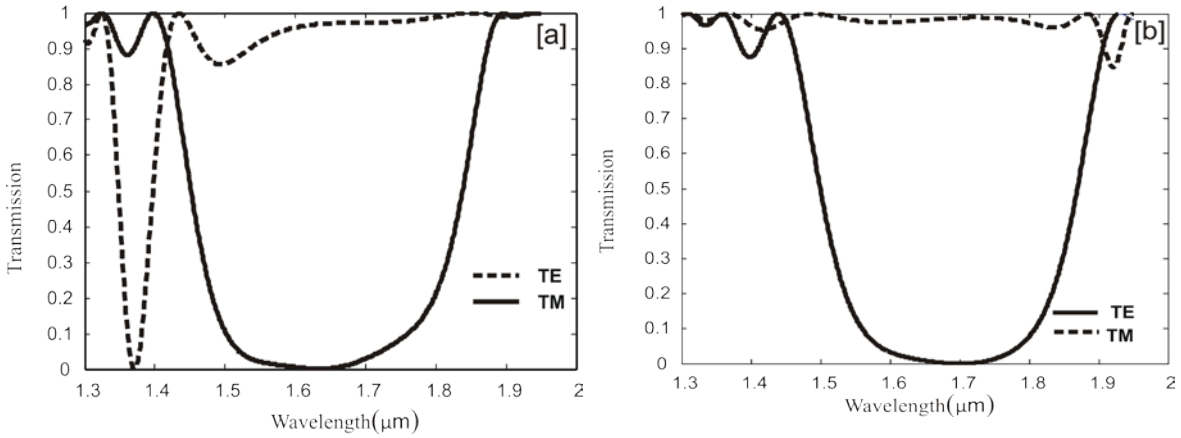


Fig. 1: Transmission spectra of designed polarization filters (a) TE-pass, (b) TM-pass.

Grating length L, grating period Λ, and corrugation height h have been optimized by PSO algorithm to obtain the desired transmission spectrum of the grating. The transmission spectra of the designed TE-pass and TM-pass filters are shown in Fig.1.

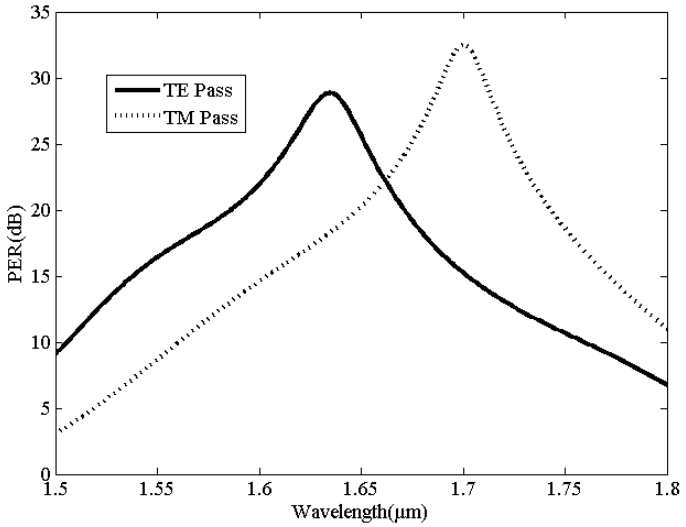


Fig. 2: Polarization Extinction Ratio for TE and TM Pass filters

Fig.1 (a) correspond to TE-pass polarizer with optimized grating parameters L = 15.4 mm, Λ = 187.5 μm, and h = 112 nm and shows a wide wavelength rejection band centered around 1.6 μm wavelength for TM polarization. The TE polarization has a transmission of more than 80%. In Fig. 1 (b) we can see TM-pass polarization filter, which correspond to grating parameters L = 15.4 mm, Λ = 191.5 μm, and h = 112 nm. We have also calculated the polarization extinction ratio of the designed filters at different wavelengths and the results are shown in Fig. 2. We can see that for TE-pass polarization filter we have PER in excess of 20 dB over a wavelength range 1.585-1.675 μm. For TM-pass polarization filter the PER is in excess of 20 dB in the wavelength range 1.65 – 1.75 μm. Such polarization filters should be useful in WDM systems.

Conclusion

We have designed polarization filters in planar optical waveguides using LPWG. The grating parameters have been optimized to design TE-pass and TM-pass filters. The designed filters show PER in excess of 20 dB over a wavelength band as large as 100 nm.

References

1. V. Rastogi and K. S. Chiang, "Long period grating in planar optical waveguide", *Appl. Opt.* **14**, pp. 6351-6355 (2002).
2. Q Liu, K. S. Chiang and V. Rastogi, "Analysis of corrugated long period grating in slab waveguide and their polarization dependence", *J. Lightwave Technol.* **21**, pp. 3399-3405 (2003).
3. K. S. Chiang, C. K. Chow, Q. Liu, H. P. Chan, and K. P. Lor, "Band- rejection filter with widely tunable centre wavelength and contrast using metal long–period grating on polymer waveguide", *IEEE Photon. Technol. Lett*. **18**, pp. 1109-1111 (2006).
4. Y. M. Chu, K. S. Chiang, and Q. Liu, "Widely tunable optical band pass filter by use of polymer long-period waveguide gratings", *Appl. Opt*. **45**, pp. 2755-2760 (2006).

Optimization of silicon wire waveguide crossing by means of vertical coupling with a polymer waveguide

A. Tsarev[1,2], E. Kolosovsky[1]

[1] *A.V. Rzhanov Institute of Semiconductor Physics SB RAS, Novosibirsk, Russia*
tsarev@isp.nsc.ru, kolos@isp.nsc.ru
[2] *Novosibirsk State University, Novosibirsk, Russia*

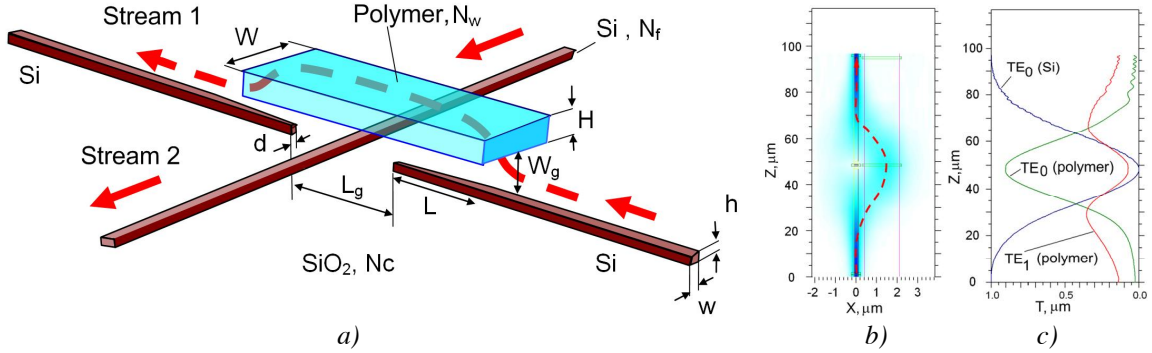
Abstract: We analyze the excellent waveguide crossing by making the optical beam to pass over the intersecting silicon wire waveguide by means of vertical up and down coupling through the silica buffer of tapered Si wires with the upper low index strip waveguide. We complete the optimization procedure by combination different methods (BPM, MoL, FDTD) which make possible to find such combinations of parameters of structure which provide (in the 35 nm spectral interval in a telecommunication range 1.55 μm) the high efficiency of crossing (98 % and above), simultaneously, for direct transmitting (the Stream 1) and a cross direction (the Stream 2), having any number (from 1 to 1024) of similar crossings.

Introduction

It is known that a good solution for the problem of cross-scattering is arranging the waveguide crossing in different spatial layers. For example, an efficient crossing has been realized in high-contrast silicon wires on the base of tunnel coupling of two vertically overlapped inverse tapers. Practical realization of the given decision requires the polysilicon [1] or silicon nitride [2] deposited technology and precision manufacturing of two oppositely directed tapers located in different layers one under the other in the strict position along the optical pass. In this paper we discuss and make optimization of alternative and much simpler structure [3-5] based on the vertical coupling of a Si wire taper with the upper low index straight polymer waveguide through the silica buffer (see Fig. 1).

Multi layer waveguide crossing

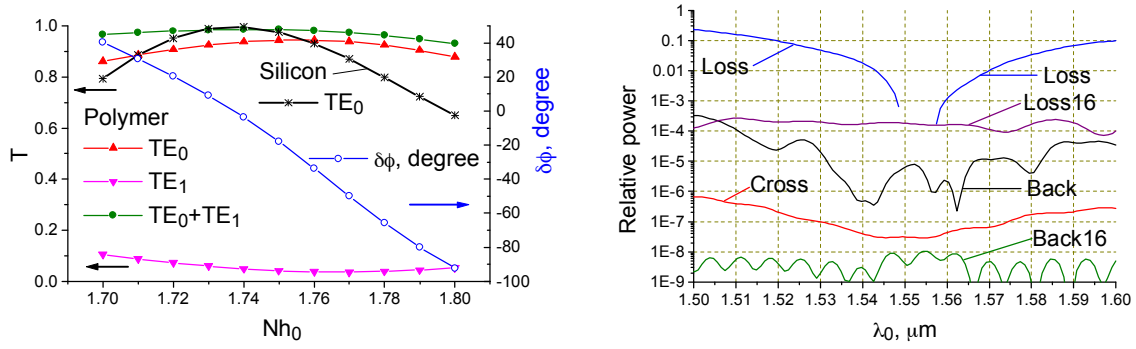
The analysis of wire crossing is executed in separate parts which are studied by different methodological approaches. Because of a great number of independent parameters (*d, h, w, H, W, L, Lg, Nw, Nf, Nc*), each of which can bring the essential contribution to the transmitting efficiency of light through a crossing area, we accomplish initial analysis by the 2D models (BPM and MoL) under effective index method (EIM) [6] approximation. Three-dimensional modeling by 3D FDTD, in all senses consuming on resources, is applied as intermediate check and at a stage of definitive testing.



a) *b)* *c)*

Fig. 1. The effective crossing of two silicon wires. The basic scheme (a); Cross-section of an electromagnetic field calculated by 2D BPM method (b); Eenergy distribution between modes along an axis of the Stream 1 (c). Lg =3 μm, H = 1.7 μm, Wg = 80 nm, L = 45 μm, Nw = 1.56, Nh = 2.95, Nh0 = 1.76, Nc=1.4, h = 220 nm, Wg = 280 nm.

The algorithm of search of optimum parameters of wire crossing is arranged by the following procedure. By the fast algorithm of 2D beam propagation method (BPM) there are determined the parameters of optimum two-dimensional structure for the Stream 1 (see Fig.1(a)). Namely, for a set of values L and Wg we find optimum value of the EIM cores index (Nh0) in a 2D waveguide (see Fig. 2 (a)). Then the further three-dimensional parameter optimization is completed by 3D FDTD starting by variation of *d*, and then by change of *Wg* (for already determined optimum value *d*). In parallel we analyze power transmitting for the Stream 2 (see Fig.1(a)) in two dimensional case by the method of lines (MoL) for an arbitrary number of crossings (from 1 till 1024) and by 3D FDTD (up to 16 crossings). As a results the joint analysis of a task in view of different methods (BPM, MoL, FDTD) has allowed to find such combinations of parameters of structure which provide (in the 35 nm spectral interval in a telecommunication range 1.55 μm, see Fig. 2(b)) the high efficiency of crossing (98 % and above), simultaneously, for direct transmitting (the Stream 1) and a cross direction (the Stream 2), having any number (from 1 to 1024) of similar crossings and a negligible cross (-70 dB) and back (-50 dB) scattering.



a) *b)*

Fig. 2. Optimization of wire crossings. The relative transmitting power T carried out by different modes of both waveguides (the left scale), and also a difference of phases δφ (the right scale) between the two first modes of a thick polymeric waveguide, as function of core index Nh0 for Wg = 180 nm in the area of crossing simulated by 2D BPM method (a); Dependence on working optical wavelength of the relative power transferred by a TE_0 mode for various streams for Wg = 340 nm, simulated by 3D FDTD(b). Loss = 1-T1(single crossing of Stream 1), Loss16=1-T16 (corresponds to 16 crossing of Stream 2), Lg =3 μm, H = 1.7 μm, W = 1.5 μm, L = 45 μm, Nf = 3.447, Nw = 1.56, Nh = 2.95, Nc=1.4, Nf = 3.447, Nw = 1.56, Nh = 3.0, Nh0 = 1.56, Nc=1.4, h = 220 nm, w = 450 nm, d = 180 nm.

Conclusion

The excellent waveguide crossing by making the optical beam to pass over the intersecting silicon wire waveguide is numerically investigated in the paper. It is realized by means of vertical up and down coupling through the silica buffer of tapered thin high index Si wires with the upper thick low index polymer strip waveguide constructed by SU-8. The optimum device provides a low loss transmitting of light in both cross direction and negligible parasitic scattering. The author acknowledges RSoft Design Group, Inc., for providing the user license for FDTD simulations [7]. *Work is executed by a support of the grant No 12-07-00018a by the Russian Fund for Basic Research.*

References

1. R.Sun, M.Beals, A.Pomerene, J.Cheng, Ching-yin Hong, L. Kimerling, and J. Michel, *Opt. Express* **16**, pp. 11682-11690 (2008).
2. Adam M. Jones, Christopher T. DeRose, Anthony L. Lentine, Douglas C. Trotter, Andrew L. Starbuck, and Robert A. Norwood, *Opt. Express* **21**, pp. 12002-12013 (2013).
3. A.V. Tsarev, *Opt. Express* **19**, pp. 13732-13737 (2011).
4. A .V. Tsarev, E. A. Kolosovskii, *QUANTUM ELECTRON* **43**, pp. 744–750 (2013).
5. A. Tsarev, *IEEE Journal of Selected Topics in Quantum Electronics* **20**, no.4, pp.1,8, (in press, JSTQE.2013.2295180).
6. K. S. Chiang, *Appl. Opt.* **25**, pp. 2169-2174 (1986).
7. Rsoft Photonic CAD Suite, version 8.0 (2007), www.rsofdesign.com.

Radiation of photonic crystals with multiple cavities

A. Tsarev[1,2], A. Shklyaev[1,2]

[1] *A.V. Rzhanov Institute of Semiconductor Physics SB RAS, Novosibirsk, Russia*
tsarev@isp.nsc.ru, alexsan@mail.ru
[2] *Novosibirsk State University, Novosibirsk, Russia*

Abstract: Two-dimension hexagonal PhCs with ordered and partially disordered cavities arrays, such as missing holes, are studied using numerical modeling by a 3D FDTD method. A PhC with an ordered array of 19 coupled cavities produces highly directive and 19 times enhanced emission, while the single peak radiation and the peak wavelength width remain about the same as those for the PhC with a single cavity. A modified PhCs with partially disordered cavities arrays are found to emit a 3 times broader and a 7 times more intense peak than those of single-cavity PhCs along with highly directive emission. The use of cavities arrays in PhCs may lead to the development of efficient Si-based light emitters.

Introduction

Effective Si-based light emitters remain the only missing component that prevents optoelectronic devices to be fabricated entirely by means of the Si technology [1-3]. The embedding of dislocations surrounded by point defects provides the formation of deep levels in the Si bandgap and produces a broad emission band around 1.5 μm [1-6]. To reduce the linewidth drastically and to enhance its intensity, microresonators as microcavities constructed as missing holes in air hole-based photonic crystals (PhCs) are typically introduced [7-17]. The main attention has been paid to designing the PhC with the cavities which provides the highest Q-factor, while the task of enhancing the radiation directivity and broaden the radiation spectrum have not yet been the subject of a targeted research. Here, for this purpose, we use the effect of interference in withdraw photonic crystal with multiple missing holes (see Fig. 1) which involves the radiation of coupled cavities arranged either in ordered or partially disordered way with respect to the PhC lattice.

The withdraw photonic crystal

The withdraw PhCs with multiple cavities arrays [Fig. 1] are constructed on the basis of the hexagonal PhC with a cavity such as missing holes. The ratio between the radius r of the air hole and PhCs lattice constant a is set to $r/a = 0.35$ for all the examined structures.

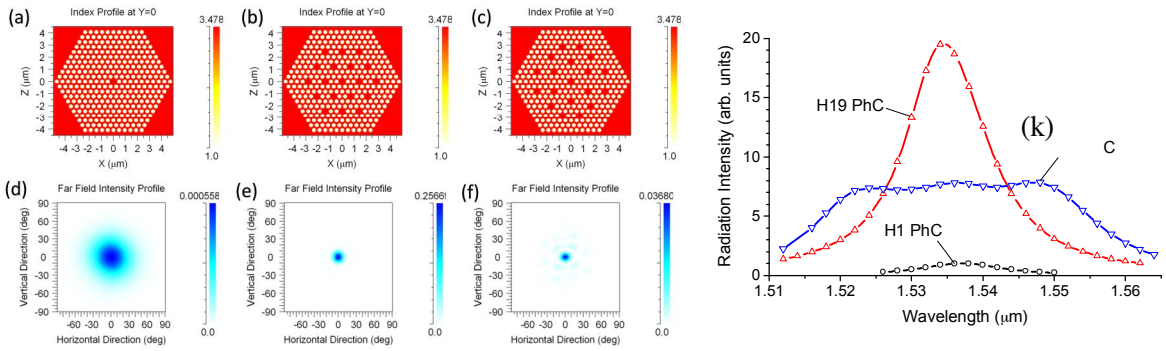


Fig. 1. PhCs with different cavities and total power radiated (to the upper hemisphere) by hexagonal PhCs with different cavities arrays. (a), (b), and (c) - refractive index distribution of withdraw PhCs with cavities named H1, H19, and H19d, respectively; (d), (e), and (f) - far field intensity of PhCs cavities H1, H19, and H19d, respectively; (k) - a radiation intensity from different withdraw PhCs.

To generate a spontaneous luminescence signal, the TE polarized pulsed or continuous wave (cw) at different optical wavelengths is launched in every PhC cavity. The signal is Gaussian-shaped and it has an asymmetrical position with respect to the missing holes centers in hexagonal PhC in the SOI structure with a 250 nm silicon slab on a 2 μm SiO_2 buffer layer. Thus, it is possible to excite and to study all the possible modes of the structure. The power and the field distribution at different cross-sections, along with the total power normally radiated to the structure plane, are calculated by 3D FDTD (see Fig. 1). The simulation area is restricted to the PhC structures nearest vicinity, and a back reflection from the bottom Si-substrate/air interface is not taken into account. This approach makes the calculation 2 times faster, but it introduces an error of about 2-5% in the evaluation of the radiation efficiency which can be neglected in this study.

A PhC with an ordered array (see Fig.1(b)) of 19 coupled cavities (H19) produces highly directive and 19 times enhanced emission, while the single peak radiation and the wavelength width remain about the same as those for the PhC with a single cavity (H1). This results in almost the same coupling efficiency of the fundamental optical mode of every cavity with the modes of the neighboring cavities thus a coupling-induced wavelength shift of the resonant mode is the same for all cavities. A modified PhC (see Fig.1(c)) with partially disordered cavities arrays (H19d) has a variation in coupling-induced wavelength shift of the resonant mode and this structure is found to emit a 3 times broader and 7 times more intense peak than those of a single-cavity PhC along with highly directive emission. The possibility of a strong enhancement of the emission intensity in certain directions may lead to the efficient Si-based light emitters fabrication. Such structures are interesting as the broadband light sources for numerous censoring applications, including fiber Bragg grating interrogation.

Conclusion

The hexagonal PhCs with coupled cavities arrays, such as missing holes, are studied using numerical modeling by a 3D FDTD method. The found array of 19 partially disordered cavities produces a box-like emission spectrum which is 3 times broader and 7 times more intense than a single-cavity emission peak. The author acknowledges RSoft Design Group, Inc., for providing the user license for FDTD simulations [18]. *Work is executed by a support of the grant No 14-19-00848 by the Russian Scientific Fund.*

References

1. R. Soref, *IEEE Journal of Selected Topics in Quantum Electronics* **12**, pp. 1678-1687 (2006).
2. B. Jalali and S. Fathpour, *J. Lightwave Tech.* **24**, pp. 4600-4615 (2006).
3. L. Pavesi, *J. Phys.: Cond. Mattter* **15**, pp. R1169–R1196 (2003).
4. N. A. Drozdov, A. A. Patrin and V. D. Tkachev, *JETP Lett.* **23**, 5 pp. 97-599 (1976).
5. A. Shakoor, R. Lo Savio, P. Cardile, S. L. Portalupi, D. Gerace, K. Welna, S. Boninelli, G. Franzo, F. Priolo, T. F. Krauss, M. Galli, L. O'Faolain, *Laser & Photonics Reviews* **7**, pp. 114-121 (2013).
6. R. Lo Savio, S. L. Portalupi, D. Gerace, A. Shakoor, T. F. Krauss, L. O'Faolain, L. C. Andreani, M. Galli, *Appl. Phys. Lett.* **98**, pp. 201106 (2011).
7. A. A. Shklyaev, A. S. Kozhukhov, V. A. Armbrister, and D. V. Gulyaev, *Appl. Surf. Sci.* **267**, pp. 40-44 (2013).
8. A. A. Shklyaev, Y. Nakamura, and M. Ichikawa, *J. Appl. Phys.* **101**, pp. 033532 (2007).
9. A. A. Shklyaev, D. V. Gulyaev, K. S. Zhuravlev, A. V. Latyshev, V. A. Armbrister and A. V. Dvurechenskii, *Optics Communications* **286**, pp. 228–232 (2013).
10. J. Xia, R. Tominaga, S. Fukamitsu, N. Usami, and Y. Shiraki, *Japanese Journal of Applied Physics* 48, pp. 2102 (2009).
11. A. Majumdar, A. Rundquist, M. Bajcsy, V. D. Dasika, S. R. Bank, and J. Vučković, *Phys. Rev. B* **86**, pp. 195312 (2012).
12. H.Altug, D.Englund, J.Vučković, *Nature Physics* **2**, pp. 484-488 (2006).
13. M. D. Weed, C. G. Williams, P. J. Delfyett, & W. V. Schoenfeld, *J. Lightwave Technol.* **31**, pp. 1426-1432 (2013).
14. Y.-J. Fu, Y.-Sh. Lee, and Sh.-Di Lin, *Opt. Lett.* **38**, pp. 4915-4918 (2013).
15. Y. Akahane, T. Asano, B. S. Song, and S. Noda, *Nature*, **425**, pp. 944-947 (2003).
16. S. L. Portalupi, M. Galli, Chr. Reardon, Th. Krauss, L. O'Faolain, L. C. Andreani, and D. Gerace, *Opt. Express* **18**, pp. 16064-16073 (2010).
17. I. Bulu, H. Caglayan, and E. Ozbay, *Appl. Phys. Lett.*, **83**, pp. 3263-3265 (2003).
18. Rsoft Photonic CAD Suite, version 8.0 (2007), www.rsofdesign.com.

Particle Patterning on Lithium Niobate waveguides via photovoltaic tweezers

M. Jubera[1], A. García-Cabañes[1], J. Olivares[2,3], J. Ramiro[4], A. Alcazar[4] and M. Carrascosa[1]

1. Universidad Autónoma de Madrid, Dept. Física de Materiales, Madrid, 28049, Spain
mariano.jubera@uam.es, angel.garcia@uam.es, m.carrascosa@uam.es
2. CMAM, Universidad Autónoma de Madrid, Madrid, 28049, Spain
3 I. Optica, Consejo Superior de Investigaciones Científicas, Madrid, Spain
4. Depto. Aerotecnia, Universidad Politécnica de Madrid, 28040 Madrid, Spain

Abstract: Successful micro and nano-particle patterning on iron doped lithium niobate waveguides using photovoltaic fields is reported. This technique previously used in bulk crystals is here applied to waveguide configuration. Well defined particle patterns are obtained using two types of planar waveguides (by proton exchanged and swift heavy ion irradiation) and metallic and dielectric neutral particles. The use of waveguide configuration has allowed a reduction of the light exposure time until 3 s, two orders of magnitude smaller than typical values used in bulk.

Dielectrophoretic (DEP) trapping and patterning of micro/nanoparticle using the electric fields generated by the bulk photovoltaic (PV) or more generally by the photorefractive (PR) effect in PR materials is an emergent field (see [1] and references therein) very promising for applications in nanophotonics and nanotechnology. Using this methodology (often called photovoltaic tweezers) remarkable patterning of dielectric dielectric and metallic particles has been achieved [1-4]. As an illustration an Al (d~70 nm) nano-particle pattern on Fe:$LiNbO_3$ is shown in fig 1.

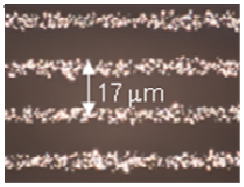


Fig1. Al nano-particle periodic pattern

In order to extend the applicability of PV tweezers in combination with integrated and/or opto-fluidic devices we have attempted particle trapping on PV photovoltaic waveguides. In this communication we present successful results for two types of Fe-doped $LiNbO_3$ waveguides obtained by soft proton exchanged (SPE) [5] and swift heavy ion irradiation (SHI) [6].

The PV fields are induced by the interference of two beams propagating through the waveguide. Then, two deposition methods have been tested: A) to blow out the particles on the sample in air or B) to immerse it in a non polar suspension of the particles. In fig. 2 we present representative results obtained with $CaCO_3$ (d~1-3 mm) in air (method A), and Al (d~70 nm) in hexane suspension (method B), for SHI waveguides. Particle patterns have been also obtained on SPE waveguides but the fringes have a lower quality and contrast.

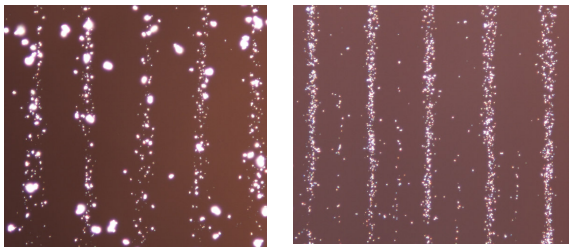


Fig 2. Microphotographs of the particle patterns deposited after sinusoidal light illumination (Λ=55 µm) during 10 min with $CaCO_3$ (left) and Al (right) particles and using method A and B respectively.

One of the potential advantages of using a waveguide configuration is the high light intensities reached in the waveguide and so, the faster recording of PV fields with regard to bulk crystals. To check the possibility of working with shorter time responses we have performed a set of experiments with decreasing times from 10 min (typical value for bulk experiments) to 3 s with $CaCO_3$ microparticles. Particle patterns have been obtained for all the time periods tested. In fig. 3 we can see the corresponding particle pattern for the shortest time of 3 s. It can be seen that a well defined and clean pattern is obtained showing the possibility of reducing two orders of magnitude the time exposure.

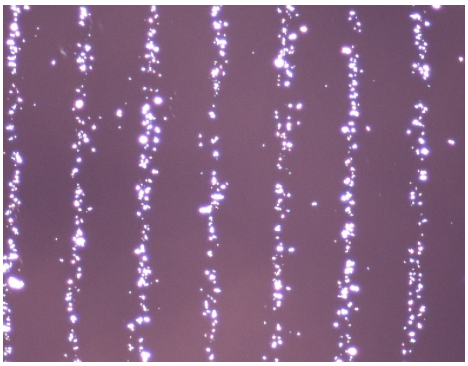


Fig 3. Microphotograph of a particle pattern deposited after sinusoidal light illumination (Λ=65 μm) during 3 s with $CaCO_3$ using method B

In summary, the use of PV tweezers in waveguide configuration allows to obtain well resolved particle patterns. It can be potentially applied to any kind of particles and enables the reduction of the PV time response. The results indicate the flexibility of this emergent methodology showing its suitability for application in integrated optical configurations.

This work was supported by grant MAT2011-28379-C03-01,-02,-03.

References

1. M. Esseling, F. Holtmann, M. Woerdemann, C. Denz, Opt. Express **18**, 17404 (2010)
2. H. Burgos et al Opt. Mat. **35** 1700 (2013)
3. H.A. Eggert, F.Y. Kuhnert, K. Buse, J.R. Adleman, D. Psaltis, Appl. Phys. Lett. 90 (2007) 241909
4. Z. Zhang, J. Wang, B. Tang, X. Tan, R.A. Rupp, L. Pan, Y. Kong, Q. Sun, J.Xu; Opt. Express 17 9981(2009)
5. O. Caballero et al. J. of Appl. Phys. **100**, 093103 (2006)
6. J. Olivares et al Nucl. Instr. Meth. B **257**, 765 (2007)

Analysis of Temperature Dependence of Ce:YIG for Athermal Waveguide Optical Isolator

Y. Shoji, T. Nemoto, T. Mizumoto

Tokyo Institute of Technology, Tokyo, Japan,
shoji.y.ad@m.titech.ac.jp

Abstract: The temperature dependence of optical properties of magneto-optic garnet Ce:YIG was analyzed for the athermal operation of the Mach-Zehnder interferometer (MZI) optical isolator composed of an SOI-based waveguide with a Ce:YIG upper cladding layer. By measuring the wavelength shift of transmittance due to temperature changes, the temperature dependences of the refractive index and magneto-optic coefficient of Ce:YIG were characterized to be 2.5×10^{-4} K^{-1} and 13 deg/cm/K, respectively. We discuss the design of an athermal waveguide optical isolator.

Introduction: A waveguide isolator is indispensable for integrated photonic circuits to realize the high-speed modulation and highly coherent operation of laser diodes. We have investigated Mach-Zehnder interferometer (MZI) based waveguide optical isolator and circulator having high optical isolation and wide operation bandwidth.[1,2] These devices are composed of a silicon-on-insulator (SOI) based photonic waveguide with a magneto-optic garnet upper cladding layer integrated using a surface activated direct bonding technique. The transmittance of MZI-based devices exhibits quasi-sinusoidal wavelength dependence. A temperature change causes the wavelength shift of transmittance characteristics due to the temperature dependences of refractive index (dn/dT) and magneto-optic coefficient ($d\theta_F/dT$). dn/dT of Si and SiO_2 are well-known at the telecom wavelength. However, dn/dT and $d\theta_F/dT$ of magneto-optic garnet Ce:YIG are unknown. In this report, in order to realize an athermal waveguide optical isolator, we investigate the dn/dT and $d\theta_F/dT$ of Ce:YIG by measuring the wavelength shift in transmittance of the MZI optical devices.

MZI-based nonreciprocal devices: Figure 1 shows a schematic of MZI-based optical isolator with silicon waveguides. The MZI has nonreciprocal and reciprocal phase shifters. The nonreciprocal phase shifter provides a phase differences of □ and + depending on the light propagation direction due to a magneto-optic effect. The reciprocal phase shifter provides a phase difference independently of the propagation direction by the asymmetric path length of MZI arm. In the transmitting direction, input light interfere constructively and is coupled to the output. On the other hand, in the isolating direction, the light launched into the device shows anti-phase interference and is radiated away from side ports. An MZI-based 4-port optical circulator can be formed by using 3 dB couplers having a 2×2 port configuration. The circular operation is achieved, since the in-phase and anti-phase interferences select the output path in a nonreciprocal manner.

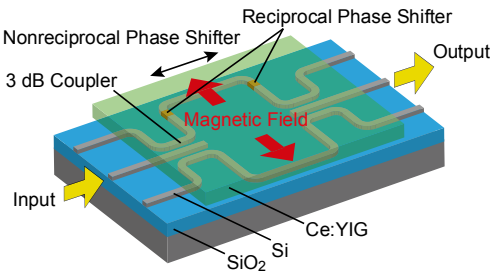


Fig. 1: Schematic of MZI based optical isolator with silicon waveguides.

Experimental results: The transmittance of isolator and circulator changes quasi-sinusoidally as a function of wavelength. With large asymmetry in the path difference between two arms, the free spectral range (FSR) of MZI interference becomes narrow and a noticeable wavelength dependence of a reciprocal phase difference 2+2 (: integer) is introduced. The wavelength shift in transmittance characteristics due to temperature changes is clearly observed in a measureable wavelength range. In this study, we fabricated an MZI circulator with a path difference of 44.7 , which corresponds to a reciprocal phase difference of m=66 at =1550 nm. The transmission spectrum of the circulator was measured using an amplified spontaneous emission light source and an optical spectrum analyzer thorough a fiber-to-fiber configuration. The temperature of the circulator was controlled from 10 °C to 75 °C using a sample stage equipped with a Peltier unit. Measured isolating wavelengths are plotted in Fig. 2 as a function of temperature. Blue and red plots correspond to adjacent isolating wavelengths with an FSR of 15 nm. Without applying magnetic field, the spectra in

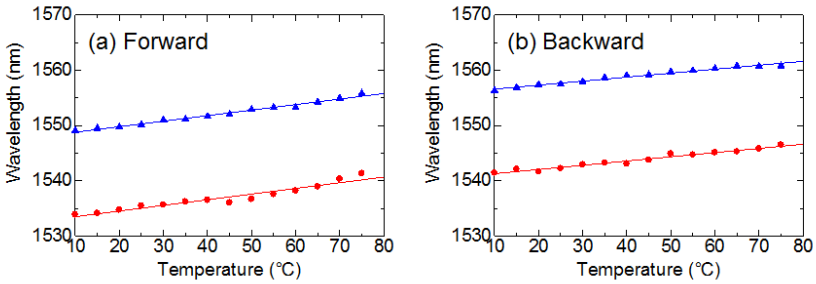


Fig. 2: Measured shift of isolating wavelengths in MZI circulator due to temperature change.

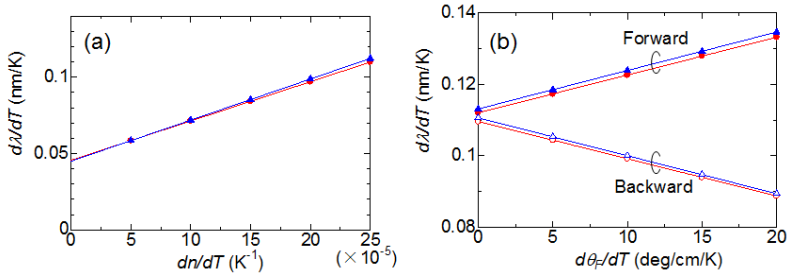


Fig. 3: Simulated wavelength shift as a function of dn/dT and $d\theta_F/dT$ of Ce:YIG.

forward and backward directions were identical due to the absence of the magneto-optic effect. By applying magnetic field, the transmission peak in the forward direction coincides with the transmission bottom in the backward direction.

Analysis of temperature dependence: Firstly, the transmission spectra was simulated by an optical mode solver using refractive indexes of Si, SiO_2, and Ce:YIG at room temperature. Then, dimensions of the Si core are corrected so that the simulated FSR agrees with measured one. Secondly, the wavelength shift due to temperature changes was simulated using dn/dT=1.86×10^{-4} K^{-1} and 1.0×10^{-5} K^{-1} for Si and SiO_2, respectively,[3] as a function of dn/dT of Ce:YIG as shown in Fig. 3(a). Since the slope of the measured wavelength shift without applying magnetic field was 0.11 nm/K, dn/dT of Ce:YIG is estimated to be 2.5×10^{-4} K^{-1}. The nonreciprocal phase shift was simulated by a perturbation theory using the Faraday rotation coefficient of Ce:YIG.[4] The wavelength shift due to temperature changes was simulated as a function of $d\theta_F/dT$ as shown in Fig. 3(b). Since the slope of the measured wavelength shift with magnetic field applied was 0.13 and 0.10 nm/K in the forward and backward directions, $d\theta_F/dT$ of Ce:YIG is estimated to be 13 deg/cm/K for θ_F= −3536 deg/cm at room temperature.

Conclusions: By measuring the wavelength shifts of an MZI nonreciprocal device, the temperature dependences of refractive index and Faraday rotation coefficient of Ce:YIG were analyzed to be 2.5×10^{-4} K^{-1} and 13 deg/cm/K, respectively. Increase in refractive index at high temperature results in an increase in a reciprocal phase difference. The Faraday rotation is decreased at high temperature, which results in a decrease in a nonreciprocal phase difference. Therefore, if we choose proper waveguide dimensions and the length of reciprocal phase shifter, deviations in nonreciprocal and reciprocal phase differences due to temperature changes are cancelled in the backward direction. Then, the athermal operation of a waveguide optical isolator is expected. For example, when the cross-sectional Si waveguide dimension is 550 nm × 220 nm and the length of reciprocal phase shifter is 4.3 μm, the wavelength shift due to a temperature change from -10 °C to 60 °C is expected to be less than 0.081 nm at ~1550 nm..

References

1. Y. Shoji, Y. Shirato, T. Mizumoto, *Jpn. J. Appl. Phys.* **53**, 022202 (2014).
2. K. Mitsuya, Y. Shoji, T. Mizumoto, *IEEE Photon. Technol. Lett.* **25**, pp. 721–723 (2013).
3. M. Harjanne, M. Kapulainen, T. Aalto, P. Heimala, *IEEE Photon. Technol. Lett.* **16**, pp. 2039–2041 (2004).
4. Y. Okamura, H. Inuzuka, H. Kikuchi, S. Yamamoto, *J. Lightwave Technol.* **LT-4**, pp. 711–714 (1986).

Study of the magneto-optical interaction in a hybrid non-reciprocal mode converter

J.P. Garayt[1], E. Jordan[2], F. Parsy[2], E. Ghibaudo[2], F. Royer[1], J-E. Broquin[2], S. Neveu[3], D. Jamon[1]

[1] Université de Lyon, F-42023 Saint Etienne, France and Université de Saint Etienne, Jean Monnet, F-42000 Saint Etienne, LT2C EA 3523,
jean.philippe.garayt@univ-st-etienne.fr, francois.royer@univ-st-etienne.fr, damien.jamon@univ-st-etienne.fr
[2] IMEP-LAHC, UMR INPG-UJF-CNRS 5130, BP 257/38 016 Grenoble Cedex, France,
elodie.jordan@imep.grenoble-inp.fr, francois.parsy@minatec.grenoble-inp.fr, elise.ghibaudo@ujf-grenoble.fr, jean-emmanuel.broquin@minatec.inpg.fr
[3] Sorbonne Universités, UPMC Univ Paris 06, UMR 8234, PHENIX, F-75005 Paris, France,
sophie.neveu@upmc.fr

Abstract: In this paper, we aim at determining the magneto-optical (MO) behavior of a TE-TM mode converter. This last is based on an hybrid interaction between a MO layer and a waveguide obtained by ion exchanged technology on glass. Comparison between measurements and theoretical behavior can be applied to give some clues for a better understanding of the MO measurements.

Introduction

In the framework of the development of optical telecommunication, lots of optical functionalities have to be integrated and, at this time, this has been achieved [1-2] for most of them. Nevertheless, optical isolation is still missing because its integration comes up against a material problem: classical MO materials, such as YIG or (Ce or Bi) substituted YIG, need high crystallization temperature (750-800°C) [3] and close lattice substrate (GGG), which make this kind of material incompatible with integration technologies. To overcome this, different approaches have been carried out, and among them the use of magnetic cobalt ferrite ($CoFe_2O_4$) nanoparticles embedded in a sol gel matrix [4]. This composite material can be coated on ion exchanged waveguides [5], and a MO mode conversion, which is a major step in the integration of an optical isolator, has been demonstrated [4]. In the following sections, we will focus on the mechanism of the MO interaction in such a hybrid structure.

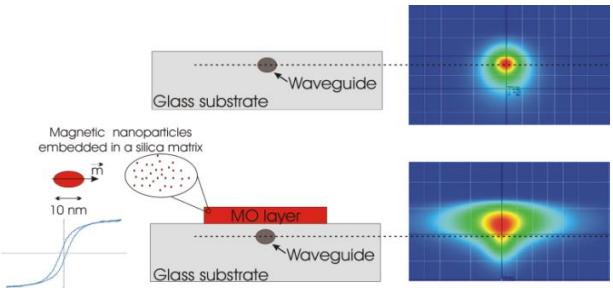


Fig. 1: Hybrid magneto-optic mode converter

Magneto-optical interaction

Free space Faraday rotation leads to a rotation of the polarization plane proportional to the magnetization of the sample. In guided configuration, as only TE and TM modes can propagate, the Faraday rotation leads to a TE-TM modal conversion which magnitude is limited by the difference between their propagation constant Δβ. According to the coupled mode theory [6], this conversion can be expressed as:

$$\frac{dA_{TE}}{dz} = iK(z).A_{TM}\,exp(i\Delta\beta z)$$
$$\frac{dA_{TM}}{dz} = iK^{*}(z).A_{TE}\,exp(-i\Delta\beta z) \quad (1)$$

Where: A_{TE} and A_{TM} are respectively the magnitude of the TE and TM modes. The coupling coefficient K(z) is proportional to the amount of modes energy confined in the MO layer, and to the

magnetization of the layer through the off-diagonal element in the dielectric tensor which is determined experimentally by the measurement of the free space Faraday rotation.

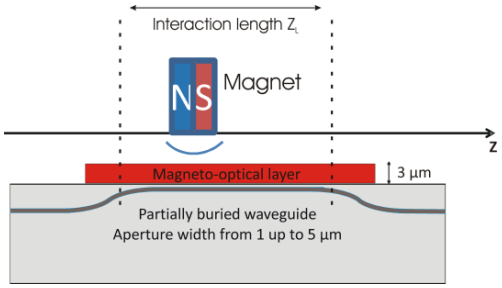


Fig. 2: partially buried waveguide

Sample preparation and characterization

Magnetic nanoparticles, issued from a magnetic liquid, are added to a sol gel solution [4]. Then, using dip coating technique, a thin film, with a specific Faraday rotation of 140°.cm^{-1}, is coated on a glass substrate containing partially buried channel waveguides made by a silver/sodium ion exchange process and followed by a selective burying process [7-8]. This last step allows both the delimitation of the interaction length Z_L and the reduction of the reflection losses due to the change of the effective index in the MO area thanks to an adiabatic transition (Fig. 2). The characterization of the MO waveguide is made via the analysis, with a lab-built polarimeter [8], of the emerging polarization under the influence of a longitudinal magnetic field. This polarization is characterized by its azimuth γ, and its ellipticity ε, with respect to the waveguide axis. A permanent neodymium magnet is moved along the whole waveguide, and the emerging polarization is recorded as a function of its position (fig. 3). At first, we can observe oscillations whose period L_B is related to the modal birefringence ($\Delta\beta = \frac{2\pi}{L_B}$) [9]. We can notice also that these oscillations exceed the interaction length: this is due to the fact that the magnetic field created by the magnet is spreading along the z axis. Thus, modeling the behavior of such MO converter, using numerically integration of the differential equations system (eq.1), requires taking into account all of these parameters by the introduction of a z dependent term in the coupling coefficient K. This will lead to the determination of the amount of power confined in the MO layer. It is, mainly due to the adiabatic transition, z dependent. Typical result is shown in fig. 3 for a 0.5mm thick neodymium magnet. The global shape of the simulated curves is globally the same as the experimental points, even if some details differ in the magnitude of the polarization angles.

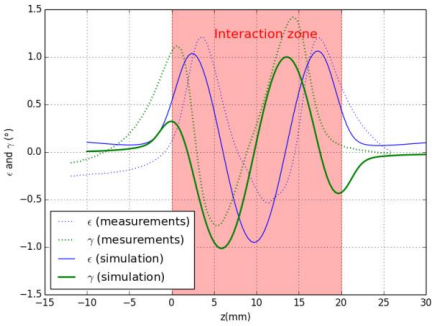


Fig.3: simulated and measured sample emerging polarization

Conclusion

Based on MO measurements, we have modelized the behavior of a MO mode converter in order to extract some information such as MO confinement in a hybrid configuration. These first results from our simulations are rather in good agreement with our measurements. Further improvements of the model will allow us to better understand all the mechanisms underlying the mode conversion in guided configuration**.**

References

1. D.F. Geraghty, D. Provenzano *et al*, Electron. Lett. **37**, n°13 (2001).
2. H. Takahashi, Y. Hibino, and I. Nishi, Opt Lett., **17**, n°7 (1992).
3. D. C. Hutchings, J. phys. D: Appl. Phys. **36**, 2222 (2003)
4. H. Amata, F. Royer *et al*, Appl. Phys. Lett., **89** (2011)
5. T. Izawa and H. Nakagome, Appl. Phys. Lett., **21**, 584-586 (1972)
6. M. Lohmeyer, N. Bahlmann, and al, Opt. Comm., **158**,189-200 (1998)
7. O. Bertoldi, J.-E. Broquin *et al*, Proceeding of Spie, **5451**, 2004
8. D. Jamon , F. Royer , F. Parsy , E. Ghibaudo and J.-E. Broquin, J. Lightw. Technol., **31**, no. 19, pp.3151 -3157 2013

Cross-Connected Notch Filter with a Flat Stopband and Double Free-Spectral-Range

Chyong-Hua Chen

National Chiao Tung University, Hisnchu, Taiwan,
chyong@mail.nctu.edu.tw

Abstract: A novel cross-connected filter constructed by a microring resonator, a multi-mode interference based crossing and a resonant loop is numerically presented. The microring resonator consists of two arc waveguides with slightly different effective indices to achieve a second-order filtering owing to the existence of the bidirectional propagation modes in the resonator. The device is numerically simulated using the scattering matrix method, functioning as a notch filter with a square stopband and double free spectral range by manipulating the length of the resonant loop and the effective indices of the arc waveguides.

Introduction: In the past decades, microring resonators (MRRs) are promising building blocks in wide applications, such as wavelength-division multiplexing (WDM) communication system, telecommunications, computer interconnects, and biochemical sensing [1-3]. For the applications of an optical channel filters in the WDM system, it is required to have a boxlike spectral shape, large out-of-band signal rejection and wide free spectral range (FSR) to ensure signal fidelity, to enhance the tolerance of signal wavelength shifts and to accommodate large channel counts. Various approaches have been proposed to enlarge the FSR, including reducing the microring radius [4], cascading serial MRRs based on Vernier effect [5-7] and merging Mach-Zehder interferometer with MRRs [8-9]. However, multiply coupled cavities are used to realize a boxlike response, giving rise to the increment of the device's size [5-8]. Here, we propose a novel cross-connected notch filter using a single MRR to realize a flat response and double FSR. This filter consists of a multimode interference (MMI) crossing, a MRR and a resonant loop connecting the throughput- and one drop-ports of the MMI crossing. The MRR is assembled by two arc waveguides with different effective indices to obtain a second-order microring filter with a flat response, and the length of the resonant loop is adjusted to realize double FSR.

Design of the cross-connected notch filter: The configuration of the proposed cross-connected notch filter is schematically depicted in Fig. 1. This filter consists of a MMI crossing and a side-coupled MRR with a radius of R_1. The throughput- and one drop ports of the MMI crossing are connected to form a large resonant loop with a length of L. The MMI crossing design is based on our previous work [10], which is compact, low loss, low crosstalk and broadband. The MRR is comprised of two arc waveguides with subtend angles of θ and $2\pi-\theta$, respectively. Two arc waveguides have different effective indices to allow both forward and backward propagating modes to travel inside the MRR and the resonant loop. The separation distance of the directional coupler between the MRR and the bus waveguide in the throughput/drop port is d, corresponding to the coupling coefficient κ.

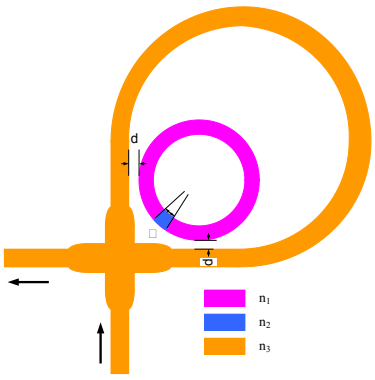


Fig.1. Schematic diagram of the proposed cross-connected notch filter

Scattering matrix approach taking into account the bidirectional coupling among these elements is used to analyze this structure [11]. Suppose that the effective indices of two arc waveguides and the resonant loop are n_1, n_2 and n_3, respectively. The attenuation coefficients for these waveguides are α. From the transfer function at the other drop port, the path length difference between the three quarters of the MRR and the resonant loop has to equal to half path length of the MRR, i.e.,

$$n_3 L - 3\pi n_1 R_1 / 2 = \pi n_1 R_1 \qquad (1)$$

This formulation indicates that the arc waveguide with subtend angle of θ arranged in the lower quarter of the MRR imperceptibly affects the FSR. Consider a structure with the following parameters: R_1=5 μm, n_1= n_3=2.33, n_2=2.53, α=0.0001 and θ=0.5. Then, the corresponding L is 39.3 μm. The coupling coefficient κ is critical to the performance of this device, and κ for each coupler is 0.99 to obtain the minimal transmission in the stopband in this case. Figure 2 shows the transmission spectrum of this structure. The FSR of 61.1 nm and the full width at half maximum (FWHM) of 7 nm are observed. The FSR of this structure is expanded roughly twice that of a single MRR, ~31 nm with a radius of 5 μm. The maximum transmission of roughly 0.97 is obtained due to the propagation loss of MRR and the loop.

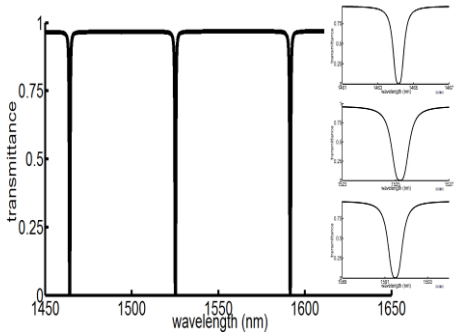


Fig. 2. Transmission spectrum of the designed notch filter

The variation of n_2 on the transmission spectrum is illustrated in Fig. 3. For each n_2, the coupling coefficient κ is optimized to obtain the minimal transmission in the stopband. We observe that a Lorentzian-shaped spectrum is obtained as n_2=2.33, and the FWHM becomes wider and the spectrum becomes U-shaped as n_2 increases. In addition, the resonant wavelength shifts to longer wavelength. As shown in the inset of Fig. 3, FSR remains the same as n_2 varies, but the crosstalk roughly at the wavelength of 1495 nm becomes more obvious owing to the phase mismatch between two resonances.

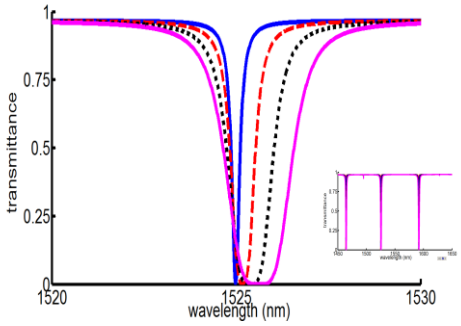


Fig. 3. Transmission spectra for n_2=2.33 (blue curve), 2.53 (red curve), 2.73(black curve) and 2.93 (magenta curve).

Conclusion:

We numerically present a compact cross-connected notch filter with a flat response and the double FSR by using scattering matrix method. This filter consists of a MMI crossing, a MRR and a resonant loop. The MRR consists of two arc waveguides where forward and backward traveling modes propagate, and then a second-order filter with a square response is obtained by adjusting the coupling coefficient κ. The double FSR is realized by controlling the length of the resonant loop roughly equal to the perimeter of five-quarter MRR. The bandwidth of this filter can be controlled by varying the effective index difference between the arc waveguides.

References

1. W. Bogaerts et al. *Laser Photonics Rev.***6**, pp. 47–73 (2012).
2. Q. Xu et al., *Nature* **435**, pp. 325-327(2005).
3. A. Melloni et al, *Opt. Lett.* **28**, pp.1567-1569 (2003).
4. Q. Xu, D. Fattal, and R. G. Beausoleil, *Opt. Express* **16**, pp. 4309–4315 (2008).
5. Y. Yanagase et al., *J. Lightwave Technol.* **20**, pp.1525-1529 (2002).
6. R. Grover et al., *J. Lightwave Technol.* **20**, pp. 900-905 (2002).
7. S. Xiao et al., *Opt. Express***15**, pp.14765–14771 (2007).
8. M. R. Watts et al., *Conference on LEOS,* CMP3 (2005).
9. L. Zhou and A. W. Poon, *Opt. Express***15**, pp. 9194–9204 (2007).
10. C.H. Chiu and C.H. Chen, *IEEE J. Quantum Electron.* **46**, pp. 656–1661 (2010).
11. J. Capmany and M. A. Muriel, *J. Lightwave Technol.* **8**, pp.1904-1919 (1990).

Loss Uniformity Improvement of Arrayed-waveguide Grating Router using Interleaved Chirped Array

H. Asakura[1] **and H. Tsuda**[1]

[1] *School of Integrated Design Engineering, Graduate School of Science and Technology, Keio University, Yokohama-shi, Kanagawa, Japan,*
askr@tsud.elec.keio.ac.jp, tsuda@elec.keio.ac.jp

Abstract: An arrayed-waveguide grating router using interleaved chirped array (IC-AWGR) is proposed. We designed 32 x 32, 50-GHz channel spacing IC-AWGR. The minimum loss of the IC-AWGR is 4.75 dB with a loss variation of 1.08 dB.

Introduction: An arrayed-waveguide grating router (AWGR) is a planar lightwave circuit which enables N frequency channels to make strictly nonblocking N x N interconnections.[1] The free spectral range (FSR) of the conventional N x N AWGR is equal to the product of N and the channel spacing. The conventional AWGR has large loss variation and the center frequency deviations of wavelength channels, depending on the combination of the input and the output ports.[2] To improve these characteristics, an uniform-loss and cyclic-frequency (ULCF) configuration or an interconnected multiple AWG configuration were reported.[1] These configurations showed good characteristics, however, the former requires a lot of couplers and waveguide crossings, the latter requires a lot of AWGs. An AWG using interleaved chirped array has been reported as multiplexer of optical cross connect.[3] However, a configuration of AWGR using interleaved chirped array has never be reported.

In this paper, we propose AWGR using interleaved chirped array (IC-AWGR) which has improved loss uniformity characteristics. We designed AWGR for newly developing thousand-band (T-band, 1000 –1260 nm) communication[4].

Principle: An IC-AWGR consists of input waveguides (1a, 2a,… 8a), slab waveguides, an arrayed-waveguide with interleaved chirping, and output waveguides (1b, 2b,… 8b). The length of the shortest waveguide in the arrayed-waveguide is L_0. The length of i-th interleaved chirping waveguide in the arrayed-waveguide, L_i, is derived by eq. (1) [3].

$$L_i = L_0 + (i - 1)\Delta L + \lambda_0/(4n_c) * \mathrm{Modulo}_2(i + 1),\ i = 1, 2, 3,\ldots \quad (1)$$

ΔL is path difference of arrayed-waveguide, λ_0 is center wavelength of the AWGR, and n_c is effective index of the arrayed-waveguide. Figure 1 shows transmission spectra of the IC-AWGR and a normal AWGR when the center input waveguide and the center output waveguide are used. The FSR of the IC-AWGR is one-half compared to the FSR of the normal AWGR. The peak transmittance is 3 dB lower than that of the normal AWG. Table 1 shows output wavelength channel relation of connection between input waveguides and output waveguides. 1a, 2a, …, and 8a are input waveguide number, 1b, 2b, …, and 8b are output waveguide number. Arabic numerals (1, 2,…, 8) mean wavelength channel number. Two wavelength channels are output, when one input waveguide and one output waveguide are used. A gray part of table 1 satisfies cyclic condition and operates as AWGR when 3rd, 4th, 5th, and 6th wavelength channels are used.

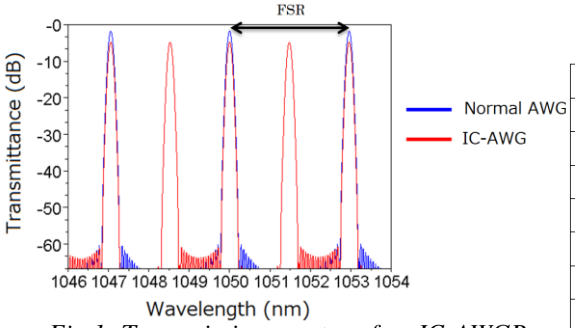


Fig.1: Transmission spectra of an IC-AWGR and a normal AWGR.

Table.1: Channel relation of connection.

In/Out	1b	2b	3b	4b	5b	6b	7b	8b
1a	2, 6	3, 7	4, 8	1, 5	2, 6	3, 7	4, 8	1, 5
2a	3, 7	4, 8	1, 5	2, 6	3, 7	4, 8	1, 5	2, 6
3a	4, 8	1, 5	2, 6	3, 7	4, 8	1, 5	2, 6	3, 7
4a	1, 5	2, 6	3, 7	4, 8	1, 5	2, 6	3, 7	4, 8
5a	2, 6	3, 7	4, 8	1, 5	2, 6	3, 7	4, 8	1, 5
6a	3, 7	4, 8	1, 5	2, 6	3, 7	4, 8	1, 5	2, 6
7a	4, 8	1, 5	2, 6	3, 7	4, 8	1, 5	2, 6	3, 7
8a	1, 5	2, 6	3, 7	4, 8	1, 5	2, 6	3, 7	4, 8

Design: The 32 x 32 IC-AWGR was designed, the center wavelength was 1050 nm, the FSR was 3200 GHz, and the channel spacing was 50 GHz. We used silica waveguides with a relative index difference of 1.5 %, and the core dimension of 4.5 μm x 4.5 μm. At the center wavelength, the effective index in arrayed-waveguide, n_c, was 1.46633, and the group index of effective index, N_c was 1.48697. The number of waveguide in arrayed-waveguide was 192, and the diffraction order was 87. The path difference, ΔL is 63.3 μm, and the length of slab waveguide was 14.8 mm.

Simulation results: Transmission characteristics of three types of AWGR were calculated. One is the IC-AWGR, and the others are normal AWGRs which have FSR equal to the product of 32 channels and 50-GHz channel spacing. The normal AWGR, which is named AWGR-A, has the same diffraction efficiency[5] as that of the IC-AWGR. The other normal AWGR, which is named AWGR-B, has low diffraction efficiency to improve loss uniformity. The AWGR-B has wide gap of 14 μm between waveguides in boundary between slab waveguide and arrayed-waveguide to reduce diffraction efficiency. The parameters of the normal AWGRs are 32 x 32, and 50-GHz channel spacing. The number of waveguide in arrayed-waveguide is 96, the diffraction order is 175, and the path difference is 125.3 μm. The former has a slab waveguide with a length of 7.4 mm, and the latter has a slab waveguide with a length of 14.8 mm. Figure 2 shows simulation results of loss characteristics. The maximum loss and the minimum loss in 32 wavelength channels for each output waveguide are indicated. In all combinations of input and output waveguides, the minimum losses of the IC-AWGR, the AWGR-A, and the AWGR-B are 4.75 dB, 1.74 dB, and 7.76 dB, respectively. The maximum losses are 5.83 dB, 6.05 dB, and 8.84 dB, respectively. Loss variations of the IC-AWGR, the AWGR-A, and the AWGR-B, which are the ratio of the maximum loss to the minimum loss, are 1.08 dB, 4.31 dB, and 1.08 dB, respectively. The loss variation of the IC-AWGR is as same as that of the AWGR-B, but the loss is smaller than it by about 3 dB. The AWGR-A has smaller loss but the loss variation is larger.

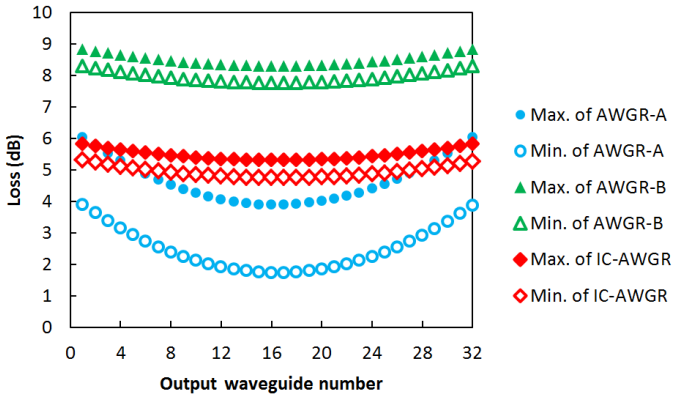


Fig. 2: Loss characteristics of AWGRs.

Conclusions: The 32 x 32, 50-GHz channel spacing AWGR using interleaved chirped array is designed. The minimum loss of the IC-AWGR is 4.75 dB with a loss variation of 1.08 dB. The IC-AWGR has better loss uniformity than that of a normal AWGR.

Acknowledgement: This research was financially supported by the National Institute of Information and Communications Technology (NICT), Japan.

References

1. S. Kamei, M. Ishii, A. Kaneko, T. Shibata, and M. Itoh, *Journal of Lightwave Technology* **27**, pp. 4097–4104 (2009).
2. H. Takahashi, K. Oda, H. Toba, and Y. Inoue, *Journal of Lightwave Technology* **13**, pp. 447–455 (1995).
3. C. R. Doerr, *IEEE Photonics Technology Letters* **10**, pp. 528–530 (1998).
4. N. Yamamoto, K. Akahane, T. Kawanishi, Y. Omigawa, H. Sotobayashi, Y. Yoshioka, and H. Takai, *Optics Express* **19**, pp. B636–B644 (2011).
5. H. Takahashi, S. Suzuki, and I. Nishi, *Journal of Lightwave Technology* **12**, pp. 989–995 (1994).

TE-TM Mode Conversion Optical Isolator Employing Halfwave Plate Integrated with Spot-Size Converters

Hideki Yokoi, **Daisuke Tamura, Yukihiro Okada**

Shibaura Institute of Technology, Tokyo, Japan,
yokoi@sic.shibaura-it.ac.jp

Abstract: A TE-TM mode conversion optical isolator consists of a nonreciprocal mode converter and a reciprocal mode converter. The reciprocal mode converter is realized by a polyimide halfwave plate inserted into a groove. In order to suppress diffraction loss, a spot-size converter was integrated at both an input facet and an output facet of the halfwave plate. By introducing the spot-size converter, the insertion loss due to the halfwave plate could be reduced to approximately 0.22 dB.

Introduction: In optical communication systems, an optical isolator is indispensable in protecting optical active devices from unwanted reflected light. An optical isolator employing a TE-TM mode conversion comprises nonreciprocal and reciprocal mode converters.[1] Therefore, complicated control of direction of magnetization is needed. To overcome the difficulties associated with the mode-conversion isolator, a hybrid optical isolator with a halfwave plate was proposed.[2] The control of direction of magnetization is required for the nonreciprocal mode converter only. In this paper, the authors report on the TE-TM mode conversion optical isolator which employs the halfwave plate integrated with spot-size converters for suppressing diffraction loss.

Device structure: Figure 1 shows a TE-TM mode conversion optical isolator with a halfwave plate. The optical isolator consists of the $\pi/4$-rad nonreciprocal mode converter and the $\pi/4$-rad reciprocal mode converter. The nonreciprocal mode converter is comprised of the magneto-optic waveguide with a $(CeY)_3Fe_5O_{12}$ (Ce:YIG) guiding layer. An external magnetic field in the longitudinal direction is applied to the magneto-optic waveguide for the nonreciprocal mode conversion. A polyimide halfwave plate is inserted into a groove fabricated in the waveguide as a $\pi/4$-rad reciprocal TE-TM mode converter.[3]

For the forward-traveling light wave, the $-\pi/4$-rad nonreciprocal mode conversion is cancelled by the $+\pi/4$-rad reciprocal mode conversion. Consequently, the polarization state of the output light wave is identical with that of the input light wave. For the backward-traveling wave, on the other hand, the nonreciprocal mode conversion changes its sign to $+\pi/4$ rad. This mode conversion is added to the reciprocal mode conversion, and the whole mode conversion amounts to $\pi/2$ rad. The polarization state of the output light wave is normal to that of the input light wave. Therefore, the device equipped with two polarizers, whose polarization azimuth is identical, at both the input port and the output port acts as an optical isolator. The optical isolator can operate for both TE mode and TM mode depending on the azimuth of the polarizers.

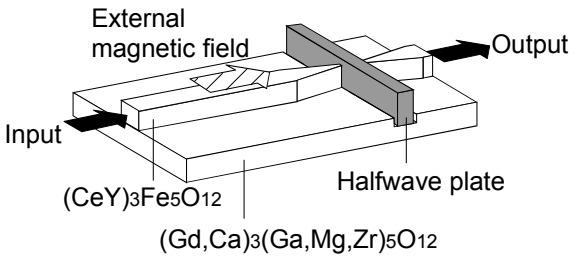


Fig. 1. TE-TM mode conversion optical isolator with Ce:YIG guiding layer.

As can be seen in Fig. 1, the polyimide halfwave plate is inserted into the groove in the magneto-optic waveguide. Propagation through the halfwave plate gives rise to diffraction loss due to the lack of an optical confinement structure. Diffraction loss was calculated when the light wave propagated in a slab waveguide with the groove. Figure 2 shows the calculated diffraction loss depending on the groove width. The refractive index of the polyimide halfwave plate was assumed to be 1.6 at 1.55 μm.[2,3] The thickness of the slab waveguide H was 1.0, 1.5, 2.0, 3.0 and 5.0 μm, respectively. Smaller the thickness H is, larger the diffraction loss is, which is derived from a small optical confinement factor. In

consideration of a single-mode condition, however, it is desirable that the magneto-optic waveguide has a small Ce:YIG core. There is a trade-off between the diffraction loss and the single-mode condition.

In order to circumvent the diffraction loss, a spot-size converter was introduced into the waveguide at both an input facet and an output facet of the halfwave plate as shown in Fig. 1. The spot-size converter was designed in order to minimize the diffraction loss at 1.55 μm. The strip height and the strip width were assumed to be 0.80 μm and 1.0 μm, respectively. The thickness of the halfwave plate was assumed to be 20 μm in the light of the thickness of the polyimide halfwave plate. In consideration of the calculated diffraction loss, the taper length and taper width were determined to be 300 μm and 0.25 μm, respectively. Figure 3(a) shows the propagation characteristics of the TE mode through the halfwave plate without the spot-size converter. The propagation loss due to the insertion of the halfwave plate without the spot-size converter was more than 20 dB. When the halfwave plate was integrated with the spot-size converter, the propagation loss was reduced to approximately 1.48 dB. Moreover, when the spot-size converter was covered by an SiO_2 cladding layer, the propagation loss was reduced to approximately 0.22 dB. Figure 3(b) shows the propagation characteristics of the TE mode through the halfwave plate integrated with the spot-size converter covered by the SiO_2 cladding layer. By introducing the spot-size converter at both facets of the halfwave plate, the magneto-optic waveguide satisfies not only a single-mode condition but also a small diffraction loss.

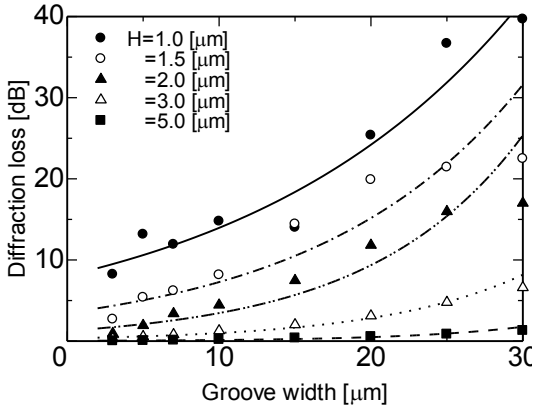


Fig. 2. Calculated diffraction loss depending on groove width.

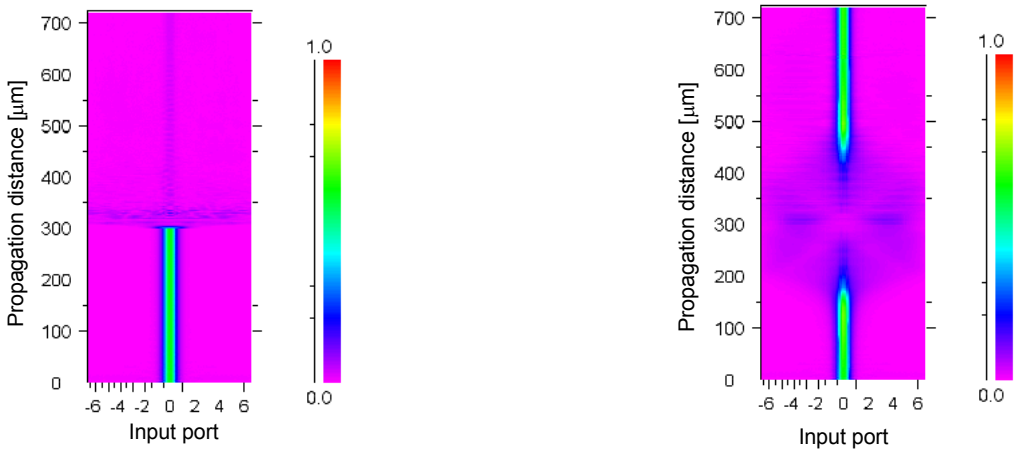


Fig. 3. Propagation characteristics of the TE mode (a) without a spot-size converter and (b) with a spot-size converter covered by a SiO_2 cladding layer.

Conclusion: We discussed an optical isolator employing a TE-TM mode conversion. The reciprocal mode converter was realized by a polyimide halfwave plate integrated with a spot-size converter. By introducing the spot-size converter for an input facet and an output facet of the halfwave plate, the propagation loss due to the halfwave plate could be reduced to approximately 0.22 dB.

References

1. J. P. Castera and G. Hepner, *IEEE Trans. Magn.* **MAG-13**, pp.1583-1585, (1977).
2. N. Sugimoto, H. Terui, A. Tate, Y. Katoh, Y. Yamada, A. Sugita, A. Shibukawa, and Y. Inoue, *J. Lightwave Technol.* **14**, pp.2537-2546, (1996).
3. S. Ando, T. Sawada, and Y. Inoue, *Electron. Lett.* **29**, pp.2143-2145, (1993).

Bandwidth and Offset Launch Investigations on a 1.4 m Multimode Polymer Spiral Waveguide

Jian Chen[1], Nikos Bamiedakis[1], Richard V. Penty[1], Ian H. White[1], Petter Westbergh[2], Anders Larsson[2]

[1] University of Cambridge, 9 JJ Thomson Avenue, Cambridge, United Kingdom, jc791@cam.ac.uk
[2] Chalmers University of Technology, SE-412 96 Göteborg, Sweden

Abstract: Bandwidth measurements are conducted on a 1.4 m long spiral polymer multimode waveguide for a SMF and 50/125 μm MMF launch and for different input offsets. The waveguide exhibits a bandwidth of at least 30 GHz for all input types, yielding a bandwidth-length product of at least 42 GHz×m, while no impact is observed on the waveguide performance due to the different spatial input offsets. The results indicate that data transmission at data rates even higher than 25 Gb/s can be achieved over such structures, thereby demonstrating the potential of multimode polymer waveguide technologies in short-reach board-level datacommunication links.

Introduction: High bandwidth short-reach optical interconnects have been of particular interest in recent years in high-performance computing and data centre environments due to the inherent drawbacks of traditional electrical interconnects such as high frequency loss, poor immunity to electromagnetic interference and heat dissipation issues.[1,2] Multimode polymer waveguides are potential candidates for use in board-level optical interconnections owing to the large bandwidth, low crosstalk and high density that they can offer. In recent years polymer materials which possess favourable optical, mechanical and thermal properties enabling cost-effective integration on printed circuits boards (PCBs) have been developed.[3,4] The use of large core size optical waveguides further offers relaxed alignment tolerances enabling therefore cost-effective board assembly.[5] However, the demand of higher and higher data rates increases for on-board interconnects, the bandwidth limitation of multimode waveguide due to modal dispersion needs to be examined. This paper presents therefore bandwidth studies and offset launch investigations on a 1.4 m long spiral waveguide, which we believe demonstrates a record performance achieving bandwidth-length product of at least 42 GHz×m for this long integrated waveguide**.**

Experimental Results: The 1.4 m long spiral waveguide is fabricated on a 6-inch glass substrate using siloxane polymer materials (Core: Dow Corning® OE-4140 Cured Optical Elastomers; cladding: OE-4141 Cured Optical Elastomer). The core and cladding materials, with bulk refractive indices of 1.52 and 1.50 respectively, are spun onto the substrate directly; and the waveguide is patterned by standard photolithographic methods.[1] The waveguide core has a cross section of 50×20 μm^2 and is sandwiched between the top and cladding layers. A vector network analyser (Agilent 8722ET) is used to measure the S_{21} parameter of the optical link with and without (back-to-back) the waveguide (Fig. 1a and 1b). The frequency response of the waveguide can be obtained from the difference between the recorded frequency response of the waveguide link and the back-to-back link. The waveguide frequency response is investigated under different launch conditions as different mode power distributions at the waveguide input can often result in different levels of multimode dispersion in the guides. A single-mode fibre (SMF) is used to emulate a restricted launch while a "typical" and a quasi-overfilled 50/125 μm multimode fibre (MMF) launch are used to investigate the waveguide performance with a broader mode power distribution at the waveguide input. The "typical" 50/125 μm MMF launch is obtained by directly butt-coupling a cleaved MMF patchcord with the VCSEL source, while the quasi-overfilled 50/125 μm MMF launch is achieved with the use of a mode mixer (Newport FM-1) before the waveguide.

An 850 nm vertical-cavity surface-emitting laser (VCSEL) (bandwidth of ~ 25 GHz)[6] is used as the transmitter, and a photodiode (VIS D30-850M) with bandwidth of 30 GHz is employed as the receiver. The VCSEL is butt-coupled to the input fibre patchcord (either SMF or 50/125 μm MMF), and a cleaved 50/125 μm MMF is used to couple the light output from the waveguide to the photodiode. Index-matching gel is used at the waveguide input and output facets to reduce the

scattering losses due to surface roughness. An Agilent NA7766A variable optical attenuator (VOA) is employed to adjust the optical power received by the photodiode. Fig. 1c, 1d and 1e show the obtained frequency response of the waveguide for the SMF, the "typical" and quasi-overfilled 50/125 µm MMF input respectively with the different horizontal input offsets. The presented results are normalised with respect to that of the back-to-back link, showing that the frequency responses remain approximately constant up to the 30 GHz instrumentation limit for all launch conditions.

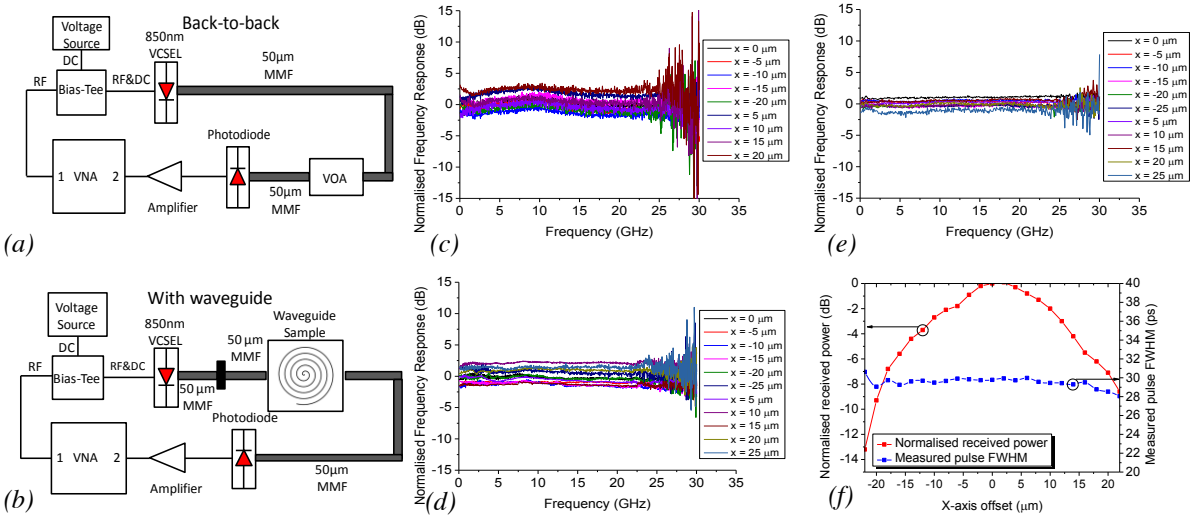


Fig. 1: Experimental set-up of the S_{21} parameter measurement for (a) the back-to-back link and (b) the waveguide link for the 50 µm MMF input. The normalised frequency response of the spiral waveguide for different offsets is shown under (c) a SMF, (d) a typical and (e) a quasi-overfilled 50 µm MMF input; (f) shows the normalised received optical power and FWHM of received signal as a function of the input position.

The dynamic performance of the waveguide is examined for a SMF input to confirm the observations obtained from the S_{21} measurement. A single pulse is generated by modulating the VCSEL with a pulse of duration ~ 23 ps and a repetition rate ~172 MHz. The optical pulse is launched into the spiral waveguide via a SMF and is collected with a 50/125 µm MMF (using a similar set-up to Fig. 1b). The received electrical signal is amplified by a 38 GHz amplifier (SHF 806E), and the FWHM of the received pulse is measured with a digital communication analyser (Agilent 86100A) for the different input positions. The FWHM of the received pulse for the back-to-back link is ~30 ps. As expected from the S_{21} measurement, the FWHM of the received pulse for the waveguide link remains relatively constant for the different input positions, with no significant pulse broadening observed (Fig. 1f). The power received at the waveguide output is also measured for the different input positions (Fig. 1f). 3 dB points are found to be ± 10 µm. Increasing offsets result in larger power coupled into higher order modes which suffer from higher bending losses along the spiral waveguide. The repeatability of the observations is confirmed through multiple measurements. The results indicate that the link's performance does not degrade under different input offsets.

Conclusions: Bandwidth measurements have been carried out on a 1.4 m long spiral polymer multimode waveguide. The results indicate that the waveguide exhibits a bandwidth of at least 30 GHz under a large range of launch conditions for all input offsets. This demonstrates the potential of transmitting data rates higher than 25 Gb/s over such structures.

Acknowledgement: The authors would like to acknowledge Dow Corning for providing the spiral polymer waveguide samples, EPSRC for supporting the work and IQE Europe for providing the epitaxial material used for the VCSEL fabrication.

References

1. N. Bamiedakis et al, *IEEE Journal of Quantum Electronics*, vol. **45**, no. 4, pp. 415–424, (2009).
2. L. Schares et al, *IEEE Journal of Selected Topics in Quantum Electronics*, vol. **12**, no. 5, pp. 1032–1044, (2006).
3. H. Ma et al, *Advanced Materials*, vol. **14**, no. 19, pp. 1339–1365, (2002).
4. L. Eldada et al, *IEEE Journal of Selected Topics in Quantum Electronics*, vol. **6**, no. 1, pp. 54–68, (2000).
5. N. Bamiedakis et al, *IEEE Trans. Compon. Packag. Manuf. Technol.*, vol. **3**, no. 4, pp. 592–600, (2013).
6. P. Westbergh, et al., *Electronics Letters*, vol. **48**, pp. 1145-1147, (2012).

Bit-Error-Rate Performance in Optical 16QAM Recognition with Integrated-Optic Circuit

Aiko Takahashi, Kensuke Inoshita, Yoshimitsu Hama, Nobuo Goto, and Shin-ichiro Yanagiya

The University of Tokushima, Tokushima, Japan,
{c501338001, goto.nobuo, syanagiya}@tokushima-u.ac.jp

Abstract: Optical processing of optical labels is expected in broadband photonic label routers. We have proposed integrated-optic circuits to recognize optical 16QAM codes. The recognition function is theoretically analyzed. We also discuss noise tolerance in the circuit, and perform numerical simulation to evaluate bit-error-rate characteristics against incident optical signal-to-noise ratio.

Introduction

In photonic networks, optical label routing will be a practically promising solution because of its simplicity and flexibility. Optical label recognition is one of key functions in label routers. Various methods to recognize optical labels in on-off-keying (OOK) and multi-level phase-shift-keying (PSK) modulation formats have been investigated.[1,2] The authors have proposed waveguide circuits for recognizing optical quadrature amplitude modulation (QAM) codes. We reported two kinds of schemes depending on whether the detecting output port is exiting minimum or maximum output.[3,4]

In this report, we discuss noise tolerance in label recognition processing by detecting minimum-output port using computer simulation, where the proposed integrated-optic circuit is modeled by parallel connection of optical discrete devices. We obtain the bit-error-rate (BER) performance.

Recognition of 16QAM Codes

The optical electric field $E_{16\mathrm{QAM}}$ can be written as $E_{16QAM} = E_0 e^{j\pi/4}\left(2e^{jn\pi/2} + e^{jm\pi/2}\right)$, where n, m=0,1,2,3. We consider recognition of the 16QAM code by cascaded connection of two circuits for QPSK code recognition.

Fig.1 shows a waveguide circuit for QPSK phase recognition circuit (QPRC) followed by phase adjustment waveguides.[5] This circuit consists of a 3-dB directional coupler, two Y-branches, and an asymmetric X-junction coupler. The output fields are related to the input fields by

$$\begin{pmatrix} E_{out}^{(1)} \\ E_{out}^{(2)} \\ E_{out}^{(3)} \\ E_{out}^{(4)} \end{pmatrix} = \frac{1}{2}\begin{pmatrix} 1 & -j \\ 1 & 1 \\ 1 & -1 \\ 1 & j \end{pmatrix}\begin{pmatrix} E_{in}^{(1)} \\ E_{in}^{(2)} \end{pmatrix}. \qquad (1)$$

Using two-stage connection of this QPRC, a proposed

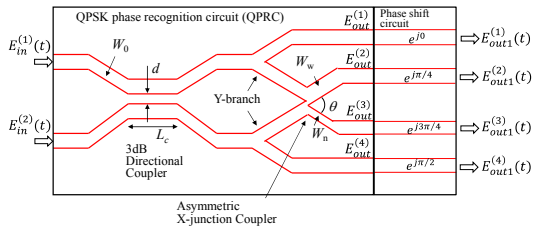


Fig.1 Optical waveguide circuit (QPRC) for recognition of QPSK code and phase shift circuit.

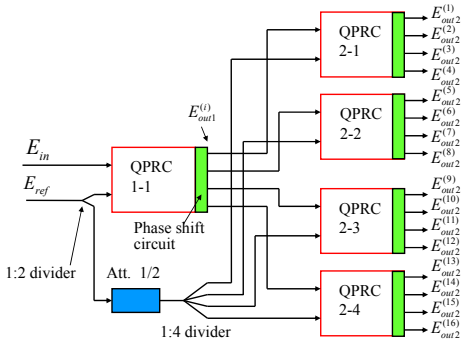


Fig.2 A recognition circuit for 16QAM codes consisting of QPRCs.

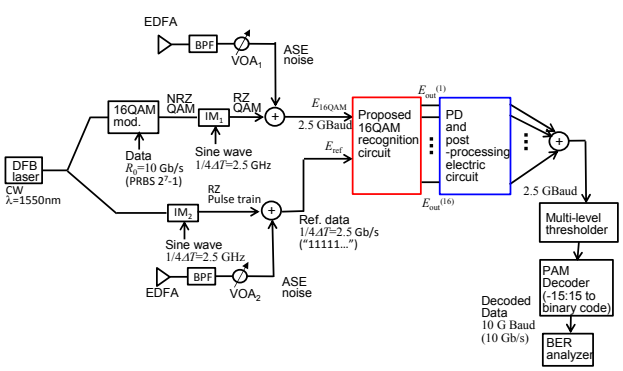


Fig.3 System diagram to evaluate noise tolerance.

circuit for recognition of 16QAM codes is formed as shown in Fig.2. The input-to-output relation is given by

$$\begin{pmatrix} E_{out2}^{(1)} \\ E_{out2}^{(2)} \\ E_{out2}^{(3)} \\ E_{out2}^{(4)} \\ E_{out2}^{(5)} \\ E_{out2}^{(6)} \\ E_{out2}^{(7)} \\ E_{out2}^{(8)} \\ E_{out2}^{(9)} \\ E_{out2}^{(10)} \\ E_{out2}^{(11)} \\ E_{out2}^{(12)} \\ E_{out2}^{(13)} \\ E_{out2}^{(14)} \\ E_{out2}^{(15)} \\ E_{out2}^{(16)} \end{pmatrix} = \frac{1}{4} \begin{pmatrix} 1 & -j3/2 \\ 1 & 1/2 - j \\ 1 & -1/2 - j \\ 1 & -j/2 \\ 1 & 1 - j/2 \\ 1 & 3/2 \\ 1 & 1/2 \\ 1 & 1 + j/2 \\ 1 & -1 - j/2 \\ 1 & -1/2 \\ 1 & -3/2 \\ 1 & -1 + j/2 \\ 1 & j/2 \\ 1 & 1/2 + j \\ 1 & -1/2 + j \\ 1 & j3/2 \end{pmatrix} \begin{pmatrix} E_{in} \\ E_{ref} \end{pmatrix}. \quad (2)$$

E_{16QAM} enters as E_{in}, and the reference signal $E_{ref} = 2\sqrt{2}E_0 e^{j\pi/4}$ enters as E_{ref} .We find that only one null output port exists for each (n,m). Although the maximum intensity of the outputs for each code depends on (n,m), the second minimum intensity is constant 0.125 E_0^2. By using inverters at each output port whose threshold is below 0.125 E_0^2, the output port having null output can be distinguished.

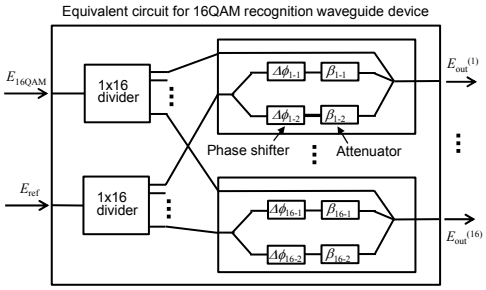
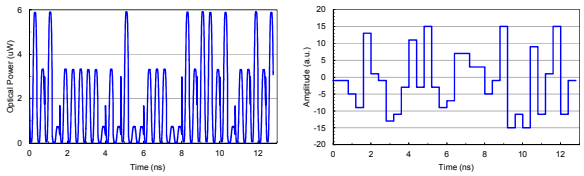


Fig.4 Equivalent circuit model for 16QAM recognition waveguide device.



(a) (b)

Fig.5 Simulated signals; (a) RZ 16QAM pulse train and (b) Output from multi-level thresholder.

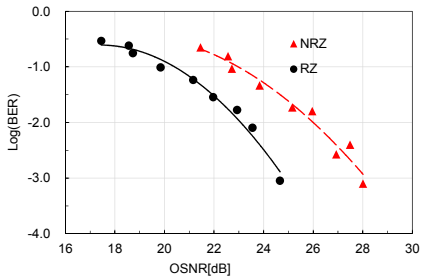


Fig.6 BER performance as a function of OSNR.

Noise Tolerance

The code recognition was numerically simulated using OptiSystem (Optiwave Systems Inc.). An optical system is shown in Fig.3. The optical waveguide circuit of Fig.2 was modeled with discrete optical devices as shown in Fig.4. A post-processing electric circuit and followed circuits of a combiner, multi-level thresholder, and a pulse amplitude demodulator can retrieve the incident 16QAM code. As optical 16QAM signal, RZ and NRZ pulse trains were considered. Fig.5 shows an example of simulated signals at input to the recognition circuit and at the output of multi-level thresholder. Simulated BER performance is shown in Fig.6 as a function of the OSNR at the input of the recognition circuit, where ASE noise was added only at the 16QAM signal as a preliminary study.

Conclusion

The optical waveguide circuit for recognition of 16QAM codes was discussed from the viewpoint of noise tolerance. We will further investigate to improve the circuit having larger noise tolerance.

Acknowledgment

This work was supported in part by JSPS KAKENHI (24360150).

References

1. H. Hiura, Y. Makimoto, N. Goto, & S. Yanagiya, *J. Lightwave Tech.*, vol.27, no.24, p.5543-5551, 2009.
2. A. Ihara, H. Kishikawa, N. Goto, and S. Yanagiya, *J. Lightwave Tech.*, vol.29, no.91, pp.1306-1313, 2011.
3. K. Inoshita, H. Kishikawa, Y. Makimoto, N. Goto, and S. Yanagiya, *J. Lightwave Tech.*, vol.31, pp.2271-2278, 2013.
4. K. Inoshita, N. Goto, and S. Yanagiya, to be published in *IEICE Trans. Electron.* 2014.
5. Y. Makimoto, H. Hiura, N. Goto, and S. Yanagiya, *J. Lightwave Tech.*, vol.27, no.1, pp.60-67, 2009.

Two beam multiplexing in a multimode periodic segmented waveguide

P. Aschieri [1], V. Doya[1] D. Makarov[2]

[1] *LPMC, UMR 7336, University of Nice Sophia, France,*
pierre.aschieri@unice.fr
[2] *V.I. Il'ichev Pacific Oceanological Institute,*
Vladivostok, Russia
makarov@poi.dvo.ru

Abstract: The purpose of this article is to show that a beam multiplexing can be achieved in Multimode Periodic Segmented Waveguide. The beam multiplexing is based on properties of ray and wave chaos that have been revealed on such device. Two incident optical beams remain collimated all along the propagation into the waveguide without interfering if their associated trajectories are constructed on resonances of the Poincaré section.

A Multimode Periodic Segmented Waveguide (MPSW), sketched in figure 1, consists in an array of high refractive index guiding segments embedded in a low refractive index substrate. These particular waveguides are well known to be very interesting for many purpose for linear an nonlinear applications in integrated optics domain [1–3]. Beside this, recent works have shown that MPSW could be promising and versatile systems in which ray and wave chaos could be studied and used.
Recent works have shown that for particular waveguide configurations, MPSW exhibits complex rays' dynamics compared to classical uniform waveguides which can be regular or chaotic depending on the initial input conditions. In the case of highly multimode waveguides, where the geometrical assumption of ray propagation remains valid, the extension of the geometric analysis to the wave domain shows reminiscence of the complex rays' dynamics. Thus, a complex and non intuitive light behaviour can be observed in MPSW such as, for example, an imput beam, properly injected in the structure, does not diffract but remains collimated during the propagation in the MPSW unlike classical waveguide where the input beam is quickly dispersed on several modes.
In order to develop such a complex ray and wave dynamics, MPSW must have a longitudinal index periodicity associated with a non harmonic (gaussian) transverse index profile for the guiding segments[4]. The complex ray dynamics can be clearly identified by the use of the Poincaré section which is a convenient and widely used representation of a periodically perturbed nonlinear system. It consists in a projection of the trajectory (x,θ,z) onto the phase plane (x,θ) at positions z=n Λ, n=1,2,3,... where Λ represents the segmentation period of the waveguide. Poincaré sections revel that the dynamic may be characterized by the presence of a parametric nonlinear resonance which manifests itself through a period-locking between two characteristic periods of the

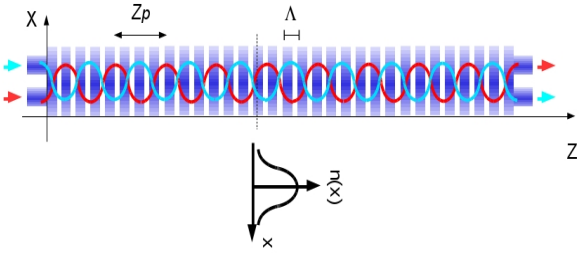


Fig 1: A schematic of a classical Multimode Periodic Segmented Waveguide with a transverse gaussian index profile in high index segments. For two beam multiplexing demonstration, two input and output waveguides have been added. A typical ray path is superimposed on the waveguide, the focusing length of the ray is Zp.

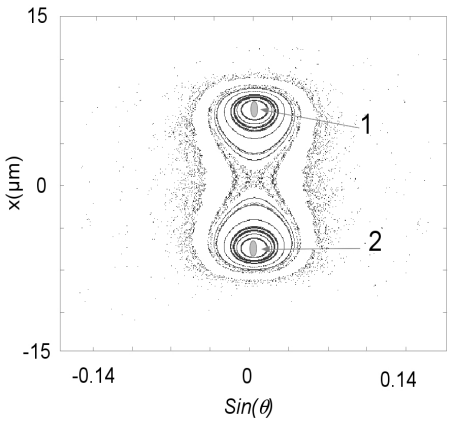


Fig 2: Poincaré section of the waveguide that exhibits two main resonances. Positions of the input beam are noted 1 and 2.

system: the segmentation period Λ and the focusing period Zp of the propagating ray. Resonances play a key role in the rays' dynamics. If an incident ray is injected in a resonance, then the ray trajectory is *trapped* and remains confined in the resonance. Thus, an incident beam propagates without diffracting into the waveguide if its associated trajectory is constructed on a resonance of the Poincaré section.
The beam multiplexing is performed in a waveguide configuration that exhibits two main resonances in the Poincaré section (see figure 2). Two beams are simultaneously injected in the two resonances of the Poincaré section (positions "1" and "2" noted on figure 2). The amplitude of the field of the second beam is reduced compared to the first beam in order to get clear picture of the two superposed beams in the waveguide. The field intensity distribution is shown in figure 3, the two beams coexist in the waveguide during the propagation without diffracting and interfering because they simultaneously occupy different positions in the phase space. The transverse field distribution of the output of the waveguide clearly demonstrates that the two input beams remain unchanged and identical to the input field profile. Regarding the propagation losses, despite the index discontinuity due to the segmentation, the calculated propagation losses are very low, 0.01 dB/cm which is two order of magnitude lower than the propagation losses induced by the waveguide fabrication process.

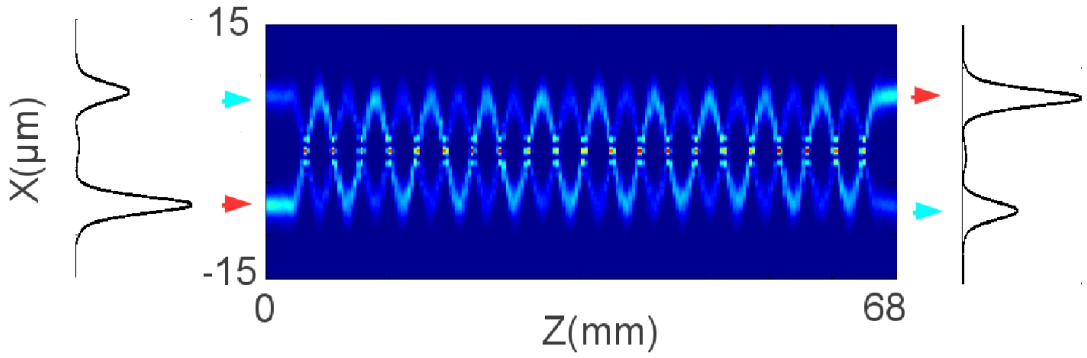


Fig 3: Two input beams injected simultaneously in the two resonances via the two input waveguides. The two Gaussian beams remain collimated without interfering each other. The output exhibits two well separated Gaussian fields.

What has mainly interested us with this work is to show that beam multiplexing can be achieved in MPSW. A simple two beams multiplexing has been numerically demonstrated which provides a preliminary numerical study of this new spatial multiplexing scheme. Nevertheless, this new kind of multiplexing may be useful to achieve specific functions in some integrated optical devices. For example, as it can be seen on figure 3, the two beams are spatially separated during the propagation excepted at the crossing point at the centre of the waveguide which means that adding an index perturbation localised in a suitable way will perturb the propagation of only one of the two beams.
This work may also precede a promising field of investigation where higher number of multiplexed beams can be obtained for various waveguide configurations that exhibits multiples resonances in the Poincaré section [4].

References

1. Z.Weissman *et al., J. Lightwave Technol*. **13**, 2053–2058 (1995).
2. D. Castaldini *et al., Opt. Express*. **17**, 17868–17873 (2009).
3. D. Bierlein *et al., Appl. Phys. Lett.*. **56**, 1725–1727 (1990).
4. P. Aschieri *et al.*, *JOSA B, 30, 3161–3167* (2013).

Design and Fabrication Technology for a Twin-Guide SOA Concept on InP membranes

Y. Jiao, D. Heiss, L. Shen, S.P. Bhat, M.K. Smit, J.J.G.M. van der Tol

COBRA Research Institute, Eindhoven University of Technology, Eindhoven, the Netherlands,
y.jiao@tue.nl, dheiss@tue.nl, lshen@tue.nl, s.p.bhat@tue.nl, m.k.smit@tue.nl, j.j.g.m.v.d.tol@tue.nl

Abstract: In this contribution we present a novel concept of a twin-guide SOA design based on the "InP membrane on Si" (IMOS) platform. As a fundamental device, this SOA design can be used for lasers with current injection and photodetectors under reverse bias in the IMOS platform. The fabrication scheme is presented in detail and the current fabrication progress will be shown.

Introduction: The InP membrane on Si (IMOS) technology [1] is a novel candidate for resolving the on-chip data communication bottleneck by adding an additional III-V photonic layer on top of electronic chips. The major advantage of this platform is the possibility to integrate passive (waveguides, filters) and active components (lasers, photodetectors) in a single membrane.

A variety of passive IMOS components have been demonstrated with good performance in past few years. However, as a fundamental element to be used in active membrane devices, the optical amplifier (SOA) is not yet demonstrated.

In this contribution, we present a novel design of a twin-guide SOA structure on the IMOS platform. The proposed SOA design can be used both in lasers and photodetectors with good predicted performance. The fabrication scheme is presented in detail and the current fabrication progress will be shown.

SOA Design: The SOA design is based on the so-called twin-guide approach. It consists of two vertically stacked waveguiding layers; for the active and the passive functions respectively. The complete SOA structure including material and layerstack information is depicted in Figure 1(a). After being bonded to a Si carrier wafer using DVS-BCB as the bonding material, the SOA layerstack consists of (from low to high): a 300 nm thick InP passive waveguiding layer; 100 nm thick n-contact layers formed by a n+-doped quaternary layer (Q1.25) and an n-doped InP layer; a bulk active region formed by 250 nm thick nominally undoped Q1.58; a p-doped InP cladding layer; a p-contact region formed by quaternary spacer layers and highly p+-doped InGaAs. To define the amplifier, 700 nm wide ridges are defined by means of dry etching until the n-doped contact layer. The designed SOA width ensures a fundamental transverse electric (TE) mode in the active region with a high confinement factor (0.55) and an affordable absorption loss (~50 cm^{-1}). The p-side of the SOA will be contacted using a Ti/Pt/Au metallization on top of the ridge, while the n-side will be contacted with Ni/Ge/Au pads parallel to the ridge with a few micrometer separation. In the passive regions, all layers except the 300 nm InP waveguiding layer are removed by a combination of dry and wet etching. The transition of the optical power between the SOA and the passive waveguide is accomplished by a taper structure, as shown in Fig. 1 (b). The 3D-FDTD simulations show a taper length of 10 µm is sufficient to transfer 95% of the light between the SOA and waveguide.

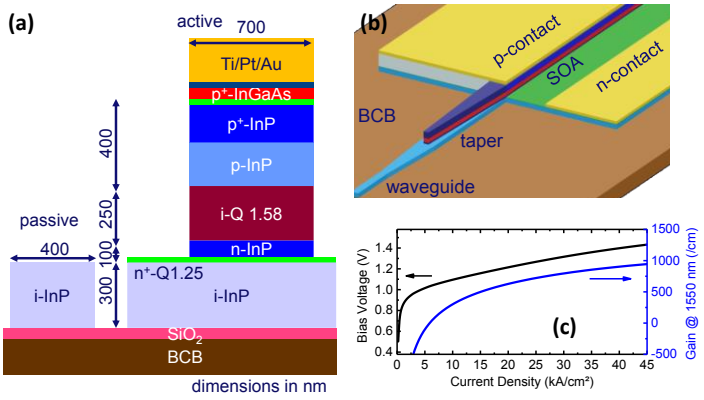


Fig. 1 (a) The schematic picture of the proposed SOA structure. (b) The 3D schematic picture of the taper structure between SOA and waveguide. (c) Simulated I-V characteristics and material gain of the active layer as a function of current density.

To estimate the material gain in the active layer, electrical simulations using a self-consistent 1D Poisson-solver (nextnano++) are performed. The corresponding I-V characteristics of the diode

(including the series resistance of the contacts) is plotted in Fig. 1(c) as black line. The material gain is then calculated from the charge carrier density as a function of the current density [2] up to 45 kA/cm . Auger recombination, radiative and surface recombination are all considered in the model using typical values from literatures. The material gain of the active layer at 1550 nm wavelength is plotted in Fig. 1(c) as a blue line. The current density to compensate the loss in the amplifier is estimated to be 6.8 kA/cm at a voltage of 1.05V.

The main advantage of this design is that all the fabrication steps will be done after bonding. This avoids problems of bonding quality and increases yield. The fabrication process to realize the SOA design is described in the next section.

Fabrication: The key fabrication steps for the twin-guide SOA structures as well as the passive waveguides are depicted in Fig. 2. The fabrication starts with the flip-chip BCB bonding of the III-V layerstack onto a SiO_2/Si carrier wafer, followed by removing the InP substrate and an InGaAs sacrificial layer wet-chemically. After bonding, the SOA pattern is defined using electron beam lithography (EBL) with C_{60}/ZEP resist and a SiN_x hard mask [3]. The pattern is finally transferred with dry etching to the III-V layerstack. The etching is stopped when the n-doped InP layer is reached (Fig. 2a)). The region for making n-type metal contact is defined with a second EBL. The SiN_x will protect the regions where n-InP and n-Q1.25 material are preserved for making the n-contacts. The n-type material at all the other regions will be removed wet-chemically (Fig. 2(b)). Two more EBLs will be performed to realize passive waveguides and fiber-grating couplers with etch depths of 300nm and 120nm, respectively, as shown in Fig. 2(c). During the final metallization step, the entire sample is covered with a 50-nm thin SiN_x layer for electrical isolation and planarized with polyimide. Finally two lift-off processes using optical lithography are performed to create the p- and n-metal contacts, as shown in Fig. 2(d). It is worth to mention that all the processings (including dry and wet etching, optical lithography, surface treatment etc.) are based on mature technologies from the COBRA standard multi-project wafer runs [4], in order to ensure the reliability of the entire fabrication.

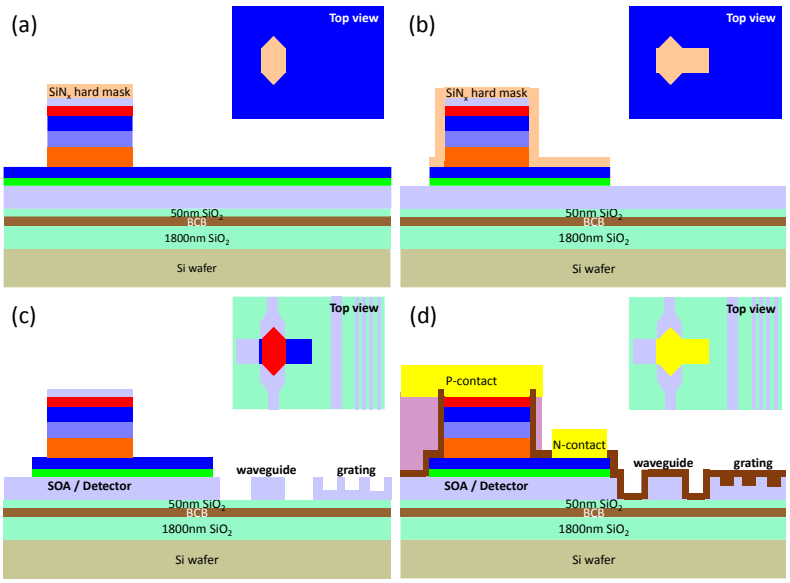


Fig. 2 (a) The first EBL step to define the SOA structure on the bonded sample. b) The second EBL step to define the n-contact region. c) The third and fourth EBL step to print the passive waveguides and fiber-grating couplers. d) The lift-off step to create p and n metal contacts.

Currently a test fabrication run of the SOA structure using the described layerstack is well underway. The SEM pictures taken in between some fabrication steps are presented in Fig. 3. First results make us confident that we can reliably fabricate laser devices in the near future.

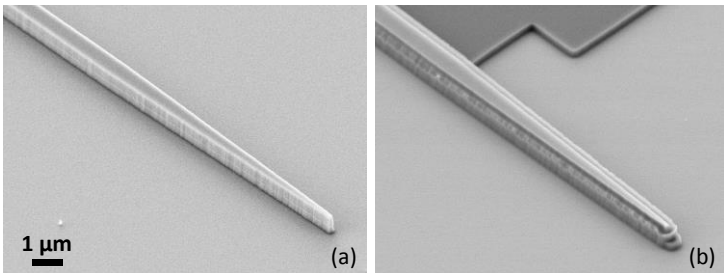


Fig. 3 The SEM picture of the taper structure of the SOA (a) after 1st EBL and dry etching to form the SOA ridge, (b) after 2nd EBL and wet etching of the n-contact material.

References

[1] J. van der Tol, *et al*., *IET Optoelectronics* **5**, pp.218-225 (2011).
[2] L.A. Coldren, *et al*., *Diode Lasers and Photonic Integrated Circuits* (Wiley, Hoboken, NJ. 2012).
[3] Y. Jiao, *et al*., *Optics Letters* **39**, pp.1645-1648 (2014).
[4] M.K. Smit, *et al*., *IET Optoelectronics* **5**, 187-194 (2011).

Photonic integrated transceivers for data read-out systems

S. Stopinski[1,2], M. Malinowski[1], R. Piramidowicz[1], D. Gajanana[2,3], M. J. van der Hoek[3], M. K. Smit[2], X. J. M. Leijtens[2]

[1] *Institute of Microelectronics and Optoelectronics, Warsaw University of Technology, Koszykowa 75, 00-662 Warsaw, Poland; S.Stopinski@imio.pw.edu.pl*
[2] *COBRA Research Institute, Eindhoven University of Technology, 5600 MB Eindhoven, the Netherlands*
[3] *Nikhef, Science Park 105, 1098 XG Amsterdam, the Netherlands*

Abstract: In this work design and characterization results of integrated optical transceivers are presented. The devices were realized as photonic integrated circuits in a generic InP-based technology. The application is a data read-out unit for a sensor network. The circuits utilize PIN photodiodes for detection of a slow speed signal and amplitude modulators, either in a Michelson or a Mach-Zehnder interferometer configuration, for data encoding. Modulation bandwidth of 16.1 GHz was measured, eye-diagrams with 11.6 dB dynamic extinction ratio were recorded and transmission of a 10 Gb/s signal over 25 km of SMF fiber with BER below 10^{-10} was achieved.

Introduction

In a distributed sensor network, the read-out system is responsible for collecting all signals generated by a large number of sensors. The system we consider here has a star topology and comprises microelectronic and optoelectronic devices located next to the sensors, and is connected with optical fibers to a central station (CS). The upstream signal, towards the CS, provides information about the monitored physical parameters, while the downstream from the CS may be used for sending a control signal to the sensor units. Figure 1 presents a scheme of an optical link between the central station and a single sensor, where the downstream is a 1.25 Gb/s digital signal, modulated with low extinction ratio (ER = 0.4 dB). At the sensor unit a fraction of the input power is tapped and the downstream signal is detected. The remaining signal is used as a carrier for modulation with high extinction ratio in order to generate the upstream signal. It is assumed that the read-out from the sensor as well as driving the modulators is performed by electronic circuitry deployed at the sensor unit.

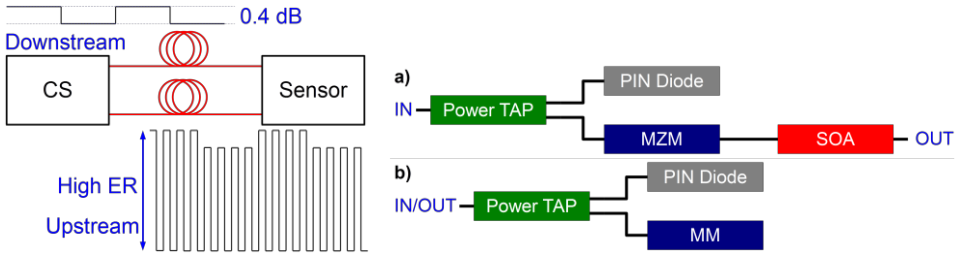


Fig. 1. Optical fiber link between the central station (CS) and a single sensor (left) transceiver circuit schemes in transmitting (a) and reflecting (b) configurations (right)

This concept, based on discrete photonic components, has been proposed and investigated by the Dutch institute for subatomic physics (Nikhef) for the data read-out system of the KM3NeT neutrino telescope experiment[1]. It utilized a 5%:95% fiber-optic power coupler, a PIN photodiode and a reflective electro-absorption modulator. In this work we demonstrate photonic integrated circuits that combine all of the functionality in a single semiconductor chip. We utilized an InP-based generic integration technology platform[2]. It supports building blocks such as passive waveguides, electro-optic phase modulators exploiting the quantum confined Stark effect[3], PIN photodiodes and semiconductor optical amplifiers.

Chip design

Figure 1 presents the block diagrams of the designed circuits. Two possible arrangements are presented. Both of them utilize a power tap, which is either a symmetric 50%:50% 1x2 MMI power splitter or a 15%:85% 2x2 MMI power coupler, and a PIN photodiode for monitoring the downstream signal. The data from the sensor is encoded onto the carrier using amplitude modulators in either

transmissive Mach-Zehnder (MZM) or reflective Michelson (MM) configuration, constructed from MMI couplers and phase modulators. Additionally, the transmitting circuits utilize a semiconductor optical amplifier in order to boost the power of the output signal. Figure 2 presents the mask layout of the transmitting circuits with two additional test circuits and a picture of a fabricated device mounted on a ceramic block for RF characterization. The chip dimensions are 6x2 mm^2.

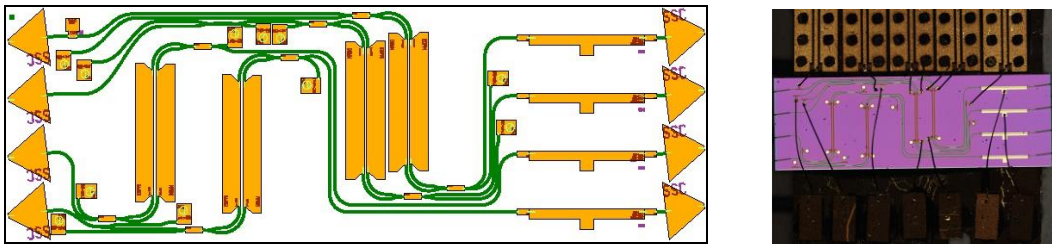


Fig. 2. Mask layout of the transceiver circuits in a transmitting configuration (left) and microscope photograph of the chip mounted for RF-characterization (right)

Characterization results

For the RF measurements the chips were mounted on ceramic submounts and the circuit components were wire-bonded to the gold DC pads and RF ground-signal-ground (G-S-G) coplanar transmission lines. The RF-response of the modulators was measured with a 67 GHz lightwave component analyzer (LCA, Agilent N4373C) by injecting CW laser light at 1550 nm and analyzing the modulated signal by the LCA. Figure 3 presents the characteristics of the S_{21} magnitude, normalized at 0 GHz, for the Mach-Zehnder and Michelson type modulators. The measured 3 dB bandwidth is 11.5 GHz and 16.1 GHz, respectively.

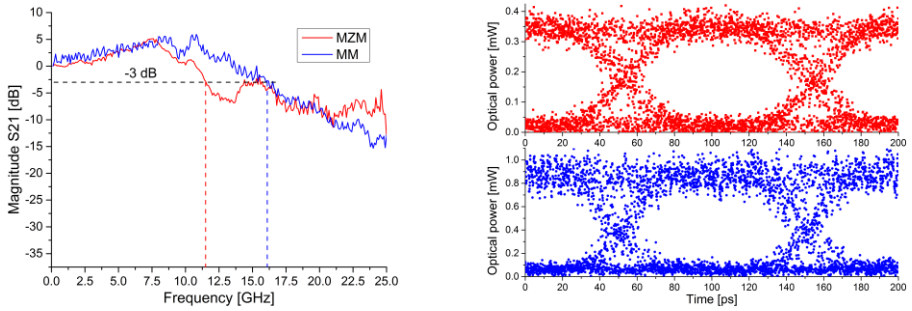


Fig. 3. Frequency response (left) and eye diagrams for an NRZ 10 Gb/s signal (right)

The measured static extinction ratio of the Mach-Zehnder modulators is 18 dB at λ = 1550 nm and the driving voltage V_π = -3.9 V. For the Michelson arrangement the ER is 25 dB and V_π = -3.0 V. Dynamic measurements were performed with the injected CW carrier at λ = 1550 nm and a pseudo random bit sequence generator which was driving the modulators. The recorded eye-diagrams for the back-to-back configuration are presented in Figure 3 for both types of modulators. In both cases the eye is wide open with the dynamic extinction ratio 11.6 dB and 11.2 dB, respectively. For the Mach-Zehnder circuits transmission of the modulated signal for back-to-back and over 25 km of SMF fiber was achieved with a bit error rate smaller than 10^{-10} (measured with Anritsu MP1764C error detector).

Conclusions

The integrated optical transceivers were designed and fabricated in a standardized generic InP technology. Their overall performance is good in terms of dynamic extinction ratio higher than 10 dB and available RF bandwidth up to 16 GHz.

Acknowledgment – This work received funding from the Seventh Framework Programme (grant NMP 228839 EuroPIC). The authors wish to thank Christophe Kazmierski from III-V Lab for submounting the chip samples.

References

1. KM3NeT Consortium, *KM3NeT Technical Design Report*, 2008, ISBN 978-90-6488-033-9
2. M. Smit et al., *IET Optoelectronics* **5**, pp. 187–194 (2011)
3. J. Weiner et al., *Applied Physics Letters* **50**, pp. 842–844 (1987).

Wavelength-Selective Nanopatterned III-V on Si Hybrid Photonic Waveguide

X.Pommarede[1], A.Talneau[1], A.Lupu[2] and H.Benisty[3]

[1] Laboratoire de Photonique et de Nanostructures, route de Nozay, F-91460 Marcoussis
anne.talneau@lpn.cnrs.fr
[2] Institut d'Electronique Fondamentale, Université d'Orsay
[3] Laboratoire Charles Fabry, UMR 8501, Institut d'Optique, CNRS, Univ Paris Sud 11, 2 Avenue Augustin Fresnel, 91127 Palaiseau cedex, France

Abstract: An heteroepitaxial bonded III-V on Si nanopatterned waveguide is demonstrating a wavelength selective behavior thanks to a super-periodicity added to its sub-wavelength, below band-gap, structuration. Effective Medium Theory has been implemented for modal effective index determination, allowing a rapid and nevertheless detailed investigation of the role of a large number of geometrical parameters. Such nanostructured waveguides offer the versatility for designing complex geometries required for hybrid advanced optical functions on silicon.

Introduction

The future of all optical networks links relies upon hybrid silicon photonics. III-V materials are still required for optical functions that silicon is not able to efficiently produce. We have developed oxide-free bonding of III-V InP-based material on nanopatterned silicon waveguides [1]. Including a sub-2D photonic bandgap structuration in the lateral claddings of the silicon waveguides provides a large versatility for tailoring the propagated optical mode, thus enabling advanced hybrid optical functions. We demonstrate here that adding further to this 2D structuration a super-periodicity in the propagation direction provides wavelength selectivity. Such a design could be implemented for example within monomode hybrid laser, allowing a large versatility for the mode shaping and selected wavelength.

For modal simulation, being in the sub-photonic band gap regime Effective Medium Theory – EMT– allows determining the modal effective index. EMT is of interest when modal behavior of optical waveguides including nanopatterns is calculated since simulation of the exact geometry requires a tiny meshing which leads to highly demanding computational resources. We have implemented EMT for fast and accurate modal calculation, thus investigating a large variation range for the several geometrical parameters.

Design of the Photonic Crystal waveguide using Effective Medium Theory

EMT has been demonstrated to fully represent a periodic nanostructured medium when its pitch Λ is much smaller than the wavelength λ, $\alpha = \Lambda/\lambda << 1$ [2-4]. The nanostructured medium behaves like a uniaxial material. The nanostructured medium is here a two dimensional Photonic Crystal -2D PC- serving as a lateral cladding for the waveguide, with propagation along the z direction (Fig.1, left), the core of the waveguide is not structured. For the structured material, in the case of electric field along the direction of invariance, the resulting permittivity of the extraordinary index is the mean value of the involved permittivities [2]. As for the ordinary index, it is obtained from the dispersion curve of a 2D PC calculated by a plane wave expansion method [5]. Both ordinary and extraordinary indices are plotted in Fig.1 right, versus the air filling factor, evidencing the uniaxial behaviour of the patterned material.

We use the commercial COMSOL RF mode solver module. We calculated the eigenmodes of a hybrid waveguide in the case of a 400nm-thick InP layer bonded on a 550nm-thick Si guiding layer, on SOI [1] , and including 2D periodic nanostructured claddings on both sides. A parametric study is performed according to the PC waveguide width *w*, varying the trench depth *H* and air-filling factor *f* (Fig.1, left). Holes parameters (*H, f*) are determined in order to provide large higher order mode selectivity, in TE polarization, according to the waveguide width *w*. When the effective index of the fundamental TE mode is obtained, the added super-periodicity is calculated to provide wavelength selectivity for 1.55μm. It consists in a single larger hole added each other longitudinal period (Fig.2-b). A 30% increase has been chosen for the larger hole to ensure the required feedback.

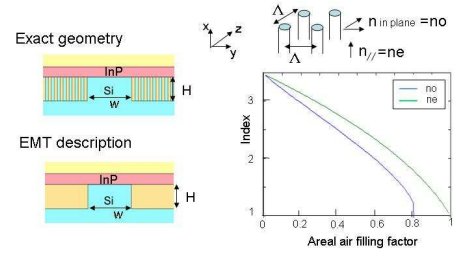


Figure 1: Left: schematic of the effective medium operating as the waveguide cladding Right : Extraordinary index and ordinary index versus areal air-filling factor

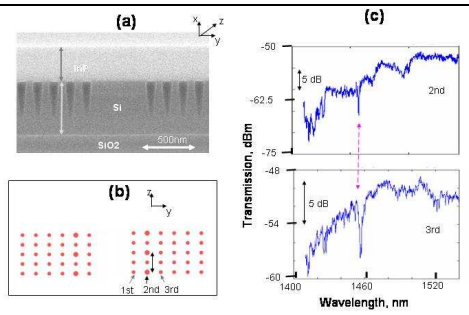


Figure 2: (a): InP membrane bonded on a PC Si waveguide on SOI , SEM view of a cleaved facet (b) : Schematic of the added super-periodicity, larger hole on the 2nd row, (c) Transmission versus wavelength evidencing the signature of the added periodicity

Fabrication and measurement of wavelength-selective hybrid waveguides

The sub-λ 2D PC parameters are the following: square lattice of holes, diameter 60nm, period in the 150 nm range, f = 12.5%. For a waveguide width w=0.6-μm, the optimal hole depth for a large higher order modes rejection in TE polarization is H=380nm. Fig.2-a is a SEM image of a hybrid waveguide cleaved facet. Two cleaved facets waveguides including 20 rows of holes on both sides, have been measured on an end-fire set-up including polarization maintaining tunable sources and injection fibre for TE polarization. Collection is performed with a microscope objective allowing simultaneous observation of the guided mode and collection in the fiber. The feedback efficiency of the added larger has been experimentally investigated changing its position from the 1st, 2nd and 3rd row (Fig.2-b). Fig.2-c shows the transmission versus wavelength, for w=0.6μm, for a 30% larger hole. The sharp dip visible at 1455nm corresponds to the feedback effect of the additional periodicity. Its spectral position is in reasonable agreement with the effective index mode calculated with EMT. When going from a larger hole on the 2nd to the 3rd row (Fig.2-c top to bottom), the feedback wavelength is not affected since the periodicity is the same. Due to the weak lateral effective index step, the feedback efficiency is almost the same. Further characterization is under progress to understand the relatively large variation in overall transmission.
Such a wavelength-selective hybrid waveguide is a good candidate for hybrid single mode laser design.

Conclusion

We have proposed and experimentally demonstrated the wavelength-selective operation of a sub-photonic band gap 2D photonic crystal hybrid waveguide, when a super-periodicity in the propagation direction has been added to the effective-medium. Effective Medium Theory has been proven to be a reliable tool for modal effective index determination, allowing designing complex geometries required for advanced optical functions.

Such an effective medium design offers a large potential for the conception of any kind of hybrid waveguide dedicated to advanced optical functions, since a tailored geometry can be easily inserted. The great advantage is that changing the geometry in order to obtain a new optical function does not require developing a new technology for material bonding, thus allowing several designs to be included within an hybrid device during a single bonding process.

Acknowledgment

This work has been supported by the national ANR project COHEDIO.

References

[1] A.Talneau et al. Appl. Phys. Lett., 102, 212101 (2013)
[2] F.T.Chen and H.G.Craighead, Opt. Lett., vol.20,no2, pp.121-123, Jan. 1995.
[3] R.Brauer and O.Bryngdahl, Appl. Opt., vol.33, no.34, pp.7875-7882 (1994).
[4] P.Lalanne, Appl. Opt.,vol.35, no.27, pp.5369-5380 (1996)
[5] C.Pang and H.Benisty, Photonics and Nanostructures Fundamental and Applications vol.11, no.2, pp.145-156 (2013)

Generic InP-based Photonic Integration Technology Platform for Long Wavelength Applications

H. Rabbani Haghighi[1], P.J. van Veldhoven[2], P.J.A. Thijs[2], T.D. Vries[1] and M. K. Smit[1]

[1]Technical University of Eindhoven (TU/e), Dept. of Electrical Engineering, Photonic Integration group, COBRA, PO Box 513 - 5600 MB, Eindhoven, the Netherlands

[2]Technical University of Eindhoven (TU/e), PSN group, 5600 MB, Eindhoven, the Netherlands

h.rabbani@tue.nl , P.J.Veldhoven@tue.nl, p.j.a.thijs@tue.nl, t.d.vries@tue.nl, M.K.Smit@tue.nl

Abstract: In this paper, a generic InP-based photonic integration technology platform for long-wavelength applications is described. This entails some information on the active-passive integration procedure followed by the steps which lead to photonic integrated circuit devices operating in 2 μm wavelength range.

Introduction

Generic photonic integration technology is an approach which offers monolithic fabrication of miniaturized photonic devices with diverse functionalities at a reduced price. This is achieved through development of a standardized integration technology with a library of fully-characterized basic building blocks including passive components, detectors, modulators and the highly-demanded lasers and optical amplifiers (SOAs). In this context, integrated circuits on Indium-phosphide (InP) substrate are of particular interest since both active and passive components are supported.[1] Since the launch of the InP-based generic integration concept in 2007 by the European Network of Excellence (ePIXnet), the COBRA research group together with some other leading partners have successfully demonstrated a number of milestones for devices operating at 1.55 μm. These achievements have triggered the idea to establish a so-called long-wavelength generic platform where devices with operating wavelengths around 2 μm can be fabricated. The wavelength range around 2 μm is of great interest since various gas species have absorption lines in this region (carbon dioxide 2.05 μm, nitrous oxide 2.13 μm and carbon monoxide 2.33 μm) and the absorption of water is very low. This offers a potential for trace-gas monitoring applications in environmental and medical diagnostics. In the next section, we will describe how the generic COBRA platform available for photonic integrated circuit (PIC) fabrication at 1.55 μm is modified for use at longer wavelengths.

Active-passive integration

There are various techniques for semiconductor active-passive integration [2, 3]. Among the reported schemes the butt-joint [4] coupling approach offers maximum flexibility in design of the integration layers. It allows for precise and independent control of thickness and doping concentration in the active and passive sections. Therefore, the COBRA approach in the long wavelength platform is based on butt-joint active-passive integration. It starts with growth of a spot-size convertor layer stack followed by a 600-nm-thick active layer which photoluminescence spectrum is shown in fig. 1.

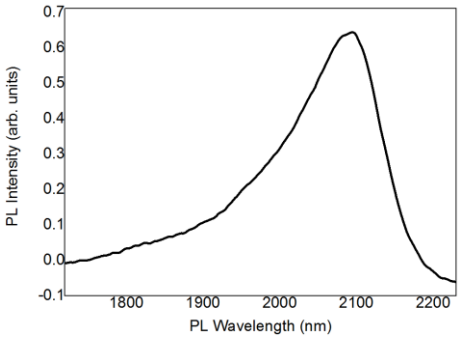


Fig. 1- Photoluminescence spectrum of the long-wavelength active material.

All these steps are done via Metal Organic Vapor Phase Epitaxy (MOVPE). In the next step, a dielectric mask (400-nm-thick layer of SiNx) is deposited and after the lithography and defining the active islands (30-μm-wide with a user-defined length), the active layer is etched away outside the masked region and replaced by a thickness-matched passive quaternary (Q1.25) layer in a regrowth step. Then, the mask layer is removed and the top p-InP cladding layer (1.5-μm-thick) followed by the

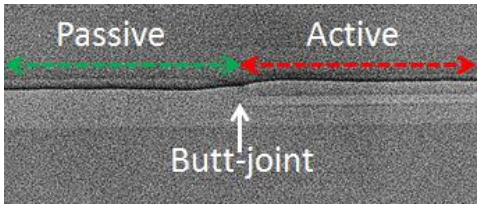


Fig. 2: SEM image of a cross-section through an active-passive butt-joint.

highly p-doped InGaAs contact layer (300-nm-thick) is grown. Fig. 2 is showing a SEM image of an active-passive butt-joint realized in the long-wavelength platform. Once the wafer is fully grown it undergoes the following processing steps:

Waveguide processing

For the waveguide processing a 600-nm-thick SiNx layer is deposited all over the grown wafer and will be used as the main etching hard mask. The pattern is then written into a positive photoresist via optical contact lithography from which it is then transferred onto the SiNx hard mask layer. The semiconductor etching is a multi-stage process and is done through dry etching, using the ICP machine with an appropriate CH_4:H_2 gas mixture. Fig.3 (left) is showing the building blocks which are achieved in the long-wavelength platform at the end of all the etching steps. Fig.3 (right) is showing a SEM top image of a smooth junction of a passive waveguide running into the active region.

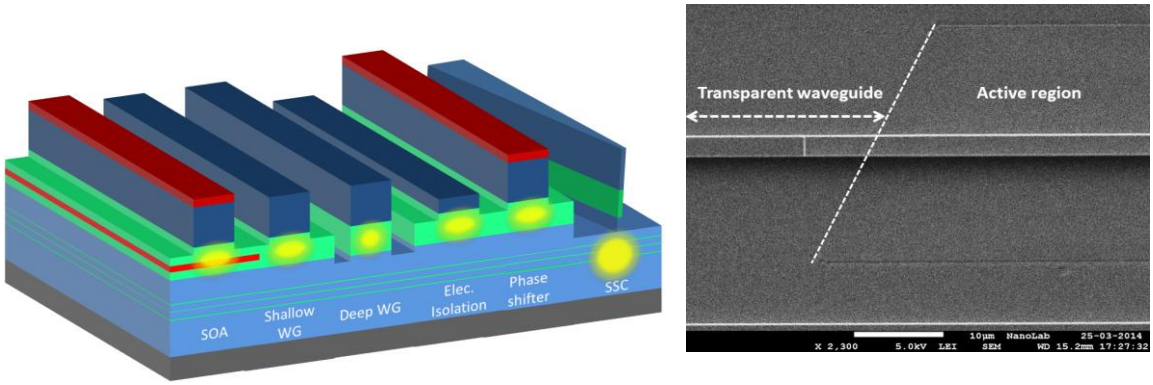


Fig. 3- (Left) Schematic of the building blocks in the long wavelength platform. From left to right, the following components are distinguishable: semiconductor optical amplifier, shallow waveguide, deep waveguide, electrical isolation, phase shifter and laterally-tapered spot-size convertor. (right) top view of the junction between active and passive.

Planarization and metallization

Once all the etching steps are done and the structures are defined, the next step is to deposit a metal layer stack on top of the p-InGaAs contact layer (the red layer on top of the structures in fig.3). However, the entire wafer needs to be planarised before p-metallization. This is done via polyimide spinning, curing at 325°C and then etching back process in polymer RIE (reactive ion etching) to expose top of the contact layer for metal deposition. Thereafter, the lift-off lithography is done followed by the p-metal evaporation. The evaporated metal layer consists of Ti, Pt, Au films with thicknesses of 60, 75, 300 nm, respectively. This is an optimized combination in order to have low contact resistance. Following the p-metal evaporation, the metal lift-off is done by using the Acetone solvent. Then, the wafer backside is cleaned and the n-metal evaporation is done with composition of again, Ti, Pt, Au and thicknesses of 60, 75, 200 nm, respectively. At last the samples are annealed at 325°C for 90 s. This last step prepares the sample for cleaving, mounting and eventual wire bonding.

Conclusion

In this paper, a description of the processing steps in the COBRA generic long-wavelength platform is given. Currently, the first long-wavelength devices are under processing. The characterization of these devices is expected in a short time.

Acknowledgements

The authors would like to gratefully acknowledge support of the EU FP7 through the PARADIGM project (ICT 257210).

References

1. M. Smit *et al*. *IET Optoelectronics*,vol 5, Issue 5, pp. 187–194, (2011).
2. T.L Koch *et al*. *IEEE journal of Quantum Electronics*. 27, pp. 641-653, (1991).
3. T..Kato *et al*. *Proc*. *Eur*. *Conf*. *On optical communication (ECOC 91)*, paper WeB7-2, (1991).
4. J.J.M. Binsma *et al*. *IEICE Trans.Electron*., vol. E80-C, pp. 675-681 (1997).

Polarization Property of a Double-layer Wire Grid Polarizer and the Mechanism of Transmission

A. Motogaito[1, 2], Y. Morishita[1], H. Miyake[1, 2], K. Hiramatsu[1, 2]

[1] Graduate School of Engineering, Mie University, Tsu, Mie, Japan,
motogaito@elec.mie-u.ac.jp, 412m248@m.mie-u.ac.jp, miyake@elec.mie-u.ac.jp, hiramatu@elec.mie-u.ac.jp
[2] The Center of Ultimate Technology on nano-Electronics, Mie University, Tsu, Mie, Japan,

Abstract: We fabricated a double-layer wire grid polarizer (WGP) and performed optical characterization to clarify the relationship between structure and polarization characteristics. For normal incidence, the fabricated double-layer WGP exhibits an extinction ratio of 30.4 dB for a period of 400 nm. The transverse magnetic (TM) transmittance peak is found to vary with the period of WGP. The peak shift can be explained on the basis of extreme transmittance phenomena exhibited by the surface plasmon polariton (SPP) of metal slit structures. It is considered that the incident light passes through the resist layer, followed by the excitation of SPP at the interface between the resist and Au. Subsequently, it combines with the transmitted light in the glass substrate, leading to strong transmitted light with TM polarization.

Introduction: The current state-of-the-art system for exposing circuit patterns in a semiconductor device or liquid crystal is by photolithography. To enhance the precision of a semiconductor structure, it is necessary to improve the resolution of the photolithographic system. This often requires a projection system with a light source of a shorter wavelength and large caliber. Besides, the effect of contrast-reducing p-polarized light in the device can be circumvented using s-polarized light. In practice, two types of polarizing elements are used to control the polarization state of a light source, namely, prism type and filter type, of which a wire grid polarizer (WGP) is a filter-type polarizer. This polarizer is considered suitable for use in electron beam lithography.

Given these advantages, in this study, we used a double-layer WGP that uses a double layer of a metal wire to realize a high optical extinction ratio when compared with the conventional WGP. Furthermore, the double-layer WGP offers the advantage of simplifying the fabrication by skipping the process of removing the resist. Besides, the simulation of polarization over the horizontal interval of the distance or a metal small-gage wire is conducted for two layers[1, 2]. However, to the best of our knowledge, there are no experimental studies reported so far on the double-layer WGP. In this study, we attempted to clarify the relationship between the structure and polarization property of a double-layer WGP and investigate the various parameters, such as period and metallic film thickness, to obtain an optimum structure.

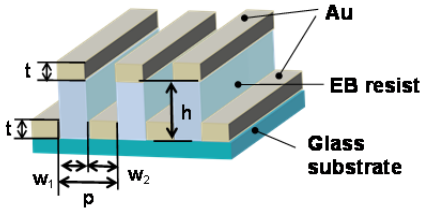


Fig. 1: Schematic diagram of WGP.

Experiments Procedure: Fig. 1 shows the schematic of the WGP made on a glass substrate using electron beam lithography system (CABL-8000, CRESTEC). The double-layer WGP was fabricated by sputtering a Au layer (SC-701MC, SANYU). Polarization measurements were performed using a red laser of wavelength λ = 635 nm. The polarization property of the fabricated double-layer WGP was characterized for different periods by varying the incident angle from 0 degree to 70 degree.

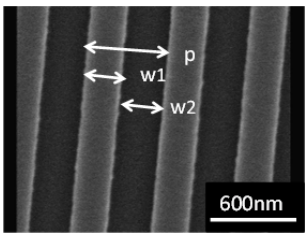


Fig. 2: Surface SEM image of WGP. p = 600 nm, $w_1 = w_2 = 300$

Experimental Results and Discussion: Fig. 2 shows the surface morphology of the double-layer WGP, as observed using SEM. As is seen, the WGP has almost the same structures.

Furthermore, we evaluated the polarization property of the fabricated double-layer WGP. Fig. 3 shows the TE and TM transmittance spectra of normal incidence for various periods.

The highest transmittance of TM polarization is obtained for a period of 400 nm. On the other hand, the transmittance of TE polarization is about 1000 times smaller than that of TM polarization. The extinction ratio for the 400-nm-period is 30.4 dB, which is almost similar to that of the commercial products. Subsequently, we characterized the dependence of TM transmittance on the incident angle. Fig. 4 shows the relationship between the period and incident angle, corresponding to the peak of TM transmittance. The peak angle is varied with the period.

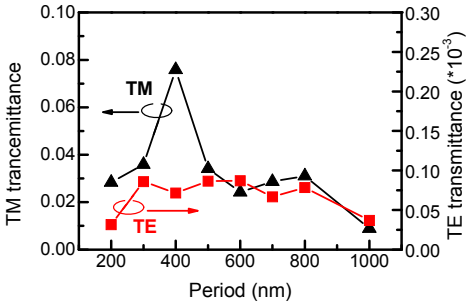


Fig. 3: TE and TM transmittance of normal incidence for various periods.

Furthermore, to consider the peak shift of the incident angle, we speculated the extreme transmission phenomena by surface plasmon[4]. For the simplified model composed of Au grating and a dielectric medium of refractive index 1.25, average of air and the resist, the dispersion relationship of surface plasmon polariton (SPP) and the incident angle excites the SPP. Fig. 5 shows the relationship between period and incident angle, which shows a peak corresponding to the TM transmittance of experimental data and calculated data. The calculated data are almost identical to the experimental data. Furthermore, the distribution of electrical field is calculated by the rigorous coupled wave analysis method. Fig. 6 shows the distribution of electrical field for a period of 316 nm and an incidence angle of 30 degree. The electrical field is concentrated at the interface of Au and the resist in the vicinity of the glass substrate. It is considered that the incident light passes through the resist layer, followed by the excitation of SPP at the interface between the resist and Au. Subsequently, it combines with the transmitted light in the glass substrate. This results in strong transmitted light with TM polarization.

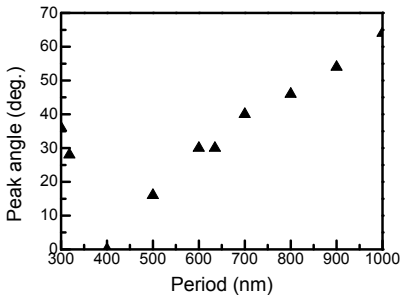


Fig. 4: Relationship between period and incident angle showing peak corresponding to TM transmittance.

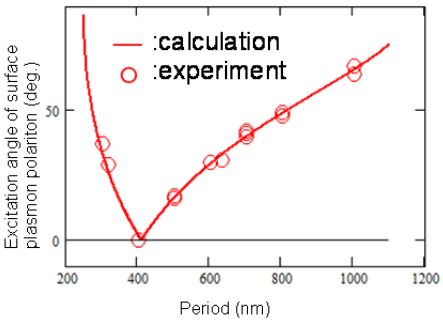


Fig. 5: Relationship between period and incident angle showing peak corresponding to TM transmittance of experimental and calculated data.

Conclusion: In summary, we clarified the relation between structure and polarization property in double-layer WGP to obtain the optimal structure. The polarization property of the fabricated double-layer WGP for the different period was characterized with the incident angle varying from 0 degree to 70 degree. The peak incident angle of TM transmittance is found to vary as a function of the period. This can be explained on the basis of the extreme transmission phenomena by surface plasmons.

Acknowledgements: This study is partly supported by Nippon Sheet Glass Foundation for Materials Science and Engineering and JSPS KAKENHI (Grant Number 25600090).

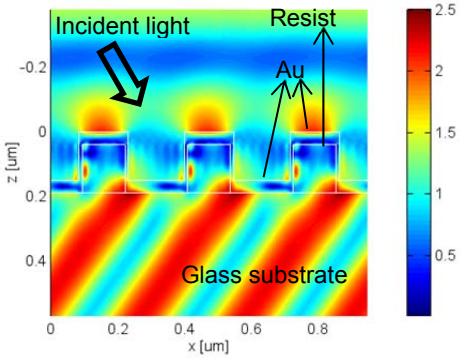


Fig. 6: Distribution of electrical field for a period of 316 nm and an incidence angle of 30 degree.

References

1. Z. Yu et al., *App. Phys. Lett.* **77**, pp. 927-929 (2000).
2. Y. Ekinci et al., *Opt. Exp.* **14**, pp. 2323-2334 (2006).
3. Z. Ye et al., *J. Opt.Soc. Am. B* **28**, pp.502-507 (2011).
4. T. W. Ebbesen et. al., *Nature* **393**, pp.667-669 (1998).

Excitation of Surface Plasmon Polariton at the GaP–Au Interface in a High-Refractive-Index Medium

A. Motogaito[1, 2], S. Nakamura[1], J. Miyazaki[1], H. Miyake[1, 2], K. Hiramatsu[1, 2]

[1] Graduate School of Engineering, Mie University, Tsu, Mie, Japan,
motogaito@elec.mie-u.ac.jp, 412m232@m.mie-u.ac.jp, 409371@m.mie-u.ac.jp, miyake@elec.mie-u.ac.jp, hiramatu@elec.mie-u.ac.jp
[2] The Center of Ultimate Technology on nano-Electronics, Mie University, Tsu, Mie, Japan,

Abstract: We demonstrated the application of GaP–Au contacts as SPP chemical sensors for a high-refractive-index medium, as verified using 2,4-dichlorotoluene ($C_7H_6Cl_2$, n = 1.55). The calculation of the dispersion relationship shows that the surface plasmon polariton (SPP) excited in GaP for incident light (λ = 635 nm) illuminated at 31.6° can be effectively used for detecting $C_7H_6Cl_2$. Subsequently, reflectance is analyzed as a function of Au thickness. The SPP excitation angle determined experimentally is found to be consistent with that of simulation data. When light is illuminated at 31.6°, the electric field is concentrated at the interface between Au and $C_7H_6Cl_2$ and is propagated along the interface. These results suggest that the SPP excited at the GaP–Au interface can be used as chemical sensors.

Introduction: In semiconductor electronic devices such as the Schottky barrier diode, the metal–semiconductor junction can act both as the Schottky contact and ohmic contact. In principle, the refractive index of a semiconductor is higher than that of transparent materials such as glass and sapphire, making semiconductors such as GaP and GaN transparent in the visible and near-ultraviolet-light regions. The combination of a semiconductor and a metallic thin film might result in the excitation of SPP at the metal–semiconductor interface. Typical examples of the application of SPP using metal and semiconductor include a silicon photodiode and luminescence enhancement of visible light light-emiiting diodes[1, 2]. On the other hand, the Kretschmann arrangement on the basis of the attenuated total reflectance method has been applied to chemical sensor. However, to use total reflection, it is difficult to detect the light reflected from a medium having a refractive index higher than 1.5, such as 2,4-dichlorotoluene ($C_7H_6Cl_2$, n = 1.55) and 1-bromonaphthalene ($C_{10}H_7Br$, n = 1.65). In this study, we focused on the semiconductor GaP, which is transparent in the visible region, has a large refractive index (3.3), and exhibits a wide band gap (2.2 eV). Its application as a chemical sensor has been attempted using the excitation of SPP at the interface between GaP and a metallic thin film. However, to the best of our knowledge, there are no detailed studies reported so far on the analysis of excitation conditions of SPP at the interface between the metal and semiconductor. In this study, we theoretically and experimentally analyzed the dependence of reflectance on the incidence angle for the interface between GaP and the Au thin film.

Calculation of Dispersion Relationship and Reflectance: When the complex dielectric constant of metal is $\varepsilon_1 = \varepsilon_1' + i\varepsilon_1''$ and that of a dielectric is ε_2, the dispersion relation at the interface of metal and dielectric is given by the following equation[3].

$$k_{sp} = \frac{\omega}{c}\sqrt{\frac{\varepsilon_1'\varepsilon_2}{\varepsilon_1' + \varepsilon_2}} + i\frac{\omega}{c}\left(\frac{\varepsilon_1'\varepsilon_2}{\varepsilon_1' + \varepsilon_2}\right)^{\frac{3}{2}} \quad (1)$$

$$k\sin\theta = \frac{2\pi n \sin\theta}{\lambda_0} = \Re e\{k_{sp}\} \quad (2)$$

The dispersion relationship is calculated for Au-$C_7H_6Cl_2$ with n = 1.55. Fig.1 shows the dispersion relationship between Re{k_{sp}} and ω. The laser light of wavelength 635 nm was used for the analysis. The angular frequency (ω_{sp}) of the exciting light is found to be $\omega_{sp} = 2.95 \times 10^{15}$ rad/s. The wavenumber k_{sp} for the exciting surface plasmon polariton (SPP) is obtained from the intersection of the dispersion curve and the light line. Furthermore, the incident angle θ in the substrate is obtained

from the following eq. (2), where k is the wavenumber of the substrate, λ_0 is the wavelength in vacuum, and n is the refractive index of the substrate. According to the dispersion relationship of Au-$C_7H_6Cl_2$, it is estimated that GaP can excite SPP at 31.0°. However, SiO_2 cannot excite the SPP.

Furthermore, the dependence of reflectance on the incident angle is calculated by the rigorous coupled wave analysis (RCWA) method. Fig.2 shows the dependence of reflectance on the incident angle for GaP/Au/$C_7H_6Cl_2$. Light of wavelength 635 nm is illuminated from the GaP substrate. The critical angle between GaP and $C_7H_6Cl_2$ is 27.9°, for which there is a rapid increase in reflectance. For an incident angle of 31.6°, reflectance decreases. In particular, the reflectance is close to 0 for 50-nm-thick Au.

Experimental Results and Discussion: The abovementioned results for GaP/Au/$C_7H_6Cl_2$ were further substantiated via fabricating a GaP–Au contact and performing reflectance measurement. The sample was fabricated by sputtering Au (MC-701, SANYU) onto a GaP (100) single crystal substrate. The dependence of reflectance on the incident angle was measured, as the p-polarized light is allowed to enter from the GaP side toward Au. The corresponding experimental results are shown in Fig.3. The reflectance becomes minimum at 31.1°, at which the SPP is excited at the Au-$C_7H_6Cl_2$ interface. This result is almost consistent with the simulation data.

Subsequently, we calculated the distribution of electric and magnetic fields when the SPP is excited. Fig.4 shows the distribution of electric field for the incident angle of 31.6°, as simulated by the RCWA method. The electric field is concentrated at the interface between Au and $C_7H_6Cl_2$ and is transmitted along the interface. These results suggest that the SPP is excited at the interface between Au and $C_7H_6Cl_2$, wherein reflectance becomes close to 0. Therefore, it can be concluded that GaP is effective in detecting $C_7H_6Cl_2$.

Conclusion: In summary, we used GaP–Au contacts as SPP chemical sensors for a high-refractive-index medium for demonstrating the detection of $C_7H_6Cl_2$. The experimental reflectance measurement results in case of $C_7H_6Cl_2$ indicate that the degrees corresponding to the excitation of SPP are consistent with the simulation data. Therefore, it can be concluded that the GaP–Au contact demonstrates the excitation of SPP, and hence can be used as chemical sensors for high-refractive-index media.

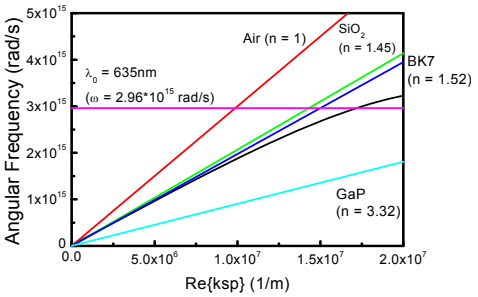


Fig. 1: Dispersion relationship between Au and $C_7H_6Cl_2$.

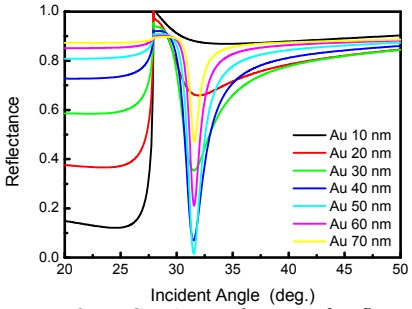


Fig. 2: RCWA simulation of reflectance depending on the incident angle.

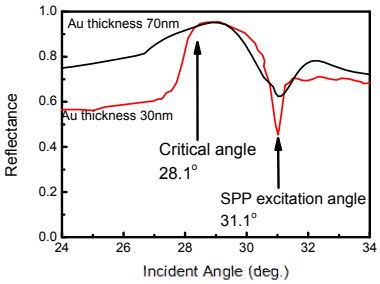


Fig. 3: Experiments of reflectance depending on the incident angle.

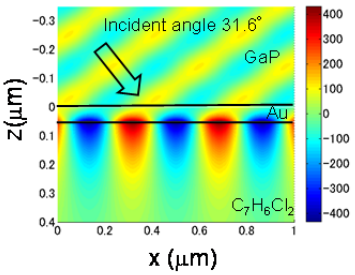


Fig. 4: Distribution of electrical field calculated by the RCWA method.

Acknowledgements: This study is partly supported by The Murata Science Foundation, Hikari-Mirai Young Scientist Grant 2010 of Optical Society of Japan, and JSPS KAKENHI (Grant Number 25600090).

References

1. T. Ishi et al., *Jpn. J. Appl. Phys.* **44**, pp.L364-L366 (2005).
2. K. Okamoto et al., *Nat. Mat.* **03**, pp.601-605 (2004).
3. K. Okamoto and Y. Kawakami, *IEEE J. Sel. Top. Quantum Electron.* **15**, pp.1199-1209 (2009).

QD-PMMA nanocomposite plasmonic waveguides

I. Suárez[1], E. P. Fitrakis[2], R. Abargues[1], P.J. Rodríguez, I. Tomkos[2] and J.P. Martínez-Pastor[1]

[1] *UMDO (Unidad Asociada al CSIC-IMM), Instituto de Ciencia de los Materiales, Universidad de Valencia, PO Box 22085, 46071 Valencia, Spain, isaac.suarez@uv.es*

[2] *Athens Information Technology, P.O. Box 68 19,5 klm, Markopoulo Ave. GR – 19002, Peania Attikis, Greece*

Abstract: In this work colloidal quantum dots (QD)-PMMA nanocomposites are proposed as a material able to compensate losses in surface plasmon polariton (SPP) propagating along a gold plasmonic waveguide. For this purpose geometrical parameters of the waveguides are optimized with the appropriate simulations prior to the fabrication of the structures. Then, a new method to measure the propagation length of the SPP is proposed to characterize the structures and to estimate the propagation length.

Introduction Nowadays there is a great concern of combining plasmonic waveguides with photonic technology. This is because the hybrid electromagnetic wave and charge surface state nature of the surface plasmon polaritons (SPP) [1] allows for unique properties like subwavelength confinement and strong electric field concentration, which could be used to miniaturize the final size of the device and reduce its power consumption in future electronic/photonic technology [2]. However, the propagation length (L_P) of SPPs is limited by the high ohmic losses in metals and. This limitation can be compensated by an appropriate design of the plasmonic waveguide. A first approach is to provide gain in the dielectric on top of the metal [3] that could amplify the SPP signal [4]. In addition, the propagation length can be increased by combining the SPP with dielectric waveguide modes [5], which usually exhibit small propagation losses. In this work a combination of both solutions is presented as a method to couple light into the SPP and to increase its L_p.

The active material proposed in this work consists of colloidal quantum dots (QD) embedded in an appropriate polymer (PMMA in our case). Such a nanocomposite is of great interest nowadays, because it combines the properties of the QDs (i.e., room temperature emission and tuning of the absorption/emission wavelengths by changing their size and composition [6]) with the technological feasibility provided by the polymer, (i.e., deposition by different solution processing methods and patterning by using either e-beam lithography or nanoimprint [7]). The use of QD-PMMA in photonics was demonstrated in Ref. 7 by using such a nanocomposite as the core of active planar waveguides. In addition, (PbS QDs)-PMMA films have already been used to compensate the losses of the SPP propagation at infrared wavelengths [8-9]. In this work (CdSe QDs)-PMMA/Au plasmonic waveguides deposited on a SiO_2/Si substrate (see Fig. 1a) are analyzed; the structures were carefully designed to optimize the light confinement in the metal together with low losses. The L_p of optical modes in the waveguide has been characterized by using a novel experimental method based on the use of a fiber tip that couples the input signal into SPP modes. An additional pump beam that is end-fire coupled into the plasmonic waveguides produces an enhancement of the SPP L_p.

Waveguide design. Figure 1a shows the structure of the CdSe-PMMA/Au plasmonic waveguides used in the present work. The Au was deposited by evaporation (30 nm thick) on a SiO_2/Si substrate (CEMAT Silicon S.A.) and the stripes (6 - 20 μm wide) by a standard lift-off process. The CdSe-PMMA nanocomposite is spin-coated by following the procedure developed in Ref.7. These plasmonic waveguides were optimized by solving the propagation constant of the guided modes with the transfer matrix method in a complex plane at the photoluminescence (PL) peak wavelength (600 nm), in a similar way as that previously reported in Ref. 10 for planar structures. The optimization consisted in achieving a maximum confinement and propagation length for the long range SPP (LR-SPP). In this way, a gold film around 30 nm thick is an appropriate trade-off between the LR-SPP confinement (increasing with thickness) and propagation length (decreasing with thickness), L_P, for which L_P = 11.7 μm and the mode confinement is around 10 % [10]. Figure 1c shows the effective refractive index of several optical modes and L_p of the LR-SPP mode as a function of the CdSe-PMMA nanocomposite thickness (lines in color and left axis). Here it is important to point out that the nanocomposite layer should ideally be thick enough to contain the whole evanescent tail of the TM fundamental mode. However, above a certain thickness ($d \approx 1100\ nm$) higher order hybrid TM modes

start to be guided and hence a thickness d=1 μm was fixed. Figure 1d depicts the LR-SPP mode confined in a stripe 6 μm wide.

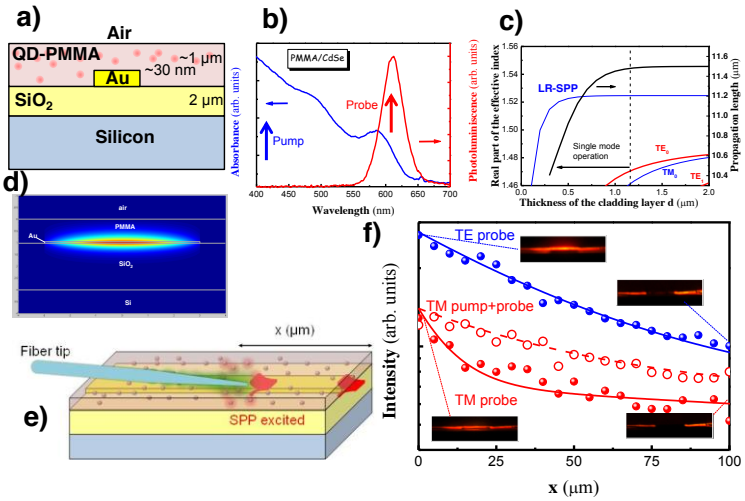


Fig. 1: a) Waveguide structure. b) Absorbance (blue line) and PL (red line) spectra of the CdSe-PMMA nanocomposite. c) Calculation of several propagating modes and propagation length in a planar structure as a function of the nanocomposite thickness. d) Simulation of the LR-SPP mode. e) Experimental set-up. f) Characterization of Lp in TE (blue) and TM (red) without (solid symbols and continuous lines) and with (hollow symbols and dashed line) end-fire coupled pumping laser. The pictures show the near field distribution in TE and TM at x=0 and x=100 μm.

Waveguide characterization. Plasmonic waveguides were characterized by exciting the PL of CdSe QDs at 533 nm with a fiber tip and recording the guided PL signal at the nearest waveguide edge, as illustrated in Fig. 1d. Figure 1f shows the signal intensity as a function of the distance between the fiber tip and the waveguide edge for TE and TM modes (blue and red solid symbols, respectively), which is fitted (continuous lines) by the sum of two exponential decays where L_P for both modes is deduced: $\sim A_1 e^{(-x/Lp1)} + A_2 e^{(-x/Lp2)}$. The shortest propagation length, L_{p1}, for TM mode corresponds to the LR-SPP and the best fit yields $L_{p1} = 11.1\ \mu m$, which is very close to the calculated value (11.4 μm, see Fig. 1c). The fit for the TE mode gives a longer L_p value (50 μm), given that this mode is centered at the dielectrics (QD-PMMA nanocomposite) and not at the metal (see pictures at x = 0 μm in Fig. 1f). The longest propagation length, L_{p2}, corresponds to the light travelling out of the metal stripe and hence is similar under both polarizations (see pictures at x=100 μm in Fig. 1f). The QD-PMMA film can be used to couple a pump beam by end-fire coupling of 404 nm laser (on the opposite face to that of detection) to compensate for the losses of the LR-SPP mode (red open symbols in Fig. 1f). Again, this experimental curve can be fitted by the same two exponential decay functions (dashed line) yielding a value for L_{p1} of around 35 μm.

Conclusions. Plasmonic waveguides based in a QD-PMMA nanocomposite are proposed. The structures are optimized to achieve optimum light confinement and low losses and are coupled to a photonic waveguide where a pump beam can be propagated with low losses. A novel experimental set-up based on a fiber tip is used to measure the LR-SPP propagation length. An enhancement of this propagation length by around 3 fold is demonstrated when PL of QDs in the nanocomposite is excited by end-fire coupling.

Acknowledgement. This work was supported through the Spanish MCINN and EU-NAVOLCHI, Grants TEC2011-29120-C05-01 and 288869 respectively.

References

1. S.A. Maier, *Plasmonics Fundamentals and Applications*, Ed., New York: Springer, (2007).
2. J. Leuthold *et al*., Optics and Photonics News, pp. 30-35, (2013).
3. P. Berini and I. De Leon, *Nature Photonics*, **6**, pp. 16-24, (2012).
4. M.C. Gather *et al*., *Nature Photonics*, **4**, pp. 457-461, (2010).
5. R.F. Oulton *et al*., *Nature Photonics*, **2**, pp. 496-500, (2008).
6. V.I. Klimov *et al*. ,Science, **28**, pp. 214-220, (2003).
7. I. Suárez *et al*., *Nanotechnology*, **22**, 435202, (2011).
8. J. Grandidier, *et al*., *Nanoletters*, **9**, pp. 2935-2939, (2009).
9. I.P. Radko *et al*., *Optics Express*, **18**, pp. 18633-18641, (2010).
10. I. Suárez *et al*., *ICTON Proceedings*, (2013).

1×3 plasmonic power splitter for various splitting ratio

Yuhsin Chang, Chyong-Hua Chen

Department of Photonics and Institute of Electro-Optical Engineering,
National Chiao Tung University, Hisnchu, Taiwan,
ysyuhsin.chang@gmail.com, chyong@mail.nctu.edu.tw

Abstract: A 1×3 plasmonic power splitter for various splitting ratio is proposed by using a rectangular ring resonator based on metal-insulator-metal waveguide. The input/output waveguides are located at which destructive/constructive interferences of this ring interferometer are occurred, respectively. Then flexible splitting ratio is realized by manipulating the output waveguide widths and the minimized reflectance in the input waveguide is numerically accomplished by adjusting the resonator's dimension.

Introduction: Plasmonic power splitters that divide an input power into two or more output ports have been considered as a key component for both signal routing and signal processing in ultrahigh-density photonic integrated circuits (PICs)[1-3]. In particular, power splitters with flexible power splitting ratio are required in many applications, such as in a communication system[4]. In addition, 1×3 splitters are required as one elementary building block to build a 1×N optical splitter[5]. Various 1×3 plasmonic splitters are proposed to manipulate the splitting ratio by adjusting the coupling lengths in the couplers[1], varying the gap widths between waveguides and the cavity[2] and shifting the waveguide positions along the multimode interference waveguide[3]. However, these splitters are high sensitive to the wavelength variation. In this work, we present a 1×3 plasmonic power splitter constructed by a rectangular ring resonator with directly-connected input and output waveguides based on the metal-insulator-metal (MIM) waveguides. The input/output waveguides are located where destructive/constructive interferences of this ring interferometer are occurred, respectively. The splitting ratio is controlled by adjusting the output waveguide widths, and the reflectance at the input waveguide is eliminated by adjusting the waveguide width of resonator. Due to the direct connection and the conditions for interferences, the qualify factor of this resonator is low, and thus this device provides the characteristics of broad bandwidth. An example of a 1x3 plasmonic power splitter is numerically demonstrated.

1×3 plasmonic splitter: The configuration of a 1×3 plasmonic splitter based on MIM waveguides is shown in Fig. 1. The input and three output waveguides are directly connected to a rectangular ring resonator. The widths of input waveguide and three output waveguides are w_{in}, $w_{out,1}$, $w_{out,2}$ and $w_{out,3}$, respectively. The width and the height of the resonator are W and H, respectively. The waveguide width of the resonator is w_r.. Due to the impedance mismatched of the T-splitter at each junction of the input/output waveguide, bidirectional propagation waves travel inside the resonator, resulting in an interference pattern of the field distribution along the resonator. Thus, to obtain three anti-nodes of the interference pattern where all the output waveguides are located, the total propagation phase in the resonator is equal to 3π. To realize the minimal reflection at the input waveguide, the input waveguide is located at one node of the interference pattern. The interference conditions related to the waveguide parameters become $\mathrm{Re}\{\beta_r\}H=0.5\pi$ and $\mathrm{Re}\{\beta_r\}W=\pi$, where $\mathrm{Re}\{\beta_r\}$is the real part of the propagation constant of the resonator. The output power in each output waveguide is proportional to its width, and then the splitting ratio of this device can be realized by adjusting the width ratio, $w_{out,1}$, $w_{out,2}$ and $w_{out,3}$. In addition, in order to minimize the reflectance, the waveguide width of the resonator w_r is adjusted to have a completely destructive interference in the input waveguide. Thus, w_r, W and H are relevant, and we iteratively obtain all design parameters to reach the desired splitting ratio and a negligible reflectance.

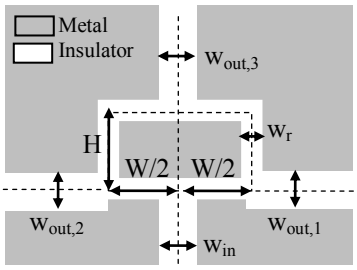


Fig. 1: Structure of the 1x3 splitter

Simulated results: We numerically exhibit an example of the 1×3 power splitter with various splitting ratio. The dielectric and metallic materials of MIM waveguides are air and silver,

respectively. The permittivity of silver is described by the Drude-Lorentz model[6]. The concerned wavelength is 1550nm. Suppose that the splitting ratio is 1:2:3. First, let w_0=$w_{out,2}$=50nm and set $w_{out,1}$=25nm, $w_{out,3}$=75nm and w_r=50nm as our initial guessing. Then, $w_{out,1}$ and $w_{out,3}$ and w_r are modified to obtain the specifications. The optimized parameters are as follows: $w_{out,1}$=15nm, $w_{out,3}$=80nm and w_r=40nm. Then, the corresponding H=259.6nm and W=519.2nm. The field evolution of this 1x3 splitter at the wavelength of 1550nm simulated by using the two-dimensional (2D) finite difference time domain (FDTD) simulator (Fullwave, RSOFT Design Inc.) is depicted in Fig. 2(a). The transmittances in the output waveguides are -8.2, -4.8 and -3.3 dB, respectively, showing the splitting ratio is approximately 1:2:3. The reflectance in the input waveguide is -32.0dB. The wavelength dependence of this device is shown in Fig. 2(b). The splitting ratio is roughly 1:2:3 over the wavelength range between 1400 and 1700nm, showing that the splitting ratio slightly vary with the wavelength. The wavelength dependence of reflectance is shown in Fig. 2(c). The reflectance in the input waveguide is less than -20dB as the wavelength ranges between 1400 and 1700nm. These simulated results show that this device has a flat and wide band due to the low qualify factor of this resonator.

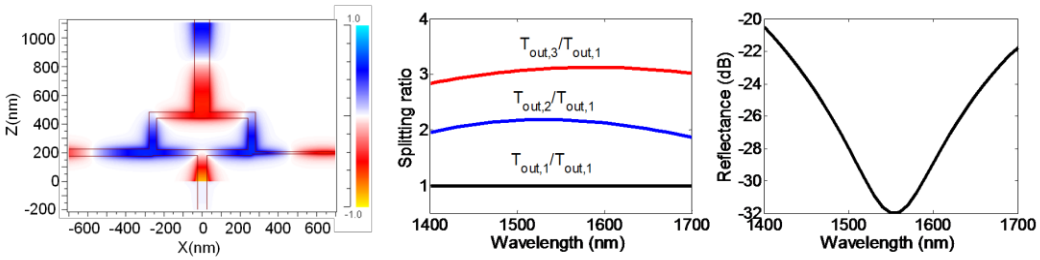


Fig. 2: (a) Field evolution (b) Splitting ratio (c) Reflectance spectrum

Conclusion: A 1×3 plasmonic power splitter constructed by a rectangular ring resonator is proposed to reach various splitting ratio for the applications in ultrahigh-density PICs. The input and output waveguides are located at the one node and three anti-nodes of the interference pattern of the field distribution along the resonator. Then, the splitting ratio is manipulated by adjusting the waveguide width ratio among the output waveguides and the minimized reflectance is obtained by adjusting the resonator dimension. Due to the direct connection and the conditions for interferences, the qualify factor of this resonator is low, and thus this device provide the characteristics of broad bandwidth. An example of the 1×3 plasmonic splitter with its dimension of 259.6nm×519.2nm and a splitting ratio of approximately 1:2:3 and reflectance below -20dB over the range of 1400 to 1700nm is numerically demonstrated.

References

1. N. Nozhat and N. Granpayeh, *Optics Communications* **284**, pp. 3449–3455, (2011).
2. Y. Guo *et al*., *Optics Express* **19**, pp. 13831–13838, (2011).
3. Y. Song *et al*., *Journal of optical* **13**, pp. 075002, (2011).
4. S. Tao *et al*., *IEEE Photonics Technology Letters* **23**, 1004–1006, (2011).
5. T.-J. Wang *et al*., *IEEE Photonics Technology Letters* **15**, 1401–1403, (2003).
6. P. B. Johnson *et al*., *Physical Review B* **6**, pp. 4370–4379, (1971).

Arbitrary coupling ratio multimode interference couplers in Silicon-on-Insulator

J.D. Doménech[1], **J.S. Fandiño**[2], **B. Gargallo**[2] **and P. Muñoz**[1,2]
[1]VLC Photonics S.L., Spain - david.domenech@vlcphotonics.com
[2]Universitat Politècnica de València, Spain - pmunoz@iteam.upv.es

Abstract

In this paper we present the experimental demonstration of Multimode Interference (MMI) couplers in Silicon-on-Insulator (SOI) technology with coupling ratios 95:05, 85:15, 75:25, 65:35 and 55:45. The couplers were designed using a rib waveguide Si cross-section with SiO_2 cladding, on a regular 220 nm film and 2 μm buried oxide SOI wafer. Set of devices were fabricated in two wafers with two different etch depths. The coupling ratios obtained match, with little deviations, the design targets for a wavelength range between 1525 and 1575 nm. Excess loss is conservatively estimated to be less than 2 dB.

I. Introduction

The Multimode Interference (MMI) coupler is widely used in high index contrast technologies, such as III-V and group IV material systems based PICs, since it is in general more compact, and preserves the coupling constant over a wide wavelength range. Since its inception [1], and the early demonstrations [2], multitude of papers have studied these devices: theory and design rules for canonical MMIs [3]–[5]; design rules and demonstration widened/narrowed body MMIs for arbitrary coupling ratios at a single wavelength [6] and reconfiguration using thermal tuning [7]; tolerance analysis [8] and design optimizations for different technologies [9], to name a few. In this paper we report on the design and experimental demonstration of arbitrary coupling ratio MMIs following the design rules from [6], supported by Beam Propagation Method (BPM) commercial software optimizations [10], on a Silicon-on-Insulator (SOI) platform.

II. Experimental results

The design of all the MMIs was carried out in three steps: i) cross-section analysis and 2D reduction [10], ii) analytical approach [6] and iii) numerical BPM optimization [10]. The cross-section consist of a rib waveguide in a standard SOI wafer with SiO_2 cladding. The devices were fabricated on two different wafers, A and B, using a 248 nm CMOS fabrication line. Wafers A and B had different etch depth for the rib waveguides, 130 nm (design) and 160 nm respectively from top of the Si film.3 dies per wafer were retained for measurements. A picture of the fabricated devices is shown in Fig. 2. All the layouts included focusing grating couplers (FGC) [11] for TE polarization. The *coupling ratios* for the MMIs were derived from the spectral traces measured at outputs. The results are given in Fig. 3, where the average coupling ratios and standard deviations in the wavelength range of the measurements are shown. They show good agreement with target coupling ratios. Deviations from the mean value are approximately in the range of ± 0.02. Note the additional etch depth of

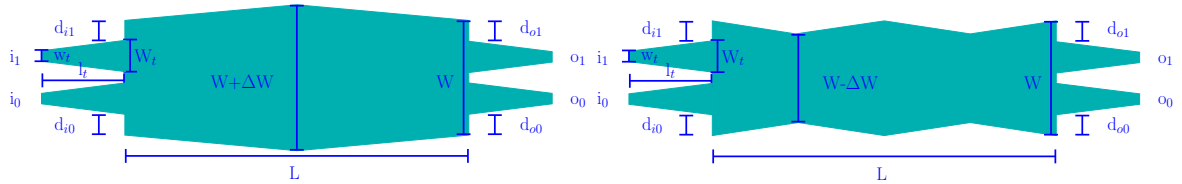


Fig. 1. Multimode Interference coupler sketches, (a) Type A, B, C, D and (b) Type B Symmetrical layout. Abbreviations: L and W, MMI body length/width; d_{io} distance of input/output waveguides from the edges of the MMI; l_t input/output taper length; w_t and W_t input/output taper narrow/wide widths.

Id	#1	#2	#3	#4	#5
Ratio	95:05	85:15	75:25	65:35	55:45
Type	B Sym	B Sym	C	D	D
L	211.95	184.55	247.18	170.36	200.04
ΔW	1.44	2.53	3.26	1.5	3.34
d_{i0},d_{i1}	1.97	1.97	1.11	0.60,2.60	0.61,2.61
d_{o0},d_{o1}	1.97	1.97	1.11	2.60,0.60	2.61,0.61
W_t	2.7	2.7	2.83	2.83	2.80
Body	Double	Double	Single	Single	Single

TABLE I
MMI design parameters, lengths and widths in μm. For all $W_t = 0.45$, L_t=50, W=10 microns.

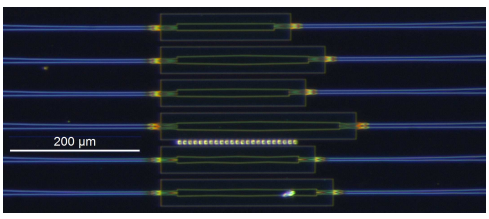
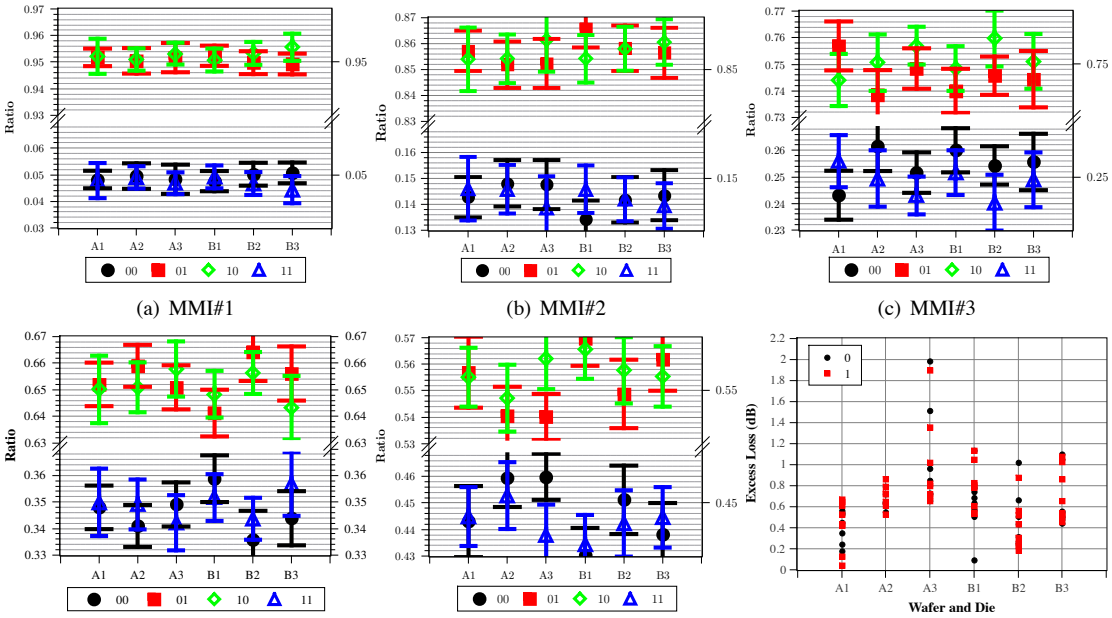


Fig. 2. Chip photograph for the fabricated MMI devices, from bottom to top MMIs #3-#7, i.e. 95:05, 85:15, 75:25, 65:35, 55:45 (non canonical) and 72:28 (canonical) splitting ratios.



(a) MMI#1 (b) MMI#2 (c) MMI#3

(d) MMI#4 (e) MMI#5 (f) EL

Fig. 3. MMIs coupling ratio average and standard deviation, $\lambda \in [1525, 1575]$ nm, wafers A y B and dies 1, 2, 3 within each wafer.

30 nm in wafer B did not change significantly the results, as reported in [9]. The ratios are calculated from spectra obtained from adjacent different outputs, through different output FGCs. Little variations (imbalance, deviation) are observed except for a few cases, and differences in the FGCs can explain the average value deviations, e.g. MMI#5 A3 in Fig. 3-(e). An estimation for the *excess loss*, EL, is derived combining the MMI measured spectra with the spectra of reference straight waveguides. The results needed to be corrected by adding 0.4 dB, accounting for the deviations due to fiber alignments and differences in FGC performance. Consequently, an absolutely accurate value for the EL cannot be derived from these measurements. Otherwise, one should resort to full in depth statistical analysis of a larger number of samples [12] [13]. However, from these calculations, the interval on which the EL lies can be estimated at the sight of Fig. 3-(e). Inferring conservative conclusions from these graph leads to an expected EL for each MMI of less than 2 dB.

III. Conclusion

In this paper the design, fabrication and measurement of MMIs with arbitrary coupling ratio in Silicon-on-Insulator technology has been reported. The design methodology consisted on a combination of theoretical first guess and numerical optimization, using the Beam Propagation Method. The devices were fabricated in two different wafers, where the waveguides had different etch depths. Very good match between the design and experimental results was obtained in terms of the coupling ratio for the devices. All the coupling ratios were attained within the design wavelength range of 1525-1575 nm with deviations as low as ± 0.02. Minor deviations were attributed to the difference in the performance of the focusing grating couplers. Furthermore, the excess loss for the MMIs was estimated from the measurements to be less than approximately 2 dB.

The authors acknowledge the Spanish CDTI NEOTEC, MICINN TEC2010-21337, MINECO TEC2013-42332-P, FEDER UPVOV 10-3E-492, FEDER UPVOV 08-3E-008, FPI BES-2011-046100 and FPU AP2010-1595.

References

[1] R. Ulrich and G. Ankele, *Appl. Physics Lett.*, vol. 27, no. 6, 1975.
[2] E. Pennings, R. Deri *et al.*, *Appl. Physics Lett.*, vol. 59, no. 16, pp. 1926–1928, 1991.
[3] L. B. Soldano and E. C. Pennings, *J. Lightwave Technol.*, vol. 13, no. 4, pp. 615–627, 1995.
[4] M. Bachmann, P. Besse, and H. Melchior, *Appl. Optics*, vol. 33, no. 18, pp. 3905–3911, 1994.
[5] ——, *Appl. Optics*, vol. 34, no. 30, pp. 6898–6910, 1995.
[6] P.-A. Besse, E. Gini *et al.*, *J. Lightwave Technol.*, vol. 14, no. 10, pp. 2286–2293, Oct 1996.
[7] J. Leuthold and C. H. Joyner, *J. Lightwave Technol.*, vol. 19, no. 5, p. 700, May 2001.
[8] P.-A. Besse, M. Bachmann *et al.*, *J. Lightwave Technol.*, vol. 12, no. 6, pp. 1004–1009, Jun 1994.
[9] R. Halir, I. Molina-Fernandez *et al.*, *J. Lightwave Technol.*, vol. 26, no. 16, pp. 2928–2936, Aug 2008.
[10] "FieldDesigner and OptoDesigner software packages," http://www.phoenixbv.com/.
[11] F. Van Laere, T. Claes *et al.*, *IEEE Photonics Technol. Lett.*, vol. 19, no. 23, pp. 1919–1921, 2007.
[12] L. He, Y. Liu *et al. IEEE Photonics Technol. Lett.*, vol. 25, no. 14, pp. 1358–1361, 2013.
[13] W. Bogaerts, M. Fiers, and P. Dumon, *IEEE J. Selected Top. in Quantum Elect.*, vol. 20, no. 4, pp. 1–8, July 2014.

The fundamentals of multi-splitting filtering technology

A. Tsarev[1,2]

[1] *A.V. Rzhanov Institute of Semiconductor Physics SB RAS, Novosibirsk, Russia*
tsarev@isp.nsc.ru
[2] *Novosibirsk State University, Novosibirsk, Russia*

Abstract: We present the general description on novel optical filter/multiplexer constructed by multiply coupled waveguides. For the study, a modified effective index method (MEIM), has been used. It correctly describes, in the 2D case both the phase and the group indexes in a 3D silicon wire waveguide and makes it possible to simulate complicated SOI structures by 2D FDTD. The silicon wire crossings are realized by means of a vertical up and down coupling through the silica buffer of tapered Si wires with the upper thick polymer waveguide. FDTD modeling prove that a short 0.26 mm multiplexer with 32 couplers has FSR 35 nm, spectral resolutions 1.4 nm, internal loss -0.7 dB and sidelobes -20 dB.

Introduction

Silicon photonics [1] creates a great amount of optical devices intended for different applications from telecom to sensors. None of them are ideal but each has some advantages related to the others. A brief description of original results which make the building blocks of multi-splitting (MS) photonic structures on silicon-on-insulator (SOI), which can be used as tunable filter or reconfigurable optical add drop multiplexer (ROADM), are discussed and reviewed in the paper.

A design of multi-splitting multiplexer

A general view of the novel multi-splitting multiplexer [2, 3] is shown in Fig. 1(a). It uses multilayer wire crossing [4, 5] (see Fig.1(b)). The input signal (In) is coming into the bottom Si wire waveguide and splits into sub-beams by multiple adiabatic directional couplers with the varying coupling ratio (different gap width) which is responsible for the filter apodization. Each of sub-beams goes further along the crossed waveguides (vertical in a structure design) and is combined in the output wire waveguide (Drop) by an appropriate set of similar couplers. The structure has a constant optical path difference of $\Delta S = L_a + L_b$. Thus, at drop optical wavelengths, all the sub-beams add in the phase along the Output wire waveguide (Drop) and produce efficient filtering. All other wavelengths pass further the coupler, cross the Drop waveguide and further combined in the output wire waveguide (Through) by an appropriate set of similar directional couplers. These couplers also have the varying coupling ratio (generally inversely respective to In and Drop bus waveguides) in order to increase the Through signal efficiency. Structure design provides the condition that the most of spitted sub-beams have the same pass difference on the way from input (In) to output (Through). Thus, all the optical wavelength which are not filtered by Drop channel will be transmitted to the Through output. As a results, the structure presented in Fig. 1(a) could be used as the optical multiplexer, as well as the optical filter.

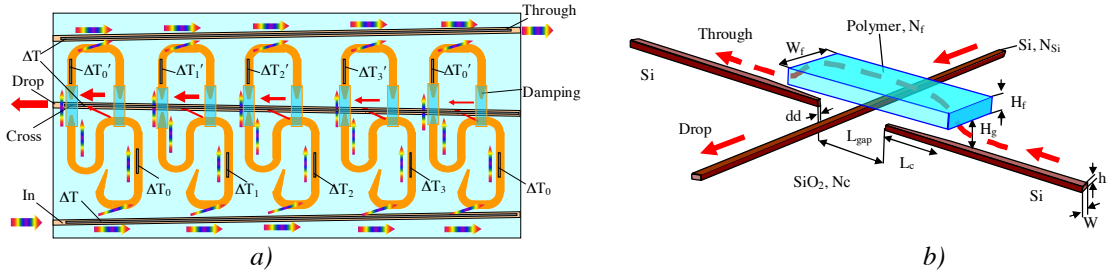
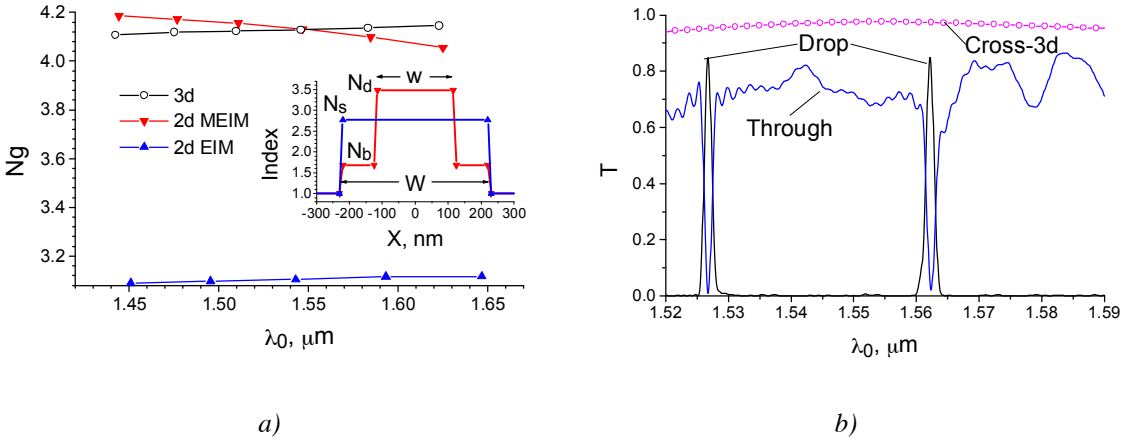


Fig. 1. The principle view of multi-splitting tunable multiplexer (a) and a basic scheme of multilayer effective crossing of two silicon wires by vertical coupling with a polymer waveguide (b).

Device examination is very complicated and the study has been divided into several interconnected parts, which are focused on one key point. The first part is devoted to the approach of multilayer waveguide crossing [4, 5] which is also suitable to construct a damper. Next part discuses the modified effective index method MEIM [6] which is optimal for direct 2D modeling of the device as it correctly (with about 1% error) describes in 2D case the phase and group index of 3D silicon wire waveguide (see Fig.2(a)). Optimum filter design [3] takes into account a constant pass-length difference and variation of coupling strength by controlling the gap between directional couplers used as power splitters. Spectrum properties of the MS filter (see Fig.2(b)) and it tuning by thermo-optic effect are examined by direct 2D modeling jointly by 2D FDTD and MEIM, and taking into account the presence of the wire crossings studied by 3D FDTD.



a) *b)*

Fig. 2. Numerical modeling of MS-multiplexer by FDTD and MEIM. Group indexes as a function of optical wavelength λ_0 for different simulation cases (a); wavelength dependence of transmitted power for Drop and Through channels of the optical multiplexer with 32 directional couplers (b). A curve Cross-3d presents waveguide crossing transmitting efficiency. In the insert are the refractive index profiles for EIM and MEIM.

Conclusion

We discuss optical properties of a new tunable optical multiplexer which utilized multiple coupled silicon wire waveguides in SOI structures. In order to provide a negligible scattering, the wire crossings are realized by means of a vertical up and down coupling through the silica buffer of tapered Si wires with the upper thick polymer waveguide. For the multiplexer study, a modified effective index method, which utilizes the combined index profile with two spatial parameters, has been used. It correctly describes, in the 2D case both the phase and the group indexes in a 3D silicon wire waveguide and makes it possible to simulate complicated SOI structures by 2D FDTD. Our FDTD modeling proves a general conception of the multiplexer on SOI and demonstrates that a short 0.26 mm structure with 32 couplers has spectral resolutions 1.4 nm, internal loss -0.7 dB and sidelobes -20 dB. It provides the wavelength tuning (without Vernier principle) within FSR 35 nm at optical wavelength 1550 nm by the four sets of thermo-optical phase shifters with $\Delta T<140$ C°. A device of 0.7 cm in size will provide a 0.05 nm filter linewidth. It is CMOS compatible. Work is executed by a support of the grant No 12-07-00018a by the Russian Fund for Basic Research. The author acknowledges RSoft Design Group, Inc., for providing the user license for FDTD simulations [7].

References

1. W. Bogaerts, S. Selvaraja, P. Dumon, J. Brouckaert, K. De Vos, D. Van Thourhout, R. Baets. *J. Sel. Top. Quantum Electron. (invited)* **16**, pp. 33-44 (2010).
2. A. Tsarev, *Proc. SPIE* **8781**, pp. 878106-878106-13 (2013).
3. A. Tsarev, *IEEE Journal of Selected Topics in Quantum Electronics*, **20**, no.4, pp.1,8, (in press, JSTQE.2013.2295180).
4. A.V. Tsarev, Opt. Express **19**, pp. 13732-13737 (2011).
5. A .V. Tsarev, E. A. Kolosovskii, QUANTUM ELECTRON **43**, pp. 744–750 (2013).
6. A.Tsarev, *Opt. Lett.* **38**, pp. 293-295 (2013).
7. Rsoft Photonic CAD Suite, version 8.0 (2007), www.rsofdesign.com.

Coherent Tunnelling Adiabatic Passage in Fiber Geometry

K. Thyagarajan[1], **Ruchi Gupta**[2]

[1] *Department of Physics, IIT Delhi, Hauz Khas, New Delhi 110016, India, ktrajan@physics.iitd.ac.in*

[2] *Department of Applied Sciences, ITM University, Sector 23A, Gurgaon, Haryana, ruchigarg19@gmail.com*

Abstract: This paper presents a mimic scheme of stimulated Raman adiabatic passage (STIRAP) in an optical fiber. An analogy is shown between the three level atomic system and the three modes of the optical fiber. It is possible to achieve an interaction using a pair of superimposed long period gratings where the fundamental core mode couples to another core mode via an intermediate cladding mode. The intermediate cladding mode gets negligibly excited and is known to work as dark mode.

Introduction:

Stimulated Raman adiabatic passage (STIRAP) technique in a three level system is the transfer of light between two levels assisted by an intermediate level with negligible excitation, thus defining the adiabatic behavior in the transfer of light. This technique has been realized in photonic integrated circuits by allowing light to couple from one waveguide to other via a central waveguide[1] wherein adiabatic transfer is ensured by maneuvering the separation between these waveguides[2]. Being the spatial analogue of STIRAP technique, the coherent tunnelling adiabatic passage (CTAP) in waveguides opens new avenues for device designing to achieve various functionalities in photonics such as mode transformers, beam splitters, polarization rotators[3-5], etc.. Adiabatic coupling in multimode waveguides has been achieved using CGPH[6] (computer generated planar holograms). We show coherent tunneling adiabatic passage in a standard SMF-28 fiber that utilizes a scheme of superimposed long period gratings (SLPGs) and involves two core modes and one cladding mode.

Analysis:

The fiber is made of fuzed silica (SiO_2) with 3.1 % GeO_2 doping in the core region. The core and cladding radii are 4.1 μm and 50 μm (etched cladding), respectively. Simulations are carried out at the wavelength of 633 nm where the geometry allows two azimuthally symmetric core modes ($LP_{0,1}$, $LP_{0,2}$) followed by cladding modes. Figure 1 shows the schematic of the fiber geometry with SLPGs. Grating I couples from fundamental core mode ($LP_{0,1}$) to the higher order cladding mode ($LP_{0,17}$) grating II couples from this selected higher order cladding mode to the $LP_{0,2}$ core mode with corresponding grating periods Λ_1 and Λ_2, respectively. L_g is the grating length which is the distance over which the three mode interaction takes place. Analysis for the three mode coupling has been carried out using standard coupled mode theory[7]. The perturbation in the refractive index profile of the fiber core that accounts for the SLPG pair is given by:

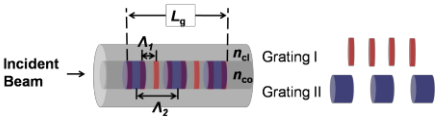


Fig. 1: Schematic of the fiber geometry showing SLPG

$$\delta n'(z) = \Delta\bar{n}'(z) + \Delta n_1(z)\sin\left(\frac{2\pi}{\Lambda_1}z\right) + \Delta n_2(z)\sin\left(\frac{2\pi}{\Lambda_2}z\right) \quad (1)$$

with $\Delta\bar{n}'(z)$ being the average z - dependent index that can be written as $\Delta n_1(z)+ \Delta n_2(z)$. Δn_1 and Δn_2 are the z - dependent peak refractive indices of grating I and grating II, respectively. The values of the cross coupling coefficients of both the gratings depend directly on these peak refractive indices, thus become z - dependent. The three mode coupled equations can be represented in the following matrix form that can be solved by simplifying into an eigen value equation:

$$\zeta'(z) = \bar{T}\zeta(z) \tag{2}$$

with:

$$\zeta(z) = \begin{bmatrix} \zeta_1 \\ \zeta_2 \\ \zeta_3 \end{bmatrix}; \zeta'(z) = \frac{d}{dz}\begin{bmatrix} \zeta_1 \\ \zeta_2 \\ \zeta_3 \end{bmatrix}; \bar{T} = \begin{bmatrix} 0 & \kappa(z) & 0 \\ -\kappa(z) & 0 & \kappa'(z) \\ 0 & -\kappa'(z) & 0 \end{bmatrix} \tag{3}$$

where $\kappa(z)$ and $\kappa'(z)$ are the cross coupling coefficients for grating I and II, respectively.

Results and Conclusion:

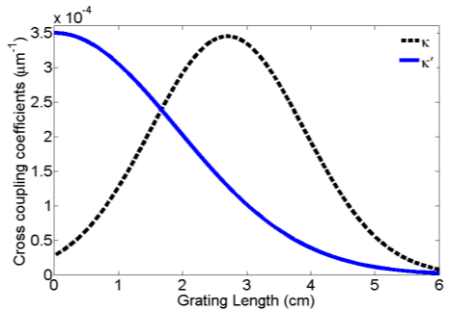


Fig. 2: Variation of cross coupling coefficients with respect to the grating length.

Figure 2 shows the variation of cross coupling coefficients for the two gratings along the grating length. It is clear from the figure that the variation follows a Gaussian profile such that the cross coupling coefficients reach the same peak value but at different positions in the grating. This comes as the direct consequence of the peak refractive index profile variation which is independent for both the gratings. As the fundamental mode is excited, coupling is stronger between the two unexcited modes than the mode which carries all light. The initial coupling between the fundamental core mode and cladding mode is weak. Thus, the scheme is counter-intuitive. Figure 3 shows the variation of fractional power in the three participating modes with respect to the grating length. It can be observed that due to the weak coupling between fundamental core mode and the cladding mode, and strong coupling between the cladding mode and $LP_{0,2}$ core mode, power launched in the $LP_{0,1}$ core mode gets immediately coupled to $LP_{0,2}$ core mode. Thus, despite the fact the power cannot be transferred without the participation of the intermediate $LP_{0,17}$ cladding mode, it gets negligibly excited. Light tunnels to the $LP_{0,2}$ mode and the intermediate cladding mode works as a dark mode. This is similar to the dark state in three level atomic system.

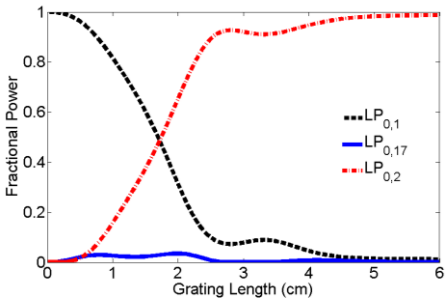


Fig. 3: Variation of power in the three modes with SLPG length.

In conclusion, an adiabatic route to power transfer between two modes via an intermediate mode that participates without getting appreciably excited is shown in optical fibers. It is realized that the dark mode exist in the fiber geometry. The result may be of interest in the optical networking and communication.

References

1. R. M. Enrich, A. Llobera, V. J. Cadarso, J. Mompart and V. Ahufinger, *IEEE Photon. Technol. Lett.* **24**, pp. 536 – 538 (2012).
2. K. Chung, T. J. Karle, M. Rab, A. D. Greentree and S. T. Hanic, *Opt. Exp.* **20**, pp. 23108 – 23116, (2012).
3. X. Sun, H. C. Liu and A. Yariv, *Opt. Lett.* **34**, pp. 280 - 282, (2009).
4. F. Dreisow, M. Ornigotti, A. Szameit, H. Heinrich, R. Keil, S. Nolte, A. Tünnermann and S. Longhi, *Appl. Phys. Lett.* **95**, 261102 (2009).
5. X. Xiong, C. L. Zou, X. F. Ren and G. C. Guo, *Opt. Exp.* **21**, 17097 - 17107, (2013).
6. T. Y. Lin, F. C. Hsiao, Y. W. Jhang, C. Hu and S. Y. Tseng, *Opt. Exp.* **20**, 24085 - 24092, (2012).
7. A. K. Ghatak and K. Thyagarajan, *Introduction to Fiber Optics*, Cambridge University Press, Cambridge, UK, 1989, Appendix F.